# Diseases of the Abdomen and Pelvis 2014-2017

SYLLABUS

IDKD

*Diagnostic Imaging and Interventional Techniques*


**Editors**

J. Hodler
R.A. Kubik-Huch
G.K. von Schulthess
Ch.L. Zollikofer



Springer

**Diseases of the Abdomen and Pelvis 2014-2017**

*Diagnostic Imaging and Interventional Techniques*

J. Hodler • R.A. Kubik-Huch • G.K. von Schulthess •
Ch.L. Zollikofer (Eds)

# DISEASES OF THE ABDOMEN AND PELVIS 2014-2017

## DIAGNOSTIC IMAGING AND INTERVENTIONAL TECHNIQUES

**46th International Diagnostic Course in Davos (IDKD)**
***Davos, March 30-April 4, 2014***

*including the*
Nuclear Medicine Satellite Course "Diamond"
Davos, March 29-30, 2014

Pediatric Radiology Satellite Course "Kangaroo"
Davos, March 29, 2014

Breast Imaging Satellite Course "Pearl"
Davos, March 29, 2014

and additional IDKD Courses 2014-2017

presented by the Foundation for the
Advancement of Education in Medical Radiology, Zurich

Springer

Editors

J. Hodler
Radiology
University Hospital
Zurich, Switzerland

R.A. Kubik-Huch
Radiology
Kantonsspital
Baden, Switzerland

G.K. von Schulthess
Nuclear Medicine
University Hospital
Zurich, Switzerland

Ch.L. Zollikofer
Kilchberg/Zurich, Switzerland

DOI 10.1007/978-88-470-5659-6

ISBN 978-88-470-5658-9 ISBN 978-88-470-5659-6 (eBook)

Springer Milan Dordrecht Heidelberg London New York

Library of Congress Control Number: 2014932003



Cover design: Simona Colombo, Milan, Italy
Typesetting: C & G di Cerri e Galassi, Cremona, Italy

Springer-Verlag Italia S.r.l., Via Decembrio 28, 20137 Milan

Springer is a part of Springer Science+Business Media (www.springer.com)

# Preface

The International Diagnostic Course in Davos (IDKD) is an unique learning experience for imaging specialists. The course is useful for experienced radiologists, imaging specialists in training and clinicians wishing to be updated on the current state of the art and the latest developments in the fields of imaging and image-guided interventions.

This organ based and disease oriented course deals with imaging of the abdomen and pelvis, and includes pediatric imaging. In addition, there will be satellite courses covering pediatric radiology and nuclear medicine of the abdomen and pelvis in more depth, and in addition a breast imaging satellite is on the program.

During the last few years there have been considerable advances in this field driven by clinical as well as technological developments. These will be highlighted in the workshops given by internationally known experts in their field. The presentations encompass all the relevant imaging modalities including ultrasound, CT, MRI, PET, and conventional radiology.

This Syllabus contains condensed versions of the topics presented in the workshops. As a result, this book offers a comprehensive review of the state-of-the art in imaging and intervention of abdominal and pelvic diseases as well as the breast.

The Syllabus is designed first to be an "aide-mémoire" for the course participants so that they can fully concentrate on the lectures and participate in the discussions without the need of taking notes. Second, the syllabus is a convenient and current update for radiologists, radiology residents, nuclear physicians and clinicians working in gastrointestinal and genitourinary subspecialities.

Additional information on IDKD courses offered can be found on the IDKD website: www.idkd.org

J. Hodler
R.A. Kubik-Huch
G.K. von Schulthess
Ch.L. Zollikofer

# Table of Contents

## Workshops

## Nuclear Medicine Satellite Course "Diamond"

## Pediatric Radiology Satellite Course "Kangaroo"



## Breast Imaging Satellite Course "Pearl"

# List of Contributors

# WORKSHOPS

# Emergency Radiology of the Abdomen and Pelvis: Imaging of the Nontraumatic and Traumatic Acute Abdomen

Jay P. Heiken[1], Douglas S. Katz[2]

[1] Mallinckrodt Institute of Radiology, Washington University School of Medicine, St. Louis, MO, USA
[2] Department of Radiology, Winthrop-University Hospital, Mineola, NY, USA

## Introduction

A very large range of disorders, from benign, self-limited conditions to processes requiring emergency surgery, can present with acute abdominal and pelvic pain. The radiologist plays a substantial role in the routine diagnosis and management of patients with these disorders. Similarly, the radiologist plays a major role in the routine evaluation as well as follow-up of selected patients with abdominal and pelvic trauma, whether blunt or penetrating. Computed tomography (CT) remains the mainstay of evaluating such patients, and protocols have evolved along with technological advancements. Ultrasound (US) has a continued important role, particularly for evaluating right upper quadrant pain, suspected gynecologic disorders, and pediatric and pregnant patients with an acute abdomen. Magnetic resonance imaging (MRI) has a growing role in initial evaluation as well as follow-up of selected patients with a variety of acute abdominal and pelvic conditions (usually nontraumatic). Although it is not possible to cover every aspect of imaging of acute nontraumatic and traumatic conditions of the abdomen and pelvis in a single chapter, an overview is presented, with key concepts and teaching points.

## Imaging Techniques

### General Considerations

Acute abdominal and pelvic pain is often nonspecific, and even under the best of circumstances physical examination findings and laboratory investigations may not reveal a diagnosis, which is why the radiologist plays such a major role in evaluating these patients. Because of their substantial limitations compared with cross-sectional imaging examinations, abdominal radiographs have a limited role but are still selectively obtained, primarily to evaluate suspected bowel obstruction and/or perforation. Multiple studies have demonstrated the superiority of CT and its impact on patient management for imaging the acute abdomen, whether in the trauma or nontrauma setting. Conventional radiographs include supine, upright, and lateral decubitus views. Multidetector CT (MDCT) is the primary imaging modality for evaluating adult patients with acute abdominal pain and for patients of all ages following acute abdominal and pelvic trauma.

### Computed Tomography

The use of CT in patients with an acute abdomen requires careful attention to protocol. In suspected or known urolithiasis, if abdominal aortic aneurysm (AAA) rupture is suspected, or if there is a suspected nontraumatic hemorrhage, then generally no contrast is administered. In most other cases of nontraumatic acute abdominal and pelvic pain, intravenous (IV)-administered contrast is generally indicated. Typically, 2-3 ml/s of an appropriate per-weight amount of iodinated contrast is administered through a peripheral IV catheter, and portal venous phase images are acquired from the dome of the diaphragm to the inferior aspect of the symphysis pubis, with routine image reconstruction in the transaxial plane using 3-mm slice thickness and 2-mm intervals. Thinner sections can be generated in selected cases, but coronal reformations should be created routinely by the technologist, sent to the Picture Archiving and Communication System (PACS), and reviewed by the radiologist. Sagittal (or other) reformations may be helpful in selected cases. The data set should be reviewed using routine abdominal windows, bone windows, and lung windows (e.g., to look for extraluminal gas and pneumothorax at the lung bases in trauma patients). Protocols can be modified by the radiologist in conjunction with the referring physician for specific situations. For example, a CT angiography protocol can be used for evaluating suspected bowel ischemia, with thin-section arterial and then routine portal venous phase images.

In the trauma setting, IV-administered contrast should be given to all patients, if possible, but orally administered contrast is not given (although water-soluble contrast given in oral and rectal combination may be indicated in selected patients with penetrating trauma to evaluate for colonic injury). Trauma CT protocols vary depending on

*Diseases of the Abdomen and Pelvis 2014-2017*,
DOI: 10.1007/978-88-470-5659-6_1 

the practice and the specific situation and are often combined with CT imaging of other portions of the body. In general, a single acquisition is obtained in the late arterial/early portal venous phase, which is then immediately checked by the radiologist. If there are substantial abnormalities on these images or if initial plain radiography of the pelvis demonstrates fractures, then a delayed (and ideally relatively low-dose) CT acquisition through the area(s) of interest can be performed to sort out the nature of injuries (i.e., whether a pseudoaneurysm versus an area of active vascular hemorrhage is present; or CT cystography can be performed in suspected bladder injury).

For a variety of reasons, orally administered contrast is used less frequently or not at all in an increasing number of practices in patients undergoing CT for nontraumatic abdominal and pelvic pain. The yield of contrast administered orally has been questioned, it adds time and minor expense, does not always reach the distal bowel, and subtle bowel wall pathology may be obscured. However, other practices prefer to give contrast orally for CT of suspected appendicitis, and/or when the patient has nonspecific abdominal pain. Oral contrast is not indicated for imaging suspected solid-organ abnormalities and suspected urinary tract and gynecologic pathology. In suspected high-grade small-bowel obstruction (SBO) or in the setting of mesenteric ischemia or gastrointestinal bleeding, positive contrast orally administered is contraindicated.

Increased attention has recently been paid to radiation exposure from diagnostic CT examinations. Although CT appropriately remains the workhorse examination for the acute abdomen, radiation dose-reduction strategies should be employed routinely, including reducing milliampere seconds (mAs) and, if available, using iterative reconstruction in conjunction with radiation dose reduction, such as lowering the kilovolt peak (kVp). Multiple CT phases should be acquired only when needed. For patients requiring repeat cross-sectional imaging examinations, alternative strategies, particularly MRI, should be seriously considered whenever feasible.

### Ultrasound

US is the initial imaging examination of choice for patients with suspected acute cholecystitis and acute gynecological abnormalities. It is also the primary method for evaluating pregnant women and pediatric patients with acute abdominal or pelvic pain in most clinical situations. Although somewhat less sensitive and specific than CT for appendicitis, US is a very good first-line imaging examination when employed by experienced radiologists (and technologists). It also can be used to evaluate the bowel wall (in patients with a body habitus permitting such evaluation) and has a role in rapidly triaging trauma patients. A variety of probes and techniques is routinely employed, including Doppler imaging and graded compression for right lower-quadrant evaluation.

### Magnetic Resonance Imaging

MRI has a growing role in imaging pregnant women with abdominal pain who have undergone a nondiagnostic US examination. In a variety of mostly retrospective, small- to medium-sized studies, MRI is shown to have high accuracy in evaluating appendicitis (Fig. 1) and has utility for

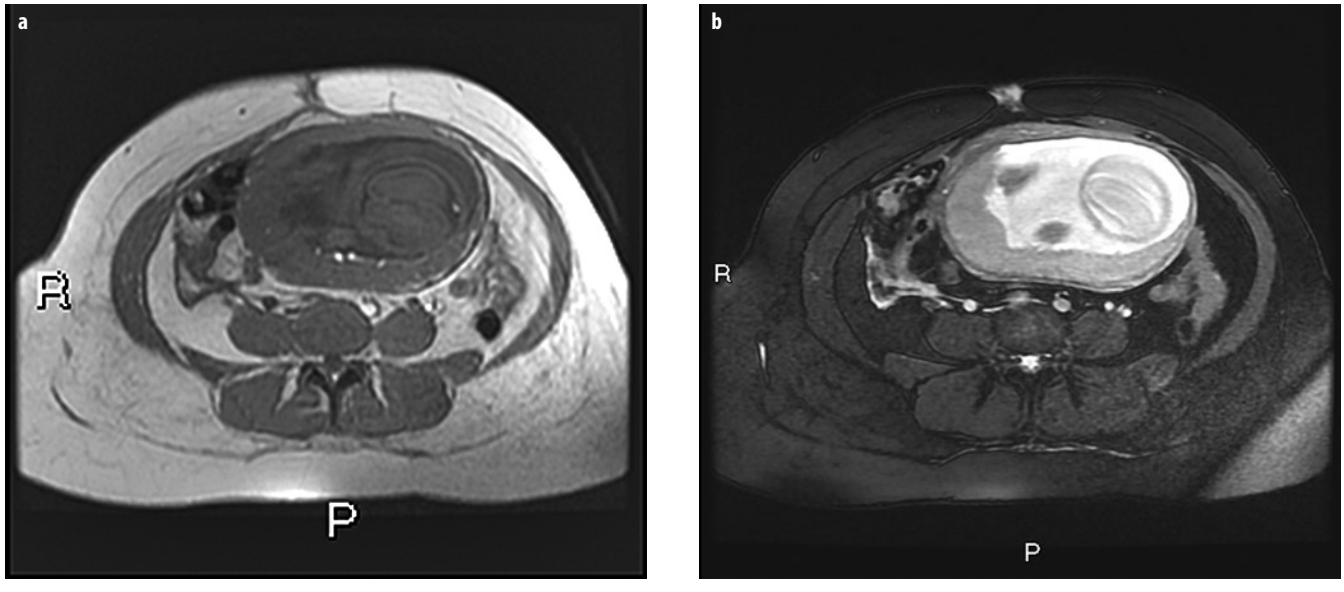


**Fig. 1 a, b.** A 30-year-old patient, 22 weeks pregnant, with right lower quadrant pain, vomiting, and elevated white blood cell count due to appendicitis, as demonstrated on magnetic resonance imaging (MRI). **a** Axial T1-weighted gradient-recalled-echo (GRE) image through the lower abdomen shows an 11-mm appendix extending posteriorly from the cecum, with inflammatory changes surrounding the more distal appendix, including fascial thickening. **b** Axial T2-weighted GRE image at the same level demonstrates the same finding. The appendix was correctly identified as being perforated on the prospective interpretation of this MRI examination, as proven at subsequent emergency surgery

identifying and evaluating alternative conditions, including other bowel pathology (such as Crohn's disease) and urinary and biliary tract pathology. Noncontrast sequences are obtained at 1.5 Tesla (or lower), with an emphasis on fast, multiplanar gradient-echo/T2-weighted sequences.

## Acute Pain in an Abdominal Quadrant

The differential diagnosis in a patient with an acute abdomen is influenced greatly by the nature and location of the pain. Therefore, imaging strategies localized to each of the four abdominal quadrants is discussed first, followed by diffuse or localized pain to the flank or the epigastric region.

### Right Upper Quadrant

Pain from gallstones, and particularly acute cholecystitis, are by far the most common disorders presenting with acute right upper quadrant pain. Other differential diagnostic considerations include hepatitis from a variety of etiologies, liver abscess, and, rarely, a ruptured liver mass (usually hepatocellular adenoma or carcinoma).

US is the imaging examination of choice for evaluating acute right upper quadrant pain. It is an accurate examination for diagnosing or excluding acute cholecystitis. Sonographic findings include gallstones, a sonographic Murphy's sign, wall thickening ⩾3 mm, and pericholecystic fluid/inflammatory changes. The more of these findings that are present, particularly gallstones combined with a sonographic Murphy's sign, the more likely acute cholecystitis is present. Isolated gallbladder wall thickening may be due to a variety of etiologies in addition to acute cholecystitis.

Recent publications show that CT and MRI are relatively accurate imaging examinations for cholecystitis, although the findings may be more subtle compared with sonography, especially early on (Fig. 2a). In our experience, patients with nonspecific abdominal pain and the eventual diagnosis of cholecystitis may be sent for CT on a relatively frequent basis rather than for sonography. Radiologists need to be aware of the potential for establishing or suggesting this diagnosis based on the initial CT findings, which are very similar to those on sonography, although pericholecystic inflammatory changes may be more obvious on CT and MRI. If the CT findings suggest cholecystitis but are not definitive, US can be performed. CT is also an excellent imaging examination for demonstrating complications of cholecystitis, including perforation/abscess formation, hemorrhage, gas (in diabetic patients with emphysematous cholecystitis), and wall gangrene (Fig. 2b). CT findings of a stone lodged in the gallbladder neck or cystic duct and areas of absent wall enhancement correlate with the need for an open rather than a laparoscopic cholecystectomy.

US, CT, and MRI are all accurate imaging examinations for diagnosing (and following-up) liver abscesses (Fig. 3), which are usually pyogenic but which also may be amebic. US usually demonstrates a round or oval hypoechoic mass or masses, which may produce low-level echoes. Occasionally, a hepatic abscess may simulate a solid (or partially solid) hepatic mass on cross-sectional imaging examinations (especially with certain *Klebsiella*

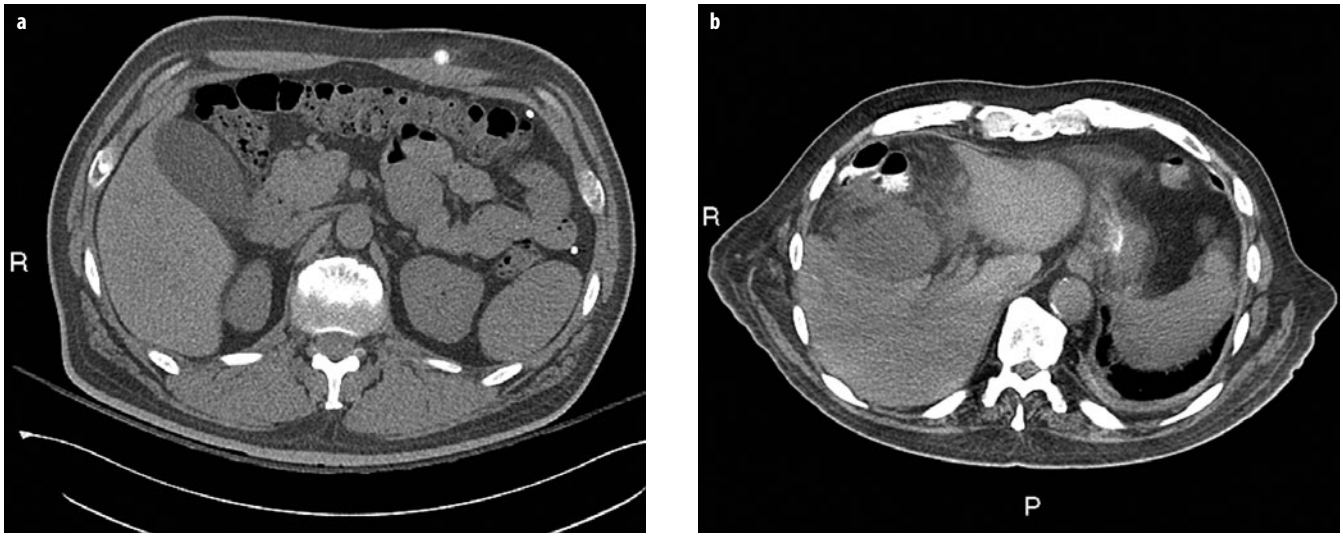


**Fig. 2 a, b.** **a** A 46-year-old man with acute right flank and right mid-abdominal pain, with suspected urolithiasis and previous gastric banding. Noncontrast computed tomography (CT) image shows a mildly distended gallbladder, with subtle wall thickening and inflammation adjacent to the gallbladder neck. CT correctly demonstrated acute cholecystitis, although subsequent ultrasound (US) findings (not shown) were more obvious and confirmatory. **b** A 76-year-old man with renal dysfunction, diabetes, and *Escherichia coli* bacteremia. Axial computed tomographic (CT) image, performed with orally administered contrast only, shows prominent focal inflammatory changes associated with a distended gallbladder, which proved to be due to gangrenous cholecystitis. There is also interposition of the hepatic flexure of the colon anterior to the liver, with associated liver remodeling. Inflammatory changes spread to the adjacent colon

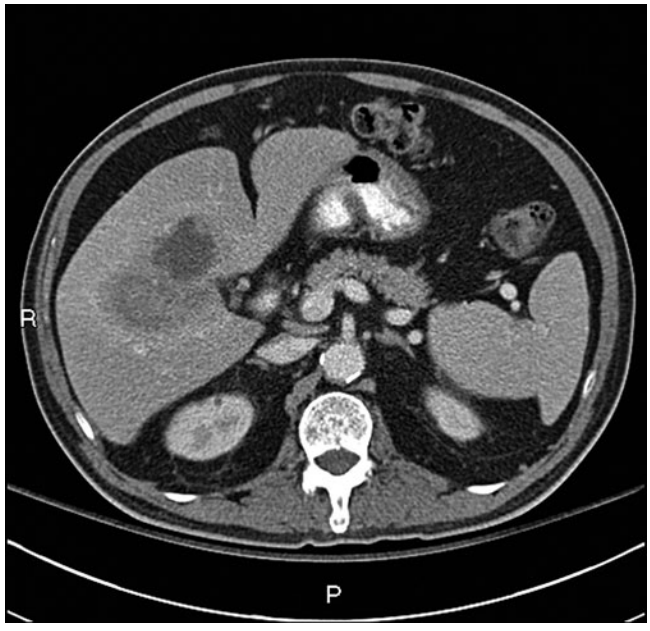


**Fig. 3.** A 73-year-old man with fever. Axial computed tomography (CT) image with contrast administered orally and intravenous (IV) demonstrates an abscess in the central liver. The posterior component is less liquified centrally than the anterior component and is associated with thrombosis of a portion of the right portal venous system

species). Pyogenic liver abscesses may be idiopathic or result from seeding from infection in the biliary tract, from the luminal gastrointestinal tract, or from the portal/mesenteric venous system. An enhancing wall and a peripheral zone of edema are common on CT and MRI but are not universally present.

Spontaneous rupture of a hepatocellular carcinoma with associated hemoperitoneum is a frequent complication in countries with a high incidence of this type of tumor; however, it is highly uncommon in Western countries (<2% of cases). Hepatocellular carcinoma is usually vascular, and tumor necrosis with associated hepatic capsular rupture and rupture of vessels within the tumor is the presumed etiology. The differential diagnosis includes spontaneous hemorrhage within a hepatic adenoma or a hepatic metastasis. Patients present with acute pain and blood loss. Rapid diagnosis and therapy are essential. Transcatheter embolization is the treatment of choice.

### Left Upper Quadrant

Although infrequent, acute left upper quadrant pain is most often caused by splenic infarction or abscess (e.g., secondary to bland or septic emboli to the spleen) (Fig. 4). It may also occur in the setting of acute gastric disorders, including gastritis and ulcer. Generally, CT is performed first, although US may occasionally be the first imaging examination. The diagnosis of gastric pathology is best established by endoscopy, although patients may present with left or right upper abdominal pain and other nonspecific signs and symptoms; CT may reveal the diagnosis when it is not clinically suspected. CT findings include focal or diffuse gastric wall thickening, increased mucosal enhancement, submucosal edema, and perigastric inflammatory changes. Focal ulceration with or without perforation also may be identified, which is generally of benign but occasionally of malignant etiology.

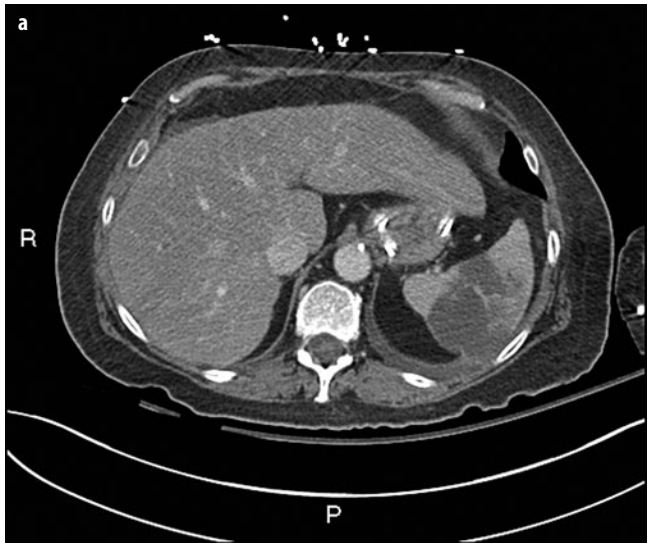


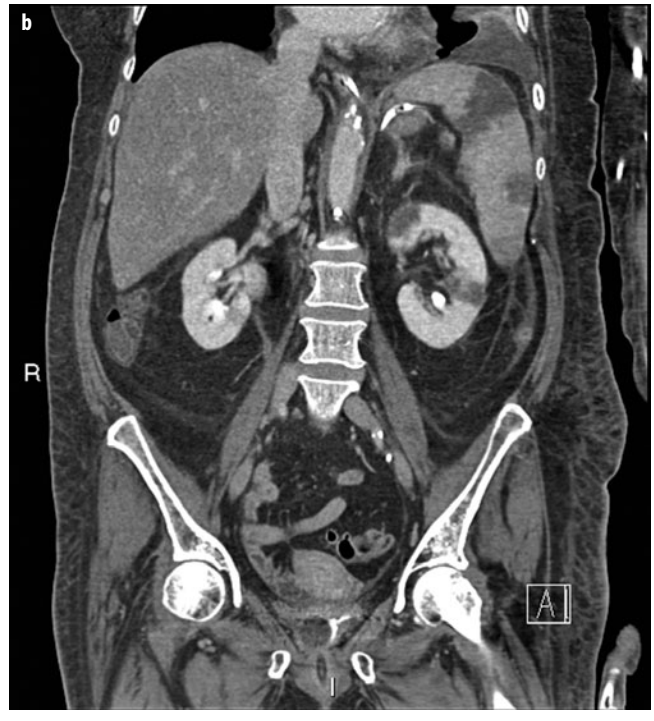


**Fig. 4 a, b.** A 65-year-old woman with fever and bacteremia and known endocarditis. **a** Axial computed tomography (CT) image with IV-administered contrast shows acute infarction in the spleen due to septic emboli. There is a small, reactive left pleural effusion. **b** Coronal CT reformation shows the extent of splenic infarction and bilateral acute renal infarcts due to septic emboli, left larger than right

Splenic infarction may be focal and less commonly global. Other etiologies of splenic infarction include marked splenomegaly with outgrowth of the splenic blood supply, and pancreatitis. Typical infarcts are wedge shaped and hypoattenuating on CT. Most splenic abscesses are secondary to hematogenous dissemination of infection and are seen primarily in immunocompromised individuals and IV drug abusers. On CT, splenic abscesses demonstrate low attenuation centrally with an enhancing rim and occasionally display central gas. Spontaneous splenic rupture can occur in patients with splenomegaly caused by hematologic malignancy or viral infection (e.g., mononucleosis).

### Right Lower Quadrant

Appendicitis is the most frequent cause of acute right lower quadrant pain and the most commonly encountered diagnosis leading to surgery. Other disorders that can present with acute right lower quadrant pain include Crohn's disease, right-sided colitis or diverticulitis, and pelvic inflammatory disease, ovarian cysts (and their complications, including rupture, hemorrhage, and torsion), and other obstetric and gynecologic conditions in women. Less common causes include omental infarction (which can also present with upper or mid right abdominal pain), epiploic appendagitis, and small-bowel diverticulitis (ileal or Meckel's).

Preoperative cross-sectional imaging continues to play an important role in diagnosing or excluding appendicitis and in identifying complications or alternative diagnoses. At most centers, even when the clinical presentation is typical (in up to one-third of patients it is not), CT usually is obtained to confirm the diagnosis and serve as a surgical road map (Fig. 5). The most specific CT finding is a thick-walled, dilated, fluid-filled appendix (occasionally containing gas), which may have one or more liths. Contrast-enhanced CT often demonstrates stratification in which the individual layers of the appendiceal wall can be identified, with mucosal hyperenhancement and submucosal edema. As the disorder progresses, there is increasing inflammation of the adjacent fat. Findings indicative of perforation include periappendiceal abscess, extraluminal gas or lith(s), defects in the appendiceal wall, and associated SBO.

Opacification of the entire appendiceal lumen is a helpful finding to exclude appendicitis if contrast is administered orally; however, as noted, some institutions/practices have eliminated the routine use of orally-administered contrast for CT of the acute abdomen. Regardless of the specific CT protocol used, interpretation depends in part on the experience of the interpreting radiologist. In a minority of cases, particularly in early and subacute/chronic appendicitis, imaging findings can be subtle. It should be noted that an appendix $>6$ mm in transverse diameter can be normal on CT if other findings of appendicitis are absent. In evaluating suspected appendicitis in children (Fig. 6) and in selected nonpregnant women of childbearing age, US is considered the initial examination of choice, if available, although CT has a higher accuracy rate. Demonstration of a swollen, noncompressible appendix $>7$ mm in diameter, with a target configuration and with pain corresponding to the site of the appendix, are the primary US criteria. Appendicolith or liths may be identified.

In pregnant women, appendicitis has a more variable presentation, and diagnosis is more challenging with all cross-sectional imaging modalities. US remains the initial imaging examination despite its poor sensitivity and specificity in this clinical setting. Noncontrast MRI is used increasingly in such patients after nondiagnostic US; it demonstrates high accuracy for the diagnosis and


**Fig. 5 a-c.** Ultrasonography (US) of acute appendicitis in a 12-year-old girl. Oblique (**a**, **b**) and transverse (**c**) views show a swollen appendix (diameter 10 mm), with a target configuration

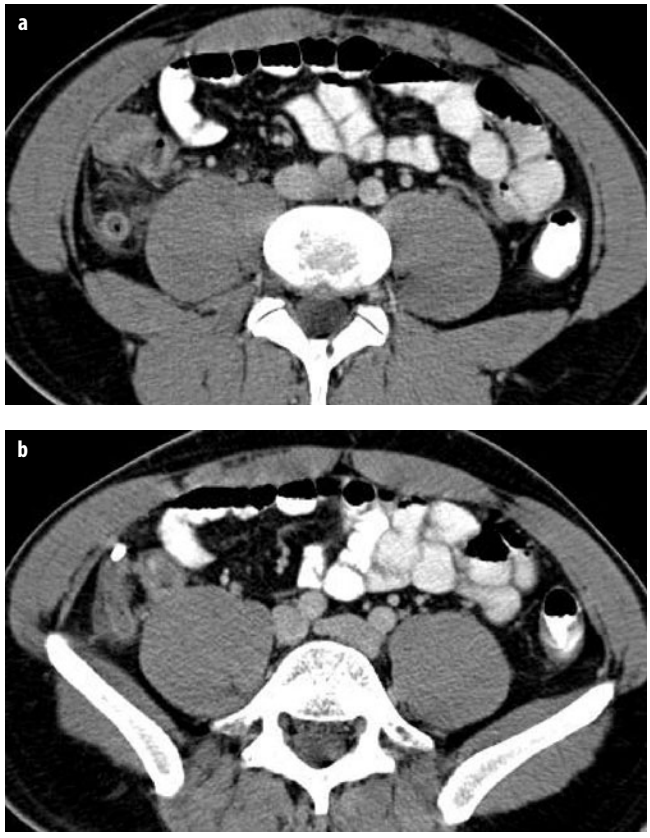



**Fig. 6 a-c.** Acute appendicitis. **a**, **b** Axial computed tomography (CT) images and **c** sagittal CT reformation demonstrate a dilated appendix in a retrocecal position, an appendicolith at the base of the appendix (**c**), and inflammatory changes of the mesenteric fat (**a**)

exclusion of appendicitis, and for the identification of alternative diagnoses. CT should be reserved as a third-line examination and used only if needed.

CT findings of right-sided diverticulitis are similar to those of the more common left-sided diverticulitis, including an inflamed diverticulum, adjacent diverticula, colonic wall thickening, and pericolonic inflammatory changes. Localized inflammation may be substantial. When considering a diagnosis of cecal diverticulitis, it is important to identify a normal appendix. Microperforation may occur, but more substantial complications, which are common in left-sided diverticulitis, such as abscess formation, fistula, and obstruction, are highly unusual in right-sided diverticulitis.

Crohn's disease is often first evaluated with CT; however, because patients with known Crohn's disease usually are young and require serial imaging, follow-up imaging with MR enterography is increasingly important to reduce radiation exposure. Cross-sectional imaging permits evaluating wall thickening and enhancement; changes of adjacent fat, vessels, and lymph nodes; and assessment of complications, including formation of abscesses, strictures, and fistulas.

## Left Lower Quadrant

Diverticulitis of the sigmoid or descending colon is a common disorder in middle-aged and older patients but also can affect young individuals. CT is the examination of choice and is typically performed with IV-administered contrast with or without orally or rectally administered contrast. Other protocols include noncontrast CT. In uncomplicated disease, CT (or MR) findings are the same as with right colonic diverticulitis. Patients with redundancy of the sigmoid colon may present with midline or right lower quadrant pain. CT also demonstrates complications, including microperforation/extraluminal gas (Fig. 7), fistula/abscess formation, and unusual complications, such as venous thrombosis, liver abscess, urinary tract obstruction, and adnexal involvement. Recent data suggest that only selected patients identified with what is believed to be left colonic diverticulitis on CT require follow-up optical colonoscopy to exclude underlying carcinoma (i.e., those with atypical and/or complicated CT findings).

Other diagnostic considerations in patients presenting with left lower quadrant pain include colitis of a variety of

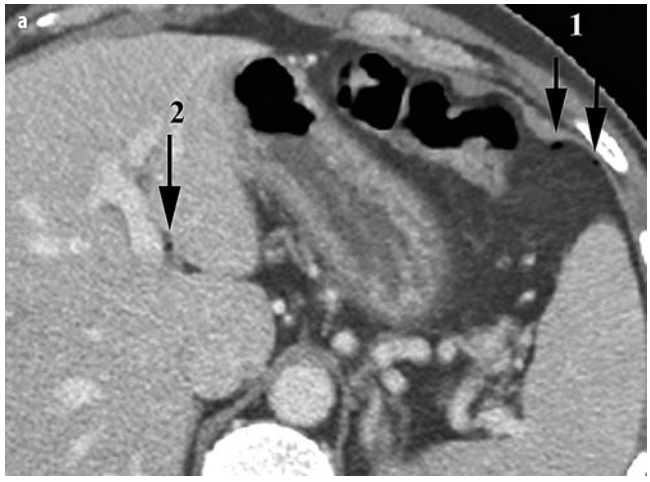


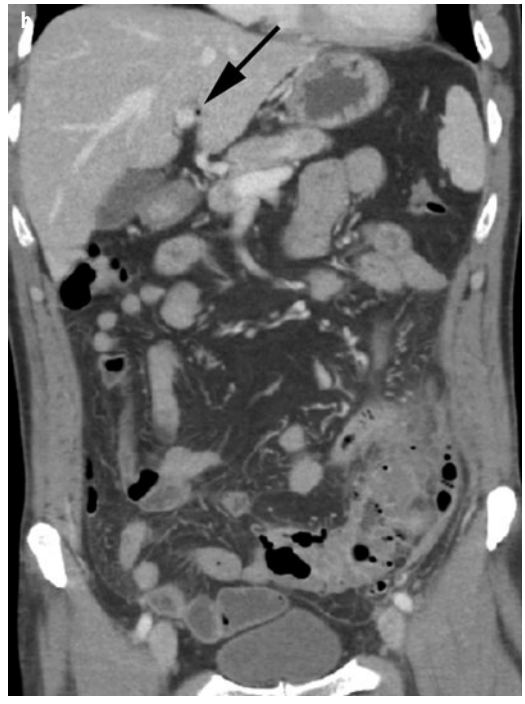


**Fig. 7 a, b.** Perforated sigmoid diverticulitis. **a** Axial computed tomography (CT) image demonstrates tiny bubbles of extraluminal gas within the left subphrenic space (*arrows, 1*) and hepatic pedicle (*arrow, 2*). **b** Coronal CT reformation shows thickened sigmoid colon, with associated diverticular disease, inflammation of the adjacent fat, and thickening of the root of the sigmoid mesocolon. Note the tiny bubble of extraluminal gas (*arrow*) within the hepatic pedicle

etiologies, including infection (especially from *Clostridium difficile* in the correct clinical setting) (Fig. 8) and ischemia; functional colonic disorders (especially constipation, and also obstruction from a variety of other etiologies); urinary tract infection; and gynecologic disease.

Epiploic appendagitis is a relatively common, self-limiting condition in which an appendage of fat along the external aspect of the colon – left side much more common than right – undergoes torsion, with subsequent venous thrombosis. CT findings include a swollen, ovoid, 1.5- to 3.5-cm fat-containing focus with peripheral thickening and associated inflammation. The adjacent colon is usually normal or nearly normal.

## Gynecologic Disorders

US is the primary imaging examination in women with suspected gynecologic pathology. Human chorionic gonadotropin (HCG) level should be checked emergently in all patients with acute, nontraumatic abdominal and pelvic pain to exclude ectopic or incidental pregnancy.



**Fig. 8 a, b.** A 73-year-old woman with abdominal pain. The patient had been on antibiotics orally for 10 days for an upper respiratory tract infection. Noncontrast coronal computed tomography (CT) reformations demonstrate moderate to marked thickening of the entire colonic wall, as well as some associated ascites, which proved to be due to *Clostridium difficile*

MRI is used increasingly as a problem-solving examination after pelvic US and for follow-up. However, because women with acute gynecologic disorders often present with nonspecific signs and symptoms, CT is ordered frequently to evaluate their abdominal pain. Therefore, radiologists interpreting CT of the acute abdomen and pelvis must be familiar with the findings of a wide variety of gynecologic disorders that may present emergently. CT can also be used selectively as a problem-solving tool in patients with known or suspected gynecologic disorders.

### Ovarian Torsion

If ovarian torsion is suspected prospectively, pelvic US is performed emergently. However, CT and MRI findings are also characteristic, are similar to US findings, and may complement US if the sonographic examination is initially equivocal. Radiologists must maintain a high index of suspicion for ovarian torsion, as the clinical presentation is variable; the possibility of torsion should be suspected if imaging findings suggest or strongly indicate this diagnosis. Cross-sectional imaging findings include an enlarged, edematous ovary with or without an associated cyst or mass (most commonly a teratoma), deviation of adnexal structures to the contralateral side, deviation of the uterus to the side of torsion, twisting of the adnexal/vascular structures, decreased ovarian vascularity, multiple peripheral ovarian follicles, inflammation of the adjacent fat, and ascites.

### Ovarian Cysts

Ovarian cysts are very common and may be complicated by hemorrhage. Associated hemoperitoneum, if present, is usually self-limited. The differential diagnosis of a hemorrhagic ovarian cyst is endometrioma. It is particularly critical to check the HCG level in a woman with otherwise unexplained hemoperitoneum to ensure that a ruptured ectopic pregnancy is not present.

### Pelvic Inflammatory Disease

Pelvic inflammatory disease (PID) is also common and has a broad spectrum of findings and presentations. If PID is known or suspected, US is done first. However, CT may initially be performed if the diagnosis is not known and the clinical presentation is nonspecific (Fig. 9). The most common causative organisms are *Gonococcus* and *Chlamydia*. Because PID most commonly results from ascending infection, it usually involves both adnexa. In the earlier stages of PID, there may be no or only subtle findings on cross-sectional imaging. There may be swelling of the ovaries and/or fallopian tubes, abnormal enhancement of the adnexal structures, and mild adjacent edema. In later stages, tubo-ovarian abscesses and/or hydrosalpinx/pyosalpinx may be identified, and adjacent organs may also be involved in complicated cases. Imaging findings include thickening and increased enhancement of the dilated, tortuous fallopian tube(s), a septated mass


**Fig. 9** A 32-year-old woman with lower abdominal pain and previously unknown pelvic inflammatory disease. Axial computed tomography (CT) image with contrast orally and IV reveals dilated, tortuous, bilateral, fluid-filled fallopian tubes containing a small amount of ascites

in the ovary or ovaries, and adjacent edema. Other presentations of PID include endometritis, cervicitis, and Fitz-Hugh-Curtis syndrome in which perihepatitis leads to increased enhancement of the liver edge.

### Other Acute Gynecologic Disorders

Other acute gynecologic disorders that can be identified on cross-sectional imaging examinations include less common forms of PID (e.g., actinomycosis), endometritis, ovarian vein thrombosis (typically following cesarean section), uterine rupture following delivery, gynecologic tumors, and complicated uterine leiomyomas (e.g., hemorrhage/degeneration, torsion, and acute prolapse).

## Acute Abdomen with Diffuse Pain

Any disorder that involves a large portion of the gastrointestinal tract or irritates the peritoneum can cause diffuse abdominal pain. The most common disorder is gastroenteritis, in which CT findings often are normal or may show mild bowel wall thickening and increased intraluminal fluid. Patients with colitis have varying degrees of colonic wall thickening/edema, with inflammation of the adjacent fat. Other important disorders that present with diffuse abdominal pain include bowel obstruction and ischemia.

### Bowel Obstruction

Bowel obstruction is a very frequent cause of abdominal pain in the emergency setting. Small-bowel obstruction

(SBO) is usually due to adhesions – more commonly in patients with previous surgery but occasionally seen in patients without prior surgery and less commonly due to hernias (external or internal), obstructing tumors, perforated appendicitis, inflammatory bowel disease, and complicated diverticulitis. Less common etiologies include gallstone ileus, intussusception, intramural small-bowel hematoma, and radiation enteritis. Large-bowel obstruction (LBO) is most commonly due to colorectal carcinoma, but diverticulitis and sigmoid or cecal volvulus are also important etiologies.

Bowel obstruction is usually diagnosed on clinical grounds and then confirmed and further evaluated as needed by imaging, typically with CT, with or without initial plain radiographs. However, frequently, the diagnosis of bowel obstruction is not clear or clinically recognized, and obstruction is established on the basis of imaging. CT reveals the presence or absence of obstruction, as well as site, level, and cause of obstruction, and permits identification of associated ischemia (Fig. 10). In SBO, the radiologist should search for the transition zone between the dilated proximal small bowel and the collapsed distal small bowel. There is often a segment of small bowel containing feces-like material just proximal to the transition zone. Review of multiplanar CT reformations is important to help identify the site of transition, which may be difficult to find conclusively on review of transaxial images alone. In a minority of cases, CT reveals a closed-loop SBO, which usually requires emergency surgery. In this situation, two points along the course of the small bowel are obstructed at a single site, usually associated with an adhesive band or hernia. Less commonly, closed-loop SBO may be due to volvulus of the small bowel.

SBO needs to be differentiated from LBO and from ileus and motility disorders involving the small and/or large bowel. Ileus of the small and/or large bowel is common after abdominal surgery and has multiple etiologies. In LBO, CT demonstrates distension of the large bowel to the point of obstruction, with collapse of the distal large bowel. The small bowel may demonstrate varying degrees of associated dilation. Colonic volvulus should be readily identified (Fig. 11), particularly on review of multiplanar reformations. A variety of CT signs are reported, and volvulus may be complicated by ischemia and subsequent perforation. Marked dilation of most or all of the colon may be seen in toxic megacolon from a variety of etiologies, as well as in pseudo-obstruction, the latter of which can also lead to subsequent volvulus. A very common cause of abdominal pain in emergency department patients is constipation, which may be of varying degrees of severity, usually without an associated focal obstructing lesion. Other motility disorders, such as scleroderma and administration of anticholinergic or opioid medications, also may lead to the need for CT in patients presenting with acute abdominal pain.

## Bowel Ischemia

Bowel ischemia has a variety of etiologies, including arterial thrombosis or embolism, venous thrombosis, hypoperfusion, and vasculitis. Occlusive disease involves the mesenteric arteries, most commonly the superior mesenteric artery, whereas bowel ischemia


**Fig. 10 a, b.** A 41-year-old woman with acute abdominal pain and gastric bypass surgery. **a** Axial computed tomography (CT) image with IV contrast and **b** coronal reformation show an anterior abdominal wall hernia containing dilated loops of small bowel, with associated mesenteric edema and thickening of the small bowel loops, representing obstruction with associated strangulation. The patient required emergency surgery

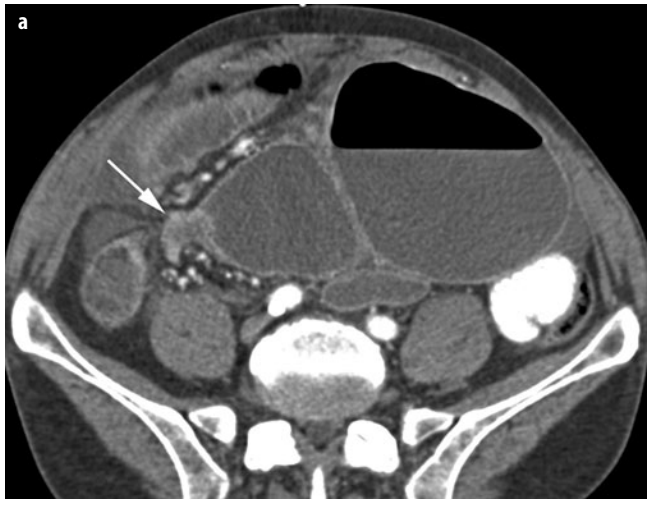


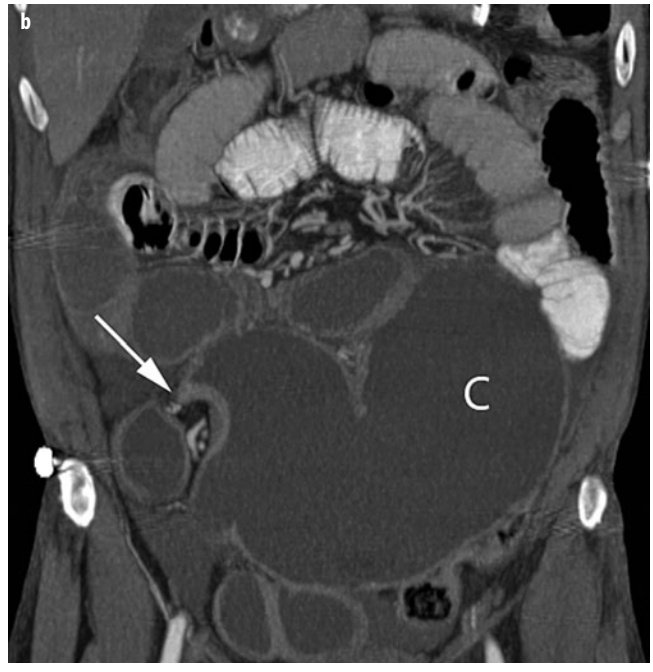


**Fig. 11 a, b.** Cecal volvulus. **a** Transverse computed tomography (CT) image and **b** coronal CT reformation demonstrate a markedly dilated cecum (*C*) located in the midline and left lower abdomen and upper pelvis. The *arrows* point to the area of colonic twisting. Note the dilated small-bowel loops due to the proximal colonic obstruction

secondary to venous thrombosis is much less common. The only direct CT (or MRI) sign of vascular impairment of the bowel is diminished wall enhancement, whereas increased bowel wall enhancement is seen in a wide variety of disorders, including in a subset of patients with bowel ischemia due to reactive hyperemia, loss of autoregulation, or compromised venous outflow. Other cross-sectional imaging findings include direct visualization of embolus or thrombus in the mesenteric arterial circulation or thrombus in the mesenteric venous circulation. Bowel distension and wall edema are nonspecific findings that may be identified in ischemia but also may be present in various infectious, inflammatory, or immunologic conditions and in primary bowel obstruction. Nonocclusive acute mesenteric ischemia is usually due to hypoperfusion secondary to severe cardiac disease; generalized decreased caliber of the arterial circulation is present.

Bowel ischemia may also be secondary to bowel obstruction, particularly a closed-loop SBO, but may also be identified secondary to large-bowel obstruction or volvulus. Focal or regional bowel wall thickening due to edema and hemorrhage may be seen on CT, with decreased bowel wall enhancement and edema adjacent to the affected bowel. With frank infarction, pneumatosis, portal/mesenteric venous gas, peritonitis/ascites, and free gas can be found.

## Bowel Perforation

Gastrointestinal perforation usually causes localized pain initially, which becomes more diffuse if peritonitis develops. Perforation due to peptic ulcer disease or a necrotic neoplasm have become less frequent due to earlier diagnosis and improved therapy (Fig. 12a). However, the incidence of perforation resulting from endoscopic procedures has increased. Perforation of the small bowel is relatively uncommon but may be secondary to a foreign body, diverticulitis, or trauma, among other possibilities. Perforation of the colon is more frequent and can occur when the colon becomes markedly dilated proximal to an obstructing lesion (e.g., tumor, volvulus) or when the colonic wall is friable (e.g., diverticulitis, ischemia, ulcerative colitis, tumor) (Fig. 12b-c).

Pneumoperitoneum can be recognized by gas under the diaphragm on an upright chest radiograph or an upright or lateral decubitus abdominal radiograph. Detection of subtle pneumoperitoneum is often difficult. As CT is much more sensitive than plain radiographs for identifying such perforations and can be used to identify the source of perforation in the vast majority of such cases, it is the examination of choice in suspected bowel perforation. Viewing CT images using lung window settings improves demonstration of small amounts of extraluminal gas.

Gas from retroperitoneal bowel perforation typically has a more mottled appearance and initially may be contained locally. As with intraperitoneal perforation, it is more readily identified and its etiology is more clearly defined on CT. Diagnostic considerations include a perforated duodenal ulcer, complicated diverticulitis, perforated colon cancer, and iatrogenic perforation.

## Acute Abdomen with Flank or Epigastric Pain

Acute flank or upper abdominal pain that radiates to the back is most commonly a manifestation of retroperitoneal pathology, particularly ureteral colic, acute pancreatitis,

and ruptured abdominal aortic aneurysm (AAA). If AAA rupture is suspected, or if retroperitoneal or other site of hemorrhage is suspected, then an emergency noncontrast CT is performed. An additional CT acquisition with IV-administered contrast can be obtained as part of the same examination, if time permits, to evaluate the vascular anatomy in more detail and determine whether there is ongoing active hemorrhage.

### Urinary Colic

The lifetime incidence of an obstructing ureteral calculus is estimated at upward of 12%. The clinical diagnosis is often not initially clear, and CT with IV-administered contrast may therefore be obtained. For evaluating known or suspected urolithiasis, noncontrast CT is the imaging examination of choice. It is extremely accurate for identifying urinary tract calculi, as well as for stone sizing, determining overall stone burden, identifying complications, and demonstrating alternative or additional significant diagnoses in upward of 10-15% of cases.

Virtually all urinary tract stones are radiopaque, regardless of their specific chemical composition. The nonsymptomatic side acts as an intrinsic control, as bilateral ureteral calculi are rare. Secondary signs of obstruction, including hydronephrosis, hydroureter, renal swelling, and perinephric and periureteric edema, are present in 95% of patients with an acute ureteral stone (Fig. 13). Coronal reformations are routinely used and may help the radiologist distinguish between a ureteral calculus and an adjacent phlebolith. Phleboliths, which are calcifications in veins, increase in incidence with age, are usually located lateral and posterior to the ureter, and typically have a tail or "comet" sign, whereas most ureteral calculi are surrounded by a rim of soft tissue. In patients who present with symptoms of renal colic but do not have a ureteral calculus, CT demonstrates a wide variety of alternative diagnoses in a substantial minority of such patients.

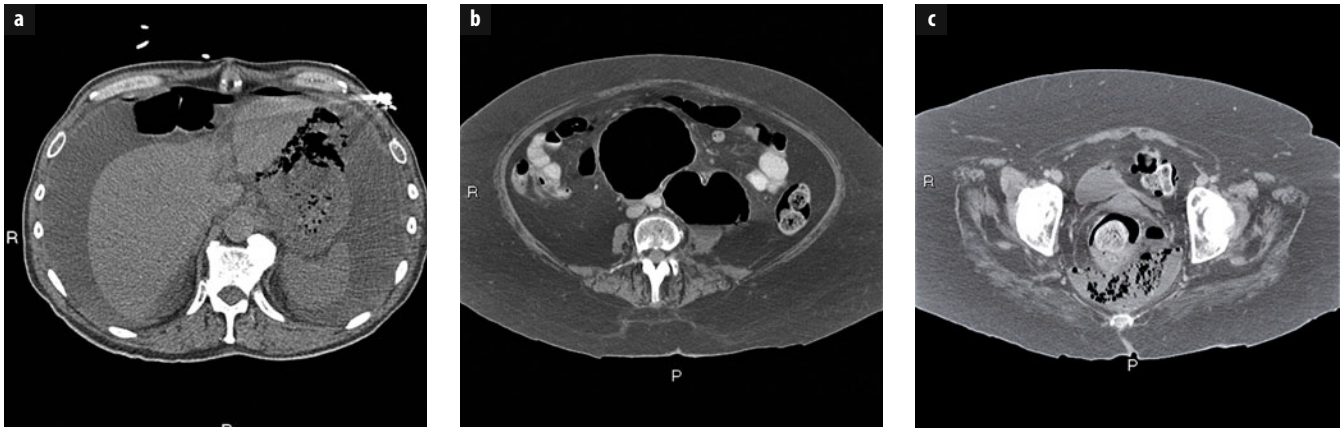


**Fig. 12 a-c.** **a** A 63-year-old man with sepsis. Noncontrast axial computed tomography (CT) image shows a large amount of ascites, free intraperitoneal gas, and a large area of gastric perforation, with gas collecting immediately anterior to the stomach and lateral to the left hepatic lobe. At surgery, there was a gastric ulcer with associated regional gastric necrosis. **b, c** A 47-year-old woman with constipation, now with pelvic pain and an elevated white blood cell count. Axial CT image with contrast orally and IV (**b**) demonstrates two large adjacent abscesses abutting the aorta. Axial CT image through the pelvis (**c**) shows a posterior rectal perforation with a large, developing abscess and a "geode" representing solid stool in the rectum. The findings were due to a perforated stercoral ulcer

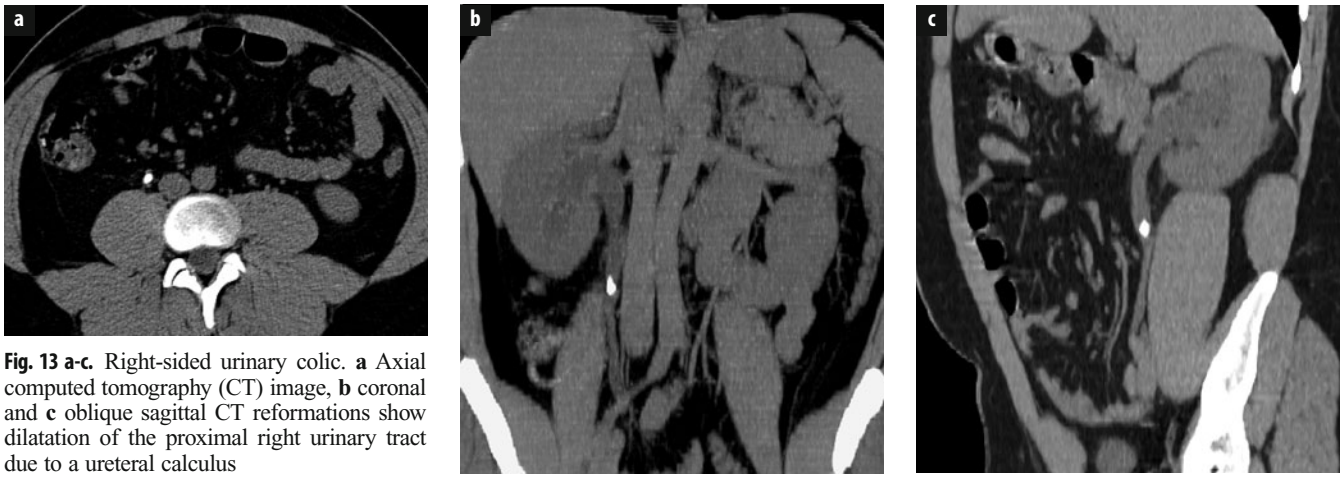


**Fig. 13 a-c.** Right-sided urinary colic. **a** Axial computed tomography (CT) image, **b** coronal and **c** oblique sagittal CT reformations show dilatation of the proximal right urinary tract due to a ureteral calculus

CT is used to determine management of patients with urolithiasis, as almost all ureteral calculi <5 mm, especially if distally located, will pass spontaneously with conservative treatment unless there is concurrent infection, in which case more aggressive management is usually indicated. Renal calculi are frequently found concurrently with ureteral calculi and occasionally may be the source of pain. Repeat CT, for short-term follow-up and for additional episodes of colic, should be used selectively, especially in younger patients, and attention should be paid to reducing radiation dose. In highly selected situations, repeat CT with IV-administered contrast is indicated to evaluate suspected superinfection or clarify an equivocal alternative diagnosis.

### Acute Pancreatitis

Pancreatitis is common and has a broad spectrum of presentations and outcomes. On initial clinical evaluation, pancreatitis is frequently confused with other disorders, and amylase and lipase levels may either be pending or not obtained. Therefore, it is important for the radiologist to identify pancreatitis, usually on CT but occasionally on sonography, when the diagnosis is not suspected clinically. The vast majority of cases are due to gallstones or alcohol abuse. Less common etiologies include trauma, interventional pancreatobiliary procedures, medications, elevated triglycerides, congenital anomalies (i.e., pancreas divisum, annular pancreas, absent dorsal pancreas), and underlying tumor. Less common presentations include chronic pancreatitis, autoimmune pancreatitis, and groove pancreatitis.

A routine CT protocol is used when pancreatitis is not specifically suspected, but a tailored protocol can be used when it is suspected or for follow-up of known pancreatitis. Specifically, no orally administered contrast is given, or else water is used as a neutral contrast agent. Contrast is administered IV, if not contraindicated, to assess for necrosis, characterize fluid collections, and identify vascular complications including venous thrombosis and pseudoaneurysm formation. Imaging is performed in a late arterial (pancreatic) phase. CT findings range from a normal or nearly normal pancreas with mild focal or diffuse peripancreatic inflammation to marked pancreatic edema and associated necrosis (Fig. 14). In the initial few days, CT findings do not necessarily correlate with patient outcome, but later in the disease course, findings have greater prognostic significance.

There are two main types of acute pancreatitis: interstitial and necrotizing. The revised Atlanta Classification System attempts to better characterize the disease process, standardize terminology, including the description of cross-sectional imaging findings, and provide better correlation with prognosis. Other CT scoring systems are also in use to characterize the findings of pancreatitis and provide prognostic information. According to the revised Atlanta Classification System, during the first 4 weeks, there may be acute peripancreatic fluid collections (APFCs) associated with interstitial pancreatitis or acute necrotic collections (ANCs) associated with necrotizing pancreatitis – the latter of which can be pancreatic and/or peripancreatic and either sterile or infected. After 4 weeks, APFCs usually resolve but can become pseudocysts, which again, may be sterile or infected; ANCs may evolve into areas of walled-off necrosis (WON), which again may be sterile or infected; pancreatic and/or peripancreatic, and sterile or infected.

CT-guided aspiration is extremely useful, when indicated, to distinguish sterile from infected necrosis/fluid collections. Additionally, MRI should be seriously considered when follow-up imaging is needed in order to reduce radiation exposure, as these patients often require multiple repeat examinations in the short term and may also have repetitive episodes of pancreatitis.

## Imaging of Abdominal and Pelvic Trauma

### Blunt Abdominal Trauma

MDCT has become the primary imaging examination for evaluating blunt abdominal trauma and has replaced diagnostic peritoneal lavage (DPL) in almost all circumstances. US plays an important role in detecting hemoperitoneum

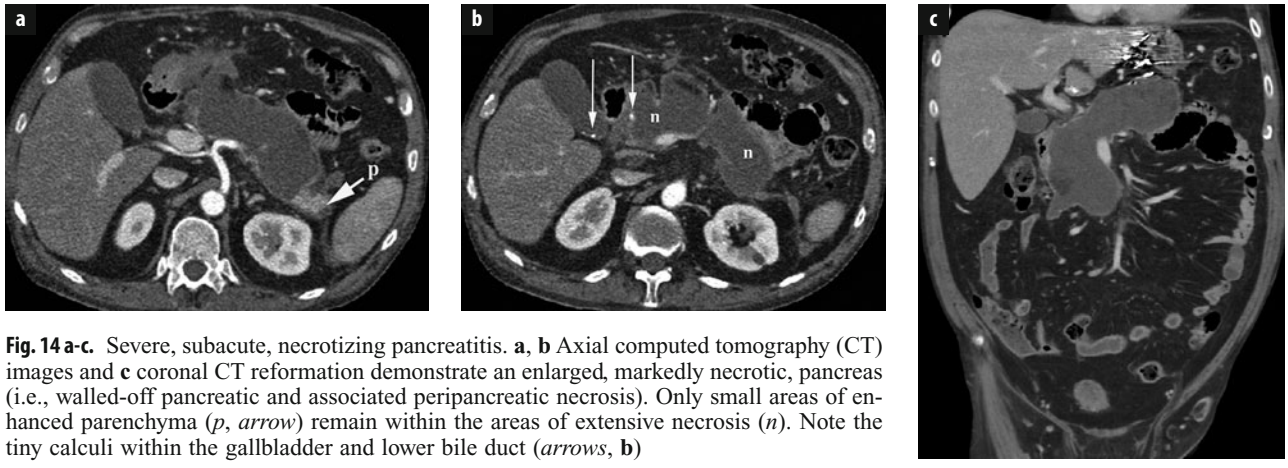


**Fig. 14 a-c.** Severe, subacute, necrotizing pancreatitis. **a**, **b** Axial computed tomography (CT) images and **c** coronal CT reformation demonstrate an enlarged, markedly necrotic, pancreas (i.e., walled-off pancreatic and associated peripancreatic necrosis). Only small areas of enhanced parenchyma (*p*, *arrow*) remain within the areas of extensive necrosis (*n*). Note the tiny calculi within the gallbladder and lower bile duct (*arrows*, **b**)

in hemodynamically unstable patients. Intra-abdominal injuries expected after blunt abdominal trauma depend upon the mechanism of injury, whether or not a restraint device was used, and patient body habitus. Knowledge of the common patterns of injury resulting from different types of motor vehicle collisions (frontal, lateral, and rear impact; sideswipe; rollover) and other traumatic events helps identify specific types of injuries, but a discussion of these factors is beyond the scope of this chapter.

## Imaging Techniques

IV-administered contrast enhancement for MDCT is critical for detecting abdominal and pelvic injuries. As noted above, images are generally obtained in the portal venous phase (~65-80 s after administration of 100-150 ml injected at 3-5 ml/s). Arterial-phase images may be helpful in some severely injured patients to demonstrate vascular injuries of solid organs that may not be apparent on portal-venous-phase images and to characterize areas of active extravasation as being either arterial or venous. When injuries are suspected on portal-venous-phase images, 5- to 10-min delayed images are helpful to detect injuries of the urinary tract and further characterize solid visceral organ injuries that involve the vasculature. Patients with suspected bladder injury should undergo CT cystography. Contrast material is no longer administered orally at almost any trauma center for patients with blunt abdominal trauma.

Focused assessment with sonography for trauma (FAST) is a limited abdominal US examination designed primarily to identify peritoneal fluid. A six-point examination is generally performed using a 3.5-MHz sector transducer. Images of the right subphrenic space (above the liver), left subphrenic space (above the spleen), hepatorenal fossa, perisplenic space (at the inferior margin of the spleen), peritoneal recess of the pelvis, and pericardium are recorded. Although FAST is 86% sensitive for detecting abdominal injuries requiring surgery, liver and spleen injuries are not always associated with hemoperitoneum, and a negative FAST does not exclude intra-abdominal injury. On the other hand, patients with a positive FAST do not always require surgery. Therefore, hemodynamically stable patients with a positive FAST should undergo MDCT for injury staging. In addition, FAST is not reliable for assessing the retroperitoneum.

## Pneumoperitoneum

On MDCT, pneumoperitoneum may consist of free gas beneath the anterior abdominal wall or small bubbles of gas trapped between leaves of the mesentery or within peritoneal recesses. Review of images using lung window settings can be helpful in identifying small amounts of intraperitoneal gas. In the setting of trauma, pneumoperitoneum is highly suggestive of bowel perforation. A localized collection of gas may be identified adjacent to the site of bowel perforation. It is important to keep in mind that pneumoperitoneum is not always present on CT scans of patients with documented bowel perforation. In addition, pneumoperitoneum may occasionally be present in patients without bowel injury but secondary to multiple other potential causes, including barotrauma, intraperitoneal spread of air from a large pneumothorax, or DPL.

## Peritoneal Fluid

In trauma patients, peritoneal fluid most commonly represents blood resulting from injury to the liver, spleen, bowel, or mesentery. In most patients, hemoperitoneum has an attenuation value ranging from 20-45 or greater Hounsfield units (HU) (Fig. 15); however, in up to one quarter of patients, hemoperitoneum has an attenuation


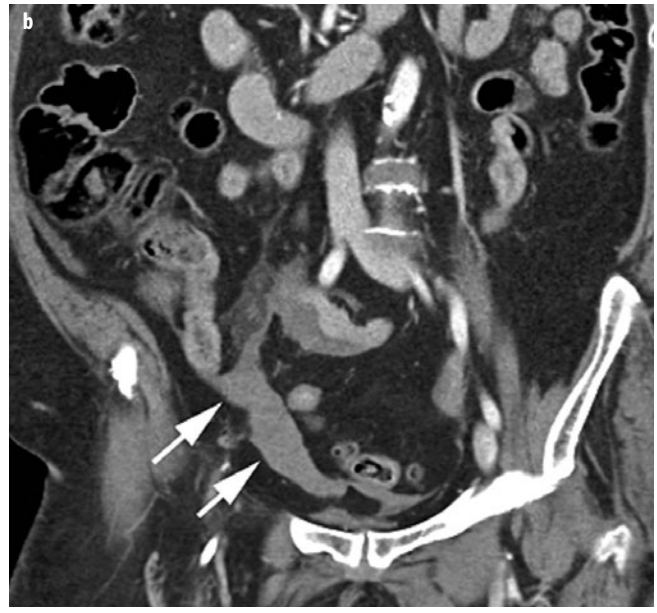


**Fig. 15 a, b.** Hemoperitoneum due to mesenteric injury from motor vehicle collision. **a** Transaxial computed tomography (CT) image demonstrates high-attenuation fluid (*arrow*) adjacent to small-bowel loops. Increased attenuation within the mesenteric fat (*arrowhead*) is due to a mesenteric contusion. **b** Coronal image shows blood layering dependently within the peritoneal cavity (*arrows*, **a** and **b**)

value <20 HU. Blood located adjacent to the source of hemorrhage is often partially clotted and higher in attenuation (the "sentinel clot" sign), which can be helpful in identifying the site of bleeding. Free peritoneal fluid in the absence of direct signs of solid or hollow visceral injury may be problematic, especially in men. However, studies show that small amounts of simple peritoneal fluid are found in up to 5% of male blunt trauma patients in the absence of hollow- or solid-organ injury. Therefore, immediate surgical intervention is not mandated in such patients, but careful review of CT images for subtle injuries, and hospital admission with close clinical follow-up and repeat CT if necessary, are recommended.

## Splenic Injuries

The spleen is the most commonly injured abdominal organ in blunt trauma. In the large majority of cases, splenic injuries can be managed nonsurgically. The need for surgical intervention is based on patient factors, clinical findings, and the CT-based splenic injury scale developed by the American Association for the Surgery of Trauma (AAST) (Table 1). The AAST splenic injury scale takes into account the size and location of splenic lacerations and hematomas. Higher-grade injuries (generally AAST grade III and higher) more often require surgical therapy; however, this grading scale is a relatively poor predictor of the success of nonsurgical management.

**Table 1.** American Association for the Surgery of Trauma (AAST) Splenic Injury Scale

| Injury grade and type | Description |
|---|---|
| I | |
| Hematoma | Subcapsular, <10% surface area |
| Laceration | Capsular tear, <1-cm parenchymal depth |
| II | |
| Hematoma | Subcapsular, 10-50% of surface area or intraparenchymal hematoma <5-cm diameter |
| Laceration | 1-3 cm parenchymal depth; does not involve trabecular vessels |
| III | |
| Hematoma | Subcapsular hematoma, >50% surface area or expanding; ruptured subcapsular or intraparenchymal hematoma; intraparenchymal hematoma >5 cm or expanding |
| Laceration | >3-cm parenchymal depth or involves trabecular vessels |
| IV | |
| Laceration | Laceration, involves segmental or hilar vessels, producing major devascularization (>25% of spleen) |
| V | |
| Laceration | Completely shattered spleen |
| Vascular | Hilar vascular injury that devascularizes spleen |

Note: Increase by one grade (up to grade III) for multiple injuries. Adapted from Moore EE, Cogbill THJ, Jurkovich GJ et al (1995) J Trauma 38:323-324, with permission from Lippincott Williams and Wilkins/Wolter Kluwer Health.

**Table 2.** Multidetector computed-tomography-based splenic injury grading system

| Injury grade | Description |
|---|---|
| I | Subcapsular hematoma <1-cm thick; laceration <1-cm parenchymal depth; parenchymal hematoma <1-cm diameter |
| II | Subcapsular hematoma 1- to 3-cm thick; laceration 1- to 3-cm parenchymal depth; parenchymal hematoma 1- to 3-cm diameter |
| III | Splenic capsular disruption; subcapsular hematoma <3-cm thick; laceration <3-cm parenchymal depth; parenchymal hematoma <3-cm thick |
| IVA | Active intraparenchymal or subcapsular splenic bleeding; splenic vascular injury (pseudoaneurysm or arteriovenous fistula); shattered spleen |
| IVB | Active intraperitoneal bleeding |

Adapted from Marmery H, Shanmuganathan K, Alexander MT, Mirvis SE (2007) AJR Am J Roentgenol 189:1421-1427, with permission from the American Journal of Roentgenology.

More recently, an MDCT-based splenic injury grading system (Table 2) was proposed that takes into account additional CT features of splenic trauma, including the presence of active hemorrhage, pseudoaneurysm, or arteriovenous (AV) fistula. Active hemorrhage appears as a localized area of hyperattenuation within the injured splenic parenchyma, which persists and grows larger on delayed images. In contradistinction, a pseudoaneurysm or AV fistula washes out on delayed-phase images. Some trauma specialists now advocate the acquisition of arterial-phase CT images of the abdomen in addition to the portal venous and delayed phase after blunt trauma, as not all vascular injuries of the spleen are identified on portal-venous and delayed-phase images. Further study is required to validate this hypothesis.

## Hepatic Injuries

Hepatic injuries are only slightly less common than splenic injuries and more frequently involve the right lobe. As with splenic injuries, the majority of blunt liver injuries are successfully managed nonoperatively. The AAST liver injury scale (Table 3) is commonly used to assess the severity of hepatic injuries. Lacerations appear as linear or branching areas of hypoattenuation that frequently travel along vascular planes. Perihilar lacerations may be associated with biliary tract injuries. As with the AAST splenic injury grading scale, the AAST liver injury grading scale has limitations in guiding clinical management. Additional useful CT findings include injury extension to the major hepatic veins (Fig. 16), presence of active bleeding into the peritoneal cavity, and presence of a large-volume hemoperitoneum. Extension to the major hepatic veins usually requires surgery to control hemorrhage, and active bleeding into the peritoneum can often be treated with endovascular interventions.

**Table 3.** American Association for the Surgery of Trauma (AAST) Liver Injury Scale

| Injury grade and type | Description |
|---|---|
| 1 | |
| Hematoma | Subcapsular, <10% surface area |
| Laceration | <1 cm in depth |
| 2 | |
| Hematoma | Subcapsular, 10-50% of surface area; intraparenchymal hematoma <10 cm in diameter |
| Laceration | 1-3 cm in depth or <10 cm in length |
| 3 | |
| Hematoma | Subcapsular, >50% surface area or expanding; ruptured subcapsular or parenchymal hematoma; intraparenchymal hematoma >10 cm or expanding |
| Laceration | >3-cm parenchymal depth |
| 4 | |
| Laceration | Parenchymal disruption involving 25-75% of hepatic lobe or one to three Couinaud segments in a single lobe |
| 5 | |
| Laceration | Parenchymal disruption involving >75% of hepatic lobe, or more than three Couinaud segments in a single lobe |
| Vascular | Juxtahepatic venous injuries (i.e., retrohepatic vena cava and/or central major hepatic veins) |
| 6 | |
| Vascular | Hepatic avulsion |

Adapted from Moore EE, Cogbill THJ, Jurkovich GJ et al. (1995) J Trauma 38:323-324, with permission from Lippincott Williams and Wilkins/Wolter Kluwer Health.

**Fig. 16.** Grade 5 liver laceration. Transaxial computed tomography (CT) image shows a large, ill-defined area of hypoattenuation surrounding the central hepatic blood vessels

## Bowel and Mesenteric Injuries

Injuries to the hollow viscera and mesentery occur in only ~5% of patients with blunt abdominal trauma, and CT findings may be subtle; however, identifying bowel and mesenteric injuries is critical, as delayed diagnosis increases morbidity and mortality rates due to peritonitis and sepsis. Bowel segments affected most commonly are the proximal jejunum and the distal ileum. The most specific signs of bowel injury are focal discontinuity of the bowel wall (transection), extraluminal orally administered contrast (when used), pneumoperitoneum, and retropneumoperitoneum. Less specific but more frequently encountered signs of bowel trauma include focal wall thickening, abnormal bowel wall enhancement, mesenteric stranding, and free intraperitoneal fluid. The association of a focal bowel abnormality with adjacent or free-fluid increases the likelihood that bowel injury is present. The most specific signs of mesenteric injury are active extravasation from a mesenteric vessel (Fig. 17), mesenteric hematoma, and abrupt termination or beading of mesenteric vessels.


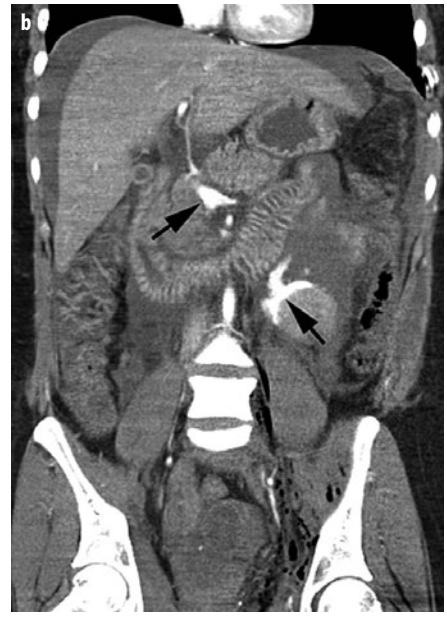


**Fig. 17 a, b.** Severe mesenteric injury in a pedestrian who was hit by a motorcycle. **a** Transaxial and **b** coronal computed tomography (CT) images demonstrate hemoperitoneum and multiple areas of active extravasation (*arrows*) within the small-bowel mesentery

Small, isolated mesenteric hematomas may not require immediate surgery and can be managed with observation. Larger hematomas and mesenteric vascular injuries have a higher risk of subsequent bowel ischemia and usually require surgical repair.

In the setting of trauma, the combination of diffuse thickening and hyperenhancement of the bowel is generally not an indication of direct bowel injury but is a component of the hypoperfusion complex, which is seen in trauma patients who have persistent hypovolemia after initial intravenous fluid resuscitation (Fig. 17). Other CT features of the hypoperfusion complex include inferior vena cava collapse, renal-vein flattening, decreased aorta caliber, delayed nephrograms, increased adrenal gland enhancement, decreased spleen enhancement, and pancreatic enlargement with peripancreatic and retroperitoneal edema. These findings are usually reversible with additional fluid resuscitation.

### Pancreatic Injuries

Pancreatic injuries typically occur after blunt trauma to the upper abdomen. Pancreatic contusions appear as focal areas of hypoattenuation or enlargement, whereas lacerations are linear, low-attenuation defects that may be superficial or extend completely through the pancreas, resulting in transection (Fig. 18). Lacerations that involve >50% of the pancreatic thickness usually cause pancreatic ductal injury. Indirect signs of pancreatic injury include fluid in the peripancreatic fat or transverse mesocolon, and thickening of the left anterior renal fascia. The injured pancreas may appear normal at CT in the first 12 h after trauma. Therefore, a 24- to 48-h repeat CT is warranted in patients who subsequently develop abdominal pain.

MR cholangiopancreatography (MRCP) may be useful to noninvasively document injury to the main pancreatic duct; however, endoscopic retrograde cholangiopancreatography (ERCP) may be necessary for diagnosis. Although some patients with pancreatic ductal injury may be treated successfully with endoscopic pancreatic duct stenting, most require surgical repair.

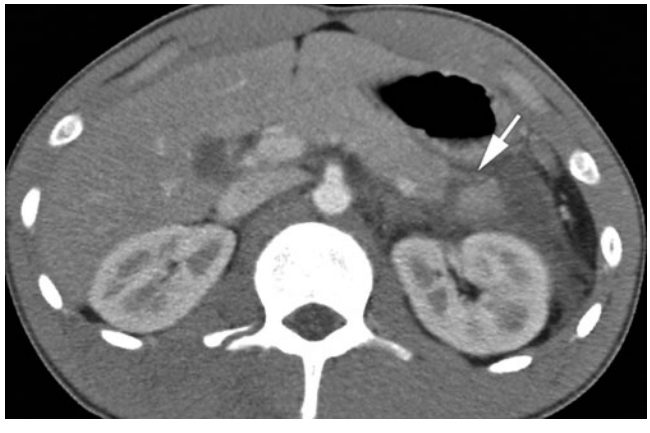

**Fig. 18.** Pancreatic laceration. Transaxial computed tomography (CT) image demonstrates a linear hypoattenuating defect (*arrow*) extending through the tail of the pancreas, which is surrounded by fluid; also note fracture of right lumbar spinal transverse process

### Urinary Tract Injuries

As with the liver and spleen, an AAST grading system classifies renal trauma severity based on the size and location of renal lacerations and hematomas (Table 4). Most renal injuries are treated conservatively, with surgical intervention reserved for collecting-system disruptions and vascular injuries (Fig. 19). Delayed CT images are necessary to assess the integrity of the collecting system. Avulsion of the renal pedicle, characterized on CT as poor or absent renal enhancement, carries a high risk of renal devascularization. Urinary bladder rupture is a complication of pelvic trauma. Patients with gross hematuria or pelvic fractures should undergo CT cystography. Intraperitoneal rupture requires surgical repair, whereas extraperitoneal rupture can be treated conservatively. However, there may be combined intraperitoneal and extraperitoneal bladder rupture in some trauma patients.

### Diaphragmatic Injuries

Diaphragmatic injuries are cause by a sudden increase in intra-abdominal pressure from blunt abdominal trauma.

CT findings include diaphragmatic discontinuity, abdominal viscera herniation into the thorax, constricted

**Table 4.** American Association for the Surgery of Trauma (AAST) Kidney Injury Scale

| Injury grade and type | Description |
|---|---|
| I | |
| Contusion | Microscopic or gross hematuria, with normal urologic studies |
| Hematoma | Subcapsular nonexpanding, without parenchymal laceration |
| II | |
| Hematoma | Nonexpanding perirenal hematoma confined to renal retroperitoneum |
| Laceration | <1-cm parenchymal depth of renal cortex, without urinary extravasation |
| III | |
| Laceration | >1-cm parenchymal depth of renal cortex, without collecting system rupture or urinary extravasation |
| IV | |
| Laceration | Parenchymal laceration extending through renal cortex, medulla, and collecting system |
| Vascular | Main renal artery or vein injury, with contained hemorrhage |
| V | |
| Laceration | Completely shattered kidney |
| Vascular | Avulsion of renal hilum, which devascularizes the kidney |

Adapted from Moore EE, Shackford SR, Pachter HL et al (1989) J Trauma 29:1664-1666, with permission from Lippincott Williams and Wilkins/Wolter Kluwer Health.

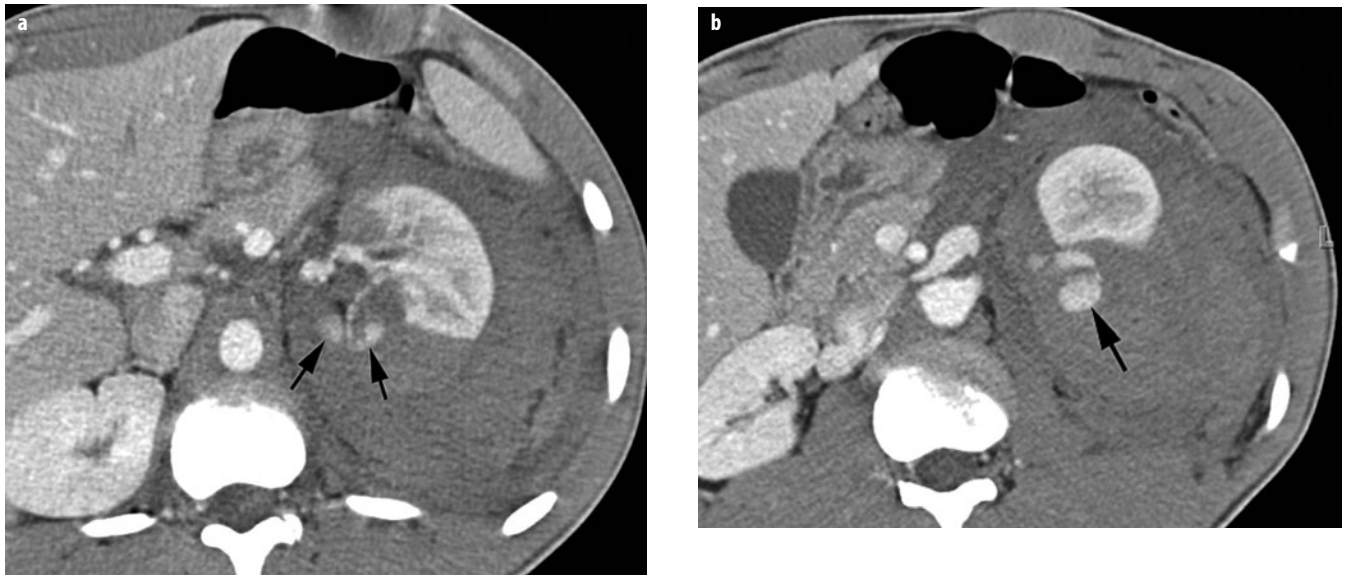


**Fig. 19 a, b.** Deep (grade III) renal laceration with active extravasation. **a, b** Transaxial computed tomography (CT) images show a deep laceration of the left kidney that extends to the renal hilum. *Arrows* (**a**, **b**) indicate active extravasation. A large hematoma surrounds the kidney and displaces it anteriorly

herniated abdominal contents through a diaphragmatic defect, and dependent position of the herniated viscera along the posterior chest wall (dependent viscera sign). Multiplanar CT imaging can be helpful in identifying diaphragmatic injuries.

### Vascular Injuries

Abdominal aortic injuries from high-speed motor vehicle collisions can be life threatening. Obvious findings include large retroperitoneal hematoma and active extravasation. More subtle injuries include pseudoaneurysm, intimal flap, and thrombosis. Thoracic aortic transection usually requires emergency surgical repair, preferably utilizing endovascular techniques, but initially, selected "minimal" aortic injuries can be closely watched without repair. Abdominal aortic injuries are most commonly caused by high-speed motor vehicle collisions in which the aorta is compressed between a lap belt and the lumbar spine. It is important to note that a substantial amount of blood loss in the retroperitoneum may be clinically occult and will not be detected with FAST. Extraperitoneal hemorrhage in the pelvis is often associated with pelvic fractures. CT angiography is useful in this setting to detect active contrast extravasation, which can be treated in most cases with endovascular embolization.

### Penetrating Abdominal Trauma

The need for surgery after a stab wound depends upon the location and depth of penetration. Wounds in any location that penetrate the peritoneum require surgical exploration because of the likelihood of bowel injury. Anterior wounds that penetrate the deep fascia usually require laparoscopy or laparotomy because of the possibility of bowel injury. In contradistinction, posterior stab wounds that penetrate the deep muscular fascia may be confined to the paraspinal muscles and may not be deep enough to penetrate the peritoneum, thus not necessitating surgical exploration. CT with contrast IV, orally, and rectally administered is useful in determining the depth of wound penetration and for the identification of organ injury, retroperitoneal hematoma, and hemoperitoneum.

Gunshot wounds are much more complex injuries that often are difficult to evaluate clinically. If clinical examination or radiographs indicate that the bullet might have crossed the bowel, laparoscopy or exploratory laparotomy is indicated, and CT is not necessary. Similarly, hemodynamically unstable patients require surgical exploration. In the remainder of hemodynamically stable patients, CT is effective in delineating the path of the bullet and for the identification of solid- and hollow-organ injuries. Solid-organ injuries are staged using the AAST criteria. Findings of bowel perforation including pneumoperitoneum and extraluminal leakage of orally or rectally administered contrast material require surgical exploration; however, small perforations of bowel may be very difficult to diagnose with CT. If CT demonstrates peritoneal fluid or the bullet path crosses the bowel in the absence of pneumoperitoneum or contrast leakage, surgical exploration is indicated.

## Conclusion

Imaging in nontraumatic abdominal and pelvic pain and following acute abdominal and pelvic trauma continues to evolve. CT, using a variety of protocols, remains the

mainstay for imaging acute traumatic and nontraumatic conditions, especially in adults, although US is frequently used as the first examination in children and in the nontrauma setting, with subsequent CT utilized in children when necessary. MRI has a growing role in imaging the abdomen and pelvis, especially for follow-up examinations in the nontrauma setting and initial imaging and following US in pregnant and pediatric patients to reduce radiation exposure. Close cooperation with the referring physician immediately prior to imaging remains essential for rapid and accurate diagnosis, as the character and location of the patient's pain and other considerations strongly influence the specific imaging examination(s) performed and the protocol(s) utilized, as well as providing imaging differential diagnosis.

## Suggested Reading


Ahn SH, Mayo-Smith WW, Murphy BL et al (2002) Acute nontraumatic abdominal pain in adult patients: abdominal radiography compared with CT evaluation. Radiology 225:159-164.

Anderson SW, Soto JA, Lucey BC et al (2009) Abdominal 64-MDCT for suspected appendicitis: the use of oral and IV contrast material versus IV contrast material only. AJR Am J Roentgenol 193:1282-1288.

Atri M, Hanson JM, Grinblat L et al (2008) Surgically important bowel and/or mesenteric injury in blunt trauma: accuracy of multidetector CT evaluation. Radiology 249:524-533.

Balthazar EJ, Robinson DL, Megibow AJ, Ranson JH (1990) Acute pancreatitis: value of CT in establishing prognosis. Radiology 174:331-336.

Boscak AR, Shanmuganathan K, Mirvis SE et al (2013) Optimizing trauma multidetector CT protocol for blunt splenic injury: need for arterial and portal venous phase scans. Radiology 268:79-88.

Desir A, Ghaye B (2012) CT of blunt diaphragmatic rupture. RadioGraphics 32:477-498.

Dewhurst C, Beddy P, Pedrosa I (2013) MRI evaluation of acute appendicitis in pregnancy. J Magn Reson Imaging 37:566-575.

Drasin TE, Anderson SW, Asandra A et al (2001) MDCT evaluation of blunt abdominal trauma: clinical significance of free intraperitoneal fluid in males with absence of identifiable injury. AJR Am J Roentgenol 191:1821-1826.

Fuks D, Mouly C, Robert B et al (2012) Acute cholecystitis: preoperative CT can help the surgeon consider conversion from laparoscopic to open cholecystectomy. Radiology 263:128-138.

Gordon RW, Anderson SW, Ozonoff A et al (2013) Blunt pancreatic trauma: evaluation with MDCT technology. Emerg Radiol 20:259-266.

Gore RM, Miller FH, Pereles FS et al (2000) Helical CT in the evaluation of the acute abdomen. AJR Am J Roentgenol 174:901-913.

Hines J, Rosenfeld J, Duncan DR et al (2013) Perforation of the mesenteric small bowel: etiologies and CT findings. Emerg Radiol 20:155-161.

Katz DS, Khalid M, Coronel EE, Mazzie JP (2013) Computed tomography imaging of the acute pelvis in females. Can Assoc Radiol J 64:108-118.

Katz DS, Klein MA, Ganson G, Hines JJ (2012) Imaging of abdominal pain in pregnancy. Radiol Clin North Am 50:149-171.

Katz DS, Scheirey CD, Bordia R et al (2013) Computed tomography of miscellaneous regional and diffuse small bowel disorders. Radiol Clin North Am 51:45-68.

Keyzer C, Cullus P, Tack D et al (2009) MDCT for suspected acute appendicitis in adults: impact of oral and IV contrast media at standard-dose and simulated low-dose techniques. AJR Am J Roentgenol 193:1272-1281.

LeBedis CA, Anderson SW, Soto JA (2012) CT imaging of blunt traumatic bowel and mesenteric injuries. Radiol Clin North Am 50:123-136.

Lee SS, Park SH (2013) Computed tomography evaluation of gastrointestinal bleeding and acute mesenteric ischemia. Radiol Clin North Am 51:29-43.

Levenson RB, Camacho MA, Horn E et al (2012) Eliminating routine oral contrast use for CT in the emergency department: impact on patient throughput and diagnosis. Emerg Radiol 19:513-517.

Lucey BC, Varghese JC, Anderson SW, Soto JA (2006) Spontaneous hemoperitoneum: a bloody mess. Emerg Radiol 14:65-75.

MacKersie AB, Lane MJ, Gerhardt RT et al (2005) Nontraumatic acute abdominal pain: unenhanced helical CT compared with three-view acute abdominal series. Radiology 237:114-122.

Marmery H, Shanmuganathan K, Alexander MT, Mirvis SE (2007) Optimization of selection of nonoperative management of blunt splenic injury: comparison of MDCT grading systems. AJR Am J Roentgenol 189:1421-1427.

Mellnick VM, McDowell C, Lubner M et al (2012) CT features of blunt abdominal aortic injury. Emerg Radiol 19:301-307.

Mirvis SE, Shanmuganagthan K (2007) Imaging hemidiaphragmatic injury. Eur Radiol 17:1411-1421.

Moore EE, Cogbill TH, Jurkovich GJ et al (1995) Organ injury scaling: spleen and liver (1994 revision). J Trauma 38:323-324.

Moore EE, Shackford SR, Pachter HL et al (1989) Organ injury scaling: spleen, liver, and kidney. J Trauma 29:1664-1666.

Orwig D, Federle MP (1989) Localized clotted blood as evidence of visceral trauma on CT: the sentinel clot sign. AJR Am J Roentgenol 153:747-749.

Pooler BD, Lawrence EM, Pickhardt PJ (2012) Alternative diagnoses to suspected appendicitis at CT. Radiology 265:733-742.

Rapp EJ, Naim F, Kadivar K et al (2013) Integrating MR imaging into the clinical workup of pregnant patients suspected of having appendicitis is associated with a lower negative laparotomy rate: a single-institution study. Radiology 267:137-144.

Rosen MP, Ding A, Blake MA et al (2011) ACR Appropriateness Criteria right lower quadrant pain - suspected appendicitis. JACR 8:749-755.

Santillan CS (2013) Computed tomography of small bowel obstruction. Radiol Clin North Am 51:17-27.

Shakespear JS, Shaaban AM, Rezvani M (2010) CT findings of acute cholecystitis and its complications. AJR Am J Roentgenol 194:1523-1529.

Singh AK, Gervais DA, Hahn PF et al (2005) Acute epiploic appendagitis and its mimics. RadioGraphics 25:1521-1534.

Smith RC, Varanelli M (2000) Diagnosis and management of acute ureterolithiasis. AJR Am J Roentgenol 175:3-6.

Soto JA, Anterson SW (2012) Multidetector CT of blunt abdominal trauma. Radiology 265:678-693.

Stojer J, van Randen A, Lameris W, Boermeester MA (2009) Imaging patients with acute abdominal pain. Radiology 253:31-46.

Stuhlfaut JW, Lucey BC, Varghese JC, Soto JA (2006) Blunt abdominal trauma: utility of 5-minute delayed CT with a reduced radiation dose. Radiology 238:473-479.

Thoeni RF (2012) The revised Atlanta classification of acute pancreatitis: its importance for the radiologist and its effect on treatment. Radiology 262:751-764.

Werner A, Diehl SJ, Farag-Soliman M, Duber C (2003) Multi-slice spiral CT in routine diagnosis of suspected acute left-sided colonic diverticulitis: a prospective study of 120 patients. Eur Radiol 13:2596-2603.

Wieseler KM, Bhargava P, Kanal KM et al (2010) Imaging in pregnant patients: examination appropriateness. RadioGraphics 30:1215-1229.

Yu J, Fulcher AS, Wang DB et al (2010) Frequency and importance of small amount of isolated pelvic free fluid detected with multidetector CT in male patients with blunt trauma. Radiology 256:799-805.

# Diseases of the Upper Gastrointestinal Tract

Marc S. Levine

University of Pennsylvania Medical Center, Philadelphia, PA, USA

## Introduction

The esophagus and stomach are susceptible to a wide spectrum of abnormalities, including inflammatory diseases, ulcers, benign and malignant tumors, and other pathologic conditions. Whereas cross-sectional imaging has become increasingly important in modern radiology practice, barium studies (particularly double-contrast barium studies) continue to have a major role in the evaluation of patients with suspected upper gastrointestinal (GI) disease.

## Esophagus

### Gastroesophageal Reflux Disease

Mild reflux esophagitis is most commonly manifested on double-contrast studies by granularity of the distal esophagus due to mucosal edema and inflammation [1]. This granularity extends proximally from the gastroesophageal junction as a continuous area of disease. Other patients may have multiple tiny ulcers in the distal esophagus or a single dominant ulcer at the gastroesophageal junction, most commonly on the posterior wall [1]. In advanced disease, the esophagus can have an irregular contour with serrated margins and decreased distensibility due to extensive ulceration, edema, and spasm. Subsequent scarring can lead to reflux-induced strictures, typically seen as smooth, tapered areas of narrowing in the distal esophagus above a hiatal hernia [1].

### Barrett's Esophagus

Barrett's esophagus arises from chronic reflux esophagitis, with replacement of the usual squamous epithelium by a metaplastic columnar epithelial lining. This condition develops in 10% of patients with reflux esophagitis and 30-40% with peptic strictures [1]. Despite its frequency, Barrett's esophagus would not be important if it were a benign entity. However, Barrett's is a premalignant condition that leads to esophageal adenocarcinoma through a gradual sequence of progressively severe epithelial dysplasia [1]. Affected patients may therefore benefit from endoscopic surveillance to detect and ablate areas of dysplasia before the development of overt carcinoma.

Classic radiologic features of Barrett's esophagus are a distinctive reticular pattern of the mucosa or a high stricture or ulcer in the esophagus [2]. In the presence of a hernia and reflux, these findings should be highly suggestive of Barrett's esofagus. However, a reticular pattern or a high stricture or ulcer is present in only 5-10% of patients with Barrett's esofagus. Nevertheless, the vast majority of patients with this condition are found to have reflux esophagitis or peptic strictures on double-contrast studies [1]. Endoscopy can therefore be reserved for patients with reflux esophagitis, peptic strictures, or other classic findings of Barrett's esofagus on double-contrast esophagography.

### Infectious Esophagitis

*Candida albicans* is by far the most common cause of opportunistic esophageal infection. *Candida* esophagitis is manifested on double-contrast studies by multiple, discrete, plaque-like lesions separated by normal intervening mucosa (Fig. 1) [3]. Patients with AIDS may develop a more fulminant form of candidiasis, which is characterized by a grossly irregular or "shaggy" esophagus due to innumerable plaques and pseudomembranes [3]. Only 50% of patients with *Candida* esophagitis have oropharyngeal candidiasis (i.e., thrush), so the absence of oropharyngeal disease in no way excludes this diagnosis [3]. In contrast, herpes esophagitis is typically manifested by small, shallow ulcers without plaques [4], whereas cytomegalovirus (CMV) and HIV esophagitis are characterized by one or more giant, flat ulcers [5]. CMV ulcers are treated with potent antiviral agents, whereas HIV ulcers are treated with steroids; therefore, endoscopy is required to differentiate CMV from HIV esophagitis before instituting therapy.

*Diseases of the Abdomen and Pelvis 2014-2017*,
DOI: 10.1007/978-88-470-5659-6_2 

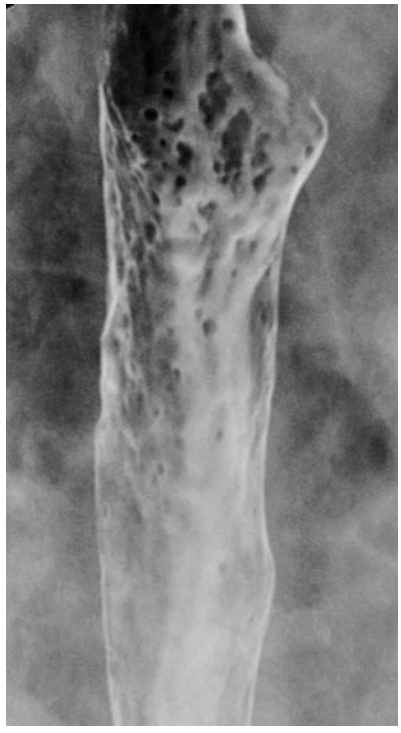

**Fig. 1.** *Candida* esophagitis: there are multiple, plaque-like lesions of varying size in the mid esophagus. Note how the lesions have discrete margins and are separated by normal, intervening mucosa. These findings are characteristic of candidiasis

**Fig. 2.** Small-caliber esophagus in eosinophilic esophagitis. There is diffuse loss of distensibility of the entire thoracic esophagus, which has a smooth, uniform contour. This young man with long-standing dysphagia and asthma had proven eosinophilic esophagitis

### Drug-Induced Esophagitis

Drug-induced esophagitis is caused by various oral medications, including tetracycline, doxycyline, potassium chloride, quinidine, alendronate, and nonsteroidal anti-inflammatory drugs (NSAIDs) [6]. These patients often have a history of ingesting the pills with little or no water immediately before retiring. As a result, the pills tend to lodge in the mid esophagus, where it is compressed by the aortic arch or left main bronchus. This can result in a focal contact esophagitis, manifested by a focal cluster of small, discrete ulcers in the mid esophagus [6]. Affected individuals may present with severe odynophagia, but there is usually rapid clinical improvement after withdrawal of the offending agent.

### Eosinophilic Esophagitis

Eosinophilic esophagitis usually occurs in young men with long-standing dysphagia and occasional food impactions. Affected patients may have an atopic history, asthma, or peripheral eosinophilia. Barium esophagography may reveal a ringed esophagus, with distinctive ring-like indentations, or a small-caliber esophagus, with diffuse loss of distensibility of the thoracic esophagus in the absence of a discrete stricture (Fig. 2) [7, 8]. The diagnosis can by confirmed by endoscopic biopsies showing >20 eosinophils per high-powered field. These patients often have a dramatic response to treatment with oral steroids or inhaled steroid preparations.

### Esophageal Carcinoma

Early esophageal cancer (EEC) is typically manifested on double-contrast studies by small, polypoid or plaque-like lesions [9]. Other patients may have superficial, spreading carcinomas with a focal cluster of poorly defined nodules and plaques that merge one with another, producing a coalescent area of disease [9]. EEC is rarely diagnosed in Western countries, because most patients develop symptoms only after the tumor has invaded the mediastinum [9]. In contrast, advanced cancers typically appear as polypoid, ulcerated, or infiltrating lesions with irregular luminal narrowing and shelf-like margins [9]. Rarely, esophageal cancers may be varicoid lesions that simulate varices due to submucosal spread of tumor.

Whereas squamous cell carcinomas tend to be located in the upper or mid esophagus, adenocarcinomas are mainly located in the distal esophagus and have a marked tendency to invade the gastric cardia and fundus. At one time, esophageal adenocarcinomas were thought to be rare lesions, because these tumors, when invading the proximal stomach, were erroneously classified as primary gastric carcinomas invading the distal esophagus. However, adenocarcinomas are now thought to constitute as many as 50% of all esophageal cancers [9], so

this is a more common malignant tumor than previously recognized.

## Stomach

### Erosive Gastritis

Erosive gastritis is usually characterized on double-contrast studies by varioliform erosions seen as punctate or slit-like collections of barium surrounded by radiolucent halos of edematous mucosa. Varioliform erosions tend to be located in the gastric antrum and are often aligned on the crests of the folds. NSAIDs are by far the most common cause of erosive gastritis, accounting for >50% of cases. Occasionally, NSAID-induced erosive gastritis may also be manifested by distinctive linear or serpiginous erosions that tend to be clustered in the gastric antrum or body or near the greater curvature [10]. These erosions are thought to result from localized mucosal injury as the dissolving NSAID tablets collect by gravity in the dependent portion of the stomach. Detection of this finding should therefore lead to careful patient questioning regarding a recent history of NSAID use, and if confirmed, the offending medication should be withdrawn.

### *Helicobacter Pylori* Gastritis

*Helicobacter pylori* gastritis can be diagnosed on barium studies by the presence of thickened folds in the antrum, body, or, less commonly, fundus of the stomach [11] (Fig. 3). Other patients with *H. pylori* may show a polypoid form of gastritis characterized by grossly thickened, lobulated folds, mimicking the appearance of Menetrier's disease, lymphoma, or even a submucosally infiltrating adenocarcinoma [11]. Endoscopy and biopsy are therefore required for a definitive diagnosis.

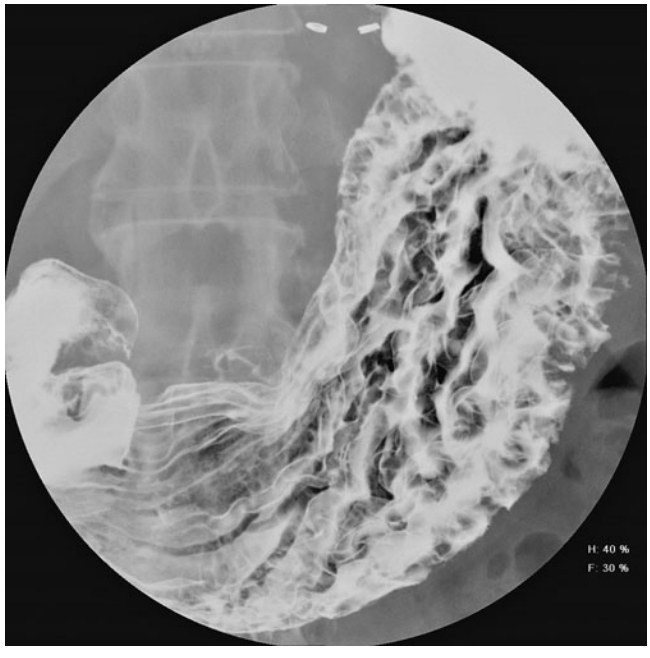


**Fig. 3.** *Helicobacter pylori gastritis*. There are considerably thickened folds in the body of the stomach due to chronic *H. pylori* gastritis. More than 90% of all patients with thickened folds in the stomach are found to have this infection.

### Gastric Ulcers

Benign gastric ulcers classically appear en face as round or ovoid barium collections, with a smooth, surrounding mound of edema and/or thin, straight folds radiating to the edge of the ulcer crater [12]. When viewed in profile, benign ulcers project beyond the gastric wall and are often associated with an ulcer mound or collar. In contrast, malignant ulcers appear en face as irregular craters within a discrete mass associated with nodularity or clubbing of adjoining folds [12]. When viewed in profile, malignant ulcers project inside the lumen within a mass that forms acute angles with the gastric wall rather than the obtuse, gently sloping angles expected for a benign mound of edema [12].

Most benign ulcers are located on the lesser curve or posterior wall of the gastric antrum or body [12]. Occasionally, however, ulcers may occur on the greater curve of the distal antrum, and the vast majority is caused by NSAIDs [12]. As NSAID-induced greater-curve ulcers enlarge, they can penetrate inferiorly into the transverse colon, producing a gastrocolic fistula [13].

Ulcer healing may be manifested not only by decrease in the size of the ulcer crater, but also by a change in shape. Ulcer healing often produces a visible scar characterized by a central pit or depression, radiating folds, and/or retraction of the adjacent gastric wall [12]. The morphology of an ulcer scar is directly related to the location of the underlying ulcer: ulcer healing on the lesser curve often leads to flattening and retraction of the adjacent gastric wall, whereas ulcer healing on the posterior wall or greater curve may lead to the development of radiating folds.

### Gastric Carcinoma

Advanced gastric cancers appear on barium studies as polypoid, ulcerated, or infiltrating lesions. Some patients have primary scirrhous carcinomas that produce a *linitis plastica*, with luminal narrowing, irregularly thickened folds, and mucosal nodularity [14]. Scirrhous carcinomas classically involve the antrum of the stomach, but 40% are confined to the body or fundus [14]. It is important to be aware of the limitations of endoscopy for diagnosing these tumors, as brushings and biopsies confirm the presence of tumor in <50% of cases [14]. Some patients therefore require repeat endoscopy or even surgery without a preoperative histologic diagnosis.

Early gastric cancer (EGC) may be manifested by small, polypoid or ulcerated lesions. Most patients in Western countries with EGC do not develop symptoms until they have advanced lesions. As a result, EGC is

unlikely to be detected as long as diagnostic tests for gastric cancer (i.e., endoscopy and barium studies) are performed only on symptomatic patients.

### Gastric Lymphoma

Although the stomach normally contains no lymphatic tissue, it is the single most common site of lymphoma in the GI tract. This apparent paradox is explained by the fact that patients with chronic *H. pylori* gastritis may develop mucosa-associated lymphoid tissue (MALT) in the stomach. This lymphoid tissue is thought to be the precursor of low-grade, B-cell, gastric MALT lymphomas that, if untreated, may undergo transformation to more high-grade lymphomas. Unlike patients with EGC, who are rarely symptomatic (see last section), patients with gastric MALT lymphoma may present with epigastric pain, dyspepsia, or other symptoms because of their underlying *H. pylori* gastritis. As a result, gastric MALT lymphomas sometimes appear on double-contrast studies as small, polypoid or ulcerated lesions indistinguishable from EGC [15]. More commonly, however, these MALT lymphomas are manifested by variably sized, round, confluent nodules (Fig. 4) [15]. When MALT lymphoma is suspected on barium studies, endoscopic biopsies should be obtained for a definitive diagnosis, as these lesions can undergo complete regression in 70-80% of patients on *H. pylori* eradication therapy (i.e., proton pump inhibitors and antibiotics) without need for surgery, radiation, or chemotherapy [15]. In contrast, advanced gastric lymphomas may be manifested by thickened folds, multiple submucosal masses, centrally ulcerated bull's-eye lesions, or giant, cavitated lesions.

**Fig. 4**. Gastric mucosa-associated lymphoid tissue (MALT) lymphoma. There is a cluster of poorly defined, rounded nodules (*arrows*) in the body of the stomach near the lesser curvature due to a proven MALT lymphoma arising in the setting of chronic *Helicobacter pylori* gastritis. When this diagnosis is suggested on barium studies, endoscopy and biopsy are required for a definitive diagnosis

## References


1. Levine MS (2008) Gastroesophageal reflux disease. In: Gore RM, Levine MS (Eds) Textbook of gastrointestinal radiology. Elsevier, Philadelphia, PA, pp 337-357.
2. Levine MS, Kressel HY, Caroline DF et al (1982) Barrett esophagus: reticular pattern of the mucosa. Radiology 147:663-667.
3. Levine MS (2008) Infectious esophagitis. In: Gore RM, Levine MS (Eds) Textbook of gastrointestinal radiology. Elsevier, Philadelphia, PA, pp 359-373.
4. Levine MS, Loevner LA, Saul SH et al (1988) Herpes esophagitis: sensitivity of double-contrast esophagography. AJR Am J Roentgenol 151:57-62.
5. Sor S, Levine MS, Kowalski TE et al (1995) Giant ulcers of the esophagus in patients with human immunodeficiency virus: clinical, radiographic, and pathologic findings. Radiology 194:447-451.
6. Levine MS (2008) Other esophagitides. In: Gore RM, Levine MS (Eds) Textbook of gastrointestinal radiology. Elsevier, Philadelphia, PA, pp 375-399.
7. Zimmerman SL, Levine MS, Rubesin SE et al (2005) Idiopathic eosinophilic esophagitis in adults: the ringed esophagus. Radiology 236:159-165.
8. White SB, Levine MS, Rubesin SE et al (2010) The small-caliber esophagus: radiographic sign of eosinophilic esophagitis. Radiology 256:127-134.
9. Levine MS, Halvorsen RA (2008) Carcinoma of the esophagus. In: Gore RM, Levine MS (Eds) Textbook of gastrointestinal radiology. Elsevier, Philadelphia, PA. pp 417-446.
10. Levine MS, Verstandig A, Laufer I (1986) Serpiginous gastric erosions caused by aspirin and other nonsteroidal anti-inflammatory drugs. AJR Am J Roentgenol 146:31-34.
11. Sohn J, Levine MS, Furth EE et al (1995) Helicobacter pylori gastritis: radiographic findings. Radiology 195:763-767.
12. Levine MS (2008) Peptic ulcers. In: Gore RM, Levine MS (Eds) Textbook of gastrointestinal radiology. Elsevier, Philadelphia, PA, pp 529-561.
13. Levine MS, Kelly MR, Laufer I et al (1993) Gastrocolic fistulas: the increasing role of aspirin. Radiology 187:359-361.
14. Levine MS, Kong V, Rubesin SE et al (1990) Scirrhous carcinoma of the stomach: radiologic and endoscopic diagnosis. Radiology 175-151-154.
15. Yoo CC, Levine MS, Furth EE et al (1998) Gastric mucosa-associated lymphoid tissue lymphoma: radiographic findings in six patients. Radiology 208:239-243.

# CT Enterography: Small Bowel Imaging That Impacts Patient Management

Joel G. Fletcher

Department of Radiology, Mayo Clinic, Rochester, MN, USA

## Overview

Computed tomography (CT) enterography and CT enteroclysis are widely performed small bowel examinations that are now widely available at many medical institutions. Their routine use and availability has impacted the understanding and management of patients with Crohn's disease and obscure gastrointestinal (GI) bleeding. The purpose of this chapter is to review patient preparation and CT acquisition for CT enterography, highlight salient features of imaging interpretation, emphasize the clinical benefit of cross-sectional CT imaging to the care of patients with Crohn's disease and obscure GI bleeding, and emphasize the complimentary role CT plays with other imaging modalities, such as magnetic resonance (MR) enterography and capsule endoscopy, in the care of these patients.

## CT Enterography

CT enterography is an abdominopelvic CT performed after patient ingestion of large volumes of enteric contrast. It provides exquisite images of the small bowel wall, lumen, and mesentery to assess for inflammation, masses, and perienteric findings. CT enterography is adapted to indication but is generally performed with neutral enteric agents that distend the bowel lumen and have low CT attenuation in order to facilitate identification of hyperenhancing inflammation or masses [1]. Intravenous (IV) contrast is administered in conjunction with oral neutral enteric contrast, with imaging for single-phase examinations generally performed during the enteric phase (i.e., approximately 50 s after initiation of IV contrast material injection) [2]. Tube current and tube potential should be adapted to patient size, with appropriate kV selection and automatic exposure control, so that radiation scanner output for CT enterography to evaluate for potential Crohn's disease is substantially less than that for routine abdominopelvic CT [3-5]. Automatic exposure control settings and tube current are increased to routine levels when performing imaging to evaluate for small bowel tumors or pancreatic disease. Unlike Crohn's disease detection, evaluation of obscure GI bleeding requires multiphase CT enterography to detect and characterize transiently enhancing vascular lesions and small bowel tumors. Multiphase CT enterography is generally performed with an arterial phase followed by enteric and delayed imaging [6, 7]. With all CT enterography methods, multiplanar images are reconstructed in three orthogonal planes to view the small bowel and its mesentery (including the origin of the mesenteric arteries), with noise reduction methods and interactive viewing on a computer workstation further improving disease conspicuity.

Radiologists should be familiar with the normal appearance of the small bowel on CT enterography. The valvulae conniventes within the jejunum have a feathery fold pattern, with fewer folds in the ileum. Using the peroral technique, the jejunal lumen will be collapsed about one third of the time [8]. Partial collapse of jejunal loops can sometimes be erroneously mistaken for a small bowel mass due to the prominent jejunal folds in the proximal bowel (Fig. 1). True masses will have abrupt borders, whereas collapsed jejunal loops are symmetric with respect to bowel lumen and will lack abrupt margins. Jejunal pathology frequently causes some degree of obstruction to highlight its presence; however, if the clinical indication for small bowel imaging is to evaluate jejunum, MR enterography, capsule endoscopy, or CT enteroclysis are better diagnostic alternatives. In the enteric phase of enhancement, the jejunum will enhance to a greater degree than the ileum [9]. Finally, the terminal ileum will often demonstrate intramural fat, which is a normal finding in the absence of hyperenhancement or wall thickening [10].

### Imaging of Inflammation

CT enterography is widely available as a cross-sectional imaging technique for adult patients with known or suspected Crohn's disease and is recommended by the American College of Radiology (ACR) as one of the most

*Diseases of the Abdomen and Pelvis 2014-2017*,
DOI: 10.1007/978-88-470-5659-6_3 

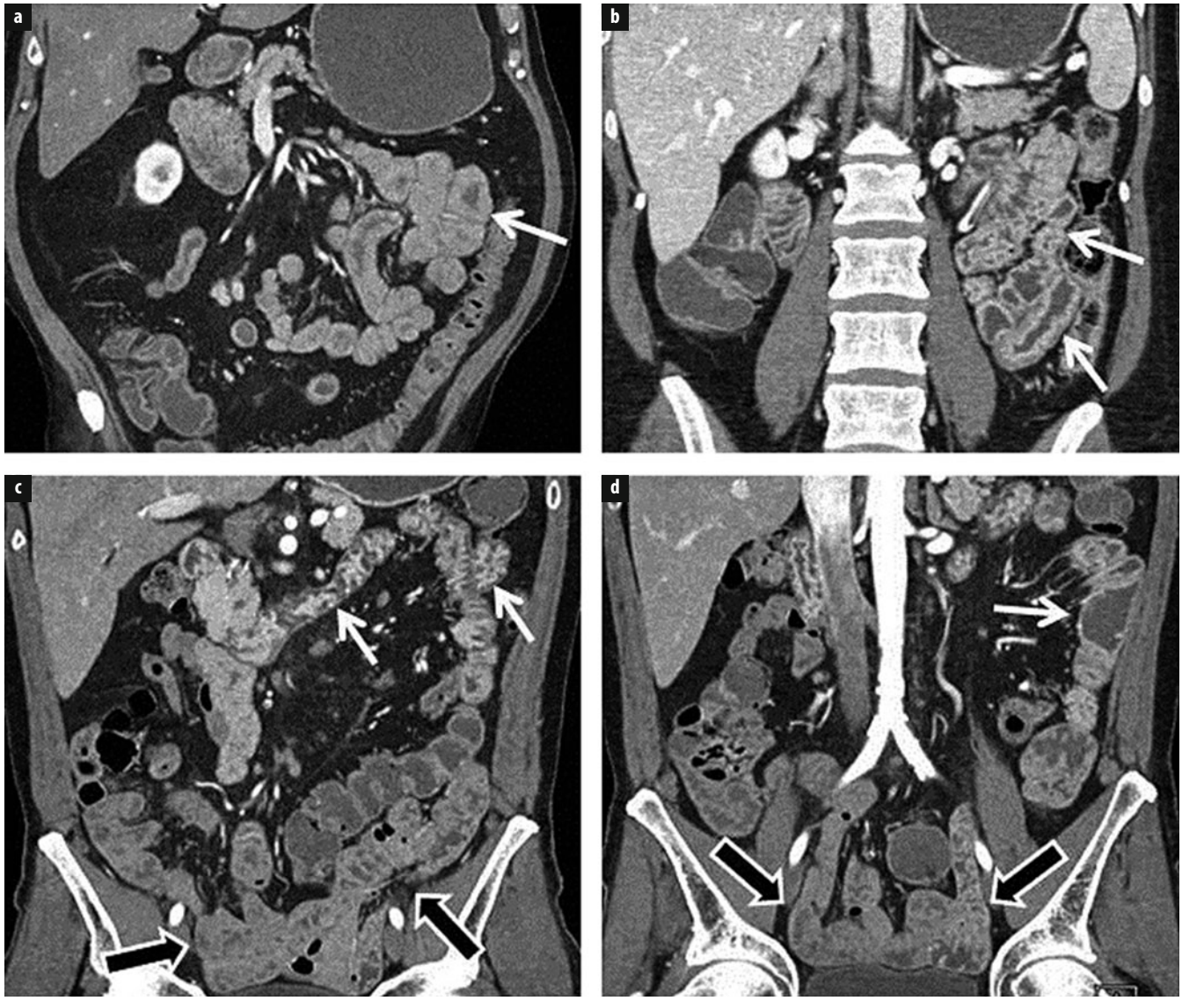


**Fig. 1 a-d.** **a** Crohn's patient with ileitis (not shown) and normal feathery jejunal folds (*arrow*). **b** Crohn's patient with jejunal inflammation manifested by asymmetric mural stratification, wall thickening, and hyperenhancement (*arrows*). **c, d** Celiac disease manifested by long-segment intramural fat in the duodenum and jejunum (**c**, *white arrows*), jejunal-fold atrophy (**d**, *white arrow*), and increased number of ileal folds (**c, d** *black arrows*)

appropriate tests for this indication. Additionally, even in centers where MR enterography is widely available to outpatients, patient volumes and symptomatic presentations to the emergency room (ER) will certainly necessitate CT imaging in patients with known Crohn's disease. Initial cross-sectional studies necessarily focused on the ability of CT enterography to identify Crohn's disease in the terminal ileum. Mural inflammation in Crohn's disease is identified by the combination of segmental mural hyperenhancement and wall thickening, which is often asymmetric and accompanied by mesenteric border fibrofatty proliferation and comb sign. However, the dichotomous decision (Crohn's present vs. absent) is no longer adequate for modern Crohn's management. The length and severity of inflamed segments should be described, in addition to their multifocality. Interpretation should also include evaluation of potential strictures (i.e., luminal narrowing with upstream dilation), penetrating and obstructing complications, the colorectum and anus, mesenteric vessels, and other extraenteric findings [11]. When fistulae are seen, they should be categorized as simple or complex, with additional description of inflammatory masses and abscesses also given (whether amenable to percutaneous drainage or not). Comparison with prior studies should be performed to determine therapeutic response and potential bowel-wall remodeling [12].

Radiologists should be aware of emerging concepts in Crohn's disease imaging that emphasize the complementarity of optical techniques, which evaluate only the mucosa, and cross-sectional techniques that visualize the

small bowel wall. Whereas optical and cross-sectional imaging findings are often synchronous, up to 50% of Crohn's patients with normal-appearing mucosa at ileoscopy will have unequivocal small bowel inflammation at CT enterography [13]. Furthermore, combining endoscopic and CT enterography findings leads to a greater correlation with serum markers of inflammation than ileocolonoscopy alone [14]. Whereas it has long been known that there is poor correlation between endoscopic and biologic markers of Crohn's activity and patient symptoms [15], recent therapeutic trials highlight the link between intestinal healing and decreasing rates of hospitalization and surgery [16]. Thus, clinical decision making increasingly relies upon objective measures rather than protean patient symptoms for disease management. Clinical decisions often involve changing medical therapy, and importantly for quiescent disease, deciding whether current regimens should continue to treat obvious inflammation. In one prospective study of >250 patients with known or suspected Crohn's disease in which gastroenterologists decided on potential management before and after CT enterography, management changes were altered by CT enterography results in 51% of patients overall [17]. CT enterography changed management decisions in nearly a quarter by excluding active inflammation, with medication changes occurring in approximately one quarter, and surgical plans being altered in 5-8%.

Segmental mural hyperenhancement and wall thickening are key findings in identifying Crohn's-related inflammation but are not specific to Crohn's disease. As mentioned, asymmetric and patchy hyperenhancement and wall thickening are pathognomonic for Crohn's disease, particularly in conjunction with fibrofatty proliferation and the comb sign [18]. Other types of inflammation that may mimic Crohn's disease can include ulcerative jejunitis from celiac disease, angioedema from angiotensin-converting enzyme (ACE) inhibitors, infectious and radiation enteritis, and tuberculous ileocolitis. Celiac disease will often be accompanied by villous atrophy in the jejunum and fold-reversal pattern in the small bowel, but will demonstrate symmetric wall thickening and hyperenhancement when ulcerative jejunitis is present, and involve long bowel segments (Fig. 1). Angioedema from ACE inhibitors will present with symptomatic abdominal pain in patients with a suggestive history. Radiation enteritis often presents with obstructive symptoms in patients who have undergone radiation therapy for cervical cancer. Primary small bowel lymphoma and carcinoid tumors can sometimes be mistaken for Crohn's disease, and small bowel carcinoid tumors and adenocarcinomas can arise in Crohn's strictures themselves. When mass-like findings at potential Crohn's-related stricture locations are worrisome (for example, in the absence of hyperenhancement as may occur in lymphoma or with suspicious lymphadenopathy), further investigation with laparoscopy or balloon-assisted endoscopy may be warranted.

Cross-sectional imaging in Crohn's disease is often used to monitor therapeutic response, as biologic agents have significant benefits but are also accompanied by risk and expense. In asymptomatic patients, MR enterography or ultrasound (US) is likely more appropriate for assessing therapeutic response [19]. Because the natural history of Crohn's disease includes the development of penetrating and stricturing disease over time, with approximately 80% of patients undergoing surgery over a 20-year time period [20], symptomatic presentation to the ER will occur, and CT is the modality of choice in the emergent setting. Radiology departments should be prepared to perform CT enterography in Crohn's patients, without enteric preparation, with low dose techniques. In the ER setting, abdominal CT results in a change in management in 81% of Crohn's disease patients and 69% of ulcerative colitis patients, emphasizing a positive benefit-to-risk ratio for CT imaging in patients with inflammatory bowel disease (IBD) [21].

### Obscure GI Bleeding

Obscure GI bleeding (OGIB) is recurrent or persistent GI bleeding in which the small bowel is the likely source of GI blood loss because of prior negative upper and lower endoscopy. OGIB is characterized as "overt" when there is visible evidence of bleeding, such as melena, hematemesis, or hematochezia, or as "occult," such as in the setting of iron-deficiency anemia or positive fecal occult blood test (FOBT). Multiphase CT enterography is an outpatient test that distends the small bowel lumen and requires a multiphase technique to evaluate for small amounts of active small bowel bleeding and identify and characterize bleeding masses, with imaging findings often suggesting the etiology of small bowel blood loss (vascular mass, tumor, inflammation, other).

Multiphase CT enterography is not used to search for acute, massive GI bleeding in the ER setting. No enteric contrast is used, and the goal of the examination is to identify the presence and site of active bleeding for treatment, or for selecting appropriate angiographic or endoscopic therapy [22]. Imaging in massive GI hemorrhage is not designed to identify or suggest bleeding etiology.

Whereas capsule endoscopy is now the first imaging test performed at many institutions in patients with OGIB, there is increasing recognition for the role of multiphase CT enterography in this challenging group of patients. CT enterography was included in the 2011 American Society for Gastrointestinal Endoscopy (ASGE) guidelines for OGIB [23], the principal reason being to identify mass lesions, which can be difficult at capsule endoscopy, as many small bowel tumors arise within the gut wall rather than the mucosa. Compared with balloon-assisted endoscopy and CT enterography, capsule endoscopy identifies about one third of such tumors. In one prospective trial, significantly more small bowel bleeding sources were identified at multiphase CT enterography than at capsule endoscopy, principally owing to the identification of small bowel masses [7]. Studies suggest that the principal benefit of CT enterography is in patients

with overt-type OGIB and those with nondiagnostic capsule endoscopy findings. The diagnostic yield of CT enterography in occult obscure GI bleeding is low. Whereas many capsule endoscopy studies focused on diagnostic yield, there is a large overlap in the prevalence of angioectasias, ulcers, and erosions in patients with OGIB and healthy volunteers.

Interpretation of multiphase CT enterography (MpCTE) data sets can be challenging owing to the large number of images with multiple phases and planes, and with inconsistent quality in the preceding endoscopic examinations. Colorectal neoplasia and vascular malformations are commonly missed at colonoscopy. Cecal and rectal arteriovenous malformations (AVMs) and varices are commonly detected at MpCTE. On this basis, interpretation is normally begun with identifying the right colic artery and vein, which is followed to the cecum, examining for enlargement and contrast within the right colic vein that may indicate a cecal AVM. To make the diagnosis of cecal AVM, this vascular shunting must be accompanied by focal (usually serpiginous), vascular wall enhancement that represents the AVM itself (Fig. 2). In a similar fashion, the superior hemorrhoidal artery is visually followed to the paired rectal vessels and rectum, where rectal vascular malformations are also detected. Colorectal masses are often best appreciated on enteric-phase images. Unsuspected cirrhosis leading to rectal or small bowel varices is frequently encountered as the cause of OGIB in this initial assessment. Thereafter, a systematic interrogation of the small bowel is performed on each imaging phase beginning with the arterial phase and ending with the delayed phase. Visual inspection is performed to identify high attenuation structures, which can signify debris, neoplasm, vascular lesions, or active bleeding. Active bleeding is characterized by the progressive accumulation of intraluminal contrast, so identifying high-attenuation structures should immediately prompt comparison between phases to look for accumulation of intraluminal contrast, in addition to 2D and 3D morphologic assessment. Sometimes, jets of extravagated contrast will be identified at the site of active bleeding. Intraluminal debris will be unchanged between phases and often possesses sharp edges, and some movement of debris may occur between phases due to peristalsis. Similarly, intraluminal filling defects and focal bowel wall thickening are compared between phases and generally represent polyps, neoplasia, or Crohn's disease; they are described subsequently. Three-dimensional interpretation using maximum intensity projection (MIP) images and interactive volume renderings (VR) is particularly helpful in the arterial phase, which will assist with identifying dilated feeding arteries and early draining veins.

### Small Bowel Tumors

MpCTE often identifies small bowel tumors before they spread to the mesentery and liver. In our experience, small carcinoid tumors are particularly frequent and often possess characteristic morphology, which makes prospective identification possible. Carcinoid tumors often present as a flat or plaque-like solitary polyp or mass lesion with intraluminal shouldering and serosal buckling or retraction, as originally described by Levy and Sobin [24]. The release of serotonin and consequent desmoplasia causes the serosal retraction underlying the polyp or mural mass. Carcinoid tumors can be difficult to identify at capsule endoscopy because the overlying mucosa may be normal. Multifocal carcinoid tumors, in which 20-30 tumorlets occur over a 20- to 30-cm bowel segment, are frequently identified at CT enterography. The routine use

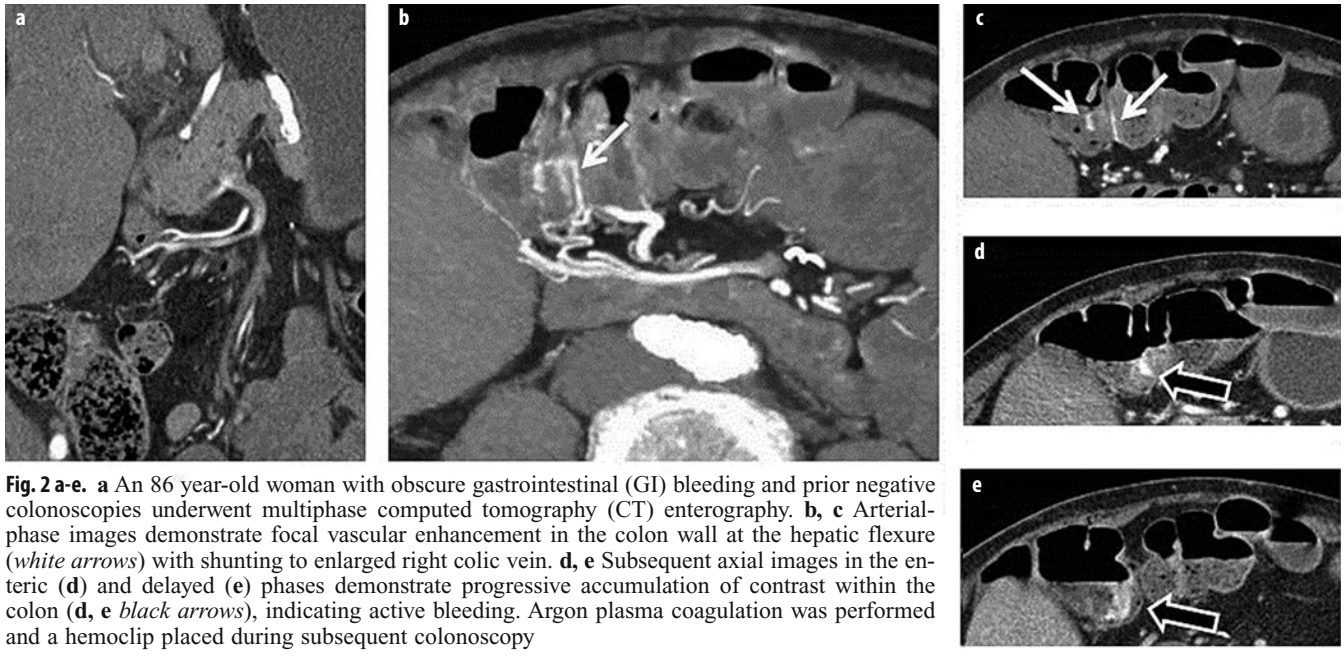


**Fig. 2 a-e.** **a** An 86 year-old woman with obscure gastrointestinal (GI) bleeding and prior negative colonoscopies underwent multiphase computed tomography (CT) enterography. **b, c** Arterial-phase images demonstrate focal vascular enhancement in the colon wall at the hepatic flexure (*white arrows*) with shunting to enlarged right colic vein. **d, e** Subsequent axial images in the enteric (**d**) and delayed (**e**) phases demonstrate progressive accumulation of contrast within the colon (**d, e** *black arrows*), indicating active bleeding. Argon plasma coagulation was performed and a hemoclip placed during subsequent colonoscopy

of CT denoising methods can increase the conspicuity of subtle small bowel lesions, such as carcinoid tumors.

Gastrointestinal stromal tumors (GISTs) of the small bowel are generally hyperenhancing, often with an exoenteric component, but may also be round intraluminal masses with varying degrees of enhancement. Similar to their appearance at routine abdominopelvic CT, primary small bowel lymphomas are hypoenhancing masses that often cause focal wall thickening or aneurysmal ulceration accompanied by localized lymphadenopathy. Melanoma and other small bowel metastases are often seen but may not be hypervascular.

### Vascular Lesions

Huprich et al. developed a simple cross-sectional classification system for vascular lesions of the small bowel that mirrors endoscopic classification [25].

#### *Angioectasias*

Angioectasias are the most frequent vascular lesion of the small bowel and are often seen in elderly individuals (3–5% in autopsy series); when identified by CT enterography or capsule endoscopy in OGIB patients, they are not considered to be the primary source of bleeding unless active bleeding is visualized. They are small, round, or plaque-like lesions best seen in the enteric phase on 3D imaging and are frequently multiple. Whereas isotropic imaging with state-of-the-art CT does permit their identification, there are frequently many more lesions seen at correlative balloon-assisted endoscopy. Angioectasias are thought to occur because arteriovenous communication develops within the small bowel in older individuals as the precapillary sphincter becomes incompetent and veins become dilated and tortuous. Indeed, prominent jejunal veins are often seen and are a normal finding in older patients.

#### *Arterial Lesions*

Arterial lesions are brightest in the arterial phase and may or may not contain draining vein. Common arterial lesions include Dieulafoy's lesions and arteriovenous fistulas and malformations. Similar to its use in angioectasias, interactive 3D imaging is particularly useful in identifying dilated veins and vascular shunting associated with these lesions.

#### *Venous Lesions*

Venous lesions are generally composed of varices, venous angiomas, and congenital lesions. Varices generally arise in the setting of Crohn's disease or (usually clinically occult) cirrhosis. Whereas venous thromboses are known to occur in Crohn's disease, it is only now becoming evident that while portal vein and superior mesenteric vein (SMV) thrombi frequently recanalize, thrombus within smaller mesenteric veins frequently does not. Small-vessel mesenteric venous thromboses can consequently lead to the formation of abnormal collateral channels through the small bowel, which eventually result in small bowel varices.

#### *Nonsteroidal Anti-Inflammatory Drug Enteropathy*

Nonsteroidal anti-inflammatory drug (NSAID) enteropathy is an increasingly recognized entity, largely due to the improved visualization of a small bowel at optical imaging and detection of small bowel diaphragms that retain endoscopic capsules. NSAID enteropathy is characterized by small bowel diaphragm(s) that demonstrate inflammation along their luminal rim, with short, symmetric, focal narrowing and hyperenhancement on multiphase CT enterography (Fig. 3). Usually, several diaphragms are clustered in a bowel segment. Unlike Crohn's disease, the focal narrowing is symmetric and often very short. A single

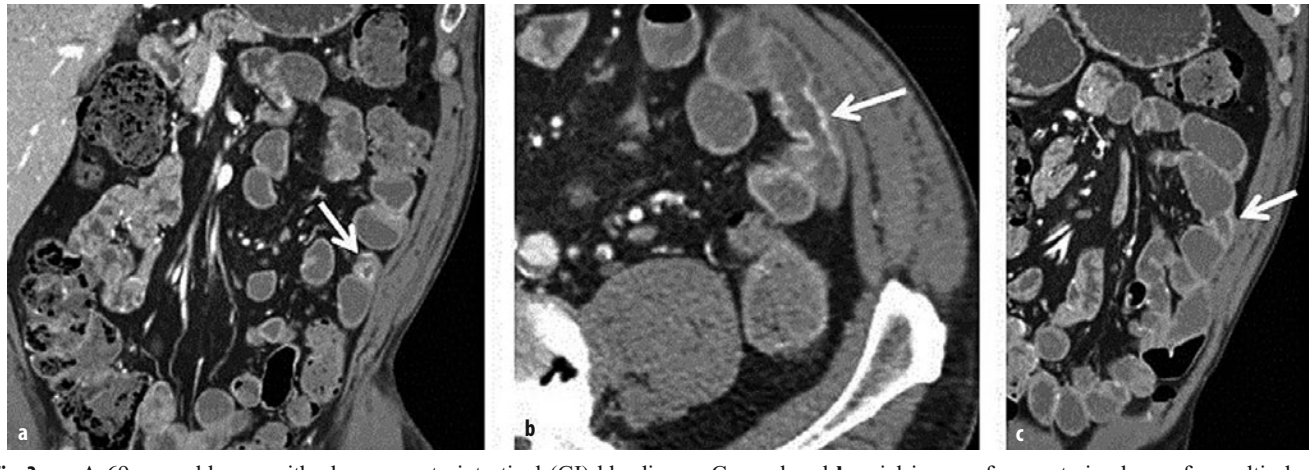


**Fig. 3 a-c.** A 69-year-old man with obscure gastrointestinal (GI) bleeding. **a** Coronal and **b** axial images from enteric phase of a multi-phase computed tomography (CT) enterography demonstrate a 1.5-cm stricture with symmetric enhancement in the proximal ileum (**a, b** *arrows*). Three other similar-appearing, short-segment strictures are seen nearby (one shown in **c**, *arrow*). Subsequent antegrade balloon-endoscopy demonstrated mid-ileal strictures with ulcerated rims, consistent with nonsteroidal anti-inflammatory drug (NSAID)-induced diaphragm disease

lesion, however, can be indistinguishable from a Crohn's stricture.

#### *Meckel's Diverticula*

Meckel's diverticula can be challenging for both capsule endoscopy (which can become entrapped within the diverticulum) and MpCTE. Meckel's diverticula can intussuscept, in which case they demonstrate the classic appearance of an inverted Meckel's diverticulum with intraluminal fat within the intussusceptum, but they can also harbor tumors and focal inflammation.

## CT Enteroclysis

CT enteroclysis is performed with the assistance of a nasojejunal tube through which large volumes of contrast can be rapidly administered. Rapid administration permits excellent distention of all small bowel loops, including the jejunum, which is often difficult to evaluate with peroral techniques alone. CT enteroclysis is usually performed to evaluate low-grade small bowel obstruction when conventional imaging proves unfruitful. A time-efficient method for performing CT enterography is to instill 1,000 cc of enteric contrast via a nasojejunal tube before any imaging is performed, after which the entire abdomen and pelvis can be imaged using CT colonography dose settings. Volumetric monitoring images can then be performed every 500 cc until contrast reaches the cecum. Neutral enteric agents are used when suspected pathologies include radiation enteritis and inflammatory conditions. Positive enteric contrast can be used when surveillance is being performed to look for filling defects, such as in patients with polyposis syndromes. When positive contrast is used, colonographic dose settings can be used as the diagnostic task becomes very similar to CT colonography, permitting large reductions in radiation dose. Visual interrogation of CT enteroclysis images is performed similar to peroral CT enterography images.

## Conclusions

Single and multiphase CT enterography are increasingly being utilized throughout the world as routine imaging techniques of the small bowel. CT acquisition is adapted to the diagnostic task required for each patient, as well as to patient size. CT enterography can be easily performed in a large variety of settings, and multiple studies show that it substantially alters patient management. CT enterography permits diagnosis of a large spectrum of small bowel diseases in addition to imaging of the perienteric mesentery, pancreas, and liver. Its use as a diagnostic tool is advocated by both radiological and gastroenterologic societies and is used increasingly in conjunction with optical imaging methods to provide a better overall assessment of small bowel disease.

## References


1. Young BM, Fletcher JG, Booya F et al (2008) Head-to-head comparison of oral contrast agents for cross-sectional enterography: small bowel distention, timing, and side effects. J Comput Assist Tomogr 32:32-38.
2. Schindera ST, Nelson RC, DeLong DM et al (2007) Multi-detector row CT of the small bowel: peak enhancement temporal window–initial experience. Radiology 243:438-444.
3. Del Gaizo AJ, Fletcher JG, Yu LF et al (2013) Reducing radiation dose in CT enterography. Radiographics 33:1109-1124.
4. Allen BC, Baker ME, Einstein DM et al (2010) Effect of altering automatic exposure control settings and quality reference mAs on radiation dose, image quality, and diagnostic efficacy in MDCT enterography of active inflammatory Crohn's disease. AJR Am J Roentgenol 195:89-100.
5. Kambadakone AR, Prakash P, Hahn PF et al (2010) Low-dose CT examinations in Crohn's disease: impact on image quality, diagnostic performance, and radiation dose. AJR Am J Roentgenol 195:78-88.
6. Huprich JE, Fletcher JG, Alexander JA et al (2008) Obscure gastrointestinal bleeding: evaluation with 64-section multiphase CT enterography–initial experience. Radiology 246: 562-571.
7. Huprich JE, Fletcher JG, Fidler JL et al (2011) Prospective blinded comparison of wireless capsule endoscopy and multiphase CT enterography in obscure gastrointestinal bleeding. Radiology 260:744-751.
8. Wold PB, Fletcher JG, Johnson CD et al (2003) Assessment of small bowel Crohn disease: noninvasive peroral CT enterography compared with other imaging methods and endoscopy—feasibility study. Radiology 229:275-281.
9. Booya F, Fletcher JG, Huprich JE et al (2006) Active Crohn disease: CT findings and interobserver agreement for enteric phase CT enterography. Radiology 241:787-795.
10. Harisinghani MG, Wittenberg J, Lee W et al (2003) Bowel wall fat halo sign in patients without intestinal disease. Am J Roentgenol 181:781-784.
11. Al-Hawary MM, Kaza RK, Platt JF (2013) CT enterography: concepts and advances in Crohn's disease imaging. Radiol Clin N Am 51:1-16.
12. Bruining DH, Loftus EV, Jr., Ehman EC et al (2011) Computed tomography enterography detects intestinal wall changes and effects of treatment in patients with Crohn's disease. Clin Gastroenterol Hepatol 9:679-683 e671.
13. Samuel S, Bruining DH, Loftus EV, Jr. et al (2012) Endoscopic skipping of the distal terminal ileum in Crohn's disease can lead to negative results from ileocolonoscopy. Clin Gastroenterol Hepatol 10:1253-1259.
14. Faubion WA, Jr., Fletcher JG, O'Byrne S et al (2013) EMerging BiomARKers in Inflammatory Bowel Disease (EMBARK) study identifies fecal calprotectin, serum MMP9, and Serum IL-22 as a novel combination of biomarkers for Crohn's disease activity: role of cross-sectional imaging. Am J Gastroenterol doi:10.1038/ajg.2013.354. [Epub ahead of print]
15. Cellier C, Sahmoud T, Froguel E et al (1994) Correlations between clinical activity, endoscopic severity, and biological parameters in colonic or ileocolonic Crohn's disease. A prospective multicentre study of 121 cases. The Groupe d'Etudes Therapeutiques des Affections Inflammatoires Digestives. Gut 35:231-235.
16. Colombel JF, Sandborn WJ, Reinisch W et al (2010) Infliximab, Azathioprine, or combination therapy for Crohn's disease. New Engl J Med 362:1383-1395.
17. Bruining DH, Siddiki HA, Fletcher JG et al (2012) Benefit of computed tomography enterography in Crohn's disease: effects on patient management and physician level of confidence. Inflamm Bowel Dis 18:219-225.
18. Meyers MA, McGuire PV (1995) Spiral CT demonstration of hypervascularity in Crohn's disease: "vascular jejunization of

the ileum" or the "comb sign". Abdominal Imaging 20:327-332.
19. Guimaraes LS, Fidler JL, Fletcher JG et al (2010) Assessment of appropriateness of indications for CT enterography in younger patients. Inflamm Bowel Dis 16:226-232.
20. Cosnes J, Cattan S, Blain A et al (2002) Long-term evolution of disease behavior of Crohn's disease. Inflamm Bowel Dis 8:244-250.
21. Israeli E, Ying S, Henderson B et al (2013) The impact of abdominal computed tomography in a tertiary referral centre emergency department on the management of patients with inflammatory bowel disease. Aliment Pharm Ther 38:513-521.
22. Lee SS, Park SH (2013) Computed tomography evaluation of gastrointestinal bleeding and acute mesenteric ischemia. Radiol Clin N Am 51:29-43.
23. ASGE Standards of Practice Committee (2010) The role of endoscopy in the management of obscure GI bleeding. Gastrointestinal Endoscopy 72:471-479.
24. Levy AD, Sobin LH (2007) From the archives of the AFIP - Gastrointestinal carcinoids: imaging features with clinicopathologic comparison. Radiographics 27:237-U219.
25. Huprich JE, Barlow JM, Hansel SL et al (2013) Multiphase CT enterography evaluation of small-bowel vascular lesions. Am J Roentgenol 201:65-72.

# MRI of the Small Bowel

Karin A. Herrmann

Department of Radiology, University Hospitals Case Medical Center, Case Western Reserve University, Cleveland, OH, USA

## Introduction

For decades, barium fluoroscopy studies have been the standard of reference to investigate small-bowel diseases. As the small bowel was not accessible to endoscopic techniques, these studies represented the only noninvasive diagnostic approach to the intestine. Both small-bowel follow-through and small-bowel enteroclysis yielded fairly good results, with sensitivities and specificities, respectively, of 98.3% and 99.3% for Crohn's disease [1] and between 61% and 95% for neoplastic disease [2], notably in assessing the intestinal mucosa due to high spatial resolution. Limitations of this technique are the almost exclusively intraluminal information, and the considerably high radiation exposure of up to 10-18 mSv. Technical advances in cross-sectional imaging by both computed tomography (CT) and magnetic resonance imaging (MRI) in the past 10 years brought about tremendous improvement of image quality in the abdomen, encouraging small-bowel imaging. Thin-section multidetector-row CT with 3D multiplanar reformations (MPR) and accelerated image acquisition plus breath-hold techniques in MRI have fostered imaging of the bowel with no or few limitations and are now considered state of the art. Both cross-sectional imaging techniques provide insight into the bowel lumen and depict mural and extramural pathology, which is essential for a comprehensive diagnostic assessment and staging of small-bowel diseases. Both imaging techniques convey far more information that conventional barium techniques [3]. MRI, in addition, has the advantage of obviating radiation exposure and is therefore particularly preferable in children, young individuals, during pregnancy, and if multiple follow-up studies are required, such as in inflammatory bowel disease (IBD).

To appropriately assess the intestine, bowel distension is essential. This can be achieved with contrast agents that typically have osmotic effects and enhance the contrast between bowel lumen and bowel wall. Depending on mode of application, the corresponding examination is called MR and CT enterography if the contrast medium is administered orally prior to examination, and MR and CT enteroclysis if a nasojejunal tube is utilized to inject the contrast agent with the help of an automatic infusion pump. In CT enteroclysis, scanning is typically performed just after completion of the filling process, resulting in a static, high-resolution data set that allows 3D postprocessing. MR enteroclysis has the advantage of providing not only static but also functional information, as repetitive scanning can be applied during the filling process.

Diagnosing small-bowel diseases with both CT and MRI is fundamentally based on morphologic criteria. Distinct imaging findings allow disease detection, diagnosis, and staging.

This chapter is designed to familiarize the participant with the technical requirements and imaging protocols for CT and MR enterography and enteroclysis; reviews typical imaging features indicating inflammatory, neoplastic, and ischemic small-bowel diseases with special focus on MRI; and provides a short overview of literature relevant to the topic.

## Duodenum

As the upper gastrointestinal (GI) tract is readily accessible to endoscopic techniques, imaging techniques are less pivotal to establishing a diagnosis. Yet, in the presence of a benign or malignant abnormality, cross-sectional imaging is helpful to assess intra- and extraluminal disease extent. As the duodenum is occasionally involved in pathologies arising from the surrounding organs, such as pancreas, bile ducts, ampulla, and papilla, these should always be considered in the differential diagnosis of duodenal pathology. Embryologic anomalies include ectopic and anular pancreas; webs and choledochocele are benign examples to be included in differential diagnostic considerations. Anular pancreas occurs in 1:20,000 births and is typically diagnosed in the early days after birth due to intestinal obstruction. During pregnancy, it can be discovered when evaluating polyhydramnios. Less frequently, it is found in young adults or incidentally at later ages and has then to be distinguished from neoplasms. Other

*Diseases of the Abdomen and Pelvis 2014-2017*,
DOI: 10.1007/978-88-470-5659-6_4 

benign nonneoplastic conditions in the duodenum include ulcerative and inflammatory disease entities, e.g., Crohn's disease (CD), and pseudoinflammatory polyps. These pathologies are typically worked up endoscopically.

### Neoplasms of the Duodenum

#### Benign Neoplasms of the Duodenum

Examples of benign neoplasms of the duodenum are lipoma, leiomyoma, neurofibroma, adenoma, Brunner gland adenoma, and polyps occurring in the duodenum. Patients are typically asymptomatic until a late stage of disease. MRI is helpful in characterizing these lesion based on their signal-intensity characteristics. Fat-containing lesions are easily identified. However, the final histopathologic diagnosis of most of these solid neoplasms is difficult to determine with MRI alone.

#### Malignant Neoplasms

Most frequent malignant neoplasms of the duodenum are adenocarcinoma, lymphoma, neuroendocrine tumors (NET), GI stromal tumors (GIST) and metastases.

##### *Adenocarcinoma*

Duodenal adenocarcinoma accounts for only 0.4% of GI tumors. By the time it becomes clinically apparent, this disease is often in an advanced stage due to locally aggressive growth. Clinical symptoms are indicative of a high-situated small-bowel obstruction and include vomiting, chronic bleeding and – if close to the ampulla – obstructive jaundice. Within the entire GI tract, the duodenum is the most common site for adenocarcinoma. Morphologically, it may appear as a well-defined, nodular mural or a diffusely infiltrating mass with spiculated borders. Another appearance is that of a diffuse or annular wall thickening causing constrictive narrowing of the lumen. On T1-weighted imaging, the tumor may be homogeneously isointense or hypointense compared with the intestinal wall and slightly hyperintense or isointense on T2-weighted imaging. Contrast enhancement is moderate and mostly homogeneous.

##### *Lymphoma*

Lymphoma of the duodenum, as in the small and large bowel, is most frequently non-Hodgkin's lymphoma (NHL). In 50% of nodal NHL, concomitant intestinal manifestations are present. Characteristic imaging features of duodenal and intestinal lymphoma are asymmetric, circumferential, mostly bulky, wall thickening or mural mass with only mild pre- and intralesional luminal dilatation. Luminal stenosis is not a predominant finding. Lymphoma may also present as multiple intraluminal polypoid masses or an exophytic extraluminal mass. Ulceration and fistula formation are not uncommon. Extraluminal desmoplastic reaction is unlikely. Associated lymphadenopathy is a helpful diagnostic hint but is not always present. Intestinal lymphoma shows moderately increased and homogeneous signal intensity on T2-weighted images compared with normal bowel wall. On T1-weighted imaging, it appears iso- or hypointense and exhibits mild to moderate and slightly inhomogeneous contrast enhancement after gadolinium administration [4].

##### *NET*

The role of CT and MRI in primary detection and diagnosis of duodenal NET is minor compared with endoscopic techniques, including endoscopic US. This is different from the important role that cross-sectional imaging has in detecting NET of the small bowel. Along with the stomach, the duodenum is a common location for NET. Typically, the lesions are small and identified on endoscopy. Occasionally, they are visible on CT and MRI as single or multiple hypervascular nodules in arterial-phase imaging. Luminal distension of the stomach, as in hydro-CT, is recommended and may help achieve a detection rate of up to 89%.

##### *GIST and other Malignancies*

GISTs are most commonly located in the stomach and small bowel and are described in the following section.

## Small Intestine

### Inflammatory Bowel Disease

The most frequent clinical application of small-bowel MRI to date is inflammatory bowel disease (IBD), with emphasis on CD. CD is a chronic inflammatory autoimmune disorder that frequently involves the small bowel but may affect the entire GI tract. CD is most commonly located in the terminal ileum (40-80%) and the colon. Involvement of the proximal ileum and jejunum is less frequent (22-40%). In imaging, CD manifestations were classified by Maglinte et al. into three categories: acute inflammatory, fibrostenotic, and fistulizing disease [5]. Due to its chronically recurrent character, different stages of CD may coexist. Discontinuity of multiple disease manifestations (skip lesions) is a characteristic feature. The morphological spectrum ranges from early superficial mucosal disease with disruption, flattening, thickening, and distortion of the fold pattern to mild or pronounced longitudinal or transverse fissures and ulcerations with cobblestone appearance; and transmural disease, with wall thickening, stenosis, and mesenteric hypervascularity. Eventually, extramural extension of the inflammation into the mesentery may occur, with development of blind sinus tracts, fistula, and micro- or macro abscesses.

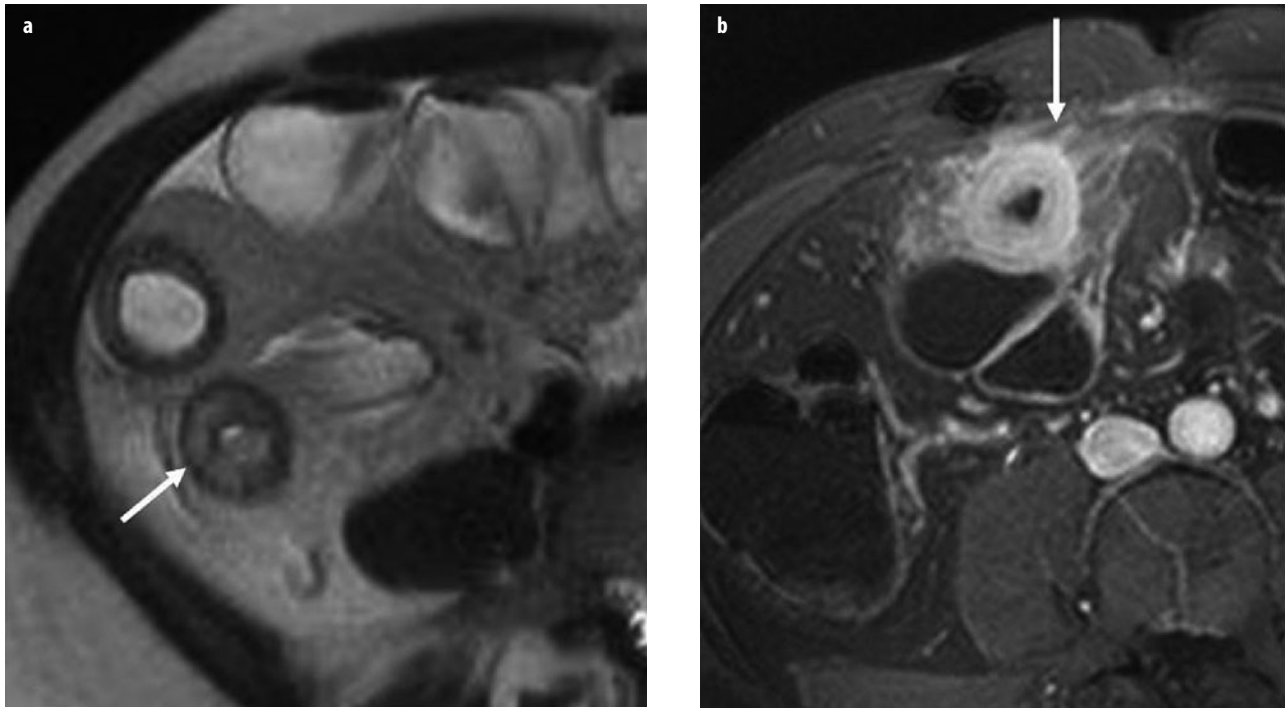


**Fig. 1 a, b.** Active Crohn's disease: magnetic resonance (MR) enteroclysis. **a** T2-weighted axial single-shot turbo spin-echo (SSH-TSE) and **b** T1-weighted postgadolinium (Gd) contrast gradient echo (GRE) with fat saturation following biphasic intraluminal contrast administration (methylcellulose). A segment of small bowel in the right lower quadrant demonstrates significant wall thickening and submucosal edema, indicated by a hyperintense layer within the intestinal wall (**a** *arrow*). There is marked transmural enhancement of the respective loop with even peri-intestinal involvement (**b** *arrow*). These signs are indicators of active Crohn's disease

### Acute Inflammatory Type

A number of imaging findings on MRI have been reported to determine acute inflammatory activity in CD: increased small-bowel wall thickening (typically >4 mm), increased mural contrast enhancement [6], submucosal edema with high signal intensity on T2-weighted images [7] (Fig. 1), presence of deep mucosal ulcers and fissures [8], and to a lesser degree mesenteric hypervascularity (comb sign) [8] and contrast-enhancing enlarged lymphadenopathy [9]. Most recent literature reports claim increased mural thickening, increased wall signal intensity on T2-weighted fat-saturated images, and layered mural enhancement to be the strongest indicators for active disease. Layered mural enhancement is also a pattern commonly associated with active disease; however, it can also be seen in coexisting fibrostenosis and scar formation [10]. It has been a challenge to define objective quantitative parameters to determine disease activity in CD. The most recent suggestion is the Magnetic Resonance Index of Activity (MaRIA) score, which is increasingly used for primary assessment and determining IBD response to therapy [11, 12].

### Early and Mild Stages

Early and mild stages of CD may present at MRI with subtle findings, such as a focal or regional disruption of the fold pattern with mildly or no increased enhancement. Superficial erosions may not be detected at all given the limited spatial resolution of MRI. In contrast to overt wall thickening and stenosis, these lesions can easily be missed on MRI, especially when distension is suboptimal. This is why MR enteroclysis compared with capsule endoscopy or invasive double-balloon endoscopy reaches an overall sensitivity of only 75-80% [13, 14]. In subacute CD and under effective treatment, wall thickening may persist initially but decreases over time. The hyperintense signal intensity from submucosal edema disappears and turns into intermediate signal intensity. Likewise, formerly increased contrast enhancement decreases.

Another important asset in MRI for assessing inflammatory bowel disease is the recent experience with diffusion weighted imaging (DWI). Preliminary data suggest that DWI and the derived quantitative apparent diffusion coefficient (ADC) demonstrate good correlation with standards of reference to detect active CD, specifically gadolinium enhancement [15]. DWI is also helpful in diagnosing internal fistula and abscess [16]. The use of DWI might be specifically beneficial in pediatric patients, in whom avoiding the use of gadolinium must be considered [17].

### Fibrostenosing Type

Fibrostenotic lesions are less conspicuous and more difficult to identify on MRI, as they typically show no wall thickening or abnormally increased enhancement. The

seemingly normal wall thickness and contrast enhancement in fibrostenosis mimic normal bowel wall. Low signal intensity on T2-weighted images with and without fat suppression reflects fibrosis but is difficult to quantify [9]. Persistent focal and fixed circumscript intestinal stenosis and marked prestenotic dilatation are the most conspicuous and reliable indicators and indirect signs of fibrous strictures.

### Fistulizing Type

Internal and external fistula and peri-/extramural abscesses represent the most severe complications of CD. They can be accurately diagnosed with MRI (92%). Fistulas are tubular inflammatory pathways between bowel loops, bowel and other hollow organs, or bowel and the abdominal wall. They are defined as internal fistulas (IF) when between bowel loops (enteroenteric) or to internal hollow organs (e.g., enterovesical). External fistulas (EF) are those that abut the skin (enterocutaneous or perianal). A vast majority of IF may remain asymptomatic or cause nonspecific symptoms, especially if located in distal bowel segments. Complex IF typically involve multiple bowel loops [18]; they are most frequently associated with bowel stenosis and symptoms of obstruction. Abnormal tubular tracts within the mesentery containing air or fluid are highly indicative of IF and are well depicted on steady-state free precession (SSFP), e.g., true fast imaging with steady-state precession (true-FISP) imaging. The outlines of IF show intermediate signal intensity on T2-weighted images, similar to the intestinal wall, and may show moderate enhancement after intravenous administration of gadolinium. For complex IF, a somewhat stellate arrangement of the bowel loops (star sign) is characteristic and has been described as a strong indicator for the presence of IF (Fig. 2) [19]. The inflamed bowel loops converge to a common center, which is often the origin of abscess formation. Urinary bladder involvement is likely when there is marked thickening of the bladder wall in the vicinity of an inflamed bowel segment [18]. A contiguous inflammatory tract between inflamed bowel and bladder wall may not always be seen.

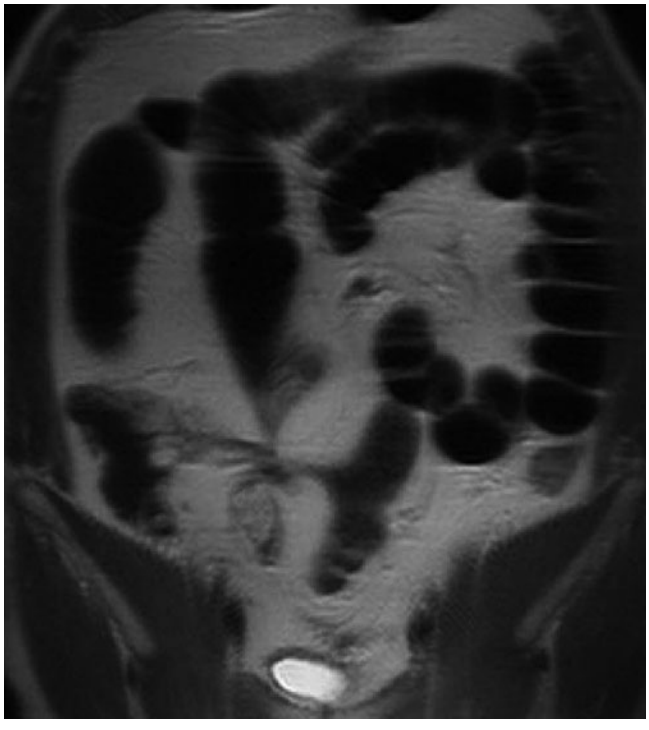

**Fig. 2.** Internal fistula in Crohn's disease: Magnetic resonance (MR) enteroclysis following negative intraluminal contrast application (Lumirem, Guerbet, France). Note stellate configuration of bowel loops in the right lower quadrant with segment stenosis; most loops demonstrate prestenotic dilatation. This configuration is characteristic and strongly predicts the presence of an internal fistula complex: enteroenteric fistula in Crohn's disease

### Differential Diagnosis of Crohn's Disease

Although less frequently a reason for imaging than CD, infectious enteritis is an important differential diagnosis to consider. Infectious enteritis is typically of bacterial origin, such as *Enterococcus*, *Salmonella*, *Yersinia*, tuberculous bacilli, and others. In immunocompromised patients, viral and fungal infections, such as cytomegalovirus (CMV), must be considered. Following bone marrow transplant, CMV and graft-versus-host disease (GVHD) are likely. Infectious enteritis presents with nonspecific findings on CT or MRI, with the main and most common feature being submucosal edema. For tuberculosis, mesenteric lymphadenopathy is a major finding and a helpful diagnostic indicator. Ischemic bowel disease is to be considered if arteriosclerosis and vascular obstruction is additionally observed.

### Small-Bowel Neoplasms

Small-bowel neoplasms are rare and account for $<5\%$ of all GI tumors. The most frequent tumor entities are adenocarcinoma, carcinoid, lymphoma, GIST, and metastases. MR enteroclysis is an effective diagnostic tool for detecting small-bowel tumors, with sensitivity, specificity, and accuracy of 86%, 98%, and 97%, respectively [20]. Small-bowel cancer incidence has risen in the past 30 years, with the greatest increase being in carcinoid tumors. Adenocarcinoma is the most common among intestinal malignant neoplasms, followed by carcinoid tumors. Following the duodenum, the jejunum is the second most common location for adenocarcinoma and typically involves the ileum. Imaging morphology for adenocarcinoma and lymphoma (Fig. 3) follows the previously described patterns (see "Duodenal Neoplasms"). Both malignancy types may complicate CD.

### NET: Carcinoid

Carcinoid tumors are neuroendocrine neoplasms and constitute approximately 2% of all GI tumors. They may be found along the entire GI tract (85%), in the pancreas,

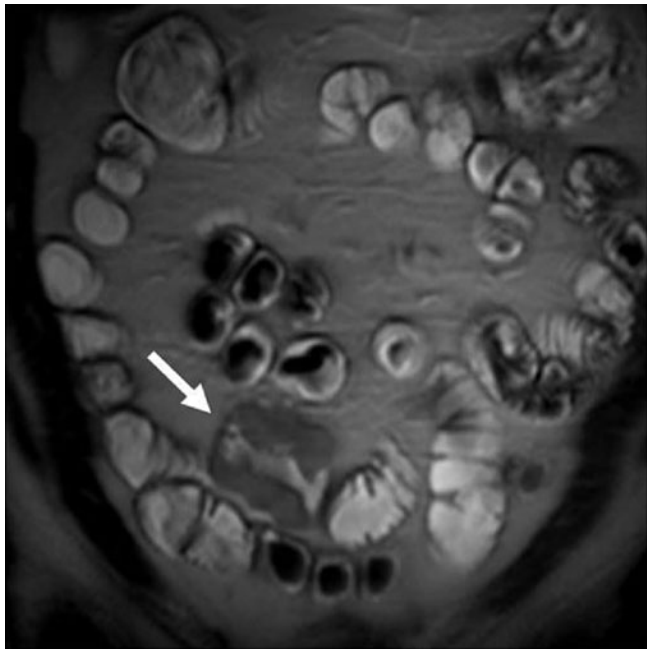

**Fig. 3.** Small-bowel lymphoma: magnetic resonance (MR) enteroclysis following biphasic intraluminal contrast application (methylcellulose). T2-weighted single-shot turbo spin-echo (SSH-TSE) images in coronal plane demonstrate appropriate filing of all small-bowel loops. A short segment with marked thickening of the small-bowel wall is noted in the lower quadrants to the right of the midline (*arrow*). Intermediate signal intensity is similar to that of the bowel wall. Note that the lumen is preserved despite significant wall thickening. Also, there is no prestenotic dilatation. This appearance is characteristic of small-bowel lymphoma

and in the lung (10%). The appendix (50%) and the ileum (~30%) are the most common primary locations. Up to 30% of intestinal carcinoids are multifocal. Carcinoids have a tendency to metastasize early to lymph nodes and liver, even when they only are 1-2 cm in size [21]. Therefore, distension of the bowel lumen in MR enteroclysis is required for better detection. Carcinoids are typically hypervascularized and therefore are best identified on contrast-enhanced T1-weighted fat-saturated gradient echo (GRE) sequences (Fig. 4). Single-shot fast spin-echo (SS-FSE) and SSFP sequence types depict these tumors less effectively as slightly hyperintense or isointense to muscle and bowel wall. Approximately one half of them appear as a nodular intraluminal mass, one third as focal wall circumferential thickening, and 20% with both characteristics [22]. If only wall thickening is present, they may easily be confounded with inflammatory disease. Desmoplastic reaction in the adjacent mesentery occurs in up to 73% of cases and can cause vascular engorgement.

## GIST

GIST represent between 0.3% and 3% of all GI tumors. They derive from the intestinal cells of Cajal and originate most often from the stomach (~70%) or small-bowel wall (20-30%). After distinct immunohistochemical preparation, they strongly express the KIT protein (CD-117) as a characteristic feature. GISTs are well delineated, noninfiltrative masses in or arising from the

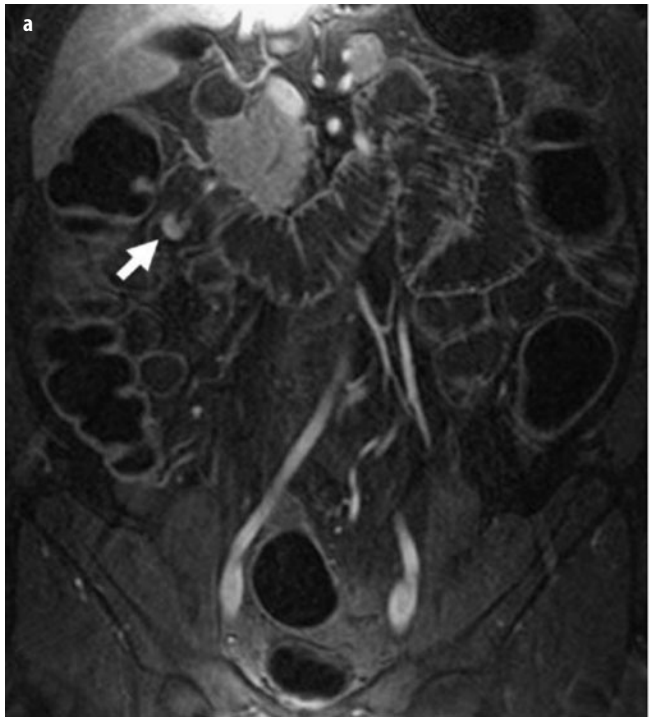


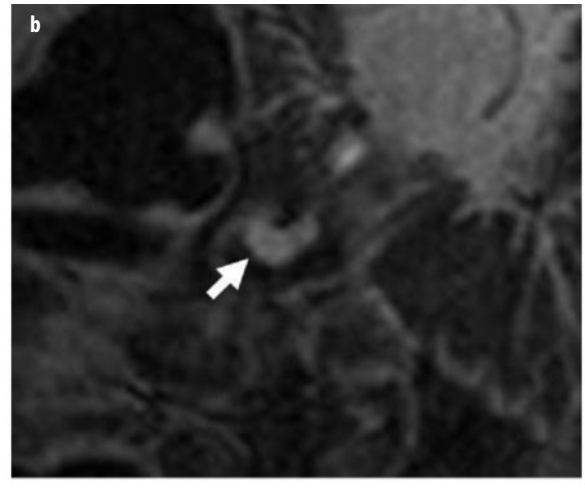


**Fig. 4 a, b.** Small-bowel carcinoid tumor (neuroendocrine tumor): magnetic resonance (MR) enteroclysis following biphasic luminal contrast application (methylcellulose). **a** T1-weighted gradient-echo (GRE) postcontrast images in coronal plane demonstrate very good distention of the entire small bowel, allowing detection of a 1.1-cm intraluminal polypoid lesion with enhancement located in the mid ileum, right upper quadrant (**a** *arrow*). **b** Magnified view better delineates the bean-shaped mass with vivid enhancement (*arrow*). There is no associated lymphatic spread or desmoplastic reaction in the mesentery. Note the mesenteric desmoplastic reaction, a characteristic feature of carcinoid tumors of the small bowel, may be absent in up to 25% of cases [22] when the tumor is small

intestinal wall, typically extraluminally, at the serosal side [23]. When <5 cm, they are slightly heterogeneous and mildly hyperintense on T2-weighted images. Larger masses are heterogeneous, with a soft-tissue rim encompassing a necrotic center. This rim is iso- or slightly hyperintense on T2-weighted images compared with the muscle and hypointense on T1-weighted images, showing heterogeneous enhancement after contrast administration. In the majority of cases, GIST do not show signs of infiltration, vessel encasement, or lymphatic spread. Primary sites of metastases from malignant GIST are liver and peritoneum. Treatment effects with tyrosine kinase inhibitors induce a loss of vascularization, translating to less contrast enhancement of the tumor and its metastases [24], which can be used for treatment monitoring.

### Other Small-Bowel Pathologies

For some small-bowel pathologies, MR enteroclysis has so far not proven to be useful. For superficial mucosal pathologies and angiodysplasia, small-bowel MRI cannot be recommended. Acute ischemia and occult GI bleeding remain the domain of CT, mainly because of availability in an emergency setting, short examination time, and high spatial resolution.

### Adhesions

Postoperative or postinflammatory small-bowel adhesions represent another important clinical condition and were formerly investigated with conventional enteroclysis using manual compression and mobilization of bowel loops. This manipulation is not practicable in MRI due to limited access to the patient inside the magnet. To date, no literature is available to support the usefulness of MR enterography or enteroclysis for small-bowel adhesions.

## References


1. Maglinte DD, Chernish SM, Kelvin FM et al (1992) Crohn disease of the small intestine: accuracy and relevance of enteroclysis. Radiology 184:541-545.
2. Bessette JR, Maglinte DD, Kelvin FM, Chernish SM (1989) Primary malignant tumors in the small bowel: a comparison of the small-bowel enema and conventional follow-through examination. AJR Am J Roentgenol 153:741-744.
3. Lee SS, Kim AY, Yang SK et al (2009) Crohn disease of the small bowel: comparison of CT enterography, MR enterography, and small-bowel follow-through as diagnostic techniques. Radiology 251:751-761.
4. Kim KW, Ha HK (2004) MRI for small bowel diseases. Magn Reson Imaging Clin N Am 12:637-650.
5. Maglinte DDT, Gourtsoyiannis N, Rex D et al (2003) Classification of small bowel Crohn's subtypes based on multimodality imaging. Radiol Clin North Am 41:285-303.
6. Sempere GAJ, Sanjuan VM, Chulia EM et al (2005) MRI evaluation of inflammatory activity in Crohn's disease. AJR Am J Roentgenol 184:1829-1835.
7. Maccioni F, Bruni A, Viscido A et al (2006) MR imaging in patients with Crohn disease: value of T2- versus T1-weighted gadolinium-enhanced MR sequences with use of an oral superparamagnetic contrast agent. Radiology 238:517-530.
8. Prassopoulos P, Papanikolaou N, Grammatikakis J et al (2003) MR enteroclysis imaging of Crohn disease. Radiographics 21 Spec No:S161-172.
9. Gourtsoyiannis N, Papanikolaou N, Grammatikakis J et al (2004) Assessment of Crohn's disease activity in the small bowel with MR and conventional enteroclysis: preliminary results. Eur Radiol 14:1017-1024.
10. Punwani S, Rodriguez-Justo M, Bainbridge A et al (2009) Mural inflammation in Crohn disease: location-matched histologic validation of MR imaging features. Radiology 252:712-720.
11. Rimola J, Ordás I, Rodriguez S et al (2011) Magnetic resonance imaging for evaluation of Crohn's disease: validation of parameters of severity and quantitative index of activity. Inflamm Bowel Dis 17:1759-1768.
12. Ordá I, Rimola J, Rodríguez S et al (2013) Accuracy of magnetic resonance enterography in assessing response to therapy and mucosal healing in patients with Crohn's disease. Gastroenterology doi: 10.1053/j.gastro.2013.10.055 [Epub ahead of print]
13. Tillack C, Seiderer J, Brand S et al (2008) Correlation of magnetic resonance enteroclysis (MRE) and wireless capsule endoscopy (CE) in the diagnosis of small bowel lesions in Crohn's disease. Inflamm Bowel Dis 14:1219-1228.
14. Seiderer J, Herrmann K, Diepolder H (2007) Double-balloon enteroscopy versus magnetic resonance enteroclysis in diagnosing suspected small-bowel Crohn's disease: results of a pilot study. Scand J Gastroenterol 42:1376-1385.
15. Hordonneau C, Buisson A, Scanzi J (2013) Diffusion-weighted magnetic resonance imaging in ileocolonic Crohn's disease: validation of quantitative index of activity. Am J Gastroenterol doi: 10.1038/ajg.2013.385. [Epub ahead of print]
16. Ream JM, Dillman JR, Adler J et al (2013) MRI diffusion-weighted imaging (DWI) in pediatric small bowel Crohn disease: correlation with MRI findings of active bowel wall inflammation. Pediatr Radiol 43:1077-1085.
17. Schmid-Tannwald C, Agrawal G, Dahi F et al (2012) Diffusion-weighted MRI: role in detecting abdominopelvic internal fistulas and sinus tracts. J Magn Reson Imaging 35:125-131.
18. Herrmann KA, Michaely HJ, Zech CJ et al (2006) Internal fistulas in Crohn disease: magnetic resonance enteroclysis. Abdom Imaging 31:675-687.
19. Herrmann KA, Michaely HJ, Seiderer J et al (2006) The "star-sign" in magnetic resonance enteroclysis: a characteristic finding of internal fistulae in Crohn's disease. Scand J Gastroenterol 41:239-241.
20. Masselli G, Polettini E, Casciani E (2009) Small-bowel neoplasms: prospective evaluation of MR enteroclysis. Radiology 251:743-750.
21. Horton KM, Kamel I, Hofmann L, Fishman EK (2004) Carcinoid tumors of the small bowel: a multi-technique imaging approach. AJR Am J Roentgenol 182:559-567.
22. Schmid-Tannwald C, Zech CJ et al (2009) Characteristic imaging features of carcinoid tumors of the small bowel in MR enteroclysis. Radiologe 49:242-245.
23. Burkill GJ, Badran M, Al-Muderis O et al (2003) Malignant gastrointestinal stromal tumor: distribution imaging features and pattern of metastatic spread. Radiology 226:527-532.
24. Schlemmer M, Sourbron SP, Schinwald N et al (2009) Perfusion patterns of metastatic gastrointestinal stromal tumor lesions under specific molecular therapy. Eur J Radiol 27:278-284.

# Infectious, Inflammatory, and Ischemic Diseases of the Colon and Rectum

Richard M. Gore, Robert Silvers

Department of Radiology, University of Chicago, North Shore University Health System, Evanston, IL, USA

## Introduction

Infectious, inflammatory, and ischemic diseases of the colon and rectum are very common causes of abdominal pain. Patients with these disorders often present with nonspecific signs and symptoms. As clinical and laboratory assessment cannot confidently identify a specific etiology in the majority of patients with acute abdominal pain, cross-sectional imaging is required. Computed tomography (CT) is the primary means of evaluating these patients because it nicely depicts pathologic changes in the colon wall, serosa, surrounding mesentery, and peritoneum. Ultrasound (US) is a readily available, real-time technique with reasonable accuracy that uses no ionizing radiation. CT provides fast assessment with high accuracy, optimal field of view, and good reproducibility. Magnetic resonance imaging (MRI) in patients with acute abdominal pain offers great clinical potential by virtue of providing a global imaging perspective, exquisite soft-tissue resolution, and high accuracy without using ionizing radiation. This presentation describes the imaging features of the common infectious, inflammatory, and ischemic disorders of the colon, provides differential diagnostic guidelines, and presents the advantages and disadvantages of the various imaging modalities in the context of optimizing patient management [1].

## Appendicitis

Acute appendicitis is the most common abdominal surgical emergency, affecting 250,000 individuals in the United States annually. The lifetime risk of developing acute appendicitis is 8.6% for men and 6.7% for women. Radiologists play a critical role in evaluating patients with suspected appendicitis and minimizing complications by confirming or excluding the diagnosis in atypical cases. They also can reduce the number of misdiagnoses and negative laparotomies, provide a correct alternate diagnosis, and manage appendiceal abscesses and postoperative complications. Indeed, with the widespread use of CT, the negative appendectomy rate has diminished from 24% to 3% [2-6].

Contrast-enhanced helical CT has a sensitivity, specificity, and accuracy >95% in the diagnosis of acute appendicitis. US with the graded compression technique is valuable, as well. Head-to-head comparative studies show that CT has a significantly higher accuracy than US in the depiction of appendicitis [7-11].

On CT, the abnormal appendix presents as a slightly distended, fluid-filled or collapsed structure approximately 0.5-2 cm in diameter (Fig. 1). The fluid within the lumen is >2.6 mm. Because of inflammatory hyperemia, the wall of the diseased appendix shows homogenous

**Fig. 1.** Appendicitis. Coronal reformatted computed tomography (CT) scan shows a dilated, inflamed, fluid-filled appendix (*arrow*) along the lateral aspect of the right psoas muscle

*Diseases of the Abdomen and Pelvis 2014-2017*,
DOI: 10.1007/978-88-470-5659-6_5 

enhancement during the arterial phase of contrast administration. The wall is circumferentially and asymmetrically thickened (usually 1-3 mm). Periappendiceal inflammation, the hallmark of appendicitis, is characterized by increased hazy density or linear stranding of adjacent mesenteric fat, by fluid-containing abscesses, and by ill-defined, heterogeneous soft-tissue densities representing a phlegmon. There may be secondary inflammatory and edematous changes with thickening of the wall of the adjacent ileum and cecum, which may mimic primary ileocolic inflammatory disease [12-14].

Contrast-enhanced CT is the preferred imaging technique in patients with suspected appendicitis. In patients who cannot receive iodinated intravenously administered contrast material, the diagnosis of acute appendicitis requires the detection of a thickened appendix (diameter >6 mm), with associated inflammatory changes in the periappendiceal fat or abnormal thickening of the right lateroconal fascia, with or without a calcified appendicolith. The detection of an appendicolith confirms a specific diagnosis of appendicitis in the appropriate clinical setting. An appendicolith can be visualized on CT in approximately 28% of adult patients (compared with 10% for plain abdominal radiographs), reflecting the higher sensitivity of CT in detecting small, intra-abdominal calcifications [15-20]. The addition of coronal and sagittal reformatted images increases confidence in establishing the correct diagnosis by virtue of more reliable demonstration of the entire appendix, surrounding fat and lymph nodes, and periappendiceal infection and inflammation.

The combination of right lower-quadrant inflammation, a phlegmon, and an abscess adjacent to the cecum is suggestive but not diagnostic of appendicitis. Indeed, if an abnormal appendix or an appendicolith is not shown, the differential diagnosis also must include Crohn's disease, cecal diverticulitis, ileal diverticulitis, perforated cecal carcinoma, and pelvic inflammatory disease. Abscesses may be found in locations distant from the cecum because of the length and position of the appendix and the patterns of fluid migration in the peritoneal cavity.

The majority (60-70%) of patients referred for cross-sectional imaging with suspected appendicitis do not have this disease. Although most patients have benign, self-limited gastrointestinal disorders, such as viral gastroenteritis, CT and US often suggest a specific alternate diagnosis [15-20]. Adnexal cysts, masses, salpingitis, and tubo-ovarian abscesses are readily shown on US. Ureteral calculi and pyelonephritis can be detected on CT and US. Enlarged lymph nodes in the right lower quadrant suggest mesenteric adenitis or infectious ileitis; mural thickening of the terminal ileum can be seen in Crohn's disease or infectious ileitis.

Although CT has a higher accuracy than US, sonography is often initially employed in pediatric and pregnant patients. MRI combines the lack of ionizing radiation exposure with high-contrast resolution, cross-sectional imaging. Initial reports on MRI in diagnosing acute appendicitis are encouraging in pregnant women [21-24].

## Diverticulitis

It is estimated that 10-25% of individuals with diverticulosis will suffer from diverticulitis. In the United States, this complication accounts for approximately 200,000 hospitalizations and a health care expenditure of $4 billion. Among patients who are hospitalized, 10-20% requires emergency operation [25-28].

Inflammatory change in the pericolic fat is the hallmark of diverticulitis on CT (Fig. 2) and is seen in 98% of cases. The extent of the inflammatory reaction is related to the size of the perforation, bacterial contamination, and host response. Mild cases may manifest as areas of slight increase in fat density adjacent to the involved colon or as fine linear strands with small, fluid collections or bubbles of extraluminal air. In sigmoid diverticulitis, the fluid is typically decompressed into the inferior portion of the combined interfascial plane. Due to hypervascularity of the inflamed area, contrast-enhanced CT scans often reveal engorged mesenteric vessels in the involved pericolic fat. Pericolic heterogeneous soft-tissue densities representing phlegmons and partially loculated fluid collections indicating abscess are seen in more severe cases. The abscess cavities usually contain air bubbles or air-fluid levels. They develop within the sigmoid mesocolon or are sealed off by the sigmoid colon and adjacent small-bowel loops. Less commonly, abscesses may form in the groin, flank, thigh, psoas muscle, subphrenic space or liver [29-33].

Diverticula are seen at the site of perforation or adjacent to it in about 80% of cases on CT. They appear as small outpouchings of air, contrast, or fecal material

**Fig. 2.** Diverticulitis. Coronal reformatted computed tomography (CT) scan demonstrates a large phlegmon in the sigmoid mesocolon (*arrows*)

projecting through the colonic wall. Symmetric mural thickening of the involved colon of approximately 4-10 mm is seen in about 70% of cases; however, if there is marked muscular hypertrophy, the wall of the colon can measure up to 2-3 cm in thickness [34].

CT can also demonstrate intramural abscesses and fistula and is helpful in patients with suspected colovesical fistulas. In the latter case, a pericolic inflammatory mass is seen involving the bladder wall; intraluminal gas confirms the diagnosis [35].

CT reports sensitivity of up to 98% when diagnosing diverticulitis. Additionally, it demonstrates disease extension, such as abscess and peritonitis remote from the colon, and can guide percutaneous abscess drainage. CT can diagnose other pathological conditions that can clinically simulate diverticulitis [29-35].

US can be used as an alternative to CT but may be limited by bowel gas and body habitus [36, 37].

## Epiploic Appendagitis

Primary epiploic appendagitis is a relatively uncommon condition that results from acute inflammation and/or torsion and infarction of the appendices epiploicae. Clinically, epiploic appendagitis can simulate diverticulitis if it occurs in the sigmoid and appendicitis if it occurs in the proximal colon. CT reveals a characteristic appearance of a small, round, or oval fat-containing mass (Fig. 3) with associated inflammatory reaction of the pericolic fat. A thrombosed central vessel can sometimes be identified centrally [38-41]. Epiploic appendagitis is a self-limited process, with clinical resolution in a few days. Follow-up CT examination may show total resolution, with shrinkage and eventual calcification of the inflamed and infarcted epiploic appendix [42, 43].

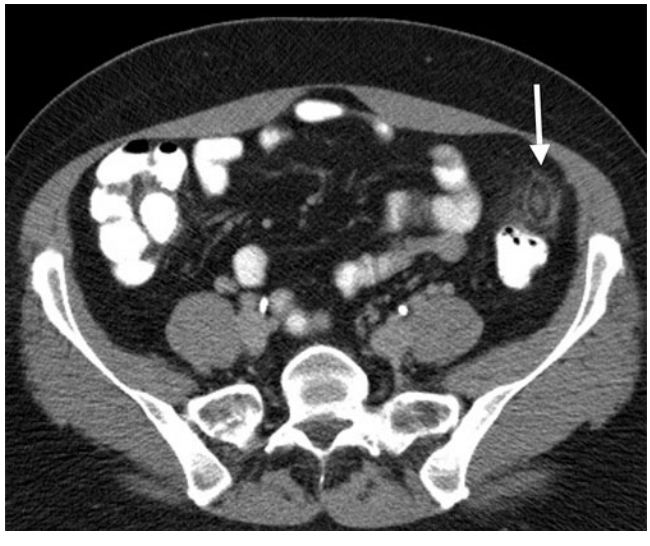

**Fig. 3.** Epiploic appendagitis. Axial computed tomography (CT) scan depicts an infarcted epiploic appendage with a central thrombosed vein (*arrow*)

## Omental Torsion and Infarction

Omental torsion and infarction are uncommon disorders. Portions of the greater omentum undergo torsion, spontaneous venous thrombosis, or both, which leads to severe abdominal pain associated with exquisite point tenderness. This usually occurs in the right lower quadrant, in which case it clinically mimics acute appendicitis, or in the right upper quadrant, in which case acute cholecystitis is simulated [44, 45].

CT demonstrates a region of increased attenuation (Fig. 4**)** within the greater omentum in the involved segment. This abnormal fat must be differentiated from an omental primary or secondary malignancy (e.g., carcinomatosis), omental infection (e.g., tuberculosis), and epiploic appendagitis. The size of the omental abnormality typically is larger in omental infarction and torsion than in epiploic appendagitis [46-49].

## Ischemic Colitis

Vascular insufficiency of the colon should be on the differential diagnosis of any elderly patient with acute or chronic abdominal pain and for all patients with a history of coronary artery disease, peripheral vascular disease, arteritis, hypotension, dehydration, or cardiac decompensation. The major cause of colonic ischemia is nonocclusive hypoperfusion disorders, but it can also be seen in the setting of arterial or venous occlusion or thrombosis [50-52].

CT manifestations of ischemic colitis depend upon its cause, chronicity, and severity. Mural thickening of the gut is the most common finding and is often associated with submucosal edema (Fig. 5). This appearance is non-

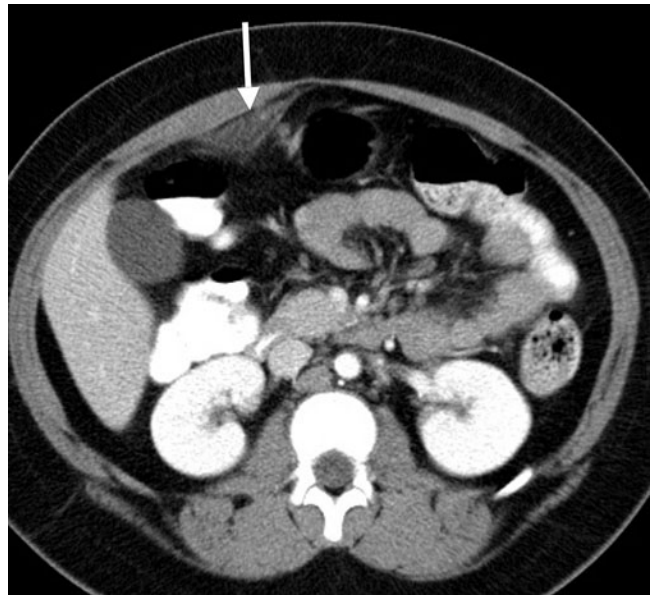

**Fig. 4.** Omental infarction. Axial computed tomography (CT) shows a focal region of abnormal omental fat (*arrow*). This area was exquisitely tender to palpation

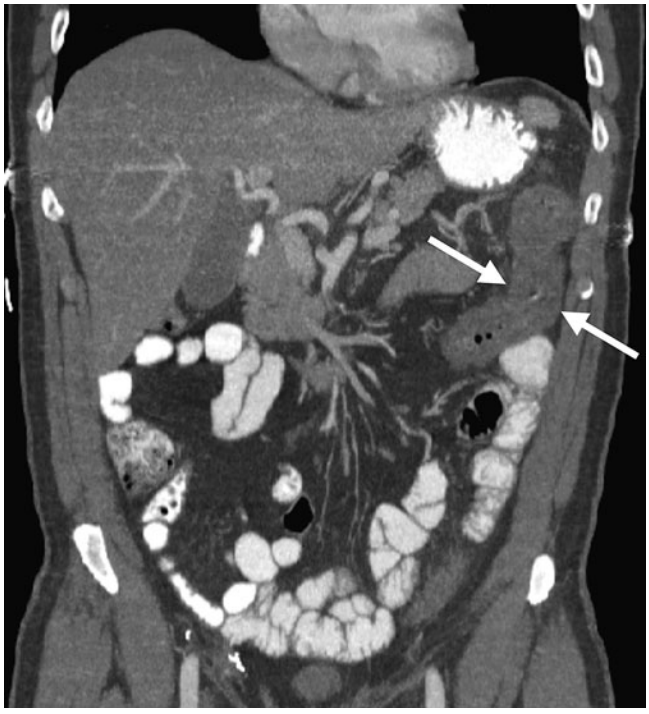

**Fig. 5.** Ischemic colitis. Coronal reformatted computed tomography (CT) reveals mural thickening of the splenic flexure of the colon (*arrows*), the most common location for colonic ischemia

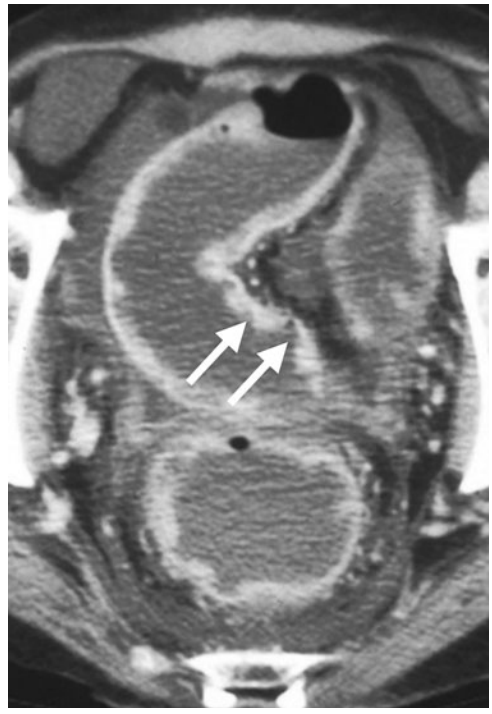

**Fig. 6.** Ulcerative colitis. Axial computed tomography (CT) demonstrates deeps ulcerations (*arrows*), with intervening surviving mucosa producing inflammatory pseudopolyps in this patient with severe disease. Notice the ascites

specific and can be seen in infectious and inflammatory colonic disease. The presence of pneumatosis or thrombus within the superior or inferior mesenteric arteries permits a specific diagnosis to be made. The distribution frequency of ischemic colitis is: left colon (32.6%), distal colon (24.6%), right colon (25.2%), transverse colon (10.2%), and pan colitis (7.3%) [53-56].

## Ulcerative Colitis

Ulcerative colitis is characterized pathologically by extensive ulceration and diffuse inflammation of the mucosa. The disease characteristically begins in the rectum and extends proximally in a contiguous fashion to involve part, or all, of the colon. Pathological changes found in the very early stages of ulcerative colitis are beneath the spatial resolution of CT. With progressive disease, submucosal edema producing a target sign may be seen. Severe mucosal ulceration can denude certain portions of the colonic wall, leading to inflammatory pseudopolyps (Fig. 6). When sufficiently large, these pseudopolyps can be visualized on CT. Mural thickening and lumen narrowing are the CT hallmarks of subacute and chronic ulcerative colitides. Mural thinning, unsuspected perforations, and pneumatosis can be detected on CT in patients with toxic megacolon. In this regard, CT can be quite helpful in determining the urgency of surgery in patients with stable abdominal radiographs yet who present a deteriorating clinical course [57-62].

In chronic ulcerative colitis, the muscularis mucosae become markedly hypertrophied, often by a factor of 40. Forceful contraction also causes shortening of the colon. The submucosa becomes thickened due to the deposition of fat or, in acute and subacute cases, edema. Submucosal thickening further contributes to lumen narrowing. Additionally, the lamina propria is thickened due to round-cell infiltration in both acute and chronic ulcerative colitis.

On CT, these mural changes produce a target or halo appearance when axially imaged: the lumen is surrounded by a ring of soft tissue density (mucosa, lamina propria, hypertrophied muscularis mucosae). This is surrounded by a low-density ring (fatty infiltration of the submucosa), which in turn is surrounded by a ring of soft tissue density (muscularis propria). This mural stratification is not specific and can also be seen in Crohn's disease, infectious enterocolitis, pseudomembranous colitis, ischemic and radiation enterocolitides, mesenteric venous thrombosis, bowel edema, and graft-versus-host disease [57-62].

There are certain CT findings that can help differentiate Crohn's colitis and ulcerative colitis. Mural stratification, i.e., the ability to visualize individual layers of bowel wall, is seen in chronic Crohn's colitis. Also, mean colon-wall thickness in chronic ulcerative colitis is 7.8 mm, significantly thinner than that observed in Crohn's colitis (11 mm). Finally, the outer contour of the thickened colonic wall is smooth and regular in 95% of ulcerative colitis cases, whereas serosal and outer mural irregularities are present in 80% of patients with Crohn's colitis [57-62].

Rectal narrowing and widening of the presacral space are hallmarks of chronic ulcerative colitis. CT depicts the anatomic alterations that underlie these rather dramatic morphologic changes. The rectal lumen is narrowed due to the previously described mural thickening that attends chronic ulcerative colitis. As a result, the rectum has a target appearance on axial scans, which should not be mistaken for the external anal sphincter, mucosal prolapse, or the levator ani muscles. The increase in the presacral space is caused by proliferation of the perirectal fat. On CT, this fat is characterized by an increased number of nodular and streaky soft tissue densities and an abnormal attenuation value 10-20 Hounsfield units (HU) higher than the normal extraperitoneal or mesenteric fat. These fatty changes relate to a number of factors, including ex vacuo replacement by fat of the void produced by rectal lumen narrowing and lipodystrophy resulting from an influx of inflammatory cells and edema. Edematous adipose tissue and enlarged lymph nodes are often observed in the perirectal region at the time of abdominoperineal resections in patients with chronic ulcerative colitis [63-66].

## Crohn's Disease

Crohn's disease most commonly affects the terminal ileum and proximal colon. The acute, active phase of Crohn's disease is characterized by focal inflammation, aphthoid ulceration with adjacent cobblestoning, an often transmural inflammatory reaction, with lymphoid aggregates and granuloma formation, fissures, fistula, and sinus tracts. The chronic and resolving phase of this disorder is associated with fibrosis and stricture formation [57-60].

US, CT, and MRI can be used to determine the presence and extent of Crohn's disease [61-74]. When Crohn's disease is limited to the mucosa, the CT scan is often normal. Although inflammatory and postinflammatory pseudopolyps may be identified on CT, the assessment of the mucosa is best reserved for barium studies and colonoscopy, which are more direct and sensitive. Crohn's disease is manifested on CT by bowel-wall thickening of 1-2 cm (Fig. 7). This thickening, which occurs in up to 83% of patients, is most frequently observed in the terminal ileum, but other portions of the small bowel, colon, duodenum, stomach, and esophagus may be similarly affected [60-74].

During the acute, noncicatrizing phase of Crohn's disease, the small bowel and colon maintain mural stratification and often have a target or double-halo appearance. As in ulcerative colitis, there is a soft-tissue density ring (corresponding to mucosa), which is surrounded by a low-density ring with an attenuation near that of water or fat (corresponding to submucosal edema or fat infiltration, respectively), which in turn is surrounded by a higher density ring (muscularis propria). Inflamed mucosa and serosa may show significant contrast enhancement following bolus contrast administration intravenously,

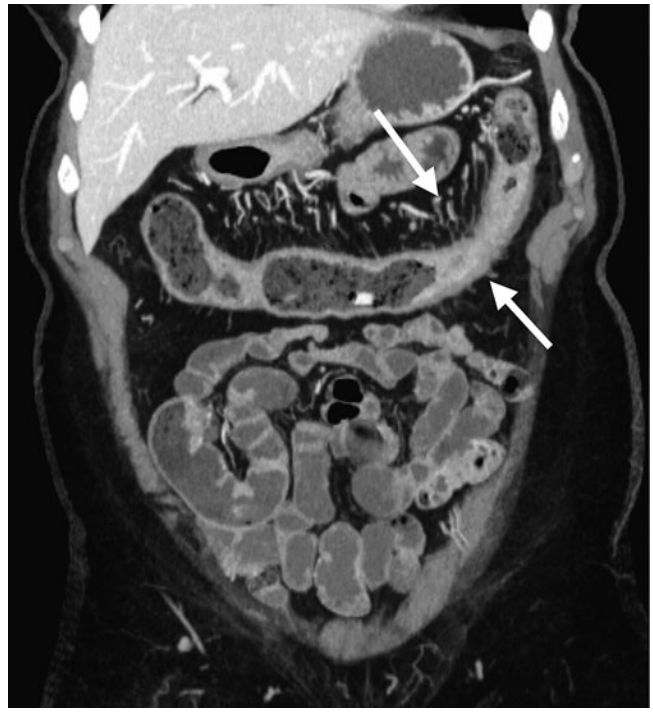

**Fig. 7.** Crohn's disease. Coronal reformatted computed tomography (CT) depicts mural thickening of the transverse colon (*arrows*) and engorgement of the vasa rectae

and the intensity of enhancement correlates with the clinical activity of the disease [60-74].

CT demonstration of mural stratification, i.e., the ability to visualize distinct mucosal, submucosal, and muscularis propria layers, indicates that transmural fibrosis has not occurred and that medical therapy may be successful in ameliorating lumen compromise. Additionally, prior to fibrosis onset, edema and inflammation of the bowel wall, which cause mural thickening and leman obstruction, are reversible to some extent. A modest decrease in wall thickness often produces a dramatic increase in lumen cross-sectional area and resolution of obstructive symptoms. Loss of mural stratification is indicative of transmural fibrosis [60-74].

In patients with long-standing Crohn's disease and transmural fibrosis, mural stratification is lost, so that the affected bowel wall typically has homogeneous attenuation on CT. Homogeneous attenuation of the thickened bowel wall suggests irreversible fibrosis, so that anti-inflammatory agents may not provide significant reduction in bowel-wall thickness. If these segments become sufficiently narrow, surgery or stricturoplasty will be necessary to relieve the obstruction.

Palpation of an abdominal mass or separation of bowel loops on a barium study in a patient with Crohn's disease evokes a large differential diagnosis: abscess, phlegmon, "creeping fat" or fibrofatty proliferation of the mesentery, bowel-wall thickening, and enlarged mesenteric lymph nodes. Each of these disorders has significantly different prognostic and therapeutic implications.

This diagnostic dilemma is further complicated by the fact that many patients are receiving immunosuppressive therapy, which can mask signs and symptoms. CT can readily differentiate the extraluminal manifestations of Crohn's disease.

Fibrofatty proliferation, also known as creeping fat of the mesentery, is the most common cause of separation of bowel loops seen on barium studies in patients with Crohn's disease. On CT, the sharp interface between bowel and mesentery is lost, and the attenuation value of the fat is elevated by 20-60 HU due to the influx of inflammatory cells and fluid. Mesenteric adenopathy with lymph nodes ranging in size between 3 and 8 mm may also be present. If these lymph nodes are >1 cm, the presence of lymphoma or carcinoma, both of which occur with greater frequency in Crohn's disease, must be excluded.

Contrast-enhanced CT scans often show hypervascularity of the involved mesentery, manifesting as vascular dilatation, tortuosity, prominence, and wide spacing of the vasa recta. These distinctive vascular changes have been called the comb sign. Identification of this hypervascularity should suggest active disease and may be useful in differentiating Crohn's from lymphoma or metastases, which tend to be hypovascular lesions.

CT enterography has become an important technique for evaluating the small bowel in patients with Crohn's disease because of its accuracy and noninvasive nature. As colonic involvement is common in patients with inflammatory bowel disease, the capability of this technique for evaluating colorectal involvement is being studied, and preliminary results are encouraging.

As patients with Crohn's disease are often young and typically will require multiple examinations, the cumulative dose of ionizing radiation from multiple CT examinations has the potential to be substantial. Accordingly, the use of an accurate technique without ionizing radiation, such as MRI, is most attractive [75-80].

## Pseudomembranous Colitis

Pseudomembranous colitis is being encountered with increasing frequency as a nosocomial infection complicating antibiotic therapy. This potentially life-threatening disorder is caused by overgrowth of *Clostridium difficile* and the subsequent release of a cytotoxic enterotoxin that causes ulceration of the colonic mucosa and formation of 2- to 3-mm pseudomembranes consisting of fibrin, mucus, sloughed epithelial cells, and leukocytes. Mild cases may demonstrate only mucosal irregularity and nodularity, with small plaque formation that cannot be detected radiologically. In advanced cases, there is thickening of haustral folds, a shaggy wall contour, and mucosal plaques [81-84].

CT shows colitis with mural thickening that may be irregular or polypoid and have a shaggy endoluminal contour. Mural thickening, which is usually 1.6-1.8 cm, is a result of submucosal edema. Mucosal and serosal enhancement is seen following intravenous administration of contrast material. The haustra are also thickened and edematous, producing the accordion pattern, which is highly suggestive of pseudomembranous colitis (Fig. 8). This pattern consists of contrast trapped between thickened haustral folds that are aligned in a parallel fashion. This appearance can sometimes simulate deep ulcerations or fissures. Pericolic stranding, ascites, pleural effusions, and subcutaneous edema are other ancillary CT findings. Complications of untreated pseudomembranous colitis include toxic megacolon, and intestinal perforation with subsequent peritonitis. CT is also useful in monitoring the response to medical therapy with vancomycin and metronidazole orally [81-84].

**Fig. 8.** Pseudomembranous colitis. Coronal reformatted computed tomography (CT) shows mural thickening of the sigmoid colon, with marked submucosal edema (*arrow*) producing the accordion sign. Note the ascites

## Typhlitis

Typhlitis (neutropenic colitis) is a potentially fatal infection of the cecum and ascending colon caused by enteric pathogens in patients with severe immunosuppression. It is most frequently seen in patients with acute leukemia receiving chemotherapy but also occurs in the setting of AIDS, aplastic anemia, multiple myeloma, and bone marrow transplantation. Bacteria, viruses, and fungi penetrate the damaged cecal mucosa and proliferate due to the profound neutropenia. There is edema and inflammation of the cecum, ascending colon, and occasionally the ileum. Fever, abdominal pain, nausea, and diarrhea are presenting symptoms. Prompt diagnosis and supportive

**Fig. 9.** Typhlitis. Axial computed tomography (CT) scan shows marked mural thickening of the cecum in this profoundly neutropenic patient being treated for leukemia

therapy with intensive antibiotic and fluid administration are required to prevent transmural necrosis and perforation. Surgical resection is indicated in patients with transmural necrosis, intramural perforation, abscess, or uncontrolled sepsis and gastrointestinal hemorrhage.

Because of the inherent risks of bowel perforation in performing barium enemas and colonoscopies in these critically ill patients, CT is the study of choice. CT demonstrates circumferential mural thickening (1-3 cm) of the cecum (Fig. 9), low-density areas within the colonic wall secondary to edema, pericolonic inflammation and fluid, and, in severe cases, pneumatosis. Clinically, CT is used to monitor a decrease in mural thickness with therapy and to detect subtle pneumoperitoneum in cases of silent perforation or necrosis [81-84].

## Differential Diagnosis of the Colitides

The differentiation of Crohn's and ulcerative colitis is important in terms of medical management, surgical options, and prognosis. This distinction can usually be made on the basis of colonoscopy with biopsy histology, double-contrast barium enema, disease distribution, and clinical course. CT can occasionally help distinguish these disorders by demonstrating differences in mural thickness, wall density, distribution of colonic involvement, as well as the presence or absence of small-bowel disease, abscess, fistula, and fibrofatty mesenteric proliferation.

Idiopathic inflammatory bowel disease must also be differentiated from infectious colitis. Although there is considerable overlap in CT findings of these disorders, there are certain differentiating features. The presence of ascites is more suggestive of an acute rather than a chronic cause of colonic inflammation. Peritoneal fluid is commonly found in acute colitides – particularly pseudomembranous, infectious, and ischemic colitis – and not in chronic inflammatory bowel disease. Ascites is only infrequently seen in patients with acute inflammatory bowel disease. Submucosal fat deposition on CT is primarily found in subacute and chronic colitides, usually ulcerative colitis, and not in acute disease.

## References


1. Bao J, Lopez JA, Huerta S (2013) Acute abdominal pain and abnormal CT findings. JAMA 310:848-849.
2. Soyer P, Dohan A, Eveno C et al (2013) Pitfalls and mimickers at 64-section helical CT that cause negative appendectomy: an analysis from 1057 appendectomies. Clin Imaging 37:895-901.
3. Sibileau E, Boulay-Coletta I, Jullès MC et al (2013) Appendicitis and diverticulitis of the colon: misleading forms. Diagn Interv Imaging 94:771-792.
4. Shademan A, Tappouni RF (2013) Pitfalls in CT diagnosis of appendicitis: pictorial essay. J Med Imaging Radiat Oncol 57:329-336.
5. Mariadason JG, Wang WN, Wallack MK et al (2012) Negative appendicectomy rate as a quality metric in the management of appendicitis: impact of computed tomography, Alvarado score and the definition of negative appendicectomy. Ann R Coll Surg Engl 94:395-401.
6. Rosen MP, Ding A, Blake MA et al (2011) ACR Appropriateness Criteria® right lower quadrant pain—suspected appendicitis. J Am Coll Radio 8:749-755.
7. Poletti PA, Platon A, De Perrot T et al (2011) Acute appendicitis: prospective evaluation of a diagnostic algorithm integrating ultrasound and low-dose CT to reduce the need of standard CT. Eur Radiol 21:2558-2566.
8. van Randen A, Laméris W, van Es HW et al (2011) A comparison of the accuracy of ultrasound and computed tomography in common diagnoses causing acute abdominal pain. Eur Radiol 21:1535-1545.
9. Kim HC, Yang DM, Kim SW et al (2012) Reassessment of CT images to improve diagnostic accuracy in patients with suspected acute appendicitis and an equivocal preoperative CT interpretation. Eur Radiol 22:1178-1185.
10. Lai V, Chan WC, Lau HY et al (2012) Diagnostic power of various computed tomography signs in diagnosing acute appendicitis. Clin Imaging 36:29-34.
11. Pooler BD, Lawrence EM, Pickhardt PJ (2012) Alternative diagnoses to suspected appendicitis at CT. Radiology 265:733-742.
12. Nelson DW, Causey MW, Porta CR et al (2013) Examining the relevance of the physician's clinical assessment and the reliance on computed tomography in diagnosing acute appendicitis. Am J Surg 205:452-456.
13. Moteki T, Ohya N, Horikoshi H (2011) Evaluation of the maximum depth of intraluminal appendiceal fluid to diagnose appendicitis with a 64-detector row CT scanner. J Comput Assist Tomogr 35:703-710.
14. Purysko AS, Remer EM, Filho HM et al (2011) Beyond appendicitis: common and uncommon gastrointestinal causes of right lower quadrant abdominal pain at multidetector CT. Radiographics 31:927-947.
15. Garcia M, Taylor G, Babcock L et al (2013) Computed tomography with intravenous contrast alone: the role of intra-abdominal fat on the ability to visualize the normal appendix in children. Acad Emerg Med 20:795-800.
16. Blumfield E, Nayak G, Srinivasan R et al (2013) Ultrasound for differentiation between perforated and nonperforated appendicitis in pediatric patients. AJR Am J Roentgenol 200:957-962.
17. Herliczek TW, Swenson DW, Mayo-Smith WW (2013) Utility of MRI after inconclusive ultrasound in pediatric patients with suspected appendicitis: retrospective review of 60 consecutive patients. AJR Am J Roentgenol 200:969-973.

18. Koo HS, Kim HC, Yang DM et al (2013) Does computed tomography have any additional value after sonography in patients with suspected acute appendicitis? J Ultrasound Med 32:1397-1403.
19. Chiu YH, Chen JD, Wang SH et al (2013) Whether intravenous contrast is necessary for CT diagnosis of acute appendicitis in adult ED patients? Acad Radiol 20:73-78.
20. Anderson SW, Soto JA, Lucey BC et al (2009) Abdominal 64-MDCT for suspected appendicitis: the use of oral and IV contrast material versus IV contrast material only. AJR Am J Roentgenol 193:1282-1288.
21. Spalluto LB, Woodfield CA, DeBenedectis CM et al (2012) MR imaging evaluation of abdominal pain during pregnancy: appendicitis and other nonobstetric causes. Radiographics 32:317-334.
22. Beddy P, Keogan MT, Sala E et al (2010) Magnetic resonance imaging for the evaluation of acute abdominal pain in pregnancy. Semin Ultrasound CT MR 31:433-441.
23. Chabanova E, Balslev I, Achiam M et al (2011) Unenhanced MR imaging in adults with clinically suspected acute appendicitis. Eur J Radiol 79:206-210.
24. Leeuwenburgh MM, Wiarda BM, Jensch S et al (2013) Accuracy and interobserver agreement between MR-non-expert radiologists and MR-experts in reading MRI for suspected appendicitis. Eur J Radiol Oct 8 [Epub ahead of print]
25. Humes DJ, Solyamani-Dodaran M, Fleming KM et al (2009) A population-based study of perforated diverticular disease incidence and associated mortality. Gastroenterology 136:1198-1205.
26. Mora Lopez L, Serra Pla S, Serra-Aracil X et al (2013) Application of a modified Neff classification to patients with uncomplicated diverticulitis. Colorectal Dis 15:1442-1447.
27. Kruis W, Morgenstern J, Schanz S (2013) Appendicitis/diverticulitis: diagnostics and conservative treatment. Dig Dis 31:69-75.
28. Sibileau E, Boulay-Coletta I, Jullès MC et al (2013) Appendicitis and diverticulitis of the colon: misleading forms. Diagn Interv Imaging 94:771-792.
29. Longstreth GF, Iyer RL, Chu LH et al (2012) Acute diverticulitis: demographic, clinical and laboratory features associated with computed tomography findings in 741 patients. Aliment Pharmacol Ther 36:886-894.
30. Hill BC, Johnson SC, Owens EK et al (2010) CT scan for suspected acute abdominal process: impact of combinations of IV, oral, and rectal contrast. World J Surg 34:699-703.
31. Ben Yaacoub I, Boulay-Coletta I, Jullès MC et al (2011) CT findings of misleading features of colonic diverticulitis. Insights Imaging 2:69-84.
32. Elmi A, Hedgire SS, Pargaonkar V et al (2013) Is early colonoscopy beneficial in patients with CT-diagnosed diverticulitis? AJR Am J Roentgenol 200:1269-1274.
33. Wilkins T, Embry K, George R (2013) Diagnosis and management of acute diverticulitis. Am Fam Physician 87:612-620.
34. Öistämö E, Hjern F, Blomqvist L et al (2013) Cancer and diverticulitis of the sigmoid colon. Differentiation with computed tomography versus magnetic resonance imaging: preliminary experiences. Acta Radiol 54:237-241.
35. Mutter D, Marescaux J (2013) Appendicitis/diverticulitis: minimally invasive surgery. Dig Dis 31:76-82.
36. Mazzei MA, Cioffi Squitieri N, Guerrini S et al (2013) Sigmoid diverticulitis: US findings. Crit Ultrasound J 5(Suppl 1):S5. doi: 10.1186/2036-7902-5-S1-S5
37. Puylaert JB (2012) Ultrasound of colon diverticulitis. Dig Dis 30:56-59.
38. Hwang JA, Kim SM, Song HJ et al (2013) Differential diagnosis of left-sided abdominal pain: primary epiploic appendagitis vs colonic diverticulitis. World J Gastroenterol 19:6842-6848.
39. Mollà E, Ripollés T, Martínez MJ et al (1998) Primary epiploic appendagitis: US and CT findings. Eur Radiol 8:435-440.
40. Bunni J, Corrigan A, Jacob K et al (2010) Epiploic appendagitis: a case report highlighting correlation between clinical features, computed tomography images and laparoscopic findings. Int J Surg 8:401-403.
41. Singh AK, Gervais DA, Hahn PF et al (2005) Acute epiploic appendagitis and its mimics. Radiographics 25:1521-1534.
42. Schnedl WJ, Krause R, Wallner-Liebmann SJ et al (2012) Primary epiploic appendagitis and successful outpatient management. Med Sci Monit 18:CS48-51.
43. Chen JH, Wu CC, Wu PH (2011) Epiploic appendagitis: an uncommon and easily misdiagnosed disease. J Dig Dis 12:448-452.
44. Sasmal PK, Tantia O, Patle N et al (2010) Omental torsion and infarction: a diagnostic dilemma and its laparoscopic management. J Laparoendosc Adv Surg Tech A 20:225-229.
45. Wertheimer J, Galloy MA, Régent D et al (2013) Radiological, clinical and histological correlations in a right segmental omental infarction due to primary torsion in a child. Diagn Interv Imaging doi:pii: S2211-5684(13)00198-8. 10.1016/j.diii.2013.05.009 [Epub ahead of print]
46. Lubner MG, Simard ML, Peterson CM et al (2013) Emergent and nonemergent nonbowel torsion: spectrum of imaging and clinical findings. Radiographics 33:155-173.
47. McClure MJ, Khalili K, Sarrazin J et al (2001) Radiological features of epiploic appendagitis and segmental omental infarction. Clin Radiol 56:819-827.
48. Kim J, Kim Y, Cho OK et al (2004) Omental torsion: CT features. Abdom Imaging 29:502-504.
49. Singh AK, Gervais DA, Lee P et al (2006) Omental infarct: CT imaging features. Abdom Imaging 31:549-554.
50. Paterno F, McGillicuddy EA, Schuster KM et al (2010) Ischemic colitis: risk factors for eventual surgery. Am J Surg 200:646-650.
51. Gore RM, Thakrar KH, Mehta UK et al (2008) Imaging in intestinal ischemic disorders. Clin Gastroenterol Hepatol 6:849-858.
52. Gore RM, Yaghmai V, Thakrar KH et al (2008) Imaging in intestinal ischemic disorders. Radiol Clin North Am 46:845-875.
53. Romano S, Romano L, Grassi R (2007) Multidetector row computed tomography findings from ischemia to infarction of the large bowel. Eur J Radiol 61:433-441.
54. Moszkowicz D, Mariani A, Trésallet C et al (2013) Ischemic colitis: the ABCs of diagnosis and surgical management. J Visc Surg 150:19-28.
55. Mazzei MA, Guerrini S, Cioffi Squitieri N et al (2013) Magnetic resonance imaging: is there a role in clinical management for acute ischemic colitis? World J Gastroenterol 19:1256-1263.
56. Reginelli A, Genovese E, Cappabianca S et al (2013) Intestinal Ischemia: US-CT findings correlations. Crit Ultrasound J 5(Suppl 1):S7.
57. Gore RM, Laufer I, Berlin JW (2008) Ulcerative and granulomatous colitis: idiopathic inflammatory bowel disease. In: Gore RM, Levine MS (Eds) Textbook of Gastrointestinal Radiology, 3rd ed. Elsevier, Philadelphia, pp 1071-1108.
58. Norsa AH, Tonolini M, Ippolito S et al (2013) Water enema multidetector CT technique and imaging of diverticulitis and chronic inflammatory bowel diseases. Insights Imaging 4:309-320.
59. Strobel D, Goertz RS, Bernatik T (2011) Diagnostics in inflammatory bowel disease: ultrasound. World J Gastroenterol 17:3192-3197.
60. Patel B, Mottola J, Sahni VA et al (2012) MDCT assessment of ulcerative colitis: radiologic analysis with clinical, endoscopic, and pathologic correlation. Abdom Imaging 37:61-69.
61. da Luz Moreira A, Vogel JD, Baker M et al (2009) Does CT influence the decision to perform colectomy in patients with severe ulcerative colitis? J Gastrointest Surg 13:504-507.
62. Thoeni RF, Cello JP (2006) CT imaging of colitis. Radiology 240:623-638.

63. Horsthuis K, Bipat S, Bennink R, Stoker J (2008) Inflammatory bowel disease diagnosed with US, MR, scintigraphy, and CT: meta analysis of prospective studies. Radiology 247:64-79.
64. Ordas I, Rimola J, Rodriguez S et al (2012) Imaging of the colon in inflammatory bowel disease: ready for prime time? Curr Drug Targets 13:1252-1260.
65. Perlman SB, Hall BS, Reichelderfer M (2013) PET/CT imaging of inflammatory bowel disease. Semin Nucl Med 43:420-426.
66. Hristova L, Soyer P, Hoeffel C et al (2013) Colorectal cancer in inflammatory bowel diseases: CT features with pathological correlation. Abdom Imaging 38:421-435.
67. Horton KM, Corl FM, Fishman EK (2000) CT evaluation of the colon: inflammatory disease. Radiographics 20:399-418.
68. Langhorst J, Kühle CA, Ajaj W et al (2007) MR colonography without bowel purgation for the assessment of inflammatory bowel diseases: diagnostic accuracy and patient acceptance. Inflamm Bowel Dis 13:1001-1008.
69. Ajaj WM, Lauenstein TC, Pelster G et al (2005) Magnetic resonance colonography for the detection of inflammatory diseases of the large bowel: quantifying the inflammatory activity. Gut 54:257-263.
70. Horsthuis K, Bipat S, Stokkers PC, Stoker J (2009) Magnetic resonance imaging for evaluation of disease activity in Crohn's disease: a systematic review. Eur Radiol 19:1450-1460.
71. Furukawa A, Saotome T, Yamasaki M et al (2004) Cross-sectional imaging in Crohn disease. Radiographics 24:689-702.
72. Rimola J, Rodríguez S, García Bosch O et al (2009) Magnetic resonance for assessment of disease activity and severity in Crohn disease. Gut 58:1113-1120.
73. Hammer MR, Podberesky DJ, Dillman JR (2013) Multidetector computed tomographic and magnetic resonance enterography in children: state of the art. Radiol Clin North Am 51:615-636.
74. Gee MS, Harisinghani MG (2011) MRI in patients with inflammatory bowel disease. J Magn Reson Imaging 33:527-534.
75. Zijta F, Stoker J (2010) Magnetic resonance imaging of the colon (colonography): results. In: Stoker J (Ed) Magnetic resonance imaging of the gastrointestinal tract. Springer Verlag, Berlin, Heidelberg, pp 185-204.
76. Rimola J, Rodriguez S, Gracia-Bosch O et al (2009) Role of 3.0-T colonography in the evaluation of inflammatory bowel disease. Radiographics 29:701-719.
77. Röttgen R, Herzog H, Lopez-Häninnen E, Felix R (2006) Bowel wall enhancement in magnetic resonance colonography for assessing activity in Crohn's disease. Clin Imaging 30:27-31.
78. Hammer MR, Podberesky DJ, Dillman JR (2013) Multidetector computed tomographic and magnetic resonance enterography in children: state of the art. Radiol Clin North Am 51:615-636.
79. Al-Hawary MM, Kaza RK, Platt JF (2013) CT enterography: concepts and advances in Crohn's disease imaging. Radiol Clin North Am 51:1-16.
80. Gee MS, Harisinghani MG (2011) MRI in patients with inflammatory bowel disease. J Magn Reson Imaging 33:527-534.
81. Regge D, Neri E, Turini F et al (2009) Role of CT colonography in inflammatory bowel disease. Eur J Radiol 69:404-408.
82. Eaton SR, Mazuski JE (2013) Overview of severe Clostridium difficile infection. Crit Care Clin 29:827-839.
83. Lee JH, Lim GY, Im SA et al (2008) Gastrointestinal complications following hematopoietic stem cell transplantation in children. Korean J Radiol 9:449-457.
84. Gluecker TM, Williamson EE, Fletcher JG et al (2003) Diseases of the cecum: a CT pictorial review. Eur Radiol 13(Suppl 4):L51-61.

# Benign Diseases of the Colon and Rectum: CT Colonography

Philippe Lefere, Stefaan Gryspeerdt

Department of Radiology, AZ Delta, Roeselare, Belgium

## Introduction

Computed tomography colonography (CTC) is established as the best alternative to optical colonoscopy (OC) for detecting polyps and tumoral lesions in the colon. In that way, it is an accepted modality after incomplete OC in patients with a contraindication for or who are unwilling to undergo OC [1]. Furthermore, CTC can be suggested for individual colorectal cancer screening and for patients with symptoms suggestive of colorectal cancer in general [2]. Adequate training and experience are considered crucial for accurate polyp detection [3]. However, besides being a champion in polyp detection, it is also very important for the radiologist to be familiar with findings of benign colonic disease and findings mimicking disease (polyps and tumors), as this will significantly reduce false-positive findings and hence superfluous OC. This issue of false-positive findings at CTC should absolutely be reduced to a minimum to avoid patient anxiety and because of increased costs. The purpose of this overview is to introduce readers to the several benign conditions of the colon that may mimic polypoid and/or malignant disease and thus enable them to distinguish findings needing further investigation and/or treatment from those who require no further investigation.

## Contraindications to CTC

CTC is NOT an indication of whenever acute colonic pathology is suspected. CTC is NOT an indication in Crohn's disease and ulcerative colytis (UC)

Before starting with CTC, it is very important to know that CTC is intended for polyp detection. This precludes its use in case of an acute clinical picture with suspicion of benign colonic pathology (acute appendicitis, acute diverticulitis, any type of colitis) and in patients with signs of obstruction, fever, or leucocytosis. Inflammatory bowel disease (IBD) (Crohn's disease, UC) is not considered a suitable indication because of the increased risk of perforation during examination. Furthermore, CTC does not add any new, significant information in these patients and can only be considered in case of incomplete OC to rule out proximal tumoral lesions. Red blood loss per anum (RBPA) is not an indication unless there are any contraindications to OC or in case OC is incomplete.

## Benign Mucosal Colonic Polyps

Whenever a polyp $\geqslant$6 mm is suspected at CTC, optical colonoscopy should be recommended.

Besides malignant tumors, polyps are the main target of CTC. According to the Paris classification, they are categorized as sessile (0-Is), pedunculated (0-Ip), or flat. Flat lesions are divided into flat elevated (0-IIa), truly flat (0-IIb), and depressed flat (0-IIc). An excavated lesion (0-III) must be considered malignant [4]. Several kinds of benign polyps may develop in the colon. The most frequent are hyperplastic polyps that, until recently, were considered totally harmless. It is now a matter of debate whether they could have some low to very low malignant potential.

Adenomas are the target of colorectal cancer screening. They are the benign triggers of pathways leading to colorectal cancer. First, there is the adenoma-carcinoma pathway, with a long period of $\pm$10 years before becoming malignant ($\pm$50% of cancers) [5]. Adenomas are subdivided in tubular, villous and tubulovillous types. The real target of CRC screening is the advanced adenoma, which is $\geqslant$10 mm and/or presents at pathology with $\geqslant$25% of villous components and/or with high-grade dysplasia. Second is the serrated neoplasia pathway ($\pm$30%). This pathway, with the hyperplastic polyp (HP), the traditional serrated adenoma (TSA), and the sessile serrated adenoma (SSA) as benign precursors was recently detected and has a different, still partly unknown behavior [6]. These lesions may be present for a long period and undergo unexpected, abrupt change to malignancy almost without a transition period. Furthermore,

*Diseases of the Abdomen and Pelvis 2014-2017*,
DOI: 10.1007/978-88-470-5659-6_6 

SSAs are particularly difficult to detect and have a high to very high malignant potential. They are mostly right sided and flat.

Every polypoid defect ⩾6 mm detected at CTC and suspected to be a polyp needs OC. They can be detected by 2D and 3D interpretation methods. In our experience, we prefer by far the primary 3D interpretation method, which is highly intuitive for detecting polyps and generates good results in combination with a appropriate colonic preparation with fecal tagging and optimal colonic distension with automated carbon dioxide ($CO_2$) inflation [7].

Whenever a polypoid defect is detected on fly-through mode (3D), the finding must be compared with the second acquisition to confirm the finding in the same position, as well as comparing it with the native images (2D) to characterize the lesion by assessing its attenuation. A polyp is characterized by homogeneous soft tissue attenuation and is frequently covered by a thin layer of tagged fluid.

We recommend primary 3D interpretation for detecting polyps. Combine this with a preparation with fecal tagging and optimal colonic distension with $CO_2$ inflation.

## Anatomy-Related Findings

### Spasm

Spasm is an important tumor mimic. Colonic distension and lumen shape depend upon the grade of contraction of the taeniae coli. These are three longitudinal muscular bands starting in the sigmoid and converging at the appendicular orifice. In the sigmoid, they are not prominent, giving a round to oval shape to the colonic lumen. From the descending to the ascending colon, they become more prominent, giving the colonic lumen its typical triangular aspect. In case of spasm, 3D shows narrowing of the lumen with a triangular aspect and with prominent taeniae. In 2D imaging, the spasm is characterized by smooth, slightly thickened, folds frequently abutting each other (kissing folds). The folds are not distorted, and there is no shoulder formation or overhanging edges. Furthermore, the spasm frequently shows a different aspect when compared on both acquisitions. It is essential to insist on optimal colonic distension with $CO_2$ insufflation, dual positioning (i.e., acquisition in supine and prone positions), and use of hyoscine-N-butylbromide (Buscopan®), if allowed in your country [8].

Troubleshooting the spasm:
- A spasm maintains the shape of the colonic lumen.
- Folds are smooth without overhanging edges or distortion.
- Always compare both 2D and 3D acquisitions.
- Use IV Buscopan®.

### Flexural Pseudotumor

The colon presents with many flexures. At each flexure, structures at the inner side are more or less compressed, causing thickening of the folds accordingly. This thickening is accentuated by the pericolic fat and its vascular structures. This entity is called a flexural pseudotumor and becomes a real tumor-mimic in case of a flexure over an acute angle with convergence of many folds. Comparing both acquisitions to detect any change in appearance and conducting a detailed analysis of both 3D and 2D images help exclude true tumoral process (Fig. 1). The fold most frequently consists of convergence of many folds. In 3D, the fold has regular, smooth contours. In 2D, sometimes pericolic fat is demonstrated in the thickened fold [8].

Troubleshooting the flexural pseudotumor:
- Smoothly thickened fold located at flexures.
- Presence of fat, convergence of folds.
- Compare both acquisitions – 3D and 2D.

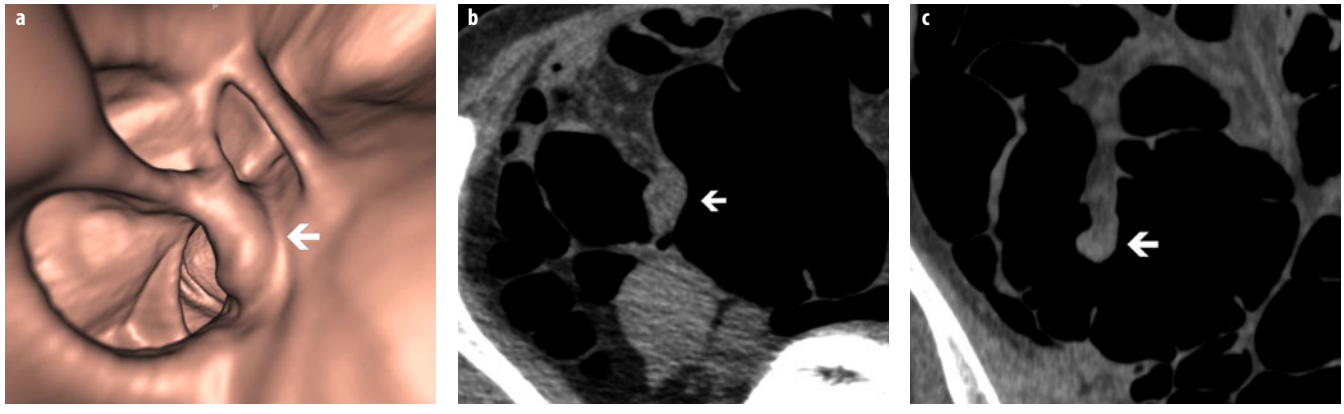


**Fig. 1 a-c.** **a** A 3D view of the ascending colon showing a smooth filling defect at the convergence of folds (*white arrow*). **b** Corresponding 2D view showing the filling defect with a soft tissue density (*white arrow*). **c** Coronal reformat showing a cecum recurvatum internum with acute flexure, causing compression of the pericolic fat and vascular structures at the inner side (*white arrow*)

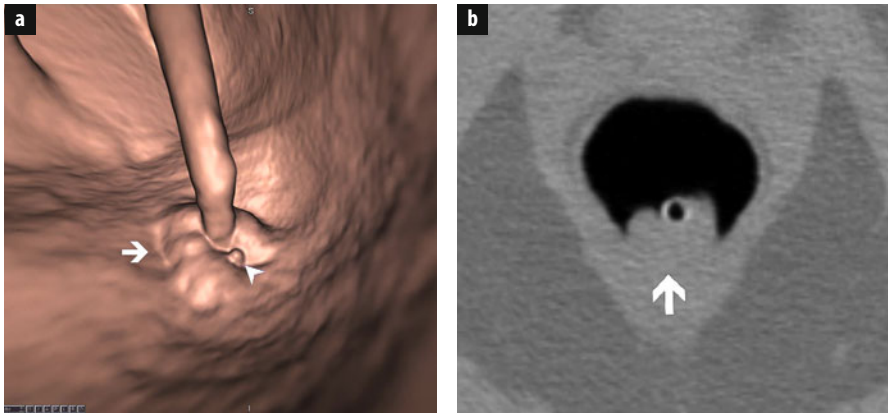


**Fig. 2 a, b.** **a** Typical 3D image of internal hemorrhoids surrounding the rectal catheter at the level of the anal margin (*white arrow*). Additional tiny polypoid defect <5 mm near the hemorrhoids (*white arrowhead*): most probably a tiny hypertrophied anal papilla. No further investigation is necessary, as this lesion is clearly <5 mm. **b** Corresponding 2D image shows internal hemorrhoids with soft issue attenuation surrounding the rectal catheter (*white arrow*)

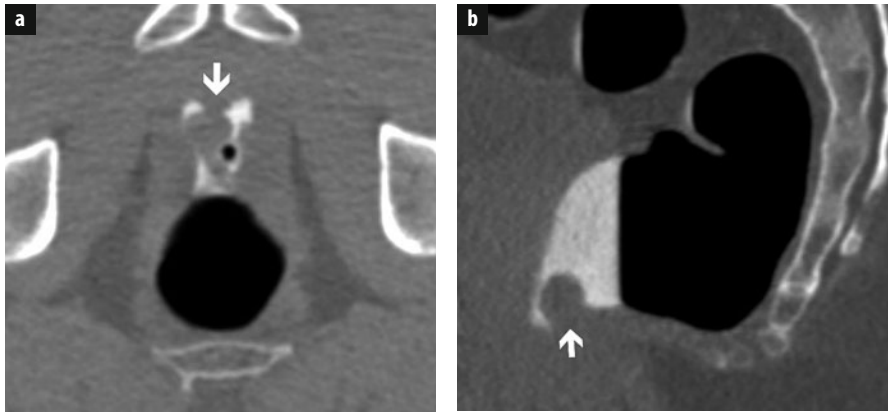


**Fig. 3 a, b.** **a** Large filling defect close to the rectal catheter and anal margin (*white arrow*). Because of this location and the fluid, this lesion is difficult to detect. **b** Sagittal reformat showing a large polypoid defect highly suspicious of a large polyp (*white arrow*). Rectoscopy revealed a large, atypical hemorrhoid. This lesion was only visible after deflation of the balloon

## Anorectal Region

The rectum is particularly difficult to inspect. Special attention is needed for the anal margin. This is done by turning the virtual camera backward toward the anal margin. Good visualization of this segment may be hampered by the rectal catheter and its small insufflated balloon, which prevents dislocation from the rectum. To obtain a good view of the region, it is mandatory to deflate the balloon before the second acquisition. Besides a true polyp or tumor, several tumor-like conditions are possible at and around the anal margin [8-10].

### *Rectal Folds*

The rectum presents with a longitudinal fold arising from the anal margin (rectal bar). This fold is located anteriorly to the rectal catheter (at 12 o'clock). In 2D, it may mimic a polyp; 3D shows its exact nature. Sometimes, more than one fold is present.

### *Hypertrophied Anal Papilla*

The hypertrophied anal papilla is a benign polypoid protrusion arising on the dentate line. It is not possible to differentiate this lesion from a true polyp. Therefore, whenever the lesion is ⩾6 mm, rectoscopy is necessary (Fig. 2).

### *Internal Hemorrhoids*

Internal hemorrhoids are varicose dilatations and arise from the superior hemorrhoidal plexus, superior to the dentate line. They typically appear as smooth filling defects surrounding the rectal catheter, with thin folds converging toward the catheter. They frequently change in appearance on both acquisitions (Fig. 2). In their atypical appearance, they appear as a polypoid lesion, which makes them look like a true polyp. Under this condition, rectoscopy is again necessary whenever the defect is ⩾6mm (Fig. 3).

### *Rectal Varix*

A rectal varix is a dilated submucosal vein causing a long, serpiginous filling defect. It frequently is less prominent, with better distension of the rectum in the prone position. The varix may appear elsewhere in the colon. It must be noted that, exceptionally, a polyp may also present as a serpiginous filling defect.

## Venous Bleb

A venous bleb is a small, venous malformation that may mimic a true polyp.

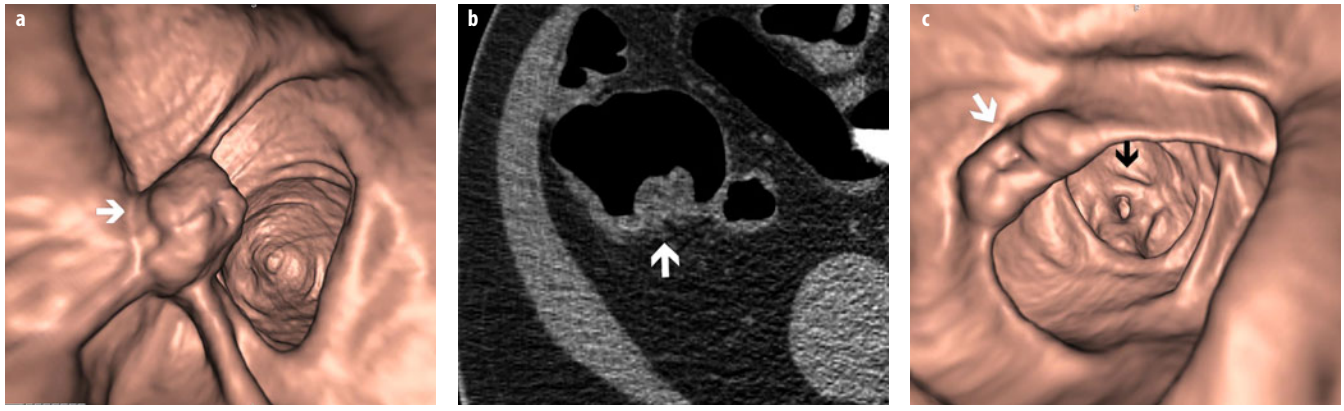


**Fig. 4 a-c.** **a** A 3D view of an enlarged ileocecal (IC) valve with distorted aspect in supine acquisition (*white arrow*). **b** Corresponding 2D view shows the enlarged IC valve with slightly inhomogeneous soft tissue density (*white arrow*). **c** Prone acquisition shows a normal IC valve (*white arrow*). On the background, a spasm with typical contraction of the taeniae gives a triangular appearance to the lumen of the ascending colon (*black arrow*)

Troubleshooting the anorectal region:
- Take special care to inspect the anal margin.
- Know the several possible benign conditions.
- Deflate the balloon before the second acquisition.
- Be strict: in case of inconclusive diagnosis, perform OC whenever a lesion is ⩾6mm.

## Cecum

First identify both ileocecal (IC) valve and appendix when examining the cecum.

As with the rectum, the cecum is challenging to examine. It is a blind-ending segment, with a lumen wider than the other colonic segments. Furthermore, special attention is needed to assess the IC valve and appendix [11].

### Ileocecal Valve

The normal IC valve consists of two folds (upper and lower lip) converging at both sides in a prominent fold, the frenulum. These characteristics make it an anatomical landmark of the cecum, which must be identified invariably. The IC valve may have several benign appearances, which must be differentiated from malignant disease.

#### *Lipomatous Transformation*

In case of lipomatous transformation, both lips of the IC valve are infiltrated with fatty tissue. On 3D, the IC valve is moderately to excessively enlarged but still shows its normal lip structure. Diagnosis is readily confirmed on 2D, with the IC valve showing typical fat attenuation (0/–100 HU).

#### *Papillary Transformation*

In case of papillary transformation, diagnosis is not always straightforward. This entity is caused by protrusion of the terminal ileum into the IC valve and is considered a normal functional status, with the IC valve preventing fluid reflux from the colon into the ileum. The normal lip-like structure becomes distorted and may appear as a bulky mass, with difficult distinction of the two lips. In 3D, a central depression is sometimes present, corresponding to the terminal ileum. Mostly, this condition still shows smooth delineation of the IC valve with some fatty infiltration on 2D imaging. The appearance frequently is different when comparing both acquisitions (Fig. 4). Sometimes a tumor is mimicked, making OC necessary.

Troubleshooting the IC valve:
- Check the IC valve in 3D and 2D on both acquisitions.
- Identify the morphology.
- Check the attenuation.

### Appendix

The appendix is another landmark in the cecum and appears as a small orifice or depression frequently located in the vicinity of a small fold. It is obvious that we need to inspect the entire appendix in 2D. Therefore, it is mandatory to know whether the patient underwent previous appendectomy. Normally, the appendix presents as a thin-walled, tubular structure, which may be filled with air or contrast. Any global or focal wall thickening should prompt further investigation to rule out malignancy (= appendectomy). Tumoral conditions of the appendix are rare and frequently asymptomatic [12].

#### *Mucocele of the Appendix*

An appendiceal mucocele corresponds to a mucus-dilated appendix. It typically is contiguous with the appendix and may present with a mural calcification. When close to the cecum, it frequently produces an extrinsic impression. This entity may correspond to a benign cyst or an obstructed appendix. A malignant cause must always be excluded. Therefore, surgery (appendectomy/right hemicolectomy) is necessary.

#### *Intussusception of the Appendix*

Intussusception of the appendix is mostly partial and asymptomatic. It produces a polypoid appearance in 3D and 2D, frequently reducing on one of both acquisitions. If not, and if the luminal defect situated at the appendiceal orifice is ⩾6mm, a true tumoral lesion must be excluded with OC.

#### *Inverted Appendiceal Stump*

Following inversion-ligation appendectomy, an older appendectomy technique, the appendiceal stump may cause a pseudopolypoid appearance. This entity cannot be differentiated from a true tumoral lesion, and once again, whenever the lesion is ⩾6 mm, OC is necessary. Furthermore, on rare occasions, a polyp or malignancy may develop in the stump [13].

Troubleshooting the appendix:
- Suspicion of significant appendicular pathology should prompt further investigation.
- Lesions ⩾6 mm at the appendicular orifice, with soft tissue attenuation, need colonoscopy.
- Tumors may develop in an appendicular stump.

## Diverticular Disease

- Myochosis causes restricted distension of the sigmoid.
- Diverticular disease creates many prominent folds with blind spots.
- Polyp detection becomes more challenging.

Diverticular disease is frequent in the Western population, with a frequency of ~30% at age 50 years and >50% at age 60 years. It is mostly located in the sigmoid. Diverticulosis is a challenge for every CTC-reader. In its early stage, the disease is characterized by myochosis: a triad of muscular thickening, taeniae shortening, and luminal narrowing. This causes restricted colonic distension, with prominent, semilunar folds and deep haustrations, making CTC interpretation more challenging. In 3D, there is restricted visualization behind the folds (blind spots), with the deep haustrations increasing these blind spots and requiring dedicated 3D inspection by turning the virtual camera around the folds. To improve colonic distension, the use of Buscopan is justified. Distension can also be improved with an additional acquisition of the affected segment with the patient in the right or left lateral decubitus position.

With myochosis progression, diverticula appear, and semilunar folds become more prominent. In 2D, diverticula are characterized by gas-filled outpouchings on the colonic wall. In 3D, they appear as a complete dark ring, which is in contrast to a polyp, which mostly presents as an incomplete or vague dark ring when viewed en face. Sometimes, this may be confusing. However, comparing 3D with 2D imaging makes differentiation straightforward.

Diverticular disease gives rise to pseudopolypoid lesions [14].

Troubleshooting diverticular disease:
- Combine 3D with 2D imaging to inspect diverticular segments.
- Look well behind the folds.
- Improve colonic distension with right/left decubitus acquisition – use Buscopan®.

### Diverticular Fecalith

Frequently, the diverticulum is impacted with fecal residue. The stool is not expelled and dries into a diverticular fecalith, protruding more or less into the colonic lumen. This causes a polypoid defect on 3D, with an aspecific aspect in the majority of cases. The solution is provided by 2D imaging in which findings are highly characteristic at all times: the diverticular fecalith almost invariably presents as a white (hyperdense) ring with hypodense center, most frequently with an air inclusion. Occasionally, a diverticular fecalith may invert into the colonic lumen, presenting as a large polyp in 3D.

### Inverted Diverticulum

A diverticulum may invert into the colonic lumen. Although it is infrequent, the radiologist must be aware of this possibility. In 3D, the inverted diverticulum resembles a true polyp. Sometimes, a central umbilication can be distinguished. In 2D, the inverted diverticulum sometimes presents with an air inclusion, which may correspond to the central umbilication. The lesions may also present with fat attenuation due to inclusion of perisigmoidal fat. Under this appearance, diagnosis is unequivocal. This is also the case whenever the diverticulum presents in the inverted status on one acquisition and in the reduced, normal status, on the other (Fig. 5). If no fat and/or air is present and there is no change in aspect, the luminal defect cannot be differentiated from a true polyp. In case this defect is ⩾6 mm, OC must be recommended.

### Polypoid Mucosal Prolapse Syndrome

Because of repetitive spasm, the mucosa thickens and elongates, causing an excess of mucosa, prolapsing in the colonic lumen as a redundant fold. This mucosal protrusion may change in shape. On both 3D and 2D, the lesion appears polypoid and cannot be differentiated from a true lesion. So again, whenever the luminal defect is ⩾6 mm, OC is necessary. The polypoid mucosal prolapse is histologically similar to the prolapse described in solitary rectal ulcer syndrome.

Troubleshooting the diverticular pseudopolyps:
- Look for the typical characteristics:
  - Diverticular fecalith: hyperdense ring with hypodense center.
  - Inverted diverticulum: air/fat inclusion, subtle depression, reducing on one acquisition.
  - Mucosal prolapse: morphology change, rare, diagnosis on CTC not possible.
- Be strict in case of equivocal findings: colonoscopy if the lesion ⩾6 mm.

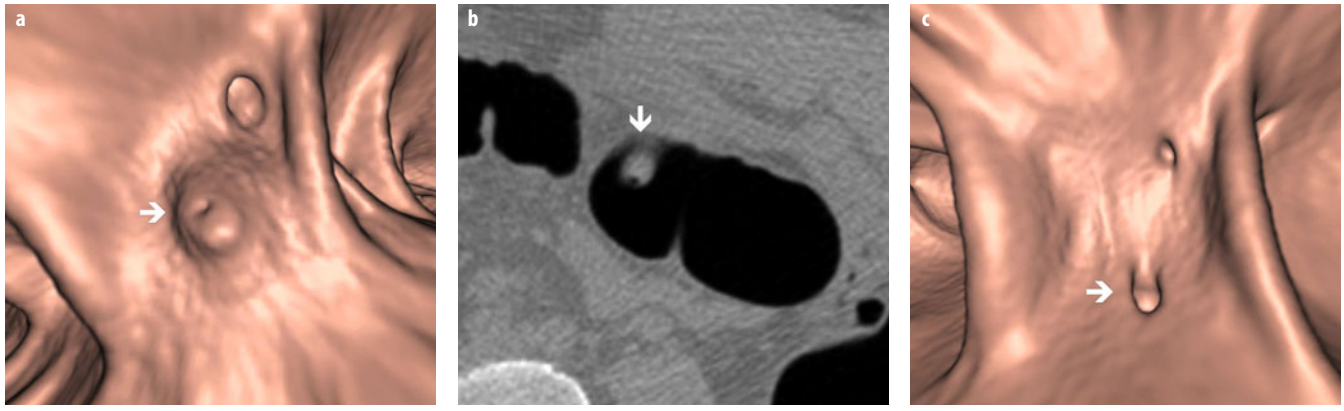


**Fig. 5 a-c.** **a** A 3D view of the sigmoid in prone position, showing a polypoid defect with central pinpoint depression (*white arrow*). **b** Corresponding 2D view showing a polypoid defect with air inclusion (*white arrow*). There is a normal diverticulum nearby. **c** The 3D view of the same segment in supine position shows two normal diverticula: the polypoid lesion with the central depression has become a diverticulum: inverted diverticulum (*white arrow*)

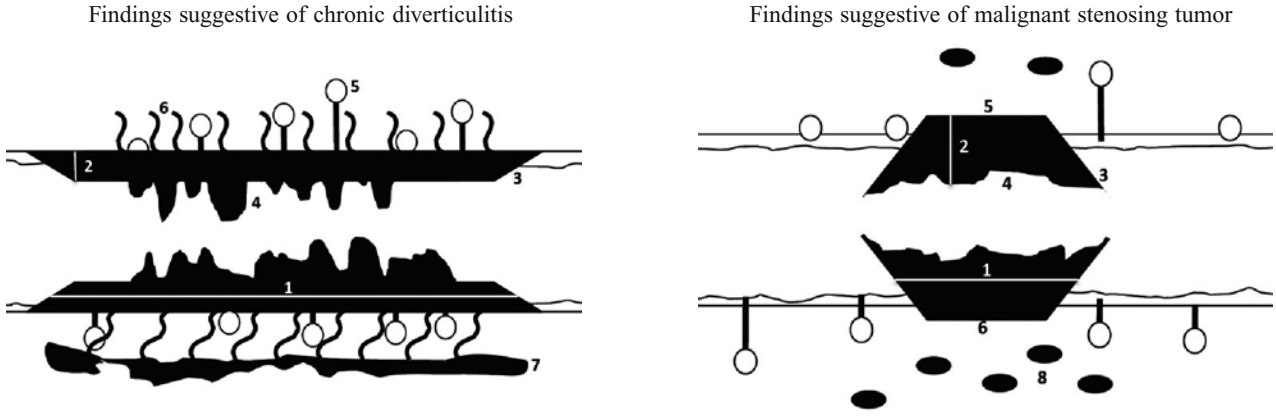


**Fig. 6.** Imaging characteristics suggestive of chronic diverticulitis on the left and of malignant stenosing tumor on the right. It is extremely important to note that these signs interfere with each other, making exact diagnosis difficult and sometimes impossible

## Chronic Diverticulitis/Fibrosis or Malignant Tumor?

- Imaging characteristics are not 100% specific, with signs frequently interchanging.
- Look for a combination of signs.
- Don't take any risk: recommend further investigation in case of doubtful imaging findings.

Patients with repetitive episodes of acute diverticulitis may present with short or long segments of important wall thickening with luminal narrowing. The patient presents with vague abdominal symptoms or no relevant symptoms at all. Differential diagnosis between fibrosis and a malignant stenosing tumor is not straightforward, and confusion may be as high as 50%. Each entity presents with imaging characteristics that, unfortunately, are not 100% specific, and interference of signs is quite frequent. Characteristics are presented in Fig. 6. In a recent study comparing both entities, we could conclude that it seems reasonable that the presence of diverticula in the affected segment, together with wall thickening over a rather long segment, a thickened fascia sign (mesosigmoid) without lymphadenopathies, cone shaped or tapered margins, and presence of more or less thickened mucosal folds, is likely to improve diagnostic accuracy for chronic diverticulitis (Fig. 7 a, c). On the inverse, absence of diverticula and the thickened fascia sign in a more prominent wall thickening, with short extension, shoulder formation or overhanging edges and distorted

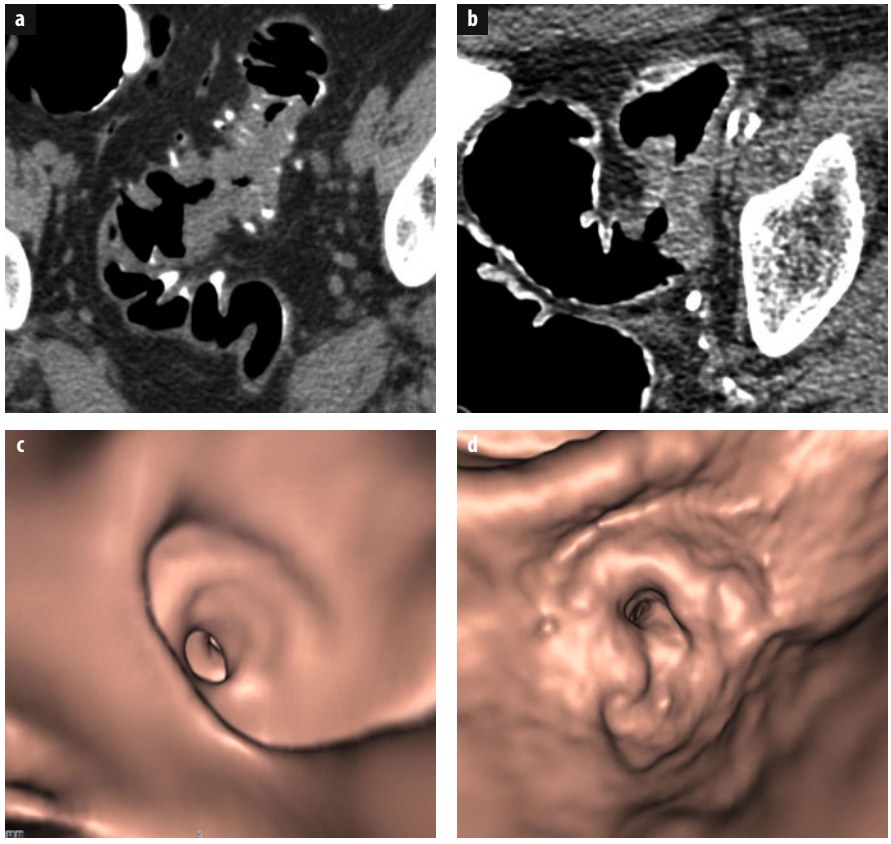


**Fig. 7 a-d. a, c** Axial image of the sigmoid showing a rather long segment with wall thickening, with diverticula throughout the thickened wall and with tapered or cone-shaped margins: chronic diverticulitis. **b, d** Axial image of the sigmoid showing a shorter segment with wall thickening, without diverticula and with shoulder formation and overhanging edges: malignant stenosing tumor

folds, are more in favor of a stenosing malignancy (Fig. 7 b, d). In case of wall thickening in patients with chronic abdominal discomfort, it is frequently decided to resect the affected segment and more so if the affected segment shows changes in imaging characteristics [15].

Troubleshooting the chronic diverticulitis versus malignancy issue:
Be aware of the overlap of imaging findings.
If present simultaneously, most specific signs for chronic diverticulitis are:
- Presence of diverticula.
- Cone-shaped margins
- Thickening of the mesosigmoid.
- Absence of lymphadenopathies.

## Benign Submucosal Tumors

Some benign submucosal tumors cannot be differentiated from significant pathology.

### Lipoma

Lipoma is the most frequent submucosal tumor in the colon. In 3D, it is characterized by a sessile, pedunculated, or even flat luminal defect with smooth borders. When sessile, it mostly has a broad base on the colonic wall. Some pedunculated lipomas present with a long pedicle and make a considerable positional shift between the two acquisitions. Large lipomas may be the source of intussusception. Final diagnosis is typically made on 2D, with the lesion showing a fat attenuation. Frequently, the mucosal layer covering the lipoma is depicted as a thin layer with soft tissue attenuation.

### Rare Submucosal Tumors

Lymphangiomas are rare, benign lesions. They may be simple, cavernous, or cystic. If cystic, it appears as cystic on 2D. However, whenever the lesion is ⩾ 6 mm, OC is necessary so that a true tumoral lesion is not overlooked (Fig. 8). There are many other rare submucosal tumors, none of which is differentiated from true polyps or tumors: leiomyoma, hemangioma, ganglioneuroma [16].

Troubleshooting benign submucosal tumors:
- Lipoma: polyp with fat attenuation, sometimes with a mucosal line.
- Lymphangioma: rare, sometimes cystic; take care if ⩾6 mm: colonoscopy.

### Pneumatosis Cystoides Coli

Pneumatosis coli is harmless in the context of CTC.

Pneumatosis coli is primary or secondary and presents with submucosal or subserosal air pockets. The primary

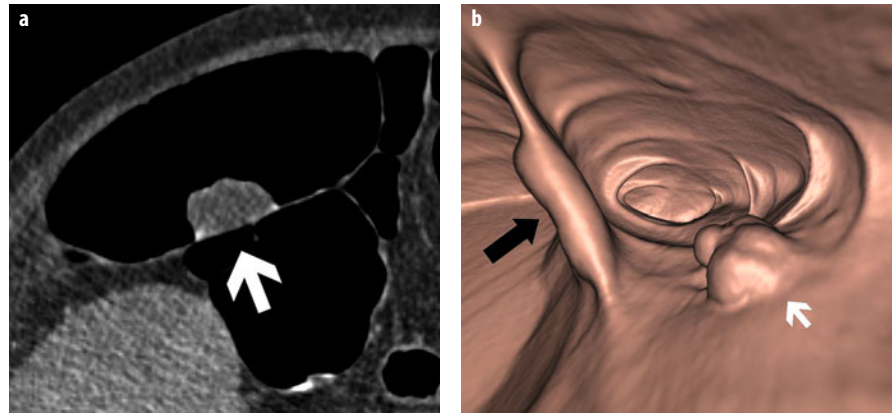


**Fig. 8 a, b.** A large polyp in the ascending colon prompting colonoscopy (*white arrow*). This lesion measures 2.5 cm and is hence suggestive of advanced adenoma. The large polyp was confirmed and diagnosed as a cystic lymphangioma at pathology. *Black arrow*, IC valve

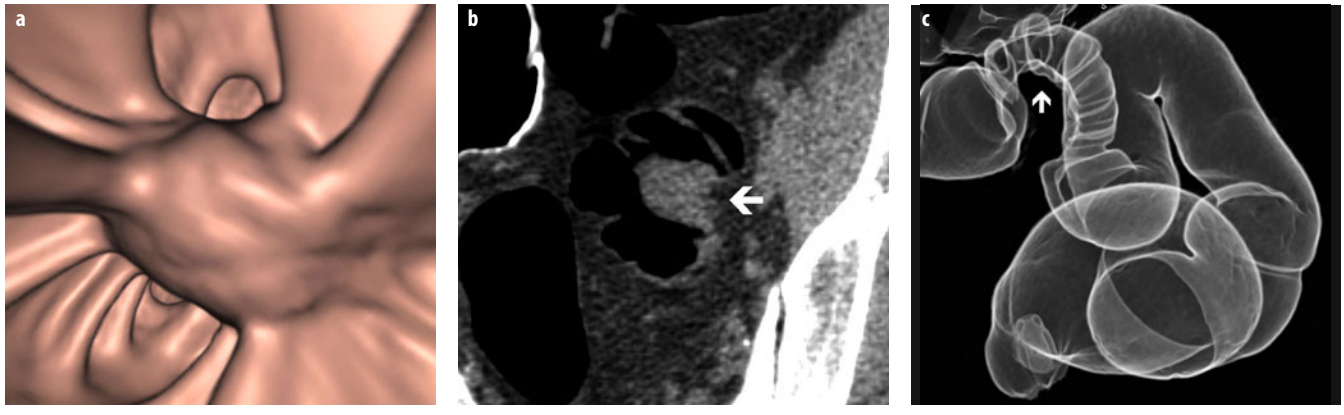


**Fig. 9 a-c.** **a** A 3D view of the sigmoid showing a thickened fold with nodular appearance in a 38-year-old woman with suspicion of endometriosis. **b** Corresponding 2D view shows a the thickened fold with homogeneous soft tissue density (*white arrow*). Image highly suggestive of deep endometriosis with luminal extension, confirmed at colonoscopy. **c** Tissue transition projection (TTP) image showing typical appearance of endometriosis: eccentric defect with slightly nodular appearance and luminal appearance (*white arrow*)

type is benign and self-limiting. The secondary type can be related to bowel-wall necrosis and may need treatment depending upon clinical presentation. Both types present with polypoid filling defects on 3D; 2D depicts air pockets. In 3D, a shine-through artefact may occur because of a segmentation artefact caused by the thin wall of the air pocket. This situation is characterized by incomplete depiction of the pocket wall. In the primary type, air pockets tend be larger, smooth, polypoid-filling defects. This type may be related to the $CO_2$ insufflation during CTC. This is a totally innocuous, asymptomatic, and self-limiting "complication", needing no further action [17]. In the secondary type, air pockets tend to be smaller and longitudinal.

Troubleshooting pneumatosis coli:
- Submucosal/subserosal air pockets.
- Mostly right sided.

### Endometriosis

Endometriosis is a condition related to growth of endometrium outside the uterus. Colonic involvement occurs mostly in the rectosigmoid and rarely in the cecum. This occurs via peritoneal implants of endometrial tissue. These implants may develop transserosal growth with submucosal extension. From there, intraluminal extension may occur in a small number of patients. According to invasion grade, CTC shows different aspects. With serosal/submucosal infiltration, there is mural thickening of a fold, with a marginal defect showing smooth delineation. This may cause loss of distension, with eccentric or circumferential narrowing. In case of extension to the mucosa, the folds become irregular and end in a polypoid lesion or mass (Fig. 9) [18].

## Miscellaneous

### Postoperative Colon

According to the technique used (end to end or side to end), the anastomosis will have a particular morphology. It should show a smooth transition with, occasionally, a subtle circumferential narrowing or ridge. In 2D, the surgical staples, if used, are easily identified. Sometimes, the staples protrude into the colonic lumen, causing a luminal defect in 3D and easily identified in 2D. Granular tissue with a polypoid aspect may develop at the anastomosis.

These pseudopolyps cannot be differentiated from true polyps. In the postoperative period, fibrosis may develop, causing a pseudotumoral narrowing at the anastomosis. CTC cannot differentiate from tumoral recurrence, and OC must be performed. One type of scar can be correctly identified on CTC. It consists of a diaphragm-like concentric narrowing of the colonic lumen, which occasionally leads to obstruction. This diaphragm develops on the stapler line [19].

- Postoperative strictures with fibrosis cannot be differentiated from tumoral recurrence.
- A diaphragm-like scar is a benign complication.

### Extrinsic Impression

Extracolonic structures may be the source of pseudopolypoid lesions arising anywhere in the colon. These are mostly normal structures: spleen, liver, kidneys, small bowel, rib, and others. Sometimes, the origin is a benign tumor: uterine fibroid, renal cyst, and others. The exact diagnosis is readily made by comparing 2D with 3D.

Troubleshooting the extrinsic impression:
Always compare 3D with 2D findings.

### Nonsteroidal-Anti-Inflammatory-Drug-Induced Colopathy: Colonic Diaphragm Disease

Chronic use of nonsteroidal anti-inflammatory drugs (NSAIDs) may cause a colopathy. This is characterized by a stricture presenting with inflammatory changes, thus making it difficult to differentiate from a malignancy. The stricture may also have a diaphragm aspect [20].

Be aware of the rare colonic diaphragm disease: think of NSAID abuse.

## References


1. Levin B, Lieberman DA, McFarland B et al. American Cancer Society Colorectal Cancer Advisory Group; US Multi-Society Task Force; American College of Radiology Colon Cancer Committee (2008) Screening and surveillance for the early detection of colorectal cancer and adenomatous polyps, 2008: a joint guideline from the American Cancer Society, the US Multi-Society Task Force on Colorectal Cancer, and the American College of Radiology. CA Cancer J Clin 58:130-160.
2. Halligan S (2013) CT colonography for investigation of patients with symptoms potentially suggestive of colorectal cancer: a review of the UK SIGGAR trials. Br J Radiol 86:20130137.doi.
3. Neri E, Halligan S, Hellström M et al (2013) The second ESGAR consensus statement on CT colonography. Eur Radiol 23: 720-729.
4. Endoscopic Classification Review Group (2005) Update on the Paris classification of superficial neoplastic lesions in the digestive tract. Endoscopy 37:570-578.
5. Ahnen DJ (2011) The American College of Gastroenterology Emily Couric Lecture—the adenoma-carcinoma sequence revisited: has the era of genetic tailoring finally arrived? Am J Gastroenterol 106:190-198.
6. Limketkai BN, Lam-Himlin D, Arnold CA et al (2013) The cutting edge of serrated polyps: a practical guide to approaching and managing serrated colon polyps. Gastrointest Endosc 77:360-375.
7. Lefere P, Silva C, Gryspeerdt S et al (2013) Teleradiology based CT colonography to screen a population group of a remote island; at average risk for colorectal cancer. Eur J Radiol 82: e262-267.
8. Lefere P, Gryspeerdt S (2011) CT colonography: avoiding traps and pitfalls. Insights Imaging 2:57-68.
9. Mang T, Gryspeerdt S, Schima W et al (2013) Evaluation of colonic lesions and pitfalls in CT colonography: a systematic approach based on morphology, attenuation and mobility. Eur J Radiol 82:1177-1186.
10. Dachman AH, Lefere P, Gryspeerdt S et al (2007) CT colonography: visualization methods, interpretation, and pitfalls. Radiol Clin North Am 45:347-359.
11. Silva AC, Beaty SD, Hara AK et al (2007) Spectrum of normal and abnormal CT appearances of the ileocecal valve and cecum with endoscopic and surgical correlation. Radiographics 27:1039-1054.
12. Pickhardt PJ, Levy AD, Rohrmann CA Jr et al (2003) Primary neoplasms of the appendix: radiologic spectrum of disease with pathologic correlation. Radiographics 23:645-662.
13. Johnson EK, Arcila ME, Steele SR (2009) Appendiceal inversion: a diagnostic and therapeutic dilemma. JSLS 13:92-95.
14. Lefere P, Gryspeerdt S, Baekelandt M et al (2003) Diverticular disease in CT colonography. Eur Radiol 13 Suppl 4:L62-74.
15. Gryspeerdt S, Lefere P (2012) Chronic diverticulitis vs. colorectal cancer: findings on CT colonography. Abdom Imaging 37:1101-1109.
16. Pickhardt PJ, Kim DH, Menias CO et al (2007) Evaluation of submucosal lesions of the large intestine: part 1. Neoplasms. Radiographics 27:1681-1692.
17. Pickhardt PJ, Kim DH, Taylor AJ (2008) Asymptomatic pneumatosis at CT colonography: a benign self-limited imaging finding distinct from perforation AJR Am J Roentgenol 190:W112-117.
18. Jeong SY, Chung DJ, Myung Yeo D et al (2013) The usefulness of computed tomographic colonography for evaluation of deep infiltrating endometriosis: comparison with magnetic resonance imaging. J Comput Assist Tomogr 37:809-814.
19. Mang T, Schima W (2013) Colorectal anastomoses. In: Mang T, Schima W (Eds) CT colonography: a guide for clinical practice. Thieme, Stuttgart, New York.
20. Munipalle PC, Garud T, Light D (2013) Diaphragmatic disease of the colon: systematic review. Colorectal Dis 15:1063-1069.

# Diseases of the Colon and Rectum: CT Colonography

C. Dan Johnson[1], Perry J. Pickhardt[2]

[1] Mayo Clinic, Scottsdale, AZ, USA
[2] University of Wisconsin, Madison, WI, USA

## Introduction

The public health need for colorectal cancer screening is compelling. Colorectal cancer is common, accounting for approximately 50,000 deaths yearly in the USA [1]. The benign precursor, adenoma, can be detected by several different imaging techniques and removal can prevent malignant transformation. The approximately 10-year polyp dwell time allows ample opportunity for patients to be screened and polyps detected and removed. Potentially, under ideal screening circumstances, an entire class of cancers could be prevented. However, barriers exist to ideal screening, including suboptimal performance of many existing colorectal screening tests, reluctant compliance by patients to follow recommended screening guidelines, and variable insurance coverage of examination charges. In many ways, computed tomography colonography (CTC) approaches an ideal screening test by addressing issues and problems inherent with other techniques. This syllabus highlights many key issues for CTC.

## Performance

The performance of CTC has undergone exhaustive testing. The Department of Defense (DoD) trial conducted by Pickhardt et al. demonstrated sensitivity similar to colonoscopy [2]; however, concerns were raised that community practices might not be able to replicate these results. The National CTC trial findings were similar to those of the Pickhardt trial and have reassured many groups that the test can be performed with high accuracy in both academic and private-practice settings [3].

Training and preferably testing of radiologists in CTC is a requirement for optimal reader performance [4]. Participation in a dedicated training program is recommended. These training sessions should provide enough time for the radiologist to become facile with a specific colonography software package and experience interpreting at least 50 proven cases. Polyp-detection testing will allow individuals an opportunity to assess whether additional training is needed before clinical implementation. In order to continue to improve reader performance, it is recommended that patients who undergoing both CTC and subsequent colonoscopy be reviewed retrospectively to assess for CTC false-positive and false-negative detections. This quality improvement review offers a rich experience for learning and gaining expertise, confidence, and competence. Strict adherence to state-of-the art CTC protocol requirements is also recommended, including stool- and fluid-tagging regimens, mechanical insufflation of the colon, thin-section data acquisition, and low-dose CT techniques [5]. It is clear that meticulous attention to all aspects of the examination and interpretation is required to achieve the best results.

## Acceptance

Approximately 40 million US adults aged ⩾50 have not undergone a sigmoidoscopy or colonoscopy within the previous 10 years or a fecal occult blood test (FOBT) within the preceding year [6]. The major disincentive for patients undergoing a full structural colorectal examination is the laxative purgation [7]. Work is being done to reduce the burden of laxation either with the use of a partial colon preparation [8] or without cathartic preparation [9]. Although not considered standard of care, evidence from feasibility trials is promising and may translate to better patient acceptance.

The advantages of CTC include the lack of required sedation and intravenous line placement, a quick return to work following the examination, and the convenience of no driving restrictions following the test; the disadvantage is that if a significant polyp is identified, patients must undergo colonoscopy and polypectomy. If same-day colonoscopy is not offered, then the patient must undergo a second bowel preparation, spend another day away from work, and experience added worry and inconvenience. In a screening population, including false-positive interpretations, the prevalence of patients being referred from CTC to colonoscopy for polypectomy

*Diseases of the Abdomen and Pelvis 2014-2017*,
DOI: 10.1007/978-88-470-5659-6_7 

is 12% when a 6-mm threshold is applied [2, 3]. This translates into an 88% chance that an individual patient will not require a second procedure, thereby mitigating concerns for redundancy. Those with a high likelihood of polyps may best be triaged to colonoscopy screening.

## Safety

The main risk for patients at CTC is colorectal perforation. The symptomatic perforation rate is estimated to be 1:20,000 examinations, and likely safer when screening patients [10]. In contrast, colonoscopy perforation rates are in the range of 1:1,000 [11], often but not always related to biopsy procedures. Bleeding can also occur following colonoscopy intervention and is more common than perforation.

Radiation risk from a CTC examination is of public concern. It is unfortunate that the risk associated with the low radiation dose required for CTC is misunderstood. The standard dose at CTC represents about 25-50% of the dose used for a standard body CT examination. This results in an average dose of approximately 2.5-5 mSv, similar to annual environmental exposures in many locales, which is without known adverse health effects. Doses at CTC can be significantly reduced further using new noise-reduction software (iterative reconstruction). The real risk of this small dose is unknown, but the Health Physics Society stated that doses in this range are associated with risks for the development of radiation-induced cancer that are either too small to measure or are nonexistent [12]. Even if a very small risk is assumed from radiation exposure at CT, it must be balanced against the risk of developing colon cancer (1:13) and the risks of other alternative procedures, including colonoscopy [13].

## Extracolonic Findings

Extracolonic abnormalities are common in patients of screening age [14, 15]. Although life-saving findings can be identified, most incidental findings are of little clinical significance but can potentially increase the cost of care if additional testing and treatment is recommended. A pragmatic approach to these findings is needed. Radiologists should only recommend follow-up studies for findings most likely to be of clinical significance. Clinicians will be grateful if within the radiological report additional testing is minimized and if patients are identified who might benefit from additional studies so recommendations can be made for them to receive optimal follow-up.

## Individual Responsibility

Maintaining high-quality radiological interpretations is a responsibility that each radiologist, each radiology practice, and the radiology specialty should assume. The American College of Radiology (ACR) has established a national CTC database within the National Radiology Data Registry (NRDR) [16]. Selected process and outcome metrics can be quickly entered online and compared with national benchmarks. These measures include process metrics related to the CT technique and the adequacy of patient preparation; outcome metrics are related to colon perforation, true-positive and false-positive rates for large ($\geqslant$1 cm) polyps, and the prevalence of significant extracolonic findings. Radiology practices seriously concerned about providing the best care are encouraged to participate in this data registry and manage their practice so benchmark metrics are achieved.

A spirit of cooperation between radiologists and gastroenterologists is needed for optimal patient care. Guidelines must be jointly developed for the appropriate use of colonography and colonoscopy and for processes that efficiently transfer patients with polyps to from CTC to colonoscopy. Practices that can do this effectively will offer patients a service of high value and will likely find they are very busy.

## Conclusions

In summary, CTC is a well-validated examination and should be available clinically. Radiologists committed to performing the examination to the highest standard must obtain the necessary education and equipment. As radiologists, we have an obligation to educate and collaborate with referring physicians on the correct use of the technique. We must be vigilant that extracolonic findings are properly reported so that only highly suspicious lesions are recommended for additional follow-up testing. Lastly, a commitment to incorporate ongoing quality measures within daily practice will ensure that patients continue to receive the highest standards of care. Radiology has an exciting opportunity to serve the public and potentially reduce the incidence of a common cancer killer.

## References

1. Siegel R, Naishadham D, Jemal A (2012) Cancer statistics, 2012. CA Cancer J Clin 62:10-29.
2. Pickhardt PJ, Choi JR, Hwang I et al (2003). Computed tomographic virtual colonoscopy to screen for colorectal neoplasia in asymptomatic adults. New Engl J Med 349:2191-2200.
3. Johnson CD, Chen MH, Toledano A et al (2008) Accuracy of CT colonography for detection of large adenomas and cancer. New Engl J Med 359:1207-1217.
4. Fletcher JG, Chen MH, Herman BA et al (2010) Can radiologist training and testing ensure high performance in CT colonography? Lessons from the National CT Colonography Trial. AJR Am J Roentgenol 195:117-125.
5. Robbins JB, Kim DH (2013) Computed Tomographic Colonography: evidence and techniques for screening. Seminars in Roentgenology 48:264-272.

6. Centers for Disease Control and Prevention (2008) Vital signs: colorectal cancer screening among adults aged 50-75 years – United States, 2008. MMWR Morb Mortal Wkly Rep 808-812.
7. Beebe TJ, Johnson CD, Stoner SM et al (2007) Assessing attitudes toward laxative preparation in colorectal cancer screening and effects on future testing: potential receptivity to computed tomographic colonography. Mayo Clinic Proceedings 82:666-671.
8. Johnson CD, Kriegshauser JS, Lund JT et al (2011) Partial preparation computed tomographic colonography: a feasibility study. Abdom Imaging 36:707-712.
9. Johnson CD, Manduca A, Fletcher JG et al (2006) Noncathartic CT colonography with stool tagging: performance with and without electronic subtraction. AJR Am J Roentgenol 190:361-366.
10. Pickhardt PJ (2006) Incidence of colonic perforation at CT colonography: review of existing data and implication for screening of asymptomatic adults. Radiology 239:313-316.
11. Waye JD, Kahn O, Auerbach ME (1996) Complications of colonoscopy and flexible sigmoidoscopy. Gastrointest Endosc Clin N Am 6:342-377.
12. Radiation risk in perspective (2010) Position Statement of the Health Physics Society, http://hps.org/documents/risk_ps010-2.pdf
13. Hendee WR, O'Connor MK (2012) Radiation risks of medical imaging: separating fact from fantasy. Radiology 264:312-321.
14. Gluecker TM, Johnson CD, Wilson LA et al (2003) Extracolonic findings at CT colonography: evaluation of prevalence and cost in a screening population. Gastroenterology 124:911-916.
15. Pickhardt PJ, Kim DH, Meiners RJ et al (2010) Colorectal and extracolonic cancers detected at screening CT colonography in 10,286 asymptomatic adults. Radiology 255:83-88.
16. American College of Radiology. National Radiology Data Registry for CT Colonography, https://nrdr.acr.org/Portal/CTC/Main/page.aspx

# How to Perform and Report Magnetic Resonance Imaging for Pelvic Floor Dysfunction: An Interactive Case-Based Approach

Rania Farouk El Sayed

Radiology Department, Cairo University, Cairo, Egypt

## Introduction

"*You look for what you know,*
*and you see what you are looking for.*"

This statement summarizes all concepts a radiologist must understand to provide the gold standard of care. My fundamental aim in teaching this course is not just to review the literature with participants but to teach vividly, interactively, and practically, which is the way students learn best. It is my belief that if this course is successful, every radiologist in attendance will be capable not only of writing a full report based on solid scientific information but also of providing state-of-the art care for patients who present for magnetic resonance imaging (MRI) for pelvic floor dysfunction (PFD). Full competence means that the radiologist will know the steps for taking a full relevant medical history, can confidently determine which radiologic studies to order to allow for a detailed diagnostic report, and know the mandatory steps for patient preparation before sending the patient to the imaging table. In this context, this review is not written in the classical chronological order but in a way that takes the reader through the actual sequence of steps for providing radiologic care for a patient with PFD. Hence, this review takes a question-and-answer form. In addition, it follows the sequence of events for best practices in radiologic assessment, starting with obtaining a thorough medical history and ending with the most advanced phase of reporting MRI findings.

The aims of this chapter are to provide a comprehensive review of MRI anatomy of the pelvic floor, which patients with PFD can benefit most from MRI, how to perform the MRI examination, and how to report MRI findings to best meet the needs of the urologist, gynecologist, and proctologist who will treat the patient.

## Learning Objectives

The objectives of this chapter are to provide the radiologist with the following skills:

- To learn how to perform and tailor MRI protocols according to specific types of main PFD
- To understand the essential anatomic, physiologic, and pathologic information necessary for reporting data for a case of PFD
- To identify the types of defects in each pelvic-support system and how to classify them according to relation with urethral, vaginal, or anal sphincter complex
- To practice reporting MRI findings in a systematic way that synthesizes data for ease of use by clinicians from several different subspecialties.

## How to Perform and Tailor MRI Protocols According to Type of Pelvic Floor Dysfunction

### History Taking

- With increasing reliance on sophisticated medical technology, it is easy to overlook the value of a patient's history in making clinical decisions. This is a particular challenge in the field of reconstructive pelvic surgery, in which anatomic aberrations are often striking but understanding the symptoms related to them is inadequate.
- Symptoms of PFD range from vague low back pain to major fecal incontinence and urinary incontinence (UI). When a patient presents for evaluation, she may be unaware that many of her symptoms may be related to PFD. The clinician should elicit a comprehensive history encompassing all pertinent areas. Symptoms are divided arbitrarily into different areas, although symptoms of all types often coexist in the same individual [1]:
  - Urinary disorders
  - Fecal disorders
  - Sexual dysfunction
  - Pelvic discomfort.

### Patient Preparation

- All patients undergo a cleansing rectal enema (using warm water) the night before the MRI examination.

*Diseases of the Abdomen and Pelvis 2014-2017*,
DOI: 10.1007/978-88-470-5659-6_8 

- For imaging the urinary bladder, patients are asked to void 2 h before the examination [2].
- With the use of 60-ml syringes, 90-120 ml of ultrasound (US) gel is placed into the rectum.
- The MRI protocol requires no oral or intravenous administration of contrast agents.
- The key element of MRI in PFD is to image the patient during maximal strain and rectal evacuation in one or more planes [3]. Patients require coaching to achieve maximal pelvic strain and defecation because pelvic organ prolapse (POP) often is only evident when a patient strains and abdominal pressure increases.

## Imaging

### Patient Position

- The patient is positioned on the MRI table with a multicoil array wrapped low around the pelvis.
- For comfort, the patient may want to bend the knees to facilitate evacuation of the gel.
- A pad is placed under the patient to avoid contamination of the MRI table; also, the pad adds more comfort to the patient when evacuating the rectum.

### Imaging Protocol

#### *Acquisition of Static MRI*

*Imaging Parameters*

- There is no standardized protocol for MRI of patients with PFD. However, the following is an example of the PFD protocol used at my institution [2], modified from my institution's original protocol to ameliorate patient complaints. We perform MRI using a pelvic phased-array coil and a 1.5-T MRI unit (Gyroscan PowerTrak 6000, Philips Medical Systems, Best, The Netherlands).
- Static images of the pelvis are acquired in three planes using T2-weighted turbo spin-echo (TSE) sequences (TR/TE 5,000/132; FOV 240-260 mm; slice thickness 5 mm; gap 0.7 mm; number of signals acquired 2; flip angle 90°; matrix 512 × 512; acquisition time 3.12 min for each sequence).

*Tailoring Static Magnetic Resonance Imaging Techniques in Certain Pelvic Floor Dysfunctions*

- In patients reporting anal incontinence or obstructed defecation, the following sequences are added for assessment of the anal sphincter complex: T2-weighted BFFE images of the anal sphincter complex are obtained (9.0/4.0; FOV 220 mm; section thickness 3 mm; number of signals acquired 8; flip angle 45°; matrix 512 × 512; acquisition time 2.12 min). In this sequence, section orientation is parallel (in the coronal plane) and perpendicular (in the axial plane) to the plane of the anal canal.
- In patients with stress urinary incontinence (SUI) and/or POP, static images of the pelvis are acquired in the axial plane with T2-weighted turbo spin-echo (TSE) but with thin slices (2-mm thick) for better evaluation of the urethral ligament [4].

#### *Acquisition of Dynamic MRI Sequences*

*Imaging Parameters*

- Dynamic sequences are performed in the sagittal, axial, and coronal planes using a balanced fast-field echo (BFFE) sequence (TR/TE 5.0/1.6 ms; FOV 300 mm; slice thickness 6-7 mm; gap 0.7 mm).
- In each plane, five slices during six phases are acquired; each phase takes 10 s. The following six phases are acquired:
  - With the patient at rest
  - During contraction of the pelvic floor (the patient is instructed to squeeze her buttocks as if trying to prevent the escape of urine)
  - During mild straining
  - During moderate straining
  - During maximum straining
  - During a repeated maximum straining sequence to ensure a maximal Valsalva maneuver (the patient is instructed to bear down as much as she can, as though she is constipated and trying to defecate)
- In the sagittal plane, the patient is asked to evacuate the injected intrarectal gel.
- With this protocol, the technique of MRI parallels that of fluoroscopic examination.

*Tailoring Dynamic Magnetic Resonance Imaging Techniques in Certain Pelvic Floor Disorders*

The following tips were added to the basic dynamic protocol [2] during a recent research project by a PhD student of whom I am PhD mentor.

- We found it very helpful in patients with obstructed defecation to increase the amount of intrarectal gel to 160 ml. Most such patients, when given less gel, frequently cannot evacuate their rectum during MRI examination while lying supine. Many earlier studies note patients' inability to evacuate the rectum as one of the main drawbacks of MRI versus conventional defecography.
- It is reported in the literature that imaging the patient during conventional defecography in the anteroposterior (AP) position (coronal plane) enhances detection of intussusception in some patients. I asked the PhD student to modify our basic protocol [2] by adding an evacuation sequence in the coronal plane. However, she modified the angle of coronal MRI defecography from zero to sections taken parallel to the anal canal. By adding the coronal evacuation sequence with its modification she also enhanced and improved visualization of the anal canal lumen in its full craniocaudal plane, which made it easier to display the evacuation process in complete detail: most important, the detection of intussusception.

By the end of this part of the examination, the radiologist will have quite a large number of images and

sequences to report. However, even with the availability of many images, it is not possible for the radiologist to accurately describe the individual patient's anatomic anomalies and pathology without understanding at least the basic anatomy of the pelvic floor and PFD pathophysiology.

## Essential Anatomic, Physiologic, and Pathologic Information for Reporting Data in Pelvic Floor Dysfunction

### Basic Essential Anatomic Considerations

- The term pelvic floor is used broadly to include all structures supporting the abdominal and pelvic cavity.
- Conceptually, pelvic floor anatomy is commonly divided into passive and active structures [5, 6] (Fig. 1).

### Passive Support Structures

These structures comprise:
- Pelvic bones
- Supportive connective tissue of the pelvis, which consists of ligaments and endopelvic fascia.

### Active Support Structures

These structures comprise:
- Pelvic floor muscles
- Neurologic wiring that results in sustained (tonic) and intermittent voluntary muscle contractions during activity.

### Integrated Multilayer System

- These passive and active components of the pelvic floor function as an integrated multilayer system that comprises four principle layers (Fig. 2). From cranial to caudal, it consists of:
  - Supportive connective tissue of the endopelvic fascia and related structures

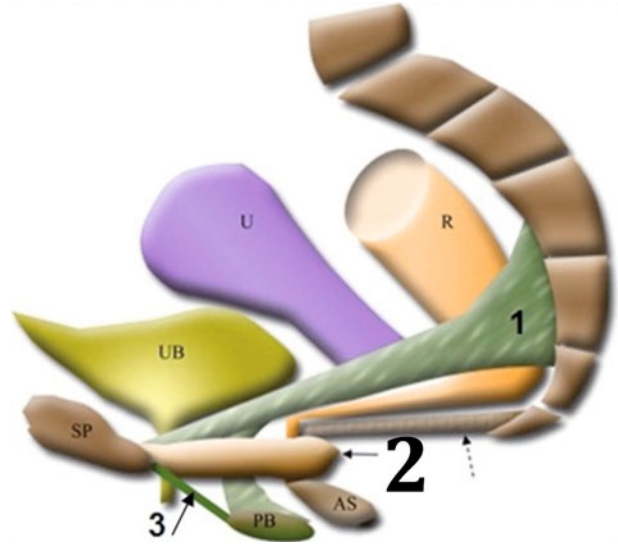


**Fig. 2.** Three-dimensional schematic drawing of the component of the pelvic floor integrated into a multilayer system, from cranial to caudal, consisting of: *1* endopelvic fascia, giving support to the uterus and upper vagina; *2* pelvic diaphragm, including the puborectalis (*solid arrows*) and iliococcygeus (*dashed arrow*); *3* urogenital diaphragm. *AS* anal sphincter complex, *PB* perineal body, *R* rectum, *SP* symphysis pubis, *U* uterus, *UB* urinary bladder. Reproduced from [7]

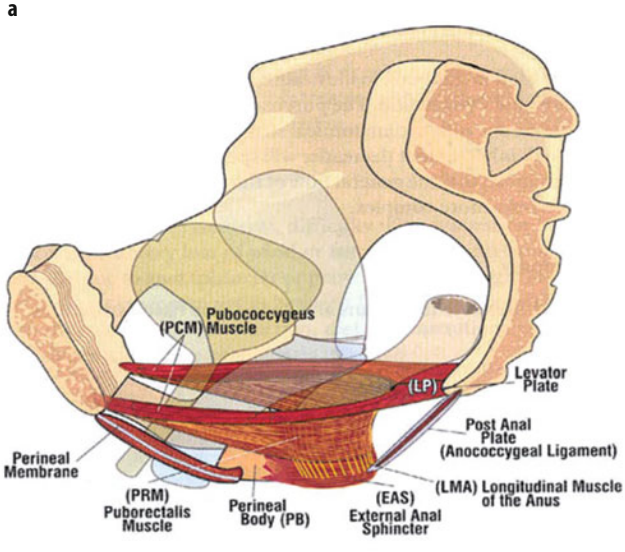


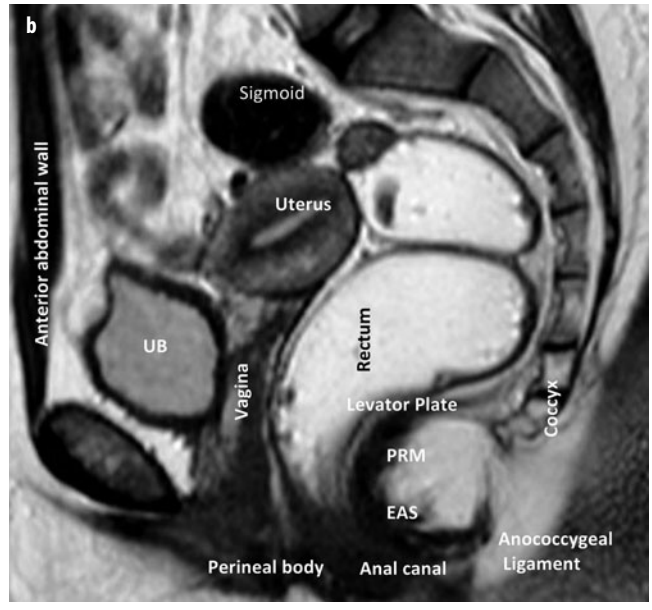


**Fig. 1 a, b.** Passive and active structures of the pelvic floor. **a** Pelvis with organs and muscles (muscles are shaded with *striations*). **b** The corresponding sagitall T2-weighted turbo spin-echo magnetic resonance images of pelvic organs, pelvic floor muscles, perineal body, and anococcygeal ligaments

  - Pelvic diaphragm
  - Perineal membrane (urogenital diaphragm)
  - Layer of superficial muscles comprising the external genital muscles
- The pelvic floor is given active support by the muscular contraction and passive elastic support by fascia and ligaments [5, 6].

*Supportive Connective Tissue of the Endopelvic Fascia and Related Structures*
The endopelvic fascia includes the parametrium and the paracolpium, giving support to the uterus and upper vagina, respectively. The paracolpium, which attaches the upper vagina to the pelvic walls, can be divided into three levels [5-8].

*Level I (Suspension)*
The portion of the vagina adjacent to the cervix (cephalic 2-3 cm of the vagina) is suspended from above by the relatively long connective tissue fibers of the upper paracolpium.

*Level II (Attachment)*
In the midportion of the vagina, the paracolpium become shorter and attaches the vaginal wall more directly to the arcus tendineus fascia pelvis at the lateral pelvic wall. This attachment stretches the vagina transversely between the bladder and rectum and has functional significance; the structural layer that supports the bladder (the pubocervical fascia) is composed of the anterior vaginal wall and its attachment through the endopelvic fascia to the pelvic wall.

*Level III (Fusion)*
Near the introitus, the vagina is fused laterally to the levator ani and posteriorly to the perineal body, whereas anteriorly it blends with the urethra. At this level, which corresponds to the region of the vagina that extends from the introitus to 2-3 cm above the hymenal ring, there is no intervening paracolpium between the vagina and its adjacent structures, contrary to the situation at levels I and II.

#### *Pelvic Diaphragm*

The pelvic diaphragm acts as a shelf supporting the pelvic organs and includes:

*Levator Ani Muscle*
This muscle consists of the puborectalis and iliococcygeus.

*Coccygeus Muscle*
It arises from the tip of the ischial spine, along the posterior margin of the internal obturator muscle. The fibers fan out and insert into the lateral side of the coccyx and the lowest part of the sacrum. This shelf-like musculotendinous structure forms the posterior part of the pelvic diaphragm.

#### *Urogenital Diaphragm*

- The urogenital diaphragm, or perineal membrane, is a fibromuscular layer directly below the pelvic diaphragm.
- Classically, it is described as a trilaminar structure, with the deep transverse perineal muscle sandwiched between the superior and inferior fascia.

#### *Superficial Muscle Layer*

This layer comprises the external genital muscles. At the most superficial of the four layers of pelvic floor lay the external genital muscles, comprising:
- Superficial transverse perinei
- Bulbospongiosus
- Ischiocavernosus.

## Pathophysiology of Pelvic Floor Dysfunction

### Urinary Incontinence

#### *Definition and Classification*

- As classified by the International Continence Society (ICS), UI of all types is defined as involuntary loss of urine that is both objectively demonstrable and socially or hygienically problematic for the patient [9, 10].
- Common subtypes of UI include SUI, urge urinary incontinence (UUI), and mixed urinary incontinence (MUI).
- Symptom of SUI is involuntary leakage on effort, whereas the symptom of UUI is involuntary leakage accompanied by or immediately preceded by urgency. MUI is a combination of SUI and UUI [11].
- SUI is the most common type of incontinence in women, with 86% of incontinent women presenting with the symptoms of either pure (50%) or mixed (36%) forms of SUI [10].

#### *Pathophysiology of Urinary Incontinence*

UI is a multifaceted problem. It may be:
- Extraurethral, caused by urinary fistula or an ectopic ureter
- Urethral, caused by bladder abnormalities or sphincteric abnormalities**.** Urethral incontinence can be divided into:
  - Urethral incontinence because of abnormal detrusor function (UUI)
  - Urethral incontinence because of urethral abnormalities (SUI).

#### *Pathophysiology of Stress Urinary Incontinence*

There are also several different types of SUI [11]:
- Because of poor urethral support (most common type)
- Despite normal urethral support, because of defective sphincteric function of the vesical neck and urethra (less common type).

*Damage to the Elements of the Urethral Support System*
This could occur because of urethral trauma, resulting from childbearing. Other common causes include:
- Menopause
- Medical conditions that increase intra-abdominal pressure
- Persistent heavy lifting or straining
- Neurologic damage
- Connective tissue disorders.

*Damage to the External Sphincter*
Damage to this system can be associated with the development of SUI. Any of the urethral sphincteric components may be diminished by:
- Loss of estrogen
- Surgical trauma
- Childbearing
- Drugs that alter muscular tone
- Vascular changes
- Local damage.

## Pelvic Organ Prolapse

### *Definitions and Classification*

The term prolapse is commonly used to describe any degree of downward pelvic organ movement, including anterior vaginal prolapse (cystocele), apical or uterine prolapse, and posterior vaginal prolapse, which includes enterocele, rectocele, and perineal descent but does not include rectal prolapse.

### *Pathophysiology of Pelvic Organ Prolapse*

POP has been attributed both to (1) damage to the levator ani muscle [12] (where weakness of the levator ani may cause widening of the levator hiatus and descent of the central portion of the pelvic diaphragm), and (2) an endopelvic fascial defect [13]. However, DeLancey [14, 15] described the interaction between pelvic floor muscles and endopelvic fascia and maintained that it is not possible to determine which is responsible for prolapse – damage to muscle or damage to fascia – because these two aspects of pelvic support are intimately interdependent.

### *Factors Contributing to Pelvic Organ Prolapse*

The following factors contribute to POP [12-15]:
- Childbirth: vaginal childbirth can contribute to POP by either of two mechanisms:
  - Direct damage to the endopelvic fascial support system and walls of the vagina
  - Direct and indirect damage to the muscles and nerves of the pelvic floor.
- Connective tissue: the protein collagen is responsible for the strength of the pelvic connective tissue. Most clinicians believe that defective endopelvic connective tissue weakens the pelvic support system and hence contributes to POP.
- Pelvic neuropathies: some evidence links vaginal childbirth with pelvic neuropathies and POP. When there is denervation of the pelvic floor muscles, there may be progressive descent of the pelvic diaphragm, followed by pelvic organ descent.
- Anal incontinence: the prevalence of fecal incontinence may be as high as 17% in patients with UI and prolapse. Fecal incontinence is complex in causation, and radiologists should not oversimplify the etiology by just concentrating on mechanical damage to the sphincter.
- Other factors include:
  - Chronic and repetitive increase in intra-abdominal pressure
  - Chronic respiratory conditions associated with forceful and repetitive coughing.

## Anorectal Dysfunction

Anorectal dysfunction may be divided into two main categories: anal incontinence and constipation.

## Anal Incontinence

### *Definitions and Classification*

- Anal incontinence is a common disorder and is defined as the involuntary loss of flatus, liquid, or solid stool, causing social and hygiene problems.
- The prevalence of some degree of fecal incontinence in the general population is about 2%, rising to 7% in the elderly [16].

### *Pathophysiology*

- Overall, about 5% of the population has anal incontinence, which can develop at any age. Many factors must work in concert to achieve continence. These factors include:
  - Rectal:
    - Stool delivery: adequate consistency and volume
    - Rectal function: compliance, sensation, contractility
    - Anorectal responses: rectoanal inhibitory reflex and anal sampling.
  - Anal sphincters:
    - Intact sphincters
    - Good sphincter functions and muscle bulk
    - Coordinated contraction.
- There are many causes of incontinence that may act independently or in conjunction to compromise continence. Disorders of these components may be:
  - Neuropathic: Autonomic neuropathy is commonly associated with disorders of rectal motor complexes; there may be high-pressure contractions that exceed sphincter tone or the absence of compensatory increases of tone in the sphincter.

  - Idiopathic: Incontinence in this case is usually associated with a patulous anal sphincter and passive stretching of the puborectalis muscles.
  - Structural: Structural abnormality of and damage to continence components are confined to the anal sphincter or occur higher in the digestive track.

#### *Clinical Assessment and Investigation*

- Clinically, fecal leakage can be divided into two categories [16]:
  - Minor, when there is just staining of underwear or bedding
  - Major, when there is definite soiling considered to be a problem by the patient.
- Fecal incontinence may be divided into passive, urge, and nocturnal incontinence:
  - Passive: leakage is the main problem; stool passage occurs without patient awareness. This type of incontinence is most likely to be due to internal anal sphincter damage.
  - Urge: stool cannot be held back despite attempts to inhibit defecation. This type of incontinence is most likely to be due to external sphincter damage.
  - Nocturnal incontinence: this type suggests a neurologic causation.

### Constipation

#### *Definitions and Classification*

- It should be borne in mind that the term constipation describes a symptom – an expression of a sensation rather than a clinical sign – and is particularly subjective, meaning different things to different people. When patients are asked to define constipation, there is considerable individual variation in response. Some concentrate on frequency of bowel movements; others focus on ease of defecation and stool size and consistency.
- It is generally accepted that a satisfactory definition of constipation must include the concepts of both infrequent defecation and difficult evacuation [17]:
  - Infrequent defecation is usually defined as bowel movements that occur three or fewer per week and is most likely associated with slow transit time
  - Difficult evacuation is defined as straining during stool passage that accounts for more than 25% of the time spent in the lavatory. Its presence indicates obstructed defecation.

#### *Pathophysiology of Obstructed Dysfunction*

Broadly, there are two major types of constipation [17]:
- Slow-transit type (infrequent evacuation), in which the movement of fecal material through the colon is slow
- Outlet obstruction, in which evacuating rectal contents requires prolonged straining during stool passage.

*Slow Colonic Transit Time*

Patients who solely exhibit slow colonic transit time are likely to have idiopathic slow transit constipation.
- These individuals are almost exclusively young women who experience constitutional symptoms and abdominal bloating together with a dramatically reduced stool frequency.
- There is some evidence that the underlying abnormality is not merely confined to the colon but is more generalized. For example, many of these patients exhibit abnormal antroduodenal manometry.
- The underlying disorder remains obscure, but it is likely to be generalized sensory and autonomic neuropathy.

*Outlet Obstruction*
- Abnormal rectal evacuation may be due to functional or structural abnormalities.
  - Functional:
    - Anismus
    - Ineffective straining
    - Solitary rectal ulcer syndrome.
  - Structural:
    - Rectocele
    - Descending perineal syndrome
    - Rectal prolapse.

## Identifying Defect Types in Pelvic Support Systems and Classifying Them within Their Complexes

### Dynamic Magnetic Resonance Imaging

#### Diagnostic Criteria

Dynamic MRI is best evaluated on midsagittal true fast-imaging dynamic evacuation sequences and on sagittal, axial, and coronal images during maximum straining, when pelvic organ descent should be greatest. The following are criteria measured during maximum straining.

#### *Sagittal Plane*

- In the sagittal plane, the pubococcygeus line (PCL) is used as the reference line. It extends from the inferior border of the symphysis pubis anteriorly to the tip of the coccyx posteriorly [18].
- Descent of the bladder neck, bladder base, uterus, and anorectal junction, measured perpendicularly below the PCL, is recorded [19-23].
- Prolapse severity can be easily graded according to the "rule of three":
  - Mild: prolapse of an organ below the PCL by 3 cm
  - Moderate: prolapse of 3-6 cm
  - Severe: prolapse of >6 cm [20, 21].
- SUI is recorded as the diagnosis when loss of urine through the urethra is visualized at maximum straining. However, the absence of urine loss during MRI does not preclude the patient experiencing symptoms [2].

- Other measurements in the sagittal plane during maximum straining include:
  - The H-line, which extends from the inferior aspect of the pubic symphysis to the anorectal junction
  - The M-line, dropped as a perpendicular line from the PCL to the posterior aspect of the H-line [19-23]
  - The levator plate angle, enclosed between the levator pate and the PCL [2, 8].

#### *Axial Plane*

Regarding the levator hiatus:
- Its width is enclosed between the puborectalis muscle slings [2, 23]
- It is measured at the most inferior point of the symphysis pubis
- The transverse diameter of the muscle reflects the extent of its ballooning during straining
- It rarely exceeds 4.5 cm in women with an intact pelvic floor [2, 23].

#### *Coronal Plane*

Regarding the iliococcygeus angle:
- It is measured between the iliococcygeus muscle and the transverse plane of the pelvis in posterior coronal images at the level of the anal canal [2, 8]
- The transverse plane of the pelvis is obtained by joining the corresponding bony landmarks on the pelvic sidewalls at the level of origin of the iliococcygeus muscle from the obturator internus, usually at the level where the complete iliac blades are seen in the coronal plane [2]. This angle reflects the degree of descent and movement of the muscle [2, 8].

### Image Interpretation

#### *Five Measurements of the Support Structures*

Measurements are obtained on dynamic images in the three orthogonal planes (Fig. 3).

- In healthy volunteers with no symptoms of lower genitourinary abnormalities, mean measurements obtained during maximum straining in the three orthogonal planes are as follows [2]:
  - Length of the H-line, 5.8 ± −0.5 cm
  - Length of the M-line, 1.3 ± 0.5 cm
  - Levator plate angle, 11.7 ± 4.8
  - Width of the levator hiatus, 4.5 ± 0.7 cm
  - Iliococcygeus angle, 33.4° ± 8.2°.
- These five measurements of support structures are all considered to reflect the status and the weakness of the pelvic floor muscles [2]:
  - They have proven to be of value in identification of pelvic floor laxity and quantification of the degree of weakness
  - They are also useful for follow-up assessment.

### Static Magnetic Resonance Imaging of Pelvic Floor

- MRI can provide information on pelvic floor muscles, urethral and vaginal support, and tears in the anal sphincter.
- Analysis of static MRI is based on thorough examination of the pelvic-organ-supporting elements and characterizations of defects in each of its components (Fig. 4):
  - Urethral support system
  - Vaginal support system
  - Anal sphincter complex.

### Magnetic Resonance Imaging and Stress Urinary Incontinence

#### *Diagnostic Criteria*

The urethral support system is shown in Fig. 4a; scrutiny of the urethral support system involves imaging the following [2, 4, 8]:
- Urethral ligaments
- Endopelvic fascia (level III fascial support)
- Puborectalis muscle.

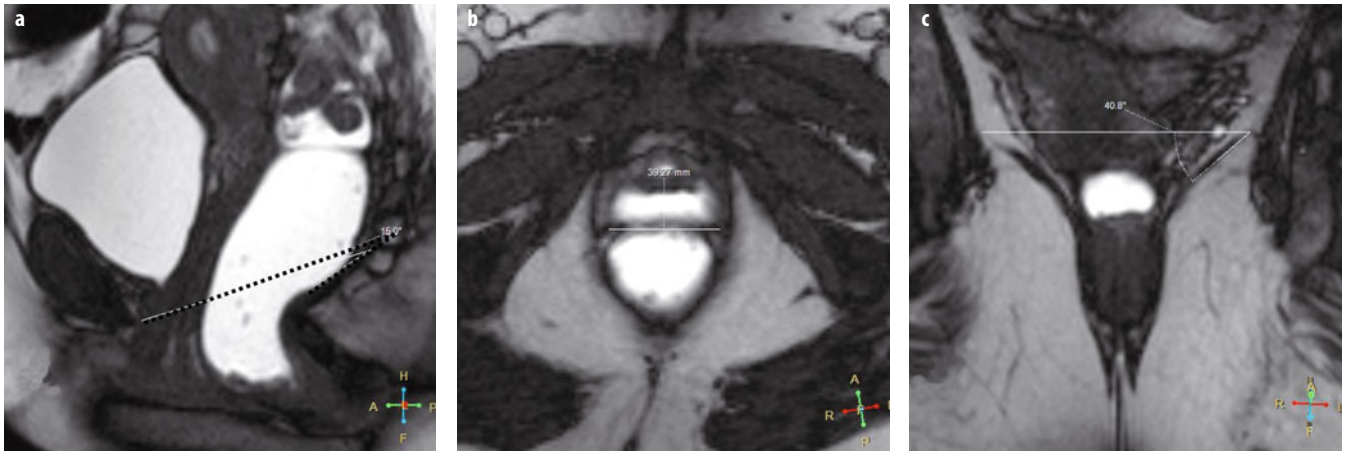


**Fig. 3 a-c.** Dynamic T2-weighted magnetic resonance images in the three orthogonal planes; all images are acquired during maximum straining. **a** Levator plate angle (*dashed line*), **b** width of levator hiatus (*solid line*), **c** iliococygeous angle (*solid line*)


**Fig. 4 a-c.** Static T2-weighted magnetic resonance images (MRI) acquired at rest summarize components of the pelvic support systems assessed in static MRIs. **a** Urethral support system, **b** vaginal support system, **c** anal sphincter complex

#### *Image Interpretation*

*Magnetic Resonance Imaging of Normal Urethral Support Systems*

- Urethral support ligaments: Evaluation of the urethral support ligaments is a meticulous process, and the radiologist will need a high level of experience to detect the different types of abnormalities. The two main groups of ligaments that should be assessed are the ventral and the dorsal urethral ligaments [2, 4].
  - The ventral urethral ligaments includes:
    - Pubourethral (PUL) ligaments:
      - Proximal
      - Intermediate
      - Distal
    - Periurethral ligament
    - Paraurethral ligaments.
  - Dorsal urethral ligament comprises:
    - Suburethral ligament, which runs retrourethral, forming suburethral sling, with a plane of cleavage between ligament and anterior vaginal wall.
- Level III endopelvic fascia: this structure supports the midurethra, which is seen centralized, with symmetrical appearance of the space of Retzius.
- Puborectalis muscle: this muscle normally shows bilateral symmetrical muscle slings with no gross evidence of defect or scarring.

*Magnetic Resonance Imaging of Abnormal Urethral Support Elements*

- Urethral ligament abnormalities are classified as follows:
  - Distortion: when internal architectural changes, waviness of the ligaments is seen
  - Defects: defined by discontinuity of the ligament with visualization of the torn parts [2].
- Level III fascial defect:
  - Assessed at the level of urethra and bladder neck
  - Recognizable by the "drooping mustache" sign, caused by the fat in the prevesical space against the bilateral sagging of the detached lower third of the anterior vaginal wall from the arcus tendineus fascia pelvis [24].
- Puborectalis muscle defect:
  - Recognizable by disruption of the normal symmetrical appearance of the muscle sling or its attachment to the symphysis pubis [2].

### Magnetic Resonance Imaging and Pelvic Organ Prolapse

#### *Diagnostic Criteria in Pelvic Organ Prolapse*

Vaginal support structures include (Fig. 4b):

- Level I endopelvic fascia, at the level of the fundus of the bladder
- Level II endopelvic fascia, at the trigone or bladder base
- Iliococcygeus muscle.

#### *Image Interpretation*

*Magnetic Resonance Imaging of Normal Vaginal Support Systems*

- Level I and II endopelvic fascia
  - Normal attachment of the pubocervical fascia, the posterior urinary bladder wall is seen as a straight line on axial MRI [2, 8, 24].
- Iliococcygeus muscle
  - Normal symmetrical appearance of the two upwardly convex muscle slings.

*Magnetic Resonance Imaging of Abnormalities in Vaginal Support Elements*

- Level I and II endopelvic fascial defect:
  - Paravaginal defect: in the axial plane, a paravaginal defect in the fascia is visualized as sagging of the fluid-filled posterior urinary bladder wall. This MRI appearance is caused by detachment of the vaginal-supporting fascia from the lateral pelvic wall, known as the saddlebags sign [24].
  - Central defect: A central defect is also indicated by sagging of the central part of the urinary bladder posterior wall [2, 18].
- Iliococcygeus muscle:
  - In the coronal plane, the iliococcygeus muscle is assessed for loss of normal symmetrical appearance of its slings [25].

  - Other abnormalities include defect or disruption of its attachment to the obturator internus muscle [2].

### Magnetic Resonance Imaging and Anorectal Dysfunction

#### *Diagnostic Criteria*

MRI has an important role in visualizing the anal sphincter. High-resolution techniques using phased-array coil and endoanal MRI have been evaluated for both clinical use and research.

#### *Image Interpretation*

*Magnetic Resonance Imaging of the Normal Anal Sphincter*
MRI allows detailed visualization of the normal anatomy and pathologic conditions of the anal sphincter. On axial T2-weighted BFFE images, the consecutive layers of the anal sphincter from the lumen outward include (Fig. 4c):
- Innermost high-signal intensity layer (combined mucosa and submucosa)
- Low-signal-intensity layer (submucosal smooth muscle)
- Internal anal sphincter (homogenous intermediate to high signal intensity), visible as a continuation of the smooth muscle of the rectum
- Deep external anal sphincter (low to intermediate signal intensity), which surrounds the lower part of the internal sphincter
- Puborectal muscle, which swings around the upper part of the external sphincter and is continued cranially by the levator ani muscle.

*Magnetic Resonance Imaging of Anal Sphincter Abnormalities*
Anal sphincter lesions are classified according to [2]:
- Lesion site:
  - External anal sphincter
  - Internal anal sphincter.
- Lesion type:
  - Structural change, which may be in the form of either defect or scarring:
    - Tears or defect: sphincteric defect is defined as a discontinuity of the muscle ring
    - Scarring: low-signal-intensity deformation of the normal pattern of the muscle layer.
  - Volume change:
    - Focal volume change:
      - Thinning
      - Thickening.
    - Diffuse volume change:
      - Atrophy: may occur without trauma; may be related to neurologic degeneration from denervation and aging
      - Atrophy of the external sphincter: defined as extreme generalized thinning. On coronal images, the thickness of all anal muscles may be compared; such comparison makes external sphincteric atrophy easy to detect.

## Correlation between Static and Dynamic Magnetic Resonance Images

### Current Treatment and Reported Recurrence Rate of Pelvic Floor Dysfunction

Although multiple factors predispose for PFD, the precise pathologic mechanism is poorly understood, and treatment is often started regardless of the specific anatomic lesion involved, possibly because one of the following factors [8]:
- Lack of understanding of normal anatomy and physiology of the pelvic floor
- Lack of solid data on selection criteria for the various surgical techniques and sparsity of data on the outcome of different procedures.

### The Clinician's Needs

- Several clinicians specializing in the field of PFD stated that a "wide variety of surgical procedures have been used, with several based on weak scientific evidence."
- Most of those clinicians stated that the optimal approach to treatment must be individualized for each patient on the basis of the symptom complex and the specific anatomic and structural abnormalities.
- What had long been missing was a tool for accurately defining the anatomic and structural abnormalities in each patient [2, 8, 26].

### The Radiologist's Role

- All diagnostic modalities, including physical examination and standard MRI assessment, are directed toward two basic goals in the clinical and radiologic assessment of POP:
  - To determine whether prolapse of a specific organ is indeed present
  - To determine the degree of prolapse.
- However, the author of this chapter, as do others, believes that as new modalities of evaluation emerge, anatomic concepts of form and function change.
- With changing concepts, it is necessary to reexamine and redefine the underlying anatomy, which requires a functional classification system based on scientific evidence [2, 8]. On the basis of the new three-part pelvic support system classification developed in my institution [2], a correlative analytic approach was created that can provide better data for treatment planning.
- The basis of this approach is simultaneous analysis of findings obtained from both static and dynamic MRI of the same patient to determine whether a particular anatomic defect in the pelvic support system detected on static images is associated with a specific dysfunction on dynamic images. The most prominent type of defect is reported as the predominant defect.

- In this context [2, 8]:
  - SUI was found to be associated with structural defects in the urethral support elements and not with bladder-neck descent.
  - In regard to POP:
    - The integrated MRI analytical approach makes it possible to differentiate whether POP is caused by defects in the endopelvic fascia, by levator muscle weakness, or by abnormalities in both the endopelvic fascia and the levator muscles.
    - Therefore, instead of the clinician focusing on a "dropped bladder," the radiologist can use combined analysis of both imaging modalities to provide the clinician with complete mapping of the site and types of defects. This includes pinpointing to the clinician the specific underlying defect that caused the bladder to drop
    - In regard to anal incontinence, levator muscle weakness may lead to incontinence in the absence of anal sphincter defects [2].

### Merits of Combined Analysis of Static and Dynamic Magnetic Resonance Imaging on Patient Treatment and Therapy Options

The success of advanced pelvic floor imaging for treatment planning will be determined not only by whether treatment is affected by new information provided by imaging modality but also by whether this information ultimately reduces complication rates and substantially improves clinical outcomes.

My institution's correlative analytical approach converts static and dynamic MRI from two separate types of images into an integrated system that offers the following benefits [8]:

- More precise identification of the underlying anatomic defect responsible for symptoms in individual patients with PFD
- Differentiation of the underlying anatomic defect when any two patients have the same symptoms
- Individualized approaches to defect treatment that may minimize the risk of surgical failure, dysfunction recurrence, and reoperation.

This approach can enhance collaboration between radiologist and clinician to the benefit of the patient because it provides a common language through which the radiologist can effectively communicate imaging findings.

## Acknowledgements

Medical editor Katharine O'Moore-Klopf, ELS (East Setauket, NY, USA) provided professional English-language editing of this article.

Tagwa Ahmed Adam Idris, radiology resident, Cairo University, Egypt, contributed to the cases submitted for the teaching course and the images contained herein.

## References

1. Maglinte DDT, Kelvin PM, Fitzgerald K et al (1999) Association of compartments defects in pelvic floor dysfunction. AJR Am J Roentgenol 172:439-444.
2. El Sayed RF, Mashed SE, Farag A et al (2008) Pelvic floor dysfunction: assessment with combined analysis of static and dynamic MR imaging findings. Radiology 248:518-530.
3. Woodfield CA, Krishnamoorthy S, Hampton BS, Brody JM (2010) Imaging pelvic floor disorders: trend toward comprehensive MRI. AJR Am J Roentgenol 194:1640-1649.
4. El Sayed RF, Morsy MM, El Mashed SM, Abdul-Azim MS (2007) Anatomy of the urethral supporting ligaments defined by dissection, histology, and MRI of female cadavers and MRI of healthy nulliparous women. AJR Am J Roentgenol 189:1145-1157.
5. Strohbehn K (1998) Normal pelvic floor anatomy. Obstet Gynecol Clin North Am 25:683-705.
6. DeLancey JO (1994) The anatomy of pelvic floor. Curr Opin Obstet Gynecol 6:313-316.
7. Petros PEP (2007) Overview. In: Petros PEP (ed) The female pelvic floor. Function, dysfunction and management according to the integral theory, 2nd edition. Springer, Berlin, pp 3-4.
8. El Sayed Rf (2013) The urogynecological side of pelvic floor MRI: the clinician's needs and the radiologist's role. Abdom Imaging 38:912-929.
9. Abrams P, Cardozo L, Fall M et al (2002) The standardisation of terminology of lower urinary tract function: report from the standardization sub-committee of the international continence society. Neurourol Urodyn 21:167-178.
10. Fultz NH, Burgio K, Diokno AC et al (2003) Burden of stress urinary incontinence for community-dwelling women. Am J Obstet Gynecol 189:1275-1282.
11. Hannestad YS, Rortveit G, Sandvik H, Hunskaar S (2000) A community-based epidemiological survey of female urinary incontinence: the Norwegian EPINCONT study. Epidemiology of Incontinence in the County of Nord-Trøndelag. J Clin Epidemiol 53:1150-1157.
12. El Sayed RF (2009) Female pelvic floor dysfunction. In: Morcos SK, Thomsen HS (Eds) Imaging in genitourinary medicine: a problem-oriented approach. Wiley-Blackwell, Chichester, pp 399-413.
13. Yang A, Mostwin JL, Rosenshein NB, Zerhouni EA (1991) Pelvic floor descent in women: dynamic evaluation with fast MR imaging and cinematic display. Radiology 179:25-33.
14. Mengert WF (1936) Mechanics of uterine support and position. Am J Obstet Gynecol 31:775-782.
15. DeLancey JO (1993) Anatomy and biomechanics of genital prolapse. Clin Obstet Gynecol 36:897-909.
16. DeLancey JO (2003) Functional anatomy of the pelvic floor. In: Bartram CI, DeLancey JO, Halligan S et al (Eds) Imaging pelvic floor disorders. Springer, New York, pp 27-38.
17. El Sayed RF, Fielding JR, El Mashed S et al (2005) Preoperative and postoperative magnetic resonance imaging of female pelvicfloor dysfunction: correlation with clinical findings. J Women's Imaging 7:163-180.
18. Kelvin FM, Pannu HK (2003) Dynamic cystoproctography: fluoroscopic and MR techniques for evaluating pelvic organ prolapse. In: Bartram CI, DeLancey JO, Halligan S et al (Eds) Imaging pelvic floor disorders. Springer, New York, pp 51-56.
19. Goh V, Halligan S, Kaplan G et al (2000) Dynamic MRI of the pelvic floor in asymptomatic subjects. AJR Am J Roentgenol 174:661-666.
20. Lienemann A, Anthuber C, Baron A et al (1997) Dynamic MR colpocystorectography assessing pelvic floor descent. Eur Radiol 7:1309-1317.
21. Goh V, Halligan S, Kaplan G et al (2000) Dynamic MRI of the pelvic floor in asymptomatic subjects. AJR Am J Roentgenol 174:661-666.
22. Comiter CV, Vasavada SF, Barbaric ZL et al (1999) Grading pelvic prolapse and pelvic floor relaxation using dynamic magnetic resonance imaging. Urology 3:454-457.

23. Fielding JR (2002) Practical MR imaging of female pelvic floor weakness. Radiographics 22:295-304.
24. Huddleston HT, Dunnihoo DR, Huddleston PM, Meyers PC (1995) Magnetic resonance imaging of defects in DeLancey's vaginal support levels I, II, and III. Am J Obstet Gynecol 172: 1778-1784.
25. Klutke CG, Siegel CL (1995) Functional female pelvic anatomy. Urol Clin N Am 22:487-498.
26. McCarthy TA (1991) Medical history and physical examination. In: Ostergard DR, Bent AE (Eds) Urogynecology and urodynamics theory and practice, 3rd edition. Williams & Wilkins, Baltimore, pp 99-101.

# MR Defecography: Clinical Indications, Technical Aspects, Reference Lines and Findings

Francesca Maccioni

Department of Radiological Sciences, Oncology and Pathology, Sapienza University of Rome, Rome, Italy

## Introduction

The female pelvic floor is divided in three main functional and anatomic compartments: the anterior, supporting the bladder and urethra; the middle, supporting the vagina and uterus; and the posterior or anorectal compartment [1, 2]. When the pelvic floor is damaged in its fascial, muscular, or neural components at the level of any of its three compartments, several pelvic floor dysfunctions or disorders (PFD) may arise [3]. Although the etiology of pelvic floor failure is multifactorial, obstetric lesions are considered primary causes of pelvic floor damage due to vaginal birth traumas, such as prolonged second stage of labor; forceps delivery; and multiple deliveries. As pelvic floor muscles and fasciae act as a unique functional entity, dysfunctions of the posterior compartment are usually associated with various dysfunctions of the anterior and middle urogenital compartments, as well. PFD are therefore characterized by a variable association of pelvic organ prolapse and functional disturbances [4] involving bladder (urinary incontinence and voiding dysfunction), vagina and/or uterus (sexual dysfunctions), and rectum [obstructed defecation syndrome (ODS)]. ODS is the main functional disorder of the posterior pelvic floor compartment and consists of severe constipation due to inadequate evacuation of fecal contents from the rectum. Different mechanical and functional rectal disorders may cause this syndrome, including rectocele, rectal invagination, rectal prolapse, and puborectalis muscle dyskinesia. ODS, pelvic organ prolapse (POP), and urinary incontinence are the most common PFD and are found in nearly 50% of multiparous women >50 years of age, with a negative impact on quality of life (QOL) and frequent need of invasive surgical treatments [3-5]. Correct diagnosis of the specific anorectal or urogenital dysfunction and identification of all associated disorders are mandatory for effective surgical or conservative treatment and to reduce postsurgical recurrences.

Dynamic MRI provides excellent morphological and functional display of the pelvic floor like no other imaging modality [6-8]. Different MRI techniques for dynamic evaluation of the pelvic floor have been proposed, particularly for evaluating the posterior compartment and related anorectal disorders, each one with several advantages and disadvantages. Several reference lines and grading systems have also been adopted for MRI grading of these disorders, in correlation with clinical grading systems. All these issues need to be analyzed and discussed.

## Functional Anatomy of the Pelvic Floor and Posterior Pelvic Floor Disorders (PPFD)

A comprehensive understanding of the pelvic floor's complex anatomy is necessary to understand the specific lesions underlying PPFD and to explain the frequent association of disorders in different pelvic compartments. The pelvic floor is an integrated system composed of an active component, the striated muscles; and a passive support system, the suspensory ligaments and fascial coverings; and is associated with an intricate neural network. It not only provides support for the pelvic viscera (bladder, bowel, uterus) but maintains their functioning, thanks to the combined action of the two major pelvic floor structures: the levator ani muscle (LAM), and the endopelvic fascia [2-4].

### Levator Ani Muscle

The LAM has two main components: the iliococcygeus and pubococcygeus muscles. Various muscle subdivisions are assigned to the medial portions of the pubococcygeus in order to reflect the attachments of the muscle to the urethra, vagina, anus, and rectum. These subdivisions are referred to as the puboure thralis, pubovaginalis, puboanalis, and puborectalis, or collectively, as the pubovisceralis.

*Diseases of the Abdomen and Pelvis 2014-2017*,
DOI: 10.1007/978-88-470-5659-6_9 

Overall, the LAM is categorized into five different muscle groups: pubourethralis, pubovaginalis, puboanalis, puborectalis, and ileococcygeus. More posteriorly, the pelvic diaphragm becomes continuous with the ischiococcygeus muscle. The LAM contracts continuously, providing tone to the pelvic floor against stress coming from gravity and intra-abdominal pressure. LAM contraction closes the urogenital hiatus and compresses urethra, vagina, and anorectal junction (ARJ) in the direction of the pubic bone. Furthermore, the puborectalis component of the LAM, called the puborectal muscle, is an intrinsic and relevant part of the anal sphincter complex. It plays a primary role in the defecation process, acting as a sling that opens and closes access to the anal canal. Relaxation of the puborectal muscle, in fact, opens the anorectal angle (ARA); its contraction closes this angle, thus impeding defecation.

#### Endopelvic Fascia

The endopelvic fascia is a layer of connective tissue that connects and attaches the uterus and vagina to the pelvic bones [1, 2]. Pelvic organs are supported by a series of fascial (ligamental) and elastic condensations of the endopelvic fascia, which support the uterus and vagina, preventing genital organ prolapse.

#### Pubocervical Fascia

The anterior portion of the endopelvic fascia, the pubocervical fascia, extends from the anterior vaginal wall to the pubis and supports the bladder. Damage to this ligament may cause urethral hypermobility and urinary incontinence.

#### Rectovaginal Fascia

The posterior portion of the endopelvic fascia forms the rectovaginal fascia, called Denonvilliers aponeurosis, composed of thin, connective tissue in the rectovaginal septum. It further extends, along with the cardinal and uterosacral ligaments (parametrium), from the posterior cervix and vaginal wall toward the sacrum [1, 2]. Damage to or weakness of this fascia represents a major cause of rectocele.

#### Obstetric Lesions

Obstetric lesions are considered primary causes of pelvic floor damage. Lesions of the iliococcygeus muscles are more frequent in the first phase of delivery, whereas the pubococcygeus muscles may be damaged in the second phase; midline episiotomy or forceps delivery are associated with anal sphincter rupture [3, 5]. During delivery, damage to the anterior portion of the endopelvic fascia (pubocervical fascia) may determine urethral hypermobility and/or cystocele, whereas a lesion of its posterior portion, the rectovaginal fascia, may result in an anterior rectocele or enterocele [6]. Pudendal nerve impairment during vaginal delivery for ischemic and mechanical factors diminishes the LAM's capability for providing adequate pelvic support. Other causes of pelvic floor weakness include ageing, obesity, hysterectomy, and the patient's genetic predisposition.

### Diagnosis and Clinical Management of PPFD

With regard to disorders of the anorectal compartment, identification of the specific anorectal dysfunction leading to ODS is fundamental for planning an effective treatment and directing the patient toward surgical or conservative management [6-8]. ODS may be sustained either by mechanical causes (e.g., rectal prolapse, rectal descent, rectal invagination, rectocele, enterocele) or by a functional disorder (puborectalis syndrome). The distinction between mechanical or functional causes is crucial, as mechanical obstructions are usually directed toward surgical treatment (e.g., rectopexy or transanal rectal resection); functional obstructions are directed toward conservative therapy (biofeedback). Furthermore, the presence of urogenital disorders associated with PPFD significantly determines the choice of surgical procedure, usually requiring a more extensive surgical approach [7]. Surgical techniques for PPFDs are continuously evolving in order to provide a more affective and comprehensive repair of the pelvic floor and to improve long-term results.

Hence, although functional gastroenterologists and colorectal surgeons are primarily involved in ODS management, a multidisciplinary team, often called a pelvic floor unit, is strongly recommended that includes urogynecologists, physicians, radiologists, physiotherapists, and specialized nurses.

PPFD diagnosis is demanding and is achieved by associating clinic history, physical examination, physiological testing, and diagnostic radiologic tools [6-10). The clinical examination alone either underestimates or results in misdiagnosis of the site of prolapse in >50-90% of patients and is therefore unreliable for assessing evacuation abnormalities.

The more widely used physiological tests include anorectal manometry, electromyography, and rectal balloon expulsion test [11]. Manometry is useful for differentiating functional disorders, particularly for detecting impaired relaxation of the puborectalis muscle and anal sphincter. Endoanal ultrasound is widely used in patients with fecal incontinence to detect tears of the anal sphincters frequently associated with PFDs as results of obstetric traumas. Transperineal US is increasingly used to image the pelvic floor in static and dynamic conditions [10-12].

The main diagnostic tools for PPFD evaluation include conventional defecography (or dynamic proctography) and dynamic magnetic resonance imaging of the pelvic floor (DPF-MRI) or MR defecography [5, 8, 12-17].

Conventional defecography has always played a central role in assessing ODS, as it can detect both functional and

anatomical anorectal disorders with high accuracy [14-17]. Limits of defecography include the projectional display, failure to define the frequently associated abnormalities of the anterior and middle compartments, and its inability to depict perirectal soft tissues. Its diagnostic accuracy has been improved, however, by simultaneous opacification of bladder, vagina, and small bowel (colpocystodefecography) [15], although the examination becomes longer, more uncomfortable for the patient, and more expensive. Furthermore, conventional fluoroscopic defecography exposes the patient to a considerable radiation dose: gonadal dose in female patients is nearly 20-25 mSv or higher [18].

DPF-MRI has emerged has a valuable alternative technique for assessing PFD and staging POP [6, 7, 13]. Thanks to its multiplanar capability and high soft tissue contrast, MRI allows comprehensive morphologic and functional evaluation of all three compartments at the same time, without the use of ionizing radiation. It enables real-time assessment of functional diseases with dynamic acquisitions, similar to conventional defecography [6-8]. The main limit of MRI is the obliged supine position for patient imaging, which is necessary if a closed 1.5-Tesla magnet is used. The supine position of MR defecography has been criticized because defecation evaluation is not under physiological conditions [19, 20]. MR defecography can also be performed with an open magnet, which allows a physiological sitting position; open magnets are, however, less diffuse and characterized by a lower magnetic field with lower technical performance [5, 19, 20]. Comparative studies performed with open and closed magnets have ultimately established a good concordance between results obtained in the sitting and the supine position, thus validating the use of closed MRI for assessing defecation [19]. However, there is less availability of open magnets in clinical settings; whereas conventional closed MRI units are widely available and more accessible.

## Dynamic MRI and MR Defecography

A standardized technique for MRI evaluation of posterior pelvic floor dysfunctions is not yet available because of the heterogeneity of MRI equipment, available sequences, and rectal contrast agents [7]. Several authors [19-22] suggest performing this examination by filling the rectum with various contrast media (US gel, mashed potatoes mixed with gadolinium, etc). Others recommend no rectal filling [23], some consider complete rectal evacuation as the main part of the exam (MR defecography), some base the exam mostly on functional maneuvers (DPF-MRI), whereas others prefer imaging the patient in the left lateral rather than the supine position [24].

Each technique has specific advantages and limitations. No rectal contrast agent can reproduce the consistency of normal or hard stools; rather, gel or mashed potatoes mimic diarrheal feces [7]. Complete evacuation inside the gantry of a closed MRI unit certainly is not a physiological process and is uncomfortable for the patient [7]. Independent of the choice of one technique over the other, in order to obtain an effective DPF-MRI with the patient in the supine position, several technical aspects are crucial [7].

First, before the examination, the patient should always be fully informed and trained in order to best perform the different functional maneuvers necessary.

Second, both static and dynamic acquisitions at rest and during functional maneuvers (contraction and straining) are needed for an exhaustive examination, independent of the rectal contrast used [7, 25].

Third, the urinary bladder should not be excessively full but neither should it be empty (containing ~50-100 cc).

Fourth, the choice of rectal contrast agent determines the choice of dynamic fast sequences (mashed potatoes and gadolinium require fast T1-weighted sequences; rectal gel is well depicted both with fast T2-weighted and balanced steady-state sequences; air is best displayed with fast T2-weighted sequences).

Fifth, the evacuation phase should always be performed or at least substituted by repeated maximal straining.

In our experience [7], we alternatively use two different functional MRI techniques, according to patient compliance and scheduled examination time; it is performed with the patient in the supine position using a standard, 1.5-Tesla, closed MRI unit. In all cases, we ask the patient to preliminary clean the rectum with two water clysters or microclysters approximately 12 and 2 h before the examination for hygienic reasons.

An MRI technique is based on the use of a Foley catheter to distend the rectum, defined as the air-balloon technique (Figs. 2, 3). The end-balloon is distended in the rectum with 15-20 cc of saline solution and inflated with ~300 cc of room air; the balloon mimics solid fecal material, whereas the air distends the rectum. The pelvic floor is examined at rest, during contraction, and at straining on static and dynamic images. The static functional examination lasts approximately 10 min, including five consecutive T2-weighted half-Fourier-acquisition single-shot turbo spin-echo (HASTE) sequences (6 mm thick, 0.15 mm distance factor, 25 parallel slices, 25-s acquisition time) on axial, sagittal, and coronal planes at rest. It is then repeated on the sagittal plane with the patient holding the maximum pelvic contraction for 25 s and then straining for an additional 25 s. The dynamic functional phase is acquired (6-mm-thick slice per second on mid-sagittal plane) for approximately 50 s, starting with the rest position, then with the patient contracting pelvic floor muscles progressively to a maximum, straining progressively in the last 30-40 s, and finally relaxing (Figs. 2, 3). The phase of maximal straining is repeated several times (2-3 times routinely) to obtain better results; an evacuation phase may be obtained by asking the patient to try to expel the balloon. The overall examination time is approximately 15-20 min, including patient positioning.

The other MRI technique is usually defined as MR defecography, or the gel-filling technique. The rectum is

first filled with gel (180-200 cc), then static and dynamic images are acquired with a final evacuation phase. Overall examination time is ~20-25 min, including patient positioning and rectal filling.

Gel allows better rectal distension and a clearer evaluation of the evacuation phase and thus is more effective in diagnosing rectal invagination. However, being a one-shot technique, it may underestimate some pathologic events, such as rectoceles or enteroceles; once the gel has been eliminated, if the rectal dysfunction has not emerged, it may be completely missed. Balloon and air filling allow several repetitions of maximal straining and evacuation phases, thus increasing the possibility of detecting the particular pelvic dysfunction. Moreover, filling with gel may prevent descent of the bladder and vaginal vault, whereas distension with air does not. By using gel, the entire examination becomes slightly longer and less comfortable and hygienic for the patient. According to our experience, both techniques are valuable; if needed, they may be associated in the same imaging session in order to obtain maximal diagnostic accuracy. In our experience, the air-balloon MRI showed a tendency to underestimate rectal invagination or small rectoceles, whereas gel MRI occasionally completely missed even large rectoceles, cystoceles, and enteroceles.

## Reference Lines and Grading Systems for PPFD

To date, several landmarks and lines for measuring and staging POP on MRI have been proposed. The two most widely used lines are the pubococcygeal line (PCL), which connects the inferior aspect of the pubic symphysis to the last coccygeal joint, and the midpubic line (MPL), extending caudally along the long mid axis of the pubic symphysis [5, 25-27]. The coccyx area is the attachment point for important components of the pelvic floor, such as the pubococcygeal muscle, puborectal muscle, and pubovesical ligaments; thus, the PCL practically represents the line of the pelvic floor [25-27]. With the advent of the POP Quantification (POP-Q) system for clinical staging of POP in 1996, clinical measurements of pelvic organ position during pelvic examination used the hymenal ring as a reference line; the MPL was subsequently developed in order to correspond more closely to the location of the hymen than in earlier systems [7, 25-28].

To date, neither the PCL nor the MPL has shown better agreement with clinical staging [28]. Hence, the choice of reference line for MRI interpretation may be dependent on radiologist experience and referring physician preference. Once the reference line is chosen, grading pelvic dysfunctions and POP is performed by measuring the perpendicular distance from the anatomical landmark of each compartment to the reference line. In the anterior compartment, the reference point is the most inferior aspect of the bladder base. In the apical compartment, it is the uterine cervix, or the vaginal apex in case of previous hysterectomy. In the posterior compartment, it is the AJR (Figs. 1 and 2) [7, 25-27].

### Pubococcygeal Line

Using the PCL-POP staging system at the level of any pelvic compartment, a prolapse is considered small if the reference point is 1-3 cm below the PCL, moderate if between 3 and 6 cm below the PCL, and large if >6 cm below the PCL. The "rule of three" is useful in grading POP using the PCL system: prolapse of an organ below the

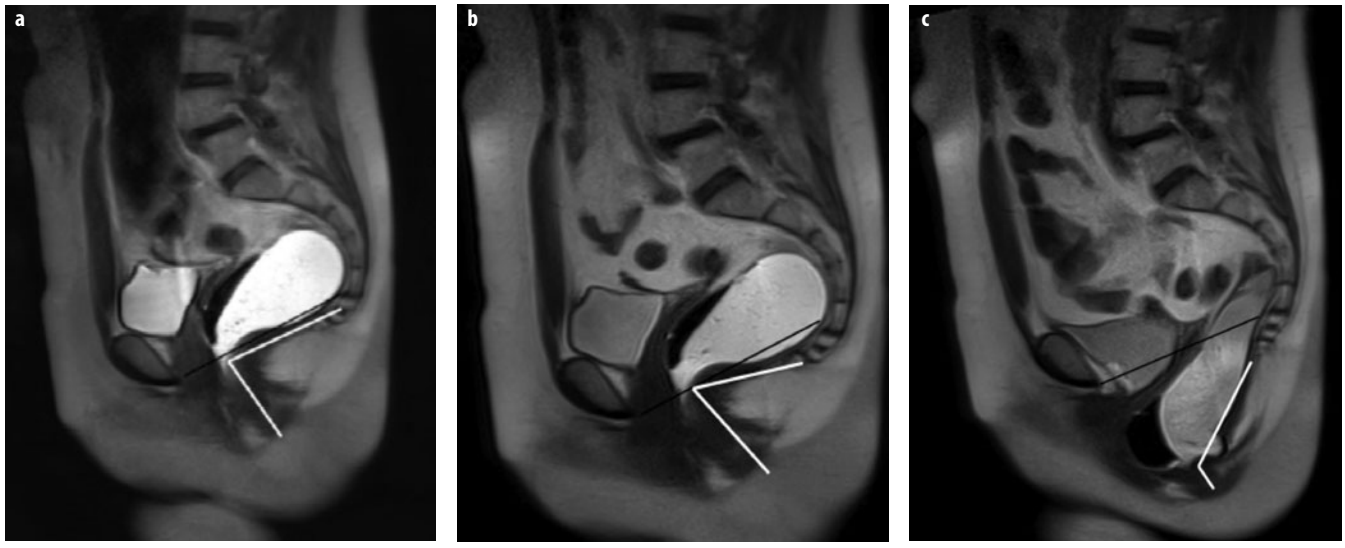


**Fig. 1 a-c.** Anorectal angle variations. **a** Sagittal T2-weighted image at rest after rectal filling with gel. The pubococcygeal line (PCL) (*black line*). At rest, the anorectal angle (ARA) (*white line*) is approximately 85°. The anorectal junction (ARJ) corresponds to the apex of the angle and it is placed at the level of the PCL. **b** Sagittal T2-weighted image during contraction of the pelvic floor: the ARA (*white line*) is reduced to <80°. **c** In this patient with obstructed defecation syndrome (ODS), during straining, the ARA opens >130° due to rectal prolapse (>160°) and is associated with severe ARJ prolapse (>6 cm)

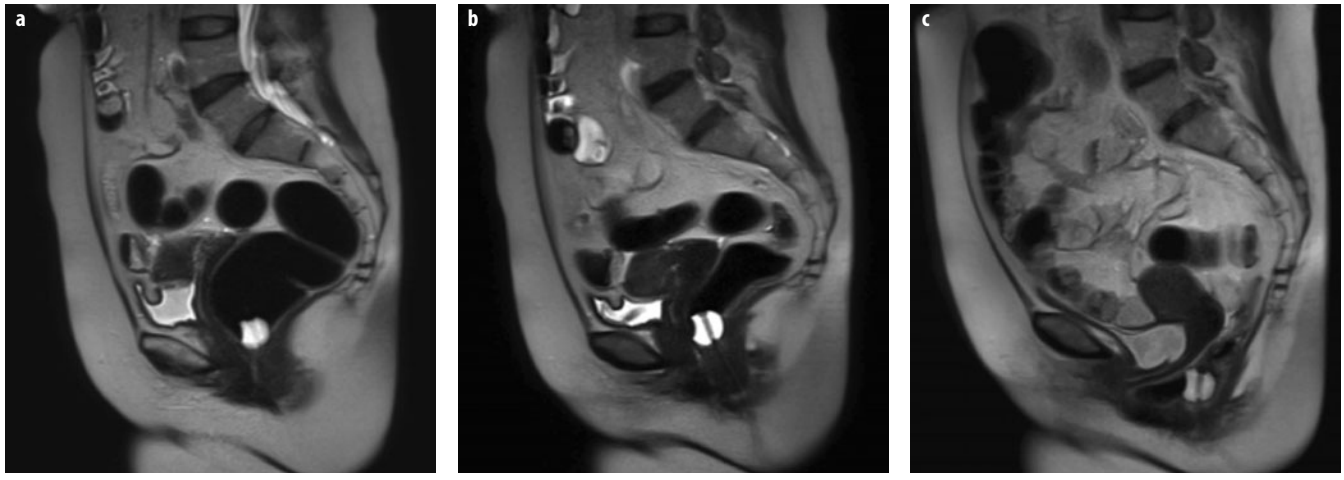


**Fig. 2 a-c.** Anorectal angle (ARA) variations. **a** Sagittal T2-weighted image at rest after rectal distension with air through a balloon Foley catheter. At rest, the ARA is approximately 90°. The anorectal junction (ARJ) corresponds to the balloon filled with fluid. **b** Sagittal T2-weighted image during contraction of the pelvic floor: the ARA reduces to <90°. **c** In this patient with obstructed defecation syndrome (ODS), during straining, the ARA opens >130° due to the rectal prolapse (>160°) and is associated with severe ARJ prolapse (>6 cm), cystocele, and colpocele. An anterior rectocele with rectal invagination is also visible

PCL by ⩽3 cm is mild, by 3-6 cm is moderate, and by >6 cm is severe [5, 25-27].

### Midpubic Line

Using the MPL-POP staging system, any POP is classified as stage 0 when the reference point is 3 cm above the MPL, stage 1 if >1 cm above the MPL, stage 2 if ⩽1 cm below the MPL, stage 3 if >1 cm below the MPL, and stage 4 represents complete organ eversion.

### H Line, M Line, Organ Prolapse System

Another grading system is the H line, M line, organ prolapse (HMO) system, which is based on H and M lines [26]. The H line extends from the inferior aspect of the pubic bone to the posterior wall of the rectum, representing pelvis hiatus widening; the M line, which extends perpendicularly from the PCL to the H line, represents hiatal descent. The HMO system is applied to a midsagittal image obtained during maximal patient straining.

Using the PCL as the main anatomical landmark is certainly easier for the radiologists. In a healthy patient at rest, the base of the bladder, the upper third of the vagina, and the peritoneal cavity should project superior to the PCL (Figs. 1 and 2). The distance from the PCL to the bladder base, uterine cervix, and ARJ, measured on images obtained when the patient is at rest and at maximal pelvic strain or evacuation, indicates prolapse severity. The same reference parameters used in conventional defecography may be adopted for DPF-MRI. The ARA is the angle formed by a line along the posterior border of the rectum and a line along the central axis of the anal canal. Its changes express the functioning of the puborectalis muscle: when the pelvic floor and puborectalis contract, the angle closes (squeezing), whereas during straining and evacuation, it opens.

In our experience, and according to other authors, in healthy individuals in the supine position, the ARA at rest is between 85 and 95° [7]. During squeezing (maximal pelvic floor contraction), pelvic organs elevate in relationship to the PCL, sharpening the ARA by 10-15° (due to contraction of the puborectal muscle). During straining and defecation, the ARA becomes more obtuse, typically by 15-25°, than when measured at rest.

## Posterior Pelvic Floor Dysfunctions

### Rectocele

Rectocele is defined as an outpouching or bulging of the anterior rectal wall that develops during defecation. It is observed in most parous women (78-99%) but is rarely seen in men. The underlying etiology of a rectocele is weakening of the support structures of the pelvic floor, particularly of the rectovaginal fascia [29]. Several factors may increase the risk of developing a rectocele, such as vaginal birth trauma (multiple, difficult, or prolonged deliveries; forceps delivery; perineal tears), constipation with chronically increased intra-abdominal pressure, hysterectomy, aging, and congenital or inherited weaknesses of the pelvic floor support system [29].

Most rectoceles develop anteriorly due to weakness of the structures sustaining the anterior rectal wall. A rectocele rarely develops posterolaterally; in this case, the lesion – a posterior perineal hernia – occurs laterally through a puborectalis muscle defect rather than in the midline [6-8, 29]. Rectal invagination is frequently associated with rectoceles [6-8, 21, 29]. Anterior rectoceles are specifi-

cally associated with rectal wall invagination and infolding of the posterior rectal wall. Rectoceles are also frequently associated with enteroceles and anismus; enteroceles or peritoneoceles may act as compensatory dysfunctions, improving evacuation from the rectocele and reducing fecal trapping.

Symptoms related to rectocele may be primarily vaginal (bulging, dyspareunia) or rectal (defecatory dysfunction, constipation, and sensation of incomplete evacuation). Fecal trapping in the rectocele leads many patients to empty it by digitating and pressing on the posterior wall of the vagina or perineum.

Sensitivity of the clinical examination in rectocele diagnosis varies from 31% to 80% [3, 4, 29] and is generally unable to distinguish an enterocele from a high rectocele. For these reasons, dynamic MRI during maximal straining and/or evacuation is clinically useful to identify and grade rectoceles (Fig. 3). Clinically relevant symptomatic rectoceles >3 cm are easily detected at supine MR defecography and DPF-MRI (Figs. 1-4). Rectoceles <2 cm are considered normal features in most parous women rather than clinically relevant features [6-8, 29]. At MRI, a rectocele is measured during the phase of maximal straining and evacuation as the distance between anal midline and the anterior rectal wall or as the depth of wall protrusion beyond the expected anterior rectal wall. At MRI, rectoceles are graded as small if <2cm, mild as being between 2 and 4 cm, and large if >4 cm [7, 19]. By using this staging system, MRI sensitivity in detecting large rectoceles (>3.5 cm) ranges between 87% and 100% [19, 20].

## Rectal Intussusception

Rectal intussusception is invagination of the rectal wall [6-8, 29] located either anteriorly, posteriorly, or circumferentially, and may involve the full thickness of the rectal wall or the mucosa only. Rectal intussusception is classified as intrarectal if it remains within the rectum, intra-anal if it extends inside the anal canal, or extra-anal if it passes the anal sphincter; the latter is also called complete or full rectal prolapse [18, 19]. Rectal intussusception is unlikely to obstruct defecation, but it can cause a sensation of incomplete emptying. If the invagination progresses becoming intra-anal, patients most likely experience a sensation of incomplete defecation due to outlet obstruction. Invagination may also cause sequestration of a rectocele, with contents returning into the rectum during relaxation, thus resulting in incomplete evacuation and OD as well (Figs. 2 and 4).

## Enterocele

Herniation of the pelvic peritoneal sac into the rectogenital pouch (pouch of Douglas) may contain fat (the so called peritoneocele), small-bowel loops (properly defined as enterocele), or sigmoid colon (defined as sigmoidocele). In patients with PFDs the incidence of enteroceles ranges between 17% and 37%, being more common in women and frequently associated with rectoceles [29, 30]. Uterus removal increases the risk of enterocele, causing separation of the anterior (pubocervical) and

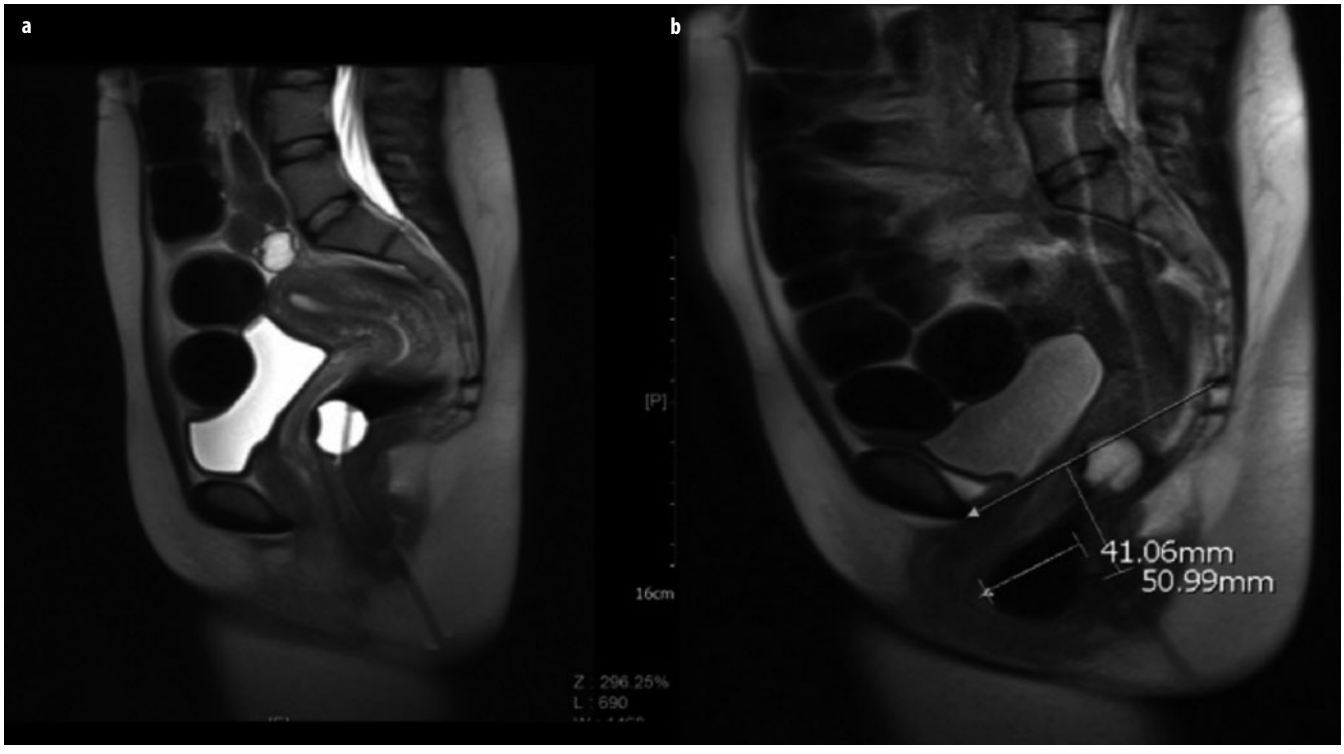


**Fig. 3 a, b.** Rectocele. **a** Sagittal T2-weighted image at rest after rectal filling with air through a balloon catheter. **b** During straining, a large anterior rectocele develops (>4 cm) and is associated with prolapsed anorectal junction (ARJ) (>5 cm)

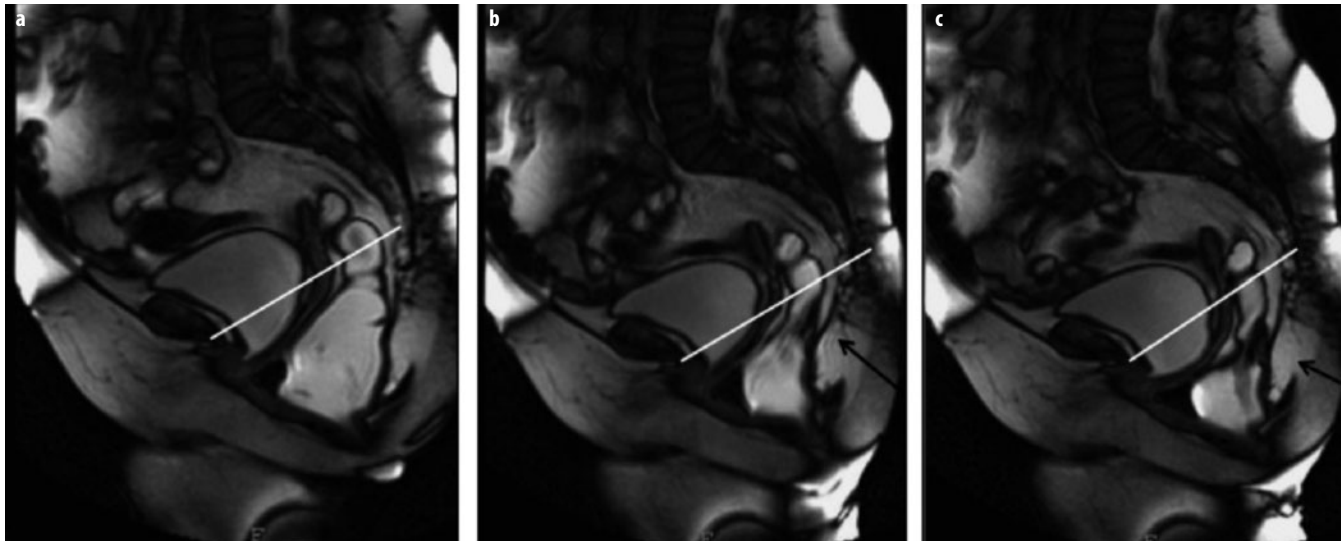


**Fig. 4 a-c.** Rectocele with rectal invagination during progressive straining. **a** Sagittal balanced image after filling with rectal gel shows an anterior rectocele (>3 cm) associated with prolapsed anorectal junction (ARJ) (>5 cm). **b** Progressive straining shows rectal invagination above the rectocele. **c** Rectal invagination and rectocele are more evident at maximum straining during evacuation

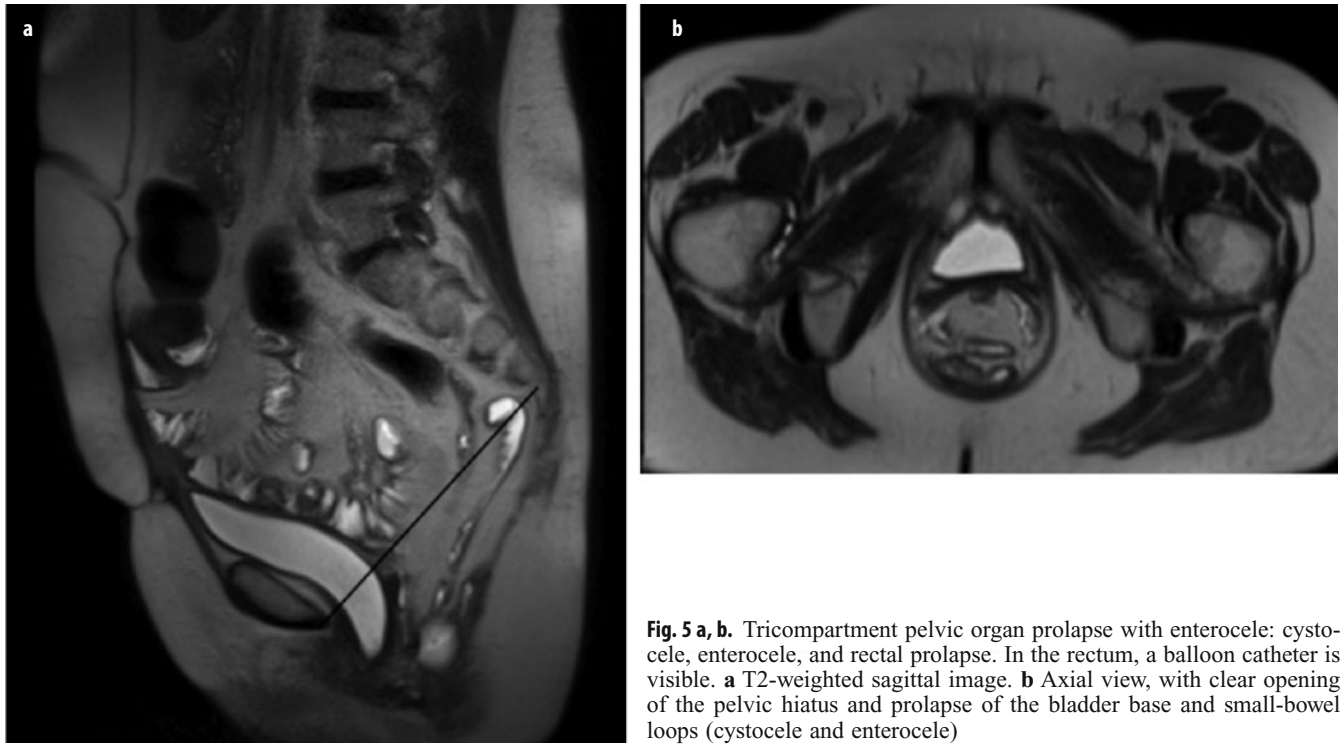


**Fig. 5 a, b.** Tricompartment pelvic organ prolapse with enterocele: cystocele, enterocele, and rectal prolapse. In the rectum, a balloon catheter is visible. **a** T2-weighted sagittal image. **b** Axial view, with clear opening of the pelvic hiatus and prolapse of the bladder base and small-bowel loops (cystocele and enterocele)

posterior (rectovaginal) fascia [8]. Enteroceles may be symptomatic, causing a dragging sensation in the pelvis, or give a sense of fullness and incomplete evacuation and occasionally cause lower abdominal pain. Usually, however, an enterocele does not impair evacuation. According to several authors, MRI is superior to dynamic cystocolpoproctography, which failed to demonstrate up to 20% of enteroceles (Fig. 5).

## Rectal and Perineal Descent

Rectal descent is descent (>3 cm) of the ARJ below the PCL, often combined with rectocele and abnormal descent of the middle and anterior pelvic floor compartments, to variable extents [8, 30]. Generalized pelvic floor weakness is also defined as descending perineal syndrome. One of the main causes is thought to be excessive

and repetitive straining. Other causes are weak pelvic floor muscles caused by pudendal nerve impairment following childbirth trauma or neuropathy [3, 8]. On MR defecography, it is considered mild when between 3 and 5 cm and severe when >5 cm (Fig. 5). The landmark sign for the posterior compartment is the position of the ARJ with respect to the PCL. Abnormal herniation of the bladder below the PCL (cystocele), representing anterior compartment descent, and descent of the vaginal vault (uterovaginal prolapse), representing middle compartment descent, are associated with severe PPFD in >50% of cases [5-8, 20, 30].

### Anismus

Anismus, or spastic pelvic floor syndrome (dyskinetic puborectal syndrome or pelvic floor dyssynergy), is characterized by lack or insufficient relaxation of the puborectal muscle and external anal sphincter during defecation [6-8]. Anismus determines constipation and incomplete defecation due to a paradoxical contraction of the puborectal muscle during straining and defecation, without significant variation in the ARA in the different functional phases (rest, squeezing, straining). At dynamic MRI, paradoxical contraction of the puborectal muscle during straining and defecation causes minimal or absent variation in the ARA in all functional phases (at rest; during contraction, straining, and evacuation). At maximal straining, despite the increasing intra-abdominal pressure, the ARA does not open; hence, defecation and evacuation cannot progress [7, 8]. Unlike in other pelvic floor disorders, anismus requires conservative treatment such as biofeedback therapy. Not uncommonly, however, it may be associated with rectocele or other mechanical disorders. In these cases, conservative treatment always precedes surgery.

## Conclusions

Dynamic pelvic floor MRI provides morphological and functional information on pelvic floor structures. Thanks to its comprehensive diagnostic approach, MRI can facilitate accurate diagnosis and grading of most urogenital and anorectal PFDs without radiation exposure, independent of the technique used. Managing PFDs, particularly ODS, is rapidly evolving, and long-term results are expected to improve. Strict cooperation between radiologists and clinicians is needed for effective therapeutic planning of PFD.

## References


1. DeLancey JOL (1993) Anatomy and biomechanics of genital prolapse. Clin Obstet Gynecol 36:897-909.
2. DeLancey JOL (1994) The anatomy of pelvic floor. Curr Opin Obstet Gynecol 6:313-316.
3. Olsen AL, Smith VJ, Bergstrom JO et al (1997) Epidemiology of surgically managed pelvic organ prolapsed and urinary incontinence. Obstet Gynecol 89:501-506.
4. Elneil S (2009) Complex pelvic floor failure and associated problems. Best Practice & Research Clinical Gastroenterology 23555-23573.
5. Subak LL, Waetjen LE, van den Eeden S et al (2001) Cost of pelvic organ prolapse surgery in the United States. Obstet Gynecol 98.
6. Mortele KJ, Fairhurst J (2007) Dynamic MR defecography of the posterior compartment: indications, technique and MRI features. Eur J Radiol 61:462-472.
7. Maccioni F (2013) Functional disorders of the anorectal compartment of the pelvic floor: clinical and diagnostic value of dynamic MRI. Abdom Imaging 38:930-951.
8. Fielding JR (2002) Practical MR imaging of female pelvic floor weakness. Radiographics 22:295–304.
9. Ganeshan A, Anderson EM, Upponi S et al (2008) Imaging of obstructed defecation. Clin Radiol 63:18-26.
10. Stoker J, Halligan S, Bartram C (2001) Pelvic floor imaging. Radiology 218:1.
11. Bharucha AE (2006) Update of tests of colon and rectal structure function. J Clin Gastroenterol 40:96-103.
12. Karasik S. Spettel CM (1997) The role of parity and hysterectomy on the development of pelvic floor abnormalities revealed by defecography. AJR Am J Roentgenol 169:1555-1558.
13. Elshazly WG, ElNekady Hassan H (2010) Role of dynamic magnetic resonance imaging in management of obstructed defecation 2627 case series. Intern J Surg 274-282.
14. Kelvin FM, Maglinte DD, Hornback JA et al (1992) Pelvic prolapse: assessment with evacuation proctography (defecography). Radiology 184:547e51.
15. Kelvin FM, Maglinte DDT, Hale DS, Benson JT (2000) Female pelvic organ prolapse: a comparison of triphasic dynamic MR imaging and triphasic fluoroscopic cystocoloproctography. AJR Am J Roentgenol 174:81-88.
16. Maglinte DDT, Bartram C (2007) Dynamic imaging of posterior compartment pelvic floor dysfunction by evacuation proctography: techniques, indications, results and limitations. Eur J Radiol 61:454-461.
17. Maglinte DDT, Bartram CI, Hale DA et al (2011) Functional imaging of the pelvic floor. Radiology 258:23-29.
18. Goei R, Kemerink G (1990) Radiation dose in defecography. Radiology 176:137.
19. Bertschinger KM, Hetzer FH, Roos JE et al (2001) Dynamic MR imaging of the pelvic floor performed with patient sitting in an open-magnet unit versus with patient supine in a closed-magnet unit. Radiology 223:501-508.
20. Roos JE, Weishaupt D, Wildermuth S et al (2002) Experience of 4 years with open MR defecography: pictorial review of anorectal anatomy and disease. Radiographics 22:817-832.
21. Pannu HK, Kaufman HS, Cundiff GW et al (2000) Dynamic MR imaging of pelvic organ prolapse: spectrum of abnormalities. Radiographics 20:1567-1582.
22. Solopova AE, Hetzer FH, Marincek B et al (2008) MR defecography: prospective comparison of two rectal enema compositions. AJR Am J Roentgenol 190:118-124.
23. Flusberg M, Sahni VA, Erturk SM et al (2011) Dynamic MR defecography: assessment of the usefulness of the defecation phase. AJR Am J Roentgenol 196:W394-W399.
24. Law JM, Fielding JR (2008) MRI of pelvic floor dysfunctions. Review. AJR Am J Roentgenol 191:S45-S53.
25. El Sayed RF, El Mashed S, Farag A (2008) Pelvic floor dysfunction: assessment with combined analysis of static and dynamic MR Imaging findings. Radiology 248:518-539.
26. Reiner CS, Weishaupt D (2013) Dynamic pelvic floor imaging: MRI techniques and imaging parameters. Abdom Imaging 38:903-911.

27. Betschart C, Chen L, Ashton-Miller JA et al (2013) On pelvic reference lines and the MR evaluation of genital prolapse: a proposal for standardization using the Pelvic Inclination Correction System. Int Urogynecol J 24:1421-1428.
28. Woodfield CA, Krishnamoorthy S, Hampton BS (2010) Imaging pelvic floor disorders: trend toward comprehensive MRI. AJR Am J Roentgenol 194:1640-1649.
29. Felt-Bersma RJ, Cuesta MA (2001) Rectal prolapse, rectal intus-susception, rectocele, and solitary rectal ulcer syndrome. Gastroenterol Clin North Am 30:199-222.
30. Broekhuis SR, Hendrik JCM, Jurgen JF (2010) Perineal descent and patients' symptoms of anorectal dysfunction, pelvic organ prolapse, and urinary incontinence. Int Urogynecol J 21:721-729.

# Diffuse Liver Disease: Cirrhosis and Vascular Diseases

Tobias J. Heye, Elmar M. Merkle

Department of Radiology, University Hospital Basel, Basel, Switzerland

## Cirrhosis

A variety of diseases may lead to liver cirrhosis, with alcohol abuse, viral hepatitis, and steatohepatitis being the most common entities in the Western world. Liver cirrhosis is one of the main risk factors for developing hepatocellular carcinoma (HCC). The radiologist's role in the workup of patients with liver cirrhosis is of utmost importance, as imaging findings oftentimes serve as the basis for selecting the most appropriate treatment strategy, e.g., surgical resection, locoregional therapy, or transplantation. Commonly, the radiologist is faced with the following questions:

Is there any imaging evidence for diffuse liver disease, such as fibrosis or cirrhosis?

Are there any focal hepatic lesions – benign, premalignant, or malignant? What is the exact size of these lesions? Is there any vascular infiltration/complication?

What is the most appropriate imaging modality to further workup/follow-up focal lesions in the cirrhotic liver? What is an appropriate time interval?

How does the radiologist's report impact the patient's treatment options?

Are there any signs of potentially life-threatening complications from cirrhosis, e.g., portal hypertension with gastroesophageal varices?

To answer all these questions, radiologists must be familiar with both the imaging appearance of liver cirrhosis and guidelines for staging and treatment strategies used at their home institution for focal lesions such as HCC.

### Appearance of Liver Cirrhosis on Cross-Sectional Imaging Modalities

Liver cirrhosis, representing irreversible hepatic fibrosis bridging the portal tracts, affects the organ's contour and the size of hepatic lobes and segments, and may cause benign or malignant focal lesions. Processes associated with cirrhosis include ascites and evidence of portal hypertension. Splenomegaly is the most common finding of portal hypertension, oftentimes associated with Gamna-Gandy bodies (Fig. 1). These fibrosiderotic nodules are composed of fibrous tissue and elastic fibers with deposition of iron and calcium salts, best appreciated on gradient echo MR images due to the lack of a 180° refocusing pulse. Besides cases of congestive splenomegaly, e.g., cirrhosis, Gamna-Gandy bodies can be seen in sickle cell anemia and hemochromatosis. Varices are often found in liver cirrhosis. These collateral vessels are seen as enhancing, tortuous vessels in the paraesophageal and gastric cardial region, porta hepatis, peritoneal cavity, retroperitoneum, and even passing through the liver via paraumbilical collaterals (Fig. 2). Another common finding in patients with liver cirrhosis is the presence of mesenteric, omental, or retroperitoneal edema. Edema is usually mild but may be severe in up to 25% of patients.

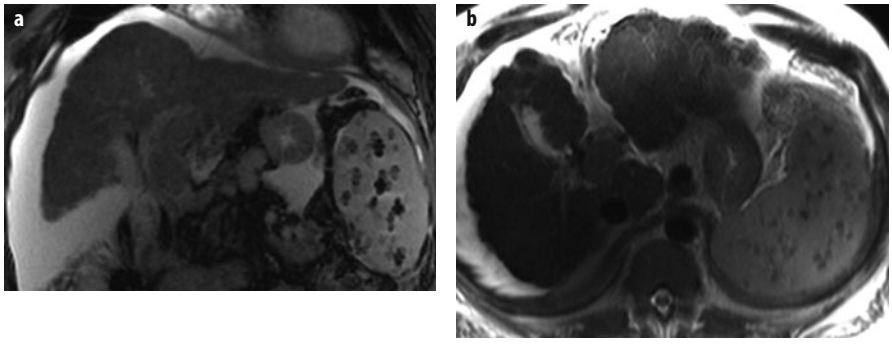


**Fig. 1 a, b.** **a** Coronal steady state with free precession magnetic resonance (MR) image shows irregular liver contour and massive ascites. Of note are the fibrosiderotic nodules, also known as Gamna-Gandy bodies, causing marked susceptibility artifacts within the spleen. **b** Corresponding axial turbo spin-echo T2-weighted MR image shows irregular liver contour and massive ascites. Note susceptibility artifacts within the spleen are less pronounced due to the pulse-sequence design (180° refocusing pulse)

*Diseases of the Abdomen and Pelvis 2014-2017*,
DOI: 10.1007/978-88-470-5659-6_10 

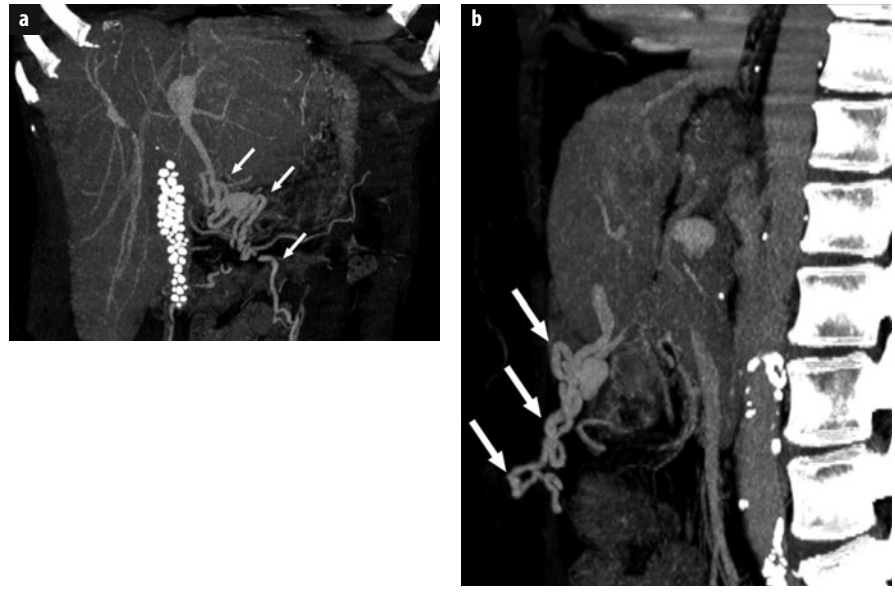


**Fig. 2 a, b.** **a** Postcontrast coronal thick-slice maximum intensity projection from a multidetector computed tomography (MDCT) data set of a 59-year-old woman with liver cirrhosis and recanalized paraumbilical veins (*arrows*). Note calcified gallstones. **b** Corresponding sagittal view

Adenopathy can be seen in the porta hepatis and the peripancreatic region in some cases. Occasionally, these nodes can be large and bulky, mimicking neoplastic involvement. These lymph nodes are most prominent in cases of primary biliary cirrhosis.

Cirrhosis markedly distorts the hepatic parenchyma, producing either a smooth, nodular, or lobular appearance of the hepatic capsule in the majority of cases. Margins that are either smooth or deformed by multiple small nodules are typical in micronodular cirrhosis. These micronodules underlying the surface of the liver are often not visualized at computed tomography (CT) or magnetic resonance imaging (MRI). At present, high-resolution transabdominal sonography with a 7.5-MHz transducer may represent the best imaging tool for visualizing these small nodules. Coarse nodularity of the margin is the result of macronodular cirrhosis. Finally, a lobular liver is usually caused by marked segmental atrophy and hypertrophy rather than by large regenerative nodules. Tremendous overlap in the frequency of smooth and nodular livers among different causes of cirrhosis usually prevents etiological distinction.

Approximately 25% of end-stage cirrhotic livers appear normal in size and shape in all cross-sectional imaging modalities; another third may be diffusely atrophic. The majority of end-stage cirrhotic livers exhibit a combination of segmental hypertrophy and atrophy, with the predominant finding being hypertrophy of liver segments 1-3. Focal atrophy is most common in segments 4-8 and may range from mild to complete involution of the affected segments. Occasionally, segments 2/3 and 5/7 may be atrophic. This is most often seen in patients with primary sclerosing cholangitis. Another rare finding in patients with primary sclerosing cholangitis is a higher attenuation in segment 1, causing a pseudotumor in the caudate lobe. Diffuse hypertrophy, however, may be seen in patients with primary biliary cirrhosis.

Approximately 25% of all patients with end-stage cirrhosis show an inhomogeneous appearance in all parts of the liver on unenhanced CT, T2-weighted magnetic resonance (MR) images, and T1-weighted images acquired during the hepatocyte phase following administration of a combined (extracellular and hepatobiliary) gadolinium-containing contrast agent, such as gadoxetate or gadobenate [1, 2]. On cross-sectional imaging, four different patterns of diffuse fibrosis may be seen:

– Patchy, poorly defined regions of low attenuation on unenhanced CT (or hypointensity on T1-weighted and hyperintensity on T2-weighted MRI)
– Thin, perilobular bands of low attenuation on unenhanced CT
– Thick, fibrosis bridging of low attenuation surrounding regenerative nodules (most commonly seen in patients with primary biliary cirrhosis)
– Diffuse fibrosis causing high-attenuation perivascular cuffing (most commonly seen in patients with primary biliary cirrhosis).

A commonly used scoring system to grade diffuse fibrosis is the METAVIR score, originally developed to grade fibrosis in hepatitis C patients. METAVIR scores are defined by fibrosis (F) stage:

– F0 No fibrosis
– F1 Portal fibrosis without septa
– F2 Portal fibrosis with rare septa
– F3 Numerous septa without cirrhosis
– F4 Cirrhosis.

Besides diffuse fibrosis, as mentioned above, radiologists must be familiar with an entity called focal or confluent hepatic fibrosis. In patients with liver cirrhosis, focal fibrosis can be confused with HCC due to an overlap of imaging features. Focal fibrosis usually appears bright on T2-weighted MR images, dark on unenhanced T1-weighted images, and demonstrates delayed enhancement following extracellular contrast agent administration (Fig. 3). Focal confluent fibrosis may be seen in all types of cirrhosis; it occurs most commonly in primary

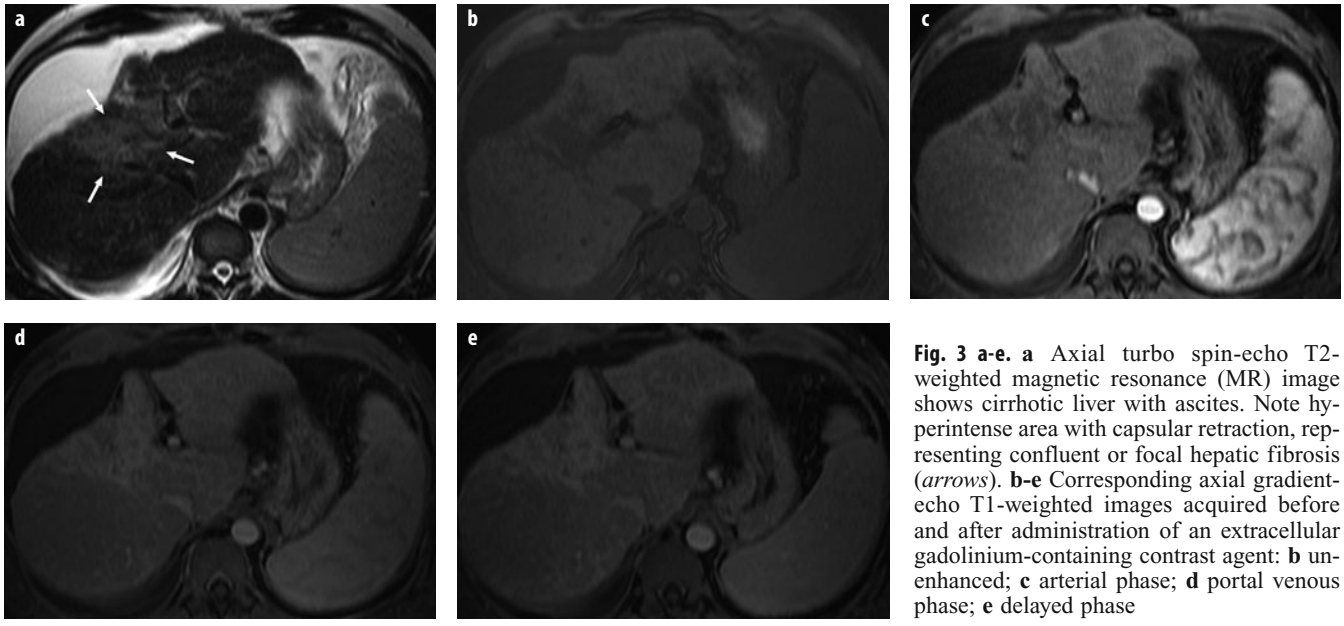


**Fig. 3 a-e. a** Axial turbo spin-echo T2-weighted magnetic resonance (MR) image shows cirrhotic liver with ascites. Note hyperintense area with capsular retraction, representing confluent or focal hepatic fibrosis (*arrows*). **b-e** Corresponding axial gradient-echo T1-weighted images acquired before and after administration of an extracellular gadolinium-containing contrast agent: **b** unenhanced; **c** arterial phase; **d** portal venous phase; **e** delayed phase

sclerosing cholangitis, and least commonly in primary biliary cirrhosis [3]. Additional imaging features are: (1) focal retraction of the liver capsule over the area of fibrosis, (2) incomplete involvement of liver segments with accompanying atrophy, and (3) characteristic location in segments 4a, 4b, 5, and 8, with a wedge-shaped structure radiating from the porta hepatis.

### Spectrum of Focal Lesions in Liver Cirrhosis

Another characteristic sign of liver cirrhosis is the development of a spectrum of focal lesions ranging from benign regenerative nodules to malignant HCC. In 1995, the International Working Party introduced a new nomenclature for hepatocellular nodules, replacing former pathological descriptions such as adenomatous hyperplasia, macroregenerative nodule, and other terms with the term dysplastic nodule [4]. Currently, focal liver lesions in cirrhosis are classified as:

- Regenerative nodules
- Low-grade dysplastic nodules
- High-grade dysplastic nodules
- Dysplastic nodule with a HCC subfocus
- Well-differentiated HCC
- Poorly differentiated HCC.

### Regenerative Nodules

By definition, regenerative nodules are present in all cirrhotic livers; however, these nodules are visualized in only 25% of unenhanced CT scans and approximately 50% of MR images. These nodules may present as high-attenuation lesions on unenhanced CT due to their iron and/or glycogen content, or simply because they are surrounded by lower-attenuation fibrosis. On portal venous phase contrast-enhanced scans, these nodules are rarely revealed. On MR images, these focal lesions can appear hypo-, iso-, or hyperintense on T1-weighted images, with isointense being the most usual and hyperintense the most unusual. On T2-weighted images, they typically appear as hypointense nodules (iron causes local magnetic field inhomogeneities, with decrease of liver signal intensity due to shortening of the T2 relaxation time). Following the administration of a gadolinium-containing extracellular contrast agent (GBCA), regenerative nodules usually appear hypointense during arterial and portal venous phases and become more isointense during the equilibrium and delayed phases. Using a combined gadolinium-containing contrast agent, such as gadoxetate, regenerative nodules generally demonstrate contrast uptake and excretion during the hepatocyte phase due to preserved hepatocellular function and intact organic ion transporters; therefore, regenerative nodules demonstrate signal intensity similar to that of background liver during the hepatocyte phase.

### Dysplastic Nodules

Dysplastic nodules develop from regenerative nodules and contain atypical hepatocytes but do not have definite features of malignancy on histology. They are present in 15-25% of cirrhotic livers and are histologically classified as low or high grade, depending on the degree of dedifferentiation. High-grade dysplastic nodules are considered premalignant and can undergo malignant transformation in a period as short as 4 months and are rarely detected by CT. If detected, they may appear slightly hyper- or isodense on unenhanced scans. On MR imaging, they appear iso- or hyperintense on T1-weighted images and iso- to hypointense on T2-weighted images. Following administration of an extracellular contrast agent, dysplastic nodules usually are hypodense/hypointense during the arterial, portal venous, and delayed

phases. However, these lesions occasionally demonstrate hyperenhancement during the arterial phase, thus mimicking HCC. Using a combined MR contrast agent such as gadoxetate, their appearance during the hepatocyte phase varies [2, 5, 6]. As with regenerative nodules, dysplastic nodules receive their blood supply mainly from the portal vein, although high-grade nodules may develop arterial hypervascularity. With progression of atypia, the number of expressed organic ion transporters decreases, reducing their ability to take up gadolinium ethoxybenzyl diethylenetriamine pentaacetic acid (Gd-EOB-DTPA). In the hepatocyte phase of gadoxetate, nodules that retain their ability to take up the agent but not excrete it appear homogenously or heterogeneously hyperintense due to intracellular cholestasis, whereas nodules that have lost their ability to take up the agent appear hypointense. Such hypointense nodules can be mistaken for HCCs in the hepatocyte phase. On the other hand, MR imaging with hepatobiliary contrast agents is the only modality that can detect these premalignant lesions [7] and open the window for the treatment of early HCC.

#### Hepatocellular Carcinoma

HCC is a malignant neoplasm composed of dedifferentiated hepatocytes. In cirrhotic livers, HCC usually develops from dysplastic nodules. HCC is solitary in about 50% of cases, multifocal in approximately 40%, and diffuse in <10%. The vascular supply of HCC is mainly arterial through neoangiogenesis, with markedly reduced or absent portal supply. Approximately 80-90% of all HCCs demonstrates arterial hypervascularity on CT/MR imaging after a bolus injection of extracellular contrast agent. Hyperenhancement is independent of histopathologic grade. After arterial-phase hyperenhancement, HCCs typically show washout in the delayed phases, with signal intensity being lower than that of background liver parenchyma (Fig. 4). Some hypervascular HCCs, however, may not show washout and so may be difficult to see on delayed phases. In these cases, administering a combined MR contrast agent may be beneficial for demonstrating an HCC as a hypointense mass during the hepatobiliary phase (Fig. 5).

Ten to 20% of HCCs are hypovascular and enhance less than surrounding liver parenchyma in the arterial phase. This is presumably from loss of arterial and portal blood supply and the absence of arterial neoangiogenesis. Typically, hypovascular HCCs are small, well-differentiated tumors, although poorly differentiated; infiltrating HCCs also may be hypovascular. Such hypovascular tumors may be difficult to detect on dynamic GBCA-enhanced MR images despite being large and biologically aggressive. Upon gadoxetate administration, the contrast behavior of typical HCCs in the dynamic phases (arterial, portovenous, equilibrium) is comparable

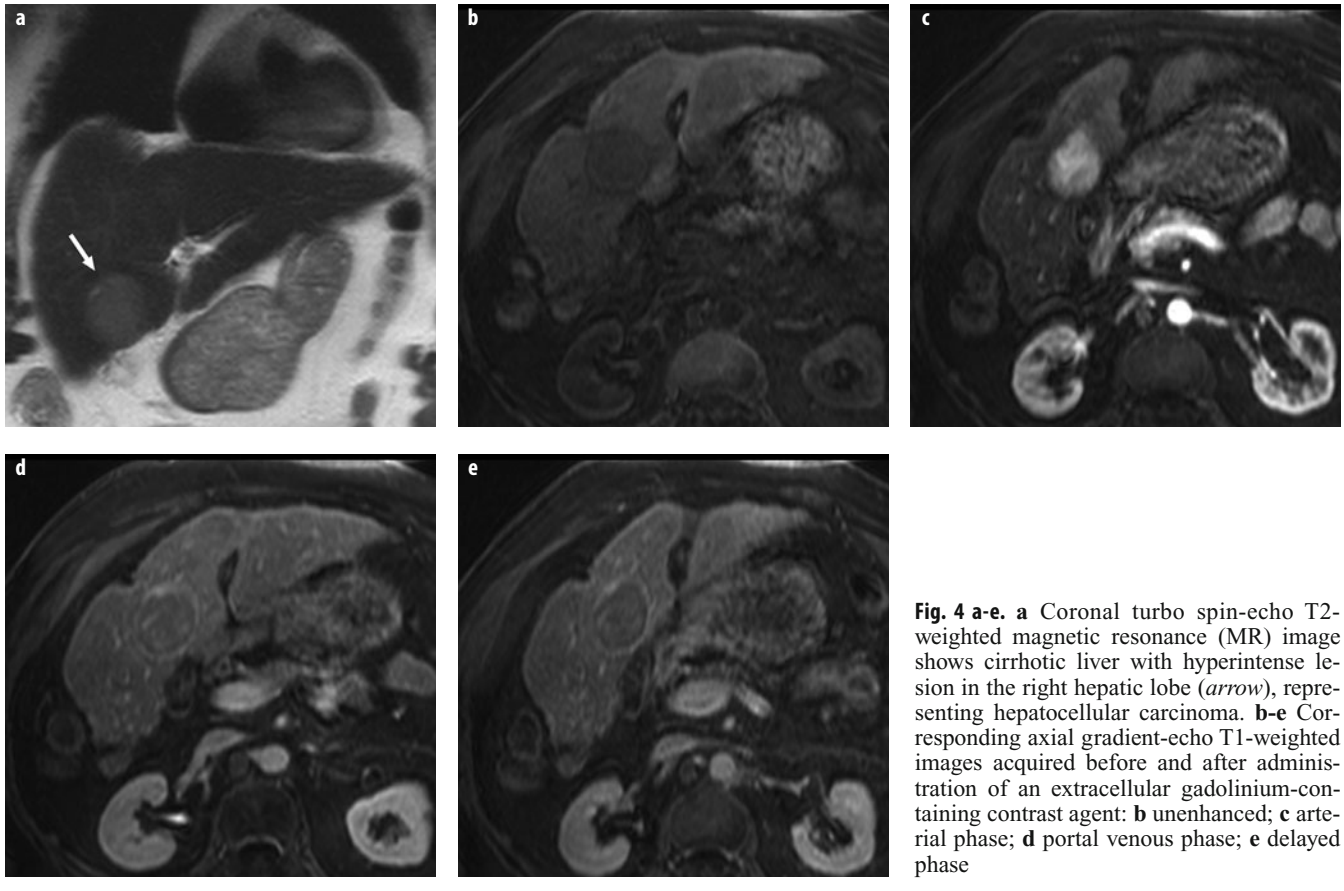


**Fig. 4 a-e.** **a** Coronal turbo spin-echo T2-weighted magnetic resonance (MR) image shows cirrhotic liver with hyperintense lesion in the right hepatic lobe (*arrow*), representing hepatocellular carcinoma. **b-e** Corresponding axial gradient-echo T1-weighted images acquired before and after administration of an extracellular gadolinium-containing contrast agent: **b** unenhanced; **c** arterial phase; **d** portal venous phase; **e** delayed phase


**Fig. 5 a-h.** **a** Transverse ultrasound (US) of the right hepatic lobe in a 60-year-old patient with liver cirrhosis shows a hypoechogenic mass (*arrows*)) suspicious for a hepatocellular carcinoma. **b-d** Corresponding dynamic contrast-enhanced computed tomography (CT): **b** arterial phase; **c** portal venous phase; **d** delayed phase. **e-h** Corresponding dynamic gradient-echo T1-weighed magnetic resonance (MR) images acquired after administration of gadoxetate, a combined gadolinium-containing contrast agent; **e** arterial phase; **f** portal venous phase; **g** delayed phase; **h** hepatobiliary phase

with that of extracellular GBCA, i.e., arterial hyperenhancement followed by rapid washout, except that washout may appear more rapid with gadoxetate because the background liver parenchyma progressively enhances [8]. The degree of peripheral rim enhancement may be similar to or lower than that seen with extracellular GBCAs, depending on the gadoxetate dose used. In the hepatocyte phase, typical HCCs are well-delineated areas of low signal intensity relative to surrounding liver parenchyma, as they do not have the ability to take up gadoxetate. Liver-to-lesion contrast typically peaks in the hepatocyte phase, when it may exceed arterial-phase contrast by 50%. In addition, tumor margins are clearly delineated in the hepatocyte phase, potentially improving detection of HCCs not readily visible in the dynamic imaging phases. If the liver parenchyma does not enhance intensely or homogeneously, however, liver-to-lesion contrast may be low, and lesion margins may be difficult to define in the hepatocyte phase. Up to 5% of HCCs may show paradoxical uptake of gadoxetate in the hepatocyte phase, appearing as iso- or hyperintense relative to surrounding liver parenchyma.

### Staging and Treatment Strategies Commonly Used for Patients with Focal Lesions in Cirrhosis

A commonly used diagnostic algorithm for the workup of focal lesions in patients with cirrhosis or chronic hepatitis B is illustrated in Fig. 6. Of note, these recommendations do not include the use of contrast-enhanced

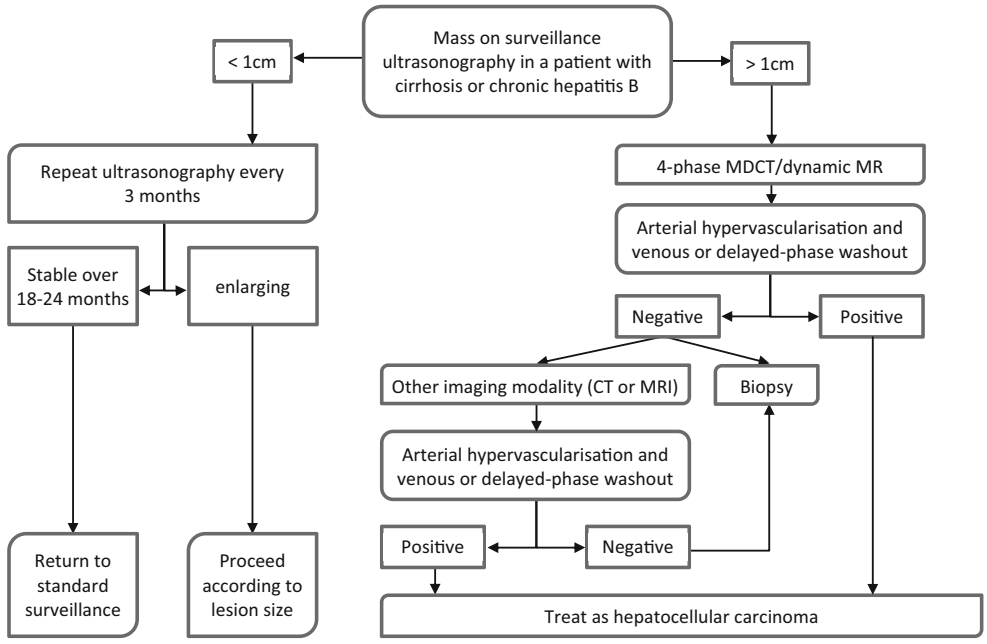


**Fig. 6.** Diagnostic algorithm for the workup of focal hepatic lesions in cirrhosis, as suggested by the Barcelona Clinic Liver Cancer Staging and Treatment Strategy

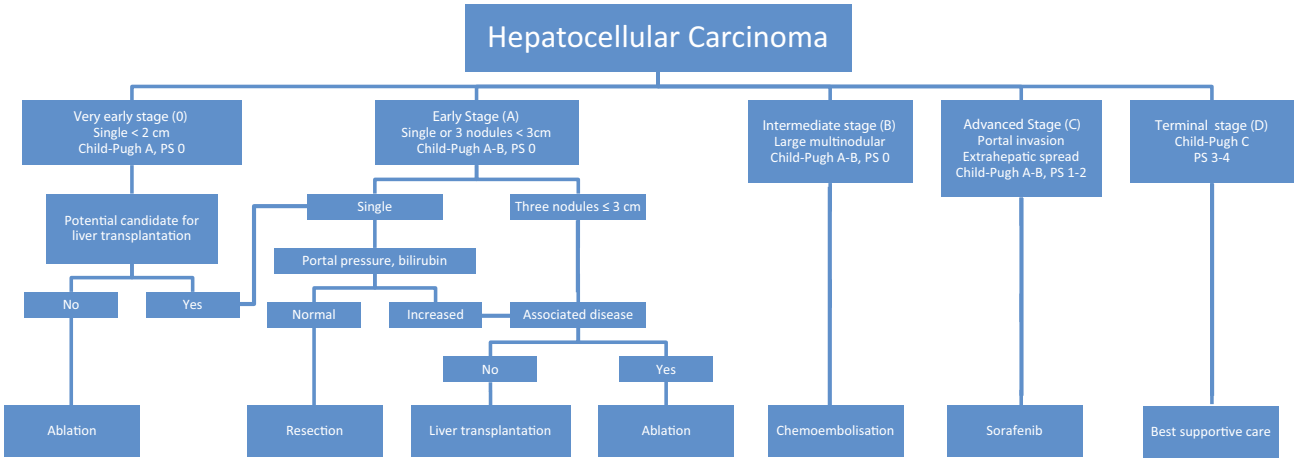


**Fig. 7.** Barcelona Clinic Liver Cancer Staging and Treatment Strategy widely used in Europe

percutaneous ultrasound (US) or MR imaging following administration of a combined gadolinium-containing contrast agent, such as gadoxetate. The Barcelona Clinic Liver Cancer (BCLC) Staging and Treatment Strategy is shown in Fig. 7. This algorithm has proven helpful, as the 5-year survival rates for curative (very early and early stages) and palliative (intermediate, advanced, and terminal stages) treatment approaches are 50-70% and 10-40%, respectively [9, 10].

## Vascular Diseases

### Portal Venous Thrombosis and Cavernous Transformation of the Portal Vein

Hypercoagulability, stasis, and disruption of vascular endothelium are known as Virchow's triad and characterize the main mechanisms leading to intravascular thrombus formation. Portal venous stasis, in particular, is often due

to parenchymal abnormalities such as cirrhosis, as well as large HCCs and pancreatic carcinoma; it is also a known complication after splenectomy. Disruption of the portal venous endothelium can occur in association with sepsis, direct trauma, schistosomiasis, chronic inflammatory bowel disease, and pylephlebitis and is a complication after direct catheterization.

Portal venous thrombosis has been described as a transient disease; however, spontaneous revascularization is rare once the portal venous thrombus has reached smaller intrahepatic branches. In this case, portoportal venous channels may form to maintain portal perfusion. In the porta hepatis, a meshwork of finely to markedly enlarged serpentine-type vessels can also be seen. Intrahepatically, portal venous shunt formation from one segmental portal vein to another can occur. Simultaneously, portosystemic collateral channels may form. Chronic occlusion of the portal vein or one of its main segmental branches may be accompanied by segmental atrophy of the affected hepatic segments, as well as compensatory hypertrophy of the other segments.

Multidetector CT (MDCT) and MR imaging of the hepatic vasculature are capable of demonstrating portal venous thrombosis and cavernous transformations during the portal venous imaging phase. Cavernous transformations can present a sponge-like mass effect. In particular, hepatic MR imaging with multiple arterial and portal-venous-phase acquisitions contributes important information in the diagnostic workup. As an indirect sign, occlusion of a larger intrahepatic branch of the portal vein is usually accompanied by a compensatory hyperenhancement on arterial-phase images of this segment, which is caused by the so-called arterial buffer reaction. Portal vein patency can be confirmed or excluded by performing flow-sensitive gradient-echo sequences, such as steady state with free precession.

### Budd-Chiari Syndrome

The description of classic Budd-Chiari syndrome focuses on a combination of portal venous hypertension and hepatomegaly due to an obstruction of hepatic venous drainage. The leading characteristic of Budd-Chiari syndrome is obstruction of venous outflow from the sinusoidal bed of the liver, with subsequent development of slowly increasing portal venous hypertension. Budd-Chiari syndrome type 1 involves occlusion of the inferior vena cava (IVC), potentially with secondary occlusion of hepatic veins; type 2 involves occlusion of the major hepatic veins; type 3 involves veno-occlusive liver disease or progressive thrombotic occlusion of small centrilobular veins.

Hepatic venous outflow stasis may be related to membranous obstruction of the IVC, constrictive pericarditis, atrial myxoma, cardiac insufficiency, Hodgkin's disease, cirrhosis, HCC, hematoma, or abscess; rarely, it may be related to mass effects from hepatic metastases, cholangiocarcinomas, or adrenal-renal carcinomas.

The role of MDCT and MR imaging of the hepatic vasculature in the specific settings of suspected, confirmed, or treated Budd-Chiari syndrome includes identifying vascular anatomy, detecting intrahepatic or extrahepatic masses, parenchymal evaluation, and assessing shunt patencies in cavoatrial, mesocaval, and mesoatrial vascular bypass situations. Any visualized reduction in vascular caliber of the hepatic veins or missing connections to the IVC, or their complete absence, can be part of the imaging spectrum. In addition, existence of newly formed but less competent intrahepatic collateral veins can be observed.

Alteration to venous drainage ultimately leads to peripheral hepatic atrophy; compensatory hypertrophy of central parenchymal segments or the caudate lobe, which usually have an independent, separate venous drainage directly onto the IVC, can be observed. MDCT provides direct visualization of thrombotic material that can occlude or narrow veins or shunts. At hepatic MR imaging, flow-void analysis and phase-contrast angiographic techniques depict and quantify flow, including depicting flow reversal.

### Liver Disease in Congestive Heart Failure

Passive hepatic congestion due to chronic failure of the right side of the heart may appear as widening and splaying of the central hepatic veins and overall hepatomegaly. The combination of decreased venous blood flow, increased venous pressure, and hypoxemia leads to diffuse cellular necrosis. Long standing diffuse cellular necrosis induces diffuse hepatic fibrosis with a micronodular cirrhotic pattern, a condition also known as "nutmeg" liver. Macroscopically, hepatic MDCT and MR imaging may demonstrate cirrhotic changes as a nonspecific imaging finding. However, microscopically, the hepatic architecture remains intact.

### Hepatic Arterial Obstruction and Intrahepatic Arteriovenous Fistulas

Significant hepatic artery stenosis or occlusion is a much rarer entity, commonly associated with liver transplantation. The arterial anastomosis of the donor liver to the native vessel trunk can be significantly narrowed initially and may subsequently thrombose. In patients who have not undergone transplantation, an embolic occlusion is the most common cause of hepatic arterial compromise. The hepatic artery constitutes only ~25% of blood flow to the liver, supplying mainly the endothelium of the intrahepatic bile ducts and fibrous hepatic tissue.

Contrast-enhanced MDCT and MR imaging show diffusely diminished enhancement of the hepatic parenchyma in cases of severe hepatic artery stenosis or occlusion. High-resolution MDCT and MR imaging of the porta hepatis can demonstrate the exact location of the culprit arterial thrombus or enable quantification of the degree of stenosis.

Intrahepatic arteriovenous fistulas are connections between hepatic arteries and hepatic veins as well as between hepatic arteries and portal veins. Diffuse intrahepatic distribution patterns are seen in hereditary hemorrhagic telangiectasia, also known as Osler disease; solitary occurrences of arteriovenous fistulas are most often related to liver biopsies or surgical procedures. Functionally, the increased arterial perfusion of the liver tissue leads to secondary hypertrophy; severe cases may show signs of right-sided heart failure. Significant dilatation of the draining vein is frequently observed, and in the case of arterial portal venous shunts, the resultant increased portal venous pressure may lead to further symptoms of portal venous hypertension.

Both MDCT and dynamic contrast-enhanced MR imaging are capable of depicting early venous drainage that occurs during the hepatic arterial phase and help estimate the functional significance of the fistula.

### Liver Infarction

Infarction of hepatic parenchyma is rare, in large part because of the dual blood supply provided by hepatic arteries and portal veins. Therefore, noticeable infarcts of hepatic parenchyma are possible only if both sources of hepatic blood supply are substantially compromised, as in acute shock trauma and hypercoagulability, as well as in preeclampsia or hemolytic anemia, elevated liver enzymes, low platelet (HELLP) syndrome and as a vascular complication after liver transplantation.

At contrast-enhanced MDCT, the typical appearance of smaller liver infarcts is a peripheral wedge-shaped area of low attenuation. Larger infarcts may demonstrate a more geographic distribution. At MR imaging, lesions are typically hypointense on T1-weighted images but hyperintense on T2-weighted images. Although the diagnosis of liver infarction is evident in most cases, it may be confused with focal fatty infiltration, abscess, or even a tumor.

## References

1. Ringe KI, Husarik DB, Sirlin CB, Merkle EM (2010) Gadoxetate disodium-enhanced MRI of the liver: part 1, protocol optimization and lesion appearance in the noncirrhotic liver. AJR Am J Roentgenol 195:13-28.
2. Cruite I, Schroeder M, Merkle EM, Sirlin CB (2010) Gadoxetate-enhanced MR imaging of the liver: Part 2: Protocol optimization and lesion appearance in the cirrhotic liver. AJR Am J Roentgenol 195:29-41.
3. Husarik DB, Gupta RT, Ringe KI et al (2011) Contrast enhanced liver MRI in patients with primary sclerosing cholangitis: inverse appearance of focal confluent fibrosis on delayed phase MR images with hepatocyte specific versus extracellular gadolinium based contrast agents. Acad Radiol 18:1549-1554.
4. Anon (1995) Terminology of nodular hepatocellular lesions. Hepatology 22:983-993.
5. Chou CT, Chen YL, Su WW et al (2010) Characterization of cirrhotic nodules with gadoxetic acid-enhanced magnetic resonance imaging: the efficacy of hepatocyte-phase imaging. J Magn Reson Imaging 32: 895-902.
6. Rhee H, Kim MJ, Park MS, Kim KA (2012) Differentiation of early hepatocellular carcinoma from benign hepatocellular nodules on gadoxetic acid-enhanced MRI. Br J Radiol 85: e837–e844.
7. Bartolozzi C, Battaglia V, Bargellini I et al (2013) Contrast-enhanced magnetic resonance imaging of 102 nodules in cirrhosis: correlation with histological findings on explanted livers. Abdom Imaging 38:290-296.
8. Zech CJ, Reiser MF, Herrmann KA (2009) Imaging of hepatocellular carcinoma by computed tomography and magnetic resonance imaging: state of the art. Dig Dis 27:114-124.
9. Bruix J, Sherman M (2011) Management of hepatocellular carcinoma: an update. Hepatology 53:1020-1022.
10. Forner A, Llovet JM, Bruix J (2012) Hepatocellular carcinoma. Lancet 379:1245-1255.

# Imaging of Diffuse and Inflammatory Liver Disease

Pablo R. Ros

University Hospitals Case Medical Center, Case Western Reserve University, Cleveland, OH, USA

## Introduction

The role of imaging in the detection, characterization, and follow-up of diffuse liver disease has increased due to advances in cross-sectional imaging. Diffuse liver disease is classified classically along pathogenesis into cirrhosis, vascular, congenital, metabolic and storage, and neoplastic. This chapter discusses the last four categories and includes both diffuse and focal inflammatory/infectious diseases. Elsewhere in this syllabus, cirrhosis and vascular diseases are reviewed.

## Metabolic and Storage Diseases

### Steatosis

Hepatic steatosis results from a variety of abnormal processes, including increased production or mobilization of fatty acids (e.g., obesity, steroid use) or decreased hepatic clearance of fatty acids due to hepatocellular injury (e.g., alcoholic liver disease, viral hepatitis). Histopathologically, the hallmark of all forms of fatty liver is accumulation of fat globules within hepatocytes. The distribution of steatosis can be variable, ranging from focal, to regional, to diffuse. Diffuse steatosis is common and estimated to occur in ~30 % of obese patients. Patients with steatosis are usually asymptomatic, although some individuals may present with right upper quadrant pain or abnormal liver function parameters.

Non-alcohol-related liver steatosis is also known as nonalcoholic fatty liver disease (NAFLD). Histopathologic findings of NAFLD vary from steatosis alone to steatosis with inflammation, necrosis, and fibrosis. At the most severe end of the NAFLD spectrum is nonalcoholic steatohepatitis (NASH) with or without cirrhosis. Histopathologic findings of NASH include steatosis (predominately macrovesicular), mixed lobular inflammation, and hepatocellular ballooning. Unlike steatosis alone, NASH may progress to cirrhosis.

Computed tomography (CT) easily identifies diffuse steatosis. The attenuation value of normal liver is usually 8 HU greater on average than that of spleen on noncontrast CT images. In patients with fatty change, however, an abnormally decreased density will be demonstrated, typically 10 HU and 25 HU less than the spleen on noncontrast CT and contrast-enhanced CT images, respectively. The diagnosis of hepatic steatosis is more reliably made on noncontrast images.

Undoubtedly the most sensitive technique to detect fatty change of the liver is the use of in-phase and out-of-phase gradient echo magnetic resonance imaging (GRE-MRI) pulse sequences (Fig. 1). Multiecho sequences, MR spectroscopy, and other MR techniques have been successfully proposed to quantify the fat burden in the liver. Conjoint iron deposition, however, may be a confounding factor in estimating the fat fraction based on dual-echo chemical-shift imaging. The fat fraction may be overestimated, and therefore, the component of iron deposition requires correction, as suggested by Kang et al.

Hepatic fatty change is, however, not always uniform, but it can present as a focal area of steatosis in an otherwise normal liver (focal steatosis) or as subtotal fatty change with sparing of certain areas (focal sparing). On imaging, several features allow accurate identification of focal fatty change or focal spared areas: (1) the typical periligamentous and periportal location, (2) lack of mass effect, (3) sharply angulated boundaries of the area, (4) nonspherical shape, (5) absence of vascular displacement or distortion, and (6) lobar or segmental distribution.

### Iron Overload

Iron overload states are categorized in hemochromatosis, where the iron accumulates preferentially within hepatocytes, and in hemosiderosis, where it is deposited in the Kupffer cells.

#### Primary Hemochromatosis

Hereditary or primary hemochromatosis is an autosomal recessive disorder of iron metabolism characterized by

*Diseases of the Abdomen and Pelvis 2014-2017*,
DOI: 10.1007/978-88-470-5659-6_11 

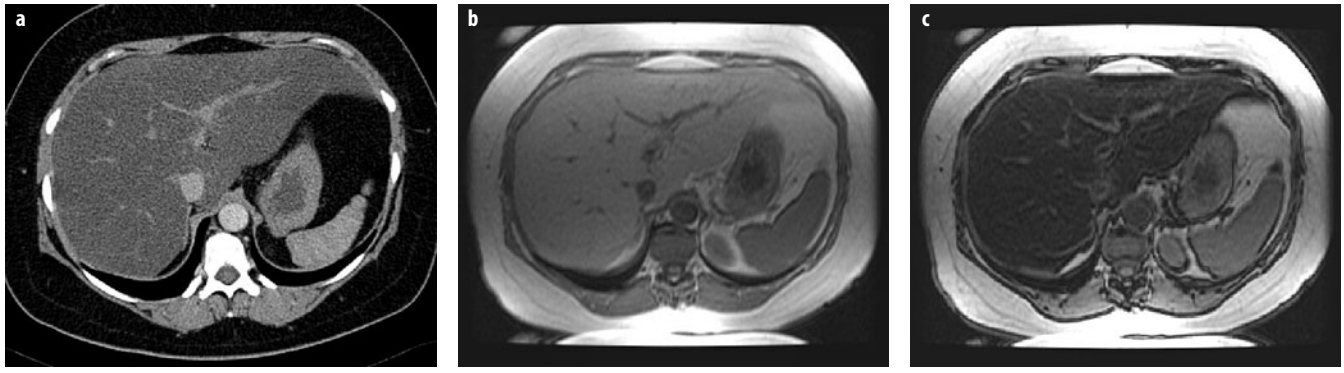


**Fig. 1 a-c.** Diffuse fatty liver. A 41-year-old woman presenting with epigastric pain. **a** Axial contrast-enhanced computed tomography image demonstrates diffuse low attenuation of the liver without displacement of the hepatic vessels. **b** In-phase and **c** out-of-phase T1-weighted images show significant signal drop in the liver on the out-of-phase images. Reproduced from Hodler J, von Schulthess GK, Zollikofer ChL (Eds) (2010) Diseases of the Abdomen and Pelvis 2010-2013. Springer-Verlag Italia, Milan, pp. 56-60

abnormal absorption of iron from the gut with subsequent excessive deposition into hepatocytes, pancreatic acinar cells, myocardium, joints, endocrine glands, and skin. In addition, reticuloendothelial system (RES) cells in patients with primary hemochromatosis are abnormal and unable to store processed iron effectively. As a consequence, patients with primary hemochromatosis do not accumulate iron into the RES. Clinical findings of cirrhosis and its complications [portal hypertension, development of hepatocellular carcinoma (HCC)] predominate in patients with long-lasting disease.

On CT, excessive storage of iron into hepatocytes will result in an overall increased density. However, this CT appearance of a hyperdense liver is nonspecific, as similar features can be seen with gold deposition and in Wilson's disease, type IV glycogen storage disease, and following amiodarone administration. Performing noncontrast CT in patients with suspected hemochromatosis is important because excessive iron cannot be detected in the setting of enhancing parenchyma.

MRI is far more specific than any other imaging modality for characterizing iron overload due to the magnetic susceptibility effect of iron. The superparamagnetic effect of accumulated iron in hepatocytes results in significant reduction of signal intensity on T2-weighted images. Comparison of liver signal intensity with that of paraspinal muscles provides a useful internal control. HCCs, complicating 35% of patients with advanced hemochromatosis, are usually easily detected on both T1- and T2-weighted images due to the background of decreased liver signal intensity.

## Hemosiderosis

In patients with hemosiderosis or siderosis, due to either transfusional iron overload states or dyserythropoiesis (e.g., thalassemia major, sideroblastic anemia, pyruvate kinase deficiency, chronic liver disease), the excessive iron is processed and accumulates in organs containing reticuloendothelial cells, including liver, spleen, and bone marrow.

**Fig. 2.** Hemosiderosis. A 45-year-old woman with long history of sickle cell anemia requiring multiple transfusions. Axial nonenhanced computed tomography image demonstrates increased attenuation of the liver. Reproduced from Hodler J, von Schulthess GK, Zollikofer ChL (Eds) (2010) Diseases of the Abdomen and Pelvis 2010-2013. Springer-Verlag Italia, Milan, pp. 56-60

On CT, there is diffuse, increased attenuation of liver and spleen (Fig. 2). On MRI, the extrahepatic signal intensity changes in the spleen and bone marrow distinguish primary hemochromatosis from hemosiderosis. Although in general the clinical significance of transfusional iron overload states is negligible, patients with chronic hemosiderosis can develop symptoms similar to those of the primary form, as well as cirrhosis and HCC.

## Wilson Disease

Wilson disease, also known as hepatolenticular degeneration, is a rare autosomal recessive abnormality of copper metabolism characterized by accumulation of toxic

levels of copper in the brain, cornea (Kayser-Fleischer rings), and liver, the latter being due to impaired biliary excretion. Hepatic deposition of copper, predominantly seen in periportal areas and along the hepatic sinusoids, evokes an inflammatory reaction resulting in acute hepatitis with fatty change. Subsequently, chronic hepatitis may result in liver fibrosis and eventually macronodular cirrhosis.

Due to copper's high atomic number, a hyperdense liver may be seen on unenhanced CT scans. However, this finding is not universally present, and usually only nonspecific signs such as hepatomegaly, fatty change, and – in advanced cases – cirrhosis are observed. During the early stage of the disease, due to ionic copper paramagnetism, MRI can be valuable by demonstrating focal copper depositions as multiple nodular lesions, typically appearing hyperintense and hypointense on T1- and T2-weighted images, respectively, as described by Cheon et al.

### Amyloidosis

Amyloidosis consists of deposition of fibrils of protein-mucopolysaccharide complexes throughout the body and is classified based on the biochemical composition of the amyloid fibrils. Primary amyloidosis is due to the deposition of immunoglobin light chains and is associated with multiple myeloma and monoclonal gammopathy. Secondary amyloidosis is due to deposition of amyloid A protein and is associated with chronic infection, rheumatoid arthritis, and malignancies. Exceeded only by the spleen and kidney, the liver is the third most common solid organ prone to this deposition.

Hepatic amyloidosis has a nonspecific imaging appearance. The most common finding is diffuse hepatomegaly. CT sporadically demonstrates focal areas of low attenuation within the liver, corresponding to sites of amyloid deposition (amyloid pseudotumor). Patients may present with a picture of jaundice, which is due to intrahepatic cholestasis.

## Neoplastic Diseases

### Metastatic Disease

Neoplastic infiltration due to diffuse metastatic disease can occur with many primary tumors. Melanoma, malignant neuroendocrine tumors, pancreatic adenocarcinoma, breast carcinoma, and colonic adenocarcinoma are some of the more commonly encountered causes of diffuse hepatic metastatic disease.

CT appearances of hepatic metastases depend on lesion vascularity compared with normal liver parenchyma. Diffuse metastatic involvement may produce only subtle imaging findings and be only detectable through indirect features, such as diffuse parenchymal heterogeneity, vascular and architectural distortion, or alterations of the liver contour. The latter, particularly seen in patients with treated breast cancer metastases, has been reported as the pseudocirrhosis sign (Fig. 3). In addition, treated breast cancer metastases may mimic the appearance of liver hemangiomata.

**Fig. 3.** Diffuse metastatic breast cancer (pseudocirrhosis pattern). A 43-year old woman treated for metastatic breast cancer. Axial contrast-enhanced computed tomography image demonstrate several small, low-density lesions in the liver and a nodular contour of the liver due to hepatic capsular retraction. Reproduced from Hodler J, von Schulthess GK, Zollikofer ChL (Eds) (2010) Diseases of the Abdomen and Pelvis 2010-2013. Springer-Verlag Italia, Milano, pp. 56-60

### Lymphoma

Lymphoma can infiltrate the liver both primarily and secondarily. Primary lymphoma of the liver is extremely rare. Conversely, the liver is often secondarily involved in both Hodgkin's and non-Hodgkin's lymphoma. Typically, the liver parenchyma is diffusely infiltrated with microscopic nests of neoplastic cells, without significant architectural distortion, and therefore, lymphomatous involvement is difficult to detect by imaging alone. Associated abnormalities, such as splenomegaly and lymphadenopathy, may narrow the differential diagnosis.

## Diffuse Infectious and Inflammatory Diseases

### Fungal Infections

Hepatosplenic fungal infection is a clinical manifestation of disseminated fungal disease in patients with hematologic malignancies or compromise of the immunologic system. The reported prevalence of fungal dissemination ranges from 20% to 40%. Most hepatic fungal microabscesses occur in leukemia patients and are caused by *Candida albicans*.

### Candidiasis

*C. albicans* in the liver may evoke little or no inflammatory reaction, cause a superlative response, or occasionally produce granulomas. The typical histologic pattern of hepatic candidiasis is characterized by microabscesses, with the yeast or pseudohyphal forms of the fungus in the center of the lesion and a surrounding area of necrosis and polymorphonuclear infiltrate.

At contrast-enhanced CT, fungal microabscesses usually appear as multiple round, discrete areas of low attenuation, generally ranging from 2 to 20 mm (Fig. 4). These microabscesses usually enhance centrally after intravenous administration of contrast medium, although peripheral enhancement may occur.

At MRI, the untreated nodules are rounded lesions $<1$ cm in diameter, are minimally hypointense on T1-weighted and gadolinium-enhanced images, and are markedly hyperintense on T2-weighted images. After treatment, lesions appear mildly to moderately hyperintense on T1- and T2-weighted images and demonstrate enhancement on gadolinium-enhanced images. A dark ring is usually seen around these lesions with all sequences. Completely treated lesions are minimally hypointense on T1-weighted images, isointense to mildly hyperintense on T2-weighted images, moderately hypointense on early gadolinium-enhanced images, and minimally hypointense on delayed gadolinium-enhanced images. MRI is superior to CT and US for detecting these fungal foci.

### Granulomatous Diseases

Granulomatous hepatitis is associated with a wide variety of conditions, most commonly with sarcoidosis, tuberculosis, and histoplasmosis. Hepatic granulomas usually appear as discrete, sharply defined nodules consisting of aggregates of epithelioid cells by a rim of mononuclear cells, predominantly lymphocytes.

**Fig. 4.** Hepatic candidiasis. A 66-year-old woman with leukemia presenting with abnormal liver function tests. Axial contrast-enhanced computed tomography image demonstrates multiple small, low-attenuation lesions seen throughout the liver and spleen. Splenomegaly and bilateral pleural effusions are also present. Reproduced from Hodler J, von Schulthess GK, Zollikofer ChL (Eds) (2010) Diseases of the Abdomen and Pelvis 2010-2013. Springer-Verlag Italia, Milan, pp. 56-60

### Sarcoidosis

Sarcoidosis is a multisystem disorder of unknown pathogenesis characterized by noncaseating granulomas. Although it may involve almost any organ in the body, pulmonary sarcoidosis is most common. Sarcoidosis of the liver is also relatively frequently seen, but the granulomas are usually not macroscopically detectable and thus may not produce focal abnormalities on imaging studies. Classically, the granulomas develop in a periportal location, resulting in periportal fibrosis, cirrhosis, and eventually portal hypertension.

Hepatic contrast-enhanced CT may typically reveal multiple, diffuse, small, low-density areas in both liver and spleen. MRI features of hepatic sarcoidosis are also nonspecific and include organomegaly, multiple low-signal-intensity lesions relative to background parenchyma with all sequences, increased periportal signal, irregularity of portal and hepatic vein branches, and patchy areas of heterogeneous signal. Literature reports by Semelka et al. confirm the nonspecific appearance but describes large central regenerative nodules and wedge-shaped areas of peripheral parenchymal atrophy as characteristic features.

### Tuberculosis

Tuberculosis (TB) is one of the most common infectious diseases worldwide. Generally, tuberculosis in the liver presents as either miliary or focal form. Focal hepatic TB is further subdivided into nodular (i.e., tuberculous abscess and tuberculoma) and tubular or hepatobiliary tuberculosis (i.e., tuberculosis involving intrahepatic ducts). Hepatic miliary TB is most common and is reported to occur in 50-80% of all patients with terminal pulmonary TB. Miliary TB is usually not detected by imaging. Hepatomegaly may be the only radiological abnormality.

In the healing stage of TB, CT may show diffuse hepatic calcifications (~50% of cases). Reported CT findings of nodular TB are nonspecific and include hypoattenuating lesions both before and after intravenous application of contrast administration.

At MRI, lesions are hypointense on T1-weighted and hypo- to isointense on T2-weighted images. TB lesions differently enhance after gadolinium administration. Because of these rather nonspecific findings with all imaging techniques, percutaneous liver biopsy is necessary.

### Histoplasmosis

Histoplasmosis is the most common cause of fungal infection in the Ohio River Valley of the United States;

99% of patients exposed to histoplasmosis develop only subclinical infections. Liver involvement is common in disseminated histoplasmosis, which usually originates in the lungs. The most common hepatic findings include portal lymphohistiocytotic inflammation, and discrete, well-delineated granulomas. In patients with healed histoplasmosis, the presence of small, punctate calcifications scattered throughout the liver and spleen is a typical but nonspecific finding.

### Parasitic Infections

#### Schistosomiasis

*Schistosoma japonicum, S. hematobium,* and *S. mansoni* are the three most important species that infect humans. These organisms live in the bowel lumen and lay eggs in the mesenteric veins. The eggs may then embolize to the portal vein. The eggs themselves do not survive and subsequently calcify. Chronic infections with either *S. japonicum* or *S. mansoni* result in formation of cirrhosis and the risk of HCC development. Histologically, schistosomiasis is characterized by white, pinhead-sized granulomas scattered throughout the liver. At the center of each granuloma is a schistosome egg. In severe infections, the surface of the liver shows granulomatous involvement and widespread fibrous portal enlargement (pipe-stem fibrosis).

At CT, the most pathognomonic pattern is the presence of calcified septa, usually aligned perpendicular to the liver capsule (tortoise shell or turtleback appearance).

### Viral Infections

#### Viral Hepatitis

Acute viral hepatitis is a systemic infection that affects the liver and is usually caused by one of five viral agents: hepatitis A virus (HAV), hepatitis B virus (HBV), hepatitis C virus (HCV), the HBV-associated delta agent hepatitis D virus (HDV), and hepatitis E virus (HEV). A vast array of other viruses may also produce hepatitis, including herpes, yellow fever, rubella, Coxsackie, and adenovirus. The diagnosis of acute hepatitis is usually based on serologic, virologic, and clinical findings. Probably the most important role of radiology in patients with acute hepatitis is to help rule out other diseases that produce similar clinical and biochemical abnormalities, such as extrahepatic cholestasis, diffuse metastatic disease, and cirrhosis.

At CT and MRI, findings in acute viral hepatitis are nonspecific and include hepatomegaly and periportal edema. At CT, heterogeneous enhancement and well-defined regions of low attenuation may be present. At MRI, periportal edema appears as high-signal-intensity areas on T2-weighted images. Involved areas may be normal or demonstrate decreased signal intensity on T1-weighted images and increased signal intensity on T2-weighted images. There is also impaired uptake of liver-specific agents. Extrahepatic findings in patients with severe acute hepatitis include gallbladder wall thickening due to edema and, infrequently, ascites. In chronic hepatitis, CT and MRI features resemble those of early-stage liver cirrhosis. Periportal lymphadenopathy may be the sole detectable abnormality in both acute and chronic hepatitis.

#### HIV Infection

The liver and biliary tracts are frequent sites of involvement during the course of HIV infection. Coinfection with HBV and HCV is particularly common due to the shared means of transmission of these viruses with HIV. AIDS-related cholangiopathy is the newest common manifestation. At CT, inflammation of the gallbladder or biliary tree manifests as mural thickening or abnormal contrast enhancement. MR cholangiopancreatography (CP) is more sensitive and specific than US or CT in depicting mural irregularity of extrahepatic ducts that results from the exuberant periductal inflammation, focal mucosal ulcers, and interstitial edema found in AIDS-related cholangitis.

### Uncommon Hepatic Infections

#### Cat-Scratch Disease

Cat-scratch disease is an infection that affects immunocompetent children or adolescents. It is caused by *Bartonella henselae*, a gram-negative bacillus usually introduced by the scratch of a cat. Cat-scratch disease takes many forms – from regional lymphadenitis to disseminated infection. The typical clinical manifestation of cat-scratch disease is painful lymphadenopathy proximal to the site of inoculation. Disseminated infection is seen in 5-10% of cases. In the abdomen, multiple granulomas ranging from 3 to 30 mm may form in the liver and spleen, with or without hepatosplenomegaly. Histopathologic findings include vascular proliferative lesions (peliosis hepatis) and necrotizing granulomatous lesions.

At unenhanced CT, lesions are hypoattenuating relative to normal parenchyma. Three different patterns at contrast-enhanced CT have been described: (a) persistent hypoattenuation relative to the liver, (b) isoattenuation relative to surrounding tissues, and (c) marginal enhancement. Only a few MRI studies of cat-scratch disease have been described. The lesions appear as low-signal-intensity nodules on T1-weighted MRI and as high-signal-intensity nodules on T2-weighted images. Peripheral enhancement may be seen on gadolinium-enhanced T1-weighted images.

#### Bacillary Angiomatosis

Bacillary angiomatosis is also a manifestation of infection by *B. henselae* but in immunocompromised patients. This

is the same organism that causes cat-scratch disease in nonimmunocompromised patients. It is characterized by localized areas of vascular proliferation that may affect the skin, airway, mucous membranes, visceral organs, bone, and brain. Contrast-enhanced CT may demonstrate multiple diffuse low- or high-attenuation lesions <1 cm scattered throughout the hepatic parenchyma. Ascites, mild periportal edema, and intrahepatic biliary ductal dilatation may occur. These imaging features are nonspecific and must be distinguished, especially in AIDS patients, from hepatic abscesses related to other bacteria, viruses, or fungi; AIDS-related lymphoma; Kaposi sarcoma; and, less commonly, disseminated *Pneumocystis carinii* infection.

## Focal Infections

### Bacterial (Pyogenic) Abscess

Pyogenic abscess, although uncommon in the antibiotic era, is still challenging clinically, as its presentation is quite variable – from profound septicemia to chronic, indolent symptoms.

Enhanced CT can reliably diagnose >90% of hepatic pyogenic abscesses, revealing two main patterns: multiple microabscesses (disseminated or clustered), and large macroabscesses. By virtue of its good spatial and contrast resolution, CT is the single best method for detecting hepatic abscess, with a sensitivity as high as 97%. On CT scans, abscesses appear as generally rounded masses that are hypodense on both contrast and noncontrast scans. Central gas, either as air bubbles or an airfluid level, is a specific sign, but it is present in <20% of cases. A thick, enhancing, peripheral rim is also noted.

At MRI, air within the abscess appears as a signal void and is therefore more difficult to differentiate from calcifications. However, the shape and location (air-fluid level) should enable the correct diagnosis. After administration of gadolinium diethylenetriamine pentaacetic acid (DTPA), abscesses typically show rim enhancement (the double target sign). Small lesions (<1 cm) may enhance homogeneously, mimicking hemangiomas. Percutaneous image-guided aspiration followed by drainage is the method of choice for definitive diagnosis and treatment, with success in >90% of cases.

### Amebic Abscess

Hepatic abscess is the most common extraintestinal manifestation of amebiasis, affecting ~10% of patients with amebiasis. Although rare in the continental United States, 10% of the world's population is infected with *Entamoeba histolytica*. Clinically, patients with amebic abscess are more acutely ill than patients with pyogenic abscess, with high fever and right upper quadrant pain. Diagnosis is made by positive serologic amebic titers, although they have false-negative rates of almost 20%.

CT demonstrates well the extrahepatic extensions to chest wall, pleura, or adjacent viscera. Percutaneous catheter drainage of an amebic abscess is rarely necessary due to the effectiveness of amebicidal therapy. Occasionally, percutaneous drainage is needed in large, symptomatic abscesses with poor response to medical therapy; suspected bacterial superinfection; and threatening intrapericardial rupture. CT appearance of amebic abscess is variable and nonspecific. Lesions are usually peripheral, round or oval areas of low attenuation (10-20 HU). A peripheral rim of slightly higher attenuation can be seen on noncontrast scans and shows marked enhancement after administration of contrast material.

On MRI, amebic liver abscesses are spherical and usually solitary lesions, with a hyperintense center on T2-weighted and a hypointense center on T1-weighted images. The abscess wall is thick, and on gadolinium-enhanced images, the enhancement pattern is similar to that of pyogenic abscess.

### Echinococcal Disease

Hydatid disease has two main forms affecting humans: *Echinococcus granulosus* and *E. multilocularis* or *Polyporus alveolaris*. These infections have well-defined and different geographic distributions. The pathologic and imaging findings differ dramatically between these parasites.

On CT scans, *E. granulosus* appears as unilocular or multilocular welldefined cysts with either thick or thin walls. Daughter cysts are usually seen as areas of lower attenuation than the mother cyst and are usually in the periphery of the lesion. Daughter cysts can also float free in the lumen of the mother cyst; therefore, altering the patient's position during imaging may change the position of these cysts, confirming the diagnosis of echinococcal disease. Curvilinear ring like calcification is also a common feature.

On MRI, the cyst component of echinococcal cysts is similar to that of other cysts, with long T1 and T2 relaxation times. However, MRI best demonstrates the pericyst, the matrix and hydatid sand (debris consisting of freed scolices), and the daughter cysts. The pericyst usually has low signal intensity on T1 and T2 weighted images because of its fibrous component. This rim and a multiloculated or multicystic appearance are distinctive features. The hydatid matrix appears hypointense on T1-weighted images and markedly hyperintense on T2 weighted images. When present, daughter cysts are hypointense relative to the matrix on both T1- and T2-weighted images (Fig. 5). Floating membranes have low signal intensities on T1 and T2weighted images.

*E. multiloculars* appear as a solid large mass or masses, with minimal to no enhancement after intravenous administration of contrast material and possible small punctate calcification.

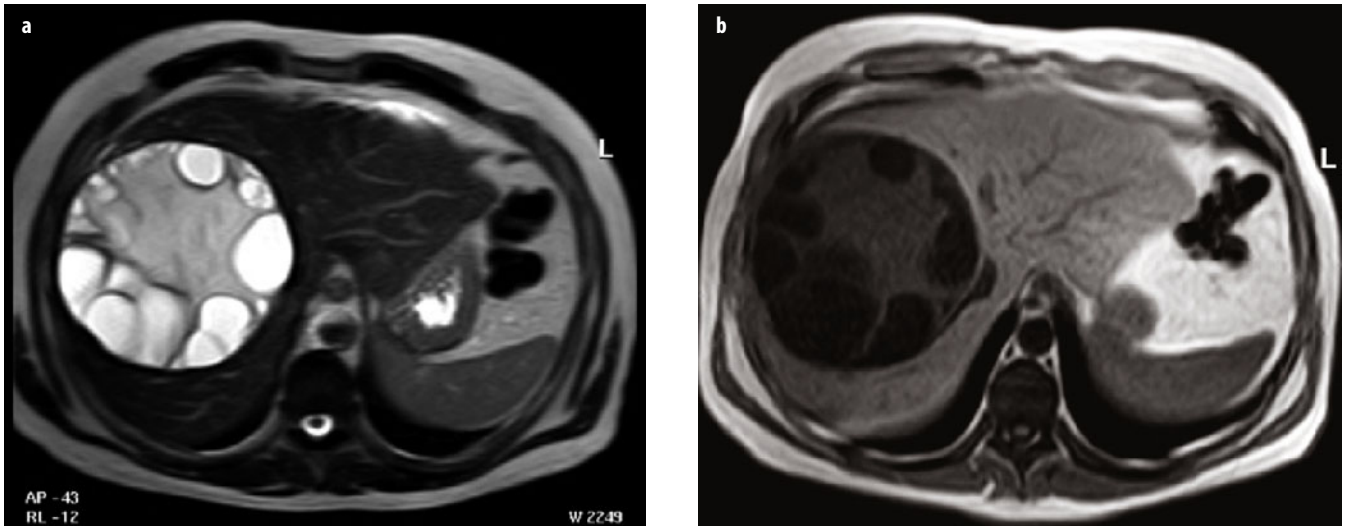


**Fig. 5 a, b.** *Echinococcus granulosus* cyst in a 28-year-old man with right upper quadrant pain. **a** Axial T2-weighted image demonstrates a large cystic mass in the right lobe of the liver surrounded by a hypointense rim and containing more hyperintense, smaller cysts in its periphery. **b** On axial T1-weighted image, the hypointense rim is well visualized and the peripheral cysts are hypointense relative to the center of the lesion. Reproduced from Hodler J, von Schulthess GK, Zollikofer ChL (Eds) (2010) Diseases of the Abdomen and Pelvis 2010-2013. Springer-Verlag Italia, Milan, pp. 56-60

## Suggested Reading


Akhan O, Ozmen MN, Dincer A et al (1996) Liver hydatid disease: long-term results of percutaneous treatment. Radiology 198:259-264.

Boll DT, Merkle EM (2009) Diffuse Liver Disease: strategies for hepatic CT and MR imaging. Radiographics 29:1591-1614.

Cheon JE, Kim IO, Seo JK et al (2010) Clinical application of liver MR imaging in Wilson's disease. Korean J Radiol 11:665-672.

Cheung H, Lai YM, Loke TK et al (1996) The imaging diagnosis of hepatic schistosomiasis japonicum sequelae. Clin Radiol 51:51-55.

Cohen EI, Wilck EJ, Shapiro RS (2006) Hepatic imaging in the 21st century. Semin Liver Dis 26:363-372.

Czermak BV, Unsinn KM, Gotwald T et al (2001) Echinococcus multilocularis revisited. AJR Am J Roentgenol 176:1207-1212.

Danon O, Duval-Arnould M, Osman Z et al (2000) Hepatic and splenic involvement in cat-scratch disease: imaging features. Abdom Imaging 25:182-183.

Doyle DJ, Hanbidge AE, O'Malley ME (2006) Imaging of hepatic infections. Clin Radiol 61:737-748.

Erturk SM, Yapici O (2013) Liver inflammatory and infectious diseases. In: Hamm B, Ros PR (Eds) Abdominal imaging. Volume II. Springer-Verlag, Berlin Heidelberg, pp 1001-1012.

Faria SC, Ganesan K, Mwangi I et al (2009) MR imaging of liver fibrosis: current state of the art. Radiographics 29:1615-1635.

Ferreira A, Ramalho M, de Campos RO (2013) Hepatic sarcoidosis: MR appearances in patients with chronic liver disease. Magn Reson Imaging 31:432-438.

Gourtsoyiannis NC, Ros PR (Eds) (2005) Radiologic-pathologic correlations from head to toe: understanding the manifestations of disease. Springer-Verlag, Berlin, Heidelberg.

Guiu B (2013) Other diffuse liver diseases: steatosis, hemochromaosis, etc. In: Hamm B, Ros PR (Eds) Abdominal imaging. Volume II. Springer-Verlag, Berlin Heidelberg, pp. 1027-1044.

Hamm B, Ros PR (Eds) (2013) Abdominal imaging. Volumes 1-4. Springer-Verlag, Berlin Heidelberg.

Hickey N, McNulty JG, Osborne H, Finucane J (1999) Acute hepatobiliary tuberculosis: a report of two cases and a review of the literature. Eur Radiol 9:886-889.

Hussain S, Reinhold C, Mitchell DG (2009) Cirrhosis and lesion characterization at MR imaging. Radiographics 29:1637-1652.

Kalovidouris A, Gouliamos A, Vlachos L et al (1994) MRI of abdominal hydatid disease. Abdom Imaging 19:489-494.

Kang BK, Yu ES, Lee SS et al (2012) Hepatic fat quantification: a prospective comparison of magnetic resonance spectroscopy and analysis methods for chemical-shift gradient echo magnetic resonance imaging with histologic assessment as the reference standard. Invest Radiol 47:368-375.

Ko S, Lee T, Ng S et al (1998) Unusual liver MR findings of Wilson's disease in an asymptomatic 2-year-old girl. Abdom Imaging 23:56-59.

Lee TY, Wan YL, Tsai CC (1994) Gas-containing liver abscess: Radiological findings and clinical significance. Abdom Imaging 19:46-52.

Marmoloya G, Karlins NL, Petrelli M, McCullough A (1990) Unusual computed tomography findings in hepatic amyloidosis. Clin Imaging 14:248.

Mergo PJ, Ros PR (1998) Imaging of diffuse liver disease. Radiol Clin North Amer 36:365-375.

Monzawz S, Ohtomo K, Oba H et al (1994) Septa in the liver of patients with chronic hepatic Schistosomiasis Japonica: MR appearance. AJR Am J Roengenol 162:1347-1351.

Moore EH, Russell LA, Klein JS et al (1995) Bacillary angiomatosis in patients with AIDS: multiorgan imaging findings. Radiology 197:67-72.

Mortele KJ, Ros PR (2001) Imaging of diffuse liver disease. Seminars in Liver Disease 21:195-212.

Mortele KJ, Ros PR (2001) Cystic focal liver lesions in the adult: differential CT and MR imaging features. RadioGraphics 21:895-910.

Mortele KJ, Ros PR (2002) MR Imaging in chronic hepatitis and cirrhosis. Seminars in Ultrasound, CT, and MRI 23:79-100.

Mortele B, Mortele KJ, Seynaeve P et al (2002) Hepatic bile duct hamartomas (von Meyenburg complexes): MR and MR cholangiography imaging findings. JCAT 26:438-443.

Mortele KJ, Segatto E, Ros PR (2004) The infected liver: radiologic-pathologic correlation. Radiographics 24:937-955.

Pastakia B, Shawker TH, Thaler M et al (1988) Hepatosplenic candidiasis: wheels within wheels. Radiology 166:417-444.

Queiroz-Andrade M, Blasbalg R, Ortega CD et al (2009) MR imaging findings of iron overload. Radiographics 29:1575-1589.
Ralls PW (2002) Inflammatory disease of the liver. Clin Liver Dis 6:203-225.
Rappaport DC, Cumming WA, Ros PR (1991) Disseminated hepatic and splenic lesions in cat-scratch disease: imaging features. AJR Am J Roentgenol 156:1227-1228.
Ros PR, Sobin LH (1994) Amyloidosis: the same cat, with different stripes. Radiology 190:14-15.
Ros PR, Taylor HM, Barreda R, Gore RM (2000) Inflammatory lesions of the liver. In: Gore RM, Levine MS (Eds) Textbook of gastrointestinal radiology, 2nd edition. WB Saunders, Philadelphia, pp 1569-1589.
Ros PR (2002) Hepatic imaging and intervention. In: Ros P, Clinics in Liver Disease. WB Saunders, Philadelphia.
Ros PR, Mortele KJ, Pelsser V, Thomas S (2013) CT/MRI of the abdomen and pelvis: a teaching file, 3rd edition. Wolters Kluver/Lippincott, Williams and Wilkins, Philadelphia.
Sakai T, Maeda M, Takabatake M et al (1995) MR imaging of hepatosplenic sarcoidosis. Radiat Med 13:39-41.
Semelka RC, Kelekis NL, Sallah S (1997) Hepatosplenic fungal disease: diagnostic accuracy and spectrum of appearances on MR imaging. AJR Am J Roentgenol 169:1311-1316.
Siegelman ES, Mitchell DG, Semelka RC (1996) Abdominal iron deposition: metabolism, MR findings, and clinical importance. Radiology 199:13-22.
Taourel P, Marty-Ane B, Charasset S et al (1993) Hydatid cyst of the liver: comparison of CT and MRI. J Comput Assist Tomogr 17:80-85.
Van Allen RJ, Katz, MD, Johnson MB et al (1992) Uncomplicated amebic liver abscess: prospective evaluation of percutaneous therapeutic aspiration. Radiology 183:827-830.
Yamamoto H, Yamashita Y, Yoshimatsu S et al (1995) Hepatocellular carcinoma in cirrhotic livers: Detection with unenhanced and iron-oxide enhanced MR imaging. Radiology 195: 106-112.

# Focal Liver Lesions

Wolfgang Schima[1], Richard Baron[2]

[1] Department of Radiology, KH Göttlicher Heiland, KH der Barmherzigen Schwestern, Sankt Josef-Krankenhaus, Vinzenzgruppe, Vienna, Austria
[2] Department of Radiology, University of Chicago, Chicago, IL, USA

## Introduction

Multidetector computed tomography (MDCT) and magnetic resonance (MR) imaging technology offers detailed insights into liver anatomy and the pathophysiology of liver disease in a way that has turned imaging into the pacemaker for the development of new therapeutic techniques. Understanding different imaging techniques and the diagnostic potential of different modalities, including contrast material utilization, is essential to optimize patient diagnoses. In the environment of cost containment, the most appropriate modality should be chosen to answer the clinical question. Ultrasonography (US) is a widely available, noninvasive, and least expensive imaging modality, but it is limited by low sensitivity and specificity unless contrast agents are used. Contrast-enhanced MDCT has emerged as the modality of choice for routine liver imaging. MR imaging is used primarily as a problem-solving technique for liver evaluation when MDCT or US is equivocal or if concern exists for malignancy in certain high-risk populations. This chapter highlights imaging of focal liver lesions and focuses on MDCT and MR imaging, and includes US in selected cases. Course participants should gain an understanding of how to optimize their CT and MR imaging protocols and how different focal liver lesions appear. The value of liver-specific MR contrast agents for noninvasive characterization of focal lesions is emphasized.

## MDCT Imaging Techniques

MDCT allows organ imaging in multiple planes rather than single sequential slices. Thus, with 64-plus-detector systems, the entire liver can be scanned within 1-4 s using a submillimeter detector configuration for high-quality multiplanar reconstructions (MPR) [1]. When viewed axially, reconstructed sections of 2.5-3 mm thickness with an overlap of 0.5-1 mm are preferred. Thinner slices do not improve lesion conspicuity and increased image noise [2] and substantially decrease specificity [3]. The amount of contrast material may depend on patient weight, but typically, 40-45 g of iodine should be administered (i.e., 120-150 ml contrast at 300-320 mg/ml iodine, equivalent to 110 ml contrast at 400 mg/ml). The total amount of iodine given determines the quality of the portal-venous imaging phase, with the goal of increasing liver attenuation through contrast enhancement by 50 HU [4]. To achieve good arterial-phase imaging, contrast material flow rate is crucial: 4-5 ml/s is recommended [5]. A variable amount of contrast material (e.g., 2 ml/kg body weight) and fixed injection duration of 30 s means that the injection rate varies according to patient weight.

Timing of image acquisition in relation to contrast material administration depends upon whether imaging is required during early arterial phase (for arterial anatomy only), late arterial phase (for hypervascular tumor detection and characterization), or venous phase (for follow-up imaging and hypovascular tumor detection). Routinely, late arterial phase imaging (with a delay of aortic transit time plus 15-18 s) [6, 7], and a venous phase scan (20-30 s interscan delay or with fixed delay of ~60-70 s) are acquired. The use of combinations of these imaging phases depends upon the individual indication [8]. Automated methods of measuring arterial enhancement (aortic transit time) on CT, often termed bolus tracking, has replaced the use of fixed scan-delay times because it provides better coincidence of scanning with peak enhancement of liver tumors (in the later arterial phase) and parenchyma (in the venous phase).

Different techniques for dose reduction and optimization of image quality were developed in recent years: automatic exposure control by tube current (mA) modulation, selection of lower tube potential (kVp), and adaptive dose shielding to minimize overscanning in the *z*-axis, to name a few. Conventional filtered back projection (FBP), the standard CT image reconstruction technique for many years, offered little potential for further

* In this chapter, figs. 2, 3, 5, 6, 9, 10, 13, 15, 17, 18, 20 are reproduced from Schima W, Baron R (2010) Focal liver lesions. In: Hodler J, von Schulthess GK, Zollikofer ChL (Eds) Diseases of the Adomen and Pelvis 2010-2013. Springer-Verlag Italia, Milano, pp. 63-74.

*Diseases of the Abdomen and Pelvis 2014-2017*,
DOI: 10.1007/978-88-470-5659-6_12 

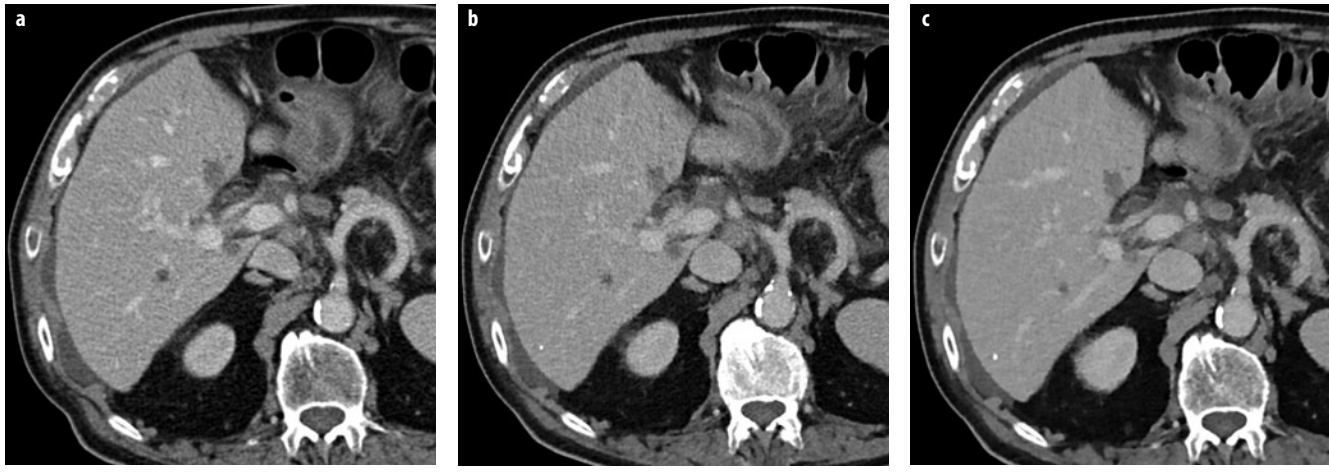


**Fig. 1 a-c.** Dose reduction using iterative reconstruction techniques at multidetector computed tomography (MDCT). **a** Normal-dose MDCT in the venous phase (120 kVp, ref. mAs 230) reconstructed with standard filtered backprojection shows colorectal liver metastases. **b** Image appearance (120 kVp, ref. mAs 150) using iterative reconstruction (SAFIRE level 3) is slightly different in general due to reduced image noise. Lesions are shown with the same conspicuity. Patient dose is reduced by 36%. **c** At higher iterative reconstruction levels (SAFIRE level 5), the image appearance is pixilated (plastic-like), especially the liver parenchyma and perirenal fat

improvements. A rather old principle, iterative reconstruction (IR), has been "rediscovered." IR uses loopwise raw data correction to reduce image noise. Thus, imaging at lower kVp or mAs, with reduced radiation dose but comparable image quality, is possible. All major manufacturers now provide iterative reconstruction techniques (SAFIRE, Siemens; iDose, Philips; ASIR, MBIR, GE Healthcare; AIDR, Toshiba) [9]. Stepwise IR reduces CT noise levels. However, high levels of IR may induce a pixilated (plastic-like) image texture, rendering image quality unacceptable [10]. A dose reduction of 38-55% is possible with IR without compromising image quality [11-13] (Fig. 1).

## MR Imaging Technique

MR examination of the liver must include unenhanced T1-weighted and T2-weighted pulse sequences and contrast-enhanced sequences. Specific pulse sequences vary by manufacturer, patient compliance, and the clinical question being addressed**.** In- and opposed-phase (or out-of-phase) T1-weighted imaging is recommended to allow for maximal tumor detection and characterization of fatty tumors and steatosis/nonsteatosis. T2-weighted pulse sequences with fat suppression provide better lesion contrast than non-fat-suppressed sequences. Diffusion-weighted imaging (DWI) has become a standard technique in liver imaging and it is now available on all scanners. In general, DWI depends upon the microscopic mobility of water, called Brownian motion, in tissue. Water-molecule diffusion (and thus the measured signal intensity) depends on tissue cellularity, tissue organization, intactness of cellular membranes, and extracellular space. Usually, low values of diffusion are found in most tumors, which are attributed to their high cellularity [14]. Thus, DWI is helpful for detecting liver metastases and hepatocellular carcinoma (HCC) [15-17]. Preliminary results show its potential for lesion characterization [18], although this is a matter of ongoing discussion [19].

Administration of contrast agents is of importance in liver MR imaging. In general, after intravenous (IV) bolus application of nonspecific (extracellular) gadolinium-based contrast agents, dynamic imaging (using breath-hold T1-weighted gradient-echo pulse sequences) is performed for lesion characterization, detecting tumors in cirrhosis, evaluating tumor response to therapy, and detecting marginal tumor recurrences following tumor ablation. Liver-specific (or hepatobiliary) MR contrast agents are available: gadobenate dimeglumine (MultiHance®, Bracco) and gadoxetic acid (Primovist® or Eovist®, Bayer Healthcare) can be administered IV as a bolus, as with nonspecific gadolinium chelates for dynamic imaging. Liver-specific agents are, to a certain degree, taken up into hepatocytes after IV injection (gadobenate dimeglumine 4-5%; gadoxetic acid ~50%). They provide T1 enhancement of liver tissue in hepatobiliary-phase imaging, which is performed 20 min (gadoxetic acid) or 1-2 h (gadobenate dimeglumine) after contrast material injection. Liver-specific agents are used to improve detection of metastases and to characterize lesions [20-23].

## Benign Hepatic Lesions

### Cysts

Cysts are common, usually asymptomatic, liver lesions with an incidence between 5% and 14% of the population. At US, hepatic cysts are anechoic, with an imperceptible wall and increased acoustic enhancement behind the cyst. On CT scans, a hepatic cyst appears as a well circum-

scribed, homogeneous mass with attenuation values similar to water (<15 HU), lacking any mural thickening or nodularity and without contrast enhancement after IV contrast material administration. Small lesions may appear to have higher attenuation measurements because of partial volume averaging. Occasionally, unenhanced scans may suggest the diagnosis of small cysts if the lesions are well visualized as hypodense, whereas very small metastases are usually not discernible on unenhanced scans. In most instances, however, these small lesions remain problematic for characterization at CT. On MR imaging examinations, cysts are well-defined, homogeneous lesions that appear hypointense on T1-weighted images and markedly hyperintense on T2-weighted images. The marked increased T2 signal intensity of even very small cysts can be very helpful to confirm the benign nature of small lesions.

### Hemangioma

Hemangioma is the most common benign liver tumor. Typical US characteristics of hemangioma include a sharply circumscribed, well-defined, hyperechoic lesion with distal acoustic enhancement. These are usually homogeneous in appearance when small. Larger hemangiomas (>4 cm) may not demonstrate all of the characteristic appearances and, in particular, are often heterogeneous in appearance.

Hemangiomas are well-defined, hypodense masses on unenhanced CT images. They are hypointense on T1-weighted and markedly hyperintense on T2-weighted images. MRI is useful in differentiating hemangiomas from solid neoplasms based on the long T2 relaxation time (=hyperintensity) of hemangioma compared with other hepatic masses [24, 25]**.** When using a relatively long T2 echo time (>140 ms), the presence of a homogeneous, bright, light-bulb-appearing lesion is characteristic of a benign lesion, either cyst or hemangioma. Exceptions to this include cystic metastases, gastrointestinal stromal tumor (GIST), and neuroendocrine tumor metastases. Hemangiomas show three distinctive patterns of enhancement at CT/MRI [26], with the key characteristic feature being that areas of lesion enhancement should closely but not exactly follow the enhancement characteristics of blood pool elsewhere [27].

Small lesions (up to ~2 cm) may show immediate and complete filling in the arterial phase, with sustained enhancement in the venous and delayed phases (type I, also termed flash filling) [28] (Fig. 2). The most common enhancement pattern is one of peripheral nodular discontinuous enhancement, which progresses with increased fill-in over time (type II). Larger lesions (>5 cm) or lesions with central thrombosis/fibrosis may lack central fill-in (type III) (Fig. 3). With liver-specific contrast agents, the appearance of hemangiomas in the dynamic arterial and venous phases is similar to that with nonspecific gadolinium chelates. However, in the delayed phase, after 3 min, there may be "pseudo washout" (hypointensity) due to early hepatocellular enhancement of liver parenchyma. In the hepatobiliary phase, hemangiomas tend to be hypointense to the parenchyma, which should not be confused with metastases (Fig. 4).

Studies indicate that noncontrast DWI may help differentiate between hemangioma and solid lesions, as the apparent diffusion coefficient (ADC) in hemangiomas is higher than in solid lesions [29].

### Focal Nodular Hyperplasia

Focal nodular hyperplasia (FNH) is a benign lesion usually of no clinical consequence other than the confusion it causes when incidentally detected during abdominal imaging examinations. The sonographic appearance of the lesion is nonspecific: the lesion may be isoechoic or slightly hypoechoic [30] to liver, whereas in patients with diffuse hepatic steatosis, it is always hypoechoic. Several common features aid in characterizing FNH lesions. One characteristic feature in larger lesions is a lobular contour, uncommon in malignant lesions. A key feature is the common visualization of central scar, present in approximately two thirds of larger lesions but only one third of small lesions (<3 cm) [31]. The central scar is most often hyperintense on T2-weighted images, with a comma-shaped or spoke-wheel appearance; this is a key differen-

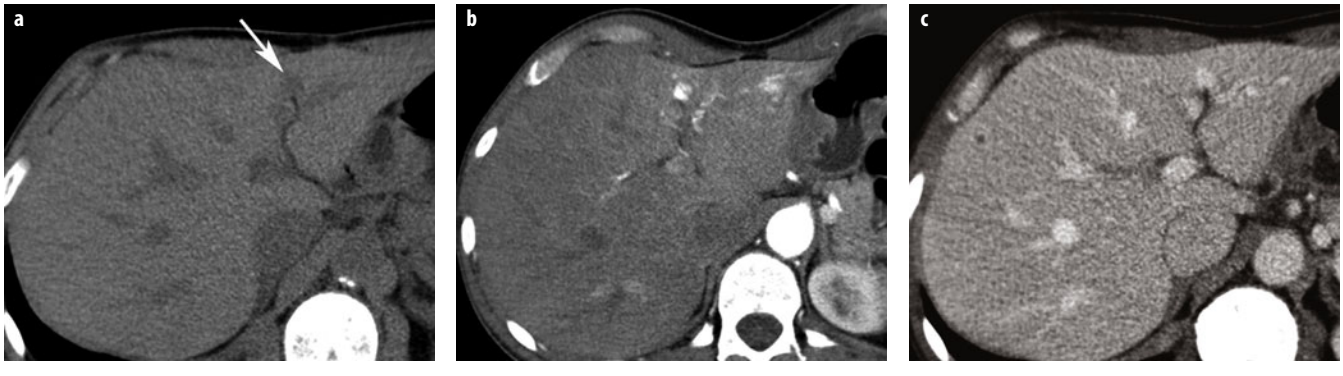


**Fig. 2 a-c.** Hemangioma type 1. **a** Unenhanced computed tomography (CT) shows a small, hypodense lesion adjacent to the falciform ligament (*arrow*). **b** Contrast-enhanced CT in the arterial phase shows rapid and complete enhancement of the hemangioma, which persists in the venous phase (**c**). Attenuation of the hemangioma in the enhanced phases is similar to that of the aorta

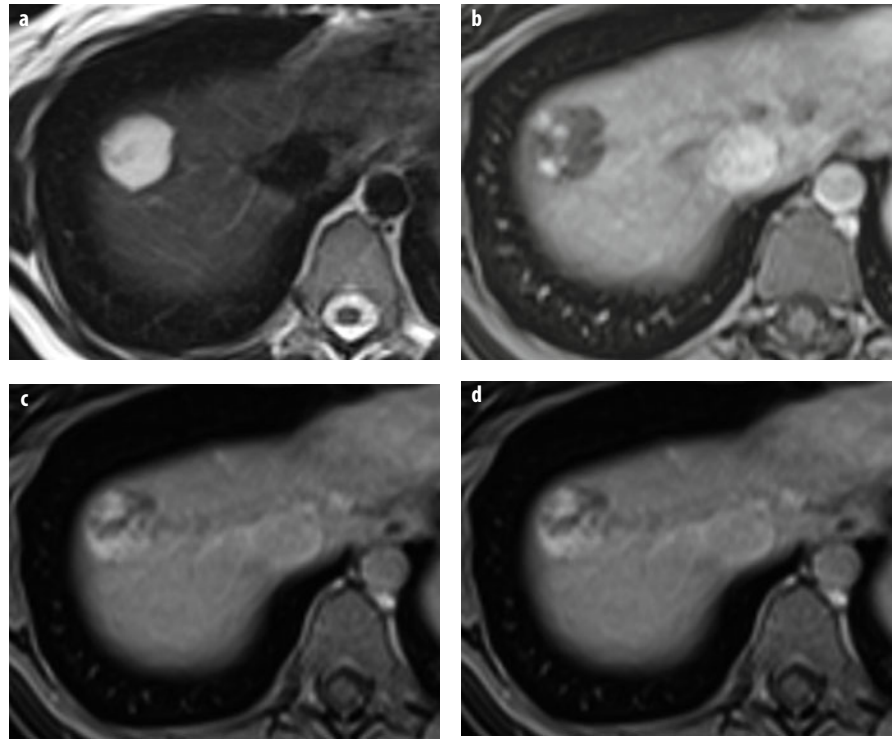


**Fig. 3 a-d.** Hemangioma type 3: nonspecific gadolinium chelates. **a** T2-weighted turbo spin-echo (TSE) image shows a very hyperintense lesion in the right lobe. **b, c** Dynamic gadolinium-enhanced T1-weighted gradient-echo (GRE) magnetic resonance (MR) images (arterial, venous, and equilibrium phases) show peripheral nodular enhancement with progressive centripetal fill-in. **d** In the equilibrium phase, after 5 min, there is no complete fill-in

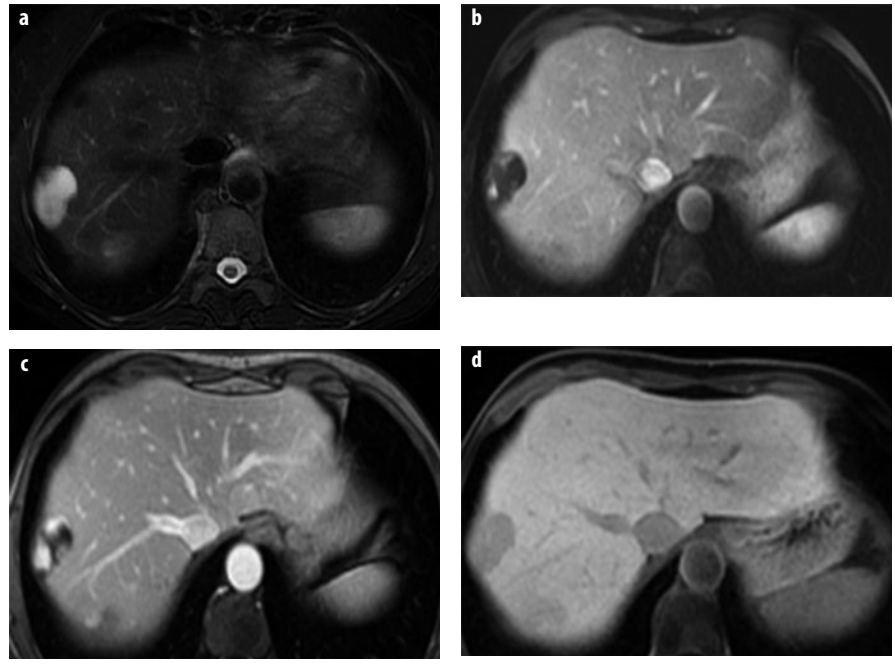


**Fig. 4 a-d.** Hemangioma type 3: gadoxetic acid. **a** T2-weighted TSE image shows a large, lobulated lesion of very high signal intensity. **b-d** Dynamic gadoxetic-acid-enhanced imaging shows peripheral nodular enhancement in the **b** arterial and **c** venous phases. In the **d** hepatobiliary phase, there is marked lesion hypointensity due to washout in the lesion and enhancement of surrounding liver parenchyma

tiating feature from fibrolamellar HCC, in which the central scar is predominately low signal on T2-weighted MR. The use of color/power Doppler US may demonstrate blood vessels within the scar [32].

FNH are isodense or minimally hypodense on unenhanced and equilibrium-phase postcontrast CT and sometimes detectable only by the mass effect on adjacent vessels. On unenhanced MR images, FNH often has signal intensity similar to hepatic parenchyma, but is usually slightly different on either T1- or T2-weighted images (Fig. 5). Due to the prominent arterial vascular supply, FNH undergoes marked homogenous enhancement during the arterial phase of contrast-enhanced CT/MR imaging, with rapid washout of contrast to isodensity/isointensity on venous-phase images [31]. The central scar often enhances on delayed scans [30], which is typical of

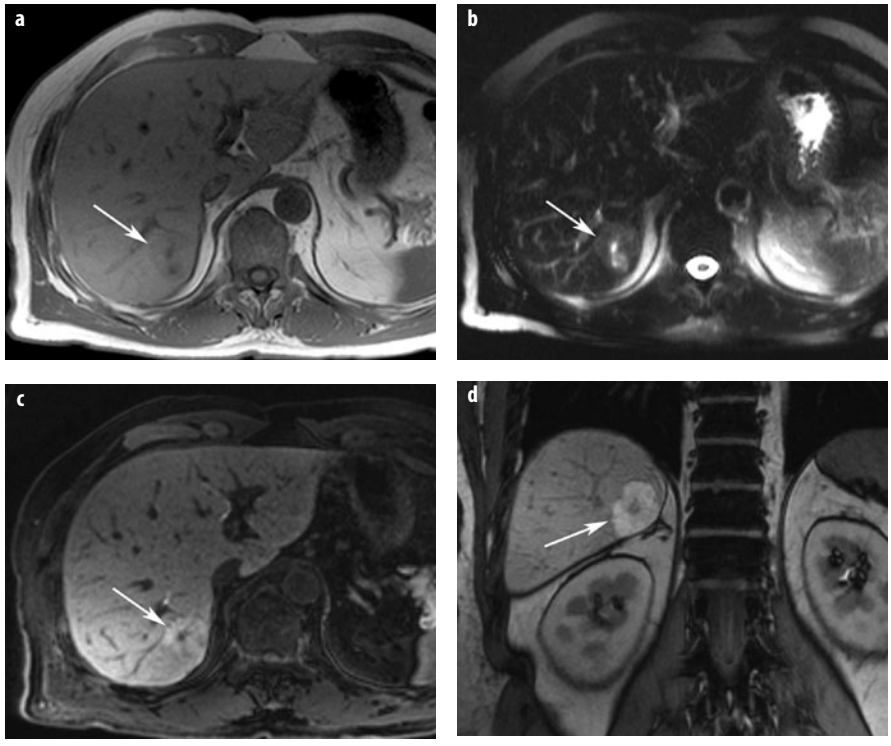


**Fig. 5 a-d.** Focal nodular hyperplasia (FNH). **a** The lesion (*arrow*) is isointense on T1-weighted image and shows a small central scar. **b** On T2-weighted images, the lesions is also isointense (*arrow*), the central T2-weighted bright scar is better discernible. **c, d** T1-weighted images with liver-specific contrast agent in axial and coronal planes show homogenous uptake of the liver-specific agent, typical for FNH (*arrow*). The central spoke-wheel scar is nicely depicted

fibrous component. Another key feature is that other than the scar, these lesions tend to be highly homogeneous in appearance, differentiating them from fibrolamellar HCC.

With liver-specific MR contrast agents, FNH shows enhancement on delayed images after administration of hepatobiliary contrast agents (such as gadoxetic acid or gadobenate dimeglumine) (Fig. 5). This feature is particularly helpful for differentiating between hypervascular metastases (which do not accumulate liver-specific agents) or hepatic adenoma and incidentally encountered FNH [28, 33]. The influence of oral contraceptives on FNH growth is still being discussed. Studies with serial imaging show that growth during follow-up is rare (3-11%) [34, 35] and that oral contraceptives do not appear to stimulate growth [35].

### Hepatocellular Adenoma

Hepatocellular adenoma (HCA), while relatively uncommon, is frequently encountered in appropriate populations due to its known association with oral contraceptive and estrogen stimulation and administration of anabolic steroids. Histologically, HCA is composed of cells resembling normal hepatocytes but lacking bile ducts. This is a key feature for histological differentiation between adenoma and FNH [35].

Reports on imaging features of adenomas stress the heterogeneous and varied appearance, with variable consistency in the commonly seen appearances often being hypervascular and when large and heterogenous due the presence of fat, necrosis, or hemorrhage [35, 36] (Fig. 6). These tumors often contain intratumoral fat, and as T1-weighted chemical-shift MR imaging is sensitive for detecting fat, this technique can be extremely helpful in characterizing adenomas. The second typical feature of adenoma is its propensity for spontaneous hemorrhage. If no tumor capsule is present, such hemorrhage may lead to spontaneous rupture with hypotension and even death.

The presence of intratumoral fat helps to narrow the differential diagnosis, as hemangioma can be excluded and metastases and FNH only very rarely contain fat. On dynamic contrast-enhanced CT or MR, adenomas usually show marked arterial-phase enhancement, with rapid transition to either iso- or hypoattenuating/intense to hepatic parenchyma on portal-venous-phase imaging. Hepatobiliary MR contrast agents (gadobenate, gadoxetic acid) are effective in differentiating small adenomas from FNH due to differences in appearance on the hepatobiliary phase (20 min-1 h). At this phase, liver parenchyma and FNH retain contrast enhancement, whereas adenomas typically do not [37, 38].

The development of genetic classification of tumors has resulted in a new understanding that HCA is not a single form of tumor but a heterogeneous group of tumors with different genetic and pathologic features and natural biology. HCA are classified into three categories based on genetic features that in many ways correlate with specific imaging [39, 40]. The most common subtype is the inflammatory adenoma, typified by intense arterial enhancement and usually lacking any demonstrable fat content (Fig. 7). These lesions often have peliotic changes and thus may retain their contrast enhancement into delayed phases

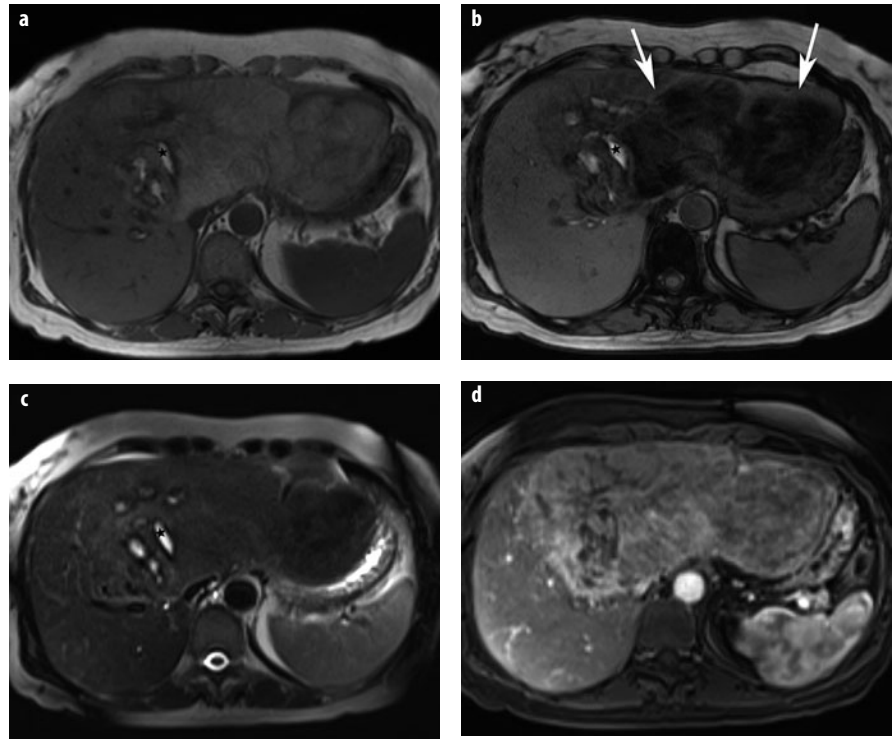


**Fig. 6 a-d.** Hepatocellular adenoma (HCA). **a** T1-weighted in-phase GRE images demonstrate a very large mass in a young woman. The mass is inhomogeneous and shows bright spots, suggestive of hemorrhage (*asterisk*). **b** Typical signal intensity drop on the opposed-phase image, indicative of intratumoral fat (*arrows*), whereas the hemorrhage (methemoglobin) does not lose signal intensity. **c** T2-weighted TSE sequence confirms the presence of hemorrhage (*asterisk*). Intratumoral fat and hemorrhage are typical for adenoma. **d** On gadolinium-enhanced image, there is moderate and inhomogeneous enhancement. In a large, very inhomogeneous adenoma, malignant degeneration cannot be ruled out radiologically. However, at surgery, the lesion was an adenoma with central hemorrhage

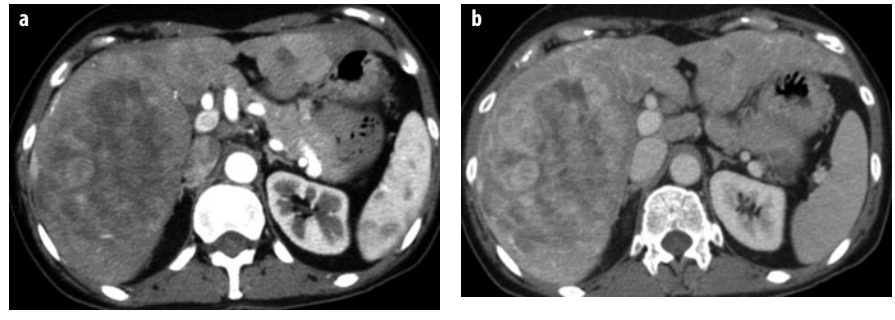


**Fig. 7 a, b.** HCA, inflammatory type. **a** Arterial-phase CT shows strong and progressive contrast enhancement, which is retained in the **b** delayed phase and is typical for peliotic changes in inflammatory adenoma

and demonstrate higher T2 signal at MR. These lesions are associated with intratumor bleeding and/or rupture and a slightly increased risk of malignant degeneration.

The second most common category, the human plasma fibronectin (HNF)-1α-mutated HCA, is seen almost exclusively in women, with almost all having a history of oral contraceptive use [39]. These lesions have a high incidence of intracellular fat deposition, resulting in associated imaging findings (Fig. 8). These lesions are the least aggressive subtype and have no risk for developing malignancy and little risk of bleeding unless they are large.

The third category of HCA represents those with β-catenin mutations. This genetic alteration has a higher association with malignant degeneration and is associated with testosterone administration and glycogen storage disease. There are no specific imaging features associated with this category, and classification can only be suggested by genetic testing from the tumor. A small percentage of adenomas remain unclassified.

## Biliary Hamartomas (von Meyenburg Complex)

Bile-duct hamartomas are congenital malformations of the ductal plate but have no connection with bile ducts. They are of no clinical significance but are incidentally encountered in patients undergoing abdominal imaging examinations. These hamartomas appear as small cystic lesions of round, oval, or irregular shape found either in the periportal region or diffusely spread throughout the liver (Fig. 9). They are usually <10 mm in diameter and lack contrast enhancement; occasionally, however, peripheral rim enhancement may simulate small hypovascular metastases [36]. If the enhancement is very thin (<2mm) and only seen on equilibrium-phase images, this is typical of fibrous component of biliary hamartomas and can help characterize these otherwise homogeneous lesions [41]. Occasionally, bile duct hamartomas can be very large, up to 20 cm, and be symptomatic from internal hemorrhage or pressure on adjacent structures [42].

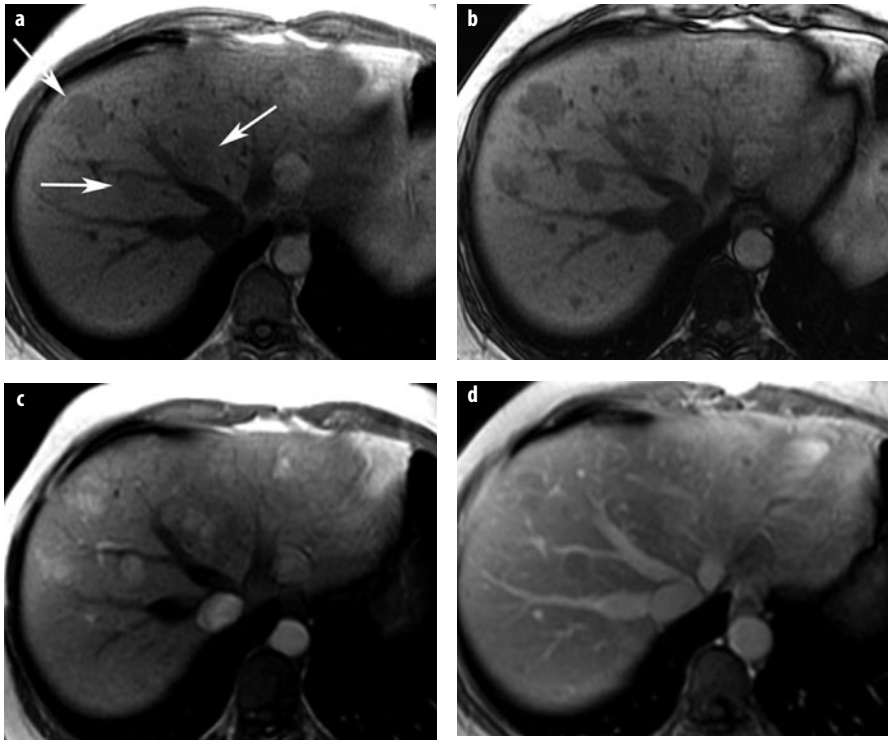


**Fig. 8 a-d.** HCA in adenomatosis. Human plasma fibronectin (HNF)-1α-mutated type. **a, b** T1-weighted GRE images: **a** in-phase image shows several mildly hypointense lesions in the right lobe (*arrows*), which show considerable signal intensity drop on the **b** opposed-phase image due to intratumoral fat. **c, d** After contrast, lesions are hypervascular in the **c** arterial-phase image, with washout in the **d** venous phase

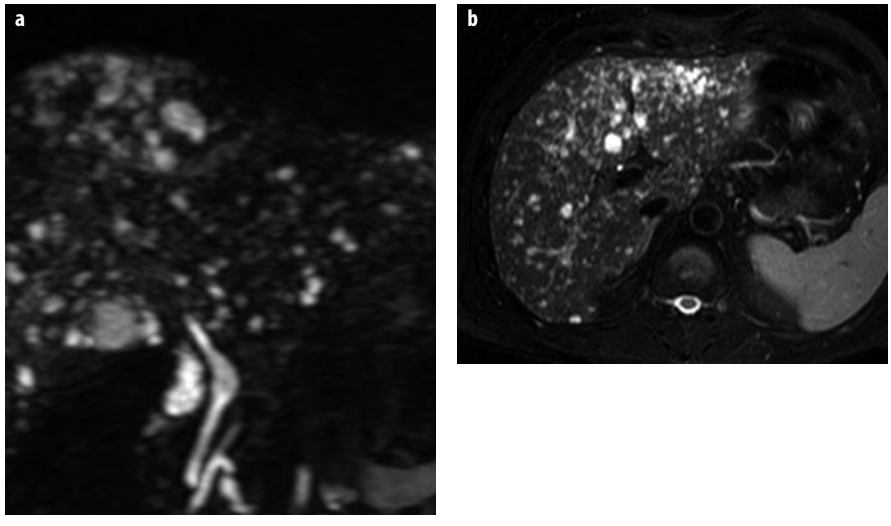


**Fig. 9 a, b.** Biliary hamartomas (von Meyenburg complex). **a, b** Coronal and axial T2-weighted images show multiple small cystic lesions of different sizes and shapes (starry-sky appearance), typical for biliary hamartomas

## Hepatic Abscess and Echinococcus

Abscess appearances can vary depending on etiology (peribiliary abscesses tend to be small and scattered adjacent to the biliary tree; hematogenous distribution via the hepatic artery or via the portal vein in appendicitis or diverticulitis tends to lead to larger lesions). US reveals a cystic lesion with internal echoes. On CT, hepatic abscess appears as a hypodense lesion with a capsule that may show enhancement; cluster sign may be noted when multiple abscesses are present as focal clusters of lesions [43]. CT appearance of hepatic abscess is nonspecific and can be mimicked by cystic or necrotic metastases. Clinical information and laboratory values play a key role in guiding the radiologic diagnosis. Though present in only a small minority of cases, central gas is highly specific for abscess (Fig. 10). On MR imaging, hepatic abscesses are hypointense relative to liver parenchyma on T1-weighted images and markedly hyperintense on T2-weighted images, often surrounded by a local area of slight T2 hyperintensity representing perilesional edema (Fig. 10).

CT appearance of amoebic liver abscess is nonspecific. It usually appears as a solitary, hypodense lesion, with an enhancing wall that may be smooth or nodular, and is

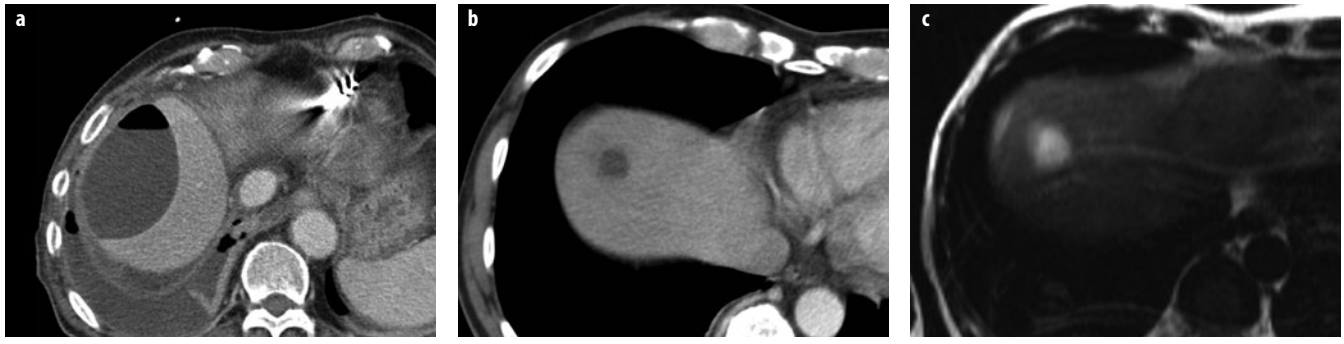


**Fig. 10 a-c.** Abscesses. **a** Typical large subcapsular abscess with an air-fluid level and a reactive pleural effusion. **b.** In another patient, computed tomography (CT) shows a small, thick-walled abscess after pancreatic surgery. **c** T2-weighted MR image of the same patient shows the thick, indistinct wall and peripheral edema

often associated with an incomplete rim of edema. With MR imaging, lesions are hypointense on T1-weighted images and heterogeneously hyperintense on T2-weighted images [44].

On CT scan, involvement of liver by *Echinococcus granulosus* (hydatid cyst) appears as unilocular or multilocular cysts with thin or thick walls and calcifications, usually with daughter cysts seen as smaller cysts, with septations at the margin of or inside the mother cyst (i.e., this appearance is quite different from a "usual" multicystic tumor). On MR imaging, the presence of a hypointense rim on T1- and T2-weighted images and a multiloculated appearance are considered to be important diagnostic features.

## Malignant Primary Tumors

### Hepatocellular Carcinoma

HCC is the most common primary liver cancer worldwide and is particularly prominent in the Asian and Mediterranean populations. In European countries, HCC is found mostly in patients with chronic liver disease (particularly hepatitis B or C, liver cirrhosis, or hemochromatosis). HCC consists of abnormal hepatocytes arranged in a typical trabecular, sinusoidal pattern. It may be solitary, multifocal, or diffusely infiltrating.

The imaging appearances of HCC can vary dramatically, but generally can be separated into appearances based on early versus late presentation. Early presentation is identified in patients with chronic liver disease, who either undergo screening for HCC with imaging or undergo frequent liver imaging due to complications of chronic liver disease. In these patients, lesions are typically small (<3 cm) and homogeneous in appearance. In noncirrhotic patients, it is usually asymptomatic, and the patient will not present for imaging until symptoms occur due to a very large lesion, usually heterogeneous in appearance.

US appearance is variable, with iso-, hypo-, or hyperechogenicity (increased echogenicity is often due to tumoral fat). Smaller lesions are typically homogeneous and larger lesions heterogeneous. A surrounding fibrous capsule is often present and relatively characteristic for HCC, appearing as a hypoechoic rim surrounding the lesion.

On unenhanced CT images, most HCCs are hypo- or isodense (the latter particularly if small). The presence of intratumoral fat can lower CT attenuation and is suggestive of primary hepatocellular tumors when seen in appropriate clinical settings; however, this can also be seen in benign adenomas, metastatic liposarcoma, or germ cell tumors in and rare benign angiomyolipomas. Due to their predominant arterial supply, many small HCCs enhance vividly in the arterial phase of hepatic contrast enhancement, becoming iso- or hypoattenuating with hepatic parenchyma in the portal-venous phase of enhancement. Delayed-phase images show most HCC lesions as hypodense compared with surrounding liver (Fig. 11). The washout of contrast in these tumors – differently from the liver parenchyma, which remains enhanced – is a key method by which to characterize HCC in patients, as many benign lesions may show arterial enhancement but most (but not all) do not exhibit this washout. Small HCCs may have a nodule-in-nodule appearance on CT and MR images, especially if the focus of HCC develops within a siderotic regenerative nodule (Fig. 12). At MR imaging, such a nodule may show higher signal intensity on T2-weighted images and display hypervascularity on arterial-phase images.

Several studies address the required phases of scanning for optimizing HCC detection and characterization. Arterial-phase imaging is the most sensitive for detecting small lesions, with highest visibility in the late arterial phase to allow time for contrast diffusion into the tumor parenchyma with no need for early arterial phase imaging [6, 45, 46]. A venous phase is always necessary for tumor detection and assessment of venous structures (Fig. 13), as well as other abdominal organs. For HCC detection, the delayed phase can detect a few lesions that would otherwise go undetected [47] and is also helpful in differentiating HCC from other benign enhancing lesions by demonstrating tumor washout greater than in the liver parenchyma [48]. Unenhanced images are important for documenting siderotic nodules as being different from

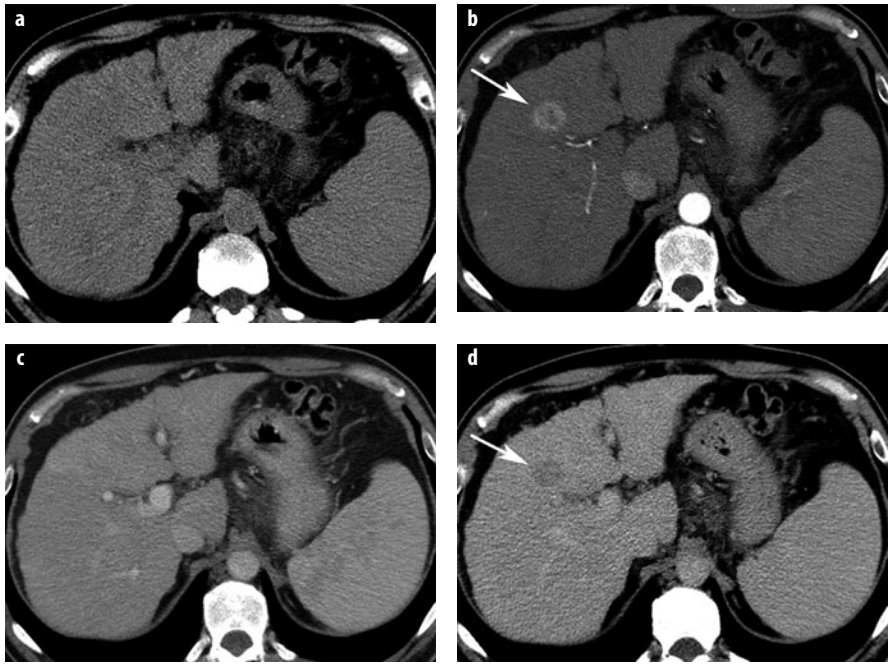


**Fig. 11 a-d.** Hepatocellular carcinoma (HCC) quadruple-phasic CT for detection and characterization. **a** Noncontrast CT shows liver cirrhosis and splenomegaly. In segment 4, a lesion is only faintly seen. **b** In the late arterial phase, a hypervascular HCC is depicted in segment 4 (*arrow*). **c** In the venous phase, the lesion is not visible. **d** The delayed-phase scan reveals lesion washout; the lesion is now hypoattenuating (*arrow*). The combination of arterial hypervascularity and washout is a highly specific sign of malignancy

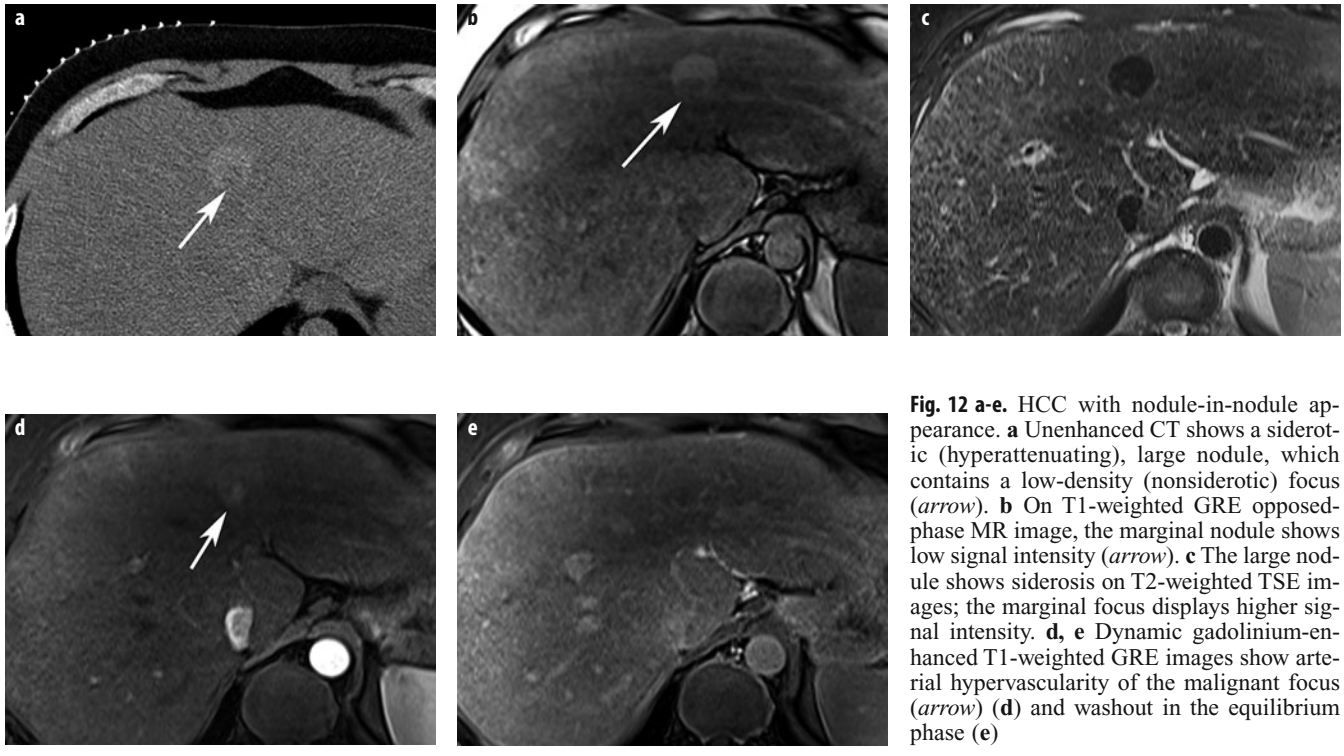


**Fig. 12 a-e.** HCC with nodule-in-nodule appearance. **a** Unenhanced CT shows a siderotic (hyperattenuating), large nodule, which contains a low-density (nonsiderotic) focus (*arrow*). **b** On T1-weighted GRE opposed-phase MR image, the marginal nodule shows low signal intensity (*arrow*). **c** The large nodule shows siderosis on T2-weighted TSE images; the marginal focus displays higher signal intensity. **d, e** Dynamic gadolinium-enhanced T1-weighted GRE images show arterial hypervascularity of the malignant focus (*arrow*) (**d**) and washout in the equilibrium phase (**e**)

arterial enhancing lesions and for detecting intratumoral fat; however, to reduce radiation dose, such images can be obtained only intermittently in those patients undergoing serial imaging examinations. It is mandatory, however, in the follow-up after chemoembolization or tumor ablation and for patients in whom hemorrhage may be suspected. In summary, a three- to four-phasic MDCT protocol is recommended by most centers to optimally detect and characterize HCC (Fig. 11). For obvious reasons relative to radiation dose, if a patient is expected to need numerous serial examinations, MR would therefore make a preferred choice.

The presence of focal hypervascularity in the arterial phase may lead to false-positive diagnoses [49]: transient

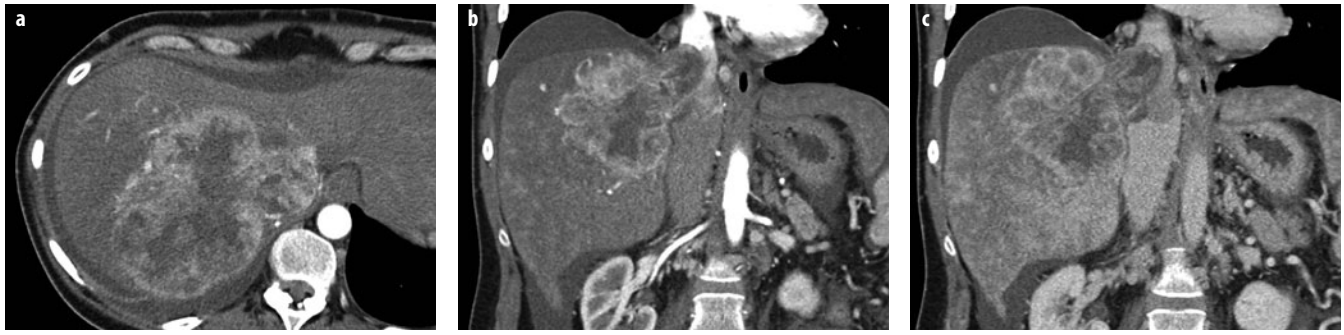


**Fig. 13 a-c.** Large HCC with tumor thrombus in the inferior vena cava (IVC). **a** Arterial-phase MDCT shows a large HCC with peripheral irregular rim enhancement, which grows into the right hepatic vein and the IVC. **b** Arterial- and **c** venous-phase images in the coronal plane better demonstrate the extension of tumor thrombus in the IVC above the diaphragm

focal enhancement of liver parenchyma during arterial phase enhancement, often termed transient hepatic attenuation differences (THAD), can be caused by a multitude of factors. In cirrhotic patients, transient focal enhancement most often is caused by arterial-portal shunting, resulting in inappropriately early focal areas of portal-venous distribution enhancement in the liver. These usually are peripheral, often wedge shaped, and are not round. Subcapsular lesions that do not show a substantial mass effect or a round nature should be evaluated carefully before suggesting the diagnosis of HCC. The combination of hyperdensity on arterial-phase images combined with washout to hypodensity on venous- or delayed-phase images, although not sensitive (33%), is a very specific (100%) feature for the presence of HCC [50] (Fig. 11). Diffusely infiltrating and small HCCs in cirrhosis may be difficult to detect with CT. The larger HCC lesions typically have a different appearance, with a mosaic appearance due to hemorrhage and fibrosis. Also, ~10% of small HCC can appear hypodense to liver and are thought to be well-differentiated lesions.

Typical MR imaging findings of larger HCC include a fibrous capsule, intratumoral septa, daughter nodules, and tumor thrombus [51]. These heterogeneous appearances are often associated with a somewhat organized internal pattern that has been termed a mosaic pattern, seen on both CT and MR [52]. Whereas most large HCC are hyperintense on T2-weighted images, small lesions, $<$3-4 cm, show a large spectrum including isointense and hypointense appearance. On T1-weighted images, HCC has similar variable signal intensity relative to hepatic parenchyma. A tumor capsule may be seen on T1-weighted and, less commonly, on T2-weighted images as hypointense (Fig. 12). Conventional gadolinium contrast imaging in HCC parallels that described for CT, with characteristic early peak contrast enhancement and delayed-phase tumor washout. These enhancement features are useful in differentiating HCC from hemangioma, which generally shows early peripheral enhancement, marked peak enhancement $>$2 min after injection, and marked pooling of contrast on delayed images. The newer liver-specific MR contrast agents (gadoxetic acid or gadobenate dimeglumine) can provide arterial, portal-venous, and equilibrium-phase contrast characteristics, as well as unique additional information in the more delayed parenchymal phase. Most often, HCC on these images lack contrast retention, which can be a characteristic feature in screening patients with chronic liver disease. However, some benign regenerating nodules may also demonstrate this effect [53]. In addition, some well-differentiated HCC may retain contrast on delayed images, and early evidence suggests gadoxetic-acid-enhanced MR may be able to classify HCC into several imaging patterns that may be associated with tumor aggressiveness and patient outcomes [54]. Whereas most HCC show washout of hepatobiliary MR contrast agents on delayed imaging (Fig. 14), some well-differentiated tumors may show enhancement. However, such enhancement is not specific for HCC and can be seen with other primary hepatocellular tumors, such as dysplastic nodules, FNH, and adenoma.

High b-value (800 s/mm$^2$) DWI may suggest the diagnosis of HCC, with restricted diffusion in the tumor appearing as a high-signal-intensity lesion. However, only ~80% of HCC demonstrate this finding, and ~25% of benign nodules also show restricted diffusion [55].

To summarize, many MR characteristics are often associated with HCC (arterial-phase hyperintensity, T2 hyperintensity, venous- or equilibrium-phase washout, hepatobiliary MR contrast agent washout on hepatobiliary-phase images, and restricted diffusion on high-b-value DWI). However, for each of these findings, there is only ~60-80% sensitivity, and benign lesions show these findings in 16-65% of cases, depending on finding, contrast agent used, and series reported [53, 55]. Based on data from numerous studies, the American Association for the Study for Liver Disease (AASLD) and the European Association for the Study of the Liver (EASL) formed recommendations for the noninvasive diagnosis of HCC in patients with chronic liver disease [56]. Lesions $\geqslant$1 cm that demonstrate arterial-phase hypervascularity and venous- or delayed-phase washout are triaged for treatment with a diagnosis of HCC. If only one of the two findings

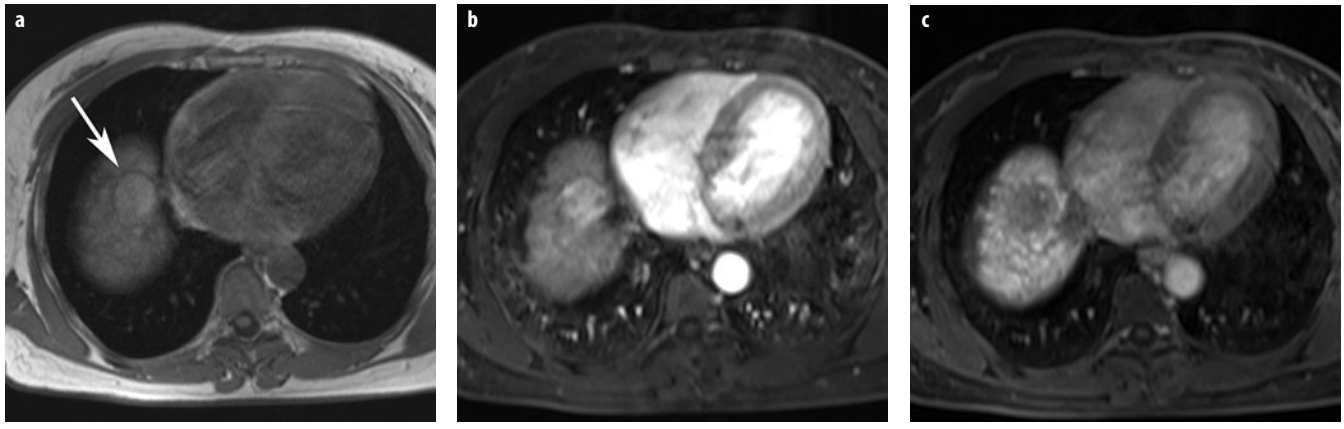


**Fig. 14 a-c.** HCC MRI with liver-specific agent (gadoxetic acid). **a** Axial T1-weighted GRE image shows an encapsulated, slightly hyperintense, mass in the dome of the liver *(arrow*). **b** Gadoxetic-acid-enhanced image shows strong enhancement in the arterial phase. **c** In the hepatobiliary phase, after 20 min, the lesion shows hypointensity due to lack of hepatocellular uptake

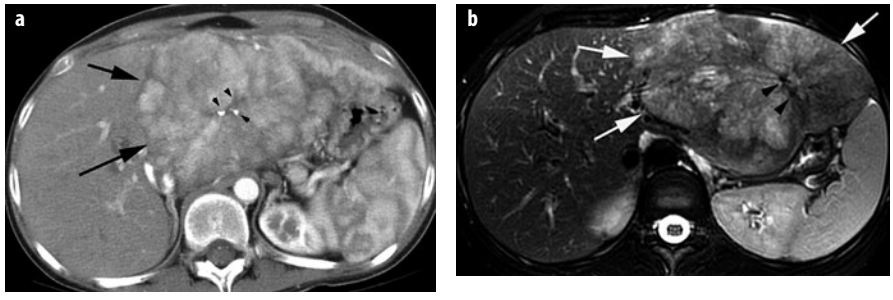


**Fig. 15 a, b.** Fibrolamellar HCC. **a** CT during the arterial phase shows typical heterogeneously enhancing mass in left lobe (*arrows*), with low-attenuation central fibrous scar with calcifications (*arrowheads*). **b** T2-weighted MRI shows large, left-lobe mass (*arrows*) with heterogeneous appearance and mildly to moderately increased signal intensity. Fibrous central scar is of very low signal intensity (*arrowheads*)

are present, then the guidelines require obtaining a different modality with contrast imaging to determine whether these findings can be verified. If the lesion remains atypical, then biopsy is recommended. For lesions $<1$ cm, the guidelines recommend repeating the examination at 3-month intervals, using the same imaging technology used to detect the lesion, to determine whether there is growth or changing character. In following up patients with chronic liver disease, development of a new nodule with any of the MR signal abnormalities discussed above should be considered worrisome for HCC, even if they do not meet the AASLD criteria for noninvasive diagnosis. These criteria were developed to be specific but are only approximately 70% sensitive [53].

It is essential for radiologists to document the number and size of all lesions meeting criteria for HCC, as treatment for these patients varies depending on these factors. It is also important to document whether vascular invasion or distant metastasis is present. The Barcelona Clinic Liver Cancer (BCLC) staging system is the most commonly used staging system, and much of it is based on imaging components [57]. Early stage (A) patients are those with a single tumor focus (and for liver transplantation requires the lesion to be $\leqslant$5 cm in maximal diameter), or if multiple, the must have three or fewer nodules $<3$ cm in diameter. These patients with chronic liver disease are often best treated with and eligible for liver transplantation. Intermediate stage (B) patients have more than three nodules or multiple nodules $\geqslant$3 cm in diameter; they are best treated with locoregional treatments and ablations. Advanced-stage (C) patients have evidence of vascular invasion and/or distant metastases and are usually triaged to receive systemic therapy with sorafenib. Terminal disease (stage C) is determined not by the extent of documented tumor but on the basis of poor liver function and patient clinical status; management consists of supportive therapies only.

### Fibrolamellar HCC

Fibrolamellar HCC (FL-HCC) is a less aggressive tumor with a better prognosis than HCC. It consists of malignant hepatocytes separated into cords by fibrous strands. On CT, FL-HCC appears as a large, well-defined vascular mass with lobulated surface and often a central scar and calcifications in up to 70% of cases [58, 59]. On MR imaging, FL-HCC appears hypointense on T1- and hyperintense on T2-weighted images, with the central scar being hypointense on both sequences (Fig. 15). This is in contrast to the scar of FNH, which is most often hyperintense on T2-weighted images. The fibrous central zones

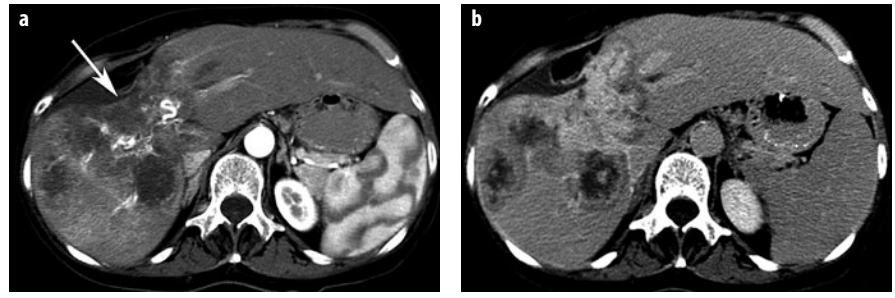


**Fig. 16 a, b.** Cholangiocellular carcinoma. **a** Contrast-enhanced CT in the arterial phase demonstrates a multicentric hypovascular mass with capsular retraction (*arrow*). **b** Delayed-phase image demonstrates typical late enhancement due to fibrous matrix

of both FNH and FL-HCC show delayed retention of conventional CT and MR contrast agents. Contrast enhancement patterns in FL-HCC are almost always heterogeneous, in contrast to those in FNH, which are almost always homogeneous.

### Cholangiocellular Carcinoma

Cholangiocellular carcinoma (CCC) is the second most common primary malignancy of the liver. Intrahepatic CCC originates from the intralobular bile ducts (in contrast to hilar CCC, which arises from a main hepatic duct or from the bifurcation). Intrahepatic CCC presents as a large mass, because the tumor does not cause symptoms in the early stages [60] (Fig. 16). According to the growth characteristics, CCC is classified as mass forming, periductal infiltrating, or intraductal growing, with the mass-forming type being most common in intrahepatic CCC [60]. At CT and MR imaging, lesions tend to be hypodense at unenhanced CT and hypointense on T1-weighted images, with peripheral enhancement at dynamic contrast-enhanced studies [61]. Delayed-phase CT/MR imaging (after 5-15 min) may show enhancement homogeneously or in the center of the lesion due to its rich fibrous stroma, which is suggestive of the diagnosis of CCC [62]. Periductal infiltrative CCC causes early segmental dilatation of bile ducts in a stage when the tumor itself may be difficult to discern [61].

In addition, there are morphologic features that can suggest the diagnosis of CCC. Peripheral lesions often demonstrate overlying capsular retraction due to the tumor's evolving scirrhous, fibrous matrix. Dilated intrahepatic bile ducts proximal to an intrahepatic CCC can also provide clues to the diagnosis, as these are rarely seen with intrahepatic metastatic lesions unless they achieve a large size and cause extrinsic compression on the common hepatic bile duct.

## Rare Primary Liver Tumors

### Biliary Cystadenoma/Cystadenocarcinomas

These tumors present a similar appearance and morphology as their mucinous counterparts in the pancreas and are seen predominately in women. Even when benign, these tumors have a propensity for malignant degeneration, and any such tumor should be considered malignant. They appear as unilocular or multilocular cystic masses, with the typical anechoic and hypoechoic US appearance and near water-like attenuation contents on CT, with peripheral soft tissue nodularity and traversing septations (Fig. 17). The greater presence of papillary excrescences, soft tissue nodularity, or septations, the more likely the lesion to be malignant [63], although this is a moot point, benign lesions can undergo malignant degeneration. The cystic areas at T1-weighted imaging are of variable signal intensity, including hyperintense to liver, presumably due to proteinaceous content. Coarse calcifications can be seen at US and CT in both cystadenoma and cystadenocarcinoma and are not a helpful differentiating feature.

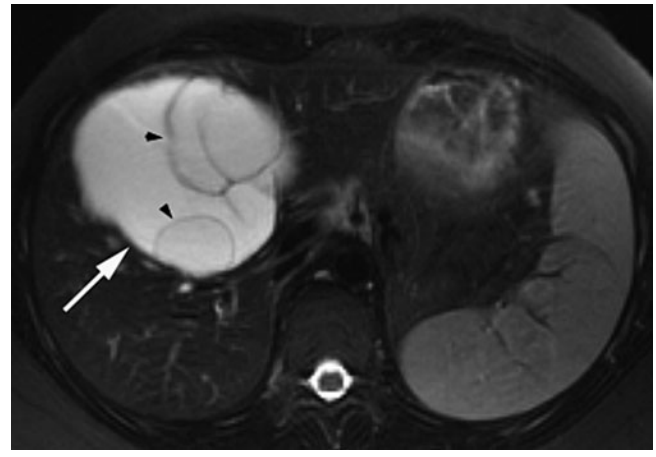

**Fig. 17.** Biliary cystadenoma. T2-weighted MR image shows very-high-signal-intensity mass (*arrow*) mostly homogeneous in appearance with exception of a few, thin internal septations (*arrowheads*).

### Hepatic Angiosarcoma

This is a rare tumor with a strong association with carcinogens such as vinyl chloride and Thorotrast; they are also seen in patients with hemochromatosis, although in the majority of patients, no known exposure to toxic agents exists. Pathologically, angiosarcoma may appear as large, solitary masses or with multiple tumor nodules of varying size. Pathologically, they may contain vascular channels that create sinusoidal spaces that can result in imaging findings in some ways simulating hemangiomas.

**Fig. 18.** Epithelioid hemangioendothelioma. Contrast-enhanced CT (portal venous phase) shows multiple, predominantly peripherally based, hypodense lesions. Note that some lesions show a laminated appearance (*arrows*). Early development of capsular retraction is present, with flattening of the capsule overlying some lesions (*arrowheads*)

The imaging appearance of angiosarcoma is most often nonspecific, being hypoattenuating on unenhanced CT, hypointense on T1-weighted MR imaging, and mildly hyperintense on T2-weighted imaging (although if prominent sinusoidal vascular spaces are present pathologically, these can be of homogeneous and very high T2-weighted signal intensity). Following iodinated or gadolinium-based contrast administration, most lesions show nonspecific heterogeneous enhancement. Potentially problematic, however, are those tumors with prominent sinusoidal vascular spaces in that CT or MR contrast enhancement characteristics of some angiosarcoma can rarely simulate that of benign hemangioma. The high MR T2-weighted signal in such lesions further compounds this problem. In most such cases, however, careful observation will reveal that tumoral enhancement does not follow characteristics of blood pool at all phases or that there are other features, such as innumerable lesions, that make hemangioma diagnosis unlikely [64, 65].

#### Epithelioid Hemangioendothelioma

Epithelioid hemangioendothelioma (EHE) is a rare tumor of vascular origin not to be confused with infantile hemangioendothelioma, a very different tumor. Primary liver tumors are characterized by the presence of multiple, peripheral-based lesions that progressively become confluent masses (Fig. 18). In addition to unusual peripheral liver distribution, a key characteristic feature is the presence of overlying capsular retraction, attributed to fibrosis and scarring within the tumor [66]. CT attenuation or MR signal intensity characteristics are nonspecific and mimic those of other tumors, although occasional tumoral calcifications may be seen. Contrast enhancement with CT or MR gadolinium chelates often shows a central zone of decreased enhancement with marked enhancement peripherally, occasionally showing concentric zones of marked enhancement (Fig. 18). Lesions often become confluent and may grow large enough to replace nearly the entire liver parenchyma.

#### Hepatic Lymphoma

This tumor is most often seen in patients with widespread non-Hodgkin's or, rarely, Hodgkin's disease. It rarely can be seen as a primary liver tumor, usually associated with an immunocompromised state, such as AIDS, or post-transplantation with immunosuppression therapy. These lesions show varying imaging appearances without any unique characteristics. CT, MR imaging, and US show focal lesions with an appearance similar to many other neoplastic lesions. Diffuse infiltrating forms can be difficult to detect with any imaging modality, although hepatomegaly may be present.

### Hepatic Metastases

At US, metastases may appear hypoechoic, isoechoic, or hyperechoic. On dynamic contrast-enhanced CT, most metastases appear hypovascular and hypodense relative to liver parenchyma on the portal-venous phase (Fig. 19). Hypervascular metastases are most commonly seen in renal cell carcinoma, neuroendocrine tumors, sarcomas, and breast tumor patients (Fig. 19). These tumors are best seen in the arterial phase and may become isodense and difficult to detect during the redistribution phase of enhancement. At MR, metastases are usually hypointense on T1-weighted and hyperintense on T2-weighted images

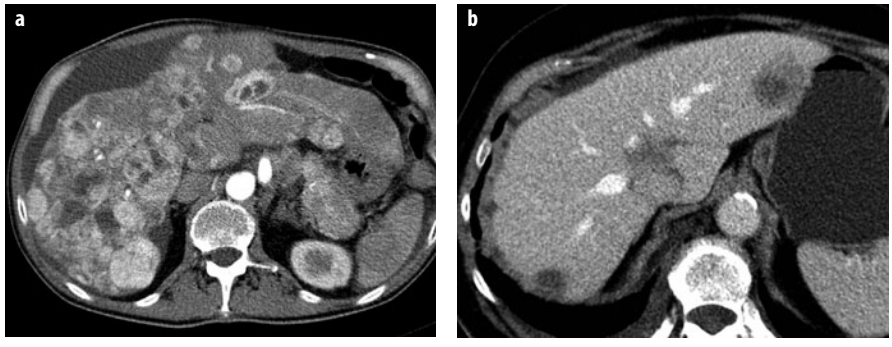


**Fig. 19 a, b.** Metastases. **a** Contrast-enhanced MDCT in the arterial phase demonstrates several predominantly hypervascular liver metastases of neuroendocrine cancer of the pancreas. **b** Contrast-enhanced MDCT in the venous phase shows typical hypovascular colorectal metastases

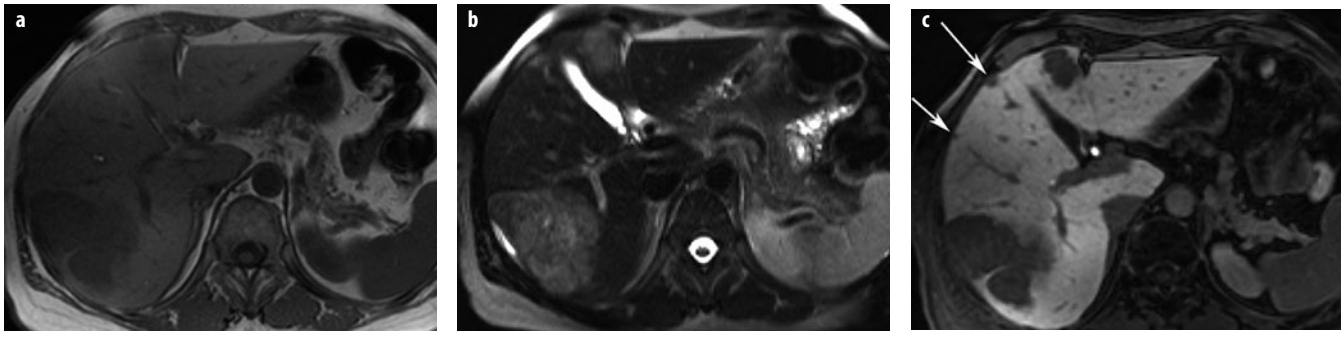


**Fig. 20 a-c.** Colorectal liver metastases at gadoxetic acid-enhanced MR imaging. **a** Unenhanced T1-weighted sequence shows two hypointense lesions in segments 6/7 and 4. **b** T2-weighted TSE pulse sequence shows the lesions to be moderately hyperintense. **c** Gadoxetic-acid-enhanced T1-weighted GRE image in the hepatobiliary phase shows two additional small subcapsular metastases (*arrows*) not seen on unenhanced MR imaging or MDCT (not shown)

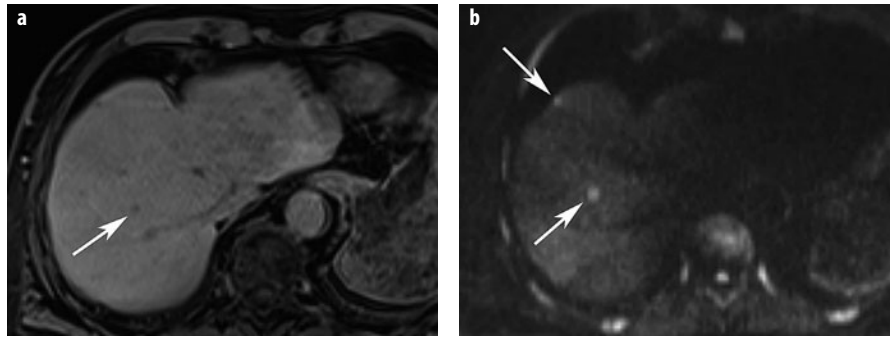


**Fig. 21 a, b.** Value of diffusion-weighted (DWI) MR imaging for detecting small metastases. **a** Contrast-enhanced MR image shows one small metastasis in the right lobe (*arrow*). There is a subtle hypointensity in the right lobe in a subcapsular location. **b** DWI clearly shows an additional metastasis (*arrows*)

[67] (Fig. 20). Peritumoral edema makes lesions appear larger on T2-weighted images and is highly suggestive of a malignant mass [68]. High signal intensity on T1-weighted sequences is typical for melanoma metastases due to the paramagnetic nature of melanin. Some lesions may have a central area of hyperintensity (target sign) on T2-weighted images, which corresponds to central necrosis. DWI with high b-values (e.g., 600-800) is very helpful for detecting small liver metastases, which may otherwise escape detection (Fig. 21). On dynamic contrast-enhanced MR imaging, metastases demonstrate enhancement characteristics similar to those described for CT. Metastases may demonstrate a hypointense rim compared with the center of the lesion on delayed images (peripheral washout sign), which is highly specific for malignancy. Most recent studies show MR imaging to be more sensitive than contrast-enhanced CT for detecting hepatic metastases [20, 22, 23], especially for detecting small lesions.

## Differential Diagnosis of Focal Liver Lesions

The approach to characterizing a focal liver lesion seen on CT begins with determining its density. If the lesion shows near water density, is homogenous in character, and has sharp margins, then a cyst should be considered and can be confirmed with US, equilibrium-phase CT, or even MR imaging (T2 bright and nonenhancing postgadolinium), which can ensure there are no solid components or mural wall lesions.

If the lesion has some enhancement, then the next analysis requires determination of whether enhancement is peripheral and nodular, with the density of enhancing portions following the same general levels of blood vessels in the arterial, venous, and delayed phases. In this case, a hemangioma may be diagnosed with high certainty.

Arterially enhancing lesions include FNH, HCA, HCC, and metastases from neuroendocrine tumors, melanoma, renal cell carcinoma, and breast cancer. In general, HCC is considered in a setting of cirrhosis and/or chronic liver disease. FNH is most likely in young women with a noncirrhotic liver and if the lesion is homogeneous and near-isodense/isointense on unenhanced CT/MR imaging with a central T2-weighted hyperintense scar. Thick, irregular, heterogeneous enhancement or the presence of peripheral washout at the delayed phase suggests a malignant mass, such as metastases, CCC, or even HCC. Liver-specific MR contrast and DWI aids in detection and characterization of focal lesions.

## References


1. Laghi A (2007) Multidetector CT (64 Slices) of the liver: examination techniques. Eur Radiol 17:675-683.
2. Weg N, Scheer MR, Gabor MP (1998) Liver lesions: improved detection with dual-detector-array CT and routine 2.5-mm thin collimation. Radiology 209:417-426.
3. Ichikawa T, Nakajima H, Nanbu A et al (2006) Effect of injection rate of contrast material on CT of hepatocellular carcinoma. AJR Am J Roentgenol 186:1413-1418.
4. Foley WD, Hoffmann RG, Quiroz FA et al (1994) Hepatic helical CT: contrast material injection protocol. Radiology 192:367-371.
5. Kim T, Murakami T, Takahashi S et al (1998) Effects of injection rates of contrast material on arterial phase hepatic CT. AJR Am J Roentgenol 171:429-432.
6. Schima W, Hammerstingl R, Catalano C et al (2006) Quadruple-phase MDCT of the liver in patients with suspected hepatocellular carcinoma: effect of contrast material flow rate. AJR Am J Roentgenol 186:1571-1579.
7. Sultana S, Awai K, Nakayama Y et al (2007) Hypervascular hepatocellular carcinomas: bolus tracking with a 40-detector CT scanner to time arterial phase imaging. Radiology 243:140-147.
8. Oliver JH, Baron RL (1996) Helical biphasic contrast-enhanced CT of the liver: technique, indications, interpretations, and pitfalls. Radiology 201:1-14.
9. Vardhanabhuti V, Loader R, Roobottom CA (2013) Assessment of image quality on effects of varying tube voltage and automatic tube current modulation with hybrid and pure iterative reconstruction techniques in abdominal/pelvic CT: a phantom study. Invest Radiol 48:167-174.
10. Singh S, Kalra M, Hsieh J et al (2010) Abdominal CT: comparison of adaptive statistical iterative and filtered back projection reconstruction techniques. Radiology 257:373-383.
11. May MS, Wüst W, Brand M et al (2011) Dose reduction in abdominal computed tomography: intraindividual comparison of image quality of full-dose standard and half-dose iterative reconstructions with dual-source computed tomography. Invest Radiol 46:465-470.
12. Gonzalez-Guindalini FD, Botelho MP, Töre HG et al (2013) MDCT of chest, abdomen, and pelvis using attenuation-based automated tube voltage selection in combination with iterative reconstruction: an intrapatient study of radiation dose and image quality. AJR Am J Roentgenol 201:1075-1082.
13. Fuentes-Orrego JM, Hayano K, Kambadakone AR et al (2013) Dose-modified 256-MDCT of the abdomen using low tube current and hybrid iterative reconstruction. Acad Radiol 20:1405-1412.
14. Padhani AR, Liu G, Chenevert TL et al (2009) Diffusion-weighted magnetic resonance imaging as a cancer biomarker: consensus and recommendations. Neoplasia 11:102-125.
15. Koh DM, Brown G, Riddell AM et al (2008) Detection of colorectal hepatic metastases using MnDPDP MR imaging and diffusion-weighted imaging (DWI) alone and in combination. Eur Radiol 18:903-910.
16. Holzapfel K, Reiser-Erkan C, Fingerle AA et al (2011) Comparison of diffusion-weighted MR imaging and multidetector-row CT in the detection of liver metastases in patients operated for pancreatic cancer. Abdom Imaging 36:179-184.
17. Vandecaveye V, De Keyzer F, Verslype C et al (2009) Diffusion-weighted MRI provides additional value to conventional dynamic contrast-enhanced MRI for detection of hepatocellular carcinoma. Eur Radiol 19:2456-2466.
18. Parikh T, Drew SJ, Lee VS et al (2008) Focal liver lesion detection and characterization with diffusion-weighted MR imaging: comparison with standard breath-hold T2-weighted imaging. Radiology 246:812-822.
19. Taouli B (2012) Diffusion-weighted MR imaging for liver lesion characterization: a critical look. Radiology 262:378-380.
20. Oudkerk M, Torres CG, Song B et al (2002) Characterization of liver lesions with mangafodipir trisodium-enhanced MR imaging: multicenter study comparing MR and dual-phase spiral CT. Radiology 223:517-524.
21. Scharitzer M, Schima W, Schober E et al (2005) Characterization of hepatocellular tumors: value of mangafodipir-enhanced magnetic resonance imaging. J Comput Assist Tomogr 29:181-190.
22. Ward J, Robinson PJ, Guthrie JA et al (2005) Liver metastases in candidates for hepatic resection: comparison of helical CT and gadolinium- and SPIO-enhanced imaging. Radiology 237:170-180.
23. Hammerstingl R, Huppertz A, Breuer J et al (2008) Diagnostic efficacy of gadoxetic acid (Primovist)-enhanced MRI and spiral CT for a therapeutic strategy: comparison with intraoperative and histopathologic findings in focal liver lesions. Eur Radiol 18:457-467.
24. Schima W, Saini S, Echeverri JA et al (1997) T2-weighted MR imaging for characterization of focal liver lesions: conventional spin-echo vs fast spin-echo. Radiology 202:389-393.
25. Farraher SW, Jara H, Chang KJ et al (2006) Differentiation of hepatocellular carcinoma and hepatic metastasis from cysts and hemangiomas with calculated T2 relaxation times and the T1/T2 relaxation times ratio. J Magn Reson Imaging 24:1333-1341.
26. Semelka RC, Brown ED, Ascher SM et al (1994) Hepatic hemangiomas: a multi-institutional study of appearance on T2-weighted and serial gadolinium-enhanced gradient-echo MR images. Radiology 192:401-406.
27. Oto A, Kulkarni K, Nishikawa R, Baron RL (2010) Contrast enhancement of hepatic hemangiomas on multiphase MDCT: can we diagnose hepatic hemangiomas by comparing enhancement with blood pool? AJR Am J Roentgenol 195:381-386.
28. Ba-Ssalamah A, Uffmann M, Saini S et al (2009) Clinical value of MRI liver-specific contrast agents: a tailored examination for a confident noninvasive diagnosis of focal liver lesions. Eur Radiol 19:342-357.
29. Vossen JA, Buijs M, Liapi E et al (2008) Receiver operating characteristic analysis of diffusion-weighted magnetic resonance imaging in differentiating hepatic hemangioma from other hypervascular liver lesions. J Comput Assist Tomogr 32:750-756.
30. Kehagias D, Moulopoulos L, Antoniou A et al (2001) Focal nodular hyperplasia: imaging findings. Eur Radiol 11:202-212.
31. Brancatelli G, Federle MP, Grazioli L et al (2001) Focal nodular hyperplasia: CT findings with emphasis on multiphasic helical CT in 78 patients. Radiology 219:61-68.
32. Uggowitzer MM, Kugler C, Mischinger HJ et al (1999) Echo-enhanced Doppler sonography of focal nodular hyperplasia of the liver. J Ultrasound Med 18:445-451.
33. Purysko AS, Remer EM, Coppa CP et al (2012) Characteristics and distinguishing features of hepatocellular adenoma and focal nodular hyperplasia on gadoxetate disodium-enhanced MRI. AJR Am J Roentgenol 198:115-123.
34. Leconte I, Van Beers BE, Lacrosse M et al (2000) Focal nodular hyperplasia: natural course observed with CT and MRI. J Comput Assist Tomogr 24:61-66.
35. Mathieu D, Kobeiter H, Maison P et al (2000) Oral contraceptive use and focal nodular hyperplasia of the liver. Gastroenterology 118:560-564.
36. Prasad SR, Sahani DV, Mino-Kenudson M et al (2008) Benign hepatic neoplasms: an update on cross-sectional imaging spectrum. J Comput Assist Tomogr 32:829-840.
37. Grazioli L, Morana G, Kirchin MA, Schneider G (2005) Accurate differentiation of focal nodular hyperplasia from hepatic adenoma at gadobenate dimeglumine-enhanced MR imaging: prospective study. Radiology 236:166-177.
38. Grazioli L, Bondioni MP, Haradome H et al (2012) Hepatocellular adenoma and focal nodular hyperplasia: value of ga-

doxetic acid-enhanced MR imaging in differential diagnosis. Radiology 262:520-529.
39. Katabathina VS, Menias CO, Shanbhogue AK et al (2011) Genetics and imaging of hepatocellular adenomas: 2011 update. Radiographics 31:1529-1543.
40. van Aalten SM, Thomeer MG, Terkivatan T et al (2011) Hepatocellular adenomas: correlation of MR imaging findings with pathologic subtype classification. Radiology 261:172-181.
41. Semelka RC, Hussain SM, Marcos HB, Woosley JT (1999) Biliary hamartomas: solitary and multiple lesions shown on current MR techniques including gadolinium enhancement. J Magn Reson Imaging 10:196-201.
42. Martin DR, Kalb B, Sarmiento JM et al (2010) Giant and complicated variants of cystic bile duct hamartomas of the liver: MRI findings and pathological correlations. J Magn Reson Imaging 31:903-911.
43. Jeffrey RB, Jr., Tolentino CS, Chang FC, Federle MP (1988) CT of small pyogenic hepatic abscesses: the cluster sign. AJR Am J Roentgenol 151:487-489.
44. Barreda R, Ros PR (1992) Diagnostic imaging of liver abscess. Crit Rev Diagn Imaging 33:29-58.
45. Laghi A, Iannaccone R, Rossi P et al (2003) Hepatocellular carcinoma: detection with triple-phase multi-detector row helical CT in patients with chronic hepatitis. Radiology 226:543-549.
46. Ichikawa T, Kitamura T, Nakajima H et al (2002) Hypervascular hepatocellular carcinoma: can double arterial phase imaging with multidetector CT improve tumor depiction in the cirrhotic liver? AJR Am J Roentgenol 179:751-758.
47. Monzawa S, Ichikawa T, Nakajima H et al (2007) Dynamic CT for detecting small hepatocellular carcinoma: usefulness of delayed phase imaging. AJR Am J Roentgenol 188:147-153.
48. Iannacone R, Laghi A, Catalano C et al (2005) Hepatocellular carcinoma: role of unenhanced and delayed-phase multi-detector row helical CT in patients with cirrhosis. Radiology 234:460-467.
49. Baron RL, Brancatelli G (2004) Computed tomographic imaging of hepatocellular carcinoma. Gastroenterology 127:S133-143.
50. Forner A, Vilana R, Ayuso C et al (2008) Diagnosis of hepatic nodules 20 mm or smaller in cirrhosis: Prospective validation of the noninvasive diagnostic criteria for hepatocellular carcinoma. Hepatology 47:97-104.
51. Tublin ME, Dodd GD, Baron RL (1997) Benign and malignant portal vein thrombosis: differentiation by CT characteristics. AJR Am J Roentgenol 168:719-723.
52. Stevens WR, Gulino SP, Batts KP et al (1996) Mosaic pattern of hepatocellular carcinoma: histologic basis for a characteristic CT appearance. J Comput Assist Tomogr 20:337-342.
53. Kim TK, Lee KH, Jang JJ et al (2011) Analysis of gadobenate dimeglumine-enhanced MR findings for characterizing small (1-2-cm) hepatic nodules in patients at high risk for hepatocellular carcinoma. Radiology 259:730-738.
54. Choi JW, Lee JM, Kim SJ et al (2013) Hepatocellular carcinoma: imaging patterns on gadoxetic acid-enhanced MR Images and their value as an imaging biomarker. Radiology 267:776-786.
55. Lee MH, Kim SH, Park MJ et al (2011) Gadoxetic acid-enhanced hepatobiliary phase MRI and high-b-value diffusion-weighted imaging to distinguish well-differentiated hepatocellular carcinomas from benign nodules in patients with chronic liver disease. AJR Am J Roentgenol 197:W868-875.
56. Bruix J, Sherman M (2011) Management of hepatocellular carcinoma: an update. Hepatology 53:1020-1022.
57. McEvoy SH, McCarthy CJ, Lavelle LP et al (2013) Hepatocellular carcinoma: illustrated guide to systematic radiologic diagnosis and staging according to guidelines of the American Association for the Study of Liver Diseases. Radiographics 33:1653-1668.
58. Ichikawa T, Federle MP, Grazioli L et al (1999) Fibrolamellar hepatocellular carcinoma: imaging and pathologic findings in 31 recent cases. Radiology 213:352-361.
59. Ichikawa T, Federle MP, Grazioli L, Marsh W (2000) Fibrolamellar hepatocellular carcinoma: pre- and posttherapy evaluation with CT and MR imaging. Radiology 217:145-151.
60. Lim JH (2003) Cholangiocarcinoma: morphologic classification according to growth pattern and imaging findings. AJR Am J Roentgenol 181:819-827.
61. Han JK, Choi BI, Kim AY et al (2002) Cholangiocarcinoma: pictorial essay of CT and cholangiographic findings. Radiographics 22:173-187.
62. Lee WJ, Lim HK, Jang KM et al (2001) Radiologic spectrum of cholangiocarcinoma: emphasis on unusual manifestations and differential diagnoses. Radiographics 21 Spec No:S97-S116.
63. Buetow PC, Buck JL, Pantongrag-Brown L et al (1995) Biliary cystadenoma and cystadenocarcinoma: clinical-imaging-pathologic correlations with emphasis on the importance of ovarian stroma. Radiology 196:805-810.
64. Peterson MS, Baron RL, Rankin SC (2000) Hepatic angiosarcoma: findings on multiphasic contrast-enhanced helical CT do not mimic hepatic hemangioma. AJR Am J Roentgenol 175:165-170.
65. Koyama T, Fletcher JG, Johnson CD et al (2002) Primary hepatic angiosarcoma: findings at CT and MR imaging. Radiology 222:667-673.
66. Miller WJ, Dodd GD, 3rd, Federle MP, Baron RL (1992) Epithelioid hemangioendothelioma of the liver: imaging findings with pathologic correlation. AJR Am J Roentgenol 159:53-57.
67. Schima W, Kulinna C, Langenberger H, Ba-Ssalamah A (2005) Liver metastases of colorectal cancer: US, CT or MR? Cancer Imaging 5 Spec No A:S149-156.
68. Lee MJ, Saini S, Compton CC, Malt RA (1991) MR demonstration of edema adjacent to a liver metastasis: pathologic correlation. AJR Am J Roentgenol 157:499-501.

# Diseases of the Gallbladder and Biliary Tree: Emphasis on Neoplasms

Byung Ihn Choi

Department of Radiology, Seoul National University Hospital, Seoul, South Korea

## Imaging Techniques

Cross-sectional imaging modalities, such as high-resolution ultrasound (US), multi-row-detector computed tomography (MDCT), and magnetic resonance imaging (MRI) with MR cholangiopancreatography (MRCP), have made considerable advances and contribute to robust biliary imaging with higher temporal and spatial resolution. Therefore, those noninvasive, cross-sectional imaging modalities are more frequently used for diagnosis and tumor staging, whereas invasive examinations, including diagnostic percutaneous transhepatic cholangiography (PTC), endoscopic retrograde cholangiography (ERC), and endoscopic US (EUS), have become less important [1, 2]. However, improvements in technical aspects of PTC and endoscopic retrograde cholangiopancreatography (ERCP) have led to the development of various interventional biliary procedures performed via both percutaneous and endoscopic routes.

US is one of the first-line imaging modalities chosen for the evaluation of biliary disease. Imaging studies that include US are essential in establishing the cause of jaundice, whether bile duct strictures are benign or malignant, and for planning management in patients with suspected biliary disease. The appropriate selection of radiological techniques is necessary to evaluate a patient with a suspected biliary disease, including cancer.

## Anomalies and Anatomic Variants of the Biliary Tree

### Anatomic Variants and Anomalies of the Gallbladder

There are various anatomic variants of the gall bladder (GB), including agenesis, duplication, Phrygian cap, diverticulum, ectopic GB, and wandering GB [3, 4]. Among them, Phrygian cap is the most common abnormality of the GB shape, with an incidence of 1-6 % of the population [3, 4]. The GB fundus is frequently folded upon itself and partially septate. When a fold or septum of the GB between the body and fundus is identified, Phrygian cap is diagnosed. Phrygian cap may be a source of confusion on imaging, but it has little clinical significance [3].

### Anatomic Variants and Anomalies of the Bile Duct

Recognizing congenital anomalies and anatomic variants of the biliary tree is important in clinical practice. Laparoscopic cholecystectomy and living-donor liver transplantation are frequently performed. The correct diagnosis of anatomic variant that may increase the risk of the bile duct injury aids in surgical planning and can prevent inadvertent complications, such as ductal ligation or structure and biliary leaks. Furthermore, congenital anomalies of the biliary tree may be undetected until adulthood, and an extensive workup is undertaken before correct diagnosis is made because symptoms and signs of the congenital anomaly are often nonspecific. Thus, in case of persistent and unexplained symptoms and signs, including cholangitis, pancreatitis, jaundice, recurrent abdominal pain, nausea, and vomiting, underlying congenital anomalies of the biliary tree should be considered.

Various kinds of congenital anomalies and anatomic variants involve the biliary tree, including aberrant or accessory biliary ducts, aberrant cystic duct insertion, choledochal cyst, and anomalous pancreaticobiliary ductal union (APBDU). Therefore, radiologists need to be familiar with these disease entities and their image features.

### Choledochal Cyst

A choledochal cyst is a relatively rare congenital cystic dilatation of the biliary tree. Women are affected four times more often than men, and 7% of choledochal cysts are found during pregnancy. The majority of choledochal cysts are diagnosed in childhood, with classic triads of obstructive jaundice, right-upper-quadrant pain, and palpable mass. However, up to 20% of choledochal cysts are recognized in adults with increasing frequency. Manifestation in adults is nonspecific, which often leads to a delay in diagnosis. The most common symptoms in adults are chronic relapsing cholangitis and jaundice. Acute

*Diseases of the Abdomen and Pelvis 2014-2017*,
DOI: 10.1007/978-88-470-5659-6_13 

pancreatitis, cholecystitis, and biliary calculi are commonly associated, and complications such as biliary obstruction, biliary cirrhosis, cyst rupture, portal vein thrombosis, and hepatic abscess wall can occur. Furthermore, tumorous conditions, including cholangiocarcinoma (CC) and GB carcinoma, have been reported frequently in a choledochal cyst [3].

There are five types of choledochal cyst [3-6]:

- Todani type I is fusiform dilatation of the extrahepatic bile duct and accounts for 80-90% of all choledochal cysts
- Todani type II presents a true diverticulum of the extrahepatic bile duct and accounts for 3% of all choledochal cysts
- Todani type III, or choledochocele, represents protrusion of a bulbous, focally dilated, intramural segment of the distal common bile duct into the duodenum; it accounts for 5% of all choledochal cysts
- Todani type IV represents the second most common type (10%) and can have both intrahepatic and extrahepatic components
- Todani type V, or Caroli disease, is a rare, congenital, biliary cystic disease manifested by cystic dilatation of the intrahepatic ducts.

#### Anomalous Pancreaticobiliary Ductal Union

APBDU is characterized by union of the distal common bile duct and pancreatic duct proximal to the duodenum, with formation of a long common channel (>15 mm). Prevalence varies from 1.5% to 3.2% [3]. According to the fusion style of the pancreatic duct and common bile duct, there are two subtypes of APBDU: P-C type and C-P type. The presence of a long common channel may allow reflux of pancreatic secretions into the biliary system and can result in the formation of a choledochal cyst. Conversely, reflux of bile into the pancreatic duct can cause pancreatitis. Associated conditions, including CC, GB cancer, choledocholithiasis, and chronic pancreatitis, may present. An anomalous junction should be diagnosed and surgically treated before pancreaticobiliary complications occur [3, 6].

### Cholangitis

There are several types of cholangitis, including primary sclerosing (PSC), recurrent pyogenic (RPC), primary biliary cirrhosis (PBC), obstructive (OC), and parasitic infestations. Sometimes, cholangitis can show characteristic findings, thus allowing correct diagnosis.

A pruned-tree appearance of the biliary tree is seen in primary sclerosing cholangitis (PSC) or recurrent pyogenic cholangitis (RPC) due to nonopacification of the peripheral bile duct. A peripheral halo sign in PBC cirrhosis indicates numerous small, rounded lesions of low T1 and T2 signal intensity surrounding portal vein branches and suggesting end-stage disease. Obstructive cholangitis is most commonly caused by choledocholithiasis. Proportionate bile duct dilatation, enhanced thickening of the bile duct wall, and enhancement of periductal hepatic parenchyma are the characteristic radiologic findings. In clonorchiasis, CT and US reveal diffuse, minimal, or mild dilatation of intrahepatic ducts, particularly in the periphery of the liver and without extrahepatic duct dilatation.

#### Primary Sclerosing Cholangitis

PSC is a chronic cholestatic liver disease of unknown cause characterized by inflammation, fibrosis, and destruction of intrahepatic and extrahepatic bile ducts. It affects male patients more commonly than female patients. PSC is commonly associated with inflammatory bowel disease (IBD), particularly ulcerative colitis, in more than half of the cases [7-9].

On direct cholangiography, multiple segmental strictures involving both the intrahepatic and the extrahepatic bile ducts are the characteristic finding of PSC, and alternating strictures and dilatations result in the beaded appearance. Ductal dilatation is usually mild and proportionately less than the degree of stricture, because periductal inflammation and fibrosis impair ductal dilatation. As fibrosis progresses, obliteration of peripheral intrahepatic ducts may give the biliary tree a pruned-tree appearance, which usually indicates the development of cirrhosis. CT findings of PSC are similar to cholangiography findings and include segmental intrahepatic and extrahepatic bile duct dilatations with multifocal strictures. Ductal-wall enhancement and periductal patchy enhancement can be seen. Intrahepatic duct stones are rarely seen. MRCP findings are similar to direct cholangiography findings and include multifocal segmental strictures alternating with mild bile duct dilatation. Ductal-wall irregularities, diverticula, and stones can be seen. On MRI, hepatic parenchymal changes may be present. T2-weighted images may reveal increased signal intensity in a peripheral wedge-shaped or fine reticular pattern, which is thought to be caused by extension of periductal inflammation to involve vascular and lymphatic channels [7-9].

#### Recurrent Pyogenic Cholangitis

RPC is characterized by intrahepatic ductal pigmented stones commonly accompanied by recurrent gram-negative bacterial infections. RPC is also known as oriental cholangiohepatitis because this disease has a propensity to occur in Asian populations. The cause of RPC is unclear, but associations with parasitic infestation such as clonorchiasis and ascariasis, portal bacteremia, and malnutrition have been suggested. RPC increases the risk of CC, with reported incidence rate of 5-6%. Chronic bile duct irritations by intrahepatic calculi, bile stasis, and bacterial infections have been proposed as responsible carcinogenic factors [7, 10, 11].

Cross-sectional imaging usually demonstrates dilated ducts containing stones and sludge. The lateral segment of the left hepatic lobe and the posterior segment of the right hepatic lobe are more commonly involved than other hepatic segments. Parenchymal atrophy of involved hepatic segments, ductal-wall enhancement and thickening, biliary strictures, hepatic abscess and biloma, segmental hepatic parenchymal enhancement, and pneumobilia are findings of RPC. As the disease progresses to cirrhosis, atrophy of left lateral and right posterior hepatic segment, along with hypertrophy of caudate lobe and left medial segment, result in round liver configuration. Cholangiography findings of RPC include intrahepatic or extrahepatic duct stones as filling defect, dilatation of extrahepatic duct and central intrahepatic duct, ductal rigidity and straightening, increased or right-angle branching pattern, decrease in arborization, acute tapering of peripheral duct, luminal irregularity, and focal strictures. MRCP findings of RPC are similar to those of direct cholangiography but are advantageous in the case of a missing duct due to severe stricture. When CC occurs in patients with hepatolithiasis, periductal soft tissue density, higher ductal enhancement than normal duct on portal-venous phase, ductal wall thickening, portal vein obliteration, and lymph node enlargement on CT images are significant findings for differentiating cancer from periductal fibrosis [7, 10, 11].

### Obstructive Cholangitis

Complete or partial bile duct obstruction leads to bile stasis and predisposes to ascending cholangitis by bacterial infection. Patients present with right-upper-quadrant pain, fever, chills, and jaundice. Benign causes of biliary obstruction are choledocholithiasis, postoperative biliary stricture, or papillary stenosis; malignant cases are CC, pancreatic carcinoma, and malignant hilar lymphadenopathy. The role of imaging is to detect biliary dilatation and determine the cause and level of obstruction. On cross-sectional imaging with contrast enhancement, ductal wall thickening and enhancement, upstream ductal dilatation, patchy periductal enhancement, and obstructive lesions per se indicate OC [7, 10].

### Parasitic Infestation in Biliary Tree

Clonorchiasis is a trematodiasis caused by chronic infestation by liver flukes, *Clonorchis sinensis*. *C. sinensis* eggs are passed in human feces, and infestation occurs by ingestion of raw fish. The worms cause obstruction of bile flow within the biliary tree and trigger inflammatory cell infiltration. As disease progresses, periductal fibrosis, ductal epithelial hyperplasia, and CC can develop. On cholangiography, *C. sinensis* appears as an ellipsoid filling defect in the intrahepatic duct measuring several millimeters. CT and US reveal diffuse and mild dilatation of intrahepatic ducts, particularly in the liver periphery, without extrahepatic duct dilatation. Mild, uniform, and disproportionate dilatation of the biliary tree from the extrahepatic duct to far peripheral ducts is the typical finding of clonorchiasis [7, 12]. Clonorchiasis increases the risk of CC [13].

*Ascaris lumbricoides* is the most prevalent human helminth worldwide. The disease is transmitted by the ingestion of food contaminated with parasitic eggs, which eventually develop into adult worms within the gastrointestinal tract [14]. The adult worms may remain within the intestines and occasionally enter the biliary system through the ampulla of Vater. Biliary colic and cholangitis may develop when worms obstruct the common duct. Worms are seen as elongated, longitudinal filling defects on cholangiography or as thin, tubular, echogenic intramural lesions on US. MRCP shows intraductal worms as a filling defect of linear low signal intensity [15].

## Cholecystitis and Adenomyomatosis

Cholecystitis is GB inflammation and is divided into acute and chronic states. Acute cholecystitis can have diverse complications, such as gangrenous cholecystitis, hemorrhagic cholecystitis, emphysematous cholecystitis, and perforation in about 4-12% [16]. Chronic cholecystitis also can have complications, including fistula, such as cholecystoduodenal fistula and cholecystocolonic fistula; xanthogranulomatous cholecystitis, which may simulate GB cancer; and porcelain GB, which has increased risk of cancer.

Adenomyomatosis of the GB, a benign, hyperplastic cholecystosis, appears as a diffuse or focal wall thickening so that it can mimic GB cancer. Therefore, radiologic differentiation is and important issue in diagnosing GB disease [16].

### Acute Cholecystitis

Acute cholecystitis is usually caused by GB outlet obstruction. Acute calculous cholecystitis indicates the obstruction is caused by gallstones. Inflammation of the GB wall starts from the mucosa and progresses to all layers unless it is treated. Typical clinical manifestation includes fever, right-upper-quadrant pain, leukocytosis, and Murphy sign [17]. Imaging is usually necessary to make a confident diagnosis. Acute cholecystitis should be differentiated from other diseases, such as peptic ulcer, liver abscess, pancreatitis, renal colic, and retrocolic appendicitis. CT features include distended GB with thickened wall, pericholecystic inflammatory change, pericholecystic fluid, and transient hepatic attenuation difference in the GB bed of the liver caused by reactive hyperemia [18]. The complication of acute cholecystitis includes gangrenous cholecystitis, hemorrhagic cholecystitis, emphysematous cholecystitis, and perforation [19, 20].

### Chronic Cholecystitis

Chronic cholecystitis results from wall damage by repeated attacks of inflammation for an extended period usually caused by gallstones, and it usually manifests as a thickened wall and luminal contraction by fibrosis and scarring. Chronic-cholecystitis-related complications include fistula, xanthogranulomatous cholecystitis, and porcelain GB [21, 22].

- Xanthogranulomatous cholecystitis is an uncommon form of chronic cholecystitis characterized by intense acute or chronic inflammation, severe proliferative fibrosis with formation of multiple yellow-brown intramural nodules, and foamy histiocytes. It can be clinically and radiologically confused with GB carcinoma because the inflammatory process often extends into neighboring organs, such as the liver, omentum, duodenum, and colon. Almost all patients have gallstones or biliary obstruction. The most frequent imaging finding is thickening of the GB wall. Characteristically, xanthogranulomatous cholecystitis often shows hypoechoic or hypodense nodules or bands in the GB wall. These characteristic intramural nodules represent abscess or xanthogranuloma [16, 21].
- Porcelain GB is a rare complication of chronic cholecystitis characterized by calcification of the GB wall. It can be detected and diagnosed on an abdominal X-ray image as a pear-shaped calcified mass in the right upper quadrant. On US, it appears as a curvilinear echogenic lesion, with shadowing in GB fossa. Most patients are asymptomatic, but surgery is recommended due to its high risk of GB cancer, especially when it has selective mucosal calcification or incomplete calcification [22].

### Adenomyomatosis

Adenomyomatosis, also termed adenomyomatosis hyperplasia, is a benign hyperplastic disease. It is relatively common, found in 2-5% of all surgical specimens of the GB [16]. Adenomyomatosis is defined as epithelial proliferation and muscular hyperplasia with Rokitansky-Aschoff sinuses. Adenomyomatosis of the GB is morphologically classified into three types: diffuse, segmental, and fundal. It may simulate GB cancer because it appears as a diffuse or localized wall thickening. Typical imaging findings are wall thickening with intramural cysts and echogenic intramural foci on US, enhancing epithelium within intramural diverticula surrounded by the relatively unenhanced hypertrophied GB muscularis (Rosary sign) on CT, and the pearl necklace sign on MR-CP images [23].

## Tumors of the Gallbladder and Biliary Tract

Most neoplasms that arise from the GB and bile ducts are malignant. Although infrequent, GB and bile duct carcinomas are not rare. GB carcinoma is the seventh most common malignancy of the gastrointestinal tract and is the most common biliary malignancy; bile duct carcinoma occurs less often. Familiarity with imaging characteristics of GB and bile duct neoplasms is important to expedite diagnosis and appropriate treatment of patients, who often present with nonspecific symptoms of right-upper-quadrant pain, jaundice, and weight loss.

### Gallbladder Cancer

Most GB carcinoma is adenocarcinoma, and its cell types can be papillary, tubular, and mucinous on microscopic pathology. The remainder are anaplastic, squamous or adenosquamous, and neuroendocrine carcinomas [24]. GB cancers can present as three major imaging features: (1) focal or diffuse wall thickening with or without irregularity of the GB wall, (2) polypoid intraluminal mass, and (3) large mass obscuring or replacing the GB, often extending into the liver. Cancer that manifests as a mass replacing the GB is the most common type of the GB cancer. Recent technologic developments in US, CT, and MR have increased the chances of detecting smaller lesions, and the detection rate of GB cancer that manifests as wall thickening is increased. However, diagnosis and differentiation from chronic cholecystitis are still not easy. Polypoid mass type is easy to detect and contributes to the increasing incidence of early GB cancer and early treatment by laparoscopic resection [24-27].

#### Focal or Diffuse Mural Thickening with or without Irregularity of the GB Wall

This is the most difficult type of GB carcinoma to diagnose and differentiate from chronic cholecystitis. Carcinomas confined to the mucosa may present as flat or slightly raised lesions, with mucosal irregularity that is difficult to appreciate on US. In advanced GB carcinomas, marked irregular wall thickening with mixed echogenicity is observed. On contrast-enhanced CT, focal malignant wall thickening shows enhancement; thus, when focal or irregular thickening of the GB wall is encountered on CT, radiologist should carefully inspect the images for bile duct dilatation, local invasion, metastasis, or lymphadenopathy with suspicion of GB carcinoma.

According to an analysis regarding enhancement patterns with high prevalence of flat GB wall thickening type of cancer on MDCT by Kim and colleagues [25], enhancement of flat-wall-thickening GB carcinoma was classified into two patterns: type 1 was a heterogeneously enhancing, one-layer, GB wall or indistinguishable layering of the GB wall; type 2 was a two-layer pattern with strongly enhancing, thick inner layer and weakly enhancing or nonenhancing, thin outer layer. Other important findings suggesting a malignant cause of GB wall thickening are stronger enhancement of the inner layer than of liver parenchyma on the portal-venous phase, irregular contour of the affected wall, and focal involvement [24, 25].

### Polypoid Intraluminal Mass

These masses are relatively easy to detect on imaging; identifying them is clinically important because they are well differentiated and more likely to be confined to the mucosa or muscularis mucosa when discovered and show good prognosis. On US, they usually appear as a fixed, homogeneous, polypoid intraluminal mass without posterior acoustic shadowing. Most have a broad base with smooth margins, although sometimes they have a narrow stalk or villous fronds. A small polypoid carcinoma can be indistinguishable from benign polypoid lesions, such as adenoma and cholesterol polyp. If the lesion is >1 cm in diameter and is not definitely benign, GB cancer should be considered. Polypoid GB cancer with sufficiently large size usually demonstrates homogeneous enhancement with adjacent GB wall thickening on contrast-enhanced CT.

### Large Mass Obscuring or Replacing the GB, Often Extending into the Liver

This is the most common type of GB carcinoma and usually invades adjacent liver parenchyma. On US, the mass presents a complex, mixed echogenicity, with area of necrosis and solid portions. Gallstones are commonly seen within the poorly defined mass. On CT scans, the mass shows irregular contrast enhancement or hypoattenuation compared with the liver parenchyma, with or without internal necrosis. Direct liver invasion or hepatoduodenal ligament invasion, satellite lesions, intrahepatic or nodal metastases, and bile duct invasion are common findings. MRI findings are similar to those of CT; however, it may be difficult to differentiate mass-replacing GB carcinoma from inflammatory and metastatic mass lesions of the GB on MRI alone [24].

### TNM Staging

The GB has a unique histologic feature, i.e., absence of a submucosa. The GB wall consists of a mucosa, lamina propria, smooth muscle layer, perimuscular connective tissue layer, and subserosa. Furthermore, there is no serosa at the attachment site to the liver and along the hepatic surface. GB carcinoma has a poor prognosis, as its late clinical presentation and anatomic factors promote early local spread. The ease by which this tumor invades the liver and surrounding structures may result from the absence of a submucosal layer in the GB wall. The cure rate for patients with GB carcinoma depends on its local stage; therefore, precise preoperative diagnosis of tumor spread is important [24].

GB carcinoma is staged surgically by the depth of invasion, extension of disease into adjacent structures, involvement of lymph nodes, and distant metastases according to the American Joint Committee on Cancer TNM staging system [27]. Recognizing known enhancement pattern and imaging criteria regarding GB carcinoma on each stage may be helpful for predicting accurate GB carcinoma stage preoperatively [24].

### Mode of Spread in GB Cancers

GB carcinoma spreads by five major routes: direct invasion of surrounding organs, lymphangitic spread, hematogenous spread, intraductal growth and spread, and peritoneal seeding [24].

### Differential Diagnosis

It is sometimes difficult to differentiate GB cancers from complicated cholecystitis with pericholecystic fluid, abscess, or severe fibrosis with adjacent organ similar to invasiveness. GB carcinoma should be suspected when abnormal GB lesions, mass, or wall thickening with prominent or extensive lymphadenopathy, hepatic metastases, and biliary obstruction at the level of the porta hepatis is present [24].

### Benign Gallbladder Tumors

Benign neoplasms originate from the epithelial and nonepithelial structures that compose the normal GB [24].

### Adenoma

Most benign neoplasms of the GB are adenomas, even though their incidence is low. They appear as polypoid, sessile, or pedunculated lesions with lobular or cauliflower-like contour and are <2 cm in size. On US, they usually appear as small, broad-based, homogeneous, echogenic masses without posterior shadowing and gravitational movement despite positional change. However, as they grow, they have a tendency to less echogenicity and greater heterogeneous echotexture [24].

Although uncommon, relatively large adenoma mimics malignant tumor of the GB, and some small, early-stage GB cancer <2 cm is now often identified; it is important to differentiate these lesions. Focal GB wall thickening adjacent to a polypoid mass and sessile lesions raise concern for malignancy, and those >1 cm on imaging modality indicate remarkable risk of malignancy.

Furthermore, age >50 years and combined gallstones are important factors predicting malignancy in polypoid GB lesions. In addition, other factors, such as solitary lesion and presence of symptoms, are considered risk factors. However, one third of adenomas are multiple lesions; a considerable portion of cholesterol polyps are single lesions, which shows that there may be overlap between benign and malignant GB neoplasms.

Otherwise, long-term clinical and US analysis demonstrate that incidentally detected GB polyps measuring ⩽6 mm may require no additional follow-up. The risk of GB malignancy resulting from incidentally detected polyps is extremely low [24].

### Gallbladder Polyp

Cholesterol polyps are the most common GB polyps and not true neoplasms. They may appear as single or multiple intraluminal-protruding polypoid lesions adherent to the GB wall and have a tendency to be observed more frequently in younger patients. Sometimes, large cholesterol polyps of the GB mimic polypoid GB carcinoma.

The predictive signs for a cholesterol polyp, which is a benign tumor, are as follows:

- A polyp observable by US but not CT scanning
- A discrepancy ⩾5 mm in the maximum diameter of the polyp between the US and CT measurements
- A smaller diameter of the polyp on CT compared with US [26].

## Cholangiocarcinoma

Bile duct cancer, or cholangiocarcinoma (CC), is a malignant tumor arising from bile duct epithelium. The incidence of CC among primary liver tumors is around 10-20%. It generally occurs during the sixth and seventh decades of life. Most common etiologies of CC are liver fluke infestation (clonorchiasis), recurrent pyogenic cholangitis (hepatolithiasis), and chronic hepatitis B or C in Eastern populations [28].

Traditionally the tumor is classified into intrahepatic (10%), hilar (50-60%), and extrahepatic (20-30%) according to location within the biliary tree. Intrahepatic CC arises from bile ducts peripheral to the secondary bifurcation of the left or right hepatic duct. Extrahepatic CC refers to a malignant tumor occurring from the left or right hepatic duct to the ampulla. Hilar CC, or Klatskin tumor, is defined as a tumor typically located at the confluence of the right and left ducts within the porta hepatis.

### Pathology

The Liver Cancer Study Group of Japan proposed a classification system based on macroscopic appearance and growth characteristics. CC can be classified into three types according to morphology and growth pattern: mass forming, periductal infiltrative, and intraductal growing. The prognosis for mass-forming and periductal-infiltrating CC is generally unfavorable, whereas it is much better for intraductal-growing CC after surgical resection [28].

- Mass-forming CC is the most common type of intrahepatic CC. It arises from the mucosa of a branch of the bile ducts in the peripheral area of the liver, invading and penetrating the bile duct wall, and spreads between hepatocyte plates. It has a propensity to invade small adjacent portal branches in the form of venous tumoral thrombi. Macroscopically, mass-forming CC is characterized by a white, firm, homogeneous, sclerotic mass with an irregular lobulated margin, typically in the absence of hemorrhage or necrosis [29].
- Periductal-infiltrating CC is the most common type of hilar CC. Arising from the mucosa of the intrahepatic or extrahepatic bile ducts, it invades the wall and penetrates to the serosa. The tumor appears as a diffuse, firm, gray-white, annular thickening of the bile duct causing almost complete obstruction of the lumen [29].
- Intraductal-growing CC is a low-grade papillary adenocarcinoma composed of innumerable frond-like infoldings of columnar epithelial cells and fibrovascular cores. Tumor cells are confined within the mucosal layer and spread superficially without invading the submucosal layer. Tumor cells are friable and may slough spontaneously from bile duct walls. Tumors are usually small, sessile, or polypoid, but sometimes a large mass may occlude an aneurysmally dilated bile duct. The biliary tract may be dilated diffusely in a lobar or segmental fashion. When an intraductal CC produces a large amount of mucin, it is called intraductal papillary mucinous neoplasm (IPMN) of the bile ducts.

### Role of Imaging

Surgical resection is the best available and potentially curative therapy for CC. Technical advances in diagnostic imaging allow better selection of surgical candidates. US accurately recognizes biliary tract dilatation and is helpful in depicting intraductal tumors. Cross-sectional imaging such as CT and MRI are the primary tools used in assessing longitudinal and lateral spread of CC and determining resectability. MDCT is a widely used, noninvasive examination for CC staging. It is an excellent imaging technique for evaluating soft tissue extent of CC and its relationship between tumor and hepatic vasculature. Fusion imaging techniques may display the tumor itself as well as the surrounding vessels and demonstrate complex anatomic relationships of bile duct cancer. These techniques seem to have a potential to improve treatment planning with MDCT. MRI in combination with MRCP can be used as a sole imaging modality for evaluating bile duct cancer. The roles of MRI combined with MRCP are to:

- Differentiate benign from malignant causes of biliary stricture
- Determine resectability in patients with bile duct cancer
- Preoperatively stage
- Differentiate between the different appearances of growth patterns.

Direct cholangiography, including ERCP and PTC is still the standard of reference for biliary extent of the tumors. [$^{18}$F]-fluorodeoxyglucose positron emission tomography (FDG-PET) is valuable for detecting unsuspected distant metastases, particularly in patients with peripheral CC because of the likelihood of distant metastases at the time of diagnosis and the high uptake in the peripheral type. Also, FDG-PET evaluates lymph node metastases more accurately than CT [29].

### Mass-Forming CC

Mass-forming CC manifests as a solitary mass in the liver parenchyma with a nodular pattern. Lesions <3 cm tend to be homogeneously hypoechoic or isoechoic, whereas tumors >3 cm are predominantly hyperechoic on US. A peripheral hypoechoic area or halo sign can be observed. However, US shows diverse echo patterns that may be hypo-, iso-, or hyperechoic; and homogeneous or heterogeneous. Peripheral ductal dilatation is occasionally associated [29].

Unenhanced CT scan may show a predominantly hypoattenuating mass. Calcification may be seen in the central portion of the lesion, especially in mucin-secreting tumors. Typical enhancement patterns on CT are marked hypoattenuation with thin, incomplete, peripheral enhancement during arterial and portal-venous phases with centripetal progression of enhancement over time. The morphology of peripheral CC on imaging as well as its histology is similar to that of metastatic adenocarcinoma, but CC is more likely to be solitary, large, and show occasional association with peripheral ductal dilatation. The peripheral portion has viable cancer cells that show incomplete rim enhancement on arterial phase and peripheral washout. The central portion contains more fibrous stroma and shows mild centripetal progression and delayed or prolonged enhancement on dynamic CT or MRI.

Other common findings include frequent capsular retraction because of desmoplastic reaction, marked hypoattenuation from mucin component, satellite nodules, extracapsular extension, lymphadenopathy, and vascular encasement within the mass. Small (<3 cm in diameter) mass-forming CCs in the cirrhotic liver show atypical enhancement patterns more frequently than do large (>3 cm) mass-forming CCs and may thus mimic HCC. Two thirds of mass-forming CCs show the typical enhancement pattern of arterial hypoattenuation and hypo-, iso-, or hyperattenuation in the portal-venous and/or equilibrium phase. One third of mass-forming CCs show an atypical enhancement pattern, such as arterial enhancement with or without washout.

On MRI, the typical appearance of the tumor is a nonencapsulated mass hypointense on T1-weighted images and hyperintense on T2-weighted sequences. The mass-forming CC is better seen on T2-weighted images and has no capsule. Central hypointensity corresponding to fibrosis and a peripheral hyperintense rim may be seen on T2-weighted images. As internal desmoplastic changes are intermingled with various degrees of fibrosis, coagulative necrosis, and mucin, signal intensity of the tumor center on T2-weighted images is variable. Enhancement patterns on gadoxetic-acid-enhanced MRI have now been reported. The most prevalent enhancement patterns of intrahepatic mass-forming CCs on gadoxetic acid-enhanced MRI are a thin peripheral rim with internal heterogeneous enhancement on dynamic-phase images and heterogeneous hypointensity with intermingled hyperintensity due to retained contrast material in fibrotic stroma on hepatobiliary-phase images. Hepatobiliary-phase imaging may aid in CC diagnosis because of increased lesion conspicuity and better delineation of daughter nodules and intrahepatic metastasis.

The contrast enhancement pattern of mass-forming CC differs from that of HCC, which typically show strong enhancement on arterial phase and washout on portal or delayed-phase images. Sclerosing HCC should be differentiated from mass-forming CC because they have abundant fibrous stroma.

There are other helpful findings for the differential diagnosis between mass-forming CC and HCC: most mass-forming CC occur in noncirrhotic livers, may show intratumoral calcifications but no intralesional fat, have no pseudocapsule, and frequently cause bile duct dilatation. Hypovascular metastases, especially from adenocarcinoma of the gastrointestinal tract, may have a similar appearance to that of mass-forming CC. Suggestive features for the diagnosis of mass-forming CC are a relatively large single tumor at discovery, few satellites nodules rather than multiple scattered nodules, and findings such as adjacent bile duct dilatation and retracted liver capsule [28-30].

### Periductal-Infiltrating CC

Periductal-infiltrating CC is characterized by growth along the bile duct appearing as elongated, speculated, or branchlike lesions. Dilatation of the intrahepatic bile duct is the most frequent abnormality seen in patients with periductal-infiltrating CC on US. Periductal-infiltrating CC is the most common type but is difficult to evaluate with sonography. Contrast-enhanced sonography can be useful for detecting and staging hilar CC in the postvascular phase.

Most periductal-infiltrating CC appears as mural and periductal soft tissue thickening or focal irregularities of the bile duct, with subsequent obstruction and prestenotic bile duct dilatation; irregular and ill-defined thickening of the ductal wall can be seen in contrast-enhanced CT or MRI, which is often hyperattenuating or hyperintense relative to the liver parenchyma in the arterial and portal-venous phase. Lobar atrophy and blood vessel crowding may be useful secondary signs. With MDCT, bile duct cancer can be correctly identified in nearly 100% of patients, and its accuracy for predicting respectability has improved to 75-90%. Multiphasic CT is helpful for assessing the relation between tumor and hepatic hilar structures. Arterial-phase images are useful for evaluating anatomic variations in hepatic arteries and arterial invasion. Portal-venous-phase images emphasize the relation between tumor and portal vein and adjacent hepatic parenchyma. Portal-venous involvement is encasement and narrowing of the vessel rather than luminal invasion. Postprocessing techniques, such as maximum intensity projection (MIP), multiplanar reformation (MPR), and volume rendering (VR) allow depiction of vascular

structures and the biliary tree with or without administration of biliary contrast media.

Adding routine coronal and sagittal reformation to standard axial images may not improve overall diagnostic accuracy in bile duct cancer with respect to tumor extent, vascular involvement, or resectability. However, more vigorous use of postprocessing techniques, such as oblique and curved reformation with VR, may increase the diagnostic confidence and has the potential to improve diagnostic accuracy in assessing tumor extent along the bile duct as well as vessel invasion [28-30].

### Intraductal CC

The most characteristic pattern of intraductal CC is diffuse ductal dilatation with multifocal papillary or sessile masses. At US, the intraductal polypoid lesion is echogenic relative to surrounding liver parenchyma. Bile ducts proximal to the tumor are dilated, and the degree of dilatation depends on the degree of obstruction. On US or CT, an intraductal mass appears as a papillary tumor or cast-like lesion within the dilated bile duct. As this lesion is usually confined to the bile duct wall, the wall appears intact. After contrast-medium injection, intraductal tumors show enhancement. In some cases, only marked intrahepatic bile duct dilatation with no obstructive mass or stricture can be detected on CT or MRI. Some papillary tumors of the bile ducts produce a large amount of mucin. Even though US, CT, and MRI might show severe dilatation of intra- and extrahepatic ducts, visible mass may not appear on images or gross examination. Bile ducts both proximal and distal to the tumor are dilated because mucin may obstruct the ampulla of Vater. Intraductal tumors may manifest as localized ductal dilatation with intraductal mass. When an intraductal papillary mass does not secrete mucin, the distal ductal dilatation is not prominent. This type of intraductal tumor may be confused with an intraductal masslike stone. The absence of contrast enhancement is useful in making the diagnosis of an intraductal masslike stone, whereas an enhancing polypoid lesion with asymmetric adjacent bile duct wall thickening is suggestive of an intraductal tumor. The most difficult type to diagnose is intraductal cast-like lesions within a mildly dilated duct. It appears as an area of mild ductal dilatation filled with intraductal soft tissue material that may show mild enhancement on CT or MRI. Rarely, intraductal tumor may appear as a focal stricture-like lesion with mild proximal ductal dilatation. The stricture may be a secondary finding of the underlying inflammation and fibrotic stricture or may itself represent a small tumor [29].

### Staging

#### Intrahepatic CC

CC staging is clinically important to identify candidates for surgical resection. The most important prognostic factors are tumor size, lymph node metastasis, multiple tumors or intrahepatic metastasis, and vascular invasion. Serosal invasion is not considered a prognostic factor. Vascular involvement is observed in 50% of cases. The presence of segmental or lobar atrophy is strongly associated with ipsilateral portal-vein encasement. The overall accuracy of detecting metastatic lymph nodes is 70-80%, and the most common error on preoperative imaging is underestimation of nodal involvement [29].

#### Extrahepatic CC

There are two staging systems used for extrahepatic CC. The first is that of the American Joint Committee on Cancer (AJCC), which incorporates extent of tumor invasion into the wall of the bile duct, as well as lymph node and distant metastases. This system is helpful in identifying prognostic subsets but is applicable only to the minority of patients who undergo surgical resection. The modified Bismuth-Corlette classification system provides an anatomical description of the tumor and is useful in determining resection or palliative treatment and type of surgery. However, it is not indicative of survival. During the staging of extrahepatic CC, the proximal and distal margins of the tumor should be clearly identified. Longitudinal spread of the tumor is related to gross morphology.

Infiltrating tumors tend to show subepithelial extension, whereas papillary tumors frequently present with long-range mucosal spread. Therefore, determining longitudinal spread must be made cautiously when a papillary tumor is found. It is also important to exclude vascular encasement of the contralateral liver lobe in hilar or extrahepatic CC before committing to partial hepatectomy and to verify vascular patency of the portal vein and hepatic artery. This usually can be accomplished by CT or MRI. Finally, regional metastases should be ruled out. However, imaging modalities are limited in determining metastatic lymph node involvement [27, 29].

### Resectability

Memorial Sloan-Kettering Cancer Center (MSKCC) has proposed a tumor-staging system that takes into consideration both vascular involvement by local tumor extension and the presence or absence of liver atrophy. This proposed T-staging system is predictive of resectability, of the likelihood of nodular or distant metastases, and of overall survival. In this staging system, T1 tumors are classified as lesions involving the biliary confluence (with or without unilateral extension to second-order biliary radicles), no portal-vein involvement, and no lobar atrophy. When tumors involve the ipsilateral portal vein or ipsilateral lobar atrophy, the lesions are considered T2. T3 tumors corresponding to the Bismuth-Corlette type 4, bilateral, or main portal-vein invasion; or Bismuth-Corlette type 3 tumors with contralateral portal-vein invasion or hepatic atrophy, are considered poor candidates for surgery. However, some Bismuth type 4 tumors with favorable anatomy or short segmental invasion of the main

portal vein may not be an absolute contraindication to attempt curative resection. Resectability also depends upon patient factors, which are essential for operation even in technically feasible cases [29].

## References


1. Choi BI, Lee JM (2013), Preoperative imaging. In: Lau WY (Ed) Hilar cholangiocarcinoma. Springer, Dordrecht Heidelberg New York London, pp 53-64.
2. Aljiffry M, Walsh MJ, Molinari M (2009) Advances in diagnosis, treatment and palliation of cholangiocarcinoma: 1990-2009. World J Gastroenterol 15:4240-4262.
3. Yu MH, Kim JH (2014) Anomalies and anatomic variants of the biliary tree. In: Choi BI (Ed) Radiology illustrated: hepatobiliary and pancreatic radiology. Springer, Heidelberg New York Dordrecht London, pp 392-394.
4. Gore RM, Fulcher AS, Taylor AJ, Ghahremani GG (2008) Anomalies and anatomic variants of the gallbladder and biliary tract. In: Gore RM, Levine MS (Eds) Textbook of gastrointestinal radiology, 3rd edition. Saunders, Philadelphia, pp 1399-1409.
5. Mortelé KJ, Rocha TC, Streeter JL et al (2006) Multimodality imaging of pancreatic and biliary congenital anomalies. Radiographics 26:715-731.
6. Yu J, Turner MA, Fulcher AS et al (2006) Congenital anomalies and normal variants of the pancreaticobiliary tract and the pancreas in adults: part 1, biliary tract. AJR Am J Roentgenol 187:1536-1543.
7. Park HS (2014) Cholangitis. In: Choi BI (Ed) Radiology illustrated: hepatobiliary and pancreatic radiology. Springer, Heidelberg New York Dordrecht London, pp 418-420.
8. Michael C, Peter FH (2011) Dilated bile ducts. In: Sahani DV, Samir AE (Eds) Abdominal imaging, 2nd ed. Saunders/Elsevier, Maryland Heights, pp 871-873.
9. Rao VA, Mehta UK, MacCarty RL (2008) Inflammatory disorders of the biliary tract. In: Gore RM, Levin MS (Eds) Textbook of gastrointestinal radiology. Vol. II, 3rd edition. Saunders/Elsevier, Philadelphia, pp 1489-1504.
10. Chan FL, Man SW, Leong LLY et al (1989) Evaluation of recurrent pyogenic cholangitis with CT: analysis of 50 patients. Radiology 170:165-169.
11. Lim JH (1991) Oriental cholangiohepatitis: pathologic, clinical and radiologic features. AJR Am J Roentgenol 157:1-8.
12. Choi BI, Park JH, Han MC et al (1989) CT findings of clonorchiasis. AJR Am J Roentgenol 152:281-284.
13. Choi BI, Park JH, Kim YI et al (1988) Peripheral cholangiocarcinoma and clonorchiasis: CT findings. Radiology 169:149-153.
14. Kubaska SM, Chew FS (1997) Biliary ascariasis. AJR Am J Roentgenol 169:492.
15. Hwang CM, Kim TK, Ha HK et al (2001) Biliary ascariasis: MR cholangiography findings in two cases. Korean J Radiol 2:175-178.
16. Lee JY (2014) Cholecystitis and adeonomyomatosis. In: Choi BI (Ed) Radiology illustrated: hepatobiliary and pancreatic radiology. Springer, Heidelberg New York Dordrecht London, pp 446-447.
17. Bedirli A, Sakrak O, Sozuer EM et al (2001) Factors effecting the complications in the natural history of acute cholecystitis. Hepatogastroenterology 48:1275-1278.
18. Bennett GL, Balthazar EJ (2003) Ultrasound and CT evaluation of emergent gallbladder pathology. Radiol Clin North Am 41:1203-1216.
19. Bennett GL, Rusinek H, Lisi V et al (2002) CT findings in acute gangrenous cholecystitis. AJR Am J Roentgenol 178:275-281.
20. Gremmels JM, Kruskal JB, Parangi S et al (2004) Hemorrhagic cholecystitis simulating gallbladder carcinoma. J Ultrasound Med 23:993-995.
21. Kim PN, Lee SH, Gong GY et al (1999) Xanthogranulomatous cholecystitis: radiologic findings with histologic correlation that focuses on intramural nodules. AJR Am J Roentgenol 172:949-953.
22. Kane RA, Jacobs R, Katz J et al (1984) Porcelain gallbladder: ultrasound and CT appearance. Radiology 152:137-141.
23. Haradome H, Ichikawa T, Sou H et al (2003) The pearl necklace sign: an imaging sign of adenomyomatosis of the gallbladder at MR cholangiopancreatography. Radiology 227:80-88.
24. Kim SJ (2014) Tumors of the gallbladder. In: Choi BI (Ed) Radiology illustrated: hepatobiliary and pancreatic radiology. Springer, Heidelberg New York Dordrecht London, pp 500-504.
25. Kim SJ (2008) Analysis of enhancement pattern of flat gallbladder wall thickening on MDCT to differentiate gallbladder cancer from cholecystitis. AJR Am J Roentgenol 191:765-71.
26. Choi JH (2008) Pre-operative predictive factors for gallbladder cholesterol polyps using conventional diagnostic imaging. World J Gastroenterol 14:6831-6834.
27. Edge SB, Byrd DR, Compton CC et al (2010) AJCC cancer staging manual, 7th edition. Springer, New York, pp 211-217.
28. Chung YE, Kim MJ, Park YN et al (2009) Varying appearances of cholangiocarcinoma: radiologic-pathologic correlation. Radiographics 29:683-700.
29. Choi JY, Han JK (2014) Cholangiocarcinoma. In: Choi BI (Ed) Radiology illustrated: hepatobiliary and pancreatic radiology. Springer, Heidelberg New York Dordrecht London, pp 470-474.
30. Lim JH (2003) Cholangiocarcinoma: morphologic classification according to growth pattern and imaging findings. AJR Am J Roentgenol 181:819-827.

# A Pattern Approach to Diseases of the Gallbladder and Bile Ducts

Angela D. Levy

Department of Radiology, Georgetown University Hospital, Washington, DC, USA

## Introduction

Patients with gallbladder and biliary disease may present with complaints of right upper quadrant or epigastric pain, fever, jaundice, pruritus, nausea, and vomiting, or they may be asymptomatic with only laboratory abnormalities. Ultrasound (US), multidetector computed tomography (MDCT), and magnetic resonance imaging (MRI) with or without magnetic resonance cholangiopancreatography (MRCP) may be used for noninvasive evaluation of patients with signs and symptoms of gallbladder and biliary disease. In many instances, noninvasive imaging will establish the diagnosis prior to endoscopic or surgical intervention. The differential diagnosis for these patients is broad and includes infectious, noninfectious inflammatory, neoplastic, and congenital disorders of the liver, gallbladder, and bile ducts. The purpose of this chapter is to discuss the approach to differential diagnosis of commonly encountered patterns during gallbladder and bile duct imaging: gallbladder wall thickening, gallbladder polyps and masses, extrahepatic and intrahepatic bile duct dilatation, and bile duct strictures. Diseases that cause these patterns are reviewed.

## Gallbladder Wall Thickening

Focal or diffuse gallbladder wall thickening may be caused by acute or chronic cholecystitis or noninflammatory conditions that produce gallbladder wall thickening, such as heart failure, cirrhosis, hepatitis, hypoalbuminemia, and renal failure. Gallbladder carcinoma may also cause gallbladder wall thickening and should be suspected with findings of a focal mass, lymphadenopathy, extension of the process to adjacent organs, hepatic metastases, or biliary obstruction at the porta hepatis level.

One of the most common causes of gallbladder wall thickening is acute cholecystitis, which should be considered when gallstones, gallbladder wall thickening, and a sonographic Murphy sign are found in patients with right upper quadrant pain (Fig. 1). Other findings that aid in the diagnosis include gallbladder distension, pericholecystic fluid, and gallbladder wall and/or liver hyperemia on color Doppler imaging. Similar findings are depicted on CT in acute cholecystitis. Increased arterial perfusion in the liver parenchyma (also called transient hepatic attenuating difference) adjacent to the gallbladder may be seen, as well as inflammatory changes in the fat surrounding the liver. Perforation may complicate cholecystitis when there is severe or long-standing inflammation. In these cases, focal disruption of the gallbladder wall may be visualized on CT or US. Complex loculated pericholecystic fluid containing echoes or dependent debris will be present when there is an adjacent abscess that results from perforation.

Gangrenous cholecystitis is another form of severe inflammation that results in gallbladder wall ischemia and necrosis. The diagnosis should be suggested when intraluminal membranes from sloughed gallbladder mucosa are seen on US. The gallbladder wall may appear striated and have irregular thickening. Often, a sonographic Murphy sign is absent in patients with gangrenous cholecystitis; CT findings are more specific. The absence of gallbladder wall enhancement is the most important feature and is indicative of ischemia (Fig. 2). Intraluminal membranes, hemorrhage, and gallbladder wall disruption are additional findings.

Xanthogranulomatous cholecystitis (XGC) is a rare form of chronic cholecystitis that resembles gallbladder carcinoma on imaging studies. The presumed etiology is intermittent cystic duct obstruction from stones. During episodes of obstruction, increased intraluminal pressure within the gallbladder causes intravasation of bile into the gallbladder wall. The intravasated bile causes a chronic, lipid-laden, inflammatory process. There is a significant overlap in CT features of XGC and gallbladder carcinoma. Both entities may demonstrate wall thickening, infiltration of the surrounding fat, hepatic invasion, and lymphadenopathy. XGC can be suggested when nodular foci are observed in the gallbladder wall (Fig. 3). Foci are hypoechoic on US and hypoattenuating on CT and represent foci of lipid-laden inflammation in the gallbladder wall.

*Diseases of the Abdomen and Pelvis 2014-2017*,
DOI: 10.1007/978-88-470-5659-6_14 

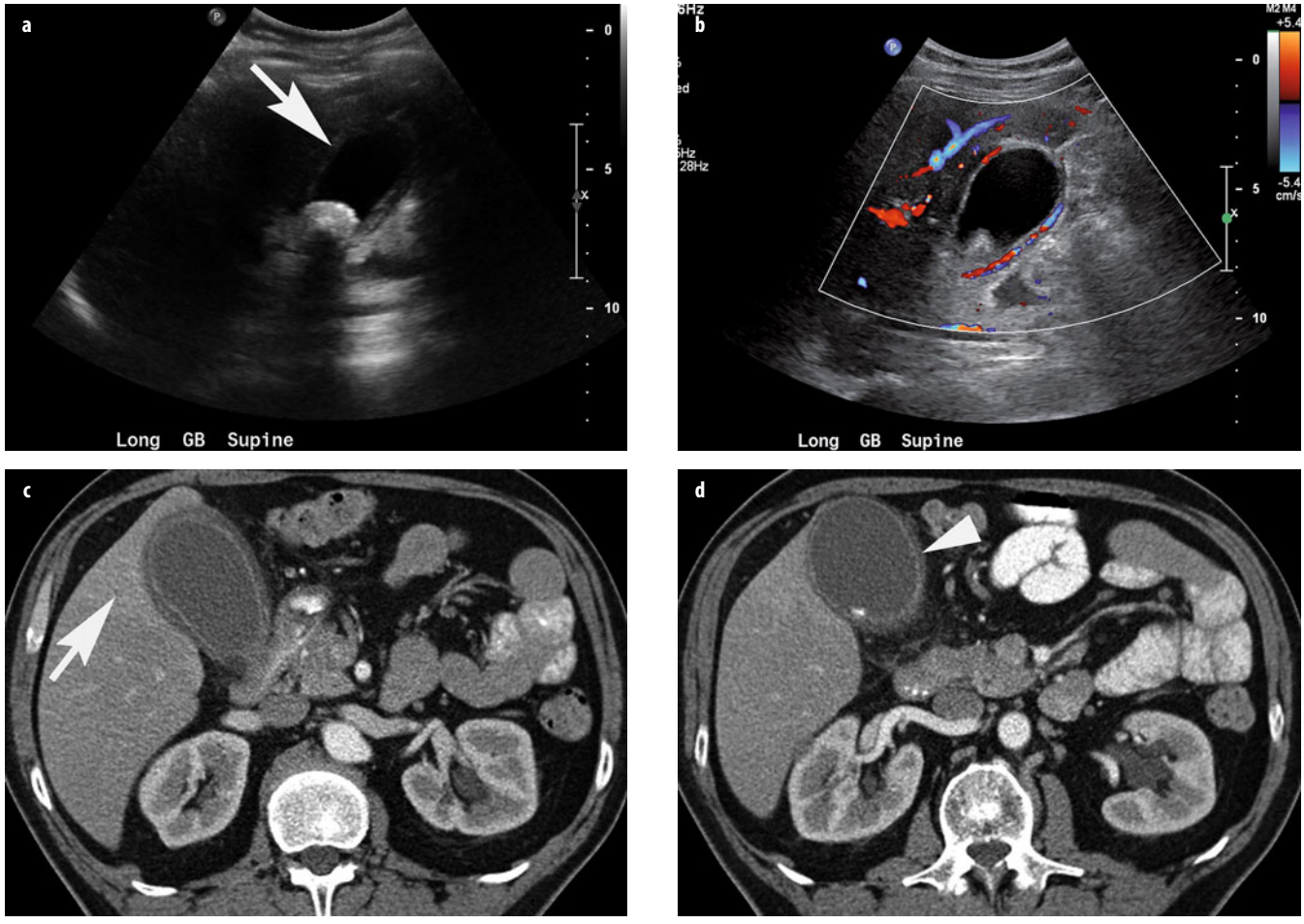


**Fig. 1 a-d.** Acute cholecystitis. **a, b** Longitudinal ultrasound (US) shows a large stone impacted in the gallbladder neck, gallbladder wall thickening (*arrow*), and gallbladder wall hyperemia on color Doppler. **c, d** Contrast-enhanced computed tomography (CT) with intravenously and orally administered contrast media shows a distended gallbladder containing a stone, gallbladder wall thickening (*arrowhead*), pericholecystic inflammation, and hyperenhancement of the adjacent liver (*arrow*)

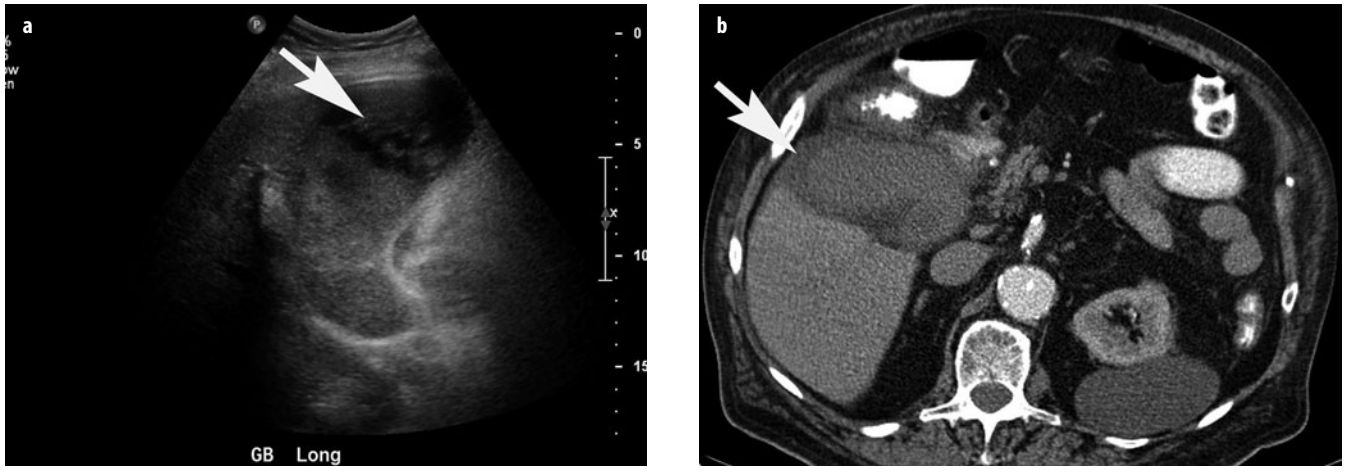


**Fig. 2 a, b.** Gangrenous cholecystitis. **a** Longitudinal ultrasound (US) shows a distended gallbladder containing sludge and intraluminal membranes (*arrow*). **b** Contrast-enhanced computed tomography (CT) using intravenously and orally administered contrast media shows nonenhancing, thick gallbladder wall (*arrow*). The high attenuation in the gallbladder lumen represents blood products

In most cases, this is difficult to differentiate prospectively from degeneration or necrosis that may be found in gallbladder carcinoma.

Adenomyomatous hyperplasia, also called adenomyomatosis, is a common benign tumor-like lesion of the gallbladder that may produce focal, segmental, or diffuse

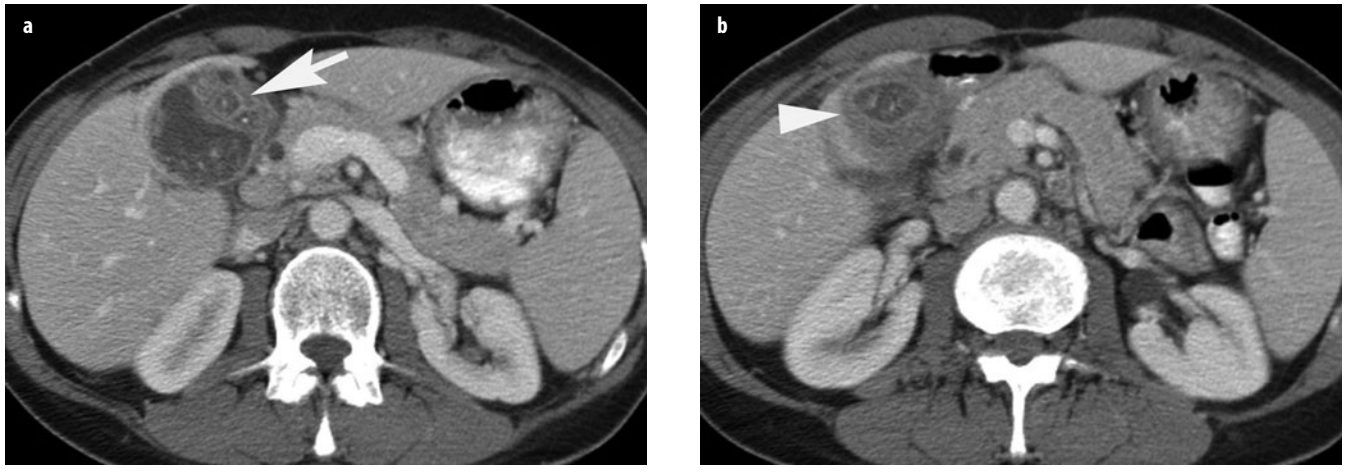


**Fig. 3 a, b.** Xanthogranulomatous cholecystitis. Contrast-enhanced computed tomography (CT) using intravenously and orally administered contrast media shows asymmetric thickening of the gallbladder wall. Round foci of hypoattenuation (**a**, *arrow*) are visible within the thickened wall. The process invades the adjacent liver (**b**, *arrowhead*)

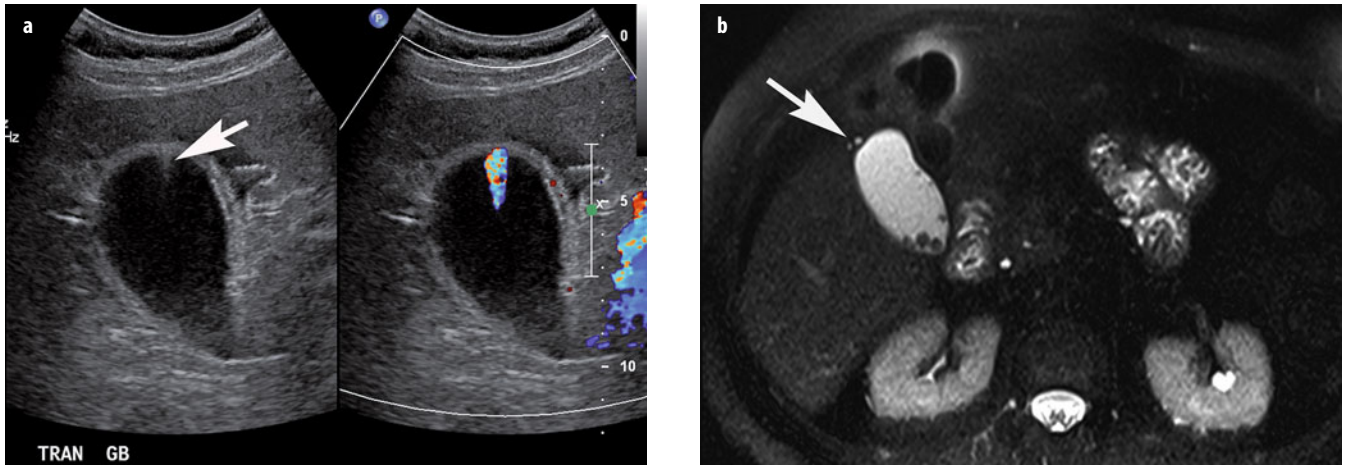


**Fig. 4 a, b.** Adenomyomatosis. **a** Ultrasound (US) shows ring-down artifact (*arrow*) emanating from a mildly thickened gallbladder wall, with twinkle color artifact on color Doppler. **b** Fat-saturated T2-weighted magnetic resonance imaging (MRI) shows two bright foci (*arrow*) in the wall of the gallbladder fundus that represent Rokitansky-Aschoff sinuses. Gallstones are also present

mural thickening. Pathologically, adenomyomatosis is characterized by hyperplasia of all layers of the gallbladder wall. Epithelial hypoplasia results in the formation of exaggerated invaginations called Rokitansky-Aschoff sinuses. Muscular hyperplasia thickens the gallbladder wall. Sonographically, adenomyomatous hyperplasia is characterized by echogenic foci that produce a characteristic reverberation artifact, commonly called ring-down artifact, emanating from the gallbladder wall. The ring-down artifact produces twinkle artifact on color Doppler (Fig. 4). Echogenic foci represent bile salts, cholesterol crystals, or small stones in Rokitansky-Aschoff sinuses. Focal or diffuse gallbladder wall thickening commonly accompanies the ring-down artifact. Focal adenomyomatosis is often localized in the gallbladder fundus. On MR, Rokitansky-Aschoff sinuses are best visualized on breath-hold T2-weighted MRI sequences as small, round foci of high T2 signal (Fig. 4) that in severe cases are visible throughout the gallbladder wall. This appearance is called the pearl-necklace sign. In cases with significant wall thickening, the finding of Rokitansky-Aschoff sinuses on MRI may be a helpful distinguishing feature from gallbladder carcinoma, which also may cause significant wall thickening.

## Gallbladder Polyps and Masses

Gallbladder polyps are commonly demonstrated as incidental findings when the gallbladder is imaged on sonography and are estimated to be present in approximately 3% of gallbladders. The differential diagnosis for a gallbladder polyp includes cholesterol polyp, adenoma, focal adenomyomatous hyperplasia, inflammatory polyp, heterotopia, neurofibroma, carcinoma, carcinoid tumor, lymphoma, and metastasis. The majority of gallbladder polyps are benign, the most common type being the cholesterol polyp, which accounts for approximately 50% of

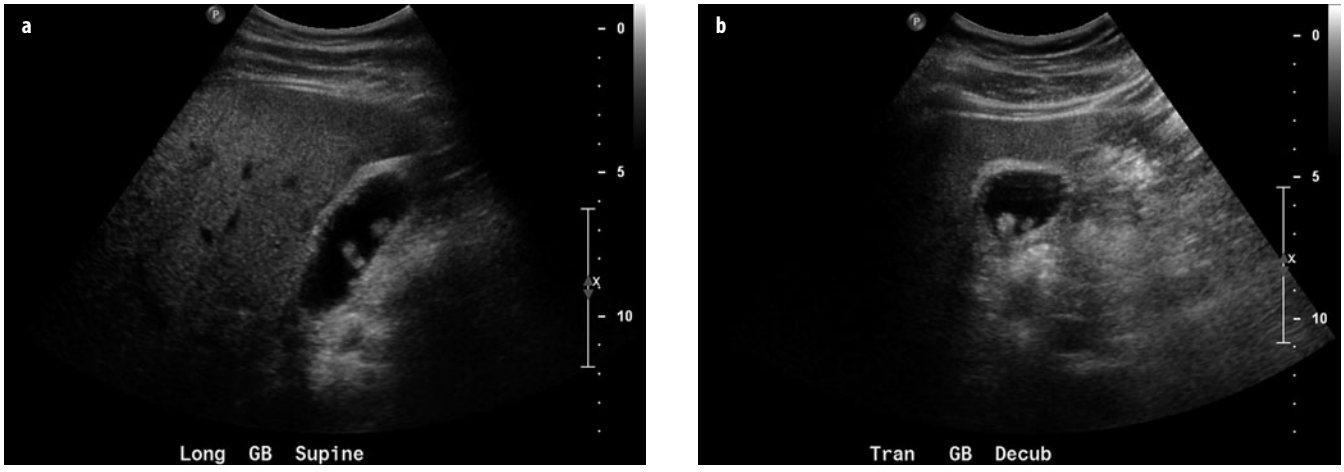


**Fig. 5 a, b.** Cholesterol polyps. Longitudinal (**a**) and transverse (**b**) ultrasound (US) images show multiple small, hyperechoic, intraluminal gallbladder polyps

all polypoid lesions. Cholesterol polyps are not neoplastic and consequently have no malignant potential. They represent focal accumulation of lipid-laden macrophages and are covered by normal gallbladder epithelium. On sonography, cholesterol polyps are typically brightly echogenic round or slightly lobulated lesions that do no produce acoustic shadowing (Fig. 5). Larger cholesterol polyps are usually less echogenic and may contain an aggregation of echogenic foci.

Adenomas and small polypoid adenocarcinomas are usually much larger than cholesterol polyps and tend to be less hypoechoic on US, presenting with a more lobular appearance. Because the incidence of neoplastic polyps increases with the increasing size of a polyp, managing gallbladder polyps is based on size. Studies show that the risk of malignancy increases for polyps $>10$ mm in size and in patients $>60$ years. The incidence of malignancy in polyps $>10$ mm ranges from 37% to 88%. Therefore, it is recommended that patients undergo cholecystectomy for asymptomatic polyps $>10$ mm. Polyps between 5 mm and 10 mm should be followed periodically by US; those $<5$ mm with classic features of cholesterol polyps can be left alone. However, at sonography, careful attention should be paid to other features that suggest malignancy, such as thickening or nodularity of the gallbladder wall; evidence of hepatic invasion, such as an indistinct margin between the liver and gallbladder; biliary duct dilatation; and peripancreatic hepatoduodenal ligament adenopathy (Fig. 6). If any features are suggestive of malignancy, MDCT or MRI should be considered to further characterize and potentially stage the mass.

## Cystic Dilatation of the Extrahepatic Bile Duct

Mechanical biliary obstruction is the most common cause of extrahepatic bile duct dilatation. Upon initial imaging, an obstructive lesion should always be suspected when biliary dilatation is present. Once an obstructive lesion is excluded, congenital etiologies of bile duct dilatation should be considered. Choledochal cyst is primarily a congenital dilatation of the extrahepatic bile duct but may also involve the intrahepatic bile ducts and cystic duct. Unlike obstructive dilatation, dilatation of choledochal cyst is typically more expansive than that usually encountered in mechanical dilatation (Fig. 7). It may be more difficult to differentiate a choledochal cyst that has mild or fusiform dilatation of the extrahepatic duct from a duct that is mildly dilated secondary to an obstructing lesion. In these cases, MRCP and/or endoscopic retrograde cholangiopancreatography (ERCP) are useful to exclude an obstructing lesion and evaluate the pancreaticobiliary junction. Anomalous pancreaticobiliary junction is commonly observed in patients with choledochal cysts and, if present, is a helpful supportive feature for diagnosing a choledochal cyst. Choledochal cysts may be complicated by stone formation and cholangitis. Furthermore, patients with choledochal cysts have a higher incidence of cholangiocarcinoma than does the general population. When cholangiocarcinoma occurs, it may arise within the cyst or elsewhere in the liver.

Rarely, pancreatic pseudocysts, echinococcal cysts, and cystic biliary neoplasms, such as biliary cystadenoma or biliary cystadenocarcinoma, may occur in or around the porta hepatis, simulating a biliary dilatation and choledochal cyst. Identifying the bile duct from the cystic structure near the porta hepatis and the appearance of rim-like calcification and enhancing septations or mural nodules should help establish the diagnosis of a biliary cystadenoma or cystadenocarcinoma. Likewise, echinococcal cysts generally present evidence of inner membranes, daughter cysts, or rim-like peripheral calcification. MR of echinococcal cysts may show a low-signal-intensity fibrous capsule and membranes on T2-weighted images.

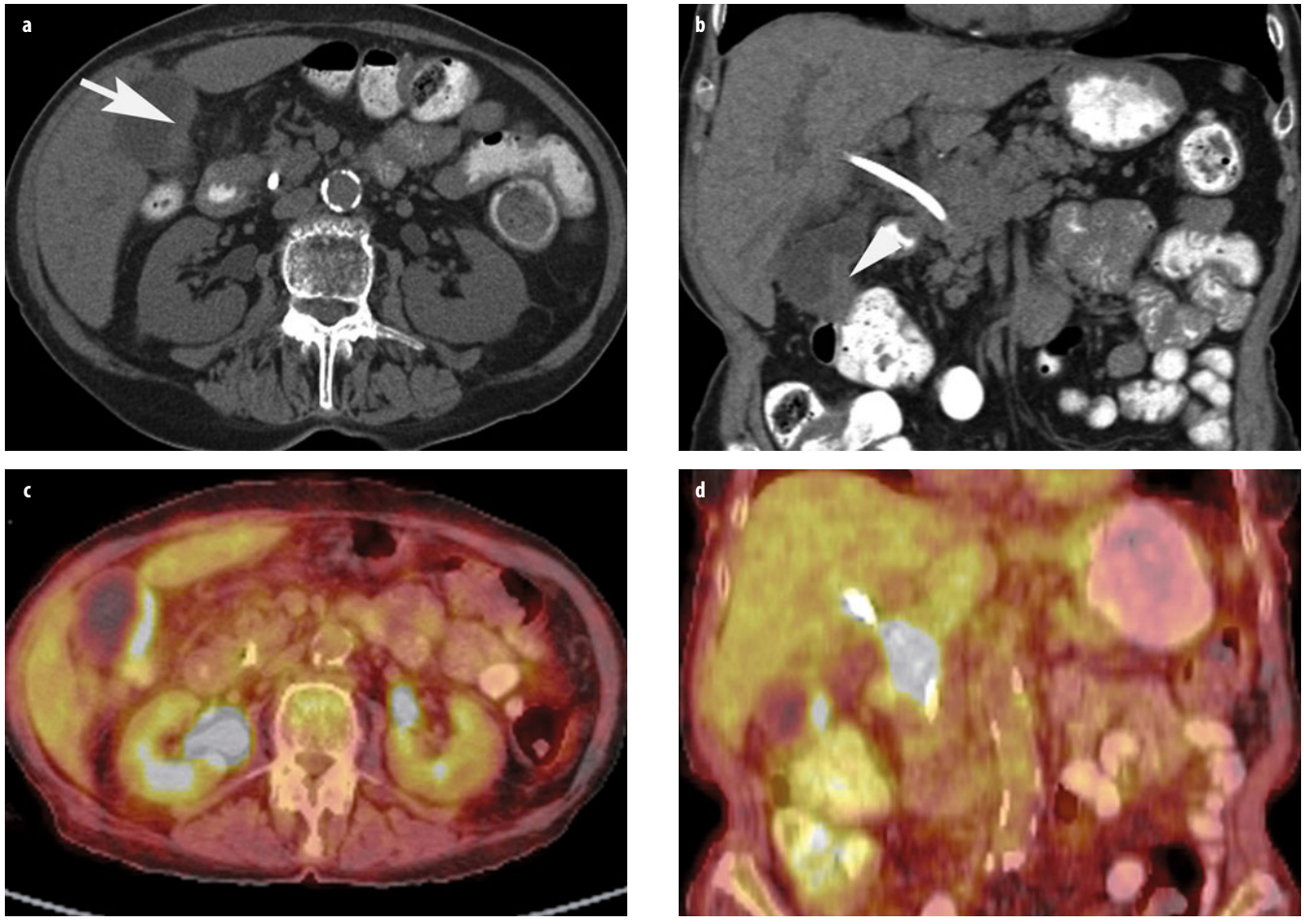


**Fig. 6 a-d.** Gallbladder carcinoma. **a, b** Contrast-enhanced computed tomography (CT) using orally administered contrast medium shows focal gallbladder wall thickening (**a**, *arrow*) with irregular margins that extends to invade the adjacent transverse colon (**b**, *arrowhead*) and hepatoduodenal ligament. A bile duct stent is in place. **c, d** Fluorine-18-deoxy-glucose ([$^{18}$F]-FDG) positron emission tomography computed tomography (PET-CT) shows metabolically active gallbladder wall thickening and a mass encasing the common bile duct that most likely represents metastatic disease

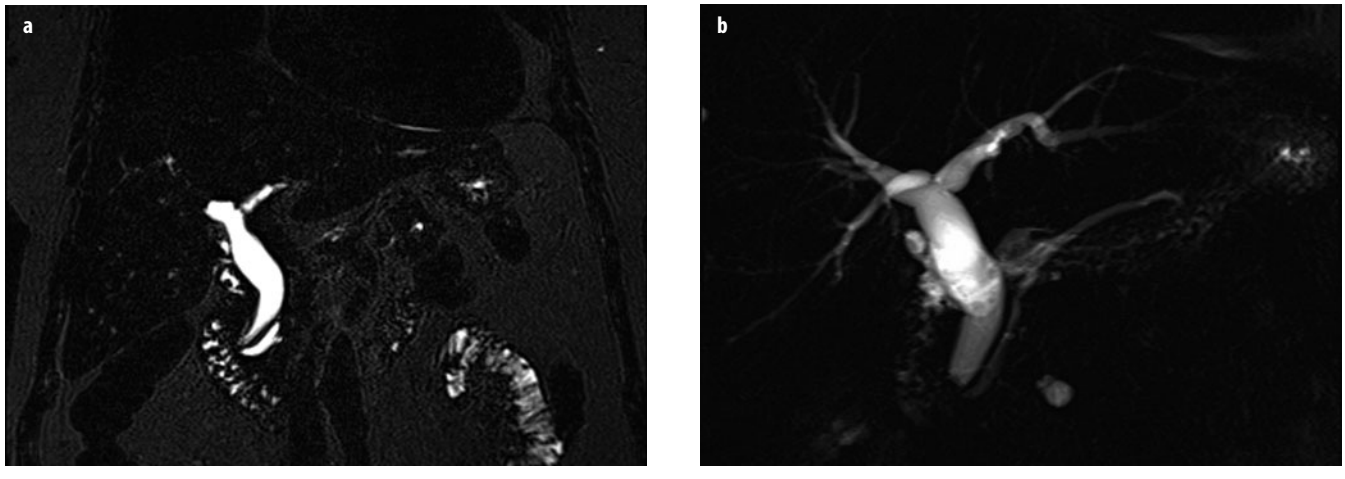


**Fig. 7 a, b.** Choledochal cyst. Coronal thin- and thick-slab magnetic resonance cholangiopancreatography (MRCP) shows fusiform dilatation of the extrahepatic bile duct and mild dilatation of the central intrahepatic ducts. The peripheral intrahepatic ducts are normal

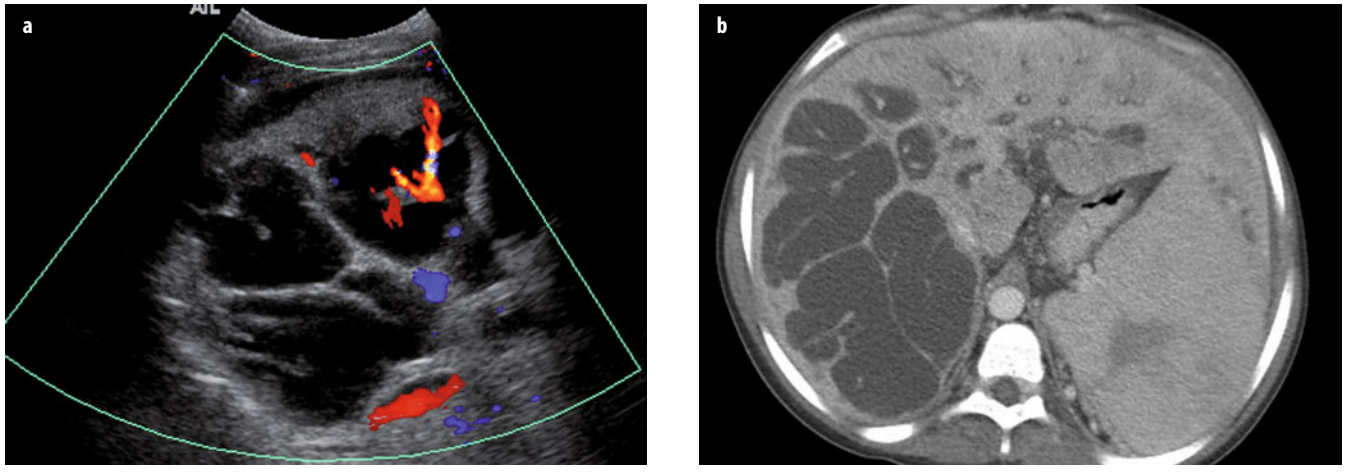


**Fig. 8 a, b.** Caroli disease. **a** Transverse ultrasound (US) image of the liver shows large cystic structures that contain a central dot and small portal venous radicles. **b** Contrast-enhanced computed tomography (CT) using intravenously administered contrast medium in the same patient shows marked dilatation of the intrahepatic bile ducts in the right lobe, with the central dot sign. The liver is cirrhotic; the spleen is enlarged and contains a focal area of infarction

## Cystic Dilatation of Intrahepatic Bile Ducts

Similar to extrahepatic duct dilatation, mechanical obstruction is the most common cause of intrahepatic bile duct dilatation. Obstruction is generally tubular, and all ducts proximal to the obstructing lesion are dilated. Nonobstructive causes of bile duct dilatation include Caroli disease, recurrent pyogenic cholangitis, and polycystic liver disease. Segmental or focal regions of intrahepatic bile duct dilatation may occur in primary sclerosing cholangitis due to stricture formation. Choledochal and peribiliary cysts should be included in the differential diagnosis of cystic intrahepatic biliary dilatation.

Caroli disease is a rare and complex disorder inherited in an autosomal recessive pattern. It is the result of abnormal remodeling of the ductal plate, which is the embryologic precursor to intrahepatic bile ducts. A spectrum of diseases ranging from congenital hepatic fibrosis to Caroli disease occurs due to abnormal ductal plate development. Caroli disease is suggested by focal or diffuse biliary dilatation that is cystic or fusiform in character (Fig. 8). Irregular bile duct walls and short strictures may also be present. When diffuse involvement is present, bile ducts converge toward the porta hepatis. Intraductal sludge, inflammatory debris, and stones may be present within the dilated ducts. MRI and MRCP are particularly useful for evaluating the extent and complications of Caroli disease. Patients may have episodes of recurrent cholangitis and stone formation from biliary stasis in the dilated ducts. They may also develop cirrhosis from chronic cholestasis or from coexisting hepatic fibrosis. The risk of cholangiocarcinoma is higher in Caroli disease patients compared with the general population.

The most important differential diagnosis for patients with suspected Caroli disease is recurrent pyogenic cholangitis, an idiopathic inflammatory disorder characterized by biliary dilatation with intrahepatic stone formation. The left hepatic lobe is more commonly involved than the right in recurrent pyogenic cholangitis. Polycystic liver disease may also mimic Caroli disease. However, in most cases, bile ducts in polycystic liver disease are intrinsically normal; only rarely will cysts communicate with bile ducts.

Although intrahepatic bile duct dilatation is a feature of primary sclerosing cholangitis, duct dilatation is typically fusiform and isolated. The degree and extent of duct dilatation in primary sclerosing cholangitis is not as severe as that in obstructive biliary dilatation, Caroli disease, or recurrent pyogenic cholangitis because fibrosis, stricture formation, and secondary cirrhosis are the major features of primary sclerosing cholangitis.

Choledochal cysts should also be considered in the differential diagnosis when both intrahepatic and extrahepatic duct dilatation is present. In general, patients with choledochal cysts will have more severe extrahepatic dilatation than intrahepatic dilatation.

Peribiliary cysts may simulate bile duct dilatation that has a beaded or saccular appearance. The bile ducts adjacent to peribiliary cysts are normal. Therefore, correct diagnosis depends upon visualization of a normal bile duct. Peribiliary cysts are almost exclusively seen in patients with chronic liver disease, such as cirrhosis, polycystic liver disease, portal hypertension, portal vein obstruction, and metastatic disease.

## Biliary Stricture

Focal narrowing or stricturing in the biliary ducts may be secondary to neoplasms, inflammation, ischemia, trauma (iatrogenic or noniatrogenic), or mass effect from an adjacent processes. The location of biliary strictures narrows the differential diagnosis. Strictures at the level of the porta hepatis (in or near the confluence of the right

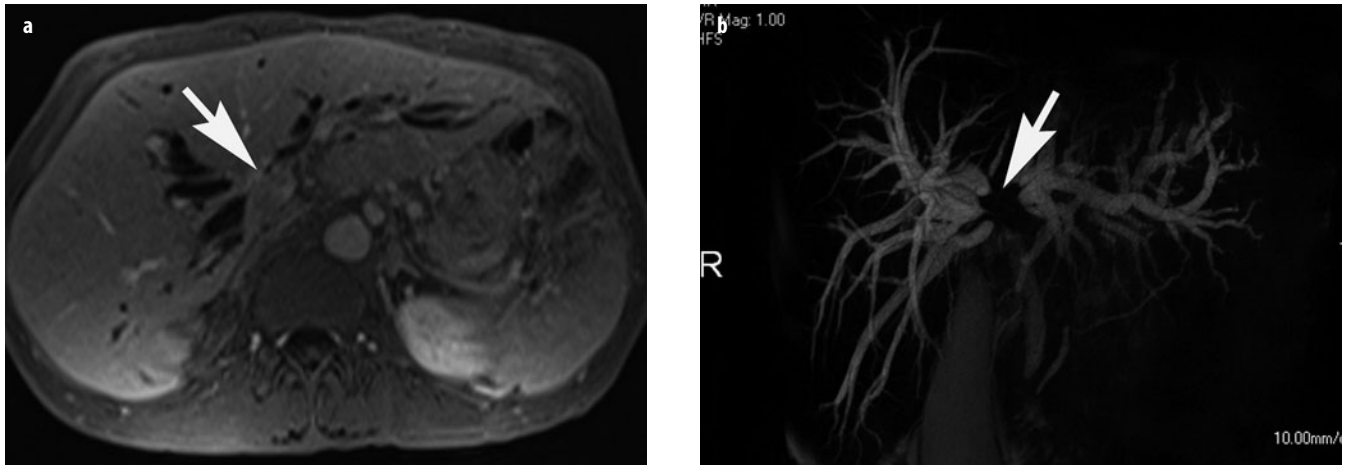


**Fig. 9 a, b.** Hilar cholangiocarcinoma. **a** Gadolinium-enhanced T1-weighted magnetic resonance image (MRI) (gadolinium administered intravenously) shows dilatation of right and left intrahepatic ducts. The ducts do not converge (*arrow*) to form the common hepatic duct. At this location there is a subtle mass. **b** Thick-slab magnetic resonance cholangiopancreatography (MRCP) shows a stricture/defect at the confluence of the intrahepatic bile ducts (*arrow*), consistent with a hilar tumor

and left hepatic ducts) may be secondary to hilar cholangiocarcinoma (Klatskin tumor) (Fig. 9), inflammation, or vascular impressions. Strictures in the mid portion of the extrahepatic bile duct are commonly related to diseases of the gallbladder, such as carcinoma that has invaded the cystic duct and hepatoduodenal ligament, or inflammatory conditions such as impaction of a stone in the cystic duct (Mirizzi syndrome). Distal extrahepatic strictures may be due to inflammatory or neoplastic diseases of the pancreas, primary carcinomas of the bile duct or ampulla, sphincter of Oddi dysfunction, stricture from stone passage, or, less commonly, infectious papillitis, which may be seen in AIDS cholangiopathy. Stricture characteristics are also important in narrowing the differential diagnosis: Benign strictures classically have smooth margins and gradually narrow the duct. In contrast, malignant strictures more often abruptly narrow or occlude the duct and have irregular margins.

## Conclusions

Knowledge of gallbladder and bile duct diseases in combination with a pattern approach to differential diagnosis on imaging findings is useful to aid in diagnosing these diseases.

## Suggested Reading

Baron RL, Campbell WL, Dodd 3rd GD (1994) Peribiliary cysts associated with severe liver disease: imaging-pathologic correlation. AJR Am J Roentgenol 162:631-636.

Baron RL, Tublin ME, Peterson MS (2002) Imaging the spectrum of biliary tract disease. Radiol Clin North Am 40:1325-1354.

Chun KA, Ha HK, Yu ES et al (1997) Xanthogranulomatous cholecystitis: CT features with emphasis on differentiation from gallbladder carcinoma. Radiology 203:93-97.

Goodman ZD, Ishak KG (1981) Xanthogranulomatous cholecystitis. Am J Surg Pathol 5:653-659.

Guy F, Cognet F, Dranssart M et al (2002) Caroli's disease: magnetic resonance imaging features. European Radiology 12:2730-2736.

Haradome H, Ichikawa T, Sou H et al (2003) The pearl necklace sign: an imaging sign of adenomyomatosis of the gallbladder at MR cholangiopancreatography. Radiology 227: 80-88.

Ishikawa O, Ohhigashi H, Imaoka S et al (1989) The difference in malignancy between pedunculated and sessile polypoid lesions of the gallbladder. Am J Gastroenterol 84:1386-1390.

Kovac JD, Jesic R, Stanisavljevic D et al (2013) MR imaging of primary sclerosing cholangitis: additional value of diffusion-weighted imaging and ADC measurement. Acta radiologica 54:242-248.

Levy AD, Murakata LA, Rohrmann CA (2001) Gallbladder carcinoma: radiologic-pathologic correlation. Radiographics 21:295-314.

Levy AD, Rohrmann CA (2003) Biliary cystic disease. Curr Probl Diagn Radiol 32:233-263.

Levy AD, Rohrmann CA, Murakata LA, Lonergan GJ (2002) Caroli's disease: radiologic spectrum with pathologic correlation. AJR Am J Roentgenol 179:1053-1057.

Masselli G, Gualdi G (2008) Hilar cholangiocarcinoma: MRI/MRCP in staging and treatment planning. Abdominal imaging 33:444-451.

Raghavendra BN, Subramanyam BR, Balthazar EJ et al (1983) Sonography of adenomyomatosis of the gallbladder: radiologic-pathologic correlation. Radiology 146:747-752.

Rubens DJ (2004) Hepatobiliary imaging and its pitfalls. Radiol Clin North Am 42:257-278.

Schulte SJ, Baron RL, Teefey SA et al (1990) CT of the extrahepatic bile ducts: wall thickness and contrast enhancement in normal and abnormal ducts. AJR Am J Roentgenol 154: 79-85.

Sugiyama M, Atomi Y, Kuroda A et al (1995) Large cholesterol polyps of the gallbladder: diagnosis by means of US and endoscopic US. Radiology 196:493-497.

Yeo D, Perini MV, Muralidharan V, Christophi C (2012) Focal intrahepatic strictures: a review of diagnosis and management. HPB 14:425-434.

Yoshimitsu K, Honda H, Jimi M et al (1999) MR diagnosis of adenomyomatosis of the gallbladder and differentiation from gallbladder carcinoma: importance of showing Rokitansky-Aschoff sinuses. AJR Am J Roentgenol 172:1535-1540.

# Diseases of the Pancreas

Thomas K. Helmberger[1], Riccardo Manfredi[2]

[1] Institute of Diagnostic and Interventional Radiology, Neuroradiology and Nuclear Medicine, Klinikum Bogenhausen, Academic Teaching Hospital, Technical University Munich, Munich, Germany
[2] Department of Radiology, University of Verona, Verona, Italy

## Introduction

Modern cross-sectional imaging with high spatial and contrast resolution allows a perfect delineation of the pancreas in its retroperitoneal home. The organ typically presents itself with a length between 12 and 15 cm and a diameter at the head area of ~2.5 cm, at the body of ~2 cm, and at the tip of the pancreatic tail of ~1.5 cm. Anatomically, the pancreatic head is defined as the area to the right of the left border of the superior mesenteric vein, the body as the area between the left border of the superior mesenteric vein and the left border of the aorta, and the tail as the area between the left border of the aorta and the hilum of the spleen. The normal pancreatic duct ranges between 1.5 mm at the tail and 3 mm at the head. Usually (~60% of cases), the pancreatic main duct (duct of Wirsung), the duct of Santorini, and the common bile duct join together within the pancreatic head, entering the duodenum via the papilla of Vater. Several conditions that affect function and integrity of the pancreas, such as developmental anomalies and neoplastic and inflammatory diseases, are discussed.

## Developmental Anomalies of the Pancreas

During embryogenesis, the pancreas is formed from a larger, dorsal bud (tail, body, parts of the head) and a small, ventral bud (rest of the head). The ventral bud migrates downward dorsal from the dorsal bud. During the union of both buds, the main pancreatic duct within the ventral bud ends via the duct of Santorini in the minor papilla. This duct then reduces to an accessory duct, whereas the main pancreatic duct of the dorsal bud merges with the duct of the former ventral bud, ending in the major papilla [1, 2]. The disturbed union of the two buds can cause three major anomalies. Pancreas divisum, a nonunion anomaly of the pancreas is found in autopsy studies with a frequency of 1-14% and is characterized by separate drainage of the main pancreatic duct via the duct of Santorini into the minor papilla and of the duct of Wirsung into the major papilla. Only 1% of individuals with pancreas divisum will develop unspecific abdominal symptoms (abdominal discomfort, most likely caused by recurrent episodes of mild pancreatitis). Therefore – albeit without real evidence – some authors consider pancreas divisum a promoting factor for pancreatic tumors based on recurrent and lately chronic focal pancreatitis [3]. In pancreas annulare, nonmigration of the ventral bud causes the ventral and dorsal buds to form a ring around the duodenum. This rare anomaly (estimated prevalence 0.01%) can be associated with other birth deformities, such as congenital duodenal atresia, mesenterium commune, oral facial defects, and Down syndrome. Clinical signs are determined by stenosis and occlusion of the duodenum. To reveal a union/migration anomaly of the pancreas, in most cases, magnetic resonance cholangiopancreatography (MRCP) will add the crucial information regarding the distorted duct configuration. The generally asymptomatic ectopic pancreatic tissue can be found in the stomach, duodenum, and ileum and very rarely in Meckel's diverticulum, gall bladder, bile duct, and spleen; autopsy studies reveal a frequency between 0.6% and 15%. Typically, pancreatic ectopic tissue is detected by endoscopy. Total agenesis of the pancreatic gland, hypoplasia of the pancreas (partial agenesis), congenital pancreatic cysts (dysontogenetic cysts, hamartosis), multiple congenital cysts associated with von-Hippel-Lindau disease (cysts also in the liver and kidneys), and cystic degenerative transformation of the pancreas in cystic fibrosis are in general rare and are identified by magnetic resonance imaging (MRI), as well as by sonography and computed tomography (CT), based on partially or completely missing organ or by solitary or multiple cysts.

## Pancreatic Neoplasms

Pancreatic tumors can be classified according to their cellular origin, enzymatic activity, and benign or malignant potential. The most recent World Health Organization (WHO) classification (2010, revised 2012) divides

*Diseases of the Abdomen and Pelvis 2014-2017*,
DOI: 10.1007/978-88-470-5659-6_15 

pancreatic tumors into primary epithelial and mesenchymal tumors, lymphomas, and secondary tumors; from a clinical-practical point of view, tumor-like lesions can be added (Table 1). In clinical reality, many of the rare and very rare tumors have no specific imaging appearance and can be differentiated only by pathology.

### Pancreatic Carcinoma

Most of the various subtypes of pancreatic carcinoma can be differentiated only by histo- and immunopathology.

### Pancreatic Ductal Adenocarcinoma

Pancreatic ductal adenocarcinoma accounts for 85-95% of all malignant pancreatic tumors (15-20% in gastrointestinal malignancies, 3% in all carcinomas). In general, most of these tumors (60-70%) are located in the pancreatic head, with 15% in the body and 5% in the tail. A multifocal or diffuse tumor spread is uncommon. Prognosis is poor, as most tumors are detected late in an advanced stage of spread. An early metastatic spread along perivascular, ductal, lymphatic, and perineural pathways is promoted by the absence of a true capsule around the organ.

For detection, staging, and follow-up, endoscopic ultrasound (US), contrast-enhanced (CE) CT, MRI, and fluorodeoxyglucose positron emission tomography (FDG-PET) may be applied [4], whereas [5] endoscopic US presents the highest accuracy in detecting small pancreatic-head and periampullary tumors and FDG-PET is superior in detecting distant metastatic spread. Nevertheless, CE-CT and MRI provide a sufficient and comprehensive display of the primary tumor and its sequelae with an accuracy of ~90% and even more [6-8].

The imaging appearance of common pancreatic adenocarcinoma is determined by its typically dense, fibrous, low-vascularized stroma, resulting in low soft-tissue density in CT and low signal on T1- and T2-weighted MRI. No or only minor enhancement (Fig. 1) is what makes the tumors best delineable to the normal glandular parenchyma on CE imaging.

The pancreatic duct may be involved depending on the primary tumor localization within the pancreas, ranging from no ductal involvement at all in peripheral tumors, to segmental obstruction due to intraductal tumor invasion (duct penetrating sign), to obstruction of both pancreatic and common bile duct (double-duct sign) in pancreatic-head tumors. The relation between tumor and ducts is noninvasively seen best on MRCP.

Assessing potential invasive local growth and metastatic spread to local and regional lymph nodes or liver, and vascular invasion completes staging of pancreatic malignancies.

Tumor margins that are blurred and not well defined are still a challenge for every imaging modality, as microscopic local invasive peritumoral spread and an inflammatory desmoplastic reaction often cannot be differentiated, causing over- or underestimation of the T stage [9, 10].

**Table 1.** Classification of pancreatic lesions modified according to the World Health Organization (WHO) (modified according to [4])

| | |
|---|---|
| Benign | Acinar cell cystadenoma<br>Serous cystadenoma, not otherwise specified (NOS) |
| Premalignant | Pancreatic intraepithelial neoplasia, grade 3 (PanIN-3)<br>Intraductal papillary mucinous neoplasm (IPMN) with low- or intermediate-grade dysplasia<br>Intraductal papillary mucinous neoplasm (IPMN) with high-grade dysplasia<br>Intraductal tubulopapillary neoplasm (ITPN)<br>Mucinous cystic neoplasm (MCN) with low- or intermediate-grade dysplasia<br>Mucinous cystic neoplasm (MCN) with high-grade dysplasia |
| Malignant | Ductal adenocarcinoma<br>Adenosquamous carcinoma<br>Mucinous adenocarcinoma<br>Hepatoid carcinoma<br>Medullary carcinoma, NOS<br>Signet-ring cell carcinoma<br>Undifferentiated carcinoma<br>Undifferentiated carcinoma with osteoclast-like cells<br>Acinar cell carcinoma<br>Acinar cell cystadenocarcinoma<br>Intraductal papillary mucinous carcinoma (IPMN) with an associated invasive carcinoma<br>Mixed acinar-ductal carcinoma<br>Mixed acinar-neuroendocrine carcinoma<br>Mixed acinar-neuroendocrine-ductal carcinoma<br>Mixed ductal-neuroendocrine carcinoma<br>Mucinous cystic neoplasm (MCN) with an associated invasive carcinoma<br>Pancreatoblastoma<br>Serous cystadenocarcinoma, NOS<br>Solid-pseudopapillary neoplasm |
| Neuroendocrine neoplasms | Pancreatic neuroendocrine microadenoma<br>Neuroendocrine tumor G1 (NET G1) / Carcinoid<br>Neuroendocrine tumor G2 (NET G2)<br>Neuroendocrine carcinoma, NOS<br>Large cell neuroendocrine carcinoma<br>Small cell neuroendocrine carcinoma<br>Enterochromaffin cell (EC), serotonin-producing neuroendocrine tumour (NET)<br>Gastrinoma, malignant<br>Glucagonoma, malignant<br>Insulin-producing carcinoma (insulinoma)<br>Somatostatinoma, malignant<br>Lipoma, malignant |
| Mesenchymal tumors | Lymphangioma, NOS<br>Lipoma, NOS<br>Solitary fibrous tumor<br>Ewing sarcoma<br>Desmoplastic small round cell tumor<br>Perivascular epithelioid cell neoplasm |
| Lymphomas | Diffuse large B-cell lymphoma (DLBCL), NOS |
| Secondary tumors | Metastases |
| Tumor-like lesions | Acute pancreatitis<br>Chronic pancreatitis<br>Groove pancreatitis<br>Autoimmune pancreatitis<br>Cystic lesions<br>Pancreas divisum<br>Pancreas annulare |

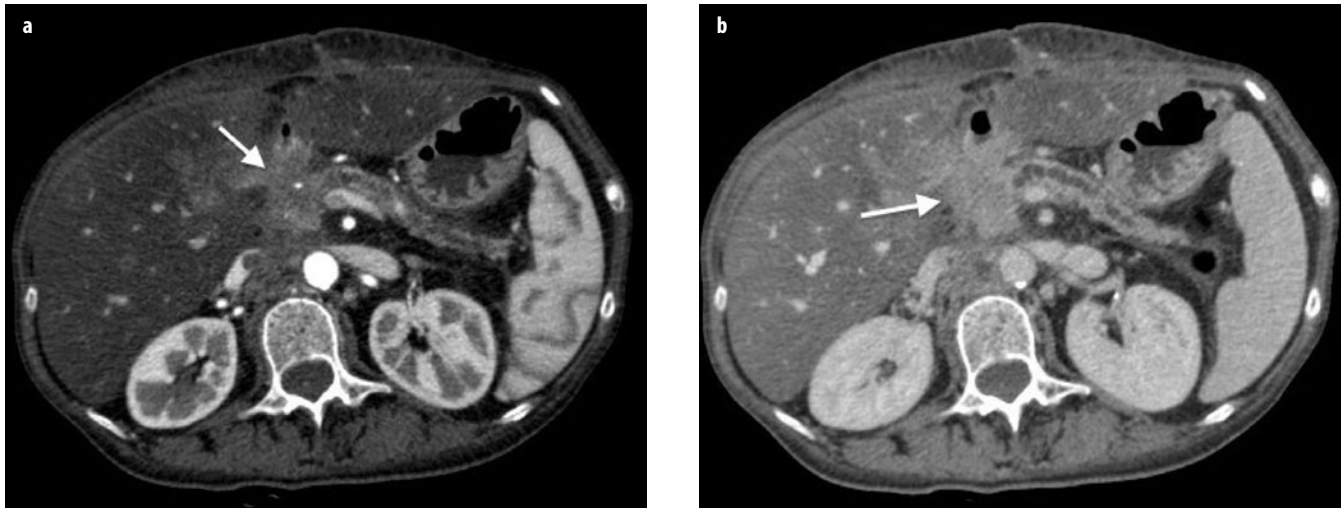


**Fig. 1 a, b.** Adenocarcinoma of the head of the pancreas locally invasive. **a** Axial contrast-enhanced computed tomography (CE-CT) during the pancreatic phase shows a hypovascular focal pancreatic lesion of the head, responsible of infiltration of the main pancreatic duct, with obstructive chronic pancreatitis and infiltration of the peripancreatic fat (*arrow*). **b** Axial CE-CT during the portal-venous phase shows infiltration of the posterior peripancreatic fat (*arrow*)


**Fig. 2 a-c.** Serous cystadenoma. **a** Axial T2-weighted turbo spin-echo image (TR/TE 4,500/102) shows a multicystic microcystic neoplasm of the head of the pancreas (*arrows*). **b** On axial fat-saturated volumetric T1-weighted gradient echo image (TR/TE 4.86/1.87 ms) during the portal-venous phase of the dynamic study following gadolinium-chelate administration, serous cystadenoma shows enhancement of the internal septa and lack of a peripheral wall. **c** On coronal magnetic resonance cholangiopancreatography (MRCP) single-shot rapid acquisition with relaxation enhancement (RARE) (TR/TE ×/110 ms), serous cystadenoma (*arrow*) is responsible of compression of the main pancreatic duct with upstream dilatation

At the time of diagnosis of the primary, about two thirds of patients will present distant metastases (lymph node 40%, hematogenous metastases to the liver 40%, peritoneal metastases 35%), which will be detected with accuracies >90% by CE-MRI and FDG-PET-CT [11, 12]. Moreover, nonresectability in pancreatic cancer is determined by vascular encasement of the superior mesenteric artery, celiac trunk, hepatic or splenic artery, and peripancreatic veins, which is highly likely if a vessel circumference is encased >50% (typical signs: decreased vessel caliber, dilated peripancreatic veins, teardrop shape of superior mesenteric vein).

### Other Tumors of Ductal Origin

This heterogeneous group of tumors includes cystic neoplasms, neuroendocrine tumors, and a variety of very rare tumors, such as pancreatoblastoma and solid pseudopapillary neoplasm.

### Serous Cystadenoma

Serous cystic neoplasms (SCN) account for ~50% of all cystic tumors, including serous cystadenomas, serous oligocystic adenomas, cystic lesions in von-Hippel-Lindau syndrome, and – rarely – serous cystadenocarcinomas [13]. The most common subtype is the benign serous cystadenoma (microcystic type), typically seen in elderly women (60-80 years of age). In most cases, the lesion is located in the pancreatic head and is composed of multiple tiny cysts separated by thin septae. Spotty calcifications and a central stellate nidus might be present (Fig. 2). About 10% of all serous cystic tumors present as an oligocystic variant, with only a few cysts of 2- to 20-mm diameter and a higher prevalence in men (30-40 years). The rare cystadenocarcinomas are usually large by the time of clinical presentation, with local invasive growth and metastases to lymph nodes and liver. Imaging diagnosis of serous cystic pancreatic lesions is ruled

by the proportion of small cysts and septae seen without CE, which may create an almost solid impression on CT, whereas cystic components still can be best appreciated by MRI. Even though the tumors can grow rather large, mismatch of tumor size, missing both ductal involvement and secondary signs of malignancy, will direct to the correct diagnosis. For differentiating oligocystic adenomas from mucinous cystic tumors, intraductal papillary mucinous neoplasms (IPMN) or walled-off cysts, tumor localization, clean clinical history, and normal ducts on MR-CP can be helpful [14, 15].

### Mucinous Cystic Neoplasm (MCN)

Mucin-producing cystic tumors, typically in middle-aged women, are characterized by a missing connection to the pancreatic ducts and the histological presence of an ovarian-like stroma. In comparison with SCN, MCN are less frequent (10% of all cystic pancreatic lesions); in general are asymptomatic; detected as solitary, large lesions arising in the body and tail of the pancreas (95%); and composed only of a few cysts with pronounced septae. As the cysts may contain mucinous, hemorrhagic, necrotic, jelly-like material, they may present intermediate and higher densities and signal intensities on CT and MRI, whereas T2-weighted MRI best displays the true cystic structure of the tumor. Nodular enhancement of the septae indicates potential malignancy, which occurs in up to 30% of MCN [16-19].

### Intraductal Papillary Mucinous Neoplasm (IPMN)

Due to increased detection rates by high-resolution imaging, IPMN is considered the most common cystic neoplasm of the pancreas and is seen more often in men than in women [17]. IPMNs may affect the main duct (28%), side branches (46%), or both ductal components (26%) based on a mucin-producing neoplasm arising from the ductal epithelium [20]. The side-branch type can be found as a solitary or multifocal duct dilatation over the entire pancreas and may also form a system of cystic dilated ducts that may mimic a microcystic appearance, as in SCN. Segmental or general dilatation is typical for the main-duct type, creating a chronic pancreatitis-like appearance. In such cases, patient history is the crucial differential diagnostic information. As main-duct-type IPMN has a low malignant potential, at least a thorough follow-up regimen should be recommend in nonsurgical cases.

### Neuroendocrine Tumors

The WHO (2010) classified these tumors mainly according to their grading (well, moderately, and poorly differentiated) and their hormone activity [gastroenteropancreatic neuroendocrine neoplasm (GEP-NEN)]. In general, these tumors are rare and account for ~5-7% of all pancreatic tumors, with the most common subtypes being insulinoma, gastrinoma, and non-hormone-active tumors. If a specific hormone release is not the leading clinical sign, imaging features of various GEP-NEN are often rather similar, which makes immunohistochemical staining a crucial issue (Fig. 3) [21].

### Insulinoma

The presentation of insulinomas – the most common GEP-NEN (60%) – is determined by hyperinsulinism (Whipple triad: i.e., starvation attack, hypoglycemia after fasting, relief by intravenous (IV) dextrose). Most tumors are solitary (95%), small (<2 cm), hypervascularized, and with a peripherally pronounced enhancement and are localized in the pancreatic body and tail [22, 23].

### Gastrinoma

Gastrinoma is the second most common GEP-NEN (20-30%) and is clinically associated with Zollinger-Ellison syndrome (peptic ulcer disease, diarrhea) due to the massively elevated gastrin blood levels. At detection, the tumors present a moderate size (mean 3 cm, ranging from 0.1 to 20 cm), and in half of the cases with multiple nodules. The vast majority of gastrinoma will arise within the gastrinoma triangle determined by the confluence of the cystic and common bile duct, the junction of the second and third portions of the duodenum, and the junction of the neck and body of the pancreas. On imaging, gastrinomas are revealed as mainly solid tumors with intermediate density and signal intensity on both CT and MRI, with moderate to strong CE. Although ~60% of such tumors are malignant, extensive metastatic spread is rare.

### Other Rare Pancreatic Neoplasm

Besides the neoplasms described above, there is still a wide variety of pancreatic tumors that – in general – can be differentiated only by specific immunohistologic staining. These rare tumors comprise a number of variably differentiated neuroendocrine tumors: carcinoid tumors, mostly without functional activity; rare, malignant pancreatoblastoma [24] in children (a large, encapsulated tumor in the pancreatic head often associated with elevated alpha-fetoprotein levels and metastases to liver and lymph nodes); acinar cell carcinoma, which are relatively large tumors predominantly seen in elderly men, with an imaging appearance similar to pancreatic adenocarcinomas and potential excessive release of serum lipase, followed by focal panniculitis and polyarthritis as a diagnostic hint [25]); solid pseudopapillary tumor (incidental in women 20-30 years of age with a M:F ratio 1:10; large, heterogeneous tumors of uncertain dignity), and occasionally children.

Mesenchymal tumors (sarcoma, cystic dermoid, lymphangioma, leiomyosarcoma, hemangiopericytoma, hemangioma, malignant fibrous histiocytoma, lympho-

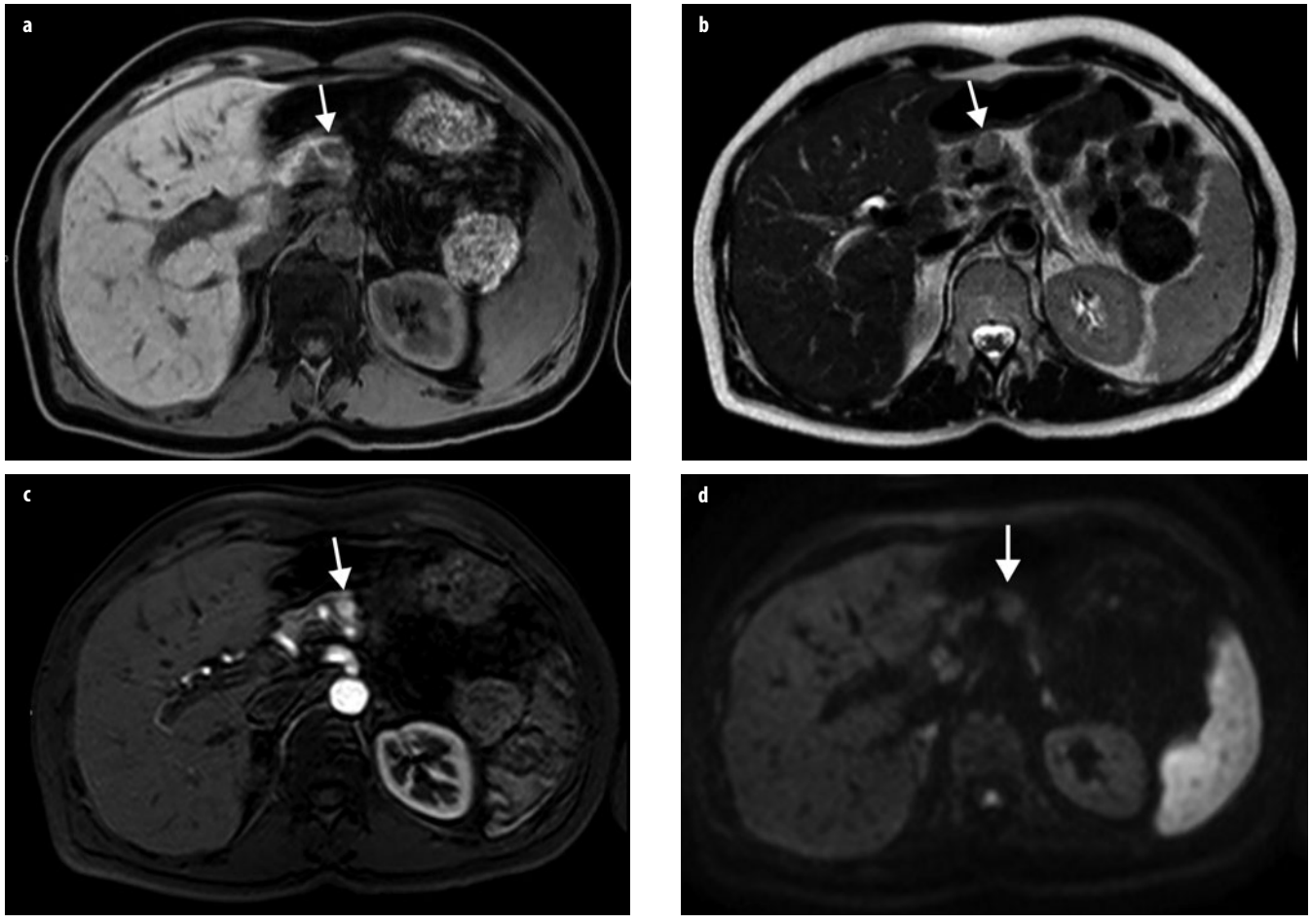


**Fig. 3 a-d.** Small neuroendocrine neoplasm. **a** Axial T1-weighted gradient echo (GRE) image (TR/TE 180/4.66 ms) with fat saturation shows a neuroendocrine neoplasm that appears hypointense compared with adjacent pancreatic parenchyma (*arrow*). **b** Axial T2-weighted turbo spin-echo (TSE) image (TR/TE 4,500/102) shows a small neuroendocrine neoplasm that appears hyperintense compared with adjacent parenchyma (*arrow*). **c** On the axial fat-saturated volumetric T1-weighted GRE image (TR/TE 4.86/1.87 ms) during the pancreatic phase of the dynamic study following gadolinium-chelate administration, the neuroendocrine neoplasm appears hyperintense compared with adjacent pancreatic parenchyma (*arrow*). **d** On axial diffusion-weighted image (DWI) (b=1000) the neuroendocrine neoplasm shows restricted diffusion (*arrow*)

epithelial cysts, primary lymphoma) and secondary tumors (secondary lymphoma, metastases) of the pancreas are very rare and may be identified by specific imaging features such as peripheral nodular enhancement on dynamic imaging or high signal intensity on T1- and T2- weighted imaging (e.g., hemangioma or lipoma). Otherwise, clinical context and histopathological examination will determine the diagnosis.

## Inflammatory Diseases of the Pancreas

In the Western world in particular, the incidence of inflammatory diseases of the pancreas is increasing. The most common causes are biliary stone disease and alcohol abuse; nevertheless, other causes, such as metabolic and systemic inflammatory diseases, are increasingly identified as promoting factors. Depending on the type and severity of the inflammatory process no, mild, or extensive morphological and functional deterioration is seen.

In general, the task of imaging is to monitor substantial structural changes and complications in acute pancreatitis, such as parenchymal integrity vs. necrosis, peripancreatic inflammation, subtile and substantial fluid collections, formation of pseudo and walled-off cysts, vascular and ductal involvement (Fig. 4). In chronic pancreatitis, differentiation of long-term parenchymal and ductal changes from similar changes caused by neoplasms, e.g., focal or complete duct dilation, focal parenchymal lesions, cystic degeneration, is mandatory to rule out potential pancreatic cancer (Fig. 5). Perfusion-weighted MRI, diffusion-weighted imaging (DWI), and FDG-PET can be helpful in such cases.

In chronic pancreatitis, as well as in groove pancreatitis (inflammatory reaction and fluid collection located in the groove between the head of the pancreas, duodenum

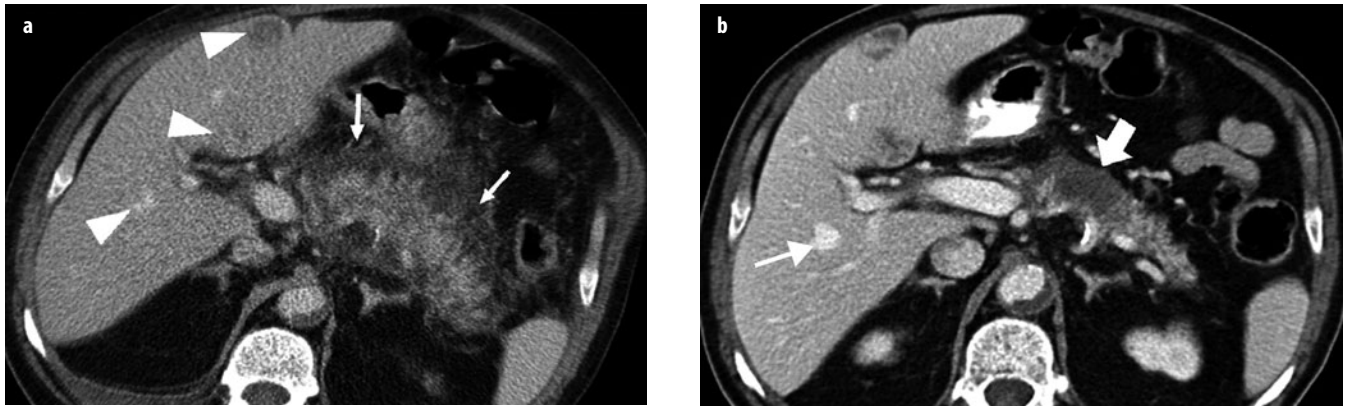


**Fig. 4 a, b.** Acute, severe pancreatitis. **a** At admission, contrast-enhanced computed tomography (CE-CT) during the venous phase displayed a fuzzy contour of the pancreatic gland together with peripancreatic exudation (*arrows*). Note the hypo- and hyperdense hepatic lesions (*arrowheads*). **b** A control scan 10 days later revealed an almost normal gland with resorption of peripancreatic fluid. However, an area showed a lack of enhancement, representing focal necrosis (*large arrow*). In the liver, one lesion turned out to be a hemangioma (*arrow*), whereas the other two lesions were small abscesses

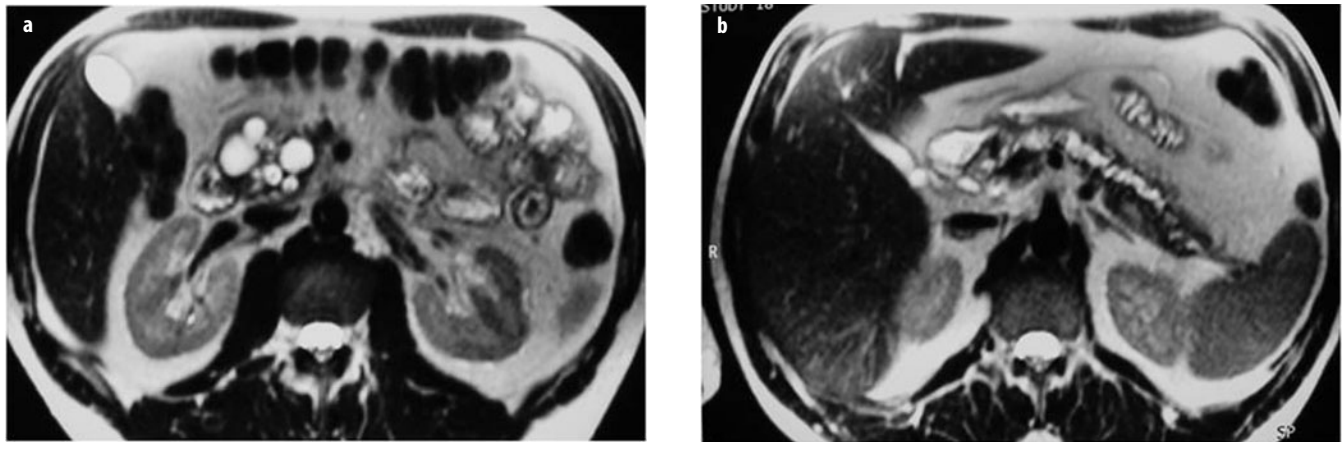


**Fig. 5 a, b.** Cholangiopancreatography (CP). **a** Cystic degeneration of the pancreatic head, together with **b** irregular dilatation of the pancreatic main duct on magnetic resonance imaging (MRI) (fast spin-echo, T2-weighted). Note the similar imaging appearance to other cystic lesions of the pancreas

and common bile duct), and autoimmune pancreatitis (AIP)[26-29].

AIP – formerly described as lymphoplasmacytic sclerosing pancreatitis with cholangitis, nonalcoholic duct-destructive chronic pancreatitis, and chronic sclerosing pancreatitis – is a relatively newly recognized syndrome of clinical and histologic findings, including hypergammaglobulinemia; elevation of serum immunoglobulin (Ig)G4; and a number of antibodies, such as antinuclear antibodies, antibodies against lactoferrin, carbonic anhydrase type II, and rheumatoid factors. Histological features are fibrosis with lymphoplasmacytic infiltration of interlobular ducts. The majority of lymphocytes are CD8+ and CD4+ T, whereas B lymphocytes are less frequent. In general, diagnosis of AIP is established by clinical signs (mild prolonged pancreatitis), laboratory, and morphological findings. An association with other autoimmune diseases, such as Sjögren syndrome, primary biliary cirrhosis, primary sclerosing cholangitis, Crohn's disease, ulcerative colitis, systemic lupus erythematosus, and retroperitoneal fibrosis, is found in a third of cases [30, 31].

At imaging, a focal (mass-forming) or diffuse (sausage-like) enlargement of the pancreas may be present. In CE studies, peripancreatic nodular or rim-like enhancement can be appreciated due to chronic peripancreatic inflammation. Focal AIP of the head that involves the pancreatic and distal common bile ducts needs differentiation from pancreatic carcinoma, thus necessitating biopsy confirmation.

## References


1. Anupindi SA (2008) Pancreatic and biliary anomalies: imaging in 2008. Pediatr Radiol 38 (Suppl 2):S267-271.
2. Yu J, Turner MA, Fulcher AS, Halvorsen RA (2006) Congenital anomalies and normal variants of the pancreaticobiliary tract and the pancreas in adults: part 2, Pancreatic duct and pancreas. AJR Am J Roentgenol 187:1544-1553.
3. Nishino T, Toki F, Oi I et al (2006) Prevalence of pancreatic and biliary tract tumors in pancreas divisum. J Gastroenterol 41:1088-1093.
4. Flejou JF (2011) [WHO Classification of digestive tumors: the fourth edition]. Ann Pathol 31(5 Suppl):S27-31.
5. Tamm EP, Bhosale PR, Lee JH (2007) Pancreatic ductal adenocarcinoma: ultrasound, computed tomography, and magnetic resonance imaging features. Semin Ultrasound CT MR 28:330-338.
6. Wong JC, Lu DS (2008) Staging of pancreatic adenocarcinoma by imaging studies. Clin Gastroenterol Hepatol 6:1301-1308.
7. Stroszczynski C, Grutzmann R, Kittner T (2008) CT and MR imaging of pancreatic cancer. Recent Results Cancer Res 177:5-14.
8. Mori H (2010) New insight of pancreatic imaging: from "unexplored" to "explored". Abdom Imaging 35:130-133.
9. Schima W, Ba-Ssalamah A, Goetzinger P et al (2007) State-of-the-art magnetic resonance imaging of pancreatic cancer. Top Magn Reson Imaging 18:421-429.
10. Edelman RR (2007) MR imaging of the pancreas: 1.5T versus 3T. Magn Reson Imaging Clin N Am 15:349-353, vi.
11. Michl P, Pauls S, Gress TM (2006) Evidence-based diagnosis and staging of pancreatic cancer. Best Pract Res Clin Gastroenterol 20:227-251.
12. Balci NC, Semelka RC (2001) Radiologic diagnosis and staging of pancreatic ductal adenocarcinoma. Eur J Radiol 38:105-112.
13. Kosmahl M, Pauser U, Peters K et al (2004) Cystic neoplasms of the pancreas and tumor-like lesions with cystic features: a review of 418 cases and a classification proposal. Virchows Arch 445:168-178.
14. Garcea G, Ong SL, Rajesh A et al (2008) Cystic lesions of the pancreas. A diagnostic and management dilemma. Pancreatology 8:236-251.
15. Freeman HJ (2008) Intraductal papillary mucinous neoplasms and other pancreatic cystic lesions. World J Gastroenterol 14:2977-2979.
16. Crippa S, Salvia R, Warshaw AL et al (2008) Mucinous cystic neoplasm of the pancreas is not an aggressive entity: lessons from 163 resected patients. Ann Surg 247:571-579.
17. Suzuki Y, Atomi Y, Sugiyama M et al (2004) Cystic neoplasm of the pancreas: a Japanese multiinstitutional study of intraductal papillary mucinous tumor and mucinous cystic tumor. Pancreas 28:241-246.
18. Song SJ, Lee JM, Kim YJ et al (2007) Differentiation of intraductal papillary mucinous neoplasms from other pancreatic cystic masses: comparison of multirow-detector CT and MR imaging using ROC analysis. J Magn Reson Imaging 26:86-93.
19. Brambs HJ, Juchems M (2008) [Cystic tumors of the pancreas]. Radiologe 48:740-751.
20. Sohn TA, Yeo CJ, Cameron JL et al (2004) Intraductal papillary mucinous neoplasms of the pancreas: an updated experience. Ann Surg 239:788-797.
21. Capelli P, Martignoni G, Pedica F et al (2009) Endocrine neoplasms of the pancreas: pathologic and genetic features. Arch Pathol Lab Med 133:350-364.
22. Tamm EP, Kim EE, Ng CS (2007) Imaging of neuroendocrine tumors. Hematol Oncol Clin North Am 21:409-432; vii.
23. Rockall AG, Reznek RH (2007) Imaging of neuroendocrine tumours (CT/MR/US). Best Pract Res Clin Endocrinol Metab 21:43-68.
24. Chung EM, Travis MD, Conran RM (2006) Pancreatic tumors in children: radiologic-pathologic correlation. Radiographics 26:1211-1238.
25. Tatli S, Mortele KJ, Levy AD et al (2005) CT and MRI features of pure acinar cell carcinoma of the pancreas in adults. AJR Am J Roentgenol 184:511-519.
26. Akisik MF, Aisen AM, Sandrasegaran K et al (2009) Assessment of chronic pancreatitis: utility of diffusion-weighted MR imaging with secretin enhancement. Radiology 250: 103-109.
27. Gillams A, Pereira S, Webster G, Lees W (2008) Correlation of MRCP quantification (MRCPQ) with conventional non-invasive pancreatic exocrine function tests. Abdom Imaging 33:469-473.
28. Agarwal B, Krishna NB, Labundy JL et al (2008) EUS and/or EUS-guided FNA in patients with CT and/or magnetic resonance imaging findings of enlarged pancreatic head or dilated pancreatic duct with or without a dilated common bile duct. Gastrointest Endosc 68:237-242.
29. Siddiqi AJ, Miller F (2007) Chronic pancreatitis: ultrasound, computed tomography, and magnetic resonance imaging features. Semin Ultrasound CT MR 28:384-394.
30. Bodily KD, Takahashi N, Fletcher JG et al (2009) Autoimmune pancreatitis: pancreatic and extrapancreatic imaging findings. AJR Am J Roentgenol 192:431-437.
31. Zandieh I, Byrne MF (2007) Autoimmune pancreatitis: a review. World J Gastroenterol 13:6327-6332.

# Adrenal Imaging

William W. Mayo-Smith[1], Isaac R. Francis[2]

[1] Department of Radiology, Warren Alpert School of Medicine Brown University, Rhode Island Hospital, Providence, RI, USA
[2] Department of Radiology, University of Michigan, Ann Arbor, MI, USA

## Introduction

The objectives of this chapter are to: (1) describe the different workups for adrenal masses, depending on clinical scenario, (2) define adrenal incidentaloma, (3) describe imaging techniques to differentiate benign from malignant adrenal masses, and (4) discuss recommended imaging algorithms of workup of an incidental adrenal mass.

The adrenal gland is made up of the catecholamine-producing medulla and the steroid-producing cortex. It is a common site of primary tumors (functional and nonfunctional) and metastases. The workup for an adrenal mass depends on the patient's clinical scenario and whether detection or characterization is the primary goal of imaging. In general, it is useful to separate the workup of an adrenal mass into one of three algorithms: detection of an adrenal tumor in a patient with a known biochemical (adrenal hormonal) abnormality; characterization of an incidental adrenal mass in a patient with a known primary malignant neoplasm; characterization of an incidental adrenal mass in a patient with no underlying malignancy.

## Detecting a Biochemically Active Adrenal Tumor

Biochemically active adrenal neoplasms originating in the adrenal cortex produce an excess of either glucocorticoids, aldosterone, or androgens; originating in the adrenal medulla causes an excess of catecholamines.

### Cushing's Syndrome

Cushing's syndrome results from an overproduction of cortisol by the adrenal cortex, and approximately 80% of these cases are due to stimulation of the adrenal glands by a pituitary adenoma. A primary adrenal cortical tumor is seen in 20% of patients with Cushing's syndrome, and $<1\%$ have ectopic production of adrenocorticotropic hormone (ACTH) by a nonpituitary neoplasm, which may be located either in the chest, abdomen, or pelvis. The workup of patients presenting with Cushing's syndrome involves a dexamethasone suppression test, pituitary magnetic resonance imaging (MRI) to look for a pituitary adenoma, and computed tomography (CT) depending on the suspected source of ACTH production. If pituitary and adrenal neoplasms are excluded and an ectopic source of hormone secretion is suspected, then a chest and abdominal/pelvis CT should be performed.

### Conn's Syndrome

Conn's syndrome results from an adrenal cortical tumor producing elevated levels of aldosterone, leading to increased sodium retention, hypertension, and potassium wasting. The diagnosis is suspected in a hypertensive patient with low serum potassium and is confirmed by measuring the ratio of serum aldosterone to renin levels. When the diagnosis is suspected based on biochemical assays, CT scans using thin collimation (2-3 mm) targeted to the adrenals is useful to attempt to differentiate a small adrenal neoplasm from bilateral hyperplasia. If findings are equivocal on CT – as is often the case, especially in the older population – then adrenal venous sampling to localize and lateralize the site of elevated aldosterone production should be performed. At some medical centers, adrenal venous sampling is the initial study of choice, especially in patients $>40$ years.

### Pheochromocytoma

Pheochromocytomas originate from the adrenal medulla and produce an excess of catecholamines, causing hypertension. These tumors are solitary and occur sporadically in the majority of cases. However, several syndromes such as multiple endocrine neoplasia (MEN) type 2 and von Hippel-Lindau, neurofibromatosis type 1, can be associated with these tumors. Studies show that about 25% of pheochromocytomas may be familial. Patients with mutations in the succinate dehydrogenase

*Diseases of the Abdomen and Pelvis 2014-2017*,
DOI: 10.1007/978-88-470-5659-6_16 

subunits have a high risk of developing pheochromocytomas and paragangliomas. The most appropriate first-line test is measuring plasma metanephrines. If these are equivocal, then urinary metanephrines can be measured. Once the biochemical diagnosis has been established, the primary role of the radiologist is to determine the site of origin of the pheochromocytoma. More than 95% of pheochromocytomas originate in the adrenal glands; therefore, CT or MRI examination of the abdomen and pelvis is sufficient. Extra-adrenal paragangliomas also can occur along the sympathetic chain. MRI of pheochromocytoma typically demonstrates a T2-weighted hyperintense mass, although the finding is nonspecific, as pheochromocytomas can also have intermediate signal intensity on T2-weighted images, thus simulating adrenal cortical carcinoma; also, other adrenal lesions can be T2 hyperintense (adrenal cysts and hemangiomas/lymphangiomas). Whereas metaiodobenzylguanidine (MIBG) scintigraphy has high specificity (>95%) for diagnosing pheochromocytoma, its sensitivity is only 77-90%. Studies suggest that MIBG scintigraphy should be used selectively and only in patients with familial or hereditary disorders in detecting metastatic disease and in patients with biochemical evidence for pheochromocytoma and negative CT or MRI. These studies also conclude that MIBG scintigraphy offers no added advantage in patients with biochemical evidence for a pheochromocytoma, no hereditary or familial diseases, and a unilateral adrenal mass detected on CT or MRI [1, 2]. The standard treatment of a biochemically active adrenal tumor is open or laparoscopic resection.

## Staging Patients with Known Underlying Extra-Adrenal Malignancy

Evaluating the adrenal gland in the oncology patient is complicated because the gland is a frequent site of metastases, but benign adrenal adenomas are much more common (detected in 2-5% of autopsy series). Thus, the presence of an adrenal mass in these patients does not necessarily implicate metastases. The role of imaging in the oncology patient is to detect an abnormality of the adrenal gland and characterize it as either benign or malignant. Positron emission tomography (PET) imaging is being used more frequently in the staging of neoplasms in oncology patients. Adrenal metastases tend to demonstrate increased activity, having a greater uptake relative to the liver, whereas most benign adenomas do not. Studies confirm the high sensitivity of PET/CT in detecting malignant lesions, but the specificity is lower (87-97%). This loss of specificity is attributable to a small number of adenomas and other benign lesions that mimic malignant lesions [3, 4].

Depending on the primary tumor, CT or PET/CT is a useful first-line exam to stage a known neoplasm. If the patient demonstrates multiple sites of metastatic disease, then characterization of an adrenal mass in not important. If the adrenal mass is the only abnormality, further evaluation is required to characterize the mass and differentiate an adenoma from a metastatic focus.

There are two main criteria (anatomical and physiological) used to differentiate benign adenomas from malignant adrenal masses: (1) intracellular lipid content of the adrenal mass, which represents the anatomical difference between adenomas and metastases, and (2) differences in vascular enhancement patterns, which represent the physiological difference. Approximately 80% of benign adenomas (lipid-rich adenomas) have abundant intracytoplasmic lipid in the adrenal cortex and thus are of low density on unenhanced CT or show signal loss on out-of-phase chemical-shift MRI (CS-MRI). Conversely, most metastases have little intracytoplasmic lipid and thus do not have a low density on noncontrast CT. At a threshold of 10 HU, CT has 71% sensitivity and 98% specificity for characterizing lipid-rich adrenal adenomas. Whereas a low HU is useful to characterize lipid-rich adenomas, it is estimated that up to 20% of adenomas, lipid-poor adenomas, do not contain sufficient lipid to be of low density on unenhanced CT [5-7]. Histogram analysis of adrenal masses (evaluating microscopic levels of lipid on a pixel-by-pixel basis) is rarely used to differentiate adenomas from metastases on non-contrast- and contrast-enhanced CT [8]. However, due to differing results in various studies, this approach has limited use in current clinical practice.

The physiological difference in perfusion between adenomas and metastases can be used to differentiate them. Lipid-rich and lipid-poor adenomas both enhance rapidly with intravenously administered contrast (iodinated CT contrast or MR gadolinium chelates) and also have rapid washout. Metastases also enhance vigorously with dynamic contrast, but washout is more prolonged than in adenomas. This difference in washout has been exploited to further differentiate benign from malignant adrenal lesions by comparing precontrast HU values with dynamic and 15-min delayed HU values [9, 10]. Absolute percent washout (APW) values are calculated by the formula: (HU at dynamic CT – HU at noncontrast CT)/(HU at 15-min delayed CT – HU at noncontrast CT) × 100. A value ⩾60% is diagnostic of an adenoma. Relative percent washout (RPW) is used when a noncontrast CT value is not available and the dynamic enhanced values are compared to 15-min delayed scans. RPW is calculated by the formula: [(HU dynamic CT – HU 15-min delayed CT)/HU dynamic CT ] × 100. A value ⩾40% is diagnostic of adenoma. Specificity for adenoma diagnosis using these washout threshold values is >90%. Dual-energy CT is also used to characterize lipid-rich adenomas using virtual unenhanced images. For adrenal masses >1 cm, specificity for characterizing a lesion as being benign was 100% in a small series of 42 patients with 51 adrenal masses [11].

Adenomas can be differentiated from metastases using CS-MRI if the patient has a nondiagnostic CT, is allergic

to iodinated contrast, or in young patients in whom radiation exposure is a concern [12, 13]. Most adrenal adenomas contain sufficient intracellular lipid and lose signal on the out-of-phase image compared with the spleen. Visual analysis is adequate in most cases to make this observation, but quantitative methods, such as signal-intensity index, may also be useful [14 ,15]. Diffusion-weighted imaging is used to help differentiate between adenomas and malignant masses but with limited success, as in most studies, adenomas and malignant lesions both demonstrate restricted diffusion [16-19].

If CT, MRI, or PET findings are equivocal, adrenal biopsy using CT guidance should be performed, particularly to stage a lung carcinoma in a patient who has no other sites of metastatic disease, as this may determine whether surgical resection is a therapeutic option. The role of adrenal biopsy has evolved in the last few years; in addition to the above indication of an indeterminate adrenal mass, adrenal biopsy can also be used to confirm metastatic disease to the adrenal glands in patients with suspected solitary adrenal metastasis. CT-guided biopsy is safe, with a diagnostic accuracy of 96% and a 3% complication rate [20].

## Evaluation of an Incidentally Discovered Adrenal Mass

As indications for abdominal imaging (particularly CT) continue to increase, so does the detection rate of the incidental adrenal mass, given the high prevalence of adenomas in the general population (3-7%) [21-23]. In general, the overwhelming majority of incidentally discovered adrenal masses (incidentalomas) are benign in a patient with no known malignancy [24]. An adrenal incidentaloma is defined as "an unsuspected and asymptomatic mass (measuring $\geqslant$1 cm) detected on imaging exams obtained for other purposes".

Risk factors for an incidental adrenal mass being malignant include lesion size, change in size, and patient history of malignancy. For patients with no history of malignancy, most small ($<$4 cm) incidentally discovered adrenal masses are benign, and an extensive and costly workup is usually not justified. Endocrinologists may recommend biochemical workup and imaging follow-up to exclude functioning adrenal tumors for all adrenal incidentalomas [25]; however, hyperfunctioning adrenal tumors rarely present as an incidental adrenal mass, so this practice is coming under scrutiny [26].

If an adrenal incidentaloma has imaging features diagnostic of a benign lesion, such as a lipid-rich adenoma ($\leqslant$10 HU on CT) or myelolipoma, no additional workup or follow-up imaging is needed. Adrenal masses that have been stable for at least 1 year according to prior imaging exams are benign, with no need for imaging follow-up. However, if the lesion is enlarging, then it may be prudent to proceed to adrenal biopsy or resection. A common scenario is an adrenal incidentaloma that measures $>$10 HU on initial, intravenously administered, contrast-enhanced CT. What is the best way to proceed in this scenario? Statistically, the lesion is most likely benign, and a history of known malignancy is important [24]. If there is no history of malignancy, either no further imaging or a follow-up unenhanced CT or CS-MRI exam in 12 months can be considered. However, if there is a history of malignancy or there are suspicious imaging features on contrast-enhanced CT (central necrosis, irregular margins), then one should proceed with an unenhanced CT or CS-MRI; if these exams do not confirm that the lesion is a lipid-rich adenoma, an adrenal protocol CT with washout calculations is recommended [27]. If the lesion does not have the imaging and washout features of a benign lesion, then a biopsy or an adrenalectomy may be appropriate.

In patients with a prior history of cancer and an adrenal mass of any size, if imaging features on contrast-enhanced CT are not diagnostic for a benign lesion and there is no prior imaging, one can consider an unenhanced CT or CS-MRI or PET imaging. If the lesion does not behave like a typical adenoma, then one should proceed to adrenal CT with washout. If the lesion shows neither washout features of an adenoma nor findings of an adenoma on PET imaging, then a biopsy should be considered. Patient history of malignancy is an important risk factor for adrenal metastatic disease, as no imaging features are diagnostic on routine portal venous phase contrast enhanced CT performed for other reasons [27]. In patients with no history of cancer and an adrenal mass $>$4 cm, resection should be considered; but if there is a history of prior cancer, then a PET scan or a biopsy is recommended [27]. An algorithm for treating an adrenal incidentaloma published in the *Journal of the American College of Radiology* is shown in Fig. 1 [28]. Preliminary evidence suggests that adoption of these recommendations leads to a more standardized approach to the incidentally discovered adrenal mass [29].

## Adrenal Cortical Carcinoma

Adrenal cortical tumors are rare with a frequency of 1-2 per million and are mostly sporadic, but can be associated with several syndromes, the most common ones being multiple endocrine neoplasia type I (MEN-I), Li-Fraumeni syndrome, Carney complex, and Beckwith-Weidemann syndrome. The majority of tumors are usually large at presentation (typically over 6 cm), and have areas of degeneration and necrosis, with calcification. Heterogeneous enhancement is typically seen with IV contrast administration. Tumor extension into the inferior vena cava is an uncommon occurrence. They can either present as hyperfunctioning or nonfunctioning tumors. When they are hyperfunctioning, patients usually present with Cushing syndrome, and less commonly with virilization, and feminization. Nonfunctioning tumors are usually very large at presentation [30-32].

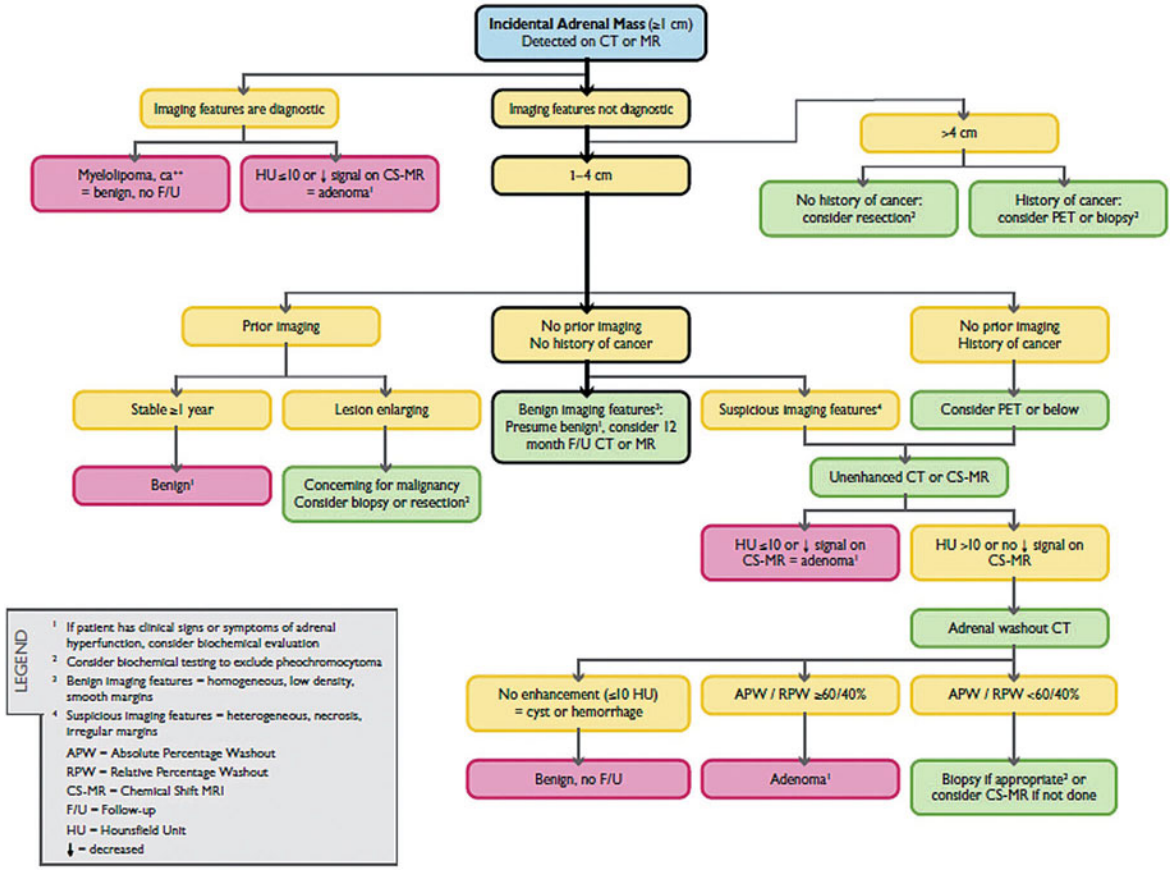


**Fig. 1.** Algorithm for evaluating an adrenal incidentaloma (reproduced with permission from [28])

## References


1. Miskulin J, Shulkin BL, Doherty GM et al (2003) Is preoperative iodine 123 metaiodobenzylguanidine scintigraphy routinely necessary before initial adrenalectomy for pheochromocytoma? Surgery 134:918-923.
2. Greenblatt DY, Shenker Y, Chen H (2008) The utility of metaiodobenzylguanidine (MIBG) scintigraphy in patients with pheochromocytoma. Ann Surg Oncol 15:900-905.
3. Boland GW, Blake MA, Holalkere NS, Hahn PF (2009) PET/CT for the characterization of adrenal masses in patients with cancer: qualitative versus quantitative accuracy in 150 consecutive patients. AJR Am J Roentgenol 192:956-962.
4. Groussin L, Bonardel G, Silvéra S et al (2009) 18F-Fluoro deoxyglucose positron emission tomography for the diagnosis of adrenocortical tumors: a prospective study in 77 operated patients. J Clin Endocrinol Metab 94:1713-1722.
5. Lee MJ, Hahn PF, Papanicolaou N et al (1991) Benign and malignant adrenal masses: CT distinction with attenuation coeff icients, size, and observer analysis. Radiology 179:415-418.
6. Korobkin, M, Brodeur FJ, Francis IR et al (1998) CT time-attenuation washout curves of adrenal adenomas and nonadenomas. AJR Am J Roentgenol 170:747-752.
7. Boland GW, Lee MJ, Gazelle GS et al (1998) Characterization of adrenal masses using unenhanced CT: an analysis of the CT literature. AJR Am J Roentgenol 171:201-204.
8. Bae KT, Fuangtharnthip P, Prasad SR et al (2003) Adrenal masses: CT characterization with histogram analysis method. Radiology 228:735-742.
9. Korobkin M, Giordano TJ, Brodeur FJ (1996) Adrenal adenomas: relationship between histologic lipid and CT and MR findings. Radiology 200:743-747.
10. Caoili EM, Korobkin M, Francis IR et al (2002) Adrenal masses: characterization with combined unenhanced and delayed enhanced CT. Radiology 222:629-633.
11. Gnannt R, Fischer M, Goetti R et al (2012) Dual-energy CT for characterization of the incidental adrenal mass: preliminary observations. Am J Roentgenol 198:138-144.
12. Tsushima Y, Ishizaka H, Matsumoto M (1993) Adrenal masses: differentiation with chemical shift, fast low-angle shot MR imaging. Radiology 186:705.
13. Israel GM, Korobkin M, Wang C et al (2004) Comparison of unenhanced CT and chemical shift MRI in evaluating lipid-rich adrenal adenomas. AJR Am J Roentgenol 183:215-219.
14. Fujiyoshi F, Nakajo M, Fukukura Y, Tsuchimochi S (2003) Characterization of adrenal tumors by chemical shift fast low-angle shot MR imaging: comparison of four methods of quantitative evaluation. AJR Am J Roentgenol 180:1649-1657.
15. Mayo-Smith WW, Lee MJ, McNicholas MM et al (1995) Characterization of adrenal masses (5 cm) by use of chemical shift MR imaging: observer performance versus quantitative measures. AJR Am J Roentgenol 165:91-95.
16. Tsushima Y, Takahashi-Taketomi A, Endo K (2009) Diagnostic utility of diffusion-weighted MR imaging and apparent diffusion coefficient value for the diagnosis of adrenal tumors. J Magn Reson Imaging 29:112-117.
17. Miller FH, Wang Y, McCarthy RJ et al (2010) Utility of diffusion-weighted MRI in characterization of adrenal lesions. Am J Roentgenol 194:W179-185.

18. Sandrasegaran K, Patel AA, Ramaswamy R et al (2011) Characterization of adrenal masses with diffusion weighted imaging. Am J Roentgenol 197:132-138.
19. Song J, Zhang C, Liu Q et al (2012) Utility of chemical shift and diffusion-weighted imaging in characterization of hyperattenuating adrenal lesions at 3.0T. Eur J Radiol 81:2137-4320.
20. Silverman SG, Mueller PR, Pinkney LP et al (1993) Predictive value of image-guided adrenal biopsy: analysis of results of 101 biopsies. Radiology 187:715-718.
21. Grumbach MM, Biller BM, Braunstein GD et al (2003) Management of the clinically inapparent adrenal mass ("incidentaloma"). Ann Intern Med 138:424-429.
22. Young WF (2007) Clinical practice. The incidentally discovered adrenal mass. N Engl J Med 356:601-610.
23. Choyke PL (2006) ACR Appropriateness Criteria on incidentally discovered adrenal mass. J Am Coll Radiol 3:498-504.
24. Song JH, Chaudhry FS, Mayo-Smith WW (2008) The incidental adrenal mass on CT: Prevalence of adrenal disease in 1049 consecutive adrenal masses in patients with no known malignancy. AJR Am J Roentgenol 190:1163-1168.
25. NIH state-of-the-science statement on management of the clinically inapparent adrenal mass ("incidentaloma") (2002) NIH Consens State Sci Statements 19:1-25.
26. Boland GW, Blake MA, Hahn PF, Mayo-Smith WW (2008) Imaging characterization of adrenal incidentalomas: principles, techniques and algorithms. Radiology 249:756-775.
27. Song JH, Grand DJ, Beland MD et al (2013) Morphologic features of 211 adrenal masses at initial contrast-enhanced CT: can we differentiate benign from malignant lesions using imaging features alone? AJR Am J Roentgenol 201:1248-1253.
28. Berland LL, Silverman SG, Gore RM et al (2010) Managing incidental findings on abdominal CT: White Paper of the American College of Radiology Incidental Findings Committee. J Am Coll Radiol 7:754-773.
29. Berland LL, Silverman SG, Megibow AJ, Mayo-Smith WW (2013) American College of Radiology Members' Response to Journal of American College of Radiology White Paper on the Management of Incidental Abdominal CT Findings. J Am Coll Radiol doi: 10.1016/j.jacr.2013.06.002. [Epub ahead of print]
30. Bharwani N, Rockall AG, Sahdev A et al (2011) Adrenocortical carcinoma: the range of appearances on CT and MRI. AJR Am J Roentgenol 196:W706-W714.
31. Schlund JF, Kenney PJ, Brown ED et al (1995) Adrenocorticalcarcinoma: MR imaging appearance with current techniques. J Magn Reson Imaging 5:171-174.
32. Chiche L, Dousset B, Kieffer E, Chapuis Y(2006) Adrenocortical carcinoma extending into the inferior vena cava: presentation of a 15-patient series and review of the literature. Surgery 139:15-27.

# Renal Tumors

Lejla Aganovic[1], Richard H. Cohan[2]

[1] University of Michigan, Ann Arbor, MI, USA
[2] University of California at San Diego, San Diego, CA, USA

## Introduction

Here we review recent advances in renal mass imaging, primarily with computed tomography (CT) and magnetic resonance imaging (MRI), and discuss developments in the use of imaging for identifying renal masses, differentiating benign from malignant renal lesions, and assessing patients following renal mass treatment.

## Ultrasonography

Although noncontrast ultrasound (US) evaluates the internal morphology of cystic lesions with greater detail than computed tomography (CT), it is not as sensitive as CT or MRI in detecting renal masses. Furthermore, US is limited in its ability to characterize renal masses, and most consider it diagnostically definitive only when it identifies a renal mass as a simple cyst.

## CT and MRI Techniques

Several phases of renal contrast-enhancement have been identified on CT and MRI. During the arterial phase, which begins ~20 s after bolus injection of contrast material, renal arteries and renal cortex enhance briskly. During the corticomedullary phase (CMP), which occurs ~60-70 s after contrast injection begins, arterial enhancement diminishes, although corticomedullary differentiation persists, with the renal medulla remaining hypoenhancing. During the nephrographic phase (NP), which usually begins 90-100 s after contrast injection starts, renal parenchymal enhancement is homogeneous. There is no corticomedullary differentiation. During the excretory phase (EP), which begins at ~120-180 s, renal parenchymal enhancement remains homogeneous but diminished. Contrast material is now seen in the renal collecting systems.

Thorough CT evaluation of a patient with a known or suspected renal mass requires that at least two series be obtained: unenhanced and NP or EP images [1]. The vast majority of renal cell carcinomas (RCCs) measure $\geqslant$20 Hounsfield units (HU) and $\leqslant$70 HU on precontrast images [2], with lesions outside of this range nearly always representing simple or hyperdense cysts. Most solid renal masses, including RCC, demonstrate enhancement of $\geqslant$15-20 HU on NP images; however, some NP-enhancing masses do not demonstrate enhancement on CMP images.

MRI examinations to evaluate a known or suspected mass should include T1-weighted sequences obtained before and after gadolinium (Gd) administration [3], and T2- and diffusion-weighted sequences. When assessing renal lesions on MRI, it is extremely important to determine whether there is contrast enhancement (which can be used to differentiate benign cysts from neoplasms). Unlike CT, where contrast enhancement can be quantitatively assessed by measuring changes in HU between pre- and postcontrast images, detecting enhancement on MRI can represent a diagnostic challenge, especially in lesions that have high signal on precontrast T1-weighted images (such as lesions with hemorrhagic or proteinaceous material). In such cases, subtraction imaging (where precontrast T1-weighted images are digitally subtracted from postcontrast T1-weighted images) is a valuable postprocessing technique, with any remaining signal representing true enhancement [3]. Additional MRI techniques that may be helpful include fat suppression and in- and opposed-phase imaging.

## Very Small Renal Masses

Most renal masses detected with CT and some detected with MRI cannot be characterized due to their small size. For CT, this is felt to be true for renal masses $<$1.5 cm in diameter. Accurate attenuation measurements in these lesions are often problematic due to volume averaging and pseudoenhancement. Because very small renal masses are so common, further assessment of all of these lesions is not feasible, even though a few will be cancers. Follow-up imaging of tiny renal masses should be

*Diseases of the Abdomen and Pelvis 2014-2017*,
DOI: 10.1007/978-88-470-5659-6_17 

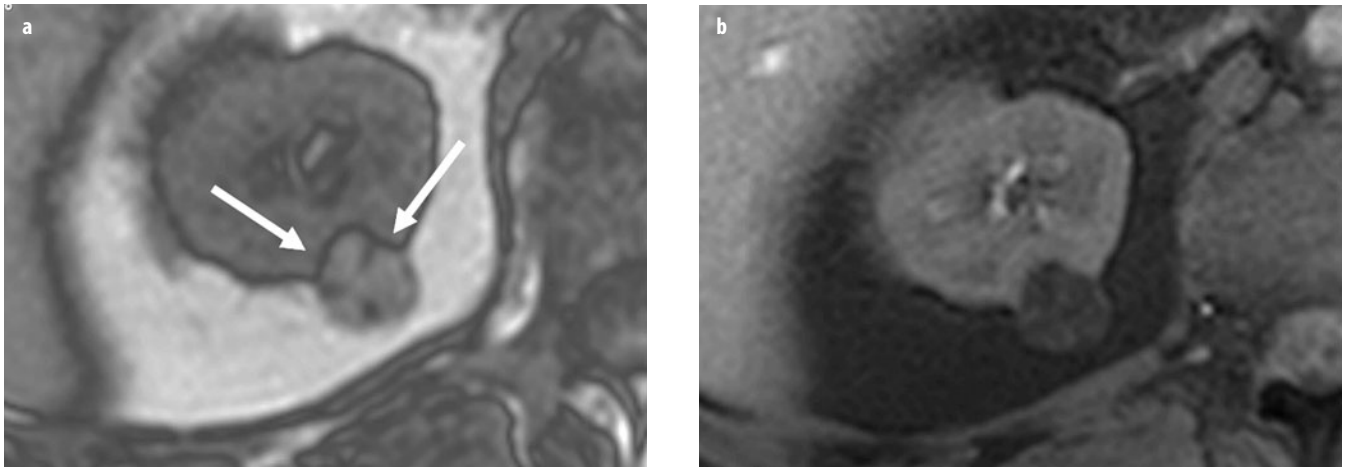


**Fig. 1 a, b.** **a** Axial opposed-phase T1-weighted magnetic resonance image (MRI) shows hyperintense mass in the upper pole of the left kidney. India ink artifact (*arrows*) is present at the interface of renal mass and kidney, which is diagnostic of angiomyolipomas (AML). **b** The mass loses signal on fat-suppression images, confirming the diagnosis of AML

performed only when: (a) heterogeneity suggests that a lesion may not be a simple cyst, (b) the lesion is detected in a young patient (<40 years), or (c) a new small mass is seen in a patient at high-risk for renal malignancy (such as in those with von Hippel-Lindau, hereditary papillary RCC, or hereditary leiomyomatosis-RCC syndromes) [4]. In these instances, further evaluation with MRI can be performed and/or by obtaining long-term imaging follow-up (up to 5 years). Even if a mass being followed is later found to be a small cancer, follow-up can be obtained in most cases without change in tumor stage. Most small RCC grow slowly, with a mean growth rate of 0.4-0.5 cm/year [5]. In fact, on a 6-month follow-up examination, the typical growth of a RCC is near the range of CT measurement error (2-3 mm).

## Cystic Renal Masses

In 1986, Bosniak described his CT cyst classification system [6], categorizing cysts according to their likelihood of being malignant. This system has undergone a number of revisions, with a more recent version published in 2005 [7]. According to Bosniak, lesions with no or minimal complexity on CT, classified as category I or II lesions, are nearly always benign and do not require follow-up. Only a tiny percentage of these contain malignant cells. Category IIF lesions require imaging follow-up with immediate MRI and/or with surveillance imaging (usually with CT), as a few of these are malignant. When these follow-up studies are interpreted, it must be remembered that both benign and malignant lesions can enlarge over time. Therefore, it is important to assess cystic lesions for increasing complexity (such as development of new wall thickening or nodularity), which is the best predictor of malignancy. Bosniak category III and IV cysts should be treated in most patients, as many of these are cancers, and imaging distinction between benign and malignant lesions is not possible.

When the Bosniak system is used with MRI, ~80% of cystic masses demonstrate similar complexity, as seen on CT, but the remainder appear more complex, revealing additional septations, wall or septal thickening, or subtle enhancement [8]. Whereas this is due in part to the ability of MRI to detect some internal cyst features not visible with CT, MRI is also more prone to artifacts.

## Angiomyolipomas

Whereas nearly all angiomyolipomas (AMLs) are echogenic on US, so are many small RCCs. Acoustic shadowing has been identified posterior to some echogenic AMLs but not posterior to echogenic RCCs; this finding is not accepted as conclusive evidence of an AML at many institutions. Thus, echogenic masses generally are evaluated further with CT or MRI to determine whether macroscopic fat is present [9]. If macroscopic fat is identified on CT or MRI, then the mass can be diagnosed as an AML (with only case-reportable exceptions).

On CT, visualization of even small areas within a renal mass measuring ⩽−10 HU is considered diagnostic of macroscopic fat and of an AML [10]. On MRI, such fat typically has high T1 and T2 signal and loses signal with fat suppression. On opposed-phase chemical-shift imaging, there is a characteristic “India ink” artifact at fat-water interfaces in the AML and between the AML and adjacent renal tissue (Fig. 1) [11].

Occasionally, AMLs can be highly exophytic and difficult to differentiate from perinephric liposarcomas. This is an important distinction given the different treatments and prognoses for these two neoplasms. Imaging features have been identified to facilitate differentiation. Fatty perinephric masses are more likely to be exophytic AMLs if they contain large vessels that extend to the renal

cortex or if they are associated with a renal parenchymal defect [12].

Some AMLs do not contain easily identifiable macroscopic fat. Many studies attempted to identify small foci of fat in these minimal fat-containing AMLs (mfAMLs) in the hope that this might permit these lesions to be correctly distinguished from other solid renal neoplasms. The utility of unenhanced CT attenuation, CT histograms, and quantitatively assessed fat on MRI have been assessed in permitting such distinctions to be made [13-15]. However, results are mixed. In some studies, mfAMLs contained more measureable fat than RCC, whereas this was not the case in others.

Additional CT and MRI features independent of fat detection have also been evaluated. On CT, mfAMLs generally have higher unenhanced attenuation than normal renal parenchyma. However, papillary RCC can also demonstrate this feature, although usually not to as great an extent [16]. Unlike many papillary cancers, mfAMLs frequently demonstrate identifiable intratumoral vessels and pronounced enhancement after contrast material administration [16]. On MRI, a diagnosis of mfAML should be considered (albeit not definitively) if a solid mass demonstrates low signal intensity on T2-weighted sequences. Whereas these MRI characteristics are not seen in the majority of RCCs, they can also be encountered in papillary RCCs. As with CT, mfAMLs also usually demonstrate more contrast enhancement on MRI than do papillary renal neoplasms.

## Differentiating Other Solid Renal Masses

### Differences in Tumor Morphology

Nearly all malignant and many benign solid renal masses typically do not contain macroscopic fat. The malignancies include all RCC types, including clear cell (most common), papillary, chromophobe, collecting duct, and medullary cancers, and the more recently described XP11.2 translocation RCC. Upper-tract urothelial cancers and primitive neuroectodermal neoplasms also can present as solid renal masses.

Benign solid renal masses that contain little or no fat include the aforementioned mfAMLs, oncocytomas, papillary adenomas, and renomedullary interstitial cell tumors, and more rarely, metanephric neoplasms, hemangiomas and lymphangiomas, leiomyomas, juxtaglomerular tumors, and mixed epithelial and stromal tumors.

Many papers have attempted to distinguish among various non- or minimal-fat- containing solid renal masses on CT and MRI. A few characteristic imaging features for the different neoplasms are summarized here.

### Oncocytoma

Oncocytomas may contain central scars that can be detected on imaging studies; however, this feature is not diagnostic. Necrosis in RCC and scars in oncocytomas are usually indistinguishable from one another. Further, most oncocytomas evaluated on CT do not contain identifiable central scars [17]. Following contrast material administration, on CMP images, most oncocytomas demonstrate less mean enhancement than do clear cell RCC; however, there is overlap [18]. In contrast to clear cell RCC, peak oncocytoma enhancement usually does not occur until the NP [19]. In one study of small renal masses ($<$4 cm), only oncocytomas demonstrated $>$50% washout on delayed-phase images [20].

Another imaging feature to differentiate oncocytoma from RCC is segmental enhancement inversion (SEI), in which two differently enhancing components identified on CMP images reverse their attenuation on EP images, with the initially higher attenuation briskly enhancing component becoming lower in attenuation than the initially lower attenuation less intensely enhancing component. In one study, SEI was seen in 17 of 33 small ($<$4 cm) oncocytomas [21]. Detecting this feature has not been consistent, however. In another publication, this finding was noted in only one of 16 small oncocytomas [22].

### Clear Cell RCC

Clear cell cancers often present as heterogeneous, solid renal cortical masses, with low-attenuation cystic and brisky enhancing components (compared with other RCC cell types). On CT and MRI, clear cell carcinomas usually demonstrate considerably greater and peak enhancement on CMP images than papillary or chromophobe RCCs [18, 19, 23]. Clear cell carcinomas also commonly enhance more heterogeneously (Fig. 2).

**Fig. 2.** Clear cell renal cell carcinoma (RCC). Contrast-enhanced computed tomography (CT) image during the corticomedullary phase (CMP) demonstrates a heterogeneously and briskly enhancing right renal mass, consistent with a clear cell RCC

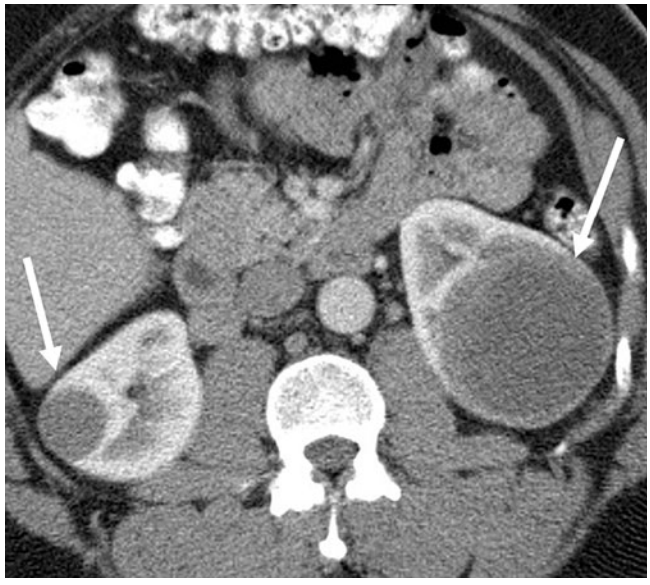

**Fig. 3.** Papillary renal cell carcinoma (RCC). Contrast-enhanced computed tomography (CT) image demonstrates bilateral renal masses (*arrows*) that are hypoenhancing and homogeneous, consistent with papillary RCC

### Papillary RCC

On contrast-enhanced CT or MRI, the most common two papillary subtypes, the better-prognosis type 1 tumors and the more aggressive type II tumors both tend to demonstrate better well-defined margins, greater homogeneity, and lesser and greater delayed enhancement than other RCC cell types (Fig. 3) [24, 25]. Papillary cancers do not demonstrate peak enhancement until NP and/or EP. On MRI, many papillary cancers demonstrate characteristic T2-signal hypointensity [26]. In comparison, only a small minority of clear cell RCC are T2 hypointense [26].

### Uncommon RCC Types

In comparison with other types of RCC, medullary, collecting duct, and XP11.2 translocation cancers generally arise in the medulla. Whereas collecting-duct cancers frequently occur in older adults, renal medullary and XP11.2 cancers are usually encountered in young patients, with XP11.2 RCC accounting for about one third of pediatric RCC [27]. Medullary RCC typically develops in patients with sickle cell trait [28].

### Urothelial Neoplasms

It can occasionally be difficult to distinguish centrally located RCC from urothelial cancers; however, several features can be used to suggest that a centrally located renal mass is a urothelial rather than a RCC, including an epicenter in the renal collecting system, a renal pelvic-filling defect, preservation of normal renal contour, lack of cystic/necrotic areas, homogeneous enhancement with contrast material, and extension toward the ureteropelvic junction [29].

### Other Types

Other abnormalities that can produce centrally located renal masses include renal lymphoma and renal artery aneurysms.

### Solid Renal Mass Growth Rates

One cannot rely on differences in growth rates to distinguish among different RCC cell types. In one series, for example, neither the initial size of a detected RCC nor its cell type predicted the likelihood that the cancer would be more or less likely to grow quickly.

As with complex cystic renal masses, benign and malignant solid renal masses can remain stable in size or enlarge, with growth rates of both types of lesions usually being slow and similar [30]. It is suggested that growth of a renal mass can only be considered suggestive of malignancy when such growth is unusually rapid (>5 mm within 12 months) [31].

### Current Status of Imaging for Solid Renal Mass Differentiation

Due to overlap of many of the above-described imaging findings, we believe that, at the present time, imaging differentiation of malignant from benign non-fat-containing solid renal masses (or of various types of malignant solid renal masses) is not possible in any given case. This once was not felt to be an important problem, as it was believed that the vast majority of solid renal masses were RCC. It has become apparent that a sizeable minority of small solid renal masses are benign: about 20% of solid renal masses <4 cm in diameter are benign [32], with the frequency of benign tumors being even greater for smaller lesions [32].

Given the substantial overlap in imaging features of benign and malignant lesions, an increasing number of institutions perform biopsies of many, or even all, detected solid renal masses. Although there was some hesitation about performing biopsies of masses that could represent RCC due to concerns about diagnostic errors, tract seeding, or bleeding, it is now widely accepted that percutaneous biopsy of a solid renal mass can be performed accurately and safely in the vast majority of patients [33]. In particular, percutaneous biopsy differentiation of oncocytomas is now considered reliable in most patients, with only a few biopsies of oncocytic tumors being indeterminate [34, 35]. Even if biopsy is generally accurate in determining whether a renal mass is benign or malignant and in assessing RCC cell type, debate about whether a percutaneous biopsy might occasionally underestimate the grade of an RCC by failing to sample the portion that contains

the most aggressive cells. It is not yet clear whether undergrading will be a clinically significant problem.

## Pretreatment Assessment of RCC

CT and MRI (preferably obtained during the portal venous phase) are highly accurate in staging and localizing RCC, with specific TNM staging provided in Table 1.

The greatest RCC staging problem relates to determining whether there is tumor extension through the capsule and into renal sinus fat (stage T3a). It is highly common to identify increased stranding in the perinephric fat adjacent to a RCC. Whereas capsular invasion is unlikely if no such stranding is present, when stranding is identified, it could be due to tumor extension or to benign causes (perinephric vessels, edema). In one study of 109 patients, linear and/or nodular changes were noted in the perinephric fat in 55 patients, only 26 of whom were ultimately determined to have stage T3a disease [36]. Not surprisingly, nodular stranding was more predictive of tumor invasion, but it is not definitive.

**Table 1.** Tumor/note/metastasis (TNM) staging of renal cell carcinoma

| Stage | Feature |
|---|---|
| Tumor | |
| T1a | ⩽4 cm in greatest dimension and limited to the kidney |
| T1b | >4-7 cm in greatest dimension and limited to the kidney |
| T2a | 7-10 cm in greatest dimension and limited to the kidney |
| T2b | >10 cm in greatest dimension and limited to the kidney |
| T3a | Gross extension into the renal vein or its segmental branches or invading perirenal or renal sinus fat |
| T3b | Gross extension into the inferior vena cava (IVC) below the diaphragm |
| T3c | Gross extension into the IVC above the diaphragm or invading the IVC wall |
| T4 | Invasion beyond the perinephric fascia or into the ipsilateral adrenal gland |
| Node | |
| N0 | No lymph node metastases |
| N1 | Regional lymph node metastases |
| Metastasis | |
| M0 | No distant metastases |
| M1 | Distant metastasis |

Many urologists now recommend that renal nephrometry scoring be performed in addition to staging prior to surgery, as nephrometry can contribute to decisions concerning whether partial nephrectomy can be performed safely and may also predict the likelihood of posttreatment complications, with masses receiving higher scores being more problematic [37]. A recommended nephrometry scoring system is listed in Table 2.

## RCC Management

Once a diagnosis of RCC is made, treatment choice depends upon preoperative imaging characteristics of each tumor and the patient's condition. There is migration toward active surveillance in a subgroup of patients with small renal masses (⩽4 cm). Active surveillance is recommended in tumors with favorable prognosis, such as type 1 papillary RCC and chromophobe RCC [33]. Low-grade (Fuhrman grade 1) clear cell RCC has been included in this group. Active surveillance can also be considered in the elderly and/or poor operative candidates.

One recommended active surveillance protocol includes obtaining follow-up CT or MRI every 6 months for 1 year, followed by annual imaging, with treatment considered only if or when a mass exceeds 4 cm in diameter or if a followed mass demonstrates rapid growth (of >5 mm in maximal diameter in 1 year), regardless of size [31].

Once a decision has been made to intervene in a solid renal mass, a variety of treatment options are available. Percutaneous thermal ablation is performed with increasing frequency but is reserved most often for small masses (<4 cm) in patients who are not good operative candidates, have renal insufficiency, or have multiple renal neoplasms. Based upon early studies, the cure rate for percutaneous thermal ablation is comparable with that for surgery. Masses in almost any location in the kidney now can be treated effectively.

Currently, many urologists have migrated from using open total and partial nephrectomy to laparoscopic procedures, because, as is the case with percutaneous thermal ablation, laparoscopic nephrectomy is associated with considerably less perioperative morbidity and a shorter length of hospital stay [38].

**Table 2.** Recommended nephrometry scoring system

| Feature | 1 point | 2 points | 3 points |
|---|---|---|---|
| R = diameter | ⩽4 cm | >4-<7 cm | ⩾7 cm |
| E = exophytic | ⩾50% | <50% | Completely endophytic |
| N = nearness to collecting system or renal sinus | ⩾7 mm | >4-<7 mm | ⩽4 mm |
| A = anterior or posterior | No points; merely list mass as A, P, or neither | | |
| L = location with respect to polar lines | Above upper or below lower polar line | Crosses polar line | >50% of mass crosses polar or midline or is entirely interlobar |

## Imaging after Treatment

Both CT and MRI are used widely to image patients after treatment for RCC. After successful thermal ablation, there is initial expansion of the ablation site. At first, some enhancement may be detected normally in the ablation bed, likely in granulation tissue. This "normal" enhancement, which can be focal or diffuse, gradually resolves [39, 40]. As time passes, the ablation bed and adjacent change in the perinephric fat typically decrease in size but rarely disappear entirely. Other characteristic "normal" findings include fat invagination between the ablation bed and normal renal parenchyma, and a perilesional halo, which can make the ablation cavity mimic an AML.

Close-interval follow-up should be performed after ablation (for example, at 1, 3, 6, and 12 months), as tumor recurrences are usually detected within the first few months of the procedure [41]. Recurrent or residual tumor should be suspected after ablation when the ablation bed increases in size, when there is increased perinephric nodularity, or when persistent or new areas of brisk enhancement are detected, particularly in mass-like areas (nodular and/or crescentic) and/or increasing in size. These are often located at the interface between the ablation bed and adjacent renal parenchyma [41].

Imaging appearance after laparoscopic partial nephrectomy has also been described [42]. Hemostatic material, such as FloSeal, Gelfoam, Surgicel, and renal bolsters, when inserted after partial nephrectomy, can be mistaken for areas of infection or recurrent tumor. Gore-Tex mesh may be inserted along the nephrectomy site, appearing as a linear area of high attenuation along the renal margin.

After partial or total nephrectomy, recurrent tumors may occur in the surgical bed or at regional or distant sites. Surgical-bed recurrences may initially be difficult to differentiate from postoperative scarring/fibrosis, although recurrent tumor often demonstrates increased enhancement and enlarges over time [42]. Regional and distant metastases from RCC usually appear in lymph nodes, liver, adrenal glands, lungs, and bones. Metastases to the adrenal glands from clear cell RCC can be problematic, as they may contain large amounts of intracellular fat. Similar to adenomas, they may demonstrate low signal intensity on opposed-phase MRI. Due to their hypervascularity, they can also demonstrate pronounced (>60%) washout on delayed enhanced CT.

RCC metastasizes to the pancreas more commonly than do other neoplasms. For this reason, the pancreas should be carefully assessed in patients being followed after treatment for RCC [43]. Patients treated laparoscopically rarely develop tumor implants along laparoscopic port sites (which may be posterior and retroperitoneal or anterior and transperitoneal), in the mesentery, or along the peritoneum [42].

## References


1 Cohan RH, Sherman LS, Korobkin M et al (1995) Renal masses: assessment of corticomedullary-phase and nephrographic-phase CT scans. Radiology 196:445-451.
2. Pooler BD, Pickhardt PJ, O'Connor SD et al (2012) Renal cell carcinoma: attenuation values on unenhanced CT. AJR Am J Roentgenol 198:1115-1120.
3. Hecht EM, Israel GM, Krinsky GA et al (2004) Renal masses: quantitative analysis of enhancement with signal intensity measurements versus qualitative analysis of enhancement with image subtraction for diagnosing malignancy at MR imaging. Radiology 232:373-378.
4. Choyke PL (2003) Imaging of hereditary renal cancer. Radiol Clin North Am 41:1037-1051.
5. Bosniak MA, Birnbaum BA, Krinsky GA et al (1995) Small renal parenchymal neoplasms: further observations on growth. Radiology 197:589-597.
6. Bosniak MA (1986) The current radiological approach to renal cysts. Radiology 158:1-10.
7. Israel GM, Bosniak MA (2005) How I do it: evaluating renal masses. Radiology 236:441-450.
8. Israel GM, Hindman N, Bosniak MA (2004) Evaluation of cystic renal masses: comparison of CT and MR imaging by using the Bosniak classification system. Radiology 231:365-371.
9. Farrelly C, Delaney H, McDermott R et al (2008) Do all non-calcified echogenic renal lesions found on ultrasound need further evaluation with CT? Abdominal Imaging 33:44-47.
10. Davenport MS, Neville AM, Ellis JH et al (2011) Diagnosis of renal angiomyolipoma with Hounsfield Unit thresholds: effect of size and region of interest and nephrographic phase imaging. Radiology 260:158-165.
11. Israel GM, Hindman N, Hecht E et al (2005) The use of opposed-phase chemical shift MRI in the diagnosis of renal angiomyolipomas. AJR Am J Roentgenol 194:1868-1872.
12. Israel GM, Bosniak MA, Slywotzky CM et al (2005) CT differentiation of large exophytic renal angiomyolipomas and perirenal liposarcomas. AJR Am J Roentgenol 179:769-773.
13. Catalano OA, Samir AE, Sahani DV et al (2008) Pixel distribution analysis: can it be used to distinguish clear cell carcinomas from angiomyolipomas with minimal fat? Radiology 247:738-746.
14. Simpfendorfer C, Herts BR, Motta-Ramirez GA et al (2009) Angiomyolipoma with minimal fat on MDCT: can counts of negative attenuation pixels aid diagnosis? AJR Am J Roentgenol 192:438-443.
15. Kim JK, Kim HS, Jang YJ et al (2006) Renal angiomyolipoma with minimal fat: differentiation from other neoplasms at double-echo chemical shift FLASH MR imaging. Radiology 239:274-280.
16. Zhang YY, Luo S, Liu Y et al (2013) Angiomyolipoma with minimal fat: differentiation from papillary renal cell carcinoma by helical CT. Clin Radiol 68:365-370.
17. Choudhary S, Rajesh A, Mayer NJ et al (2009) Renal oncocytoma: CT features cannot reliably distinguish oncocytoma from other renal neoplasms. Clin Radiol 64:517-522.
18. Young JR, Margolis D, Sauk S et al (2013) Clear cell renal cell carcinoma: discrimination from other renal cell carcinoma subtypes and oncocytoma at multiphasic multidetector CT. Radiology 267:444-453.
19. Pierorazio PM, Hyams ES, Tsai S et al (2013) Multiphase enhancement patterns of small renal masses (<4 cm) on preoperative computed tomography: utility for distinguishing subtypes of renal cell carcinoma, angiomyolipoma, and oncocytoma. Urology 81:1265-1272.
20. Bird VG, Kanagarajah P, Morillo G et al (2011) Differentiation of oncocytoma and renal cell carcinoma in small renal masses (<4 cm): the role of 4-phase computerized tomography. World J Urol 29:787-792.

21. Woo S, Cho JY, Kim SY et al (2013) Segmental enhancement inversion of small renal oncocytoma: differences in prevalence according to tumor size. AJR Am J Roentgenol 200:1054-1059.
22. O' Malley MW, Tran P, Hanbidge A et al (2012) Small renal oncocytomas: is segmental enhancement inversion a characteristic finding at biphasic MDCT? AJR Am J Roentgenol 199:1312-1315.
23. Kim JH, Bae JH, Lee KW et al (2012) Predicting the histology of small renal masses using preoperative dynamic contrast-enhanced magnetic resonance imaging. Urology 80:872-876.
24. Sun MRM, Ngo L, Genega EM et al (2009) Renal cell carcinoma: dynamic contrast-enhanced MR imaging for differentiation of tumor subtypes- correlation with pathologic findings. Radiology 250:793-802.
25. Egbert ND, Caoili EM, Cohan RH et al (2013) Differentiation of papillary renal cell carcinoma subtypes on CT and MRI. AJR Am J Roentgenol 201:347-355.
26. Oliva MR, Glickman JN, Zou KH et al (2009) Renal cell carcinoma: T1 and T2 signal intensity characteristics of papillary and clear cell types correlated with pathology. AJR Am J Roentgenol 192:1524-1530.
27. Dang TT, Ziv E, Weinstein S et al (2012) Computed tomography and magnetic resonance imaging of adult renal cell carcinoma associated Xp11.2 translocation. J Comput Assist Tomogr 36:669-674.
28. Zhu QQ, Wang ZQ, Zhu WR et al (2013) The multislice CT findings of renal carcinoma associated with XP11.2 translocation/TFE gene fusion and collecting duct carcinoma. Acta Radiologica 54:355-362.
29. Raza SA, Sohaib SA, Sahdev A et al (2012) Centrally infiltrating renal masses on CT: differentiating intrarenal transitional cell carcinoma from centrally located renal cell carcinoma. AJR Am J Roentgenol 198:846-853.
30. Choi SJ, Jim HS, Ahn SJ et al (2012) Differentiating radiological features of rapid- and slow-growing renal cell carcinoma using multidetector computed tomography. J Comput Assist Tomogr 36:313-318.
31. Pierorazio PM, Hyams ES, Mullens JK et al (2012) Active surveillance of small renal masses. Rev Urol 14:13-19.
32. Frank I, Blute ML, Cheville JC et al (2003) Solid renal tumors: an analysis of pathological features related to tumor size. J Urol 2217-2220.
33. Halverson SJ, Kunju LP, Bhalla R et al (2013) Accuracy of determining small renal mass management with risk stratified biopsies: confirmation by final pathology. J Urol 189:441-446.
34. Shah RB, Bakshi N, Hafez KS et al (2005) Image-guided biopsy in the evaluation of renal mass lesions in contemporary urological practice: indications, adequacy, clinical impact, and limitations of the pathological diagnosis. Hum Pathol 36:1309-1315.
35. Hes O, Michal M, Kuroda N et al (2007) Vimentin reactivity in renal oncocytoma: immunohistochemical study in 234 cases. Arch Pathol Lab Med 131:1782-1788.
36. Hedgire SS, Elmi A, Nadkarni ND et al (2013) Preoperative evaluation of perinephric fat invasion in patients with renal cell carcinoma: correlation with pathological findings. Clin Imag 37:91-96.
37. Kutikov A, Uzzo RG (2009) The R.E.N.A.L. nephrometry score: a comprehensive standardized system for quantitating renal tumor size, location and depth. J Urol 182:844-853.
38. Ng CS, Wood CG, Silverman PM et al (2008) Renal cell carcinoma: diagnosis, staging, and surveillance. AJR Am J Roentgenol 191:1220-1232.
39. Davenport M, Caoili EM, Cohan RH et al (2009) MR and CT characteristics of successfully ablated renal masses status-post radiofrequency ablation. AJR Am J Roentgenol 192:1571-1578.
40 Tsivian M, Kim CY, Caso JR et al (2012) Contrast enhancement on computed tomography after renal cryoablation: an evidence of treatment failure? J Endourol 26:330-335.
41. Kawamoto S, Solomon SB, Bluemke DA et al (2009) Computed tomography and magnetic resonance imaging appearance of renal neoplasms after radiofrequency ablation and cryoablation. Semin Ultrasound CT MRI 30:67-77.
42. Lall CG, Patel HP, Fujimoto S et al (2012) Making sense of postoperative CT imaging following laparoscopic partial nephrectomy. Clin Radiol 67:675-686.
43. Corwin MT, Lamba R, Wilson M et al (2013) Renal cell carcinoma metastases to the pancreas: value of arterial imaging. Acta Radiologica 54:349-354.

# Urinary Tract Obstruction and Infection

Parvati Ramchandani[1], Harriet C. Thoeny[2]

[1] Genitourinary Radiology, Perelman School of Medicine at the University of Pennsylvania, Philadelphia, PA, USA
[2] Department of Radiology, Neuroradiology, and Nuclear Medicine, Institute of Diagnostic, Interventional, and Pediatric Radiology, Inselspital, University of Bern, Bern, Switzerland

## Urinary Tract Obstruction

Imaging plays an important role in evaluating patients with both acute and chronic urinary tract obstruction. The cause of obstruction varies greatly with patient population and geographic locale. In a series reporting on percutaneous nephrostomy drainage, urinary obstruction was related to calculus disease in 26% of patients and malignancy in 61%. Carcinoma of the bladder, cervix, and colon were the most common primaries in patients with malignancies and urinary obstruction [1]. Enlarged retroperitoneal and pelvic lymph nodes due to various malignancies, including lymphoma and testicular cancer, can also lead to secondary obstruction.

Acute ureteral obstruction is usually secondary to urolithiasis, and patients commonly present to an acute-care facility with flank pain or acute renal colic. Noncontrast helical computed tomography (CT) is often the first study performed in suspected acute obstruction, as it is a safe and rapidly performed examination, with an accuracy rate for detecting ureteral stones, the most common cause of ureteral obstruction, exceeding that of other imaging studies. Other causes of acute abdominal pain, such as appendicitis, leaking aortic aneurysm, and diverticulitis, can also be readily diagnosed and occur in 13-19% of cases (Table 1) [2-4]. Noncontrast helical CT has an overall accuracy of 97% for diagnosing ureteral stone disease, with a reported sensitivity of 97-100% and specificity of 94-96% [5-12]. This far exceeds the accuracy of sonography (US) (Table 2), as discussed below, although some controversy exists as to which imaging studies are best for investigating suspected ureteral obstruction. Intravenous urography is rarely performed in a patient presenting with acute renal colic. Regardless of composition, virtually all ureteral stones will have high attenuation values, making them readily detectable with CT. Nonmineralized matrix stones and some drug-related crystal aggregates (with protease inhibitors being a common example) may not be visible on CT images, but these are rarely encountered in routine clinical practice.

The proper technique for performing noncontrast helical CT to detect ureteral stone disease using a helical scanner is detailed below. Imaging should be performed from the top of the kidneys to the base of the bladder without intravenous or oral application of contrast material, and scans should be obtained during a single breath-hold. Using a 16- to 64-slice multidetector CT (MDCT), collimation of 1.5 mm is appropriate, with review of 5-mm contiguous images. In order to reduce radiation dose, a variable mA is used for each slice based on beam attenuation. Artificial addition of noise to a renal colic CT showed that tube current could be diminished 75% without changing the detection rate of stones >3 mm in diameter [13]. For the obese patient, a fixed mA equal to

**Table 1.** Causes of obstruction

| Computed tomography (CT) findings in acute renal colic | Hoppe [2] (2006) | Katz [3] (2000) | Ahmad [4] (2003) |
|---|---|---|---|
| Number of patients | 1,500 | 1,000 | 233 |
| Urinary stone | 69% | 62% | 68% |
| Additional *or* alternative diagnosis | 71% | 10% | 12% |
| Alternate diagnosis *only* | 24% | 7.50% | – |
| Normal | 7% | 28% | – |
| Pyelonephritis | 3% | 1% | 1% |
| RCC/renal mass | 2% | 0.40% | 1% |
| Cholecystitis | 0.30% | 0.30% | 0.40% |
| Adnexal mass | – | 2% | 2% |

*RCC* renal cell carcinoma

*Diseases of the Abdomen and Pelvis 2014-2017*,
DOI: 10.1007/978-88-470-5659-6_18 

**Table 2.** Diagnostic performance for computed tomography (CT), ultrasonography (US), and intravenous urogram (IVU) in detecting ureteral stones

| Lead author | Year of publication | No. | Stone + | Test | Sensitivity | Specificity |
|---|---|---|---|---|---|---|
| Catalano [5] | 2002 | 181 | 82 | CT | .92 | .96 |
| | | | | US/XR | .77 | .96 |
| Boulay [6] | 1999 | 51 | 49 | CT | 1.0 | .96 |
| Sheley [7] | 1999 | 180 | 87 | CT | .86 | .91 |
| Sourtzis [8] | 1999 | 36 | 36 | CT | 1.0 | 1.0 |
| | | | | IVU | .66 | 1.0 |
| Yilmaz [9] | 1998 | 97 | 64 | CT | .94 | .97 |
| | | | | US | .19 | .97 |
| | | | | IVU | .52 | .94 |
| Smith [10] | 1996 | 210 | 100 | CT | .97 | .96 |

*No.* number of patients, *Stone +* number of patients with urethral stone, *XR* plain radiography

weight in pounds will usually suffice. Expected dose is 30-40 mSv. Review of the images in cine mode on a workstation facilitates continuous identification of the ureter and workflow. Coronal and sagittal reconstructions are useful to distinguish intraureteral from extraurinary calcifications.

Because of the accuracy of CT and greater familiarity with the examination by referring physicians, especially within the emergency room, referring physicians and radiologists must be cognizant of the potential for overuse of CT in patients who present with recurrent abdominal or flank pain [14-16]. The overall rate of stone positivity on CT scanning in patients with suspected renal colic is reported to be 60-66% in several studies [12, 13]. Additionally, as discussed above, CT is the diagnostic test of choice to evaluate many acute abdominal problems, and a decrease in the stone positivity rate may not necessarily reflect overuse of CT [17].

It seems reasonable that a patient with known history of stones and the appropriate clinical findings can be treated conservatively and without imaging beyond an abdominal radiograph.

### CT Findings

In addition to direct visualization of the ureteral stone, secondary signs of ureteral obstruction on noncontrast CT scans include unilateral nephromegaly, perinephric stranding, hydronephrosis, and periureteral stranding. The combination of perinephric stranding and unilateral hydronephrosis has a positive predictive value (PPV) of 96% for the presence of stone disease. The absence of both of these signs has a negative predictive value (NPV) of 93% for excluding stone disease. CT also gives information that determines therapy. Stones that are ≤5 mm, smooth shape, and located within the distal one third of the ureter are likely to pass spontaneously [11].

The major pitfall in noncontrast helical CT when evaluating the urinary tract for stone disease is difficulty in distinguishing pelvic phleboliths from ureteral calculi. The presence of a tissue rim sign usually indicates that the calcification is a stone rather than a phlebolith, with the rim representing edema of the ureteral wall. Alternatively, absence of the tissue rim sign or presence of a comet-tail sign strongly suggests that the calcification is a phlebolith rather than a stone. In practice, the presence of two or more secondary signs of obstruction, even without clear visualization of a calcification within the ureter, indicates obstruction. If there is no history of recent stone passage and the CT scan demonstrates findings suggestive of obstruction, a contrast-enhanced study of the upper tracts may be needed to exclude a urothelial neoplasm, with additional cystoscopy to optimally evaluate the bladder.

Excretory urography (EU) is a less desirable study than unenhanced CT in an acute pain setting and has been relegated to historical significance only in evaluating patients presenting with acute colic. EU was once considered to have a potential role in evaluating pregnant patients with acute flank pain when results of US examination were negative or equivocal. However, even in this patient population, low-dose CT may be the technique of choice, as it provides a definitive and rapid diagnosis. These advantages outweigh the slightly greater radiation exposure [18, 19]. Acute colic in pregnant patients is discussed below.

US, usually combined with a plain film, is an alternative method for evaluating the obstructed or dilated urinary tract. It is often used as the first imaging procedure in patients who should avoid radiation, such as pregnant women, and children. Calculi as small as 0.5 mm may be detectable in optimal conditions. When stones are >5 mm, US has a sensitivity and specificity of 96% and nearly 100%, respectively [20]. Although US allows for excellent evaluation of the renal parenchyma and collecting system to the ureteropelvic junction, it is limited in evaluating the ureter and of soft-tissue lesions within the collecting system. The use of renal US in evaluating suspected acute ureteral obstruction is also limited because dilatation often does not develop for hours, or even days. In these cases, US findings are normal in up to 50% of patients. US alone or combined with conventional radiography has been compared with unenhanced CT. US has a much lower sensitivity, varying from 24% to 77%

[5, 21-23], compared with 92-96% for CT. In Sheafor et al.'s study that compared CT and US [21], CT depicted 22 of 23 ureteral calculi (sensitivity 96%); US depicted 14 of 23 (sensitivity 61%), which was statistically significant ($P = 0.02$). Specificity for each technique was 100%. CT can give a rapid and definitive diagnosis of urinary calculus disease, as well as other abdominal disorders with the same presentation. Identifying ureteral jets within the urinary bladder lumen on US is helpful for assessing the presence of obstruction. One study showed an absent ureteral jet in 11 of 12 patients with high-grade obstruction and in three of 11 patients with low-grade obstruction [23]. Identification of jets at the ureterovesical junctions indicates that obstruction is incomplete, and thus may be used to guide therapy. It is well recognized that renal calculi <5-7 mm, particularly in large or obese patients, may not be detected on US [25, 26]. However, US may overestimate stone size in urolithiasis by as much as 1.9 mm compared with CT, particularly stones <5 mm [27]. This is an important limitation, as it has implications for stone management.

In diuresis renography, radionuclides are injected to evaluate the urinary tract for obstruction. Because considerably less anatomic detail is available with this test than with other radiographic examinations, it is less useful in the acute setting than for follow-up or for evaluating chronic urinary tract obstruction. Diuresis renography does have the advantage of yielding objective data regarding the significance of hydronephrosis and also allows for evaluation of the function of each kidney. Administration of a diuretic, usually furosemide, augments the standard renogram and is useful in evaluating dilated urinary systems to determine whether there is physiologically significant obstruction.

Magnetic resonance urography (MRU) using rapid scanning techniques, such as half-acquisition turbo spin-echo or single-shot fast spin-echo and 3D gradient-echo contrast-enhanced sequences are used for evaluating the urinary tract. Following administration of 250 ml of normal saline and 10 mg of furosemide, kidneys and dilated ureters are very bright on T2-weighted imaging, and their stable position allows for clear imaging of the level of obstruction (Table 3). However, stones appear as signal voids and can be difficult to identify and measure on MRU. Small calculi (the majority of symptomatic stones) are difficult to detect on MR imaging (MRI). Urothelial lesions, blood clots, and debris can also mimic calculi. Noncontrast-enhanced functional MRI (fMRI) techniques, such as blood-oxygen-level-dependent (BOLD) MRI or diffusion-weighted MRI (DWI), can detect urinary obstruction in patients with renal calculi, even when the collecting system is not dilated. These sequences might be particularly useful in patients with renal impairment, children, or pregnant women. Although these techniques do not allow the detection of ureteral calculus, they provide information on the presence or absence of acute ureteral obstruction, as evidenced in a small number of patients [28, 29]. Furthermore, these techniques might be helpful in transplanted kidneys to differentiate obstruction from dilatation due to denervation. However, larger-scale studies are yet needed in order to confirm these initially promising results.

**Table 3.** Computed tomography and magnetic resonance (CTU and MRU) urography protocols

| CTU protocol |
|---|
| – No contrast orally, patient supine, 10 mg IV furosemide |
| – Axial non-contrast-enhanced abdomen |
| – Inject contrast agent IV (100 cc of 350 mgI/ml) |
| – Axial abdomen and pelvis at 75 s postinjection |
| – Axial abdomen and pelvis at 5 min postinjection |
| – Coronal reformatted images of 5-min-delay examination |
| – Review using bone and soft tissue windows |
| **MRU protocol** |
| – 250 cc IV saline – begin 15 min before imaging |
| – Patient supine, give 10 mg furosemide IV |
| – Coronal HASTE/SSFSE scout |
| – Axial abdomen HASTE/SSFSE |
| – Axial IP/OOP gradient echo image |
| – Coronal 3D TSE, HASTE or other fluid-sensitive sequence |
| If GFR <3.0 or serum Cr >3.0: STOP; DWI can be performed and might detect urothelial carcinoma in the collecting system as a lesion with impeded diffusion (bright on high b-value images and dark on the corresponding ADC map) |
| If GFR is >3.0 and suspicion for urothelial carcinoma is high: coronal 3D GRE image, such as LAVA, VIBE, with fat saturation; precontrast, 2-min, and 5-min delay |

*HASTE/SSFSE* half-Fourier-acquisition single-shot turbo spin-echo/single-shot fast spin-echo, *IP/OOP* image processing/object-oriented processing, *TSE* turbo spin-echo, *GFR* glomerular filtration rate, *Cr* creatinine, *DWI* diffusion-weighted imaging, *ADC* apparent diffusion coefficient, *GRE* gradient echo, *LAVA* liver acquisition with volume acceleration, *VIBE* volumetric interpolated breath-hold examination

In patients with renal impairment due to ureteral obstruction [30, 31], noncontrast CT is the best imaging modality to identify calculus causes of obstruction, whereas MRU is superior for identifying noncalculus causes of obstruction. In patients with normal renal function, contrast-enhanced CT can identify the presence and cause of hydronephrosis in nearly all cases [32]. MRU is particularly helpful in delineating the anatomy in patients with urinary diversion to bowel conduits [33].

An abdominal radiograph is a reasonable initial test in patients who have a history of radiopaque calculi and acute flank pain similar to that of previous pain episodes. In the absence of such a history, abdominal radiography may not be of value as an initial examination [12]. If a ureteral calculus is present on CT but not clearly identifiable on the scout view, a conventional abdominal radiograph may be useful, especially if the stone is >4-5 mm and >300 HU in density [34], for following the stone progress for management purposes. For radiodense calculi, confirmation of stone location during conservative therapy is best performed using plain films [35].

In dealing with the pregnant patient with flank pain, fetal age and estimated radiation dose is of paramount

importance. Right hydronephrosis is commonly encountered as the enlarging uterus turns slightly to the right, compressing the ureter. When an obstructing stone is suspected in either the right or left system, US should be performed first. Some urologists place a stent, based on clinical findings and severe hydronephrosis. If more imaging information is needed, a limited intravenous urogram (IVU) using a plain scout film, followed by a 10-min postinfusion delayed film, yields the least radiation in the first-trimester patient. After 20-24 weeks, IVU becomes difficult to interpret because of the enlarging uterus, and CT should be considered [19]. The expected fetal dose is approximately 16 mSv, well below that expected to cause anomalies. New fMRI techniques, such as BOLD and DWI including conventional MRI, might be ideal imaging tests in the near future.

## Urinary Tract Infection

### Acute Pyelonephritis

This is usually an ascending infection spread from the bladder, seen predominantly in females. Rarely the source of infection is hematogenous bacteremia. Diagnosis is usually made on clinical grounds and with urine analysis. Imaging may be needed to detect pyelonephritis complications or sequelae. When clinical pyelonephritis persists for >3 days after suitable antibiotic therapy has been initiated, imaging is recommended. CT is the imaging technique of choice to evaluate the kidneys for possible complications of pyelonephritis, such as abscess or obstruction. It is the most sensitive and specific test for detecting changes in acute pyelonephritis and its complications. Typical CT findings of pyelonephritis include unilateral nephromegaly, renal striations, wedge-shaped defects, and perinephric inflammatory changes. Areas of liquefaction within the renal parenchyma indicate the development of a renal abscess. CT is more sensitive than US for detecting renal abscess development and assessing its extent.

As pyelonephritis is often detected in young woman as well as in children, MRI is used increasingly in order to avoid radiation exposure in these patients. DWI is an especially safe and simple method, typically showing high signal intensity lesions on the high b-value images with low signal intensity lesions on the corresponding apparent diffusion coefficient (ADC) maps, with normal findings on morphological images (T1- and T2-weighted images). These lesions can be focal or include the entire kidney. Clinical information, however, is important to consider in order to make the correct diagnosis. Abscesses typically show focal areas of impeded diffusion (due to high viscosity), which are bright on high b-value images and dark on the corresponding ADC map, with high signal intensity lesions on the T2-weighted images and low signal intensity lesions on the T1-weighed images.

In male patients with a urinary tract infection (UTI) and/or suspected pyelonephritis, US is valuable for identifying common causes of UTI, such as epididymitis, orchitis, and prostatitis. Patients with a neurogenic bladder secondary to a spinal cord injury pose a difficult problem, as urine is usually colonized. Development of systemic symptoms should prompt rapid imaging, as these patients may not be sensate to pain, and a devastating abscess can develop quickly [36]. Finally, in order to diminish radiation dose to pregnant women, US with power Doppler may be attempted prior to CT to detect areas of aberrant blood flow. This is useful in children [37, 38].

Sequelae of pyelonephritis include changes of reflux nephropathy. These changes include renal scarring and calyceal blunting due to reflux of urine through ducts of Bellini, resulting in parenchymal scarring. Changes of reflux nephropathy include broad-based scars centered over clubbed calyces, occurring preferentially in the poles of the kidneys. Function of the affected kidney is best evaluated with radionuclide renography.

### Emphysematous Pyelonephritis

This life-threatening infection with a gas-producing organism has up to 90% mortality rate without nephrectomy. Infection is usually caused by a strain of *Escherichia coli* in diabetic patients. The diagnosis of emphysematous pyelonephritis is made when gas is seen in the renal parenchyma. CT is the most accurate technique for diagnosing emphysematous pyelonephritis and for differentiating this entity from emphysematous pyelitis or perinephric emphysematous infections. CT is also most accurate for differentiating localized gas-producing infections from diffuse emphysematous pyelonephritis; the former can be successfully treated with percutaneous drainage in combination with systemic antibiotic management.

### Granulomatous Renal Infections

Tuberculosis, xanthogranulomatous pyelonephritis (XGP), malacoplakia, and fungal infections can all affect the urinary tract.

### Renal Tuberculosis

Renal tuberculosis is usually spread hematogenously from the lungs seeding the kidneys. Symptomatic renal tuberculosis results from secondary reactivation of tuberculosis. Symptoms typically include hematuria and sterile pyuria. The earliest signs of renal tuberculosis include focal papillary necrosis and inflammation of the calyces. With disease progression, areas of fibrosis and calcification may develop. Long-standing tuberculosis may result in numerous fibrotic strictures, ureteral wall thickening, hydronephrosis, and autonephrectomy. Pyelonephritis related to Bacillus-Calmette-Guerin (BCG) therapy for urothelial carcinoma has also been reported.

#### Xanthogranulomatous Pyelonephritis

XGP, an inflammatory condition with a marked female predominance, is associated with recurrent urinary tract infections caused by proteases or *E. coli* bacteria. An infection-based stone is seen in the majority of cases. The classic radiographic triad includes reniform enlargement of the kidney, renal stone, and markedly decreased or absent renal function in the affected kidney. Localized XGP occurs in 20% of cases and can mimic renal neoplasms on imaging studies. Advanced forms of XGP can also extend beyond the kidney into the psoas muscle and even into the muscles of the back; fistulae into the adjacent bowel have also been described.

#### Malacoplakia and Fungal Infection

Both malacoplakia and fungal infections have nonspecific appearances. They are often multifocal, but a tissue diagnosis is required to exclude neoplasm. Malacoplakia constitutes congregations of histiocytes. It is more commonly seen in the bladder and ureter than in the kidney. The microscopic hallmark of malacoplakia is the Michaelis-Gutman inclusion body seen within the abnormal histiocytes. When malacoplakia involves the ureter or bladder, multiple submucosal masses are usually identified. Imaging findings are nonspecific, and tissue biopsy is required for definitive diagnosis. Fungal infections are usually seen in immunocompromised patients, including in diabetics. Debris, often present within the renal collecting system, forms a 'hand-in-glove" filling defect of the contrast-opacified calyces. It is a major challenge not to misinterpret these filling defects as malignancies, especially in patients with known urothelial carcinoma of the bladder.

#### AIDS Nephropathy

Autoimmune deficiency syndrome (HIV/AIDS) nephropathy constitutes a variety of renal pathologies. Findings are generally nonspecific, but patients with an HIV infection, renal failure, and hyperechoic nephromegaly likely have AIDS nephropathy. These sonographic findings in an AIDS patient usually indicate that the patient will develop irreversible renal failure.

#### BK Virus Nephropathy

During the last decade, strong antirejection agents have been used to improve renal allograft survival. The resulting immunosuppression has allowed a generally benign virus, known as BK, to become a deadly pathogen. It is present in the urine of 50% of transplant recipients 3 months postoperation and may cause graft failure in 10%. The method of action of this small polyomavirus is unknown. Patients with transplanted kidneys who are BK positive are treated with steroids. There is no known cure [39]. DWI can be helpful in detecting early changes due to BK virus infection in case of normal morphological findings; however, this technique is not specific, and biopsy is still the only way to make the final diagnosis.

#### Pyonephrosis

Pyonephrosis constitutes a bacterial infection of the urine associated with ureteral obstruction. If untreated, this can lead to irreversible damage to the kidney, septicemia, and even rapid demise. Pyonephrosis is best diagnosed with US. Any febrile patient with hydronephrosis should be suspected of harboring pyonephrosis. Other findings that suggest pyonephrosis include echogenic urine, and debris within the hydronephrotic calyces. DWI is also helpful in differentiating hydronephrosis from pyonephrosis, showing impeded diffusion in pyonephrosis due to high viscosity of the pus. Prompt urinary tract drainage accompanied by systemic antibiotic administration is essential in these patients. When obstruction and infection are due to ureteral calculi, retrograde ureteral catheterization and percutaneous nephrolithotomy (PCN) are equally effective in relieving the obstruction and infection; neither technique is superior to the other in promoting rapid drainage or clinical defervescence [40].

#### Schistosomiasis

Schistosomiasis of the urinary tract is caused by infection with *Schistosoma hematobium*. This is endemic in Egypt. This infection usually arises in the bladder but may spread to the ureters and kidneys via reflux to the upper tracts. Dystrophic calcifications in the wall of the bladder and ureter are typical findings and are caused by calcification of the dead ova. Typical radiographic findings include mural calcifications, ureteral strictures, and vesicoureteral reflux. Patients have a markedly increased risk for the development of squamous cell carcinoma, as well as urothelial carcinoma of the urinary tract.

### Posttherapeutic Change

One of the most common causes of urinary obstruction is pelvic cancer and its complications. Many patients with gynecologic and prostatic malignancies are treated with surgery and radiation therapy, which may cause stricturing of the ureter. The ureter may be transected or suffer thermal injury due to cauterization during hysterectomy or other pelvic surgery, leading to hydronephrosis or urinoma. Large lymphoceles are uncommon with these surgeries, but if they are present, they may compress the ureter or bladder. Ureteric obstruction secondary to stricture or fibrosis is common, as are fistulae involving the bowel and urinary tract [41].

## References


1. Farrell TA, Hicks MS (1997) A review of radiologically guided percutaneous nephrostomies in 303 patients. J Vasc Interv Radiol 8:769-774.
2. Hoppe H, Studer R, Kessler TM et al (2006). Alternate or additional findings to stone disease on unenhanced computerized tomography for acute flank pain can impact management. J. Urol 175:1725-30; discussion 1730.
3. Katz DS, Scheer M, Lumerman JH et al (2000). Alternative or additional diagnoses on unenhanced helical computed tomography for suspected renal colic: experience with 1000 consecutive examinations. Urology 56:53-57.
4. Ahmad NA, Ather MH, Rees J (2003) Incidental diagnosis of diseases on un-enhanced helical computed tomography performed for ureteric colic. BMC Urology 17:2.
5. Catalano O, Nunziata A, Altei F et al (2002) Suspected ureteral colic: primary helical CT versus selective helical CT after unenhanced radiography and sonography. AJR Am J Roentgenol 178:379-387.
6. Boulay I, Holtz P, Foley WD et al (1999) Ureteral calculi: diagnostic efficacy of helical CT and implications for treatment of patients. AJR Am J Roentgenol 172:1485-1490.
7. Sheley RC, Semonsen KG, Quinn SF (1999) Helical CT in the evaluation of renal colic. American Journal of Emergency Medicine 17: 279-282.
8. Sourtzis S, Thibeau JF, Damry N et al (1999) Radiologic investigation of renal colic: unenhanced helical CT compared with excretory urography. AJR Am J Roentgenol 172: 1491-1494.
9. Yilmaz S, Sindel T, Arslan G et al (1998). Renal colic: comparison of spiral CT, US and IVU in the detection ureteral calculi. Eur Radiol 8:212-217.
10. Smith RC, Verga M, McCarthy S et al (1996) Diagnosis of acute flank pain: value of unenhanced helical CT. AJR Am J Roentgenol 166:97-101.
11. Fielding JR, Silverman SG, Samuel S et al (1998) Unenhanced helical CT of ureteral stones: a replacement for excretory urography in planning treatment. AJR Am J Roentgenol 171:1051-1053.
12. Levine JA, Neitlich J, Verga M et al (1997) Ureteral calculi in patients with flank pain: correlation of plain radiography with unenhanced helical CT. Radiology 204:27-31.
13. Ciaschini MW, Remer EM, Baker ME et al (2009). Urinary calculi: radiation dose reduction of 50% and 75% at CT – effect on sensitivity. Radiology 251:105-111.
14. Katz SI, Saluja S, Brink JA et al (2006). Dose associated with unenhanced CT for suspected renal colic: impact of repetitive studies. AJR Am J Roentgenol 186:1120-1124.
15. Kirpalani A, Khalili K, Lee S, Haider MA (2005). Renal colic: comparison of use and outcomes of unenhanced helical CT for emergency investigation in 1998 and 2002. Radiology 236:554-558.
16. Ha M, MacDonald RD (2004) Impact of CT scan in patients with first episode of suspected nephrolithiasis. J Emerg Med 27:225-231.
17. Kenney PJ (2003) CT evaluation of urinary lithiasis. Radiol Clin N Am 41:979-999.
18. LeRoy AJ (2006) Imaging of acute maternal diseases in pregnancy. Categorical course in diagnostic radiology at 92nd scientific assembly and annual meeting, Chicago, IL, RSNA. Genitourinary radiology syllabus 271-279.
19. Fielding JR, Washburn D (2005) Imaging the pregnant patient: a uniform approach. J Women's Imaging 7:16-21.
20. Middleton WD, Dodds WJ, Lawson TL, Foley WD (1988) Renal calculi: sensitivity for detection with US. Radiology 167:239-244.
21. Sheafor DH, Hertzberg BS, Kelly S (2000) Freed. Nonenhanced helical CT and US in the emergency evaluation of patients with renal colic: prospective comparison. Radiology 217:792-797.
22. Fowler KAB, Locken JA, Duchesne JH, Williamson MR (2002) US for detecting renal calculi with nonenhanced CT as a reference standard. Radiology 222:109-113.
23. Tublin ME, Dodd GD, Verdile VP (1994). Acute renal colic: diagnosis with duplex Doppler US. Radiology 193:697-701.
24. Burge HJ, Middleton WD, McClennan BL, Hildebolt CF (1991) Ureteral jets in healthy subjects and in patients with unilateral ureteral calculi: comparison with color Doppler US. Radiology 180:437-442.
25. Eisner BH, McQuaid JW, Hyams E, Matlaga BR (2011) Nephrolithiasis: what surgeons need to know. AJR Am J Roentgenol 196:1274-1278.
26. E-Sabih D, Khan AN, Craig M, Worrall JA (2004) Sonographic mimics of renal calculi. J Ultrasond Med 23:1361-1367.
27. Ray AA, Ghiculete D, Pace KT, Honey RJ (2010) Limitations to ultrasound in the detection and measurement of urinary tract calculi. Urology 76:295-300.
28. Thoeny HC, Kessler TM, Simon-Zoula S et al (2008) Renal oxygenation changes during acute unilateral ureteral obstruction: assessment with blood oxygen level-dependent MR imaging–initial experience. Radiology 247:754-761.
29. Thoeny HC, Binser T, Roth B et al (2009) Noninvasive assessment of acute ureteral obstruction with diffusion-weighted MR imaging: a prospective study. Radiology 252:721-728.
30. Shokeir AA, El-Diasty T, Eassa W et al (2004). Diagnosis of ureteral obstruction in patients with compromised renal function: the role of noninvasive imaging modalities. J Urol 171:2303-2306.
31. Shokeir AA, El-Diasty T, Eassa W et al (2004). Diagnosis of noncalcareous hydronephrosis: role of magnetic resonance urography and noncontrast computed tomography. Urology 63:225-229.
32. El-Ghar MEA, Shokheir AA, El-Diasty T et al (2004) Contrast enhanced spiral computerized tomography in patients with chronic obstructive uropathy and normal serum creatinine: a single session for anatomical and functional assessment. J Urol 172:985-988.
33. Zielonko J, Studniarek M, Markuszewski M (2003) MR Urography of obstructive uropathy: diagnostic value of the method in selected clinical groups. Eur Radiol 13:802-809.
34. Zagoria RJ, Khatod EG, Chen MYM (2001) Abdominal radiography after CT reveals urinary calculi: a method to predict usefulness of abdominal radiography on the basis of size and CT attenuation of calculi. AJR Am J Roentgenol 176:1117-1122.
35. Assi Z, Platt JF, Francis IR et al (2000) Sensitivity of CT scout radiography and abdominal radiography for revealing ureteral calculi on helical CT: implications for radiologic follow-up. AJR Am J Roentgenol 175:333-337.
36. Rubenstein JN, Schaeffer AJ (2003) Managing complicated urinary tract infections. The urologic view. Infect Dis Clin N Am 17:333-351.
37. Dacher J, Pfister C, Monroc M et al (1996) Power Doppler sonographic pattern of acute pyelonephritis in children: comparison with CT. AJR Am J Roentgenol 166:1451-1455.
38. Majd M, Nussbaum Blask AR, Markle BM et al (2001) Acute pyelonephritis: comparison with Tc99m-DMSA SPECT, spiral CT, MR imaging, and power Doppler US in an experimental pig model. Radiology 218:101-108.
39. Wiseman AC (2009) Polyomavirus nephropathy: a current perspective and clinical considerations. Am J Kidney Dis 54:131-142.
40. Pearle MS, Pierce HL, Miller GL et al (1996) Optimal method of urgent decompression of the collecting system for obstruction and infection due to ureteral calculi. J Urol 160:1260-1264.
41. Yablon CM, Banner MP, Ramchandani P et al (2004) Complications of prostate cancer treatment: spectrum of imaging findings. Radiographics 24:S181-194.

# Benign Diseases of the Uterus

Susan Ascher[1], Caroline Reinhold[2]

[1] Georgetown University School of Medicine, Georgetown University Hospital, Washington, DC, USA
[2] Gynecology and Internal Medicine, McGill University Health Center, Montreal, Quebec, Canada

## Introduction

Endovaginal ultrasonography (EVUS) remains the procedure of choice for initial evaluation of benign diseases of the female genital tract. When EVUS findings are indeterminate, further evaluation is typically performed with magnetic resonance imaging (MRI) due to its excellent soft tissue differentiation, multiplanar capabilities, and absence of ionizing radiation. MRI is thus well suited for imaging women of reproductive age. It is used as a problem-solving tool in benign uterine disease – for example, uterine malformations, and adenomyosis, and to select appropriate candidates for therapies such as myomectomy and uterine artery embolization. It is also increasingly used in the pregnant patient for both fetal and maternal indications. The role of computed tomography (CT) is limited in the evaluation of benign disease of the female pelvis and is usually employed in an emergency situation, such as in an acute abdomen caused by ovarian torsion or pelvic inflammatory disease.

## Anatomy of the Uterus

In women of reproductive age, the uterus is ~6-9 cm in length and varies in appearance according to menstrual cycle. On EVUS, the thickness of the endometrium in premenopausal women increases progressively during the menstrual cycle: from 3 to 8 mm in the proliferative phase to 8 to 12 mm or greater in the secretory phase. The echotexture of the endometrium also varies. The endometrium is hypo- to isoechoic in the mid proliferative phase and becomes trilaminar in the periovulatory phase; in the secretory phase, it becomes echogenic and may have a nodular appearance. In the inner myometrium, subjacent to the endometrium, a thin, hypoechoic line is visible, called the subendometrial halo. This line does not correspond anatomically to the junctional zone on MRI and is typically thinner. The remainder of the myometrium is of intermediate echogenicity. Sonographic studies of endometrial thickness in postmenopausal women suggest an upper limit of 5 mm in patients not on hormone replacement and 8 mm for patients receiving hormonal therapy. EVUS is highly sensitive for detecting endometrial pathology when these cutoff values are used as guidelines to determine which patients would benefit from endometrial sampling [1]. The presence of endometrial widening on EVUS may be nonspecific and may be due to endometrial hyperplasia, polyps, or carcinoma.

The uterine zonal anatomy on MRI is best depicted using sagittal T2-weighted (T2-W) images (Fig. 1). In pre-

**Fig. 1.** Normal magnetic resonance imaging (MRI) of the uterine anatomy on sagittal 3D T2-weighted multiplanar reconstruction (MPR) of the uterus and cervix demonstrates normal zonal anatomy. There are three zones identifiable in the uterus: hyperintense endometrium, hypointense junctional zone (*arrow*), and intermediate signal intensity of the outer myometrium. Four zones are distinguished in the cervix: hyperintense mucus within the endocervical canal, intermediate signal intensity of the cervical mucosa (*arrowhead*), hypointense cervical stroma, and intermediate signal intensity of the outer smooth muscle

*Diseases of the Abdomen and Pelvis 2014-2017*,
DOI: 10.1007/978-88-470-5659-6_19 

menopausal women, three distinct zones are recognized:
– High-signal-intensity (SI) endometrium of varying thickness, depending on menstrual cycle
– Hypointense junctional zone, anatomically corresponding to the innermost layer of the myometrium
– Outer layer of the myometrium of intermediate SI.

Four zones are distinguished in the cervix by high-resolution MRI:
– Hyperintense mucus within the endocervical canal
– Cervical mucosa (plicae palmatae) of intermediate to high SI
– Hypointense cervical stroma surrounding the mucosa
– Additional layer of intermediate SI in continuity with the uterine myometrium representing smooth muscle.

In postmenopausal patients, the uterine corpus but not the cervix regresses and decreases in size. On dynamic gadolinium-enhanced images, the endometrium is hypovascular relative to the myometrium and becomes iso- or hyperintense on delayed scans.

## MRI Technique

If possible, patients should be scheduled in the second half of the menstrual cycle, as the thickness of the endometrial stripe increases during the follicular and secretory phase and thus the normal zonal anatomy of the uterus can be better appreciated. The objective of patient preparation is to obtain the best possible image quality while making the examination as comfortable as possible for the patient. To minimize motion artifact induced by bowel peristaltics, patients are advised to fast from 6 to 8 hours before the procedure. Unless contraindicated, intravenous or intramuscular injection of peristaltic inhibitors, i.e. glucagon or butyl-scopolamine, is recommended to further decrease artifacts. An empty urinary bladder minimizes ghosting artifact from patient motion. In addition, an empty bladder maintains the uterus in a more caudal position in the pelvis, away from small-bowel loops, and assures that the normally visible fat plane between the uterus and urinary bladder, an important criteria to exclude tumor invasion of the bladder wall in oncologic patients, will not be obliterated. Examinations are usually performed with the patient in the supine position using a body-flex phased array MR surface coil; in pregnant patients in the third trimester, imaging may also be performed in an oblique or lateral-decubitus position.

Depending on the clinical questions, one or several fast sequences of the upper abdomen should be performed, e.g., cine steady-state free-precession sequence [true fast imaging with steady-state precession (True-FISP); fast-imaging with steady-state acquisition (FIESTA)] in the coronal and axial plane and a T1-weighted (T1-W) gradient echo (GRE) sequence, to exclude ascites, enlarged retroperitoneal lymph nodes, hydronephrosis, or renal agenesis in patients with congenital uterine malformations.

T1-W sequences are standard for assessing the small pelvis. Although uncommon, lipomatous tumors of the uterus can only be accurately diagnosed with an additional fat-suppressed T1-W sequence using chemical presaturation to distinguish fat from blood, mucin, or other proteinaceous material, which remain of high SI. Alternatively, a T1-W 3D Dixon GRE sequence allows for T1-W in-phase, T1-W out-of-phase, T1-W water excitation, and T1-W fat excitation images within a single breathhold. Routine use of this sequence helps standardize imaging protocols without additional exam time.

T2-W images are most important for assessing the uterus, whereas sagittal sections are best suited to image it. Oblique coronal and axial slice orientation according to the long and short axis of the endometrial cavity should be applied for assessing uterine and cervical pathologies. It is important to train MR technologists on how to acquire these oblique sequences if physician supervision is not possible. The short-axis coronal oblique sequence (perpendicular to the long-axis of the endometrial cavity) is particularly valuable for assessing localized endometrial pathology and evaluating junctional zone thickness. It is also valuable for determining the extent of a uterine septum. A T2-W sequence performed parallel to the long axis of the endometrial cavity is critical to characterize the external uterine contour in patients with Müllerian duct anomalies. As this series is so important for classifying uterine anomalies, it is best performed earlier in the examination, prior to bladder filling that often displaces the uterus as it becomes increasingly distended. If the fundal contour is inadequately characterized by T2-W images, T1-W images parallel to the long axis can help characterize the external contour due to increased contrast between the myometrial fundal contour and the overlying fat. Software advances allow for 3D T2-W acquisition, facilitating postprocessing of the uterus in any plane and potentially obviating the need to acquire individual orthogonal 2D T2-W sequences. However, there is a trade off between acquisition time and left-to-right coverage, which is the result of trying to acquire nearly isotropic voxels for optimum multiplanar reconstruction.

Imaging of the uterus should be performed using the smallest possible field of view (FOV) (20-24 cm), thin sections (4-5 mm), and the largest possible matrix size appropriate to each individual sequence. These imaging parameters provide important anatomic detail, which becomes critical when imaging uterine anomalies and endometrial pathology. When imaging large leiomyomas, section thickness and FOV may need to be adjusted accordingly. However, when establishing the myometrial origin of a subserosal leiomyoma, thin sections at the level of the pedicle are frequently helpful.

We added an axial echoplanar diffusion-weighted (DW) MRI sequence of the small pelvis to our clinical routine protocol. DWI, well established for intracranial imaging, is a functional technique in which contrast derives from the random motion of water molecules within the extracellular tissue. It has a potential for identifying pelvic tumors, i.e., to differentiate benign from malignant lesions, and has a high sensitivity to detect iliac lymph nodes.

Gadolinium-enhanced imaging is not needed for most benign conditions but can be useful in selected pathologies. We routinely perform contrast-enhanced imaging in patients referred for evaluation of endometrial pathology. In addition, contrast-enhanced imaging is performed in patients with symptomatic leiomyomas scheduled for laparoscopic surgery or uterine artery embolization, in the latter case with additional MR angiography (MRA) of the iliac arteries. Vascularity can help predict treatment response, and enhancement may help distinguish a benign fibroid from a malignant leiomyosarcoma.

## Congenital Uterine Anomalies

Between the 6th and 11th weeks of gestation, the paired Müllerian ducts undergo descent, fusion, and septum resorption to form the uterus, fallopian tubes, cervix, and upper two thirds of the vagina [2]. Müllerian duct anomalies (MDA) occur when this process either fails or is interrupted. Depending on the anomaly, some patients may be asymptomatic, with normal fertility and obstetric outcomes, whereas others may have primary amenorrhea, menstrual irregularities, infertility, obstetric complications, and/or endometriosis. The reported prevalence of MDA varies widely: 1-5% in the general population and 13-25% in women with recurrent fetal loss [3]. Ovaries and external genitalia/distal one third of the vagina are spared because they originate from the primitive yolk sac and sinovaginal bud, respectively; renal anomalies are present in 30-50% of women with MDA [4].

Buttram and Gibbons classified MDAs in 1979, and a revised classification by the American Society for Reproductive Medicine (formerly the American Fertility Society) was published in 1988 [5, 6] (Fig. 2); appropriate classification is critical to ensure proper treatment. Whereas most anomalies can be assigned a subtype, some defy specific classification and are best described anatomically rather than "forced" into a category.

When an MDA is suspected, US is the most commonly performed exam and may be diagnostic, especially if a 3D US is performed. However, MRI remains the preferred imaging technique in patients where EVUS is not possible due to vaginal agenesis, in patients with complex uterine anomalies, and especially when surgical intervention is contemplated. In multiple studies, MRI shows excellent agreement with MDA subtype classifications [7].

### Class I: Müllerian Agenesis and Hypoplasia

Müllerian agenesis and hypoplasia anomalies (10%) occur early in gestation and are the result of some degree of failure of the Müllerian ducts prior to fusion [2]. The most extreme and common form of class I MDA is the Mayer-Rokitansky-Küster-Hauser syndrome: agenesis of the vagina, cervix, and uterus in 90% of cases. In 10%, there is a rudimentary uterus present. Ovaries are morphologically and biochemically normal, but they may be located outside the pelvis. Treatment is focused on enabling sexual function by creating a neovagina. At imaging, fatty and connective tissue appears in the expected location of

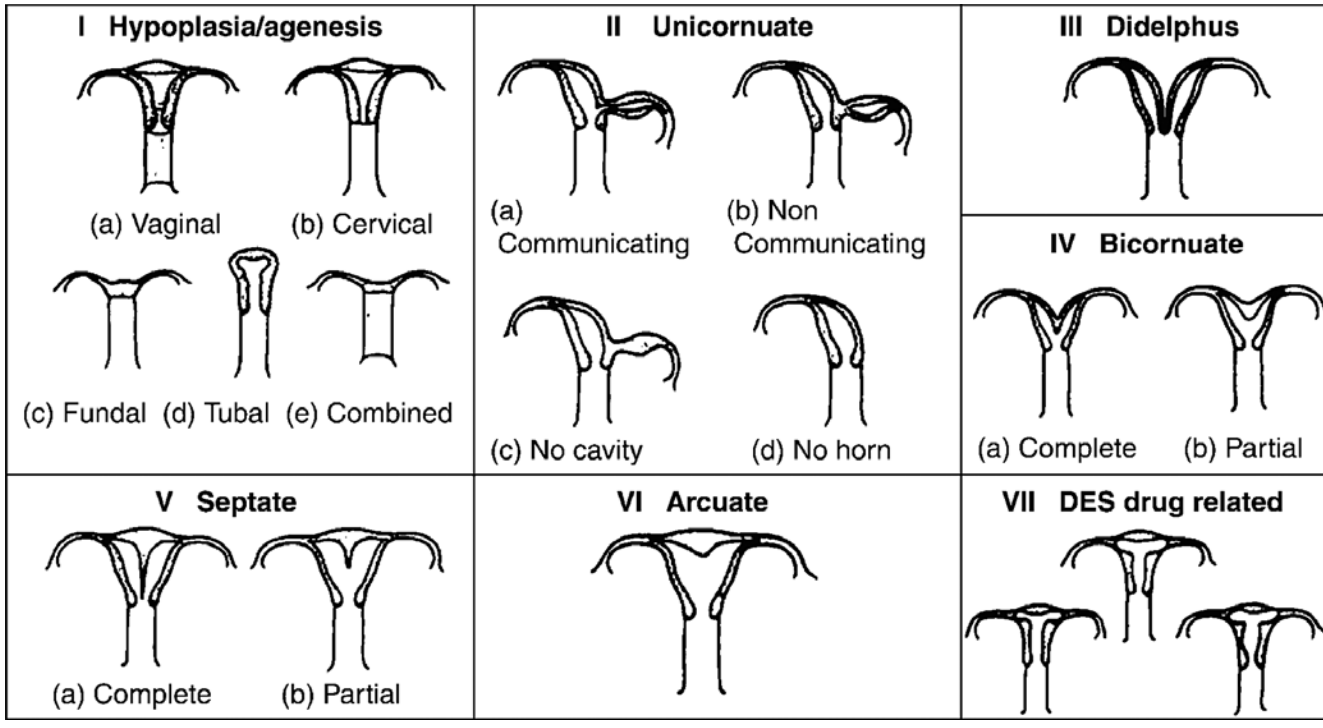


**Fig. 2.** Classification system of Müllerian duct anomalies developed by the American Fertility Society [6]

**Fig. 3** Müllerian duct anomalies (MDA): Mayer-Rokitansky-Küster-Hauser Syndrome. Axial T2-weighted magnetic resonance image (MRI) in a woman with primary amenorrhea demonstrates the upper urethra anteriorly (*arrow*) and rectum posteriorly (*arrowhead*). A normal upper vagina is not present. The transverse plane highlights the fibrofatty tissue in the expected location of the vagina

the upper two thirds of the vagina and is best seen on transverse images (Fig. 3). A truncated vagina may be seen between the urethra anteriorly and the rectum posteriorly.

### Class II: Unicornuate Uterus

Unicornuate uterus (20%) is the result of normal development of one Müllerian duct, with either complete agenesis or some degree of arrested development of the contralateral duct. There are four subtypes of unicornuate uterus:

– No rudimentary horn
– Rudimentary horn without a cavity
– Rudimentary horn with communicating cavity
– Rudimentary horn with noncommunicating cavity.

There is a high association with renal anomalies, especially renal agenesis, ipsilateral to the rudimentary horn (40%). Only patients with cavitary rudimentary horns require surgical excision. This is done to prevent hematometra and/or obstetric complications to include uterine rupture [8].

At imaging, the unicornuate uterus is deviated to one side of the pelvis, and the endometrium is described as "banana" or "bullet" shaped (Fig. 4). Uterine zonal anatomy is preserved, as is the endometrial-to-myometrial ratio [9]. Appearance of the rudimentary horn varies by subtype. A noncavitary rudimentary horn images as diffuse low to intermediate SI. A cavitary rudimentary horn displays normal zonal anatomy. If noncommunicating, the endometrial cavity may be distended with blood, and/or there may be imaging manifestations of endometriosis.

### Class III: Uterus Didelphys

Uterus didelphys (5%) results from complete failure of Müllerian duct fusion. Most patients have two distinct uterine horns, cervices, and upper vaginas [3]. A transverse hemivaginal septum is often present, with ipsilateral obstruction and hematometrocolpos. If present, this septum is excised. Patients with obstructed uterus didelphys are more likely than others to have ipsilateral renal agenesis [4]. Patients without a transverse hemivaginal septum are asymptomatic and require no invasive therapy.

At imaging, two widely divergent and symmetric uterine horns, two separate cervices ("owl eyes"), and two separate upper vaginas are noted (Fig. 5). There is no communication between the paired endometrial or endocervical cavities. A fundal cleft >1 cm is always present [10]. Uterine zonal anatomy and endometrial-to-myometrial

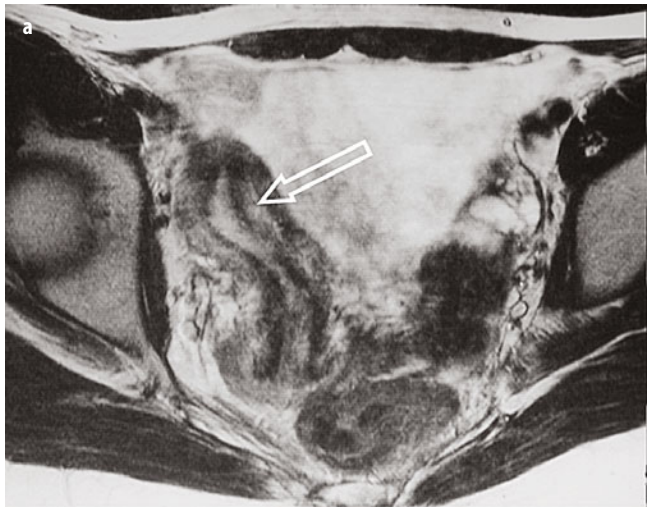



**Fig. 4 a, b.** **a** Müllerian duct anomalies (MDA): unicornuate uterus. Axial T2-weighted magnetic resonance images (MRI) show: **a** right-sided "banana"-shaped unicornuate uterus (*open arrow*) and **b** smaller, noncommunicating cavitary horn (*arrowhead*)

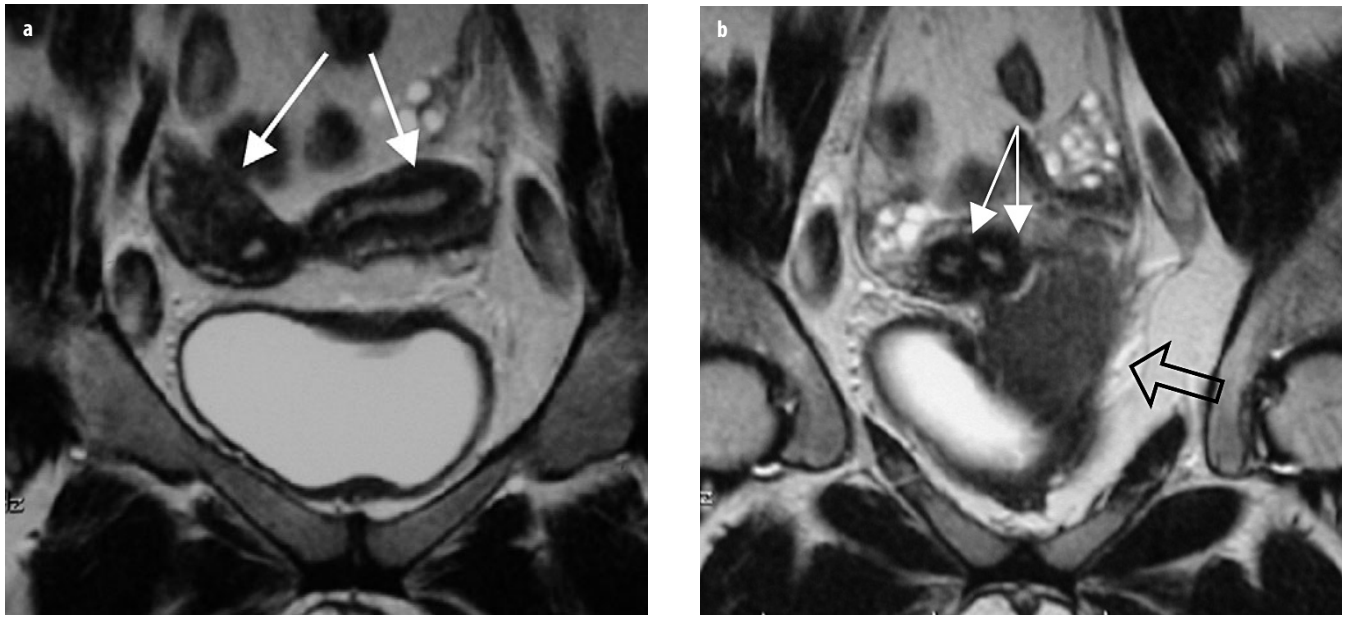


**Fig. 5 a, b.** Müllerian duct anomalies (MDA): uterus didelphys. Coronal T2-weighted magnetic resonance images (MRI) demonstrate: **a** two divergent uterine horns (*arrows*) and **b** separate cervices (*solid arrows*). There is no communication between the paired cavities. A transverse left hemivaginal septum obstructs the ipsilateral vagina, leading to left hematocolpos (*open arrow*, **b**)

ratio are preserved in both horns. If there is an obstructing transverse hemivaginal septum, the affected side will be distended, with high SI blood products on T1-W sequences.

### Class IV: Bicornuate Uterus

Bicornuate uterus (10%) results from incomplete fusion of the Müllerian ducts. The uterine horns are duplicated, and there may be a single (bicornuate unicollis) or a duplicated (bicornuate bicollis) cervix. Communication of the endometrial or endocervical canals is necessary to make the diagnosis. In one fourth of cases, there will also be a longitudinal vaginal septum, and distinction with uterus didelphys can be challenging. In the absence of symptoms, no treatment is necessary. If a patient is symptomatic (dyspareunia and/or hematocolpos), a vaginal septoplasty is warranted [11, 12].

Imaging features include two symmetric uterine horns separated by a deep (>1 cm) fundal cleft (Fig. 6). In a bicornuate unicollis uterus, the endometrial canal is heart shaped, with visible communication between the two sides. In a bicornuate bicollis uterus, the two cervices mimic "owl eyes" of an uterus didelphys. Communication between segments allows diagnosing bicornuate bicollis with confidence.

### Class V: Septate Uterus

Septate uterus (55%) results from some degree of failure of uterovaginal septum resorption. The septum may be complete, extending at least to the external os or into the vagina, in one fourth of patients [13]. A partial septum ends proximal to the external os. The composition of the septum is variable and often myometrial proximally and more fibrous distally [9, 14]. The hallmark of the septate

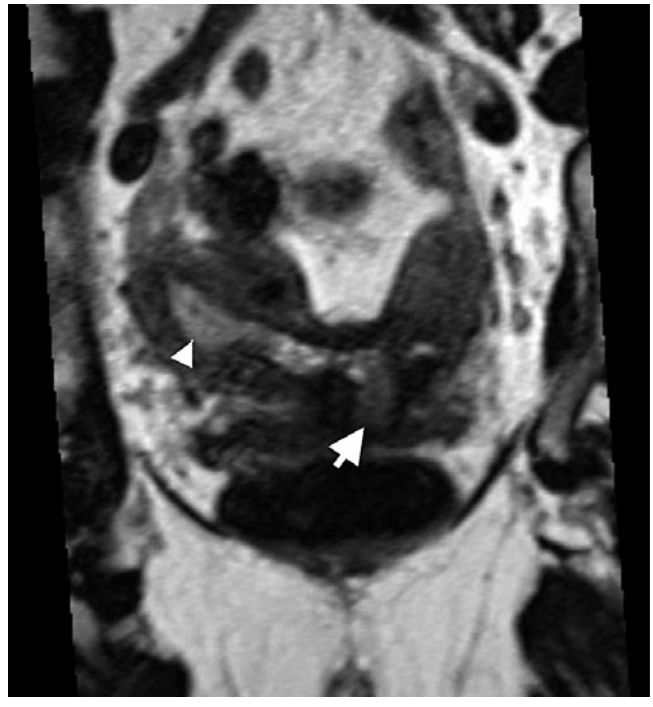

**Fig. 6** Müllerian duct anomalies (MDA): bicornuate uterus. 3D T2-weighted multiplanar reconstruction (MPR) magnetic resonance image (MRI) in the true coronal plane of the uterus demonstrates divergent uterine horns with a common cervix (*arrow*), consistent with bicornuate unicollis uterus. Note the polyp distending the right endometrial canal (*arrowhead*)

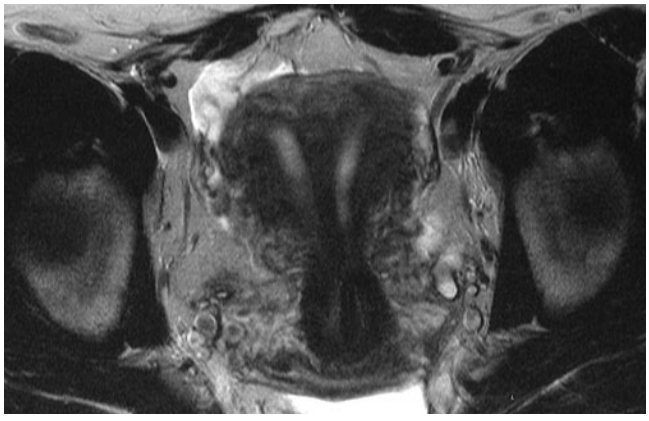

**Fig. 7.** Müllerian duct anomalies (MDA): septate uterus. T2-weighted magnetic resonance image (MRI) obtained in the true coronal plane of the uterus shows two symmetric uterine horns and cervices, with an intervening septum consistent with a complete, septate uterus. Note the straight fundal contour

uterus is a convex, flat, or minimally concave fundal contour. Fetal wastage is common in women with a septate uterus, and the spontaneous abortion rate is 65%. Treatment reflects the makeup of the septum. That is, if the septum is primarily fibrous, a hysteroscopic septoplasty can be performed with good results. If, however, the septum is primarily myometrial, a combined laparoscopic-hysteroscopic surgical approach is warranted [15].

At imaging, the uterus is normal in size, with normal zonal anatomy and endometrial-to-myometrial ratio. The fundal region may have a cleft ⩽1 cm (Fig. 7). It is critical to describe whether the septum is partial or complete and its imaging characteristics, that is, smooth muscle and/or fibrous tissue [14].

#### Class VI: Arcuate Uterus

Arcuate uterus results when there is near complete resorption of the uterovaginal septum, with a mild indentation of the endometrial cavity at the level of the fundus. Fertility and obstetric outcomes are usually normal [16]. Treatment is reserved for women with habitual fetal loss.

At imaging, the uterus is normal in size and morphology, without a deep fundal cleft. A myometrial broad-based indentation of the endometrial canal is present.

#### Class VII: DES Uterus

DES uterus is caused by maternal ingestion of diethylstilbestrol prescribed to prevent miscarriage in high-risk women. It leads to uterine, cervical, fallopian tube, and vaginal anomalies and is linked to the development of clear cell carcinoma in female offspring. Uterine malformations include a T-shaped, small, and hypoplastic uterus, narrowed fundal endometrial canal, widened lower uterine segment, irregular endometrial margins, and intraluminal filling defects [17, 18]. Cervical changes include hypoplasia, anterior cervical ridge, cervical collar, and pseudopolyposis [18]. Fallopian tube anomalies include truncation, saccular outpouchings, and fimbria deformities.

At MRI, the uterus is hypoplastic, with a T-shaped endometrial canal. Focal junctional zone thickening, called constriction bands, results in narrowing and irregularity of the endometrial canal [2].

## Benign Conditions of the Vagina, Cervix, and Uterus

### Cysts

- Bartholin's cysts are caused by retained secretions within the vulvovaginal glands, mostly as a result of chronic inflammation or trauma. They are located in the posterolateral parts of the lower vagina and vulva.
- Nabothian cysts are retention cysts of the cervical glands and clefts.
- Gartner duct cysts represent remnants of the caudal end of the Wolffian or mesonephric ducts and are typically located in the anterolateral wall of the vagina above the inferior margin of the symphysis pubis.
- Müllerian cysts, representing embryologic remnants of Müllerian (paramesonephric) ducts, are the most common congenital cysts of the female genital tract and can be found from the introitus to the cornua. They are typically lined by mucinous, columnar epithelium. At the level of the vagina, they are most commonly located anterolaterally and are indistinguishable from Gartner duct cysts. The majority of Müllerian cysts are small and asymptomatic. Large, symptomatic cysts require excision.

### Endometrial Polyps

Endometrial polyps are among the most common pathologic lesions of the uterine corpus. Patients with postmenopausal bleeding and endometrial polyps usually undergo endometrial sampling and polyp removal [19]. Endometrial polyps have a variable appearance at EVUS but are typically echogenic, with an intact overlying endometrium or subendometrial halo. A vascular pedicle is usually identified at color/power Doppler imaging. On T2-W images, polyps present as masses that are slightly hypointense or isointense relative to the normal endometrium. Large polyps are frequently heterogeneous in SI [20]. On T2-W sequences, the fibrous core is seen as a hypointense area within a polyp; the addition of gadolinium-enhanced sequences significantly improves detection rate (Fig. 8). Endometrial polyps show a variable degree of enhancement after gadolinium administration. Small polyps enhance early and are well delineated against the hypointense endometrial complex on early dynamic scans. In addition, a vascular stalk can frequently be identified during the arterial phase.

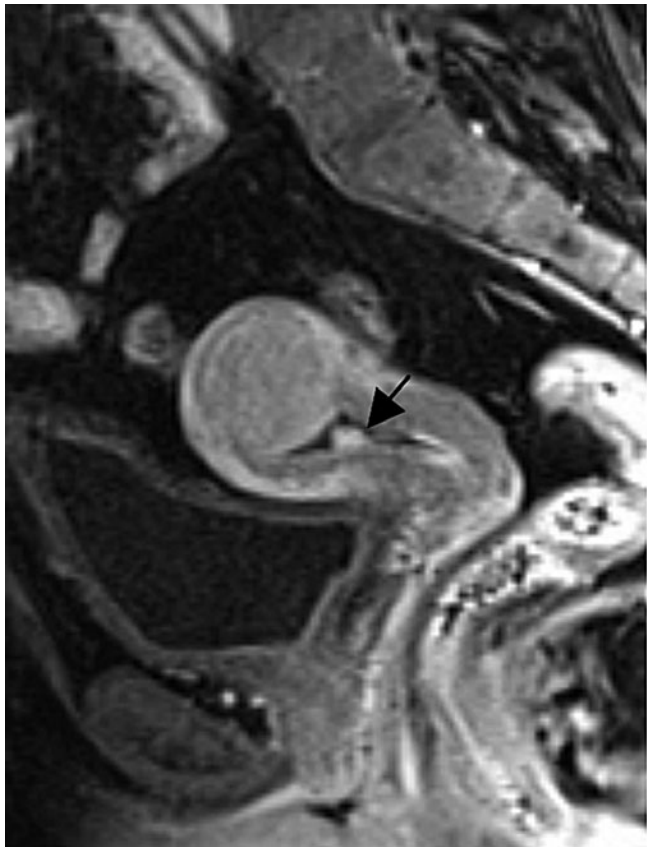

**Fig. 8.** Endometrial polyp. Contrast-enhanced sagittal fat-suppressed T1-weighted magnetic resonance image (MRI) shows an enhancing lower-uterine-segment polyp (*arrow*). A fundal intramural leiomyoma with a submucosal component enhances less than the polyp

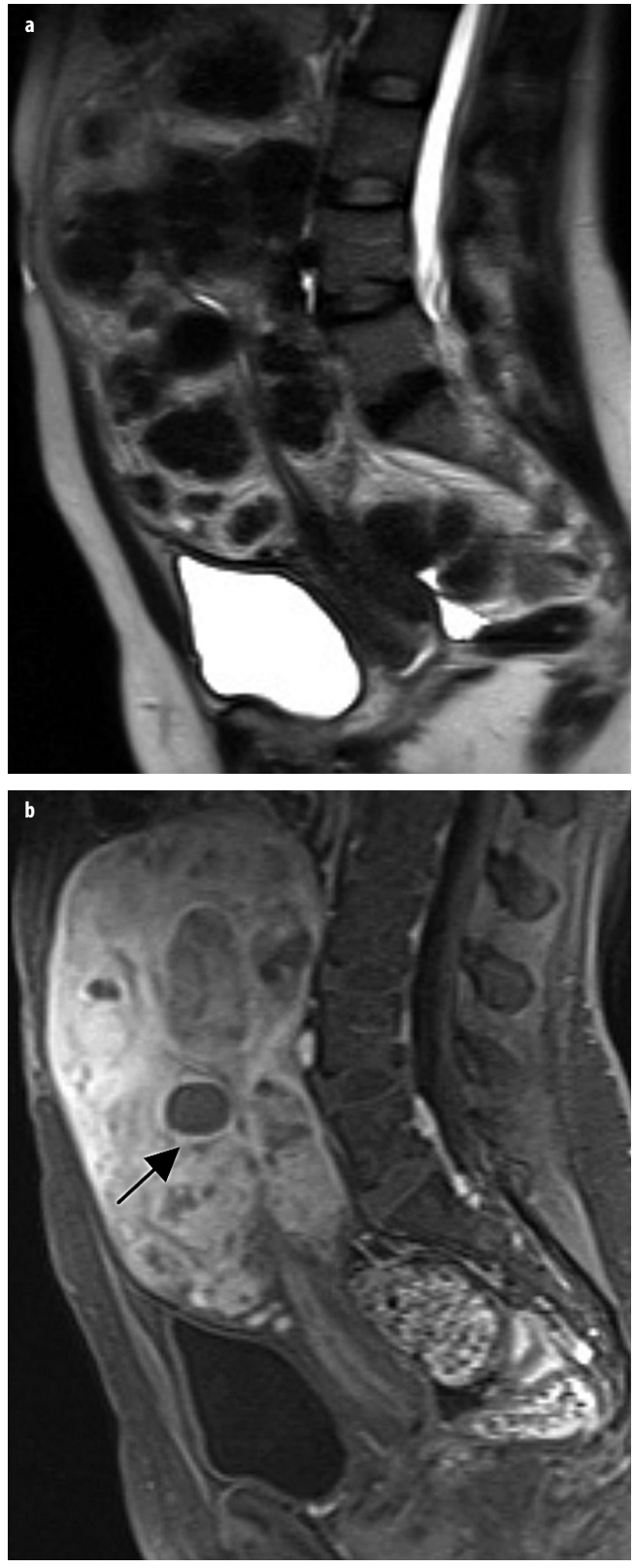


**Fig. 9 a, b.** Leiomyomata. **a** Sagittal T2-weighted magnetic resonance image (MRI) demonstrates an enlarged uterus with multiple, well-defined low signal-intensity leiomyomas. **b** Contrast-enhanced sagittal fat-suppressed T1-weighted MRI shows variable enhancement of the leiomyomata. Note a degenerated avascular leiomyoma in the anterior corpus (*arrow*, **b**)

### Endometrial Synechia

Endometrial synechia result from traumatic injury to the endometrium and may be demonstrated on EVUS and MRI; sonohysterography improves detection. In severe cases of Asherman's syndrome, synechiae may result in infertility, recurrent pregnancy loss, and amenorrhea. On EVUS, synechiae present as echogenic or hypoechoic bands traversing the endometrial cavity. These bands can be thick and broad or thin and easily disrupted on sonohysterography. On MRI, they are hypointense on T2-W sequences and usually show enhancement after gadolinium.

### Leiomyomas

MRI is useful for distinguishing leiomyomas from other myometrial pathology and solid pelvic masses, especially in patients with nondiagnostic or equivocal ultrasound (US) findings. A mass of intermediate SI on T1-W that is low SI on T2-W MRI images and splays the uterine serosa or myometrium allows the confident diagnosis of leiomyoma [21] (Fig. 9). The presence of feeding vessels originating in the myometrium further supports the uterine ori-

gin of the mass. However, if a mass is adjacent to the uterus and is of intermediate or high SI relative to the myometrium on T2-W images, the differential diagnosis includes both degenerated leiomyoma and extrauterine tumors (benign and malignant). In these patients, the diagnosis of leiomyoma should be reserved only for cases in which the uterine origin of the mass is firmly established. Occasionally, it may be difficult to distinguish a pedunculated subserosal leiomyoma from an ovarian fibroma, as both lesions may be hypointense on T2-W images. This distinction is likely not significant, as the latter is rarely malignant [21]. Submucosal leiomyomas are usually distinguished from endometrial polyps by identifying their myometrial origin and low SI on T2-W images.

Symptomatic leiomyomata are a burden for the women affected, as well as for society. In the United States, symptomatic leiomyomata remain the number one cause of hysterectomies per year and cost up to US $34.4 billion annually, reflecting direct costs of providing care and indirect costs associated with lost work days and pregnancy-related issues [22]. These statistics have led to an increase in uterine-conserving therapies for affected women [23]. MRI provides a comprehensive evaluation for potential candidates for uterine artery embolization (UAE); it accurately displays size, number, and location [24]. Additionally, in at least 20% of cases, it identifies autoinfarcted, comorbid, or alternative conditions that preclude UAE as primary therapy [25]. Following UAE, MRI helps assess treatment response and identify complications, such as leiomyoma delivery and pyomyoma [26-28].

Malignant degeneration of a leiomyoma is a rare occurrence [29]. Echogenicity or signal characteristics may not reliably distinguish a benign leiomyoma from a leiomyosarcoma. However, if a leiomyoma suddenly enlarges, especially after menopause, and/or if it has an irregular or indistinct border, intratumoral hemorrhage, intermediate or heterogenous T2-W SI, and/or restricted diffusion, the possibility of sarcomatous transformation should be considered [30].

**Fig. 10.** Adenomyosis. Sagittal T2-weighted magnetic resonance image (MRI) demonstrates an enlarged globular uterus with diffuse junctional-zone widening. Punctate high-signal-intensity foci (*arrows*) are distributed throughout the widened junctional zone. Note multiple nabothian cysts in the anterior cervical lip and debris in the posterior vaginal fornix

### Adenomyosis

Leiomyomas must also be differentiated from uterine adenomyosis, although these conditions frequently coexist. Differentiating the two entities may be critical, because uterine-conserving therapy is established for leiomyomas; whereas hysterectomy remains the definitive treatment for debilitating adenomyosis. MRI is extremely accurate in making this distinction, especially in patients with diffuse adenomyosis with junctional-zone widening >12 mm and foci of increased signal on T2-W sequences (Fig. 10) [31]. The hyperintense foci correspond to the heterotopic endometrial tissue. The surrounding muscular hyperplasia results in the low-SI myometrial lesion or junctional-zone widening. Hemorrhagic foci can be seen on T1-W sequences in ~20% of patients due to the presence of progesterone receptors. However, imaging features of focal adenomyosis can overlap with those of leiomyomas [31-33]. Imaging characteristics that favor the diagnosis of focal adenomyosis include:

- A lesion with poorly defined margins
- A lesion that is elliptical in shape extending along the endometrium
- A lesion that has little mass effect upon the endometrium relative to its size
- A lesion with high SI striations radiating from the endometrium into the myometrium.

Cystic adenomyosis needs to be differentiated from a leiomyoma with central hemorrhagic degeneration or a unicornuate uterus with an obstructed, noncommunicating rudimentary horn.

### Myometrial Contraction

Another entity that may mimic a leiomyoma or adenomyosis is a myometrial contraction. Myometrial contractions are transient and usually change or resolve over the course of the exam. Contractions image as hypoechoic or low-SI lesions within the myometrium that deform the endometrium while sparing the outer uterine contour.

### Uterine Peristalsis

Uterine peristalsis, which represents a rhythmic contraction of the inner myometrium and is most marked during the menstrual and periovulatory phase, can present as diffuse widening of the junctional zone. Kinematic sequences using a T2-W single-shot fast-spin-echo (SSFSE) or half-Fourier-acquisition single-shot turbo spin-echo (haste) can differentiate true from apparent widening of the junctional zone.

## MRI in Pregnancy

There is no clinical or experimental evidence of teratogenic or other adverse fetal effects from MRI in pregnancy. The technique is well suited for imaging pregnant women for maternal indications, including mapping fibroids that may interfere with labor and causes of acute pelvic pain (e.g., red degeneration of fibroids or other pelvic pathology).

## Conclusion

MRI is a powerful imaging modality that provides a comprehensive examination of the female pelvis.

## References


1. Smith-Bindman R, Kerlikowske K, Feldstein VA et al (1998) Endovaginal ultrasound to exclude endometrial cancer and other endometrial abnormalities. JAMA 280:1510-7.
2. Troiano RN, McCarthy SM (2004) Müllerian duct anomalies: imaging and clinical issues. Radiology 233:19-34.
3. Behr SC, Coutier JL, Qayyum A (2012) Imaging of Müllerian duct anomalies. RadioGraphics 32:1619-1620.
4. Li S, Qayyum A, Coakley FV, Hricak H (2000) Association of renal agenesis and müllerian duct anomalies. J Comput Assist Tomogr 24:829-834.
5. Buttram VC Jr, Gibbons WE (1979) Müllerian anomalies: a proposed classification. (An analysis of 144 cases.) Fertil Steril 32:40-46.
6. The American Fertility Society classifications of adnexal adhesions, distal tubal occlusion, tubal occlusion secondary to tubal ligation, tubal pregnancies, müllerian anomalies and intrauterine adhesions (1988). Fertil Steril 49:944-955.
7. Mueller GC, Hussain HK, Smith YR et al (2007) Müllerian duct anomalies: comparison of MRI diagnosis and clinical diagnosis. AJR Am J Roentgenol 189:1294-1302.
8. Jayasinghe Y, Rane A, Stalewski H, Grover S (2005) The presentation and early diagnosis of the rudimentary uterine horn. Obstet Gynecol 105:1456-1467.
9. Pellerito JS, McCarthy SM, Doyle MB et al (1992) Diagnosis of uterine anomalies: relative accuracy of MR imaging, endovaginal sonography, and hysterosalpingography. Radiology 183:795-800.
10. Fedele L, Dorta M, Brioschi D et al (1989) Magnetic resonance evaluation of double uteri. Obstet Gynecol 74:844-847.
11. Miller RJ, Breech LL (2008) Surgical correction of vaginal anomalies. Clin Obstet Gynecol 51:223-236.
12. Rackow BW, Arici A (2007) Reproductive performance of women with müllerian anomalies. Curr Opin Obstet Gynecol 19:229-237.
13. Propst AM, Hill JA 3rd (2000) Anatomic factors associated with recurrent pregnancy loss. Semin Reprod Med 18:341-350.
14. Zreik TG, Troiano RN, Ghoussoub RA et al (1998) Myometrial tissue in uterine septa. J Am Assoc Gynecol Laparosc 5:155-160.
15. Chandler TM, Machan LS, Cooperberg PL et al (2009) Müllerian duct anomalies: from diagnosis to intervention. Br J Radiol 82:1034-1042.
16. Tulandi T, Arronet GH, McInnes RA (1980) Arcuate and bicornuate uterine anomalies and infertility. Fertil Steril 34:362-364.
17. Kaufman RH, Adam E, Binder GL, Gerthoffer E (1980) Upper genital tract changes and pregnancy outcome in offspring exposed in utero to diethylstilbestrol. Am J Obstet Gynecol 137:299-308.
18. Goldberg JM, Falcone T (1999) Effect of diethylstilbestrol on reproductive function. Fertil Steril 72:1-7.
19. Sheth S, Hamper UM, Kurman RJ (1993) Thickened endometrium in the postmenopausal woman; sonographic-pathologic coorelation. Radiology 187:135-139.
20. Grasel RP, Outwater EK, Siegelman ES et al (2000) Endometrial polyps: MR imaging features and distinction from endometrial carcinoma. Radiology 214:47-52.
21. Hricak H, Tscholakoff D, Heinrichs L et al (1986) Uterine leiomyomas: correlation of MR histopathologic findings, and symptoms. Radiology 158:385-391.
22. Cardozo ER, Clark D, Banks NK et al (2012) The estimated annual cost of uterine leiomyomata in the United States. Am J Obstet Gynecol 206:21.e1-9.
23. Jacobson GF, Shaber RE, Armstrong MA, Hung Y-Y (2007) Changes in rates of hysterectomy and uterine conserving procedures for treatment of uterine leiomyoma. Am J Obstet Gynecol 196:601.e1-6.
24. Jha RC, Ascher SM, Imaoka I, Spies JB (2000) Symptomatic fibroleiomyomata: MR imaging of the uterus before and after uterine artery embolization. Radiology 217:228-35.
25. Nikolaidis PN, Siddiqi AH, Carr JC et al (2005) Incidence of nonviable leiomyomas on contrast material enhanced pelvic MR imaging in patients referred for uterine artery embolization. J Vasc Interv Radiol 16:1465-1471.
26. Kroencke TJ, Scheurig C, Poellinger A et al (2010) Uterine artery embolization for leiomyomas: percentage of infarction predicts clinical outcome. Radiology 255:834-841.
27. Kitamura Y, Ascher SM, Cooper C et al (2005) Imaging manifestations of complications associated with uterine artery embolization. RadioGraphics 25:S119-32.
28. Radeleff B, Eiers M, Bellemann N et al (2010) Expulsion of dominant submucosal fibroids after uterine artery embolization. Eur J Radiol 75:e57-63.
29. Shah SH, Jagannathan JP, Krajewski K et al (2012) Uterine sarcoma: then and now. AJR Am J Roentgenol 199:213-223.
30. Thomassin-Naggara, Dechoux S, Bonneau C et al (2013) How to differentiate benign from malignant myometrial tumors using MR imaging. Eur Radiol 23:2306-2314.
31. Reinhold C, McCarthy S, Bret PM et al (1996) Diffuse adenomyosis: comparison of endovaginal US and MR imaging with histopathologic correlation. Radiology 199:151-158.
32. Togashi K, Ozasa H, Konishi I et al (1989) Enlarged uterus: differentiation between adenomyosis and leiomyoma with MR imaging. Radiology 171:531-534.
33. Mark AS, Hricak H, Heinrichs LW et al (1987) Adenomyosis and leiomyoma: differential diagnosis with MR imaging. Radiology 163:527-529.

# Malignant Tumors of the Uterus

H. Alberto Vargas[1], John A. Spencer[2]

[1] Memorial Sloan-Kettering Cancer Center, New York, NY, USA
[2] Clinical Radiology, St James's Institute of Oncology, Leeds, West Yorkshire, UK

## Overview

Primary malignant tumors of the uterus include:
1. Tumors of the uterine cervix
   – 80% are squamous carcinomas arising from the ectocervix
   – 15% are adenocarcinomas from the endocervical canal.
2. Tumors of the endometrium
   – 90% are type 1 tumors: endometrioid carcinoma grades 1 and 2
   – 10% are more aggressive type 2 tumors: grade 3 endometrioid and clear cell carcinoma, papillary serous carcinoma, and poorly differentiated tumors.
3. Uterine sarcomas
   – Endometrial stromal sarcoma (ESS) and adenosarcoma arising from the stroma of the uterus
   – Leiomyosarcoma arising from its smooth muscle.

## Role of Imaging

– Ultrasound (US) can be used to determine which women with postmenopausal bleeding (PMB) should undergo hysteroscopy.
– Magnetic resonance imaging (MRI) is the primary tool for staging cervical and endometrial cancer.
– Computed tomography (CT)-positron emission tomography (CT-PET) is a valuable adjunct for metastatic assessment of advanced cervical and endometrial cancers as well as aggressive uterine sarcomas.

## Tumors of the Uterine Cervix

Cervical cancer is the second most common female cancer worldwide and the fifth most common cause of female cancer death. It affects about 16 per 100,000 women and kills about 9 per 100,000 per annum. In industrialized countries, the incidence of cervical cancer is lower and is falling due to public health measures, including screening by cervical smear cytology and vaccination against human papilloma virus (HPV).

### Diagnosis and Primary Treatment

The cardinal symptom of early cervical cancer is vaginal bleeding, particularly intermenstrual and postcoital bleeding. Histologic diagnosis follows colposcopic biopsy and an initial estimation of tumor extent from conization of the cervix or loop biopsy [large loop excision of the transitional zone (LLETZ)]. Early disease up to stages IB2/IIA1 (Table 1) is suitable for radical surgical treatment (Wertheim hysterectomy). Some small, confined cervical tumors are suitable for trachelectomy with fertility preservation. Most tumors ⩾4 cm and/or of higher stage are now considered for chemoradiotherapy (CRT).

### Staging

All cancers are staged in the same way if they are believed to be primary cervical cancer. The International Federation of Gynecology and Obstetrics (FIGO) system for staging is most widely used but does not include lymph node status [1]. It is primarily a clinical and pathologic system. The 2009 revision of FIGO staging (Table 1) made the concession that information from cross-sectional imaging should be recorded [1].

The American Joint Committee on Cancer (AJCC) TNM staging scheme works as for most other cancers. Stages T1-T4 are similar to FIGO stages I–IVa, but it includes additional nodal (N) and distant spread (M) staging categories [2].

### Key Points of TNM (AJCC) Staging

Regarding lymph node spread, N1 indicates pelvic spread but M1 indicates spread to paraortic or inguinal nodes [2]. NX is used when nodes cannot be assessed [2].

*Diseases of the Abdomen and Pelvis 2014-2017*,
DOI: 10.1007/978-88-470-5659-6_20 

**Table 1.** Revised FIGO staging of cervical carcinoma 2009 [1]

| Stage | Characteristic |
|---|---|
| Stage 0 | Cervical intraepithelial neoplasia (CIN 3) |
| Stage I | Confined to cervix |
| IA | Invasive carcinoma only diagnosed by microscopy |
| IA1 | Stromal invasion <3 mm in depth and <7 mm in extension |
| IA2 | Stromal invasion >3 mm depth and not >5 mm and extension <7 mm |
| IB | Visible lesions limited to the cervix or preclinical cancers >stage 1A |
| IB1 | Clinically visible tumor ≤4 cm in greatest dimension |
| IB2 | Clinically visible tumor >4 cm in greatest dimension |
| Stage II | Beyond cervix though not to pelvic sidewall or lower third of vagina |
| IIA | With upper vaginal but without parametrial invasion |
| IIA1 | Clinically visible tumor ≤4 cm in greatest dimension |
| IIA2 | Clinically visible tumor >4 cm in greatest dimension |
| IIB | With parametrial invasion |
| Stage III | Lower vaginal or pelvic sidewall spread |
| IIIA | Tumor involves lower third of the vagina with no extension to pelvic sidewall |
| IIIB | Extension to pelvic sidewall or causing obstructive uropathy |
| Stage IV | Extension beyond pelvis or biopsy proven to involve the mucosa of the bladder or the rectum |
| IVA | Extension beyond pelvis or rectal/bladder invasion |
| IVB | Distant organ spread |

*FIGO* International Federation of Gynecology and Obstetrics, *CIN* carcinoma in situ

## MRI Technique and Pearls for Cervical Cancer Staging

The imaging mainstay is T2-weighted imaging (T2-WI), comprising a sagittal sequence of the pelvis and a small field of view (SFOV) inclined axial sequence perpendicular to the endocervical canal (Fig. 1). In some cases, imaging along the plane of the endocervical canal better depicts lateral extension of the tumor. In the normal cervix, a low signal intensity (SI) stromal ring surrounds high SI mucosa. Tumors in premenopausal women are more commonly exophytic, filling the vagina. In postmenopausal (PM) women, they are more commonly endophytic within the barrel of the cervix.

### Stage I

Stage IA tumors are usually completely excised in the diagnostic biopsy. MRI shows only features of this artefact. Stage IB tumors have brighter T2-W SI than the dark, fibromuscular, cervical stroma. The key imaging sign of stage IB disease is preservation of a continuous intact low T2-W SI stromal ring of the cervix around the tumor [3].

### Stage II

Stage IIB tumors interrupt or breach this "black ring" and may extend into the surrounding parametrial fat (Fig. 2). Stage IIA tumors invade the low T2-W SI wall of the upper vagina but do not breach this black ring.

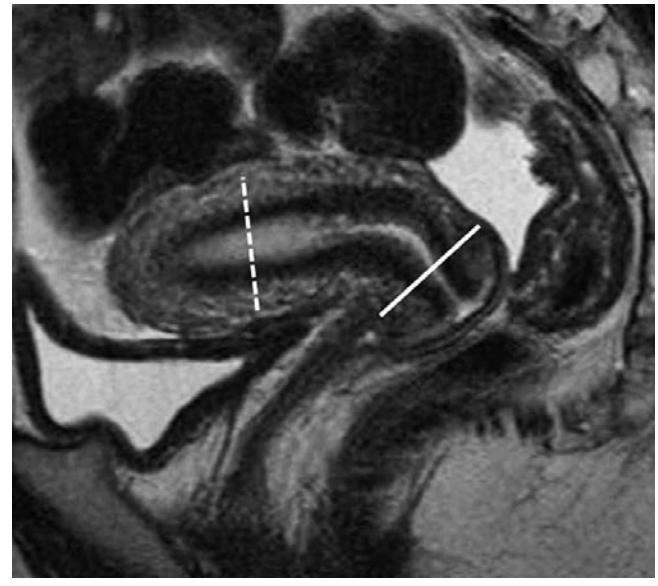

**Fig. 1.** Sagittal T2-weighted image of the normal uterus showing zonal anatomy and planes used for small field-of-view imaging of cervical cancer (*solid white line*) and endometrial cancer (*dashed white line*)

### Stage III

Stage IIIA tumors invade the lower vagina, and this involvement may be better appreciated clinically. Stage IIIB tumors extend within 3 mm of or show abutment with the low-SI internal obturator, levator ani, and pyriform muscles and the iliac vessels, or show ureteric involvement with a hydroureter above this level.

### Stage IV

Stage IVA tumors show loss or interruption of the low-SI bladder or rectal wall, and tumor invading through the mucosa is diagnostic. Bladder bullous edema alone does not qualify stage IVA disease (Fig. 3a).

### Alternative Imaging Sequences

Alternative sequences that may be used include diffusion-weighted imaging (DWI) and dynamic contrast-enhanced (DCE) MRI. There is no consensus as to which other sequences should be used for staging pelvic lymph node metastasis and other abdominal spread, suffice to say that they should cover the pelvis and abdomen up to the renal hila and employ at least two orthogonal planes and both T1-W and T2-W images. A pelvic lymph node >9 mm in maximum small-axis dimension (MSAD) is concerning due to pelvic nodal metastasis [4], as is any lymph node showing necrosis (Fig. 4). Smaller nodes seen in the parametrium or the rectal envelope are concerning for metastasis. Examinations performed to assess treatment response should aim for reproducibility with earlier MRI studies. Examinations performed for suspected treatment complications should be tailored to the specific concern.

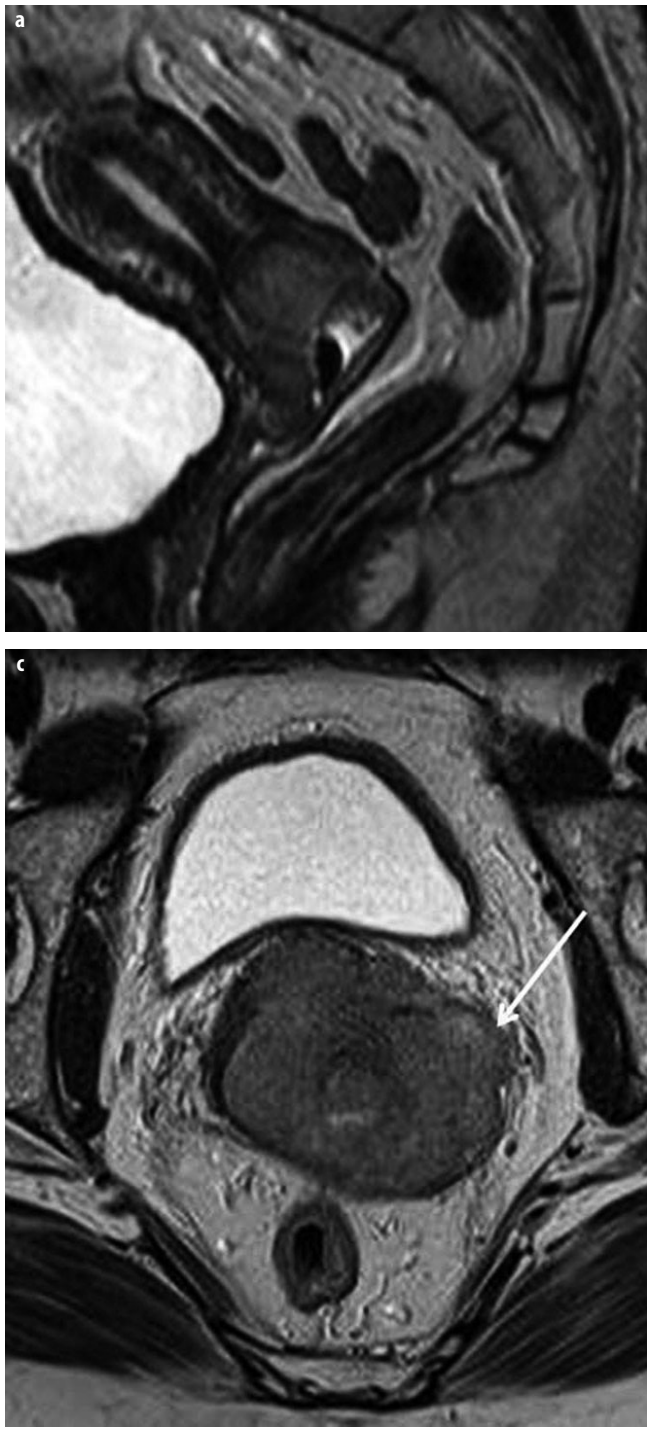


**Fig. 2 a-c.** **a** Sagittal T2-weighted image of stage IB cervical cancer with **b** corresponding inclined small field-of-view image showing an intact and complete T2 dark stromal ring (*yellow arrows*) and **c** a different and large stage IIB cancer with breach of the left side of the stromal ring and parametrial invasion (*white arrow*)

Pelvic insufficiency fractures are not uncommon [5], but metastases are very rare. Coronal T1-W and short-tau inversion recovery (STIR) imaging is valuable, particularly when inclined along the long axis of the sacrum (Fig. 5). With suspected vesicovaginal and rectovaginal fistulae, T2-WI should include sagittal (Fig. 3b) and inclined axial imaging along the suspected axis of the fistulous track. Adjunct sequences of value include STIR to increasing conspicuity of T2 signal abnormalities or fat-suppressed (FS) CE T1-W imaging [6]. MR urography can help assess ureteric involvement.

MRI is thus a valuable technique for investigating cervical cancer throughout the patient pathway, from treatment planning, through response assessment, to evaluation of the treated patient for suspected recurrence or therapy complications.

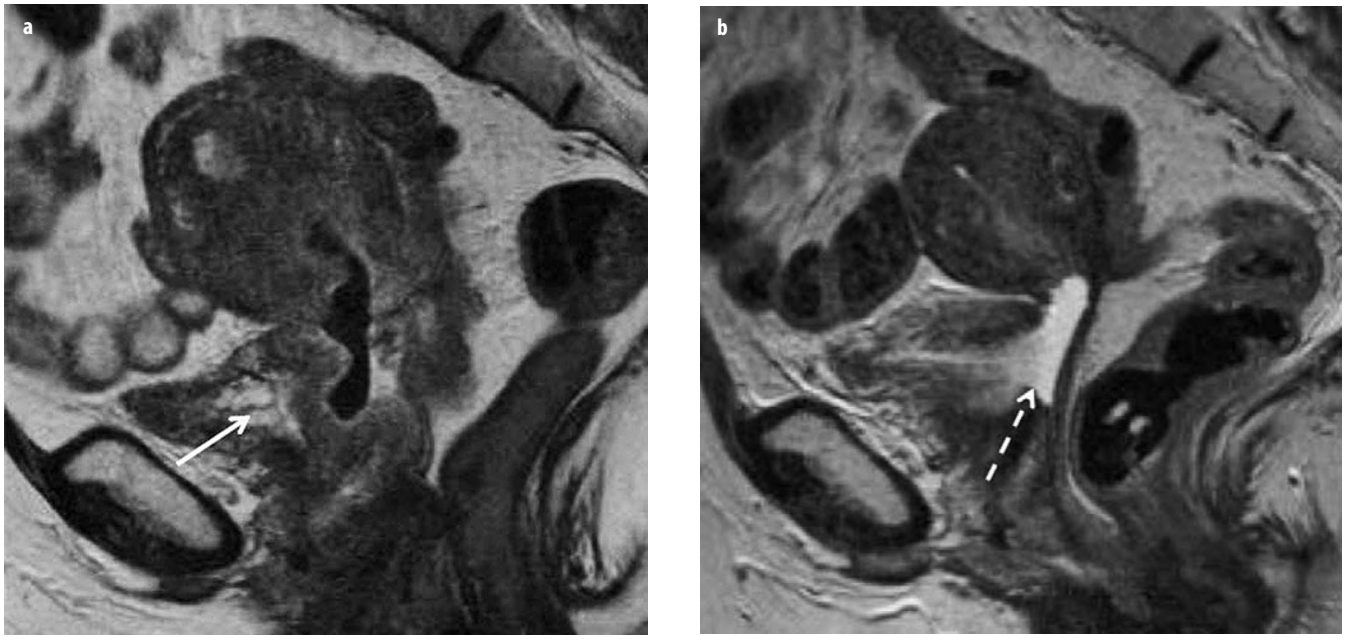


**Fig. 3 a, b.** **a** Sagittal T2-weighted image of a large stage II cervical cancer invading the upper vagina and outer wall of the bladder. Note the presence of bullous edema of the bladder (*solid arrow*) but no frank invasion of the lumen; **b** development of a vesicovaginal fistula postchemoradiation therapy (*dashed arrow*)

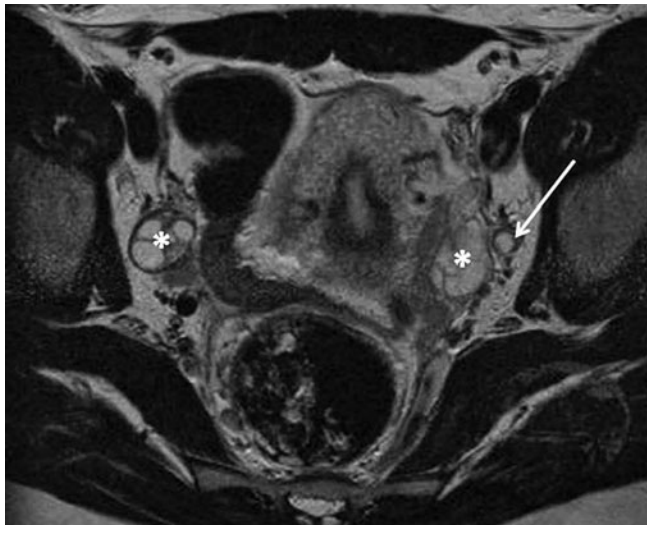

**Fig. 4.** Axial T2-weighted image of the pelvis showing both ovaries (*asterisks*) and a necrotic lymph node (*arrow*) in the left obturator group

## Tumors of the Endometrium

Endometrial carcinoma is the commonest gynecological cancer in industrialized countries. More than 90% occur in PM women. Risk factors include conditions leading to increased estrogenic exposure, e.g., hormone replacement therapy, obesity, tamoxifen use, nulliparity, polycystic ovary disease, and genetic predisposition (e.g., Lynch syndrome).

### Diagnosis

PMB after >6 months of amenorrhoea, is the cardinal symptom. With PMB, an US endometrial thickness (ET) of ⩽5 mm has a 98% exclusion value [7]. Diagnosis is made by endometrial biopsy. Hysteroscopy allows a directed biopsy.

### Staging and Primary Treatment

Staging is most commonly performed according to the FIGO surgical-pathological staging system (Table 2) [1]. Surgery includes a total abdominal hysterectomy with

**Table 2.** Revised FIGO staging of endometrial carcinoma 2009 [1]

| Stage | Characteristic |
|---|---|
| Stage I | Confined to uterus |
| IA | Tumor confined to the uterus, no or <50% myometrial invasion |
| IB | Tumor confined to the uterus, ⩾50% myometrial invasion |
| Stage II | Cervical stromal invasion |
| Stage III | Local or regional spread |
| IIIA | Tumor invades serosa or adnexa |
| IIIB | Vaginal and/or parametrial involvement |
| IIIC1 | Pelvic lymph node involvement |
| IIIC2 | Para-aortic lymph node involvement |
| Stage IV | Extension beyond pelvis or involvement of the bladder or the bowel mucosa |
| IVA | Tumor invades bladder mucosa and/or bowel mucosa |
| IVB | Distant metastasis |

*FIGO* International Federation of Gynecology and Obstetrics

bilateral salpingo-oophorectomy and peritoneal washings. The practice of pelvic/retroperitoneal lymph node dissection (LND) varies. Stage IA tumors do not usually undergo LND, and thus their MRI identification alters treatment. Identification of stage II disease may alter surgical approach or anticipate the need for adjuvant brachytherapy. Location of lymph node disease may direct the LND procedure.

The AJCC TNM staging [2] can also be used as per most other cancers with T1 to T4 stages similar to FIGO stages I-IVa, N stage similar to FIGO stage IIIC, and metastatic (M) spread similar to FIGO stage IVB.

#### Key Points of FIGO and TNM (AJCC) Staging

Nodal metastasis in endometrial cancer is included in both systems. FIGO stage IIIC1 (TNM stage N1) indicates spread to pelvic lymph nodes, and FIGO stage IIIC2 (TNM stage N2) indicates spread to retroperitoneal lymph nodes.

### MR Imaging Technique and Pearls for Endometrial Cancer Staging

The normal uterine anatomy consists of three distinct zones: T2-WI shows high-SI endometrium, surrounded by low-SI junctional zone (inner myometrium), which itself is surrounded by intermediate-SI outer myometrium (Fig. 1). Endometrial cancer is usually isointense to the myometrium on T1-WI and has lower SI than the endometrium on T2-WI [8]. On dynamic multiphase CE 3D T1-WI, the tumor enhances more slowly and less avidly than the adjacent myometrium. On DWI, tumors demonstrate high SI with corresponding low SI on the apparent diffusion coefficient (ADC) maps.

#### Stage I

Stage I tumors account for >80% of cases. High-resolution small FOV axial oblique T2-WI perpendicular to the endometrial stripe (Fig. 1) is essential to evaluate the depth of myometrial invasion and discriminate between stage IA (<50% myometrial invasion) and stage IB (⩾50% myometrial invasion) [8] (Fig. 6). Gadolinium-enhanced T1-WI (especially delayed 2- to 5-min postgadolinium injection) facilitates evaluation of myometrial invasion, providing maximum tumor-to-myometrium contrast (Fig. 6). Use of high-resolution, FS, gradient echo (GRE) imaging is advised and allows multiple and multiplanar acquisitions at 60-180 s pos-injection. DW-MRI may also be useful [9] (Fig. 6). Peritumoral inflammation can lead to overestimation of myometrial invasion on MRI. Pitfalls in assessing myometrial invasion also include leiomyomas, adenomyosis, loss of junctional zone definition, and myometrial compression by polypoid tumor.

#### Stage II

Stage II tumors with cervical stromal invasion are represented by intermediate- to high-SI tumor disrupting the normal low-SI cervical stroma on T2-WI, similar to that seen in Fig. 2a. Use of dynamic postcontrast T1-WI is useful in distinguishing between cervical invasion and polypoidal endometrial tumor protruding into the endocervix. Enhancement of cervical mucosa on postcontrast images can confidently exclude cervical stroma invasion [10].

#### Stage III

Stage IIIA tumors show disruption of the T2 hypointense SI of uterine serosa, irregular uterine contour on T2-WI; loss

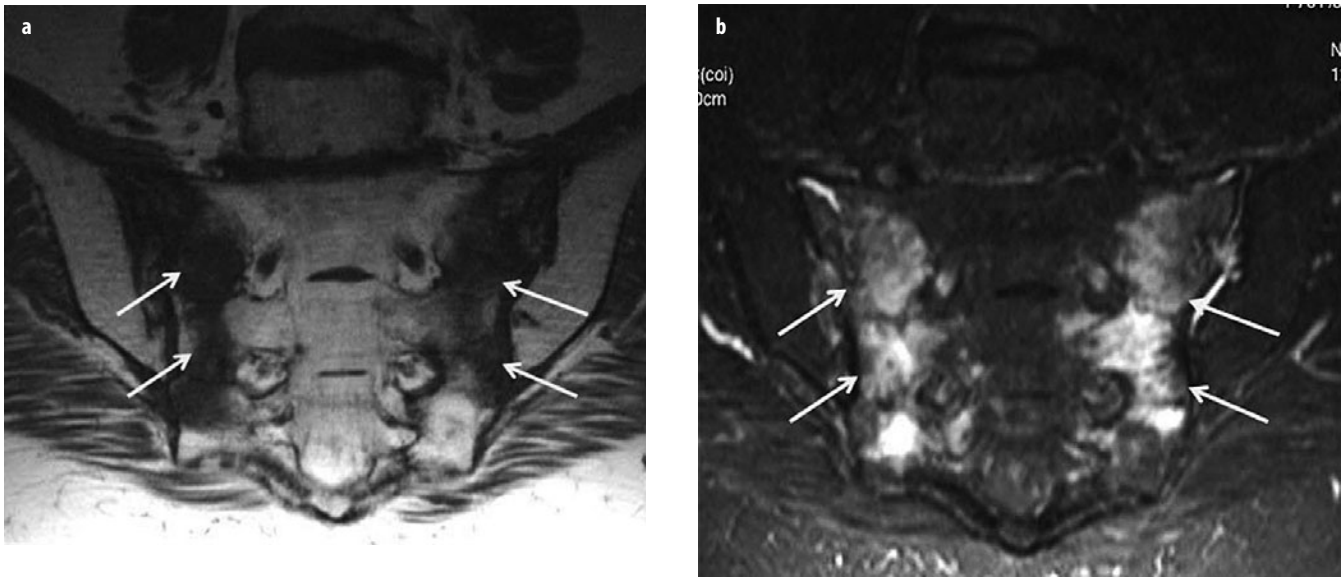


**Fig. 5 a, b.** **a** Inclined coronal T1-weighted image and **b** short-tau inversion recovery (STIR) image showing bilateral sacral stress fractures postradiation therapy (*arrows*)

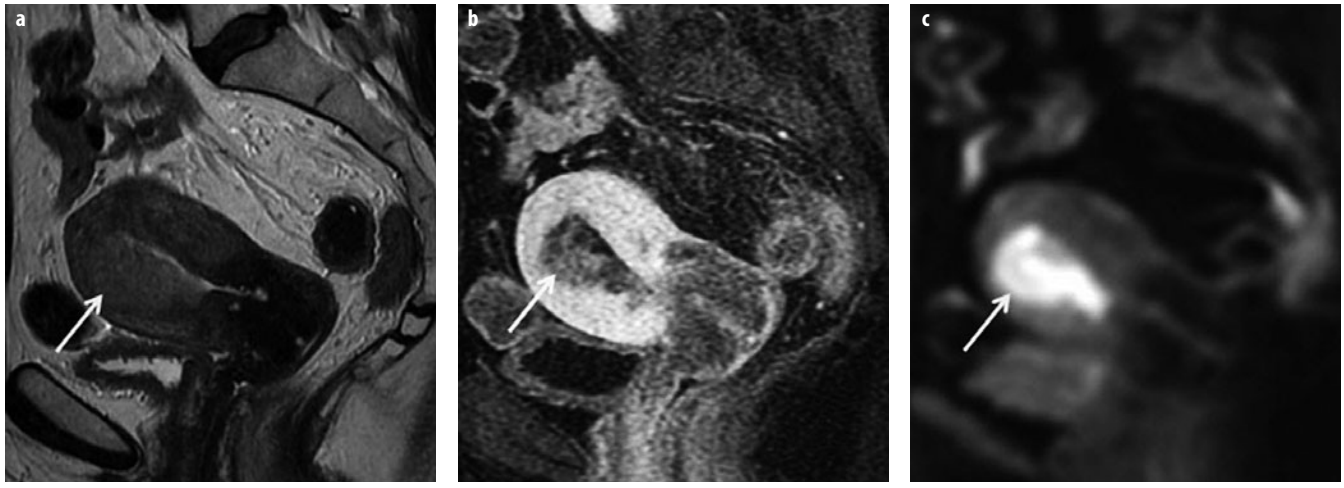


**Fig. 6 a-c.** **a** Sagittal T2-weighted, **b** sagittal contrast-enhanced T1-weighted, and **c** sagittal diffusion-weighted images of a stage IB endometrial cancer with >50% myometrial depth invasion (*arrows*)

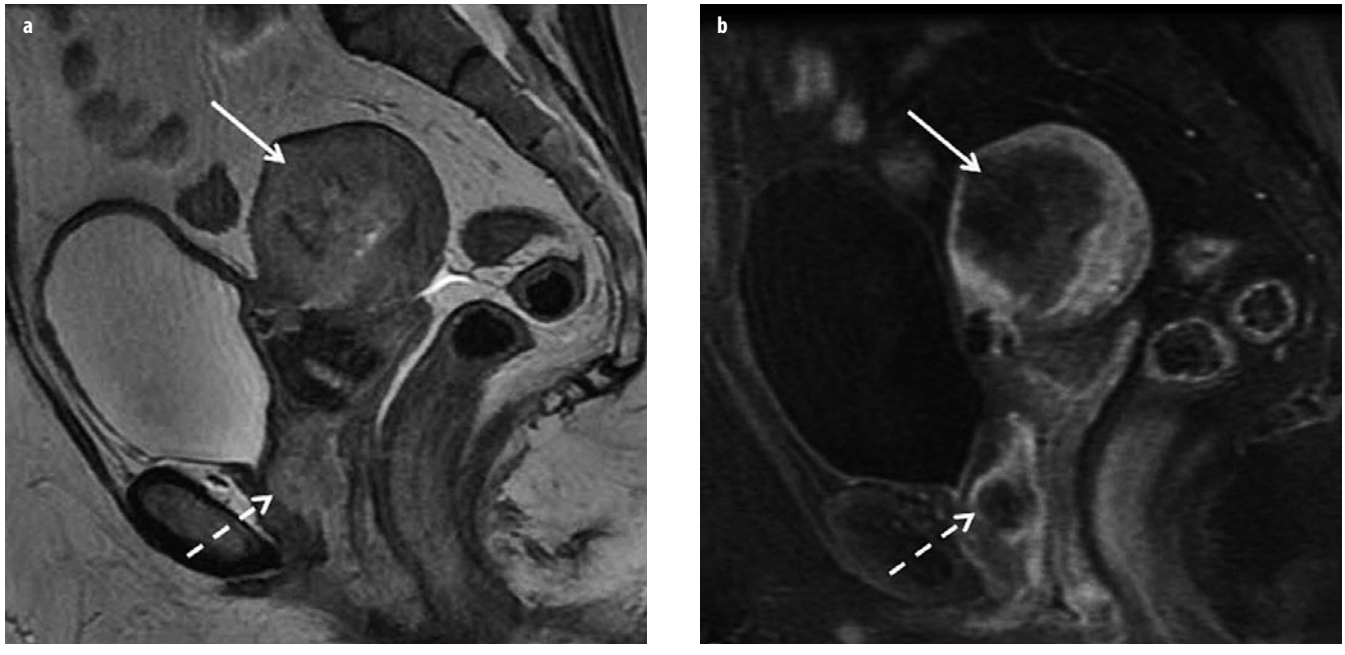


**Fig. 7 a, b.** **a** Sagittal T2-weighted and **b** sagittal contrast-enhanced T1-weighted images of a stage IIIB endometrial cancer with >50% myometrial depth invasion (*solid arrow*), as well as vaginal "drop" involvement (*dashed arrow*)

of normal rim of enhancement of outer myometrium on CE T1-WI indicates serosal involvement. Tumor deposits may be identified in the adnexa, even in the absence of serosal invasion, especially with high-grade, clear-cell, or serous papillary tumors. DWI can aid in detecting these cases. In stage IIIB disease, tumor invades the upper vagina, indicated by segmental loss of the low SI of the vaginal wall on T2-WI (Fig. 7). The presence of enlarged regional and/or para-aortic lymph nodes indicates stage IIIC disease.

### Stage IV

Stage IVA tumors show similar features to equivalent stage of cervical cancer.

### MRI Following Primary Treatment

MRI has a limited role in treatment monitoring, and there is no role for routine imaging surveillance after primary treatment. It is valuable for assessing suspected recurrence and when clinical assessment is limited.

## Uterine Sarcomas

These sarcomas are rare, accounting for ~3% of malignancies of the uterine corpus. They are difficult to diagnose preoperatively, as they are not accessible to colposcopic or endoscopic biopsy. Their imaging appearances overlap with

those of uterine fibroids (leiomyomata), which may undergo a wide variety of degenerations, thus mimicking malignant disease. Hence, diagnosis is often an unexpected result after simple hysterectomy performed for fibroid disease.

### Staging and Primary Treatment

The 2009 FIGO revision separated endometrial carcinoma from uterine sarcoma [11]. Individual staging schemes are now described for leiomyosarcoma and there is a combined scheme for ESS/adenosarcoma. Carcinosarcoma, formerly malignant mixed Müllerian tumor (MMMT), is staged as for endometrial carcinoma [11]. The scheme for leiomyosarcoma reflects tumor size.

#### Stage I

Leiomyosarcoma confined to the uterus and $<5$ cm are stage IA; those $>5$ cm are stage IB [11].

#### Stages II and III

Stage II tumors have pelvic extension, and stage III tumors involve abdominal sites, which excludes simple extension of the uterine tumor itself up into the abdominal cavity [11].

The scheme for ESS and adenosarcoma has similarities to that for endometrial carcinoma, emphasizing depth invasion rather than tumor size for early local spread. Otherwise, it resembles that for leiomyosarcoma with extrauterine spread.

## References


1. Pecorelli S (2009) Revised FIGO staging for carcinoma of the vulva, cervix, and endometrium. Int J Gynaecol Obstet 105:103-104.
2. Edge SB, Byrd DR, Compton CC et al (2010) AJCC Cancer Staging Manual, 7th ed. Springer, New York.
3. Subak LL, Hricak H, Powell CB et al (1995) Cervical carcinoma: computed tomography and magnetic resonance imaging for preoperative staging. Obstet Gynecol 86:43-50.
4. Choi HJ, Kim SH, Seo SS et al (2006) MRI for pretreatment lymph node staging in uterine cervical cancer. AJR Am J Roentgenol 187:W538-543.
5. Kwon JW, Huh SJ, Yoon YC et al (2008) Pelvic bone complications after radiation therapy of uterine cervical cancer: evaluation with MRI. AJR Am J Roentgenol 191:987-994.
6. Healy JC, Phillips RR, Reznek RH et al (1996) The MR appearance of vaginal fistulas. AJR Am J Roentgenol 167:1487-1489.
7. Gupta JK, Chien PF, Voit D et al (2002) Ultrasonographic endometrial thickness for diagnosing endometrial pathology in women with postmenopausal bleeding: a meta-analysis. Acta Obstet Gynecol Scand 81:799-816.
8. Sala E, Rockall AG, Freeman SJ et al (2013) The added role of MR imaging in treatment stratification of patients with gynecologic malignancies: what the radiologist needs to know. Radiology 266:717-740.
9. Hori M, Kim T, Onishi H et al (2013) Endometrial cancer: preoperative staging using three-dimensional T2-weighted turbo spin-echo and diffusion-weighted MR imaging at 3.0 T: a prospective comparative study. Eur Radiol 23:2296-2305.
10. Ascher SM, Reinhold C (2002) Imaging of cancer of the endometrium. Radiol Clin North Am 40:563-576.
11. Prat J (2009) FIGO staging for uterine sarcomas. Int J Gynaecol Obstet 104:177-178.

# Adnexal Diseases

Evis Sala[1], Andrea Rockall[2]

[1] Department of Radiology, Memorial Sloan-Kettering Cancer Center, New York, NY, USA
[2] Department of Radiology, Imperial College Healthcare NHS Trust, London, UK

## Introduction

The differential diagnosis for adnexal masses is wide, encompassing a range of benign, borderline, and malignant entities. The majority of adnexal masses are benign, but identifying malignant lesions is of paramount importance. Risk stratification is based on age, menopausal status, imaging features, and tumor markers. Imaging evaluation should be used in combination with the patient's age, menopausal status, history, clinical examination, and tumor markers [i.e., cancer antigen 125 (CA 125)] in order to derive an appropriate differential diagnosis. However, diagnosis may ultimately depend on histological confirmation. Magnetic resonance imaging (MRI) is an adjunct to ultrasound (US) in characterizing adnexal masses, with well-established imaging criteria for malignant ovarian tumors.

## Imaging Modalities Used in Evaluating the Adnexal Mass

### Ultrasound (US)

In evaluating adnexal masses, a combination of transabdominal ultrasound (TAUS) and transvaginal ultrasound (TVUS) should routinely be used. TAUS allows assessing large adnexal masses that will not be adequately evaluated on TVUS alone, as well as detecting ancillary features such as the presence of ascites, hydronephrosis, pleural effusions, and peritoneal and omental disease. TVUS, using high-frequency TV probes, provides high-resolution images of the adnexa allowing differentiation between cystic and solid adnexal masses, and improving characterization. Imaging features suspicious for malignancy include: wall irregularity, thick septations ($>$3mm), papillary projections, solid components, size ($>$4cm) [1-4]. Color and Doppler US have been proposed as further ways to distinguish between malignant and benign adnexal masses [5]. Ovarian tumors have low-resistance Doppler waveform, with a pulsatility index (PI) $<$1.0 or a resistance index (RI) $<-0.4$ to $-0.8$ [6, 7]. However, these values overlap with other conditions, such as inflammatory masses, endometriomas, benign vascular masses, corpus luteal cysts, and ectopic pregnancies. When color Doppler and US morphology is combined, sensitivities and specificities in evaluating an adnexal mass are higher than for either method alone.

### Magnetic Resonance Imaging (MRI)

MRI is recommended as a second-line investigation for characterizing complex adnexal masses indeterminate on US [8-11]. MRI gives superb contrast resolution and involves nonionizing radiation. Studies show high diagnostic sensitivity (67-100%) and specificity (77-100%) [12-18]. Typical protocols include both T1- and T2-weighted imaging (WI) sequences, with imaging acquisition performed in three planes. High-resolution axial oblique fast spin-echo (FSE) T2-WI taken parallel to the ovarian axis, the long axis of the uterus, are useful in assessing nonovarian origin of a parauterine mass (i.e., pedunculated uterine leiomyoma), whereas coronal FSE T2-WI is extremely helpful in evaluating complex adnexal lesions. Presence of bridging vessels between the mass and the myometrium or the claws of the uterine myometrium are associated with uterine origin. Ovary beak sign may suggest the ovarian origin. Adnexal lesions can be characterized by their specific signal characteristics on T1-and T2-WI. Simple fluid has homogeneous low signal on T1-WI and high signal intensity (SI) on T2-WI. Fat and hemorrhage have high SI on T1-WI. Fat suppression (FS) on T1-W sequences is used to differentiate these entities. If the adnexal lesion demonstrates low or intermediate SI on T1-WI and low SI on T2-WI, these characteristics suggest fibrotic and/or smooth muscle components. Multiphase contrast-enhanced (CE) MRI after intravenous administration of gadolinium is useful for characterizing adnexal masses. Solid components will demonstrate enhancement, enabling the distinction between debris or retracting clot in the cyst wall from papillary projections. Subtraction images are essential to

*Diseases of the Abdomen and Pelvis 2014-2017*,
DOI: 10.1007/978-88-470-5659-6_21 

evaluate enhancing nodules within a background of hyperintense T1-W lesion. Gadolinium also improves peritoneal and omental implant detection in case of ovarian carcinoma. Dynamic CE (DCE) MRI is not yet routinely performed when evaluating adnexal masses. Preliminary studies demonstrate the value of DCE-MRI in characterizing ovarian epithelial tumors, with early enhancement patterns being able to distinguish benign, borderline, and invasive tumors [19-21]. The use of diffusion-weighted imaging (DWI) is debatable, with one recent study showing no significant difference in apparent diffusion coefficient (ADC) values between malignant and benign adnexal lesions [22].

#### Computed Tomography (CT)

Contrast-enhanced computed tomography (CE-CT) is not routinely recommended for evaluating adnexal masses as it has poor contrast resolution and involves ionizing radiation. In women with acute pelvic pain, CT is generally used in the emergency settings when US is inconclusive. If ovarian carcinoma is suspected on US, staging is performed with CT.

#### Positron Emission Tomography/Computed Tomography (PET/CT)

Fluoro-2-deoxy-D-glucose (FDG) positron emission tomography (PET)/CT has a limited role in characterizing adnexal lesions. FDG physiological uptake can be seen in ovarian follicles and corpus luteum cysts in premenopausal patients. FDG uptake can also be seen in certain benign ovarian and as well as inflammatory and infectious processes. PET/CT is increasingly used in evaluating patients with malignant gynecological conditions and is valuable in cases of suspected recurrence.

## Benign Adnexal Masses

### Benign Cystic Ovarian Tumors

#### Ovarian Cysts

Functional cysts are most common in women of reproductive age and include either follicular cysts or corpus luteum cysts following hemorrhage within a corpus luteum. A simple cyst appears as a unilocular structure and ranges in size from 3-8 cm, with absence of solid internal components. On US, these cysts appear thin walled and anechoic, with posterior acoustic enhancement. Differential would include a serous cystadenoma or a paraovarian cyst. On MRI, simple adnexal cysts show typical low SI on T1-WI and high SI on T2-WI, with no enhancement post gadolinium. Corpus luteum cysts appearance on US is described as being lace like, often demonstrating a ring of vascularity on color Doppler. On MRI, it may demonstrate high SI on T1-WI and FS T1-WI (blood products), with bright enhancement of the cyst rim, which may be thick walled and crenulated.

#### Endometriomas

These occur in patients with endometriosis, defined as presence of endometrial glandular tissue outside of the uterus. Endometriomas are large cystic lesions containing blood products. They typically appear as unilocular or multilocular adnexal masses on US, with uniform low-level echoes. Distinction between endometrioma and hemorrhagic cysts may be difficult, although the latter should resolve on follow up US. On MRI (Fig. 1), endometriomas may appear as multicystic adnexal masses that show high SI on T1-WI and low SI on T2-WI due the presence of blood. Shading is described on T2-WI, where chronic hemorrhage and high viscosity results in T2 shortening. Fibrous adhesions may be present in the cul-de-sac, seen as low SI bands (Fig. 1).

#### Dermoid Cysts (Mature Cystic Teratomas)

On US, dermoid cysts may demonstrate several characteristic features such as:
- Fat fluid level
- "White ball" within part of or all the lesion (representing dermoid plug consisting of hair and sebum)
- "Tip of the iceberg" appearance, in which a diffuse or partly echogenic mass is seen with sound attenuation
- "Dermoid mesh," consisting of long, echogenic lines and dots within the cyst fluid, corresponding to hair floating within the cyst cavity.

Often, if shadowing is present, it may be confused with adjacent bowel. US features may overlap with other entities, such as endometriomas or ovarian carcinomas. On CT, they are recognized due to the presence of macroscopic fat and calcifications. On MRI, the fat component will demonstrate high SI on both T1- and T2-WI, with the lipid-laden cyst fluid demonstrating a similar high SI on T1- and intermediate SI on T2-WI. It is important to distinguish a dermoid cyst from an endometrioma, as both can show high SI on T1-WI. Chemical-shift artefact will be seen at the fat-fluid interface in dermoid cysts as bright or dark bands along the frequency-encoding gradient. Use of frequency-selective FS enables dermoid cysts (which appear as low SI) to be distinguished from hemorrhagic lesions or endometriomas (which retain high SI) (Fig. 2). Rarely, a cancer may develop within a dermoid cyst, most frequently a squamous cell cancer.

#### Serous and Mucinous Cystadenomas

Serous and mucinous cystadenomas are classified as surface epithelial tumors. Serous cystadenomas are classically described on US as thin-walled unilocular or bilocular cystic lesions, with a homogenous echotexture, thin regular septa (when present), and no vegetations (Fig. 3). Unlike functional cysts, cystadenomas will persist

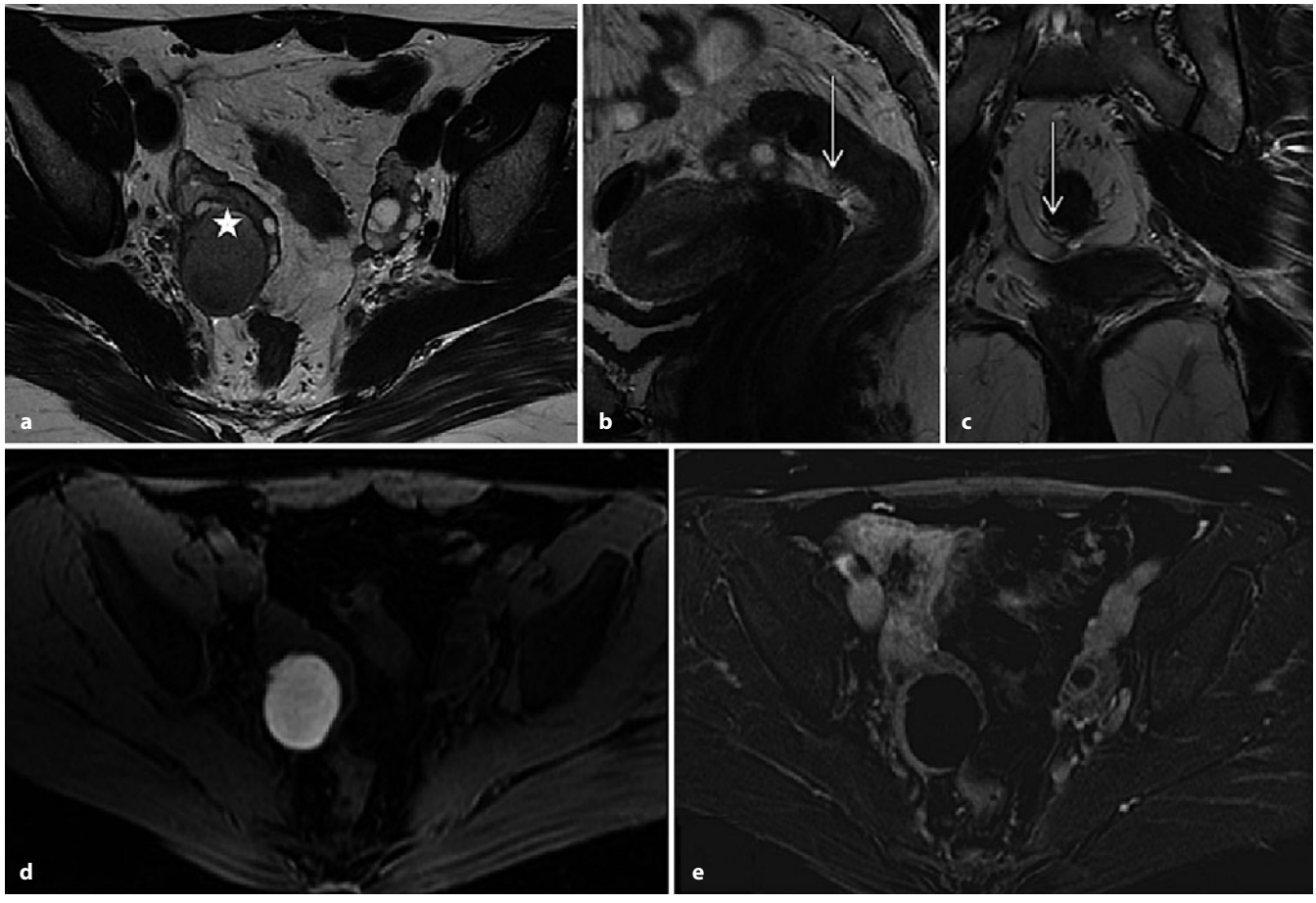


**Fig. 1 a-e.** Ovarian endometrioma. **a** Axial fast-spin-echo T2-weighted imaging (FSE T2-WI) shows unilocular right cystic ovarian lesion (*asterisk*) demonstrating diffuse hypointensity (i.e., shading effect) relating to chronic hemorrhage. **b** Sagittal and **c** coronal T2-WI show some fibrous adhesions in the pouch of Douglas (*arrows*). **d** Axial fat-suppressed (FS) T1-WI confirms presence of blood product inside the lesion. **e** Subtraction gadolinium-enhanced FS T1-WI demonstrates absence of mural solid nodules. These findings are suggestive of endometriosis

unchanged over one or two menstrual cycles and may increase in size. In comparison with serous cystadenomas, mucinous cystadenomas are more often multilocular, containing fluid of different echotextures. As with serous cystadenoma, they have a smooth wall, thin septa (<3 mm) and no vegetations. On MRI, cysts in mucinous tumors demonstrate various signal intensities on T1- and T2-WI, giving rise to the so-called "stained-glass" appearance. This is because on T1-WI locules with watery mucin generate lower SI than locules with thicker mucin. The opposite is generated on T2-WI.

### Benign Solid Ovarian Tumors

These tumors include ovarian fibromas, thecomas, adenofibromas, and Brenner tumors. Fibrotic tumors account for approximately 5% of all ovarian tumors.

#### Fibromas/Fibrothecomas

They are the most common solid benign tumors of the ovary. Fibromas and fibrothecomas may mimic pedunculated myomas on US, appearing as well-circumscribed, hypoechoic, and solid round or oval tumors with sound attenuation. On color Doppler, they are usually hypovascular. Fibromas are sometimes associated with ascites and pleural effusion (Meigs syndrome). On MRI, due to the extensive collagen content and hyalinized tissue, fibromas and fibrotic component of fibrothecomas appear as intermediate SI masses on T1- and low SI masses on T2-WI. There may be scattered foci of high SI on T2-WI due to cystic degeneration or edema. Calcification may occur, seen as foci of signal voids on T1- and T2-WI. After administration of gadolinium, there is typically delayed low-level enhancement. Thecomas contain a prominent lipid component that can be demonstrated on chemical-shift imaging or on frequency-selective FS-MRI. Due to estrogen secretion, endometrial hyperplasia may be present.

#### Brenner Tumors

Brenner tumors are transitional cell tumors of the ovary. The majority is benign, but borderline and malignant types can also arise. Benign tumors are usually unilateral, small

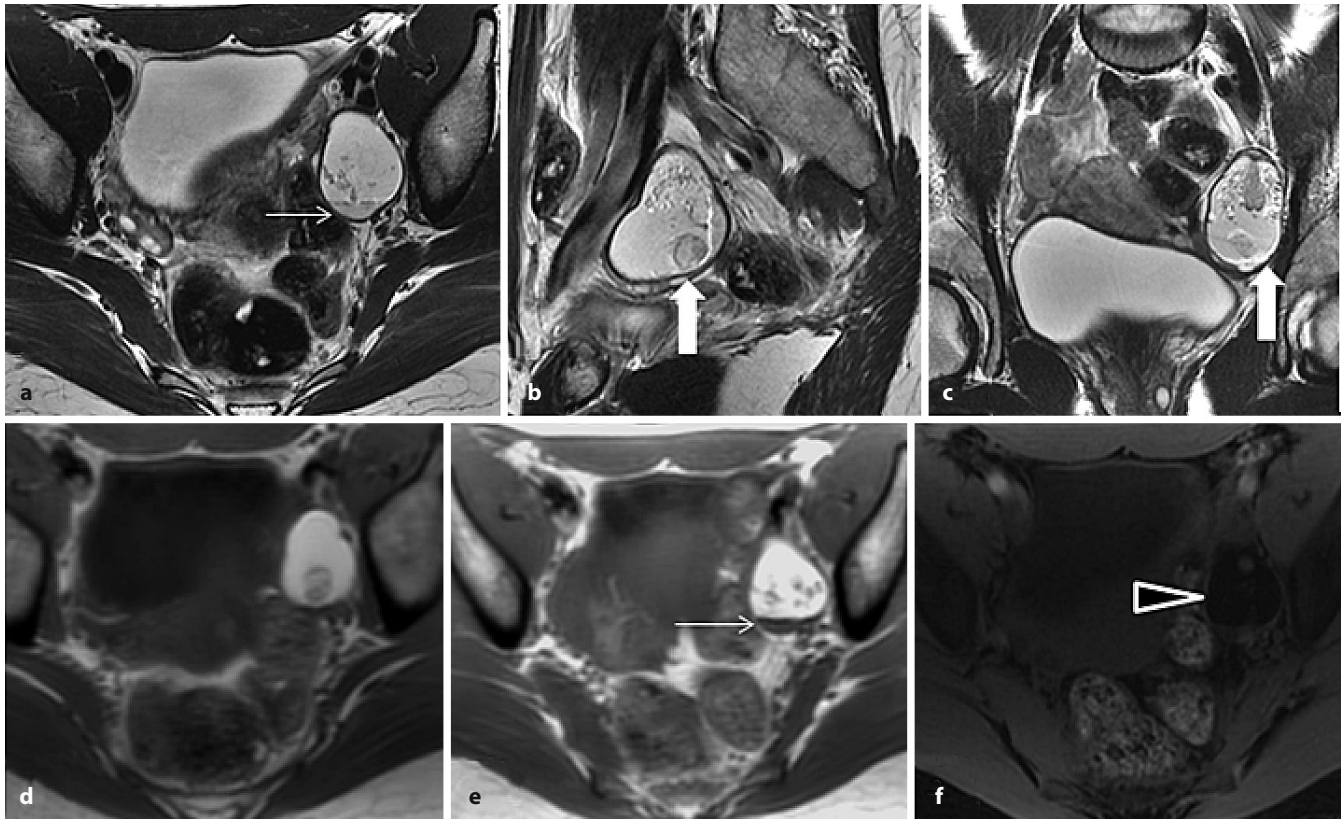


**Fig. 2 a-f.** Mature ovarian cystic teratoma. **a** Axial, **b** sagittal, and **c** coronal fast-spin-echo T2-weighted images (FSE T2-WI) show high T2-signal-intensity unilocular left cystic ovarian lesion, with hypointense mural protrusions (i.e., dermoid plug; *large arrow* in **b** and **c**). **d, e** On axial T1-WI, lesion demonstrates high signal intensity characterized signal drop on **f** fat-saturated (FS) T1-WI (*arrowhead*) due to lipid content, with evidence of fluid-lipid level (*thin arrow* in **a** and **e**)

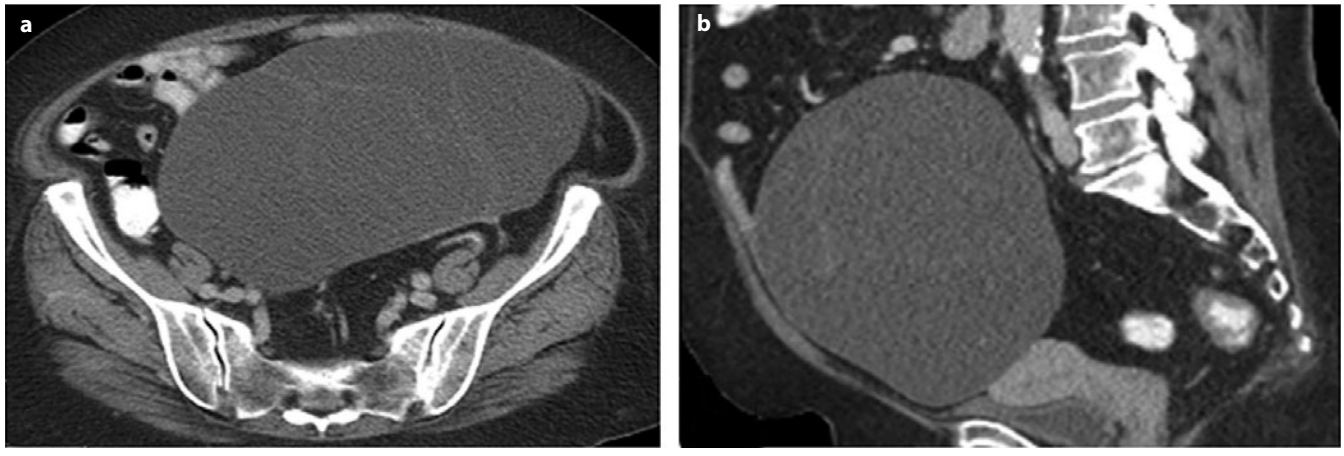


**Fig. 3 a, b.** Serous ovarian cystoadenoma. **a** Axial and **b** sagittal contrast-enhanced computed tomography (CE-CT) images show cystic pelvic mass with smooth margin and internal thin, regular septa, without evidence of solid mural enhancing nodules

(<5 cm), and hypoechoic on US. Extensive calcification is characteristic, resulting in posterior acoustic shadowing on US. On MRI, the benign type appears solid and of low SI on both T1- and T2-WI. They demonstrate lower SI on T2-WI than other solid tumors. Ipsilateral ovarian tumors (e.g., mucinous cystadenomas) may be present in 30% of cases, and endometrial hyperplasia can also occur.

### Borderline and Malignant Ovarian Tumors

Tumors such as these include surface epithelial tumors (serous cystadenocarcinomas, mucinous cystadenocarcinomas, endometrioid, and clear-cell carcinomas), sex cord-stromal tumors (granulosa cell and Sertoli-Leydig cell tumors), and germ cell tumors. Less common malig-

nant tumors are mixed Müllerian tumors, undifferentiated carcinomas, carcinoids, and lymphomas.

Borderline serous tumors account for 10-15% of all ovarian serous tumors and are bilateral in 30% of cases. Likelihood of malignancy increases with the presence of septations, mural nodules, and papillary projections (Fig. 4). MRI features suspicious for malignancy include: mass >4 cm, cystic lesion with solid component, irregular wall thickness >3 mm, septal thickness >3 mm, presence of papillary projections or nodules, and presence of solid mass with necrosis and early, bright contrast enhancement [23, 24]. In addition, ancillary criteria for suspected malignancy include: direct local invasion, peritoneal deposits, enlarged lymph nodes, and ascites. DW-MRI is highly sensitive and specific in detecting the extent of peritoneal disease. CE-CT remains the technique of choice for staging ovarian carcinoma (Fig. 5).

## Algorithm for Evaluating the Incidental Adnexal Mass

In general, a cystic mass (either simple or complex), in a young adult woman <30 years of age, is most likely to represent a functional cyst, endometrioma, tuboovarian abscess, dermoid cyst, or cystadenoma. Only a small percentage of these patients will have borderline or frank malignancy masses. If imaging suggests a frankly malignant tumor, the most likely differential in this age group would be a malignant germ-cell or sex-cord stromal tumor (granulosa-cell tumor) rather than a surface epithelial tumor. In premenopausal patients between 40 and 49 years, cystadenomas contribute a larger percentage. With increasing age, the likelihood of malignancy increases, with a 10-15% malignancy risk in premenopausal patients compared with 45% in postmenopausal patients. The majority of malignant tumors in older patients are of epithelial

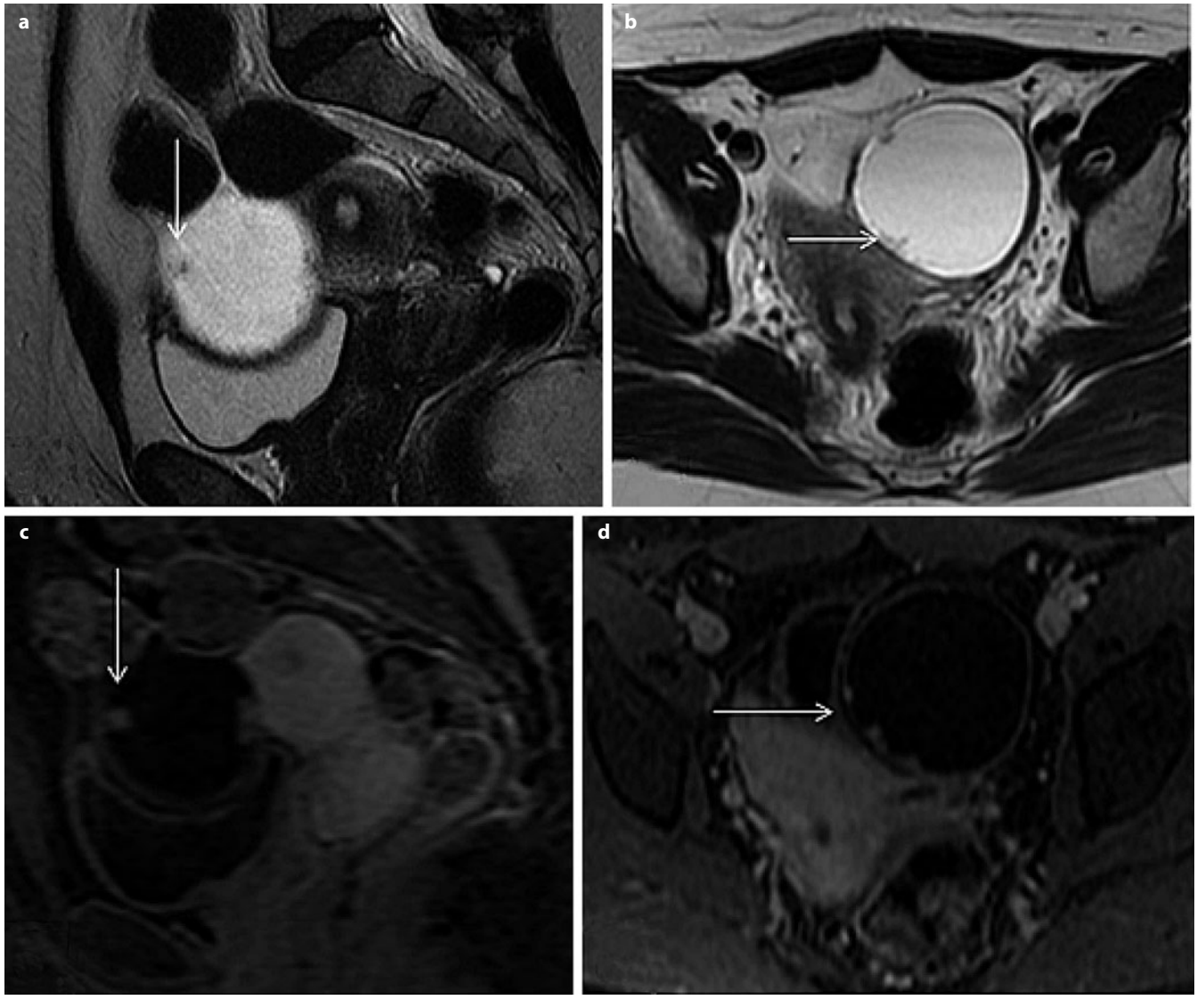


**Fig. 4 a-d.** Serous borderline ovarian tumor. **a** Sagittal and **b** axial fast-spin-echo T2-weighted image (FSE T2-WI) show unilocular, thin-walled cystic lesion, with intermediate signal intensity T2 papillary projections (*arrows* in **a** and **b**). **c, d** Sagittal and axial gadolinium-enhanced fat-saturated (FS) T1-WI confirm the presence of solid papillary projections, characterized by contrast enhancement


**Fig. 5 a-c.** Stage IC serous papillary ovarian carcinoma. **a** Axial, **b** sagittal, and **c** coronal contrast-enhanced computed tomography (CE-CT) images show complex cystic pelvic mass with thick septa and solid enhancing component

origin. Cancer antigen 125 (CA 125) is elevated in 90% of cases of advanced ovarian cancer. It can also be elevated in other benign conditions, such as fibroids, adenomyosis, pelvic inflammatory disease, endometriosis, renal disease, hepatic disease, and benign ovarian tumors.

An incidental unilocular ovarian cyst found in the premenopausal patient requires no further management unless it is symptomatic or, due to its size, there is a risk of torsion [1]. In postmenopausal patients, unilocular cysts can be managed conservatively with repeat TVUS if there is no increase in cyst diameter or complexity and serum CA 125 is normal. If there is a complex cystic or solid lesion on US, further assessment is recommended. The European Society of Urogenital Radiology (ESUR) provided an algorithmic approach for characterizing MRI indeterminate adnexal masses on US [25]. If ovarian carcinoma is suspected on US, staging is performed with CT [26].

## References


1. Levine D, Brown DL, Andreotti RF et al (2010) Management of asymptomatic ovarian and other adnexal cysts imaged at US: Society of Radiologists in Ultrasound Consensus Conference Statement. Radiology 256:943-954.
2. Timmerman D, Ameye L, Fischerova D et al (2010) Simple ultrasound rules to distinguish between benign and malignant adnexal masses before surgery: prospective validation by IOTA group. BMJ 341:c6839.
3. Timmerman D, Valentin L, Bourne TH et al; International Ovarian Tumor Analysis (IOTA) Group (2000) Terms, definitions and measurements to describe the sonographic features of adnexal tumors: a consensus opinion from the International Ovarian Tumor Analysis (IOTA) Group. Ultrasound Obstet Gynecol 16:500-505. Review.
4. Buy JN, Ghossain MA, Hugol D et al (1996) Characterization of adnexal masses: combination of color Doppler and conventional sonography compared with spectral Doppler analysis alone and conventional sonography alone. AJR Am J Roentgenol 166:385-393.
5. Caruso A, Caforio L, Testa AC et al (1996) Transvaginal color Doppler ultrasonography in the presurgical characterization of adnexal masses. Gynecol Oncol 63:184-191.
6. Carter JR, Lau M, Fowler JM et al (1995) Blood flow characteristics of ovarian tumors: implications for ovarian cancer screening. Am J Obstet Gynecol 172:901-907.
7. Guerriero S, Ajossa S, Risalvato A et al (1998) Diagnosis of adnexal malignancies by using color Doppler energy imaging as a secondary test in persistent masses. Ultrasound Obstet Gynecol 11:277-282.
8. Yamashita Y, Torashima M, Hatanaka Y et al (1995) Adnexal masses: accuracy of characterization with transvaginal US and precontrast and postcontrast MR imaging. Radiology 194:557-565.
9. Komatsu T, Konishi I, Mandai M et al (1996) Adnexal masses: transvaginal US and gadolinium-enhanced MR imaging assessment of intratumoral structure. Radiology 198:109-115.
10. Hata K, Hata T, Manabe A et al (1992) A critical evaluation of transvaginal Doppler studies, transvaginal sonography, magnetic resonance imaging, and CA 125 in detecting ovarian cancer. Obstet Gynecol 80:922-926.
11. Yamashita Y, Hatanaka Y, Torashima M et al (1997) Characterization of sonographically indeterminate ovarian tumors with MR imaging: a logistic regression analysis. Acta Radiol 38:572-577.
12. Buist MR, Golding RP, Burger CW et al (1994) Comparative evaluation of diagnostic methods in ovarian carcinoma with emphasis on CT and MRI. Gynecol Oncol 52:191-198.
13. Grab D, Flock F, Stohr I et al (2000) Classification of asymptomatic adnexal masses by ultrasound, magnetic resonance imaging, and positron emission tomography. Gynecol Oncol 77:454-459.
14. Hricak H, Chen M, Coakley FV et al (2000) Complex adnexal masses: detection and characterization with MR imaging—multivariate analysis. Radiology 214:39-46.
15. Huber S, Medl M, Baumann L et al (2002) Value of ultrasound and magnetic resonance imaging in the preoperative evaluation of suspected ovarian masses. Anticancer Res 22:2501-2507.
16. Jain KA, Friedman DL, Pettinger TW et al (1993) Adnexal masses: comparison of specificity of endovaginal US and pelvic MR imaging. Radiology 186:697-704.
17. Sohaib SA, Mills TD, Sahdev A et al (2005) The role of magnetic resonance imaging and ultrasound in patients with adnexal masses. Clin Radiol 60:340-348.
18. Kurtz AB, Tsimikas JV, Tempany CM et al (1999) Diagnosis and staging of ovarian cancer: comparative values of Doppler and conventional US, CT, and MR imaging correlated with surgery and histopathologic analysis—report of the Radiology Diagnostic Oncology Group. Radiology 212:19-27.
19. Thomassin-Naggara I, Darai E, Cuenod CA et al (2008) Dynamic contrast-enhanced magnetic resonance imaging: a useful tool for characterizing ovarian epithelial tumors. J Magn Reson Imaging 28:111-120.
20. Thomassin-Naggara I, Bazot M, Darai E (2008) Epithelial ovarian tumors: value of dynamic contrast-enhanced MR imaging and correlation with tumor angiogenesis. Radiology 248:148-159.

21. Thomassin-Naggara I, Aubert E, Rockall A et al (2013) Adnexal masses: development and preliminary validation of an MR imaging scoring system. Radiology 267:432-443.
22. Fujii S, Kakite S, Nishihara K (2008) Diagnostic accuracy of diffusion-weighted imaging in differentiating benign from malignant ovarian lesions. J Magn Reson Imaging 28:1149-1156.
23. Bernardin L, Dilks P, Liyanage S (2012) Effectiveness of semi-quantitative multiphase dynamic contrast-enhanced MRI as a predictor of malignancy in complex adnexal masses: radiological and pathological correlation. Eur Radiol 22:880-890.
24. Thomassin-Naggara I, Aubert E, Rockall A et al (2013) Adnexal Masses: Development and Preliminary Validation of an MR Imaging Scoring System. Radiology 267:432-443.
25. Spencer JA, Forstner R, Cunha TM, Kinkel K; ESUR Female Imaging Sub-Committee (2010) ESUR guidelines for MR imaging of the sonographically indeterminate adnexal mass: an algorithmic approach. Eur Radiol 20:25-35.
26. Forstner R, Sala E, Kinkel K, Spencer JA (2010) ESUR guidelines: ovarian cancer staging and follow-up. Eur Radiol 20:2773-2780.

# Imaging of the Male Pelvis: Scrotum

Brent J. Wagner

Department of Radiology, Reading Health System, West Reading, PA, USA

## Introduction

Scrotal imaging, particularly with ultrasound (US), is a critical tool for accurate and rapid diagnosis of a variety of acute and subacute conditions. This review presents a framework for assessing abnormal imaging findings in adults based on four major categories: neoplastic, inflammatory, traumatic, and vascular. Miscellaneous conditions, including mimics for malignant neoplasms, are also presented, in addition to basic clinical background to allow radiologists to provide refined interpretations in the context of current management algorithms.

## Neoplastic Disease

The first step in assessing an intrascrotal mass is establishing its location as intratesticular vs extratesticular location. Among intratesticular lesions, the most common are germ-cell tumors (GCT). Although subtypes have been described, the major types are seminoma, embryonal carcinoma, yolk-sac tumor, teratoma, and choriocarcinoma. GCT account for ~95% of testicular neoplasms, and almost all are malignant. Within this broad category, it is useful to divide the tumors into seminoma and nonseminomatous GCT (NSGCT) based on two fundamental characteristics of tumor biology: seminoma is (1) highly radiosensitive and (2) generally less aggressive than most cases of NSGCT. Pure seminomas account for about half of all testicular GCT; most of the remainder are mixed, comprising more than one type of nonseminomatous tumor histology, although pure forms of NSGCT occasionally occur [1-3].

Lesions typically present as a palpable mass, but it is important to remember that up to 10% of testicular neoplasms will present acutely with pain (with or without hemorrhage), and patients with a hematoma after minimal trauma may harbor a malignant tumor masked by the acute finding. Aggressive tumors (especially NSGCT) may present with metastasis to lung or bone or symptoms secondary to a large retroperitoneal mass, which may produce back pain (with or without hydronephrosis) [2].

Because background testicular parenchymal echogenicity is generally high, almost all neoplasms (unless calcified) are hypoechoic (Fig. 1). Although the lesions are well marginated, the borders may be difficult to assess if the tumor replaces most or all the testis. In general, compared with NSGCT, seminomas occur in older patients (>30), are more homogeneous on sonography or magnetic resonance imaging (MRI) [4], and are more often diagnosed at an early stage. On T2-weighted imaging, most GCT are hypointense relative to the high-signal background of the testis [1, 4].

Staging involves clinical, pathologic, radiologic, and serum-tumor-marker data [1]. In broad categories, tumors limited to the testis are stage I, those with retroperitoneal nodal involvement are stage II, and those with distant disease are stage III [1]. Nodal disease is usually initially assessed with computed tomography (CT), although MRI has assumed a greater role in recent years in view of concerns regarding radiation exposure in this group of men who are typically between 20 and 40 years of age at the time of diagnosis. This is especially relevant for

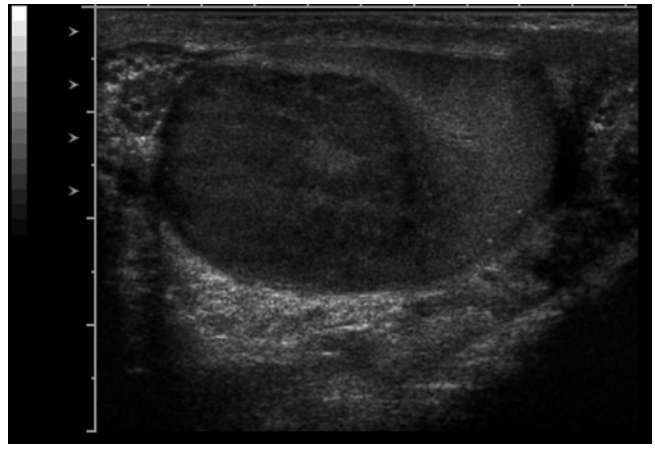

**Fig. 1.** Seminoma. Sonogram demonstrates a minimally heterogeneous, well-marginated intratesticular mass

*Diseases of the Abdomen and Pelvis 2014-2017*,
DOI: 10.1007/978-88-470-5659-6_22 

follow-up in patients with seminoma who not only have a generally favorable prognosis (including response to salvage regimens when needed) but also are frequently offered observation rather than prophylactic therapeutic radiation [5]. Fluorodeoxyglucose positron emission tomography (FDG PET) is not presently included in the initial staging of testicular malignancy due to a lack of evidence to support its routine use [1, 6]. Results have been somewhat mixed, however, in the setting of follow-up after initial treatment; FDG PET may have a role in certain patients (especially those with nonspecific findings when evaluating for active tumor, specifically for seminoma patients being followed to assess response after chemotherapy) [5].

Regardless of stage, nearly all patients with suspected testicular neoplasm are managed surgically (orchiectomy), which is intended to not only provide pathologic confirmation but also to treat the primary tumor. In patients who, based on age (e.g., <30) and imaging features (e.g., heterogeneity or calcification) have a higher likelihood of NSGCT, preorchiectomy CT may warrant consideration, as some clinicians will consider contemporaneous retroperitoneal lymph node dissection if the CT is negative for pathologically enlarged nodes (enlarged nodes, >8 mm, are presumptive evidence of stage II disease). Because most surgeons will await final pathologic confirmation before determining management, the differentiation of NSGCT vs seminoma is rarely of critical importance.

### Testicular Microlithiasis

The topic of testicular microlithiasis (TML) has been the source of considerable controversy in the imaging and urologic communities over the past 20 years [7, 8]. There is little debate that TML, when defined as at least five calcifications in a single sonographic field (Fig. 2), is associated with both intratubular germ-cell neoplasia (a malignant precursor) [9] and an empirically demonstrated increased risk of malignant GCT. Some authors point to a lack of a significant associated risk but often fail to recognize that accepting a very broad definition of TML (e.g., any isolated calcification) incorrectly defines a very large population, which dilutes the importance of the disease by decreasing the specificity of the finding. Many radiologists continue to recommend sonographic follow-up for patients with convincing evidence for TML, especially in younger individuals (e.g., <40 years) [10].

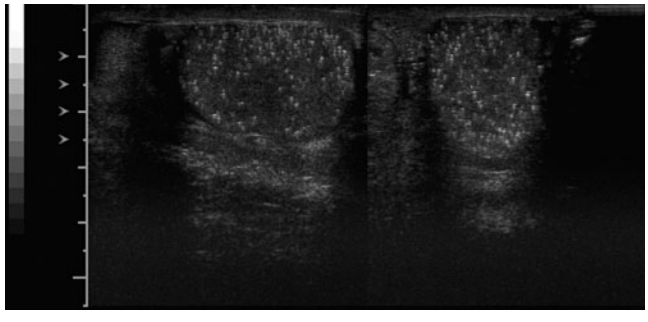

**Fig. 2.** Testicular microlithiasis. Innumerable echogenic foci in both testes

### Gonadal Stromal Tumors

Gonadal stromal tumors (GST) account for <10% of testicular neoplasms and include Leydig cell and Sertoli tumors. These are often incidental findings although may cause gynecomastia. For practical purposes, they are almost always benign but are surgically removed to confirm the diagnosis; imaging and clinical features do not allow differentiation from the more common malignant GCT mentioned above [3].

### Lymphoma

Lymphoma is usually seen in older patients than those affected by GCT. More importantly, almost all patients with testicular lymphoma have known disease prior to the development of scrotal signs or symptoms. The epididymis may be affected, but testis involvement is more common. Whereas the appearance may overlap with that of GCT, lymphoma is more likely to be multifocal or even bilateral [3]. Conspicuous hypervascularity on Doppler US imaging compared with the more common primary neoplasms has been described. It is difficult to differentiate lymphomatous from leukemic involvement of the testis, although, as noted above, the diagnosis is usually known before the patient presents for scrotal imaging.

### Extratesticular Neoplasms

Extratesticular neoplasms in adults are uncommon. The two most common lesions are lipomas and adenomatoid tumors. Lipomas are rarely a clinical or imaging challenge to diagnose. Adenomatoid tumors are well-marginated, benign, solid masses that may be ignored when small but may be removed if large enough to cause pain or if there is concern regarding the diagnosis [11].

### Mesothelioma

Mesothelioma is a rare but aggressive scrotal neoplasm that arises from the tunica. It is far more likely to arise from the pleura or peritoneum than the scrotum and is typically a locally advanced process at the time of initial presentation. Hydrocele or hematocele is commonly seen, and soft tissue nodules of the tunica may be surrounded by fluid. Whereas findings are nonspecific and may mimic unusual soft tissue malignancies, such as leiomyosarcoma, imaging and clinical findings will mitigate for surgical diagnosis and treatment [11].

### Papillary Cystadenomas

Papillary cystadenomas of the epididymis are extremely rare but may be seen in 20-25% of patients with von

Hippel-Lindau disease. The lesions are benign, solid, well-marginated, and may be difficult to differentiate from the more common adenomatoid tumors.

### Tubular Ectasia

Tubular ectasia is not neoplastic but may be mistaken for a mass lesion. The finding is the result of dilatation of the rete testis, with elongated, anechoic channels that converge to the epididymis. Etiology in most cases is uncertain, although obstructive pathophysiology (e.g., postvasectomy) is associated. A nonspherical linear process with angulated margins and, usually, distinct anechoic channels will allow for confident diagnosis. When sonographic findings are atypical, MRI will allow confirmation by demonstrating a well-marginated T2-hyperintense focus [12].

### Epidermoid Cysts

Epidermoid cysts are nonneoplastic inclusion cysts and are well-marginated spherical lesions often characterized by alternating rings of hypo- and hyperechogenicity with a layered appearance. They are benign but are almost always removed surgically because they cannot be differentiated from a malignant GCT with absolute certainty. However, if the radiologist can suggest the diagnosis preoperatively, the patient may be spared orchiectomy and instead be treated with simple enucleation of the mass [11].

## Inflammatory Disease

The most common cause of acute scrotal pain is epididymitis, with or without orchitis. Most patients with epididymo-orchitis are managed conservatively (i.e., without surgery), and imaging is performed to exclude torsion or unusual infectious complications. The most common organisms are *Escherichia coli* species, but *Chlamydia* and gonorrhea are not unusual. Many patients with presumed epididymitis will have no abnormal imaging findings, but many will demonstrate heterogeneous enlargement of the epididymis on grey scale and hyperemia on color or amplitude Doppler US. Hydrocele, with or without internal complicating features (pyocele), is often seen. Although only 20% of patients with epididymitis have coexistent orchitis, such patients are at risk for abscess formation and focal or diffuse infarction.

The most severe form of scrotal infection is necrotizing fasciitis (Fournier's gangrene). This does not originate from the testis or epididymis but begins in the subcutaneous tissues, often in older patients with diabetes mellitus and associated vasculopathy. The clinical presentation may overlap with other scrotal pathology, and the radiologist must be alert to the possibility, paying careful attention to the combination of scrotal skin thickening (edema) and increased echogenicity (secondary to subcutaneous gas, Fig. 3). Treatment is urgent, extensive debridement; the prognosis is poor, and many patients succumb despite aggressive therapy [13].

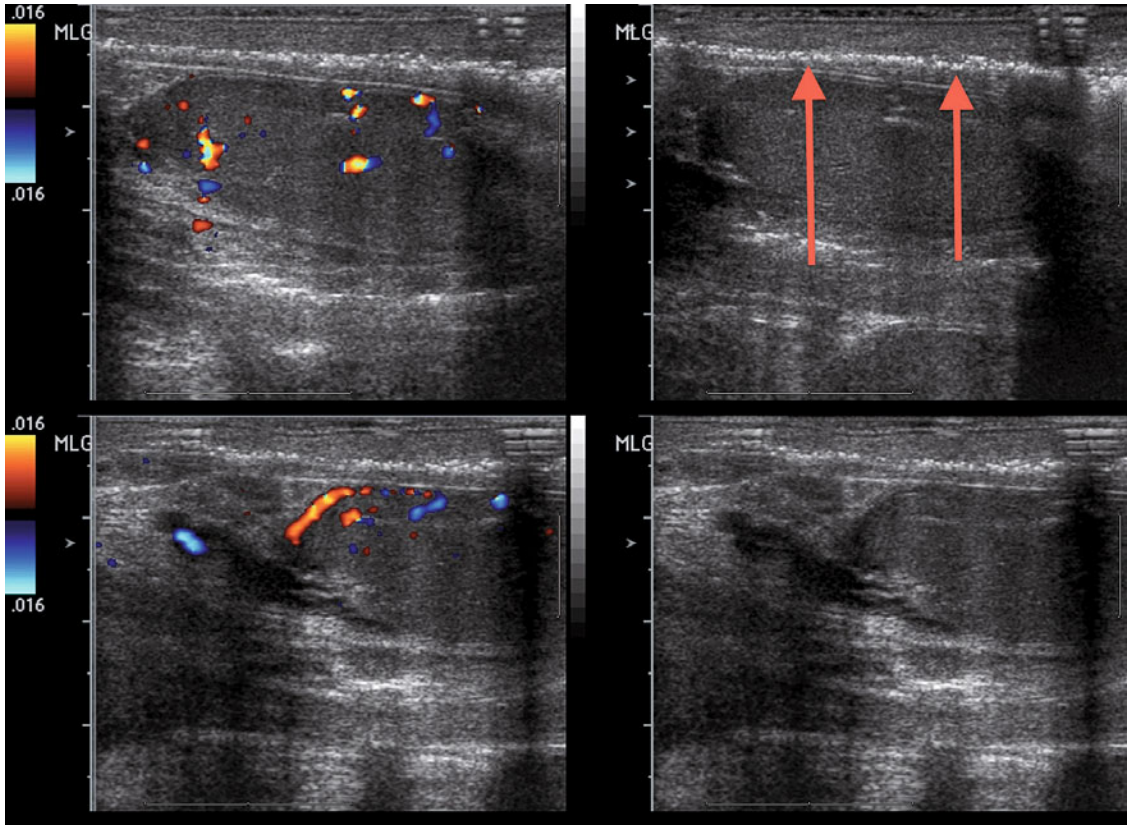


**Fig. 3.** Fournier's gangrene. Nonshadowing echogenicity (*arrows*) in the scrotal wall compatible with gas

## Traumatic Injury

Injury to the testis is nearly always evaluated with sonography. Most patients with scrotal pain and swelling will have, at most, a hematocele. However, diagnostic possibilities also include contusion, intratesticular hematoma, fracture, or rupture (disruption of the tunica albuginea with protrusion of the parenchyma) [13]. Sonographic demonstration of discontinuity, heterogeneity, and contour abnormality are findings that support the diagnosis of rupture [10]; this is important in determining surgical decision making, as most patients with an intact tunica will not require surgical exploration. Most authors recognize that these can be challenging cases due to a combination of patient discomfort and surrounding hematocele; when imaging findings are equivocal, surgery is often performed as a precaution.

## Vascular Disorders

Vascular disorders not only include global ischemia resulting from spermatic cord torsion but a variety of less common disease states that may cause segmental infarction (including severe orchitis and vasculitis) [13, 14]. Patients with torsion usually have an acute presentation with severe unilateral scrotal pain that may be preceded by minor trauma [15]. Color or amplitude (power) Doppler US will usually be subjectively decreased on the affected side. When evaluating the lack of symmetry of the testis on color Doppler, it is critical to know the location of the symptoms. Specifically, if the symptoms lateralize to the side of decreased flow, the diagnosis is likely torsion. In contrast, if the symptoms are associated with the side of relatively increased flow signal, the diagnosis is most likely infection (epididymo-orchitis). However, minor variations of arterial spectral Doppler waveforms may be seen early, including absence of the dicrotic notch or increased resistance (decreased or absent diastolic flow). The latter finding may also be seen in early stages of torsion, when venous flow is altered but arterial flow is still seen on color Doppler.

Most authors agree that significant grey-scale findings (heterogeneity and decreased echogenicity) are indicative that the ischemia has progressed to infarction. Despite such imaging findings to suggest that emergent surgery is not likely to significantly alter the outcome, most urologists will operate without delay in the hopes that surgical detorsion might allow testis salvage.

## References


1. Kreydin EI, Barrisford GW, Feldman AS, Preston MA (2013) Testicular cancer: what the radiologist needs to know. AJR Am J Roentgen 200:1215-1225.
2. Appelbaum L, Gaitini D, Dogra V (2013) Scrotal ultrasound in adults. Semin Ultrasound CT MRI 34:257-273.
3. Woodward PJ, Sohaey R, O'Donoghue MJ, Green DE (2002) Tumors and tumorlike lesions of the testis: radiologic-pathologic correlation. Radiographics 22:189-216.
4. Tsili AC, Argyropoulou MI, Astrakas LG et al (2013) Dynamic contrast-enhanced subtraction MRI for characterizing intratesticular mass lesions. AJR Am J Roentgen 200:578-585.
5. Kollmannsberger C, Tyldesley S, Moore C et al (2011) Evolution in management of testicular seminoma: population-based outcomes with selective utilization of active therapies. Ann Oncol 22:808-814.
6. Brunereau L, Bruyère F, Linassier C, Baulieu J-L (2012) The role of imaging in staging and monitoring testicular cancer. Diagnostic and Interventional Imaging 93:310-318.
7. Lam DL, Gerscovich EO, Kuo MC, McGahan JP (2007) Testicular microlithiasis: our experience of 10 years. J Ultrasound Med 26:867-873.
8. Costabile RA (2007) How worrisome is testicular microlithiasis? Curr Opin Urol 17:419-423.
9. Tan IB, Ang KK, Ching BC et al (2010) Testicular microlithiasis predicts concurrent testicular germ cell tumors and intratubular germ cell neoplasia of unclassified type in adults. Cancer 116:4520-4532.
10. Aganovic L, Cassidy F (2012) Imaging of the scrotum. Radiol Clin N Am 50:1145-1165.
11. Woodward PJ, Schwab CM, Sesterhenn IA (2003) Extratesticular scrotal masses: radiologic-pathologic correlation. Radiographics 23:215-240.
12. Mohrs OK, Thoms H, Egner T et al (2012) MRI of patients with suspected scrotal or testicular lesions: diagnostic value in daily practice. AJR Am J Roentgen 199:609-615.
13. Avery LL, Scheinfeld MH (2013) Imaging of penile and scrotal emergencies. RadioGraphics 33:721-740.
14. Aquino M, Nghiem H, Jafri SZ et al (2013) Segmental testicular infarction: sonographic findings and pathologic correlation. J Ultrasound Med 32:365-372.
15. Lubner MG, Simard ML, Peterson CM et al (2013) Emergent and nonemergent nonbowel torsion: spectrum of imaging and clinical findings. RadioGraphics 33:155-173.

# Multiparametric Magnetic Resonance Imaging in Prostate Cancer Detection

Tahir Durmus, Alexander Baur, Bernd Hamm

Department of Radiology, Charité, Universitätsmedizin Berlin, Berlin, Germany

## Introduction

Prostate cancer is the most common malignancy in men, but only about 10% of patients die from that cancer. While the incidence rate in the last 30 years has increased fourfold, the mortality rate has decreased over the last 20 years [1]. This can be primarily attributed to the early detection of prostate cancer as a result of the common practice of testing the prostate-specific antigen (PSA) in peripheral blood. Trendsetting studies indicate that the current diagnostic and therapeutic approach must be fundamentally rethought. Wilt et al. could not show a significant reduction in mortality rate for patients with a localized tumor who underwent a radical prostatectomy compared with patients who were simply monitored [2]. In addition to possible postoperative complications, radical prostatectomy was associated with a significantly higher morbidity rate (incontinence, erectile dysfunction) [2]. As with radical prostatectomy, radiation therapy is also associated with significant side effects, such as loss of potency, in up to 50% of patients [3]. Although prostate cancer can be effectively treated in many cases by radical therapies following early diagnosis, not all patients seem to benefit from such treatments. Therefore, new management strategies, such as active surveillance and watchful waiting, as well as organ-preserving focal therapy options, are being evaluated in studies.

Selecting the most suitable diagnostic and therapeutic approach for the individual patient is a significant challenge. As a matter of fact, magnetic resonance imaging (MRI), with its multiparametric imaging, is shaking the foundations of established diagnostic and therapeutic paradigms and is now being used for planning diagnostic punctures and radical treatments. In the future, it will become increasingly important for patient stratification with regard to therapeutic approach and treatment monitoring [4].

This chapter provides an overview of the status of multiparametric MRI of the prostate and an interpretation of relevant findings. The role of multiparametric MRI in diagnosing prostate cancer, including systematic and targeted biopsy and its potential in conservative and minimally invasive treatments, is also discussed.

## Multiparametric MRI of the Prostate

Due to its high soft tissue contrast, high resolution, and ability to simultaneously image functional parameters, MRI provides the best visualization of the prostate compared with other imaging methods. In the case of MRI scanners with a field strength of 1.5 T, it is advantageous to use a dedicated endorectal coil, particularly for local staging of prostate cancer [5]. With MRI scanners with a field strength of 3 T and the associated higher signal-to-noise ratio (SNR), image quality is so good even without an endorectal coil that the coil is not necessary for detection purposes. This should result in greater patient acceptance and should further support the broader use of multiparametric MRI in the coming years.

Multiparametric MRI refers to the combination of morphological sequences and functional imaging techniques. Standard T2-weighted (T2w) and T1-weighted (T1w) turbo-spin-echo (TSE) sequences are used to visualize morphology, whereas diffusion-weighted imaging (DWI), dynamic contrast-enhanced imaging (DCE), and MR spectroscopic imaging can be combined for functional sequences.

### Morphological Imaging: T2- and T1-Weighted Imaging

High-resolution axial T2-TSE is the backbone of every MRI of the prostate. This is typically supplemented by a sagittal and possibly a coronal T2-TSE sequence, which facilitates evaluation of the seminal vesicles in particular. T2w imaging allows precise visualization of the zonal anatomy of the prostate, showing peripheral, central, and transition zones (Fig. 1a). Moreover, nodular, glandular,

* This chapter has been reproduced, with permission, from Rofo. Durmus T, Baur A, Hamm B (2014) Multiparametric magnetic resonance imaging in the detection of prostate cancer. Fortschr Röntgenstr, DOI: 10.1055/s-0034-1365937.

*Diseases of the Abdomen and Pelvis 2014-2017*,
DOI: 10.1007/978-88-470-5659-6_23 

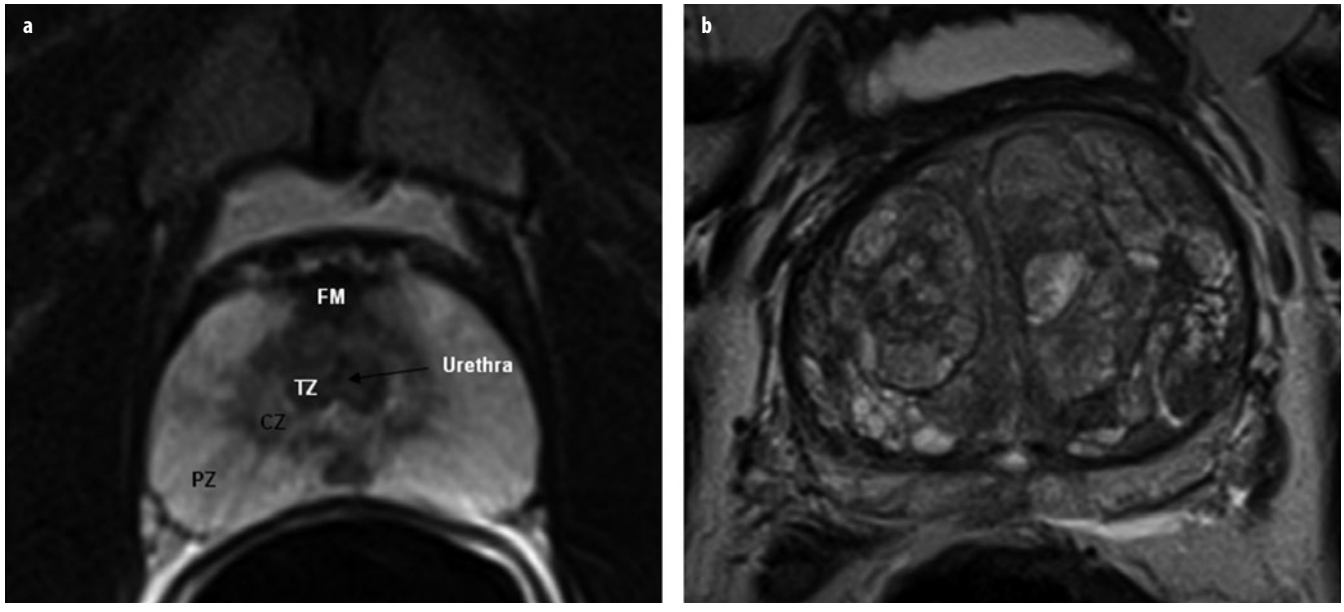


**Fig. 1 a, b.** **a** Normal prostate of a 30-year-old man. The transition zone (*TZ*) is still highly localized around the urethra. It is surrounded by the central zone (*CZ*) in the basal segments and by fibromuscular tissue (*FM*). The majority of the prostate is composed of the peripheral zone (*PZ*). **b** Nodular changes in benign prostate hyperplasia in an older patient enlarge the transition zone with consecutive compression of central and peripheral zones

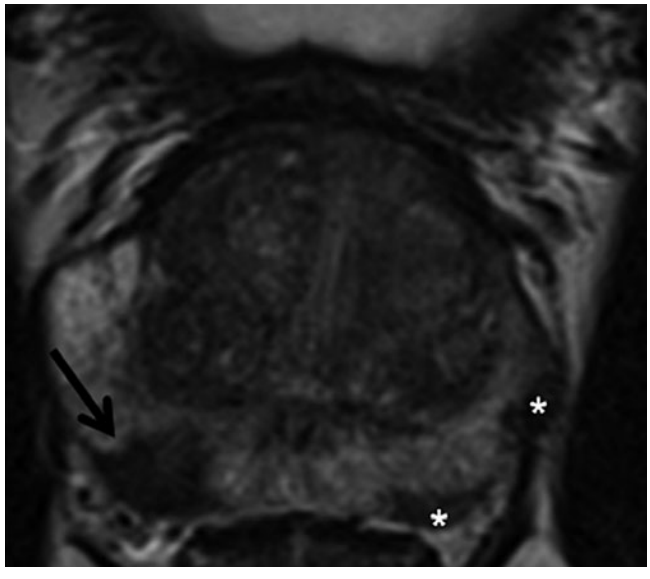

**Fig. 2.** Prostate cancer of the peripheral zone: Axial T2-weighted turbo-spin-echo (TSE) sequence with a hypointense lesion on the right side in the peripheral zone (*arrow*). After targeted biopsy under magnetic resonance imaging (MRI) guidance, an acinar prostate adenocarcinoma with a Gleason score of 3 + 4 = 7 was detected. The additional, smaller foci on the left side of the peripheral zone should also be mentioned (*)

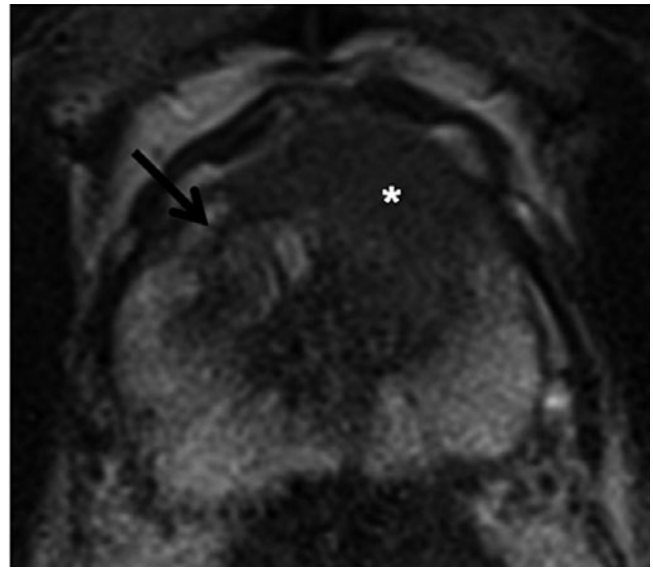

**Fig. 3.** Prostate cancer of the transition zone: Axial T2-weighted turbo-spin-echo (TSE) with homogeneously hypointense lesion ventral left paramedian (*). Whereas the benign hyperplastic nodule has a distinct hypointense border on the right in the transition zone (*arrow*), the border around the focus is unclear (erased charcoal sign). There is a ventral protrusion in the contour of the cancer

stromal, and cystic changes in benign prostate hyperplasia (BPH) can be reliably visualized (Fig. 1b). Prostate carcinomas can be detected in T2w imaging on the basis of their low signal classic oval shape, as well as their space-occupying nature once they reach a certain size (Figs. 2 and 3). The diagnostic accuracy of T2w imaging alone is highly variable according to the literature. This is primarily due to differences in study design (e.g., prostatectomy versus biopsy as reference standard, type of reading, detection versus staging) and in the examined study population (e.g., patients with known prostate cancer versus patients after multiple biopsies). For T2w imaging without functional sequences, sensitivity and specificity for prostate cancer are approximately 57-83% and 62-82%,

respectively [6, 7]. The diagnostic limitations of T2w imaging alone are due to the often similar nature of regularly occurring acute and chronic inflammation of the prostate and hemorrhages, which also cause a hypointense pattern in T2w imaging. Prostatitis typically has a striated, slightly hypointense, appearance and sometimes cannot be morphologically differentiated from prostate cancer in T2w imaging (Figs. 4 and 5). Hemorrhages have a very variable appearance in T2w imaging and can be detected in T1w imaging on the basis of their hyperintensity (Fig. 6a, b). As bleeding is a regular occurrence after biopsy, MRI of the prostate should not be performed until at least 6-8 weeks after biopsy in order to avoid unnecessary diagnostic impediments. However, hemorrhages can also persist for several months. Therefore, it is useful to know that bleeding can also serve as a diagnostic detection aid. In a hyperintense prostate on T1w imaging, due to postbioptic hemorrhagic changes, hypointense island-like areas that correlate with hypointense areas on T2w images can be an indication of prostate cancer (hemorrhage exclusion sign) [8]. It is presumed that the anticoagulative effect of the citrate, which is highly concentrated in normal prostate tissue but is low in cancer tissue, results in increased bleeding. Well-vascularized and perfused cancer tissue is probably also a better site of degradation for bleeding residues than normal prostate tissue. With respect to a more exact diagnosis in the case of bleeding residues, DWI and MR spectroscopy are particularly advantageous [9, 10]. At present, morphological imaging should normally be combined with at least two functional sequences in order to significantly increase MRI sensitivity and specificity [11-13]. These will be introduced in the following.

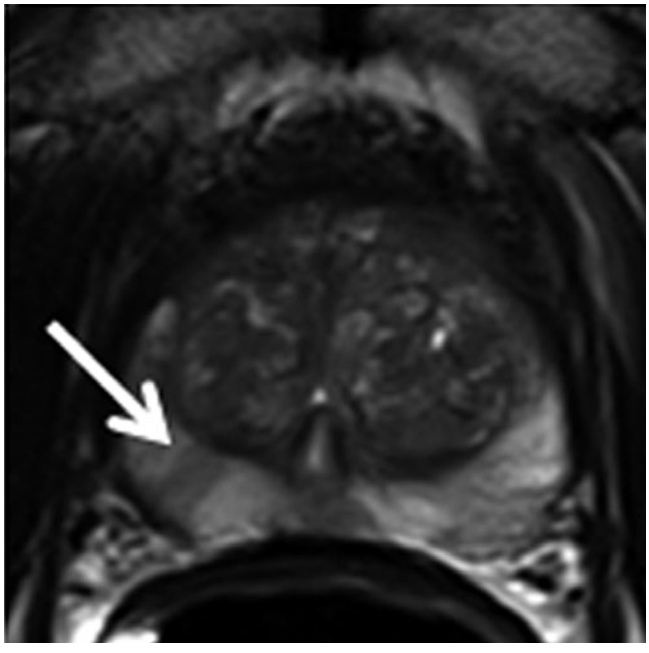

**Fig. 4.** Prostatitis: Axial T2-weighted turbo-spin-echo (TSE) with slightly hypointense, striated changes on both sides (*arrow*), diagnosed in histology as chronic prostatitis

## Diffusion-Weighted Imaging

DWI visualizes the Brownian molecular motion of water. It has become an important part of oncological

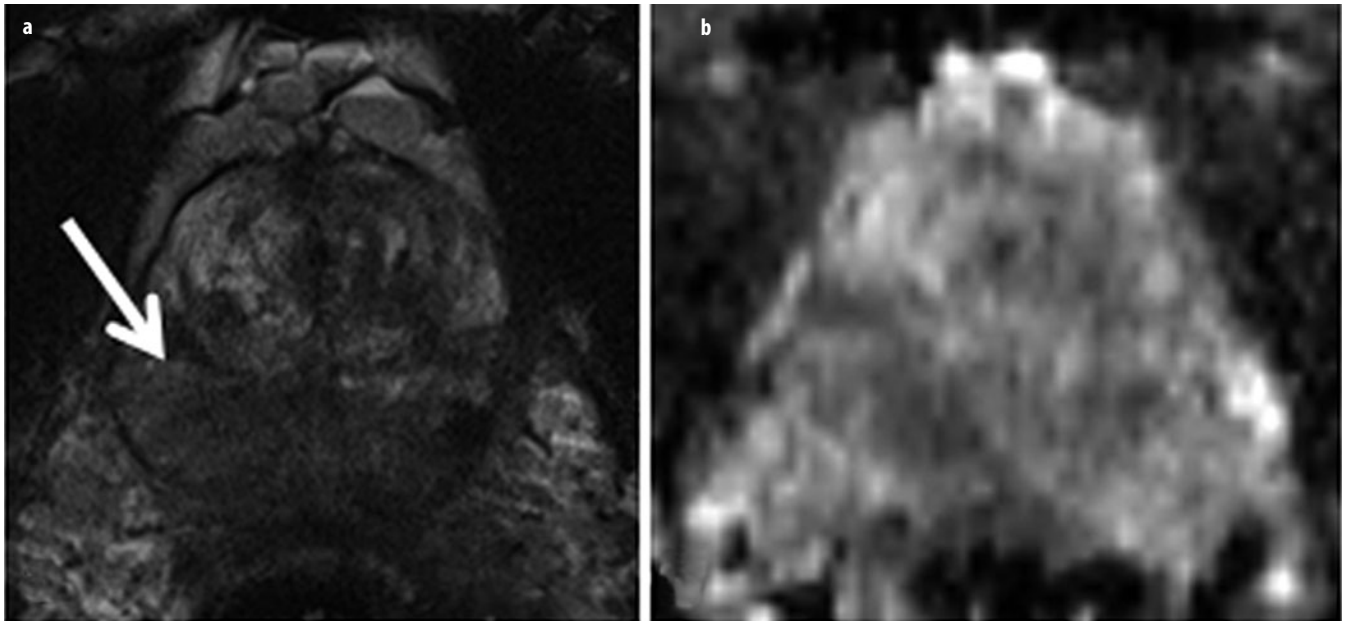


**Fig. 5 a, b.** Granulomatous prostatitis. **a** Axial T2-weighted turbo-spin-echo (TSE) and **b** corresponding apparent diffusion coefficient (ADC) map of a patient with prostate-specific-antigen (PSA) values between 6-8 ng/ml and three transrectal ultrasound (US)-guided biopsies without detecting cancer. The extensive and partially significantly T2-weighted hypointense changes (*arrow*) were diagnosed as granulomatous prostatitis after targeted magnetic resonance imaging (MRI)-guided biopsy. The finding in T2-weighted imaging would also be consistent with imaging of an advanced, diffusely growing prostate cancer

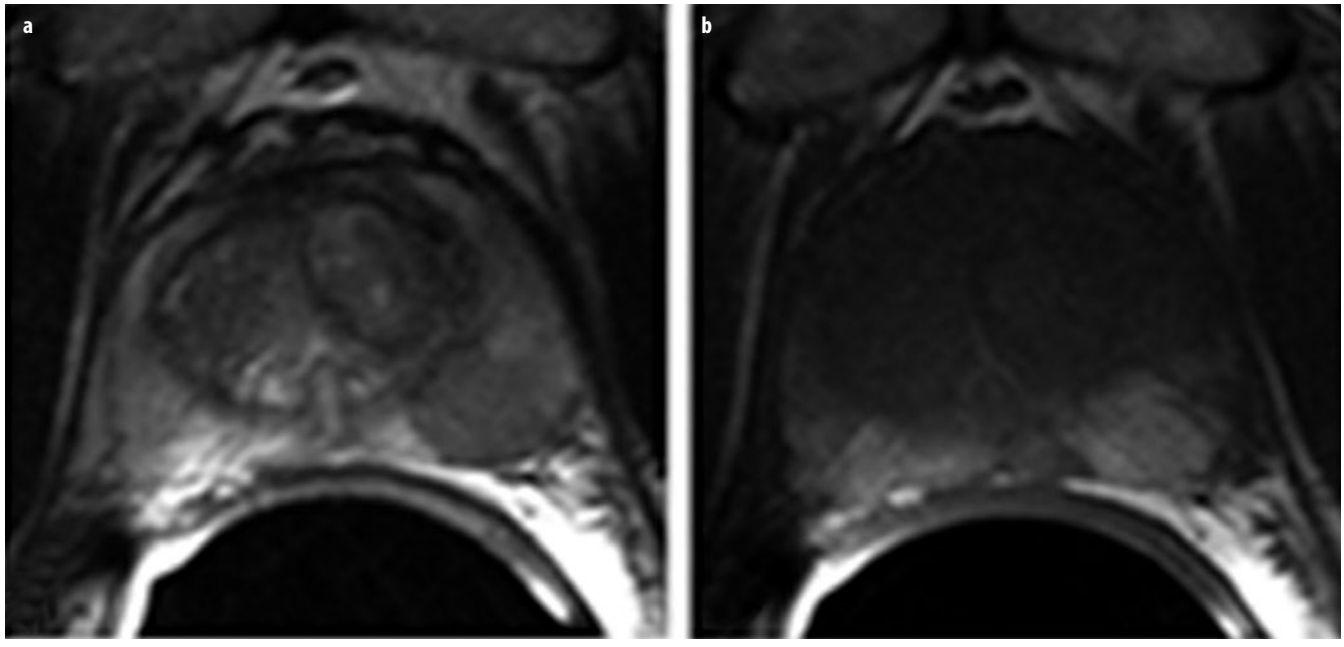


**Fig. 6 a, b.** Postpuncture bleeding. **a** Bleeding can be mistaken for prostate cancer in T2-weighted turbo-spin-echo magnetic resonance imaging (TSE-MRI) due to its hypointense appearance. **b** Hyperintense postpuncture hemorrhagic changes can be detected on both sides in the peripheral zone in the corresponding axial T1-weighted TSE slice

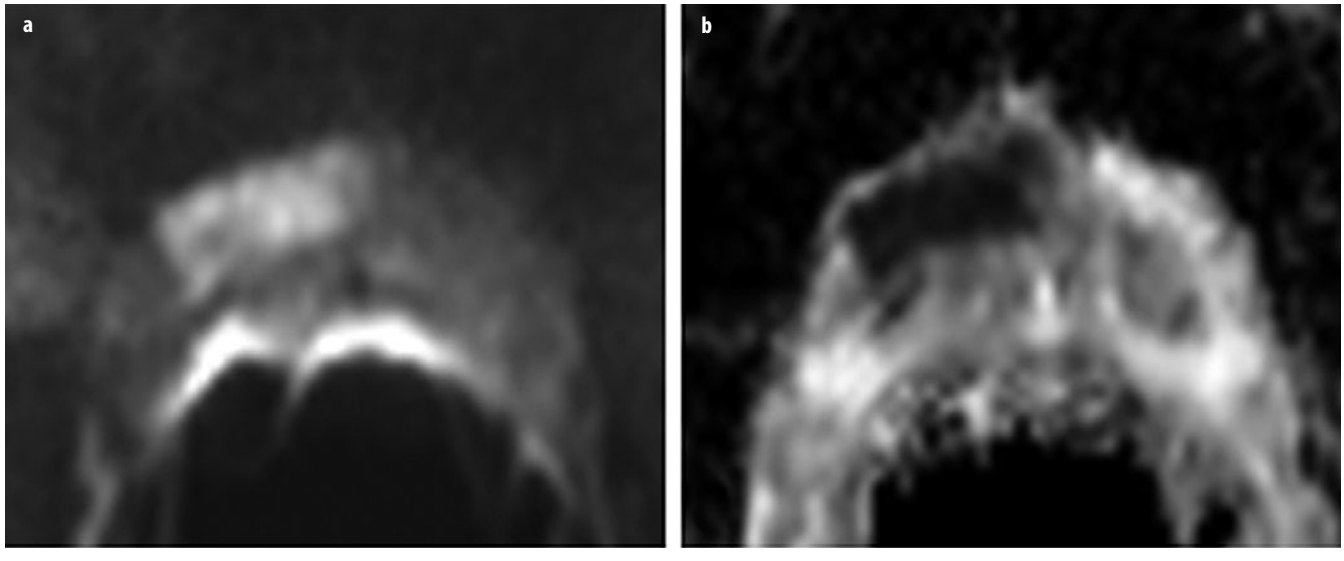


**Fig. 7 a, b.** **a** Axial diffusion-weighted imaging (DWI) with a b-value of 1,000 shows a lesion ventral right with a hyperintense signal. **b** This area has low signal intensity in the corresponding apparent diffusion coefficient (ADC) map. With normal diffusion, the peripheral zone of the prostate has high signal intensity in ADC and low signal intensity in b-1,000. After prostatectomy, an acinar prostate adenocarcinoma with a Gleason score of 4 + 3 = 7 was diagnosed ventral right

imaging, as malignant tumors are typically composed of densely arranged cells in which their numerous membranes limit this Brownian molecular motion [14]. Prostate cancers are thus visualized on highly diffusion-weighted images (typically upper b-values of 800-1,000 s/mm$^2$ in prostate imaging) as areas with high signal intensity (Fig. 7a). Diffusion coefficients [apparent diffusion coefficient (ADC)] can be calculated from the diffusion-weighted data. In ADC maps, areas with normal diffusion can then be differentiated as having high signal intensity and those with diffusion restriction as having comparatively low signal intensity (Fig. 7b). Most studies show that DWI is a very useful addition to morphological imaging and can increase sensitivity in particular by 10-25% [15-17]. Since hyperplastic stromal nodules can have pronounced diffusion restriction in BPH, DWI

must be evaluated together with morphological imaging (T2w), especially when assessing the central portions of the prostate gland [16].

Studies have increasingly examined the capabilities of DWI with respect to evaluating the aggressiveness of prostate cancer. Such studies show that the ADC value has a negative correlation with the Gleason score, i.e., low ADC values are seen primarily in high-grade, aggressive prostate cancers [15, 18]. Results regarding the ability to differentiate low-grade (Gleason score 3 + 3 = 6) and high-grade (Gleason score >4 + 3 = 7) tumors in the peripheral zone are very promising, since they may be able to help to better determine patient risk potential [19, 20]. However, since there can still be relevant overlapping of ADC values in different Gleason groups, additional studies are needed to implement this grading potential of DWI in clinical routine. DWI will play an important role in differentiating patients with a low risk from those with a high risk and separating them with respect to management [21].

### Dynamic Contrast-Enhanced MRI

Contrast-enhanced MRI sequences can be used to assess tissue vascularity and permeability. Gadolinium-containing extracellular T1w contrast agent is typically administered intravenously for this purpose [22]. Fast T1w gradient-echo (GRE) sequences with a temporal resolution of 4-10 s are primarily used in prostate imaging. Measurements should be performed over a period of up to approximately 5 min after contrast agent application [13]. Enhancement can be displayed in the form of curves over time, thus helping to characterize tissues. Prostate cancers are characterized by fast washin (early peak enhancement) and fast washout compared with healthy tissue (type III curve). Enhancement typically increases steadily (type I) in the given measurement time in cancer-free tissue, whereas a curve with a plateau (type II) occurs relatively frequently in both healthy and cancerous tissue [22]. On the basis of enhancement curves, gadolinium concentrations in tissue and tissue-transport constants in the direction of the tumor interstitium ($K^{trans}$) and back in the direction of the blood plasma ($k_{ep}$) can be calculated using suitable mathematical models (two-compartment Tofts model). Prostate cancers are characterized by an increase in the tissue-transport constants, which can be displayed using color coding in pharmacokinetic parameter maps (Fig. 8) [23]. Available studies do not provide a clear conclusion regarding improvement of prostate cancer detection via DCE. Some studies showed an improvement in diagnostic accuracy of conventional MRI (T2w and T1w) when supplemented by DCE imaging [24, 25]. However, it is problematic in DCE that hyperplastic nodules in BPH can enhance and wash out quickly, like prostate carcinoma foci, and $K^{trans}$ and $k_{ep}$ can be accordingly increased, thus limiting sensitivity and specificity, particularly in the central portions of the prostate gland [26, 27]. In addition, inflammation can often have greater vascularity and tissue permeability, which also limits its sensitivity and specificity in detecting prostate cancer. However, local staging of prostate cancer and detection of local tumor relapses after definitive therapy can be significantly

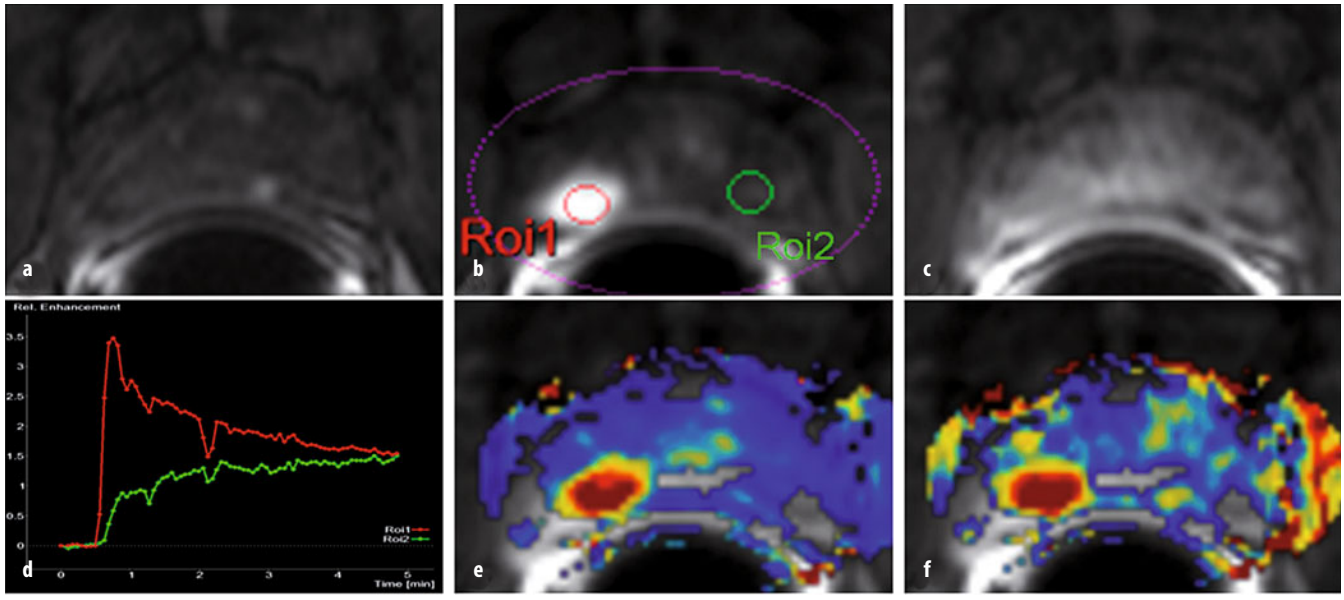


**Fig. 8 a-f.** **a** Unenhanced axial T1-weighted gradient echo (GRE) sequence. **b** After contrast agent administration, an area with early enhancement is seen on the *right* in the peripheral zone (ROI1), with **c** significant washout in the late-phase image. **d** Enhancement can be graphically shown as signal intensity (SI)/time curve. A type III curve (*red*) with early enhancement is a typical finding in prostate cancer, whereas healthy prostate tissue is characterized by a steady, slow washin (type I, *green*). Parameter maps represent an alternative. **e, f** High-transport constants ($K^{trans}$ and $k_{ep,}$ respectively) confirm suspicion of prostate cancer. In this example, a minimally differentiated prostate adenocarcinoma with a Gleason score of 4 + 5 = 9 was diagnosed after prostatectomy

improved using dynamic T1w sequences, with good spatial resolution [28, 29].

#### MR Spectroscopy

MR spectroscopy allows spatially resolved visualization of chemical substances in an organ. The healthy prostate gland produces an ample amount of a citrate-containing secretion, resulting in a high citrate content and a low choline level. In prostate cancer, the choline level is significantly elevated and the citrate content reduced due to the metaplastic processes of cell membranes. The relationship between these two metabolites can therefore be used as a measure of malignancy [30]. MR spectroscopy increases MRI specificity, in particular, but can also be used to evaluate tumor volume [31, 32]. The diagnostic accuracy of morphological MRI can be increased by MR spectroscopy from 52% to 75% [10].

The basic requirement for good spectral resolution of the individual metabolites is a homogeneous magnetic field in the field of measurement and sufficient suppression of the fat and water signal during the measurement. In addition to sequence adjustments, this usually requires multiple shimming steps and saturation bands around the prostate to be manually adjusted to the individual prostate anatomy. Together with these preparations, MR spectroscopy at 1.5 T requires a measurement time of 13-20 min. Evaluation and interpretation are complex and often only possible after appropriate physical adjustments. Even if in the near future automatic segmentation algorithms are able to automatically detect the prostate, thus minimizing measurement preparations, MR spectroscopy will remain limited in its daily use due to the significant time investment and the high level of physical-medical expertise required.

### Structured Interpretation and Communication of MRI Findings in the Prostate

In 2012, the European Society of Urogenital Radiology (ESUR) created the Magnetic Resonance Prostate Imaging Reporting and Data System (MR PI-RADS) as part of its MRI guidelines for prostate imaging [13]. Based on the Breast Imaging Reporting and Data System (BI-RADS), a standardized method for reporting multiparametric MRI of the prostate for detecting prostate cancer, was proposed here. The goal was to standardize image interpretation and to simplify communication between the radiologist and colleagues in other departments.

Based on clearly defined criteria according to PI-RADS, every lesion suspicious for tumor within the prostate is assigned a point value between 1 and 5 for every sequence performed as part of multiparametric MRI (consisting of at least T2w, DWI, and DCE). Moreover, a total point value is calculated for every lesion suspicious for tumor [33]. Thus, a statement regarding the probability of the presence of a clinically significant prostate cancer should be possible: a point value of 1 means that a lesion is probably benign, whereas a point value of 5 indicates a high probability of malignancy. The development of PI-RADS and criteria contained therein for the assignment of point values are based on published literature and an expert consensus. Since being published in February 2012, PI-RADS has been evaluated in multiple studies.

The point values of T2w, DWI, and DCE were added to form a total point value for lesions suspicious for tumor. Good and reproducible diagnostic accuracy was documented for the total point values calculated in this manner [33-37].

Standardization of image interpretation in research and the clinical routine is an important milestone that should accelerate the acceptance of multiparametric MRI in the coming years. The results of clinical studies should be easier to compare using PI-RADS. Moreover, PI-RADS makes it possible to formulate guidelines for diagnostic clarification and perhaps even for treating prostate cancer. The present data indicate that a biopsy should be performed in PI-RADS $\geqslant$4 lesions, whereas monitoring via MRI and PSA could be sufficient in lesions with PI-RADS $\leqslant$3.

### MRI and Prostate Biopsy

The standard prostate biopsy is the transrectal ultrasound (TRUS)-guided systematic prostate biopsy. Urological studies in particular show that the detection rate increases as expected with the number of samples so that approximately six samples are taken from each lateral lobe in accordance with the recommendations of the professional associations [38, 39]. However, the entire context of the diagnostic weaknesses of TRUS biopsy only becomes clear with MRI and visualization of prostate cancer [40]. The rate of carcinomas in the ventral portion of the prostate gland, as well as in an extreme lateral position in the peripheral zone and on the apex of the gland, is significant in patients with multiple negative US-guided biopsies. It was shown that patients with a diagnosis of prostate cancer in the ventral portions of the gland have a higher clinical risk than those with a diagnosis of prostate cancer in the peripheral zone [41].

#### Direct MRI-Guided Biopsies

In all direct MRI-guided biopsy techniques, MRI is performed during the biopsy and the images are used to guide the biopsy needle. Therefore, the biopsy equipment must be MRI compatible. MRI-guided biopsies should be performed on a 1.5-T or 3-T unit, since exact visualization of lesions during biopsy is of essential importance. Direct MRI-guided biopsies can be performed via transgluteal, transperineal, and transrectal access [41-43]. Transrectal biopsy is the most common and most accepted direct MRI-guided biopsy technique, since there are no special requirements regarding anesthesia or sterility in contrast to the transperineal and transgluteal methods.

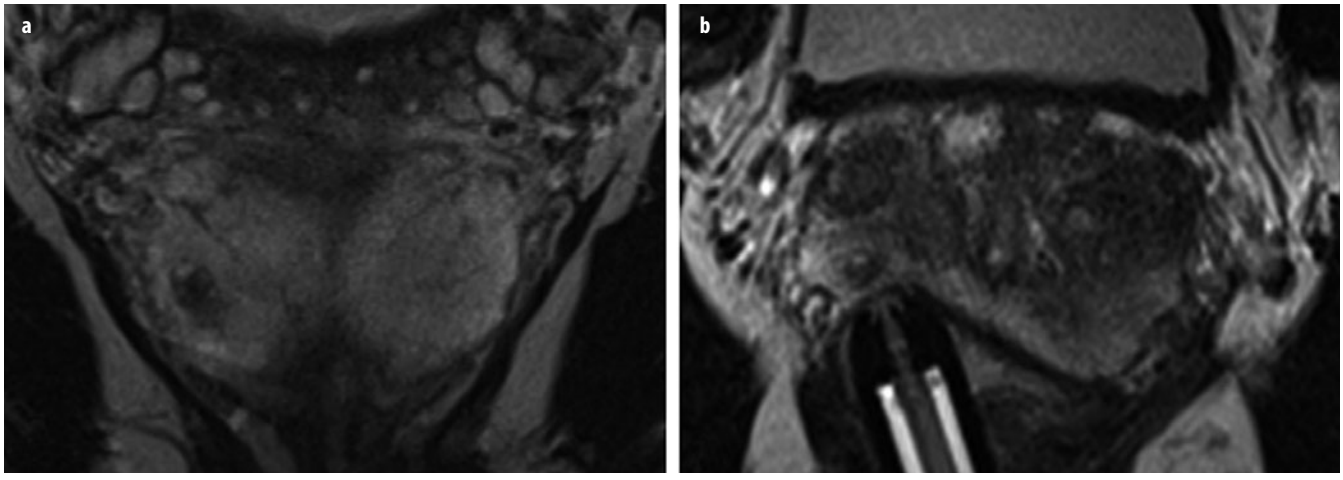


**Fig. 9 a, b.** Patient with a negative ultrasound (US)-guided biopsy in history and increasing prostate-specific antigen (PSA) value; 12 ng/ml at the time of magnetic resonance imaging (MRI). **a** Coronal T2-weighted turbo-spin-echo (TSE) with lesion suspicious for cancer measuring a maximum of 5 × 7 mm in the peripheral zone. **b** Targeted biopsy under direct MRI guidance yielded a total sample length of 12 mm, with 4 mm of an acinar prostate adenocarcinoma (Gleason score 3 + 3 = 6)

Transrectal MRI-guided biopsy is typically performed after simply coating the rectal mucous membrane with a disinfecting and locally anesthetizing gel [44]. The patient is premedicated with antibiotics, as in standard transrectal US-guided biopsies. Transrectal MRI-guided biopsy can be evaluated as the most exact prostate biopsy method on the basis of current data (Fig. 9): in populations with multiple negative systematic US-guided biopsies, detection rates of 41-59% could be achieved with direct MRI-guided prostate biopsy, with the majority of tumors being classified as clinically relevant [41, 45-47]. As shown in Fig. 9, the targeted clarification of non-clinically-relevant cancers is also important, since this can resolve the diagnostic dilemma of an increasing PSA with a negative biopsy, thus creating a foundation for noninvasive and minimally invasive strategies, such as active surveillance or focal therapy.

### MRI/US Fusion Biopsy

A multiparametric MRI scan is performed prior to every targeted biopsy to identify lesions suspicious for carcinoma and to evaluate whether targeted biopsy techniques are suitable. A possibility for improving reporting would be to create a drawing of the location of the suspicious focus in addition to the written findings. This drawing can then be used during a planned biopsy to perform a greater number of biopsies in certain regions of the prostate. The procedure is similar for cognitive fusion, in which US-guided biopsy is performed immediately after viewing the MRI scan. The objective here is to evaluate the regions suspicious on MRI in a targeted manner and to identify focal lesions on the B-mode image [48]. The prostate must be viewed in both modalities on the same – or at least a comparable – image plane. Otherwise, it is extremely difficult to recognize complex structures in the prostate. Navigation is facilitated by detecting the urethra, prominent hyperplastic nodules, or cysts. Puech et al. detected 15% more clinically relevant cancers per TRUS biopsy in their study by viewing MRI images immediately prior to biopsy [48]. However, cognitive fusion can be expected to be highly examiner dependent. Therefore, software-based fusion of MRI data sets with US images would be desirable. Software on the latest US devices can fuse previously imported MRI data sets three dimensionally and in real time with the B-mode image of a US examination. An electromagnetic unit coupled to the US probe to track probe movement is positioned next to the patient table during the biopsy for this purpose [48, 49]. By selecting individual reference points on MRI and B-mode images, MRI images are adjusted and moved in parallel with the US scan (Fig. 10). This makes it possible to use the US probe to navigate to and biopsy lesions evaluated as being suspicious for cancer in the preceding multiparametric MRI scan [49]. Software-supported 3D real-time fusion is currently under intense evaluation. Multiple workgroups were already able to document a significantly higher detection rate of clinically relevant prostate cancers compared with systematic US-guided biopsy [49-51].

To date, different direct MRI-guided biopsy techniques and MRI/US fusion biopsy have not been evaluated in a direct comparison with respect to MRI preparation and examination time, cost, and diagnostic accuracy. However, the possibility of software-based fusion of MRI and US images in real time is a milestone in the bioptic diagnosis of prostate cancer and will probably be used more widely in coming years.

### MRI for Active Surveillance

Not all patients with prostate cancer benefit from radical surgery or radiation therapy, particularly when considering possible peri- and posttherapeutic complications,

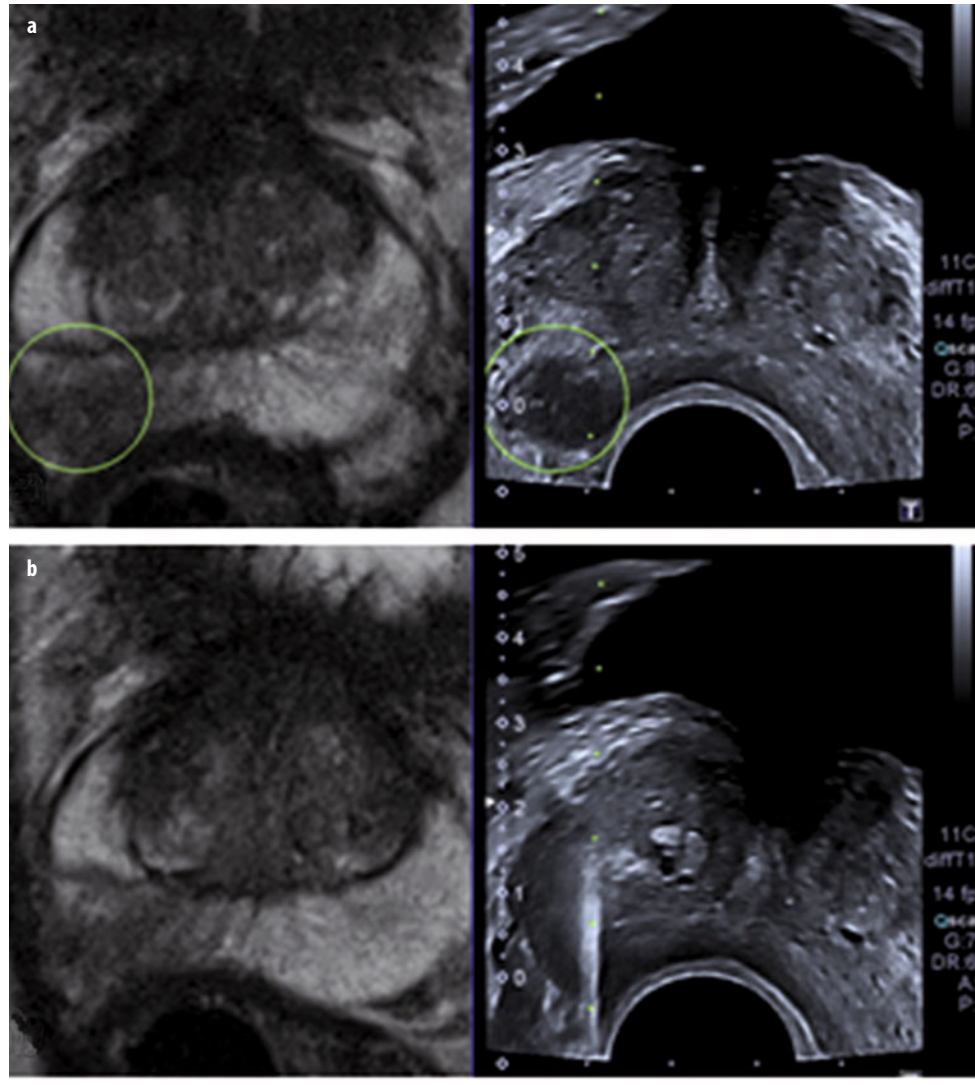


**Fig. 10 a, b.** Magnetic resonance imaging (MRI)-ultrasound (US) 3D fusion in real time. After MRI images [*right*, T2-weighted turbo-spin-echo (TSE) axial] are imported, freely selectable reference points are selected in the T2-weighted and B-mode image. **a** Based on this information, the two data sets are combined by software so that the T2-weighted image is adjusted in accordance with US probe movement, so that – as shown in this example – it is possible to navigate to the lesion suspicious for tumor in the right peripheral zone. **b** After the lesion is precisely targeted, it can be biopsied under US guidance

including incontinence and erectile dysfunction [2]. In particular, patients with low-grade prostate cancer (Gleason ⩽6) can benefit from surveillance and watchful waiting. Multiparametric MRI can play a significant role in identifying suitable patients [52]. In patients under surveillance, multiparametric MRI can help during follow-up to detect paraclinical parameters, such as PSA value and rebiopsy results, as well as any tumor progress, and to initiate appropriate treatment. Such progress can be detected on the basis of an increase in size but in the future also on the basis of changes in functional sequences such as DWI and DCE in terms of dedifferentiation. MRI could also significantly reduce the number of necessary rebiopsies, thus making management less invasive.

To date, multiparametric MRI has not been an integral part of diagnostic algorithms in large prospective studies for examining morbidity and mortality among patients under watchful waiting or active surveillance. However, the role of multiparametric MRI is being explicitly examined in studies in progress regarding this topic. Corresponding evidence-based data can therefore be expected in the near future.

## MRI and Minimally Invasive Therapies

A number of minimally invasive, focal, organ-preserving methods have been used in recent years as further alternatives to the radical treatment of prostate cancer. The goal of these methods is to ablate tumor tissue within the prostate while maintaining tumor-free areas of the prostate gland and preserving periprostatic tissue and structures. These procedures seek to avoid typical peri- and postoperative complications. From the histopathological processing of prostatectomy specimens, it is known that prostate cancer is usually multifocal. However, a so-called "index lesion," a tumor focus that is significant on the basis of size and differentiation (Gleason score), seems to be decisive for patient prognosis also in these patients [53]. The goal of a minimally invasive treatment must therefore not necessarily be to achieve tumor-free

status but to ablate significant tumor foci. Imaging per multiparametric MRI makes it possible to determine the exact location of relevant tumor foci in order to guide focal therapies, as in diagnostic biopsies [54]. The methods used to date for the prostate include cryotherapy, high-intensity focused US, and laser-induced thermoablation [55]. Other methods, such as irreversible electroporation (IRE), are being evaluated [56].

Significant tumor foci that are generally accessible for ablation can be identified via multiparametric MRI. Moreover, MRI will become increasingly important in the image-guided use of locally ablative procedures [54, 55]. PSA value remains a valuable marker for follow-up evaluation and for detecting relapses. The exact role that multiparametric MRI will play in treatment monitoring after minimally invasive therapy and as an instrument in long-term follow-up must be examined in the coming years.

## References


1. Siegel R, Naishadham D, Jemal A (2012) Cancer statistics, 2012. CA Cancer J Clin 62:10-29.
2. Wilt TJ, Brawer MK, Jones KM et al (2012) Radical prostatectomy versus observation for localized prostate cancer. N Engl J Med 367:203-213.
3. Zelefsky MJ, Chan H, Hunt M et al (2006) Long-term outcome of high dose intensity modulated radiation therapy for patients with clinically localized prostate cancer. J Urol 176:1415-1419.
4. Padhani AR (2011) Integrating multiparametric prostate MRI into clinical practice. Cancer Imaging 11:S27-S37.
5. Beyersdorff D, Darsow U, Stephan C et al (2003) [MRI of prostate cancer using three different coil systems: image quality, tumor detection, and staging]. Rofo 175:799-805.
6. Nakashima J, Tanimoto A, Imai Y et al (2004) Endorectal MRI for prediction of tumor site, tumor size, and local extension of prostate cancer. Urology 64:101-105.
7. Beyersdorff D, Taupitz M, Winkelmann B et al (2002) Patients with a history of elevated prostate-specific antigen levels and negative transrectal US-guided quadrant or sextant biopsy results: value of MR imaging. Radiology 224:701-706.
8. Barrett T, Vargas HA, Akin O et al (2012) Value of the hemorrhage exclusion sign on T1-weighted prostate MR images for the detection of prostate cancer. Radiology 263:751-757.
9. Rosenkrantz AB, Kopec M, Kong X et al (2010) Prostate cancer vs. post-biopsy hemorrhage: diagnosis with T2- and diffusion-weighted imaging. J Magn Reson Imaging 31:1387-1394.
10. Kaji Y, Kurhanewicz J, Hricak H et al (1998) Localizing prostate cancer in the presence of postbiopsy changes on MR images: role of proton MR spectroscopic imaging. Radiology 206:785-790.
11. Franiel T, Stephan C, Erbersdobler A et al (2011) Areas suspicious for prostate cancer: MR-guided biopsy in patients with at least one transrectal US-guided biopsy with a negative finding–multiparametric MR imaging for detection and biopsy planning. Radiology 259:162-172.
12. Turkbey B, Pinto PA, Mani H et al (2010) Prostate cancer: value of multiparametric MR imaging at 3 T for detection-histopathologic correlation. Radiology 255:89-99.
13. Barentsz JO, Richenberg J, Clements R et al (2012) ESUR prostate MR guidelines 2012. Eur Radiol 22:746-757.
14. Turkbey B, Aras O, Karabulut N et al (2012) Diffusion-weighted MRI for detecting and monitoring cancer: a review of current applications in body imaging. Diagn Interv Radiol 18: 46-59.
15. Yagci AB, Ozari N, Aybek Z et al (2011) The value of diffusion-weighted MRI for prostate cancer detection and localization. Diagn Interv Radiol 17:130-134.
16. Haider MA, van der Kwast TH, Tanguay J et al (2007) Combined T2-weighted and diffusion-weighted MRI for localization of prostate cancer. AJR Am J Roentgenol 189:323-328.
17. Kim CK, Park BK, Lee HM et al (2007) Value of diffusion-weighted imaging for the prediction of prostate cancer location at 3T using a phased-array coil: preliminary results. Invest Radiol 42:842-847.
18. Oto A, Yang C, Kayhan A et al (2011) Diffusion-weighted and dynamic contrast-enhanced MRI of prostate cancer: correlation of quantitative MR parameters with Gleason score and tumor angiogenesis. AJR Am J Roentgenol 197:1382-1390.
19. Turkbey B, Shah VP, Pang Y et al (2011) Is apparent diffusion coefficient associated with clinical risk scores for prostate cancers that are visible on 3-T MR images? Radiology 258:488-495.
20. Hambrock T, Somford DM, Huisman HJ et al (2011) Relationship between apparent diffusion coefficients at 3.0-T MR imaging and Gleason grade in peripheral zone prostate cancer. Radiology 259:453-461.
21. Turkbey B, Bernardo M, Merino MJ et al (2012) MRI of localized prostate cancer: coming of age in the PSA era. Diagn Interv Radiol 18:34-45.
22. Durmus T, Vollnberg B, Schwenke C et al (2013) Dynamic contrast enhanced MRI of the prostate: comparison of Gadobutrol and Gd-DTPA. Rofo 185:862-868.
23. Franiel T, Hamm B, Hricak H (2011) Dynamic contrast-enhanced magnetic resonance imaging and pharmacokinetic models in prostate cancer. Eur Radiol 21:616-626.
24. Ocak I, Bernardo M, Metzger G et al (2007) Dynamic contrast-enhanced MRI of prostate cancer at 3 T: a study of pharmacokinetic parameters. AJR Am J Roentgenol 189:849.
25. Kozlowski P, Chang SD, Jones EC et al (2006) Combined diffusion-weighted and dynamic contrast-enhanced MRI for prostate cancer diagnosis–correlation with biopsy and histopathology. J Magn Reson Imaging 24:108-113.
26. Noworolski SM, Vigneron DB, Chen AP et al (2008) Dynamic contrast-enhanced MRI and MR diffusion imaging to distinguish between glandular and stromal prostatic tissues. Magn Reson Imaging 26:1071-1080.
27. Delongchamps NB, Rouanne M, Flam T et al (2011) Multiparametric magnetic resonance imaging for the detection and localization of prostate cancer: combination of T2-weighted, dynamic contrast-enhanced and diffusion-weighted imaging. BJU Int 107:1411-1418.
28. Bloch BN, Furman-Haran E, Helbich TH et al (2007) Prostate cancer: accurate determination of extracapsular extension with high-spatial-resolution dynamic contrast-enhanced and T2-weighted MR imaging–initial results. Radiology 245:176-185.
29. Cirillo S, Petracchini M, Scotti L et al (2009) Endorectal magnetic resonance imaging at 1.5 Tesla to assess local recurrence following radical prostatectomy using T2-weighted and contrast-enhanced imaging. Eur Radiol 19:761-769.
30. Scheenen TW, Futterer J, Weiland E et al (2011) Discriminating cancer from noncancer tissue in the prostate by 3-dimensional proton magnetic resonance spectroscopic imaging: a prospective multicenter validation study. Invest Radiol 46:25-33.
31. Turkbey B, Mani H, Shah V et al (2011) Multiparametric 3T prostate magnetic resonance imaging to detect cancer: histopathological correlation using prostatectomy specimens processed in customized magnetic resonance imaging based molds. J Urol 186:1818-1824.
32. Coakley FV, Kurhanewicz J, Lu Y et al (2002) Prostate cancer tumor volume: measurement with endorectal MR and MR spectroscopic imaging. Radiology 223:91-97.
33. Rothke M, Blondin D, Schlemmer HP et al (2013) PI-RADS-Klassifikation: Strukturiertes Befundungsschema fur die MRT der Prostata. Fortschr Röntgenstr 185: 253-261.

34. Portalez D, Mozer P, Cornud F et al (2012) Validation of the European Society of Urogenital Radiology scoring system for prostate cancer diagnosis on multiparametric magnetic resonance imaging in a cohort of repeat biopsy patients. Eur Urol 62:986-996.
35. Schimmoller L, Quentin M, Arsov C et al (2013) Inter-reader agreement of the ESUR score for prostate MRI using in-bore MRI-guided biopsies as the reference standard. Eur Radiol 23:3185-3190.
36. Rosenkrantz AB, Kim S, Lim RP et al (2013) Prostate cancer localization using multiparametric MR Imaging: comparison of prostate imaging reporting and data system (PI-RADS) and Likert scales. Radiology 269:482-492.
37. Quentin M, Schimmoller L, Arsov C et al (2013) 3-T in-bore MR-guided prostate biopsy based on a scoring system for target lesions characterization. Acta Radiol 54:1224-1229.
38. de la Taille A, Antiphon P, Salomon L et al (2003) Prospective evaluation of a 21-sample needle biopsy procedure designed to improve the prostate cancer detection rate. Urology 61:1181-1186.
39. Eskicorapci SY, Baydar DE, Akbal C et al (2004) An extended 10-core transrectal ultrasonography guided prostate biopsy protocol improves the detection of prostate cancer. Eur Urol 45:444-448.
40. Wefer AE, Hricak H, Vigneron DB et al (2000) Sextant localization of prostate cancer: comparison of sextant biopsy, magnetic resonance imaging and magnetic resonance spectroscopic imaging with step section histology. J Urol 164:400-404.
41. Durmus T, Reichelt U, Huppertz A et al (2013) MRI-guided biopsy of the prostate: correlation between the cancer detection rate and the number of previous negative TRUS biopsies. Diagn Interv Radiol 19:411-417.
42. Bodelle B, Naguib NN, Schulz B et al (2013) 1.5-T magnetic resonance-guided transgluteal biopsies of the prostate in patients with clinically suspected prostate cancer: technique and feasibility. Invest Radiol 48:458-463.
43. Wolter K, Decker G, Willinek WA (2013) Transperineal MR-guided stereotactic prostate biopsy utilizing a commercially available anorectal biopsy device. Rofo 185:116-120.
44. Beyersdorff D, Winkel A, Hamm B et al (2005) MR imaging-guided prostate biopsy with a closed MR unit at 1.5 T: initial results. Radiology 234:576-581.
45. Hambrock T, Somford DM, Hoeks C et al (2010) Magnetic resonance imaging guided prostate biopsy in men with repeat negative biopsies and increased prostate specific antigen. J Urol 183:520-527.
46. Hoeks CM, Schouten MG, Bomers JG et al (2012) Three-Tesla magnetic resonance-guided prostate biopsy in men with increased prostate-specific antigen and repeated, negative, random, systematic, transrectal ultrasound biopsies: detection of clinically significant prostate cancers. Eur Urol 62: 902-909.
47. Roethke M, Anastasiadis AG, Lichy M et al (2012) MRI-guided prostate biopsy detects clinically significant cancer: analysis of a cohort of 100 patients after previous negative TRUS biopsy. World J Urol 30:213-218.
48. Puech P, Rouviere O, Renard-Penna R et al (2013) Prostate cancer diagnosis: multiparametric MR-targeted biopsy with cognitive and transrectal US-MR fusion guidance versus systematic biopsy–prospective multicenter study. Radiology 268:461-469.
49. Durmus T, Stephan C, Grigoryev M et al (2013) [Detection of prostate cancer by real-time MR/ultrasound fusion-guided biopsy: 3T MRI and state of the art sonography]. Rofo 185:428-433.
50. Sonn GA, Chang E, Natarajan S et al (2013) Value of targeted prostate biopsy using magnetic resonance-ultrasound fusion in men with prior negative biopsy and elevated prostate-specific antigen. Eur Urol 10.1016/j.eururo.2013.03.025 [Epub ahead to print].
51. Walton-Diaz A, Hoang AN, Turkbey B et al (2013) Can MR-US fusion biopsy improve cancer detection in enlarged prostates? J Urol 90:2020-2025.
52. Lees K, Durve M, Parker C (2012) Active surveillance in prostate cancer. Current Opinion in Urology 22:210-215.
53. Wise AM, Stamey TA, McNeal JE et al (2002) Morphologic and clinical significance of multifocal prostate cancers in radical prostatectomy specimens. Urology 60:264-269.
54. de la Rosette J, Ahmed H, Barentsz J et al (2010) Focal therapy in prostate cancer-report from a consensus panel. J Endourol 24:775-780.
55. Bomers JG, Sedelaar JP, Barentsz JO et al (2012) MRI-guided interventions for the treatment of prostate cancer. AJR Am J Roentgenol 199:714-720.
56. van den Bos W, Muller BG, de la Rosette JJ (2013) A randomized controlled trial on focal therapy for localized prostate carcinoma: hemiablation versus complete ablation with irreversible electroporation. J Endourol 27:262-264.

# Abdominal Vascular Disease: Diagnosis and Therapy

Johannes Lammer

Cardiovascular and Interventional Radiology and Biomedical Imaging and Image-Guided Therapy, Medical University Vienna, University Clinics, Vienna, Austria

## Acute Arterial Occlusion

If acute occlusion of the abdominal aorta or branch vessels occurs, two causes have to be considered:
– Embolization
– Dissection.

### Embolization

Embolization is most common in elderly patients with atrial fibrillation, a history of myocardial infarction, and aortic aneurysm. Embolization from the heart or thoracic aorta may cause acute subtotal or total occlusion of the celiac trunk, superior mesenteric artery (SMA), inferior mesenteric artery (IMA), or renal arteries. The most common causes of embolization are:
- Atrial fibrillation
- Thoracic aortic aneurysm
- Myocardial infarction with mural thrombus formation
- Left atrial appendage thrombus
- Advanced aortic arteriosclerosis
- Penetrating arteriosclerotic ulcer
- Hypercoagulability syndrome.

Symptoms of acute ischemia are dependent upon the involved vascular territory. Embolization to the liver or spleen may cause acute right or left upper abdominal pain. Acute mesenteric ischemia typically causes severe abdominal pain and bowel paralysis. Embolization to the kidney causes flank pain, hematuria, and hypertension. In any case, severe lactate dehydrogenase (LDH) elevation indicates the ischemic nature of the acute pain. In case of complete ischemia without sufficient collateral circulation, the warm ischemic time tolerated by abdominal organs is $<6$ h. Therefore, emergent diagnosis and therapy are mandatory.

The primary diagnosis is performed using computed tomography (CT) with contrast enhancement [contrast medium (CM) 300-400 mg/ml; 4 ml/s; total bolus volume 80-120 ml; bolus care technique with 20- to 40-s delay; 2-mm collimation; pitch 2; reconstruction interval 1 mm]. In the arterial phase, the obstructing embolus and the ischemic territory can be visualized. In the delayed phase, residual perfusion through collateral arteries may be demonstrated.

Interventional treatment with a thrombectomy device and/or local intra-arterial fibrinolysis with alteplase (rt-PA) (loading dose 10 mg, infusion dose 5 mg/h) or urokinase (loading dose 250,000 IU, infusion dose 100,000 IU/h), together with a glycoprotein (G) IIb/IIIa antagonist (Abciximab; loading dose 0.25 mg/kg, infusion dose 0.125 mg/kg/h) are one option. The other option is surgery, which may be faster and enables inspection and, if necessary, resection of ischemic organs.

### Dissection

Dissection may occur in patients with chest trauma; chronic severe hypertension; or a connective tissue disease such as Marfan syndrome, Ehlers-Danlos syndrome, Loeys-Dietz syndrome (LDS), and autosomal dominant polycystic kidney disease (ADPKD). Acute types A and B aortic dissection may cause dynamic compression of the true aortic lumen due to pressurized false lumen. This can cause acute ischemia of liver, spleen, bowel, and one or both kidneys. The dissection plane may also involve one of the organ arteries causing obstruction of the true lumen. Options for interventional treatment are:
- In case of dynamic compression of the true aortic lumen, occlusion of the proximal entry into the false lumen with an aortic stent-graft will cause decompression of the false lumen and result in reopening the true lumen of the aorta and the side branches (Fig. 1).
- In case of a static compression due to a side-branch dissection, stent placement in the true lumen of the organ artery will cause reconstitution of organ perfusion.
- In case of organ perfusion through the false lumen, balloon fenestration of the intimal flap will reestablish flow into the malperfused territory.

## Chronic Arterial Occlusive Disease

In young patients, causes of chronic arterial occlusion may be:

*Diseases of the Abdomen and Pelvis 2014-2017*,
DOI: 10.1007/978-88-470-5659-6_24 

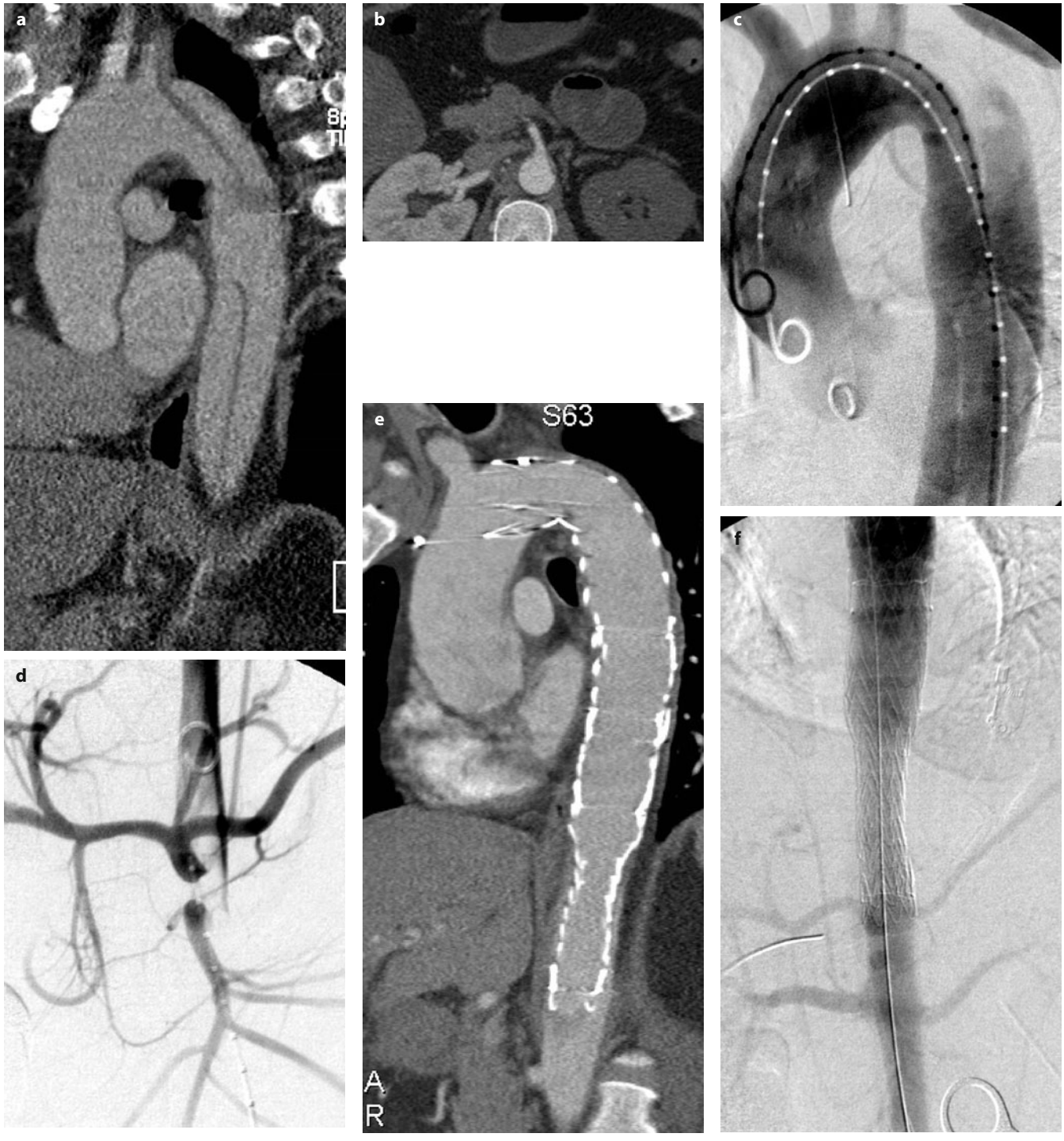


**Fig. 1 a- f.** Complicated Stanford type B aortic dissection with renal malperfusion. **a** Computed tomography (CT) demonstrating primary entry tear of type B aortic dissection. **b** CT demonstrating compression of true lumen of the aorta with left renal ischemia. **c** Aortic angiogram showing true and false lumen of type B dissection. **d** Aortography showing compression of true lumen with malperfusion of the renal arteries ("floating visceral sign"). **e** CT after stent-graft implantation and closure of primary entry tear with false lumen collapse. **f** Aortography post stent-graft implantation demonstrating spontaneous revascularization of visceral arteries

- Fibromuscular disease (FMD)
- Takayasu arteritis
- Neurofibromatosis Recklinghausen.

In elderly patients, the primary cause of chronic arterial occlusive disease is arteriosclerosis.

## Mesenteric Artery Stenosis

Between the three large mesenteric arteries (celiac artery, SMA, IMA), many collateral pathways exist:

- Pancreaticoduodenal arteries

- Arc of Buehler between celiac artery and SMA
- Arc of Riolan
- Marginal artery of Drummond between SMA and IMA.

Usually, an obstruction of more than one mesenteric artery is necessary to cause ischemic symptoms. The typical clinical symptom is "abdominal angina," with:

- Abdominal pain (94%)
- Postprandial cramps (86%)
- Weight loss (74%)
- Abdominal bruit (70%)
- Diarrhea.

The primary diagnosis is made by CT angiography, magnetic resonance angiography (MRA), or intra-arterial catheter angiography of the abdominal aorta in a lateral projection. Interventional treatment is percutaneous transluminal angioplasty (PTA) with or without secondary stent placement of the obstructed arteries.

#### Celiac Trunk Stenosis

Chronic obstruction may remain asymptomatic because of the collateral pathways through gastroduodenal and pancreatic arteries from the SMA. Causes are arteriosclerotic plaque, compression by the arcuate ligament, and carcinoma of the pancreas.

#### Superior Mesenteric Artery Stenosis

Postprandial abdominal pain, called "abdominal angina," is the leading symptom. Causes for SMA obstruction are arteriosclerosis, FMD, Takayasu arteritis, pancreatic carcinoma, and chronic pancreatitis.

#### Inferior Mesenteric Artery Stenosis

Obstruction of the IMA is most commonly observed in patients with advanced atheromatosis or partially thrombosed abdominal aortic aneurysm. Due to the collateral circulation through the arc of Riolan and the marginal artery, IMA obstruction normally remains asymptomatic.

### Renal Artery Stenosis

Renal artery stenosis (RAS) may cause hypertension and/or renal insufficiency. Acute onset of clinical symptoms and repeated flash pulmonary edema are suggestive for RAS. Etiology can be

- Arteriosclerosis in 65-75%
  - Patients >50 years
  - Male >female
  - Proximal 2 cm of renal artery
  - Atherosclerotic changes of aorta
  - Bilateral in 30%.
- FMD in 20-30%
  - Patients <50 years
  - Female:male ratio 5:1
  - Middle to distal renal artery, including branches
  - Bilateral involvement in 50-70%
  - "String of beads" appearance, aneurysms, dissections
  - No aortic disease.
- Takayasu arteritis
- Midaortic syndrome
- Morbus Recklinghausen
- Postradiation therapy.

#### RAS Diagnosis

The most appropriate algorithm for diagnosing RAS is not yet established.

#### Color Duplex Ultrasound

Color duplex ultrasound (US) is a noninvasive test but is a complex procedure that requires operator experience. An increased peak systolic velocity of >250 cm/s, a renal-to-aortic ratio of peak systolic velocity of >3.5, intrastenotic turbulence, and a flattened pulse wave in the periphery (pulsus tardus) are diagnostic criteria for RAS. The sensitivity of color duplex sonography for detecting RAS >70% is 72-92%. Color duplex US with an angiotensin-converting enzyme (ACE) inhibitor provides a positive predictive value (PPV) of 67-95% for cure or improvement after revascularization.

#### Nuclear Scan

A nuclear scan [renal scintigraphy with technetium-99m mercaptoacetyltriglycine ($^{99m}$Tc-MAG-3) or technetium-99m diethylenetriaminepentaacetic acid ($^{99m}$Tc-DTPA)] with an angiotensin-converting enzyme (ACE) inhibitor (captopril 25 mg) shows delayed tracer washout within the poststenotic kidney. However, in bilateral disease and in chronic ischemic nephropathy, tracer lateralization is less evident. In a selected population with a clinically high risk for RAS, sensitivity for detection of a unilateral RAS >70% is 51-96% (mean 82%). Its PPV, with improvement of hypertension after revascularization, is 51-100% (mean 85%). However, scintigraphy is much less sensitive in unselected patients, bilateral disease, impaired renal function, urinary obstruction, and chronic ACE inhibitor intake.

#### Newer Tests

Newer tests are gadolinium (Gd)-enhanced MRA and spiral CT angiography (CTA).

##### *Gd-Enhanced MRA*

For state-of-art MRA, high-field-strength systems with high-performance gradients are necessary for breath-hold 3D T1-weighted spoiled-gradient-echo imaging with short TR and TE. Intravenous administration of Gd contrast material (0.1 mmol/kg; flow rate 2 ml/s), a central k-space readout, and background subtraction are additional tech-

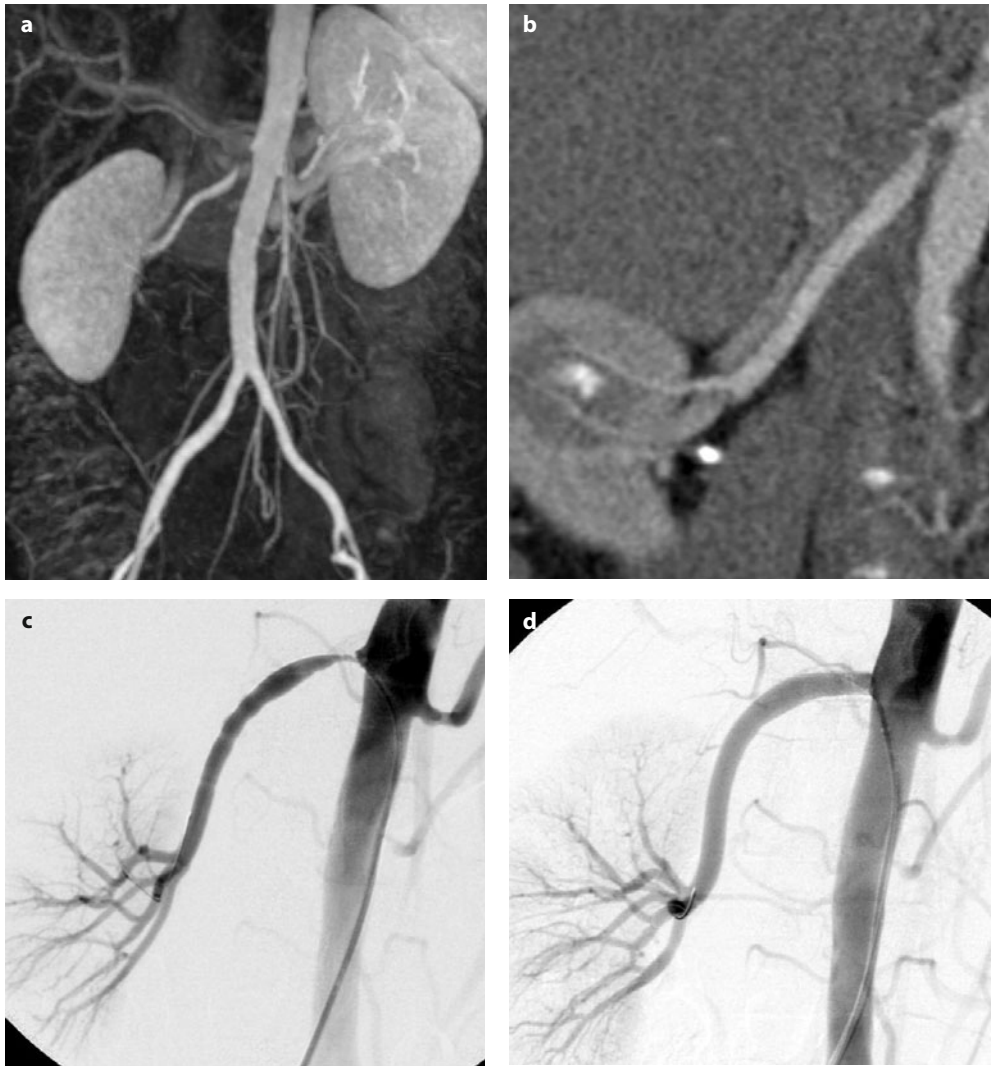


**Fig. 2 a-d.** Imaging and intervention in a patient with hypertension due to renal artery stenosis. **a** Magnetic resonance angiography (MRA) showing stenosis of right renal artery. **b** Computed tomography angiography (CTA) showing stenosis of right renal artery. **c** Arteriography showing stenosis of right renal artery. **d** Arteriography of right renal artery after stent placement

niques to improve signal-to-noise ratio (SNR) and spatial resolution. Sensitivity for detecting RAS >50% is >95% with MRA (Fig. 2). The main limitations of renal MRA are evaluation of small, accessory renal arteries and branch vessels, presence of stents, and a tendency to overestimate moderate stenoses.

### *CTA*

CTA of the renal arteries has a >95% sensitivity to detect RAS and accessory renal arteries. For high-quality opacification of renal arteries and to avoid renal vein overlap, accurate bolus planning is mandatory: density measurement during bolus rise, flow 4 ml/s, total volume 80-120 ml; multidetector (MD) scanners need less contrast. A short breath-hold acquisition, collimation (1-2 mm), pitch (1.5-6 depending on single or MD technology), reconstruction overlap (0.5-0.75) are important parameters for spatial resolution. Curved planar reconstruction (CPR, most useful for stents), volume rendering, and maximum intensity projection (MIP) are used for 3D imaging (Fig. 2).

### *Intra-Arterial Catheter Arteriography*

Intra-arterial catheter arteriography together with pressure-gradient measurement is still the "gold standard" for RAS evaluation.

## RAS Revascularization

The revascularization technique of choice is renal PTA with or without stent placement (Fig. 2). Aortorenal bypass surgery is indicated only if PTA fails. In a recently published meta-analysis, stent placement proved to be technically superior and clinically comparable with renal PTA alone. The technical success rate of stent vs. PTA was 98% vs. 77%, and the restenosis rate was 17% vs. 26%, respectively ($p<0.001$). In hypertension, the cure rate of PTA vs. stent was 10% vs. 20% and improvement rate was 53% vs. 49%, respectively. In renal insufficiency, the improvement rate was 38% vs. 30% and stabilization 41% vs. 38%, respectively. Complication rate was 11-13% [95% confidence interval (CI) 6-19] and in-hospital mortality rate 1%. In a randomized study

comparing stents vs. PTA in ostial stenoses, the technical success rate was 88% vs. 57% and the 6-month primary patency rate 75% vs. 29%, respectively. Surprisingly, randomized trials comparing the effect of PTA and drug therapy on renal hypertension did not reveal a significant benefit of PTA and stenting over continuous drug therapy. However, in a Dutch study, PTA patients required only 2.1 vs. 3.2 daily drug doses ($p<0.001$); 22/53 patients in the drug group had to be switched to the PTA group because of persistent hypertension or deterioration of renal function.

## Aneurysms

### Abdominal Aortic Aneurysm (AAA)

The incidence of AAA in European adults ⩾60 years is 2.5%. Up to 10% of patients with symptomatic peripheral arterial disease (PAD) die from aneurysm rupture. Standard treatment is open surgery. However, endovascular implantation of stent-grafts is a new, emerging technique that may replace open surgery. Since the first clinical implant of a tube stent-graft in 1990, many different designs have been developed and tested in feasibility studies. Most recently, randomized studies [Endovascular Aneurysm Repair (EVAR) 1 trial; Dutch Randomized Endovascular Aneurysm Repair (DREAM) trial] compared results of open vs. endovascular repair. In the EVAR trial, the 30-day mortality in the EVAR group was 1.7% (9/531) vs. 4.7% (24/516) in the open repair group ($p=0.009$). Four years after randomization, all-cause mortality was similar between groups (~28%; $p=0.46$), although there was a persistent reduction in aneurysm-related deaths in the EVAR group (4% vs 7%; $p=0.04$). Meanwhile, 60-80% of patients are treated by EVAR with stent-grafts.

#### Indications

Indications for endovascular treatment of AAA are the same as for open surgery:

- Diameter of the aneurysm >5.5 cm (Fig. 3)

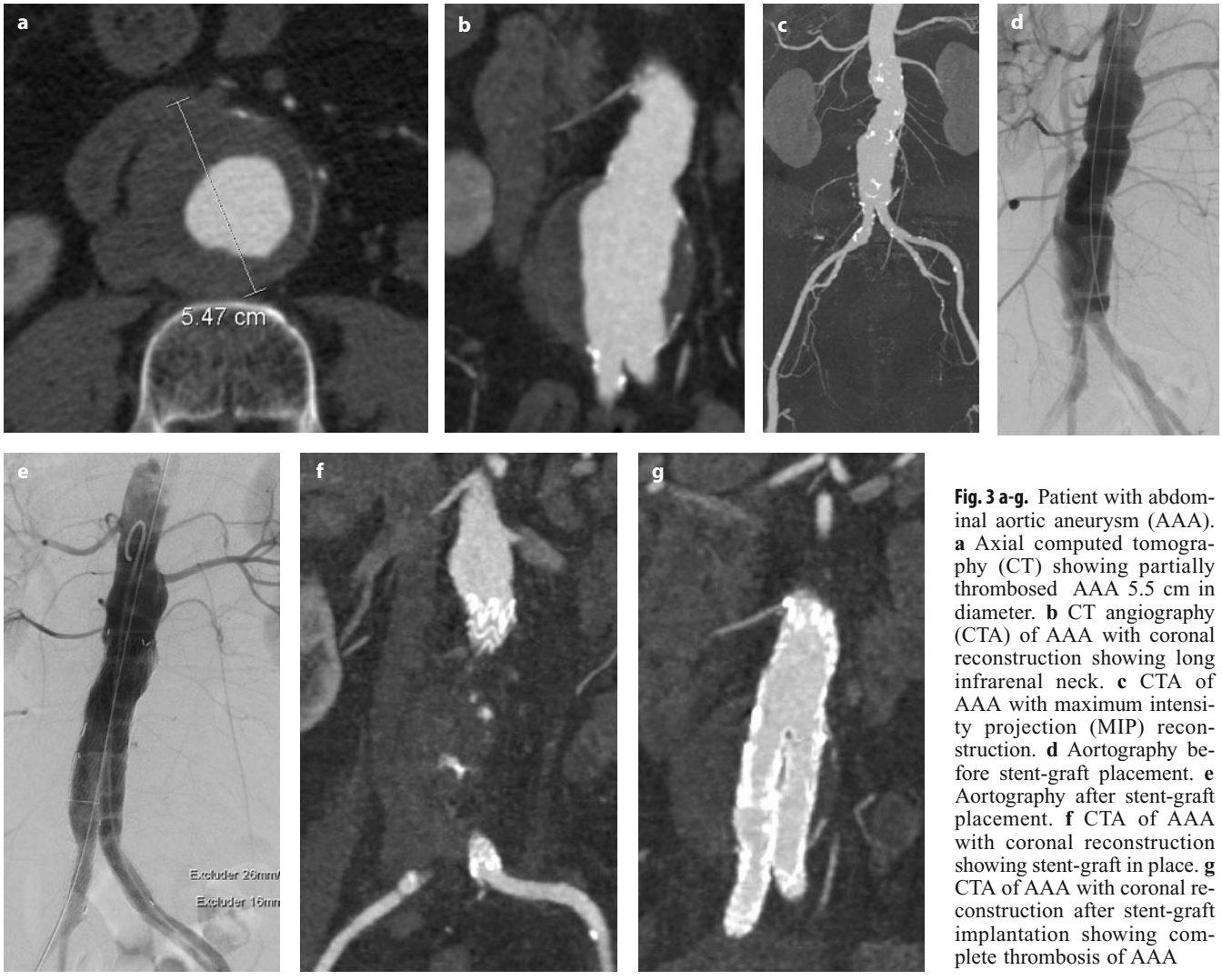


**Fig. 3 a-g.** Patient with abdominal aortic aneurysm (AAA). **a** Axial computed tomography (CT) showing partially thrombosed AAA 5.5 cm in diameter. **b** CT angiography (CTA) of AAA with coronal reconstruction showing long infrarenal neck. **c** CTA of AAA with maximum intensity projection (MIP) reconstruction. **d** Aortography before stent-graft placement. **e** Aortography after stent-graft placement. **f** CTA of AAA with coronal reconstruction showing stent-graft in place. **g** CTA of AAA with coronal reconstruction after stent-graft implantation showing complete thrombosis of AAA

- Documented growth >0.5 mm/year
- Symptomatic aneurysm (i.e., embolization, pain, ureteral compression)
- Rupture.

Specific clinical indications for the endovascular approach may be:

- Patients >75 years old
- American Society of Anesthesiologists (ASA) 3 and 4
- Hostile abdomen
- Inflammatory aneurysm, horseshoe kidney
- Severe chronic obstructive pulmonary disease (COPD).

Anatomic indications for stent-graft treatment are:

- Infrarenal neck ⩾15 mm in length
- Infrarenal neck without thrombus or severe calcification
- Angulation of the infrarenal neck <65°
- Patent celiac trunk and SMA
- Stent-graft diameter ⩾10% than neck diameter
- Iliac artery angulation <90°
- Iliac artery without thrombus or severe calcification
- More than 15-mm overlap within iliac arteries.

#### Stent-Grafts

Endovascular implantation of stent-grafts can be performed under general, epidural, or local anesthesia. The use of epidural anesthesia is a major advantage in elderly and high-risk patients.

##### *Stent-Graft Designs*

Stent-grafts have a self-expandable stent structure covered by an ultrathin polyester or expanded polytetrafluoroethylene (ePTFE) fabric. Only bifurcated stent-grafts are used for AAA treatment.

#### Imaging Before Stent-Graft Implantation

Contrast-enhanced spiral CT with multiplanar (MPR) or MIP reconstruction is the most important examination before stent-graft implantation (Fig. 3). The diameter of the landing zones (infrarenal neck, iliac arteries), maximum diameter of the aneurysm, thrombus, and calcifications can be well depicted from CT.

#### Complications

The most common complication is incomplete exclusion of the aneurysm with remaining pressurization of the aneurysm sack through an endoleak. White and May proposed a classification of endoleaks: primary (<30 days) and secondary (>30 days) endoleaks.

- Type 1: direct perfusion through the proximal (infrarenal) or distal (iliac) anastomosis
- Type 2: retrograde perfusion through branch vessels (lumbar arteries, IMA, accessory renal artery)
- Type 3: midgraft leak due to disintegration of the stent-graft (disconnection of the second iliac limb, fabric erosion)
- Type 4: fabric porosity
- Type 5: endotension.

#### Visceral Artery Aneurysm

Aneurysms of the celiac trunk and splenic, hepatic, gastroduodenal, and SM arteries are caused by arteriosclerosis, arteritis, periarterial inflammation such as pancreatitis, trauma, and soft tissue diseases such as Marfan, Ehlers-Danlos, and LDS. An aneurysm >2.5 cm in diameter should be considered for treatment to prevent rupture. Meticulous imaging, including selective catheter angiography and 3D imaging with CTA or MRA, is necessary before surgery or endovascular treatment. Endovascular options are embolization and exclusion with a stent-graft.

#### Renal Artery Aneurysm

Causes of renal artery aneurysms are arteriosclerosis, systemic vasculitis such as polyarteritis nodosa or lupus erythematosus, FMD, soft tissue disorders, and trauma. Arteriosclerotic and large aneurysms are usually calcified. The risk of rupture and chronic embolization are indications for treatment. Bypass surgery, coil embolization, and stent-graft implantation are therapeutic options.

## Therapeutic Embolization of Gastrointestinal Bleeding

### Upper Gastrointestinal (GI) Bleeding

#### Causes of Upper-GI Bleeding

- Gastroduodenal ulcer
- Proximal jejunal tumors [endocrine carcinomas, angiofibroma, melanoma metastases, arteriovenous (AV) malformation, etc.]
- Pseudoaneurysm of the gastroduodenal, pancreaticoduodenal, intrapancreatic, and splenic arteries after pancreatitis or trauma; bleeding through the ductus Wirsungianus
- Pseudoaneurysm of the hepatic artery, bleeding through the common bile duct (triad of hemobilia: abdominal colic followed by jaundice; hematemesis; melena).

#### Treating Upper-GI Bleeding

Upper GI bleedings are usually treated by endoscopic coagulation therapy. However, if endoscopic therapy fails or the bleeding source is inaccessible to endoscopy, angiographic embolization is indicated. Patients after gastric resection, with bilioenteric anastomoses, and with bleeding from hepatobiliary and pancreatic pathologies (i.e., pseudoaneurysms) should be treated primarily by angio-

graphic techniques. Because of the extensive collateral circulation in the upper abdomen, a detailed angiographic evaluation followed by embolization of all feeding arteries is required.

### Lower-GI Bleeding

In lower-GI bleeding, diagnosis and treatment is preferentially done by colonoscopy. However, in selected cases, embolization is required. For the primary diagnosis, a contrast-enhanced CT of the abdomen (CM 400 mg/ml, flow 4 ml, volume 100 ml) in arterial and delayed phases usually demonstrates nicely the area of bleeding. This helps identify the bleeding source during catheter angiography. Superselective catheterization, and bowel paralysis induced with Buscopan are mandatory when investigating a bleeding angiogram.

#### Causes of Lower-GI Bleeding

- Small-bowel tumors (endocrine carcinomas, angiofibroma, melanoma metastases, AV-malformation, etc.)
- Meckel's diverticulum
- Large-bowel diverticulum bleeding (most common cause in elderly patients)
- Hemangiomatosis and AV malformation of the colon
- Colon cancer.

Rectal bleeding due to hemorrhoidal disease has to be ruled out primarily.

#### Treatment for Lower-GI Bleeding

Lower-GI bleedings are preferentially embolized by coils.

## Treatment for Bleeding Complications after Surgery, Trauma, and Postpartum

Bleeding in the abdomen may occur from iatrogenic causes, particularly in the kidneys and liver after percutaneous interventions, trauma, and tumour. Frequent and typical locations are renal AV fistulas due to nephrostomy (Fig. 4) or biopsy, laceration of the hepatic arteries by percutaneous manipulations, psoas, and pelvic bleeding due to traumatic arterial injury and uterine artery bleeding postpartum. Temporary occlusion of the uterine artery can then be a valid alternative to emergency hysterectomy in patients with intractable bleeding due to an atonic uterus. In other locations, type, source, and area of bleeding determine the method used to safely interrupt extravasations.

### Venous Interventions

#### Transjugular Intrahepatic Portocaval Shunt

Transjugular intrahepatic portocaval shunt (TIPS) was introduced into clinical medicine at the end of the 1980s. In the meantime, a standardized technique allows safe application of this artificial connection between portal and hepatic veins to depressurize the portal venous system. The introduction of stent-grafts instead of bare stents led to improved patency of the shunt tract. TIPS is indicated in patients symptomatic of portal hypertension with:

- Acute or chronic bleeding of esophageal or gastric varices
- Intractable ascites.

Although endoscopic techniques to treat varices are competitive techniques in bleeders, in some patients with

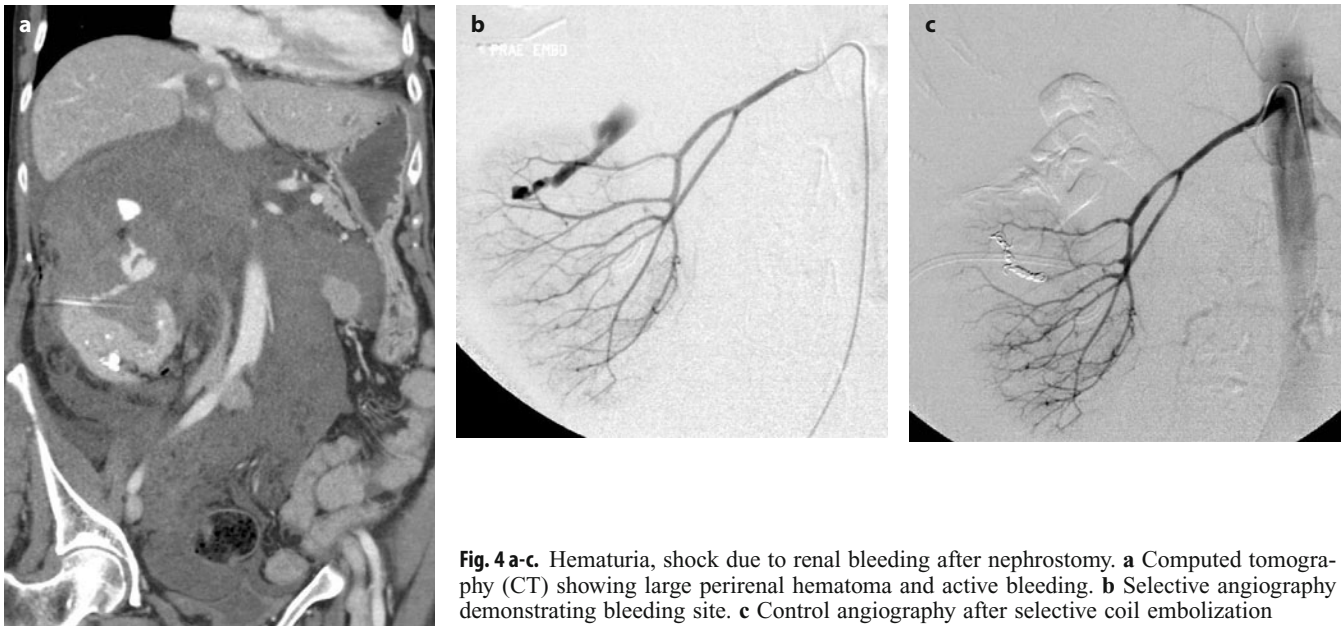


**Fig. 4 a-c.** Hematuria, shock due to renal bleeding after nephrostomy. **a** Computed tomography (CT) showing large perirenal hematoma and active bleeding. **b** Selective angiography demonstrating bleeding site. **c** Control angiography after selective coil embolization

ascites, there are few alternatives. Randomized trials, meta-analyses, and Cochrane data review analyses demonstrate that TIPS is superior to endoscopic therapy to prevent rebleeding and superior to paracenteses to remove ascites. In patients with acute or subacute Budd-Chiari syndrome, TIPS can be a life-saving procedure and help overcome the acute phase but is burdened by a relatively high rethrombosis rate. Risks after TIPS procedure are liver failure from shunted blood volume and encephalopathy.

### Embolization of Portal Vein Collaterals

In liver cirrhosis with portal hypertension, collateral pathways may develop. Pathways to the superior vena cava (SVC) are from the left gastric vein (coronary vein) and the short gastric veins to the esophageal venous plexus. This pathway may cause esophageal and gastric varices with bleeding. Pathways to the inferior vena cava (IVC) are splenorenal and mesenteric-renal shunts and umbilical and hemorrhoidal collaterals. Embolization indications are bleeding and hepatic encephalopathy.

## Suggested Reading


ASTRAL Investigators, Wheatley K, Ives N, Gray R et al (2009) Revascularization vs. medical therapy for renal artery stenosis. N Engl J Med 361:1953-1962.

Bax L, Woittiez AJ, Kouwenberg HJ et al (2009) Stent placement in patients with atherosclerotic renal artery stenosis and impaired renal function: a randomized trial. Ann Intern Med 2009 150:840-848.

Blankensteijn JD, de Jong SE, Prinssen M; Dutch Randomized Endovascular Aneurysm Management (DREAM) Trial Group (2005) Two-year outcomes after conventional or endovascular repair of abdominal aortic aneurysms. N Engl J Med 352:2398-2405.

Blum U, Voshage G, Lammer J et al (1997) Endoluminal stent-grafts for infrarenal abdominal aortic aneurysms. N Engl J Med 336:13-20.

D'Amico G, Luca A, Morabito A et al (2005) Uncovered transjugular intrahepatic portosystemic shunt for refractory ascites: a metaanalysis. Gastroenterology 129:1282-1293.

EVAR trial participants (2005) Endovascular aneurysm repair vs. open repair in patients with abdominal aortic aneurysm (EVAR trial 1): randomised controlled trial. Lancet 365:2179-2186.

Greenhalgh RM, Brown LC, Kwong GP et al; EVAR trial participants (2004) Comparison of endovascular aneurysm repair with open repair in patients with abdominal aortic aneurysm (EVAR trial 1), 30-day operative mortality results: randomised controlled trial. Lancet 364:843-848.

Kaatee R, Beek FJ, de Lange EE et al (1997) Renal artery stenosis: detection and quantification with spiral CT angiography vs. optimized digital subtraction angiography. Radiology 205:121-127.

Kasirajan K, O'Hara PJ, Gray BH et al (2001) Chronic mesenteric ischemia: open surgery vs. percutaneous angioplasty and stenting. J Vasc Surg 33:63-71.

Khan S, Tudur Smith C, Williamson P, Sutton R (2006) Portosystemic shunts vs. endoscopic therapy for variceal rebleeding in patients with cirrhosis. Cochrane Database Syst Rev 18:CD000553.

Khuroo MS, Al-Suhabani H, Al-Sebayel M et al (2005) Budd-Chiari syndrome: long-term effect on outcome with transjugular intrahepatic portosystemic shunt. J Gastroenterol Hepatol 20:1494-1502.

Laheij RJF, J Buth for the European Collaborators. Participants report. Overview of the overall patients cohort of the EUROSTAR data registry 2000.

Leertouwer TC, Gussenhoven EJ, Bosch JL et al (2000) Stent placement for renal artery stenosis: where do we stand? A meta-analysis Radiology 216:78-85.

Mann SJ, Pickering TG (1992) Detection of renovascular hypertension: state of the art 1992. Ann Intern Med 117:845-853.

Perler AB, Becker GJ (1998) Vascular intervention – a clinical approach. Visceral vascular disease. Thieme, New York Stuttgart, pp 517-637.

Prinssen M, Verhoeven EL, Buth J et al; Dutch Randomized Endovascular Aneurysm Management (DREAM) Trial Group (2004) A randomized trial comparing conventional and endovascular repair of abdominal aortic aneurysms. N Engl J Med 351:1607-1618.

Rose SC, Quigley TM, Raker EJ (1995) Revascularization for chronic mesenteric ischemia: comparison of operative arterial bypass grafting and percutaneous transluminal angioplasty. J Vasc Interv Radiol 6:339-349.

Saab S, Nieto JM, Lewis SK, Runyon BA (2006) TIPS vs. paracentesis for cirrhotic patients with refractory ascites. Cochrane Database Syst Rev 18:CD004889.

Salerno F, Cammà C, Enea M et al (2007) TIPS for refractory ascites: a meta-analysis of individual patient data. Gastroenterology 133:825-834.

Soulez G, Oliva VL, Turpin S et al (2000) Imaging of renovascular hypertension: respective values of renal scintigraphy, renal Doppler US, and MR angiography. Radiographics 20:1355-1368.

van de Ven PJ, Kaatee R, Beutler JJ et al (1999) Arterial stenting and balloon angioplasty in ostial arteriosclerotic renovascular disease: a randomized trial. Lancet 353:282-286.

Van Jaarsveld BC, Krijen P, Pieterman H et al (2000) The effect of balloon angioplasty on hypertension in atherosclerotic renal-artery stenosis. Dutch Renal Artery Stenosis Intervention Cooperative Study Group. N Engl J Med 342:1007-1014.

Webster J, Marshall F, Abdalla M et al (1998) Randomized comparison of percutaneous angioplasty vs continued medical therapy for hypertensive patients with atheromatous renal artery stenosis. Scottish and Newcastle Renal Artery Stenosis Collaborative Group. J Hum hypertens 12:329-335.

Williams DM, Lee DY (1997) Dissected aorta, parts I-III. Radiology 203:23-44.

Zheng M, Chen Y, Bai J et al (2008) TIPS vs. endoscopic therapy in the secondary prophylaxis of variceal rebleeding in cirrhotic patients: meta-analysis update. J Clin Gastroenterol 42:507-516.

# Nonvascular Abdominal Disease: Diagnosis and Therapy

Carlo Bartolozzi, Valentina Battaglia

Division of Diagnostic and Interventional Radiology, University of Pisa, Pisa, Italy

## Introduction

Nonvascular diseases can affect all abdominal parenchyma and viscera. Recent technological advances allow application of a wide range of diagnostic and interventional imaging-guided procedures for an increasing number of abdominal parenchyma. In this chapter, we focus on primitive, nonvascular pathologies of the liver and pancreas.

## Liver

### Preneoplastic Liver Lesions: Dysplasia

Dysplastic nodules (DNs) are classified as low-grade (LGDN) and high grade (HGDN), depending on the degree of cellular atypia and changes in architectural structure. HGDN are considered to be premalignant lesions that might turn into hepatocellular carcinoma (HCC) within years or even a few months [1]. Ultrasound (US) and computed tomography (CT) examinations are generally useless in characterizing DNs because of the lack of specific imaging finding. At vascular study, in fact, HGDN might show a highly variable postcontrast enhancement pattern: even if the main blood nodular supply is still provided by branches of the portal vein, the initial development of sporadic unpaired arteries might determine a slightly enhancement on the arterial phase. On the contrary, magnetic resonance imaging (MRI) demonstrates parenchymal alterations as well as intranodular components, which can play an important role in the differential diagnosis between preneoplastic and neoplastic lesions. At baseline magnetic resonance imaging (MRI) examination, DNs typically show a characteristic hyperintensity on T1-weighted imaging (WI) due to intranodular glycogen or lipids, whereas on T2-WI they may be slightly hyperintense, isointense, or even hypointense [2]. Sometimes, progression from dysplasia to HCC is detected in a very early phase, when it is possible to identify a focus of HCC within a premalignant lesion, known as a nodule within a nodule [3]. Peculiarly, on T2-WI, the typical appearance is a focus of high signal intensity located within a low-signal-intensity nodule and also showing the postcontrast signal behavior of HCC. On hepatobiliary phase, after hepatospecific contrast agent administration, DNs are generally iso- or hyperintense compared with surrounding liver parenchyma, reflecting maintenance of biliary function but also cholestasis, which occurs in so-called green nodules (Fig. 1). Nonetheless, studies show that HGDN might appear as hypointense on the hepatobiliary (HB) phase; such finding are related to premalignancy [4].

### Hepatocellular Carcinoma: Imaging Findings

Actually, the main important clue suggesting the diagnosis of HCC within cirrhosis is the identification of a typical vascular supply of the nodule, characterized by contrast-agent washin during the arterial phase and washout on the portal venous or late phase. However, a typical vascular behavior at dynamic imaging modalities is not present in the 30% of HCC [5]. In these cases, baseline and postcontrast MRI, especially after administration of hepatospecific contrast media, may lead to a definitive diagnosis of HCC. On baseline T1-WI, HCC usually appears as a hypointense nodule because of its increased cellularity, and thus its higher amount of intracellular water, whereas on baseline T2-WI, HCC usually shows mild signal hyperintensity [2]. Well differentiated HCC might not show these signal intensities on baseline sequences, resulting examination, resulting isointense on T2-WI. Although their application has not yet been introduced into diagnostic guidelines, the use of tissue-specific contrast agents may give additional information, especially in the presence of borderline lesions (DNs) or well-differentiated HCCs. Regarding hepatobiliary contrast agents, the lack of contrast uptake is strongly related to overt HCC due to the loss of normal metabolic function, whereas uptake is preserved in early HCCs, resembling that of HGDN [6]. In daily practice, the

*Diseases of the Abdomen and Pelvis 2014-2017*,
DOI: 10.1007/978-88-470-5659-6_25 

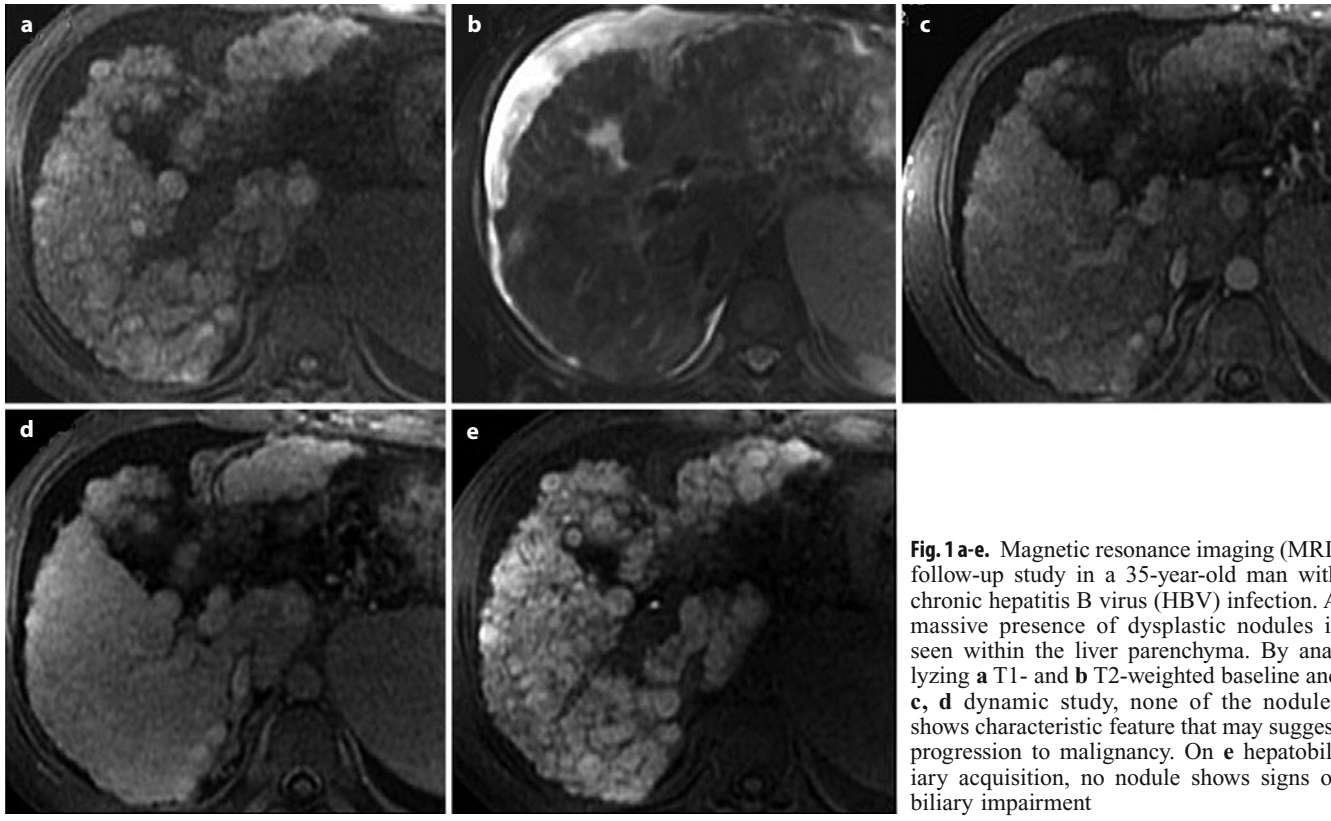


**Fig. 1 a-e.** Magnetic resonance imaging (MRI) follow-up study in a 35-year-old man with chronic hepatitis B virus (HBV) infection. A massive presence of dysplastic nodules is seen within the liver parenchyma. By analyzing **a** T1- and **b** T2-weighted baseline and **c, d** dynamic study, none of the nodules shows characteristic feature that may suggest progression to malignancy. On **e** hepatobiliary acquisition, no nodule shows signs of biliary impairment

advantages of the most recent generation of MRI contrast media can be exploited, as they illustrate the nodule's characteristic vascular and hepatospecific phases, i.e., neoangiogenesis and lack of hepatobiliary function, respectively, which allow a highly confident diagnosis of malignancy (Fig. 2).

### Therapy and Follow-up

Nowadays, the advantages of imaging-guided treatments have enlarged the therapeutic approaches of cirrhotic patients with HCC, permitting a tailored therapeutic strategy on the basis clinical and functional data and on patient staging [7]. Despite transplantation represents the best therapeutic approach for a cirrhotic patient, mini-invasive treatments, such as percutaneous ablation with radiofrequency or microwave, are actually considered a good alternative to resection. Intravascular procedures, such as chemoembolization, should instead be applied in intermediate patients with good performance status, as a palliative treatment, and in patients on waiting list for transplantation, in order to down stage those exceeding Milan's criteria [8]. Radioembolization is the newly introduced intravascular approach, reserved for patients with good performance status with large, locally advanced HCC, also involving a portal branch; this therapy permits downstaging patients otherwise classified as intermediate, who can then benefit from subsequent therapeutic approaches [9].

### Peripheral Cholangiocellular Carcinoma

Peripheral intrahepatic cholangiocellular carcinoma (IHCCC) arises from cholangiocytes of the second order of intrahepatic biliary ducts and represents 10% of all CCC; it generally occurs in the elderly (70s and 80s) and more frequently affects men than women [10]. The vast majority (95%) of these tumors are represented by adenocarcinomas. Well known risk factors for developing such neoplasm are primary sclerosing cholangitis or other chronic conditions, such as hepatolithiasis, bile stenosis, congenital hepatic fibrosis, and recurrence of biliary inflammations [11]. In recent years, moreover, the evidence of a number of concomitant chronic hepatitis C virus (HCV) infections associated with IHCCC suggests that the virus might play a role in the development of biliary neoplasm due to the common precursor (oval cell) of hepatocytes and cholangiocytes [12].

### IHCCC Classification and Prognosis

According to the Liver Cancer Study Group of Japan consensus [13], IHCCC are classified on the basis of macroscopic appearance and growth characteristics into three distinct forms: (1) mass-forming type; (2) periductal infiltrating type; (3) intraductal growing type. Different prognoses are related to different types: if the mass-forming and periductal infiltrating types usually have a poor prognosis, intraductal growing types might successfully

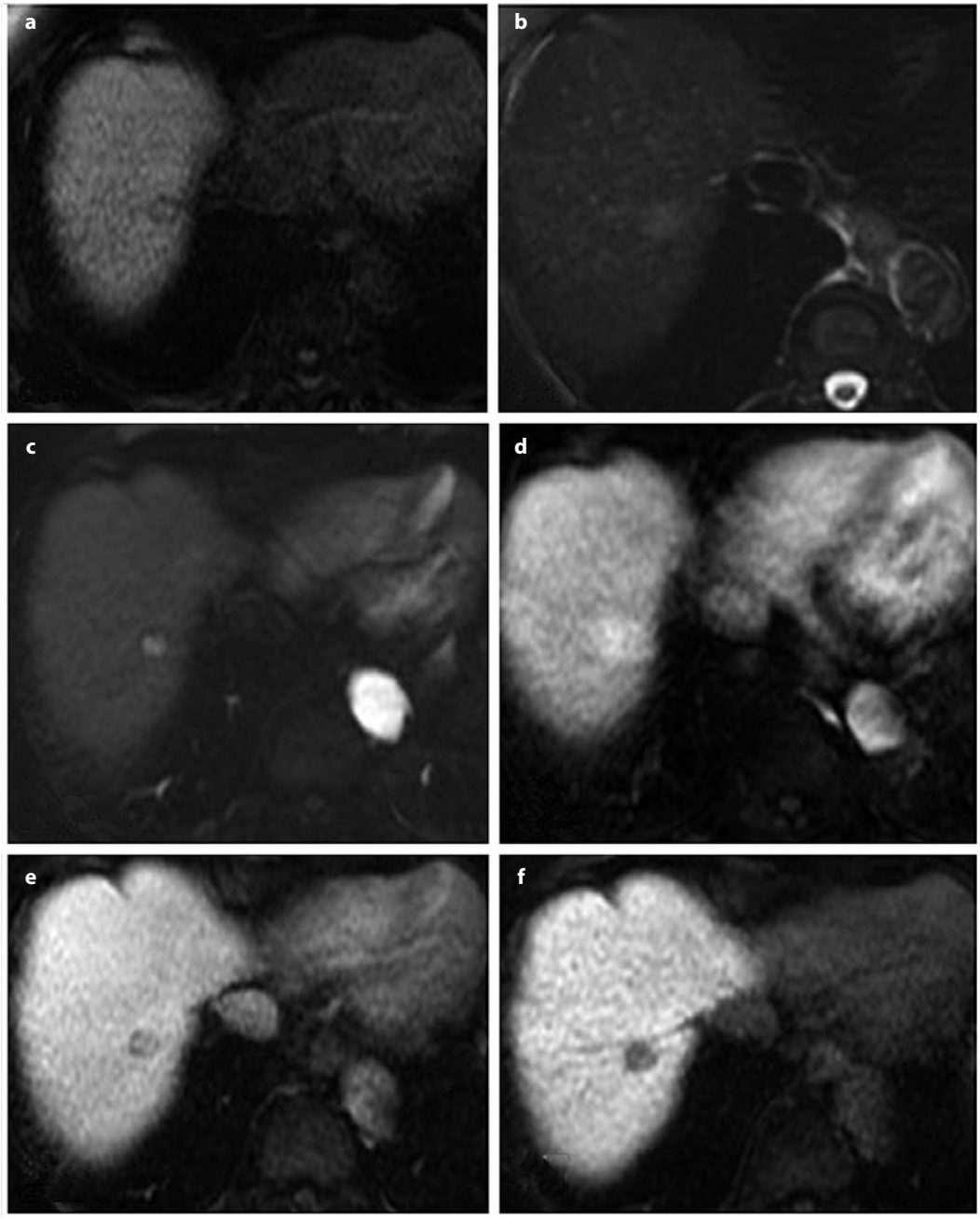


**Fig. 2 a-f.** Typical hepatocellular carcinoma (HCC) in a 77–year-old woman with chronic hepatitis C virus (HCV) infection. At magnetic resonance imaging (MRI), **a** baseline T1-weighted imaging (WI) shows the presence of a hypointense nodule of segment VII, which appears clearly hyperintense on **b** T2-WI. After gadolinium ethoxybenzyl diethylenetriamine pentaacetic acid (Gd-EOB-DTPA) administration, the nodule shows washin during the **c** early arterial phase that persists during the **d** parenchymal arterial phase and clear washout on the **e** delayed phase. **f** On hepatobiliary acquisition, the lesion appears hypointense because of complete loss of biliary activity of de-differentiated hepatocytes

benefit from surgery. As for the majority of pathological conditions, in cases of IHCCC, imaging modalities play a key role in lesion detection and characterization.

### *Mass-Forming IHCCC*

Mass-forming IHCCC appears at US as a solitary macronodule within liver parenchyma; echogenicity strictly depends on lesion dimension, as lesions $<3$ cm tend to be hypoechoic, whereas larger neoplasms can appear as slightly hyperechoic, mainly because of the large fibrous component. At multidetector CT (MDCT) examination, the lesion appears as a solitary mass or a main lesion with irregular margins, sometime surrounded by satellite nodules, appearing as a hypodense area associated with capsular retraction; dynamic study often reveals a thin rim of enhancement at the periphery of the neoplasm; on the arterial phase, whereas the central portion of the mass usually


**Fig. 3 a-c.** Peripheral mass-forming cholangiocarcinoma in a 55-year-old man. On the **a** arterial phase, it is possible to appreciate a mass-forming lesion within the dome of the liver that shows a rim like, peripheral enhancement; on **b** portal venous and **c** late phases, slight enhancement of some central portions of the lesion are appreciable. Capsular retraction of the lateral margin of segment VII is evident in all phases, as is the marginal, millimetric calcification

shows as hypodense, as it is constituted by fibrotic and necrotic areas. On delayed images, the slight enhancement of the fibrous component is detectable: such finding, together with the aforementioned capsule retraction and dilatation of the intrahepatic ducts located peripherally to the lesion, represent the most reliable elements for a confident diagnosis of IHCCC (Fig. 3). MRI shows a typically hypo/isointense mass on baseline T1-WI and slightly inhomogeneously hyperintense on baseline T2-WI, depending on the hydration of fibrous tissue and mucinous components within the lesion [14]. On the hepatobiliary phase acquired after administration of hepatospecific contrast agents, the lesion appears as hypointense in respect to the surrounding parenchyma because of the lack of functioning hepatocytes.

#### *Periductal Infiltrating IHCCC*

Periductal infiltrating IHCCC generally arise in the proximity of the hilum, thus sometimes leading to a difficult differential diagnosis from hilar primitive neoplasm (Klatskin tumor). US often shows dilation of the intrahepatic bile ducts located above the obstruction, and a hypoechoic lesion, located near the hepatic hilum, with irregular margins and mural thickening.

At MDCT, the lesion is not clearly defined, showing a slight enhancement mainly in the late phase. Portal vein branches are not frequently involved. MR cholangiopancreatography (MRCP) is largely applied in staging the neoplasm, as it can excellently and noninvasively evaluate obstructed ducts, the presence of material within them, and irregularity of duct walls, providing another clue to support the diagnosis [15].

#### *Intraductal Growing IHCCC*

Intraductal growing IHCCC presents at US as a variable dilatation of peripheral biliary ducts, usually involving an entire segment. In some ducts, and especially the more dilated ones, a single or multiple and slightly hyperechoic papillary projection might be appreciable. At MDCT, a subsegmental or segmental dilatation of peripheral biliary ducts is the major clue for suggesting this form. No clear intrahepatic mass is usually appreciable; capsular retraction is usually depicted, as well as atrophy of the involved segment. At dynamic MDCT, papillary lesions might show as slightly enhancing masses within the dilated ducts on portal venous/late phases [16]. MR may provide additional information for correct diagnosis and staging. In particular, at MRCP, it is possible to detect the presence of papillary projections within the dilated ducts, as they appear as hypointense filling defects within the bright lumen.

## Pancreas: Rare Pancreatitis

### Autoimmune Pancreatitis

Among chronic, alithiasic pancreatitis, autoimmune pancreatitis (AIP) is an unusual type of disease, representing about the 5% of cases of chronic pancreatitis. AIP is a unique, clinical entity characterized by peculiar pathologic and imaging findings, laboratory data, and effectiveness of corticosteroid therapy and is often associated with other autoimmune diseases (Sjögren's syndrome, primary sclerosing cholangitis, biliary cirrhosis). Clinically, patients complain of slight upper abdominal pain, sometimes obstructive jaundice, weight loss, and easy fatigability; lab tests might show an increased level of immunoglobulin (Ig) G, especially IgG4 subtype, and presence of autoantibodies (antinuclear antibodies, anticarbonic anhydrase antibodies, etc.), indicating the autoimmune origin of this disease [17]. Serum levels of amylase, lipase, and bilirubin may be increased. AIP can be classified as diffuse (more common) or focal, typically affecting the pancreatic head and/or uncinate process. Independently of type, the pancreatic gland shows diffuse, lymphoplasmacytic infiltration, variable degree of parenchymal atrophy, and fibrotic changes that might

involve contiguous soft tissues. Sometimes, fibroinflammatory processes involve the intrapancreatic tract of the common bile duct and small venous vessels as well.

US examination shows a homogeneous, hypoechoic, diffuse or focal enlargement of the pancreas, sometimes associated with dilation of the intrahepatic and common bile ducts. MDCT is the reference imaging technique for diagnosis and shows uniform swelling of the pancreas with well-defined outline. A characteristic sign is a rim-like capsule partially or completely surrounding the pancreas, which enhances during delayed phases, relating to fibroinflammatory changes involving the peripancreatic adipose tissue. MR examination can demonstrate a homogeneous focal or diffuse pancreatic enlargement, which generally is hyperisointense in T2-WI and hypointense in T1-WI compared with the liver. On postcontrastographic scans, the involved parenchyma shows homogeneous enhancement; the aforementioned pseudocapsule may appear as a hypointense peripheral band on both T1- and T2-WI and may show delayed enhancement [18, 19].

### Groove Pancreatitis

Another rare pathological condition that might affect the pancreas is represented by groove pancreatitis. Such uncommon, chronic inflammation originates from the groove between the head of the pancreas, the duodenum, and the last tract of the common biliary duct. The pathogenesis of groove pancreatitis is thought to be anatomical or functional obstruction of the minor papilla. Clinically, symptoms result from marked duodenal stenosis and impaired motility associated with nausea and vomiting. Occasionally, jaundice can be present. Differently from other pancreatic diseases, serum levels of carcinoembryonic antigen (CEA) and carbohydrate antigen (CA 19-9) are usually normal [20].

At imaging, it is possible to identify two distinct forms: a pure type, affecting only the groove, and a segmental type, involving the groove and the head [21]. Similarly to other chronic pathologic inflammatory diseases of the pancreas, MDCT represents the reference diagnostic technique. AT CT, imaging findings that might lead to diagnosis are cystic thickening of the duodenal wall with or without duodenal stenosis, presence of fibrous tissue within the pancreaticoduodenal groove that usually might show delayed enhancement, and common bile duct dilatation [22] (Fig. 4). MRI can provide further information in evaluating the groove area, as it shows a sheetlike mass that appears as hypointense to the pancreatic parenchyma on T1-WI and slightly hyperintense on


**Fig. 4 a-d.** Groove pancreatitis in a 44-year-old man. Multidetector computed tomography (MDCT) examination shows **a** multilocular collection (*arrows*) with well-defined margins, characteristically located between the descending tract of the duodenum and the pancreatic head; duodenal walls are clearly enhancing both on **a** arterial and **b** venous phases. No dilation of the main pancreatic duct (**b**) or the intrahepatic biliary tree (**d**) is appreciable. The head of the pancreas (**c**) is compressed; the other portions of the gland (**d**) show regular morphology and enhancement (*arrow*)

T2-WI in respect to the pancreatic gland [23]. MRCP shows a widened space between duodenum, common bile duct, and distal pancreas; moreover, the common bile duct appears to gradually taper, in contrast to the abrupt stenosis characterizing pancreatic cancer [24].

If AIP benefits from corticosteroid treatment until achieving complete resolution, groove pancreatitis is often treated surgically, especially when symptoms do not improve or the condition is difficult to distinguish from pancreatic carcinoma.

## References


1. Theise, Park YN, Kojiro M (2002) Dysplastic nodules and hepatocarcinogenesis. Clin Liver Dis 6:497-512.
2. Bartolozzi C, Cioni D, Donati F et al (2001) Focal liver lesions: MR imaging-pathologic correlation. Eur Radiol 11:1374-1388.
3. Shinmura R, Matsui O, Kobayashi S et al (2006) Cirrhotic nodules: association between MR imaging signal intensity and intranodular blood supply. Radiology 237:512-519.
4. Bartolozzi C, Battaglia V, Bargellini I et al (2013) Contrast-enhanced magnetic resonance imaging of 102 nodules in cirrhosis: correlation with histological findings on explanted livers. Abdom Imaging 38:290-296.
5. Bolondi L, Gaiani S, Celli N et al (2005) Characterization of small nodules in cirrhosis by assessment of vascularity: the problem of hypovascular hepatocellular carcinoma. Hepatology 42:27-34.
6. Bartolozzi C, Crocetti L, Lencioni R et al (2007) Biliary and reticuloendhotelial impairment in hepatocarcinogenesis: the diagnostic role of tissue specific MR contrast media. Eur Radiol 17:2519-2530.
7. Bruix J, Sherman M (2011) Management of hepatocellular carcinoma: an update. Hepatology 53:1020-1022.
8. Mazzaferro V, Regalia E, Doci R et al (1996) Liver transplantation for the treatment of small hepatocellular carcinoma in patients with cirrhosis. N Engl J Med 334:693-699.
9. Tohme S, Sukato D, Chen HW et al (2013) Yttrium-90 radiomebolization as a bridge to liver transplantation: a single institution experience. J Vasc Interv Radiol 24:1632-1638.
10. Han JK, Choi BI, Kim AY et al (2002) Cholangiocarcinoma: pictorial essay of CT and cholangiographic findings. Radiographics 22:173-187.
11. Bergquist A, Broome U (2001) Hepatobiliary and extra-hepatic malignancies in primary sclerosing cholangitis. Best Pract Res Clin Gastroenterol 15:643-656.
12. Donato F, Gelatti U, Tagger A et al (2001) Intrahepatic cholangiocarcinoma and hepatitis C and B virus infection, alcohol intake, and hepatolithiasis: a case-control study in Italy. Cancer Causes Control 12:959-964.
13. Yamasaki S (2003) Intrahepatic cholangiocarcinoma: macroscopic type and stage classification. J Hepatobiliary Pancreat Surg 10:288-291.
14. Maetani Y, Itoh K, Watanabe C et al (2001) MR imaging of intrahepatic cholangiocarcinoma with pathological correlation. AJR Am J Roentgenol 176:1499-1507.
15. Schwartz LH, Lefkowitz RA, Panicek DM et al (2003) Breath hold magnetic resonance cholangiopancreatography in the evaluation of malignant pancreaticobiliary obstruction. J Comput Assist Tomogr 27:307-314.
16. Yoon KH, Han HK, Kim CG et al (2000) Malignant papillary neoplasm of intrahepatic bile ducts: CT and histopathologic features. AJR Am J Roentgenol 175:1135-1139.
17. Sugumar A, Chari ST (2010) Diagnosis and treatment of autoimmune pancreatitis. Curr Opin Gastroenterol 26:513.
18. Shanbhogue AK, Fasih N, Surabhi VR et al (2009) A clinical and radiologic review of uncommon types and causes of pancreatitis. Radiographics 29:1003-1026.
19. Perez-Johnston R, Sainani NI, Sahani DV (2012) Imaging of chronic pancreatitis (including groove and autoimmune pancreatitis). Radiol Clin North Am 50:447-466.
20. Yamaguchi K, Tanaka M (1992) Groove pancreatitis masquerading as pancreatic carcinoma. Am J Surg 163:312-318.
21. Stolte M, Weiss W, Volkholz H et al (1982) A 10 special form of segmental pancreatitis: 'groove pancreatitis'. Hepatogastroenterology 29:198-208.
22. Mohl W, Hero-Gross R, Feifel G et al (2001) Groove pancreatitis: an important differential diagnosis to malignant stenosis of the duodenum. Dig Dis Sci 46:1034-1038.
23. Irie H, Honda H, Kuroiwa T et al (1998) MRI of groove pancreatitis. J Comput Assist Tomogr 22:651-655.
24. Levenick JM, Gordon SR, Sutton JE et al (2009) A comprehensive, case-based review of groove pancreatitis. Pancreas 38:e169-e175.

# Pathways for the Spread of Disease in the Abdomen and Pelvis

James A. Brink

Radiology, Massachusetts General Hospital, Boston, MA, USA

## Introduction

An understanding of abdominal and pelvic viscera anatomy is critical to understand and predict pathways by which disease may spread throughout the abdomen and pelvis. Of critical importance are ligamentous attachments that interconnect the intra-abdominal organs, as these are common conduits for the spread of disease. Moreover, organs and their ligamentous attachments form the boundaries of the peritoneal cavity and guide the flow of peritoneal fluid throughout the abdomen and pelvis.

There are four different pathways for the spread of disease throughout the abdomen. Using neoplastic disease as an example, intra-abdominal malignancies may spread through the bloodstream, direct invasion, via lymphatic extension, and intraperitoneal seeding. Of these, blood-borne metastasis is beyond the scope of this chapter. Direct invasion and lymphatic extension commonly occur through the peritoneal ligaments and mesenteries that interconnect the abdominal viscera. The spread of malignancy through the peritoneal cavity occurs first by seeding of the peritoneal cavity with metastatic cells that then spread via the natural flow of peritoneal fluid via the peritoneal spaces [1].

## Spread of Disease via the Peritoneal Ligaments

The peritoneal ligaments form a major network for the spread of disease in the upper abdomen, by both direct invasion and lymphatic extension. Three pairs of ligaments provide interconnections among the upper abdominal viscera: the gastrohepatic and hepatoduodenal ligaments (that together comprise the lesser omentum), the gastrosplenic and splenorenal ligaments, and the gastrocolic ligament and transverse mesocolon. In addition to interconnecting the upper abdominal organs, these ligamentous pairs connect the intraperitoneal organs to the retroperitoneum, providing a pathway of disease from the abdominal viscera to the retroperitoneum and vice versa.

### Gastrohepatic Ligament

The gastrohepatic ligament joins the lesser curvature of the stomach to the liver, extending from the fissure for the ligamentum venosum to the porta hepatis. It can be recognized on cross-sectional imaging as a fatty plane that connects the lesser curvature of the stomach to the left hepatic lobe and contains the left gastric artery, the left gastric vein or coronary vein, and associated lymphatics (Fig. 1). Lymph nodes in this structure tend to be somewhat smaller than elsewhere in the abdomen; nodes in the gastrohepatic ligament are typically considered abnormal when they exceed 8 mm in diameter [2]. Sometimes, unopacified bowel loops, the pancreatic neck, or the papillary process of the caudate lobe can mimic pathology in the gastrohepatic ligament by projecting into the expected plane of this structure [3, 4].

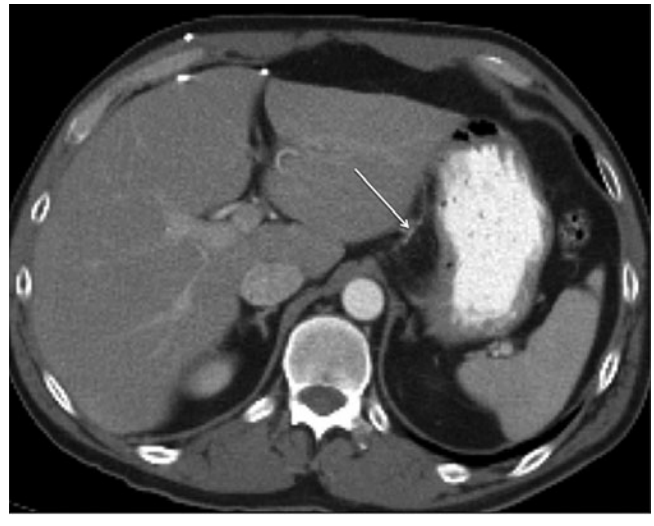

**Fig. 1.** Transaxial computed tomography (CT) image demonstrates the gastrohepatic ligament (GHL), seen as a fatty plane interposed between the lesser curvature of the stomach and the lobe of the liver. The GHL contains the left gastric artery (*arrow*), the left gastric vein (coronary vein), and associated lymphatics

*Diseases of the Abdomen and Pelvis 2014-2017*,
DOI: 10.1007/978-88-470-5659-6_26 

**Fig. 2.** Transaxial computed tomography (CT) image demonstrates a heterogenous mass centered in the gastrohepatic ligament (GHL), with invasion of the left hepatic lobe and the stomach (*arrow*). Prospectively, it was unclear as to the organ of origin, but it proved to be a hepatoma extending through the GHL to involve the stomach

Gastric disease commonly spreads to the liver and hepatic disease commonly spreads to the stomach via the gastrohepatic ligament. An important feature is that the subperitoneal areolar tissue within the ligament is continuous with the perivascular fibrous capsule of the liver (Glisson capsule). This feature provides a direct pathway from the gastrohepatic ligament into the liver parenchyma. Gastric disease can spread directly into the left lobe of the liver, and hepatic disease can readily invade the stomach via this pathway, including both neoplastic and inflammatory conditions (Fig. 2). Several types of malignancies are known to spread via lymphatic extension through the gastrohepatic ligament, including gastric and esophageal cancer. Direct invasion through the gastrohepatic ligament can also occur from gastric and esophageal cancer spreading to the liver and hepatoma and cholangiocarcinoma spreading to the stomach.

## Hepatoduodenal Ligament

The hepatoduodenal ligament is intimately related to the gastrohepatic ligament, as it forms the free edge of the gastrohepatic ligament along its rightward aspect. Together, these structures comprise the lesser omentum. The primary structures of the porta hepatis, including the common bile duct, the hepatic artery, and the portal vein, coexist within the hepatoduodenal ligament. The hepatoduodenal ligament extends from the flexure between the first and second duodenum to the porta hepatis, forming a tent-like structure extending from anterior to posterior as it courses from superior to inferior. Immediately posterior to the ligament is the foramen of Winslow, permitting access to the lesser sac [5]. Unlike nodes within the gastrohepatic ligament, which tend to be smaller than elsewhere in the abdomen, nodes at the base of the hepatoduodenal ligament at the foramen of Winslow (in the portocaval space) have an unusual morphology such that their transverse dimension is greater than their anteroposterior (AP) dimension. Typically, these nodes can be up to 2.0 cm in transverse dimension and up to 1.5 cm in AP dimension and still be normal. Unless these nodes are grossly enlarged, internal pathology can be difficult to recognize but may be suggested by a more spherical shape or central necrosis [6, 7].

A wide range of neoplastic and inflammatory conditions commonly spread via the hepatoduodenal ligament. Lymphatic extension can occur within the lymphatics in the hepatoduodenal ligament, propagating neoplastic disease in both directions (Fig. 3). Liver or biliary cancer may spread in an antegrade fashion through lymphatics in

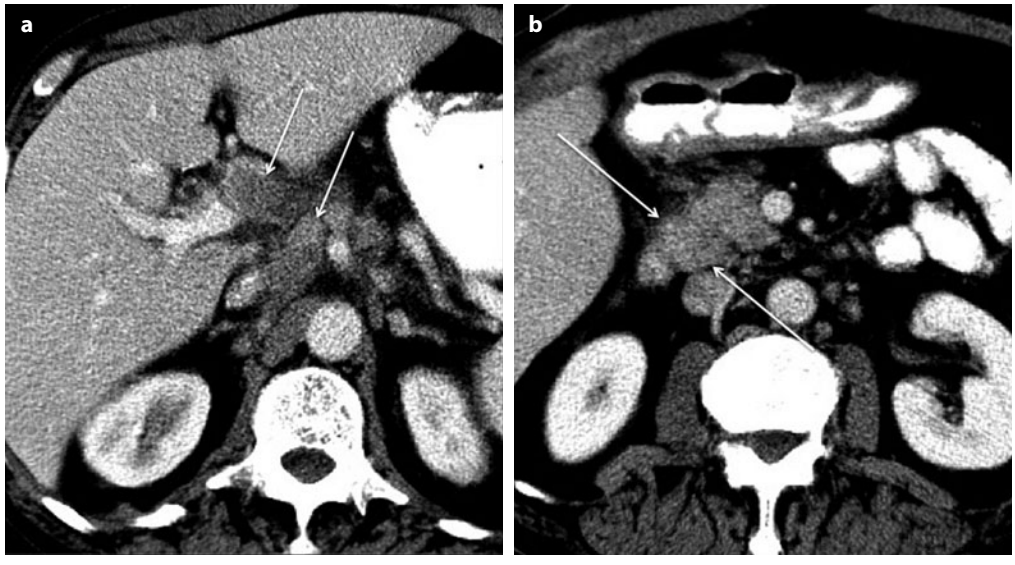


**Fig. 3 a, b.** Transaxial computed tomography (CT) images through **a** the porta hepatis and **b** the uncinate process demonstrate bulky lymphadenopathy (*arrows*) in the hepatoduodenal ligament (HDL) in a patient with gallbladder carcinoma. Tumor has spread bidirectionally within the HDL proximally (**a**) and distally to the insertion of the HDL on the second portion of the duodenum (**b**) (*arrows*)

the hepatoduodenal ligament to deposit in periduodenal and peripancreatic lymph nodes. Conversely, malignant disease in nodes surrounding the superior mesenteric artery, as may occur in the setting of pancreatic and colon cancer, can spread in a retrograde fashion up the lymphatics in the hepatoduodenal ligament to the liver. Direct invasion can also occur through the hepatoduodenal ligament, commonly involving gastric cancer arising in the lesser curvature of the stomach and spreading through the gastrohepatic ligament to the hepatoduodenal ligament and then to peripancreatic and periduodenal lymph nodes. A host of inflammatory conditions also spreads commonly through this ligament, including inflammatory conditions arising within the gall bladder and biliary tree that can spread down the ligament, as well as pancreatitis that can spread up the ligament. Vascular complications related to both neoplastic and inflammatory conditions commonly involve structures within the hepatoduodenal ligament, including the portal vein and hepatic artery. Portal venous thrombosis and hepatic arterial pseudoaneurysms may occur as complications to disease spreading within the hepatoduodenal ligament [1, 5].

### Gastrosplenic and Splenorenal Ligaments

As the gastrohepatic and hepatoduodenal ligament connect the lesser curvature of the stomach to the porta hepatis and the retroperitoneum in the right abdomen, the gastrosplenic and splenorenal ligaments connect the gastric greater curvature to the splenic hilum and the retroperitoneum in the left abdomen (Fig. 4) [8]. The superior third of the gastric greater curvature and the splenic hilum are connected by a rather thin filamentous ligament known as the gastrosplenic ligament. The left gastroepiploic and short gastric vessels and associated lymphatics reside within the ligament. Gastric disease commonly propagates to the splenic hilum through this ligament. Once reaching the spleen, both inflammatory and neoplastic disease of the stomach can invade the spleen via this pathway.

The gastrosplenic ligament is continuous with the splenorenal ligament posteriorly and medially, and thus, gastric disease spreading to the splenic hilum can continue posteriorly to the retroperitoneum. Not uncommonly, disease spreading through the splenorenal ligament can involve the tail of the pancreas and engulf the splenic vasculature (Fig. 5) [9, 10]. Similarly, pancreatic disease, both neoplastic and inflammatory, may spread via the

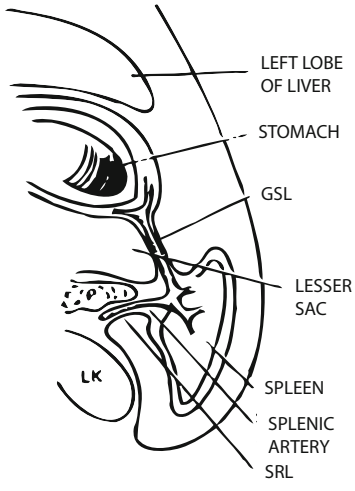


**Fig. 4.** Gastrosplenic ligament (*GSL*) and splenorenal ligament (*SRL*) comprise the left wall of the lesser sac and provide a conduit for the spread of metastatic disease from the greater curvature of the stomach to the retroperitoneum and vice versa. Reprinted from [8] with permission of Springer Science and Business Media

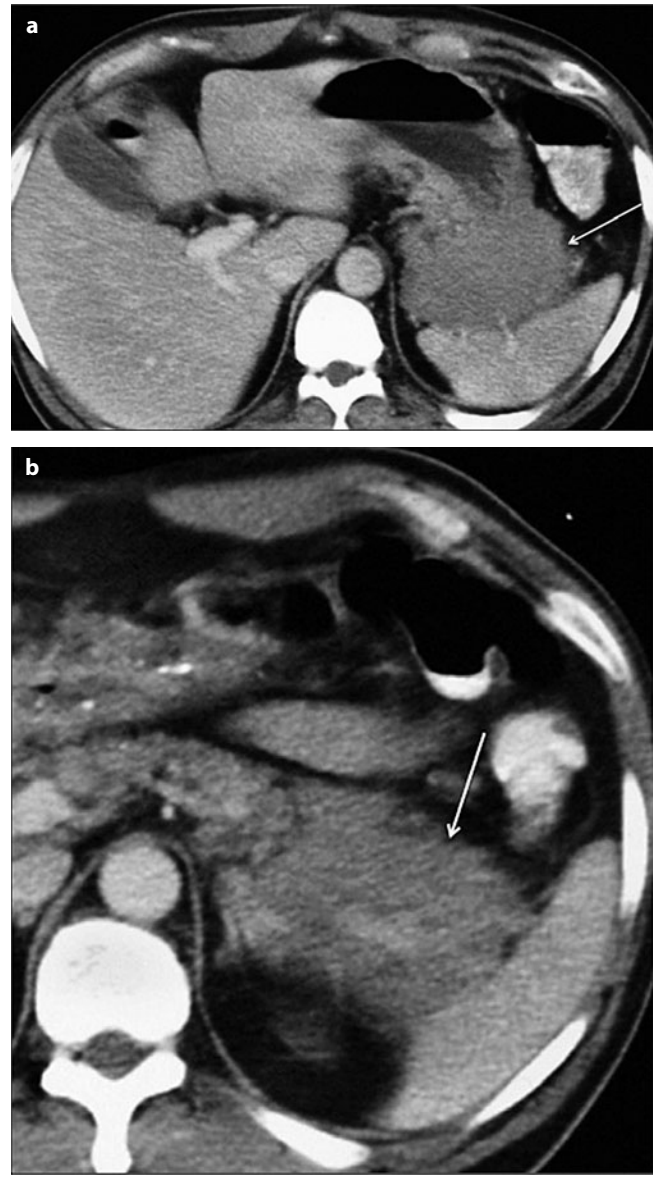


**Fig. 5 a, b.** Transaxial computed tomography (CT) images through **a** the gastrosplenic ligament (GSL) and **b** the splenorenal ligament (SRL) in a patient with lymphoma. Tumor is seen within the GSL, interposed between the gastric greater curvature and the spleen (**a**), and within the SRL, encasing the splenic vasculature (**b**) (*arrow*)

splenorenal ligament to the splenic hilum and continue on through the gastrosplenic ligament to the gastric greater curvature [1].

### Gastrocolic Ligament

In the midabdomen, the gastrocolic ligament (greater omentum) joins the inferior two thirds of the gastric greater curvature to the transverse colon (Fig. 6) [11]. In concert with the transverse mesocolon, the gastrocolic ligament provides an important conduit of disease between the stomach, transverse colon, and retroperitoneum. The gastrocolic ligament is continuous with the gastrosplenic ligament in the left abdomen, and it ends at the gastroduodenal junction near the hepatoduodenal ligament on the right. In the embryo, the gastrosplenic ligament is a long ligamentous attachment between the stomach and the retroperitoneum that gives rise to the gastrocolic ligament and the transverse mesocolon in the adult. Because the adult gastrocolic ligament results from fusion of the anterior and posterior leaves of the embryonic gastrosplenic ligament, it contains four layers of peritoneum that invest the stomach and, thus, it has a potential space within it that can fill with fluid under certain conditions. On occasion, tense ascites in the lesser sac can dissect open the potential space within the gastrocolic ligament, resulting in a cyst-like appearance within the greater omentum.

The gastroepiploic vessels and associated lymphatics reside within the gastrocolic ligament and can aid in its identification in the fatty plane that connects the stomach to the transverse colon. The gastrocolic ligament provides an important conduit of both benign and malignant disease from the inferior two thirds of the gastric greater curvature to the transverse colon and vice versa (Fig. 7). Together with the transverse mesocolon, the gastric greater curvature is connected to the retroperitoneum via the gastrocolic ligament and the transverse mesocolon. Thus, disease involving the stomach, transverse colon, and pancreas are interconnected directly by these two structures. In addition, the fatty veil of the greater omentum provides an important nidus for peritoneal metastases, as commonly occur with ovarian, gastric, colon, and pancreatic cancer [12, 13]. Finally, pancreatic tumors that spread by direct invasion locally, or gastric disease spreading to the pancreas via the gastrocolic ligament/transverse mesocolon and/or gastrosplenic/splenorenal ligaments, may encase the splenic vasculature and result in splenic venous compromise, resulting in gastroepiploic collaterals seen within the gastrocolic ligament.

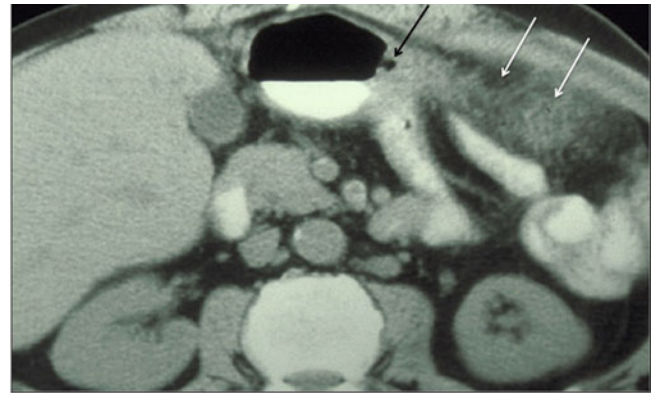

**Fig. 7.** Transaxial computed tomography (CT) image through the gastrocolic ligament (GCL) demonstrates a gastric ulcer extending into the GCL (*black arrow*) with associated inflammation in the greater omentum (*white arrows*)

### Transverse Mesocolon

In addition to providing a connection between the transverse colon and the retroperitoneum, the transverse mesocolon provides a broad conduit for disease across the midabdomen, with bare areas that link the pancreas to the transverse colon, the spleen, and the small bowel (Fig. 8). The transverse mesocolon is continuous with the duodenocolic ligament in the right abdomen, with the small-bowel mesentery in the midabdomen, and with the phrenicocolic

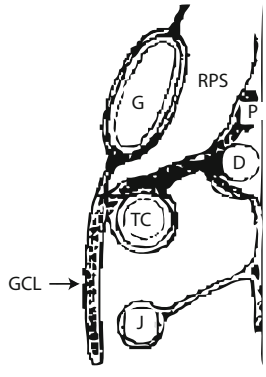


**Fig. 6.** Gastrocolic ligament (*GCL*) joins the greater curvature of the stomach (*G*) to the transverse colon (*TC*). In concert with the transverse mesocolon, a pathway of disease is formed between retroperitoneal structures such as the pancreas (*P*) and the duodenum (*D*) to the anterior aspect of the intraperitoneal cavity. *RPS*, right peritoneal space, lesser sac; *J*, jejunum. Modified from [11]

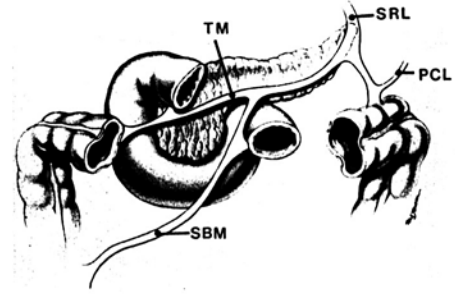


**Fig. 8.** Transverse mesocolon (*TM*) provides an important conduit for the spread of disease across the midabdomen. It is continuous with the splenorenal ligament (*SRL*) and phrenicocolic ligament (*PCL*) on the left and with the duodenocolic ligament on the right. In its midportion, it is continuous with the small-bowel mesentery (*SBM*). Reprinted from [8] with permission of Springer Science and Business Media

**Fig. 9.** Transaxial computed tomography (CT) image through the transverse mesocolon (TMC) in a patient with pancreatic adenocarcinoma demonstrates invasion of the TMC with necrotic tumor (*arrows*). The tumor in the TMC has fistulized with the transverse colon, resulting in gas accumulating within the necrotic debris

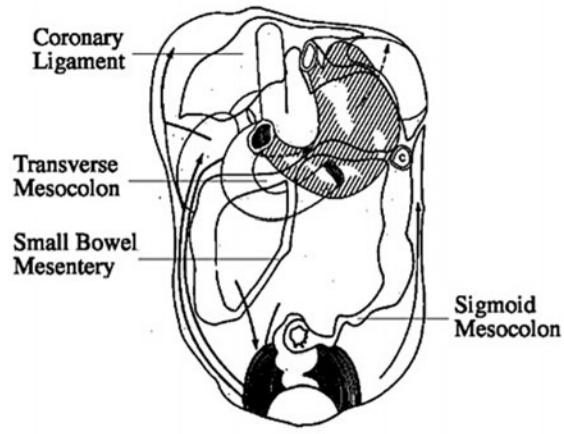


**Fig. 10.** Posterior peritoneal reflections and recesses. Intraperitoneal fluid flows naturally from the pelvis to the upper abdomen. Flow occurs preferentially through the right rather than left paracolic gutters owing to the broader diameter of the right gutter. In addition, flow in the left paracolic gutter is cut off from reaching the left subphrenic space by the phrenicocolic ligament. The transverse mesocolon (TMC) divides the abdomen into supra- and inframesocolic spaces. In the right inframesocolic space, fluid is impeded from draining into the pelvis via the small-bowel mesentery (SBM). Owing to natural holdup of fluid at the root of the SBM and sigmoid mesocolon, these structures are naturally predisposed to involvement with serosal-based metastases in the setting of peritoneal carcinomatosis. Reprinted from [8] with permission of Springer Science and Business Media

ligament and splenorenal ligaments in the left abdomen. The transverse mesocolon contains the middle colic vessels and associated lymphatics that may help identify the fatty plane interconnecting the transverse colon to the retroperitoneum at the level of the uncinate process of the pancreas. Pancreatic disease often spreads ventrally into the transverse mesocolon (Fig. 9), and inflammatory disease such as pancreatitis commonly results in adjacent fluid collections that can dissect open the potential space within the transverse mesocolon formed by fusion of the anterior and posterior leaves of the embryonic gastrosplenic ligament. Such fluid collections are sometimes confused with fluid in the lesser sac. Similarly, pancreatic carcinoma can spread ventrally into the transverse mesocolon to involve the transverse colon, and, ultimately, to involve the stomach if spread continues through the gastrocolic ligament.

The right edge of the transverse mesocolon constitutes the duodenocolic ligament, and an important feature of this ligament involves lymphatic drainage coming from the right colon. Thus, an important route for the spread of disease also exists between the right colon and the periduodenal and peripancreatic lymph nodes via the lymphatics in the right edge of the transverse mesocolon, the duodenocolic ligament [1]. When periduodenal and peripancreatic lymphadenopathy becomes severe, gastric outlet obstruction may ensue, and it is important to consider the spread of cancers involving the right colon to these nodes if the more common causes of lymphadenopathy in this region are excluded.

## Spread of Disease via Peritoneal Spaces

The natural flow of peritoneal fluid through the peritoneal spaces guides the spread of inflammatory and neoplastic disease that may occur in the peritoneal cavity. Tumors that break through the visceral peritoneum or arise from the peritoneal lining can shed cells into the peritoneal fluid. Inflammatory processes may arise de novo within the peritoneal cavity or extend into the peritoneal spaces from adjacent structures. Once intraperitoneal, these conditions may propagate through the peritoneal spaces along predictable routes. The differential diagnosis for the source of intra-abdominal pathologies is well informed by a thorough understanding of the anatomy of the peritoneal spaces. By recognizing that a disease process is intraperitoneal, one may better predict its organ of origin and its likely routes of spread (Fig. 10).

The peritoneal cavity can be subdivided into two compartments: the left peritoneal space and the right peritoneal space.

### Left Peritoneal Space

Four compartments comprise the left peritoneal space: the left anterior perihepatic space, the left posterior perihepatic space (gastrohepatic recess), the left anterior subphrenic space, and the left posterior subphrenic space (perisplenic space).

#### Left Anterior Perihepatic Space

The left anterior perihepatic space is the rightward extension of the left peritoneal space anteriorly. It is bounded

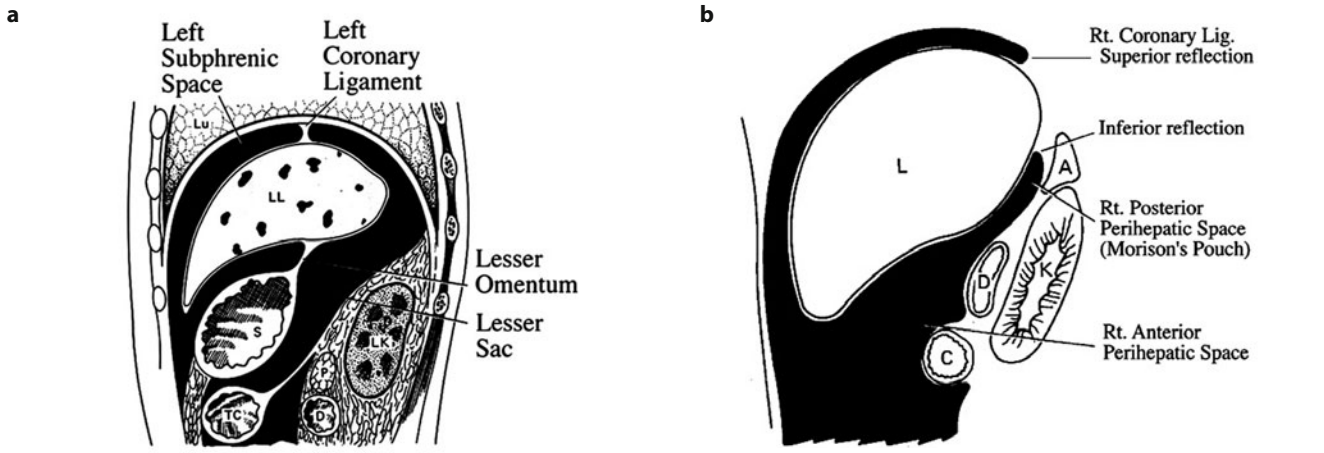


**Fig. 11 a, b.** Left and right perihepatic spaces. The **a** left and **b** right perihepatic spaces are bounded posteriorly by the coronary ligaments. The reflections of the coronary ligaments mark the site of the nonperitonealized "bare area" of the liver. *LL* left lobe of the liver, *LK* left kidney, *S* stomach, *TC* transverse colon, *P* pancreas, *D* duodenum, *Lu* lung, *L* liver (right lobe), *A* adrenal, *K* kidney, *C* colon. Reprinted from [8] with permission of Springer Science and Business Media

on the right by the falciform ligament and on the left by the anterior wall of the stomach. It extends posteriorly along the diaphragm and is limited by the left coronary ligament, the left-superior extension of the bare area of the liver (Fig. 11a).

### Left Posterior Perihepatic Space

The left posterior perihepatic space (gastrohepatic recess) follows the inferior margin of the left hepatic lobe posteriorly deep into the fissure for the ligamentum venosum. It is bounded on the left by the lateral wall of the stomach and is in close proximity to the anterior wall of the duodenal bulb, the anterior wall of the gallbladder, and the porta hepatis [9]. The lesser omentum inserts into the fissure for the ligamentum venosum and separates fluid in the gastrohepatic recess from fluid in the superior recess of the lesser sac, an extension of the right peritoneal space (see below). It is important to differentiate fluid between these two spaces, as fluid collections in the lesser sac are difficult to approach percutaneously. Conversely, a catheter guided along the inferior margin of the liver is usually sufficient to access fluid collections in the gastrohepatic recess.

### Left Anterior Subphrenic Space

The left anterior subphrenic space connects directly with the left anterior perihepatic space across the midabdomen. Unlike the right subphrenic space that communicates freely with the right paracolic gutter, the left subphrenic space is cut off from the left paracolic gutter by the phrenicocolic ligament. Thus, fluid that travels ventrally over the stomach may be relatively static compared with other locations in the peritoneal cavity, making the left subphrenic space a common site for peritoneal carcinomatosis and abscess formation in the setting of generalized peritonitis [14].

### Left Posterior Subphrenic Space

The left posterior subphrenic space (perisplenic space) is the posterior extension of the left anterior subphrenic space. Fluid in this space surrounds the superior and lateral margins of the spleen, outlining the "bare areas" of the spleen that result from insertion of the gastrosplenic and splenorenal ligaments into the splenic hilum [15-17]. Superiorly, the perisplenic space surrounds the upper margin of the spleen [18].

## Right Peritoneal Space

Three compartments comprise the right peritoneal space: the right subphrenic space/right anterior perihepatic space, the right posterior perihepatic space (hepatorenal recess/Morison's pouch), and the lesser sac.

### Right Subphrenic Space

The right subphrenic space occupies the smoothly contoured area between the right hemidiaphragm and the superolateral margin of the liver (Fig. 11b). Posteriorly, the right coronary ligament (bare area of the liver) demarcates the medial extension of the right subphrenic space [19].

### Hepatorenal Recess

The hepatorenal recess (Morison's pouch) is the posteromedial extension of the subphrenic space. The coronary ligament marks the superior aspect of the hepatorenal recess, which is located between the right lobe of the liver and the anterior border of the kidney.

### Lesser Sac

The lesser sac is comprised of superior and inferior recesses [10, 20]. The superior recess is smaller than the inferior recess, resides immediately posterior to the hepatoduodenal ligament, and communicates with the hepatorenal recess via the foramen of Winslow. Fluid in the superior recess of the lesser sac forms a typical reverse *C*-shaped configuration as it wraps around the caudate lobe (Figs. 12, 13). The gastropancreatic plicae, containing the proximal left gastric artery, is a raised peritoneal reflection along the posterior aspect of the lesser sac and serves as a useful anatomic landmark separating the superior from the inferior recesses of the lesser sac. The inferior recess of the lesser sac is bounded anteriorly by the stomach, inferoposteriorly by the transverse mesocolon, and laterally by the gastrosplenic and splenorenal ligaments. As abdominal viscera surround both compartments of the lesser sac, percutaneous drainage of lesser-sac fluid collections is problematic. A potential space may exist caudally within the greater omentum (see above) and behind the duodenum and pancreatic head, which may be responsible for peritoneal fluid collections in these locations [8].

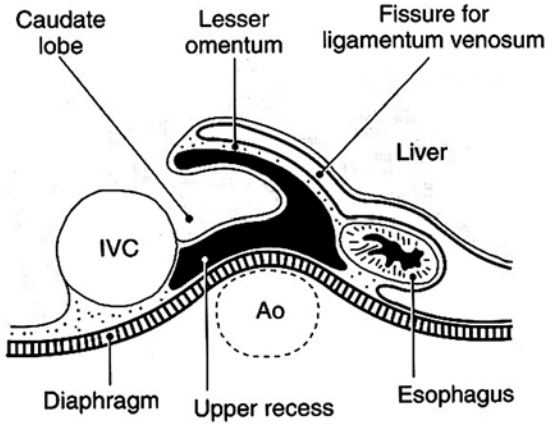


**Fig. 12.** Boundaries of the superior recess of the lesser sac may be recognized when fluid engulfs the caudate lobe. The lesser omentum separates this fluid from fluid in fissure for the ligamentum venosum, which is in continuity with the left posterior perihepatic space (gastrohepatic recess). *IVC* inferior vena cava, *Ao* aorta. Reprinted from [8] with permission of Springer Science and Business Media

**Fig. 13.** Transaxial computed tomography (CT) image through the superior recess of the lesser sac in a patient with gallbladder cancer (same patient as in Fig. 3). Malignant ascites has accumulated in the superior recess of the lesser sac (*arrows*), seen with a characteristic reverse c-shaped configuration surrounding the caudate lobe

## Summary

A working knowledge of the peritoneal ligaments, mesenteries, and spaces can provide an understanding of the pathways by which neoplastic and inflammatory disease may spread throughout the abdomen and pelvis. Intra-abdominal disease involving the intraperitoneal viscera may spread to the retroperitoneum via three pairs of ligaments. In the right abdomen, the gastrohepatic and hepatoduodenal ligaments link the lesser curvature of the stomach to the porta hepatis and retroperitoneum, respectively. In the left abdomen, the gastrosplenic and splenorenal ligaments link the superior greater curvature of the stomach to the spleen and retroperitoneum, respectively. In the mid-abdomen, the gastrocolic ligament and transverse mesocolon link the inferior greater curvature of the stomach to the transverse colon and the retroperitoneum, respectively. Recognition of disease in any of these ligamentous pairs can suggest the organ of origin and, in some cases, the location of the disease within the organ. The peritoneal spaces are defined by the peritoneal ligaments and mesenteries and guide the flow of intraperitoneal fluid throughout the peritoneal spaces. Inflammatory and neoplastic disease that arise de novo within the peritoneal cavity or has extended into the peritoneal spaces can propagate through the interconnecting peritoneal spaces along predictable pathways.

## References

1. Meyers MA, Oliphant M, Berne AS, Feldberg MAM (1987) The peritoneal ligaments and mesenteries: pathways of intraabdominal spread of disease. Radiology 163:593-604.
2. Balfe DM, Mauro MA, Koehler RE et al (1984) Gastrohepatic ligament: normal and pathologic CT anatomy. Radiology 150:485-490.
3. Auh YH, Rosen A, Rubenstein WA et al (1984) CT of the papillary process of the caudate lobe of the liver. AJR Am J Roentgenol 142:535-538.
4. Donoso L, Martinez-Noguera A, Zidan A, Lora F (1989) Papillary process of the caudate lobe of the liver: sonographic appearance. Radiology 173:631-633.
5. Weinstein JB, Heiken JP, Lee JKT et al (1985) High resolution CT of the porta hepatis and hepatoduodenal ligament. RadioGraphics 6:55-74.

6. Zirinsky K, Auh YH, Rubenstein WA et al (1985) The portacaval space: CT with MR correlation. Radiology 156:453-460.
7. Ito K, Choji T, Fujita T et al (1993) Imaging of the portacaval space. AJR Am J Roentgenol 161:329-334.
8. Meyers MA (1994) Dynamic radiology of the abdomen: Normal and pathologic anatomy. 4th ed. Springer, New York.
9. Vincent LM, Mauro MA, Mittelstaedt CA (1984) The lesser sac and gastrohepatic recess: sonographic appearance and differentiation of fluid collections. Radiology 150:515-519.
10. Dodds WJ, Foley WD, Lawson TL et al (1985) Anatomy and imaging of the lesser peritoneal sac. AJR Am J Roentgenol 144:567-575.
11. Langman J (1975) Medical Embriology. Williams and Wilkins, www.lww.com.
12. Cooper C, Jeffrey RB, Silverman PM et al (1986) Computed tomography of omental pathology. J Comput Assist Tomogr 10:62-66.
13. Rubesin SE, Levine MS, Glick SN (1986). Gastric involvement by omental cakes: radiographic findings. Gastrointest Radiol 11:223-228.
14. Halvorsen RA, Jones MA, Rice RP, Thompson WM (1982) Anterior left subphrenic abscess: characteristic plain film and CT appearance. AJR Am J Roentgenol 139:283-289.
15. Vibhakar SD, Bellon EM (1984) The bare area of the spleen: a constant CT feature of the ascitic abdomen. AJR Am J Roentgenol 141:953-955.
16. Rubenstein WA, Auh YH, Zirinsky K et al (1985) Posterior peritoneal recesses: assessment using CT. Radiology 156:461-468.
17. Love L, Demos TC, Posniak H (1985) CT of retrorenal fluid collections. AJR Am J Roentgenol 145:87-91.
18. Crass JR, Maile CW, Frick MP (1985) Catheter drainage of the left posterior subphrenic space: a reliable percutaneous approach. Gastrointest Radiol 10:397-398.
19. Rubenstein WA, Auh TH, Whalen JP, Kazem E (1983) The perihepatic spaces: computed tomographic and ultrasound imaging. Radiology 149:231-239.
20. Jeffrey RB, Federle MP, Goodman PC (1981) Computed tomography of the lesser peritoneal sac. Radiology 141:117-122.

# Abdominal Trauma

Hatem Alkadhi

Institute of Diagnostic and Interventional Radiology, University Hospital Zurich, Switzerland

## Introduction

Trauma is the fifth leading cause of death in the world and represents the leading cause of death in patients <40 years of age [1]. During the initial resuscitation period, timing and accuracy of diagnosis are essential for optimizing patient triage and therapy planning and is a major determinant of outcome of trauma patients [2]. Computed tomography (CT) represents the most important imaging modality in the evaluation of trauma patients. CT of the abdomen in trauma patients nowadays is part of a whole-body CT examination [3-6]. Recent evidence suggests that the integration of whole-body CT into early trauma care increases the chance of survival of trauma patients, most probably due to fewer missed injuries compared with X-ray and ultrasound (US) and because of a reduced delay to definitive diagnosis and patient disposition [7-9].

Regarding CT protocols in the trauma setting, it is important to consider that the trauma population usually is of young age, and therefore, the potential risk associated with radiation needs to be balanced with the benefits of the examination [10]. This holds particularly true for CT studies with multiple phases. For example, for CT evaluation of blunt splenic injury, acquisition of an arterial phase is superior to portal-venous-phase imaging for detecting pseudoaneurysms, whereas the arterial phase is inferior for detecting active bleeding and parenchymal disruption, indicating that dual-phase CT provides the best overall performance [11]. Given the increase in radiation dose in CT studies with multiple phases, it appears wise to use multiphase CT protocols in trauma patients selectively rather than routinely in order to limit the amount of radiation delivered to the patient [10]. Another option for combining the benefits of obtaining images at different contrast-medium phases yet keeping radiation doses reasonably low is the use of a split-bolus technique in which a single CT acquisition is performed for simultaneous evaluation of abdominal viscera and renal collecting system integrity, thereby limiting the number of CT series to one [12].

This chapter describes also CT imaging features of abdominal trauma to the spleen, liver, pancreas, adrenal gland, bowel, and mesentery. The chapter includes some remarks on the appropriate grading of traumatic injury in the emergency situation.

## Spleen

The spleen represents the most commonly injured abdominal organ in blunt trauma. CT is highly accurate for the diagnosis of acute traumatic splenic injury [13]. Typical findings of spleen injury are perisplenic, intrasplenic, and subcapsular hematoma; laceration, infarction, active bleeding, and contained vascular injuries such as pseudoaneurysm formation and arteriovenous fistula [14] (Fig. 1).

- Perisplenic hematoma may reflect splenic bleeding, implying capsular damage.
- Intrasplenic hematomas may be intraparenchymal or subcapsular.
- Intraparenchymal hematomas are round, ovoid, or irregular collections of blood-attenuation fluid.
- Subcapsular hematomas are crescentic peripheral collections beneath the capsular surface of the spleen [15].

## Liver

Traumatic hepatic injuries are common and can be readily diagnosed with CT. Besides liver contusions, characterized by periportal edema (or tracking) (Fig. 2a), lacerations are the most frequently identified injury in liver trauma. Lacerations are identified as predominately linear areas, often with a branching pattern, of relative hypoattenuation (Fig. 2b) [16]. Liver hematomas occur intraparenchymally, appearing as ill-defined hypoattenuating areas in the liver parenchyma; or subcapsularly, appearing as crescent-shaped hypoattenuating regions compressing the underlying liver segments. Additional important imaging findings that often guide treatment

*Diseases of the Abdomen and Pelvis 2014-2017*,
DOI: 10.1007/978-88-470-5659-6_27 


**Fig. 1 a-c.** A 66-year old female patient after blunt abdominal trauma showing multiple, rounded, high-attenuation areas in the spleen on **a** arterial-phase computed tomography (CT) images, being only faintly visualized in **b** portal-venous-phase CT. **c** Selective splenic angiogram confirms pseudoaneurysm formation (*arrowhead*) in the upper pole of the spleen. The patient underwent subsequent proximal splenic artery embolization (not shown)

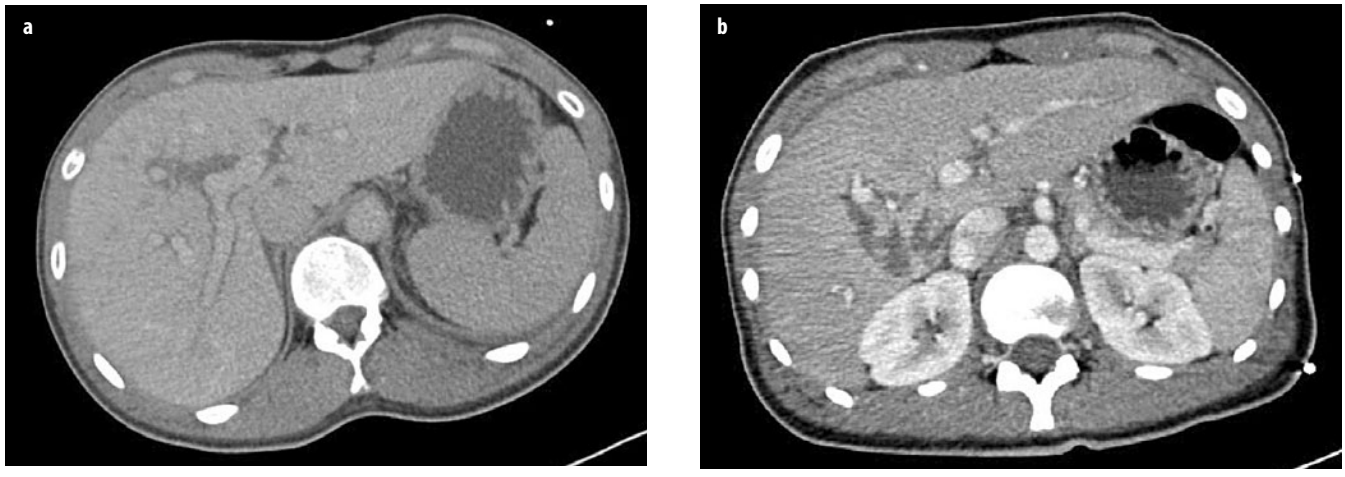


**Fig. 2 a, b.** **a** A 23-year-old female patient after blunt abdominal trauma with liver contusion predominantly affecting the right liver lobe, indicated by periportal edema (or tracking). **b** A 20-year-old female patient after blunt abdominal trauma with lacerations of liver segments I, VI, and VII

include injury to the major hepatic veins, presence of active bleeding into the peritoneal cavity, and presence of hemoperitoneum. Late complications include bile leak, biliary stricture, hepatic abscess, delayed hemorrhage, and other vascular complications [10].

## Pancreas

Blunt pancreatic trauma is an exceedingly rare but life-threatening injury with significant mortality rates. CT findings of acute pancreatic trauma may be separated into direct and indirect features [17]. Direct signs include parenchymal laceration, transection, and focal enlargement or hematoma. Lacerations, which are further classified into superficial (involving $<$50% of the parenchymal thickness) and deep (involving $>$50% of the pancreatic parenchyma), manifest as linear, irregular, low-attenuation areas within the pancreatic parenchyma (Fig. 3). Disruption of the main pancreatic duct is more likely in deep lacerations and complete transections compared with superficial lacerations [18]. Given that injury of the main pancreatic duct is the major determinant of patient outcome in pancreatic trauma, early diagnosis of pancreatic-duct injury is crucial.

## Adrenal Gland

Traumatic adrenal injury occurs in $<$5 % of cases of blunt abdominal trauma and most commonly affects the right adrenal gland [19]. The most common CT feature of adrenal injury is a round or oval hematoma expanding the gland (Fig. 4) and is present in approximately 80% of adrenal trauma cases. Average hematoma size is 2-4 cm, and mean attenuation is 55 HU. Hematomas characteristically do not enhance after contrast media administration. Due to the uncommon nature of isolated adrenal injury, if an apparent isolated injury is seen, it is critical to search for other traumatic injuries of the abdomen.

## Bowel and Mesentery

Injury to the hollow viscera and mesentery are rare, occurring in only 5% of patients who experience blunt


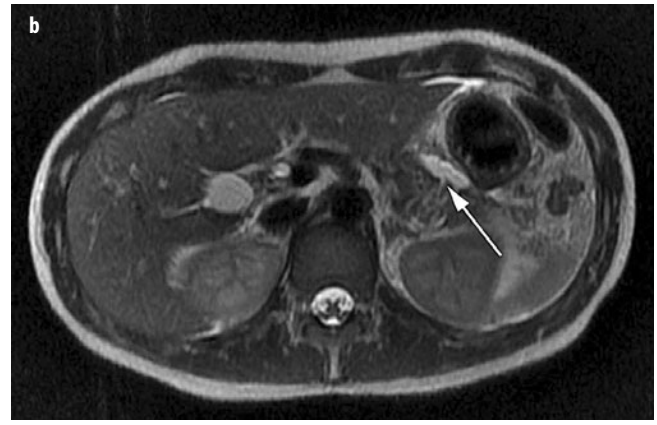


**Fig. 3 a, b.** A 21-year-old female patient after blunt abdominal trauma showing **a** deep (>50% of parenchymal thickness) transection (*arrows*) of the pancreas on computed tomography (CT). **b** Suspected main pancreatic duct injury was confirmed on T2-weighted magnetic resonance (MR) imaging, demonstrating the fracture line of the pancreas and a peripancreatic fluid collection (*arrow*)

**Fig. 4.** A 53-year-old male patient after blunt abdominal trauma showing an oval hematoma expanding the right adrenal gland (*arrow*) on computed tomography (CT) with a mean attenuation of 50 HU

abdominal trauma. At least one half of injuries to hollow viscera involve the small bowel, followed by the colon and stomach [20].

A variety of signs indicate bowel and mesenteric injury at CT, with some being sensitive and others being specific [10]. Therefore, the combination of findings increases the likelihood of a relevant injury. The specific signs of bowel injury include transection of the wall with focal discontinuity, pneumoperitoneum, and pneumoretroperitoneum.

Specific signs of mesenteric trauma include mesenteric hematoma, peritoneal extravasation of intravenous contrast-enhanced blood (Fig. 5), and abrupt termination or irregularity of the walls of mesenteric vessels. The more sensitive CT signs of bowel trauma include focal wall thickening, abnormal bowel wall enhancement, ill-defined stranding of the mesentery, and free intraperitoneal fluid. Extraluminal gas is highly suggestive for bowel perforation, with a variable amount of free gas [21].



**Fig. 5 a, b.** A 19-year-old male patient with blunt abdominal trauma showing intraperitoneal extravasation of intravenous contrast-enhanced blood and extensive hemoperitoneum due to traumatic injury to the serosal layer of the ileum and mesenteric injury with traumatic transection of a segmental branch of the superior mesenteric artery

## Traumatic Injury Grading

Fast, unequivocal communication of imaging findings by the attending radiologist is crucial in the emergency situation. Grading systems in clinical medicine should improve clarity and efficiency of communication, structuring the description of the individual patient to aid standardization of assessment, reporting, and management. This includes traumatic injury grading to the viscera detected with CT. The traditionally used grading systems in trauma patients were developed by the American Association for the Surgery of Trauma (AAST) and include various organs, such as spleen and liver. However, it must be kept in mind that matching CT imaging findings with AAST categories may be inaccurate, because the latter grading system was developed from and is reflective of findings at laparotomy [14]. Findings from CT, such as active bleeding or contained vascular lesions, which potentially are not detected during surgery, are not represented in the AAST grading system. In addition, the AAST system has repetitively shown a limited correlation with the outcome of trauma patients. Thus, other scoring systems have been proposed for various organs [22], incorporating additional findings seen at CT. Regardless of what grading scheme is used, it remains critical for emergency radiologists to use a language for reporting with which clinicians are familiar and to include in their report findings that are determinants of therapeutic interventions and surgery.

## References


1. World Health Organization (2008) WHO Statistics. http://www.who.int/whosis/whostat/2008/en/index.htlm. Accessed December 23, 2010. WHO Press, Geneva.
2. van Vugt R, Kool DR, Deunk J, Edwards MJ (2012) Effects on mortality, treatment, and time management as a result of routine use of total body computed tomography in blunt high-energy trauma patients. J Trauma Acute Care Surg 72:553-559.
3. Leidner B, Adiels M, Aspelin P et al (1998) Standardized CT examination of the multitraumatized patient. European Radiology 8:1630-1638.
4. Ptak T (2001) Experience with a continuous, single-pass whole-body multidetector CT protocol for trauma: the three-minute multiple trauma CT scan. Emergency Radiology 8:250-256.
5. Leidner B (2001) Standardized whole-body computed tomography as a screening tool in blunt multitrauma patients. Emergency Radiology 8:20-28.
6. Linsenmaier U, Wirth S, Reiser M, Korner M (2008) Diagnosis and classification of pancreatic and duodenal injuries in emergency radiology. Radiographics 28:1591-1602.
7. Sierink JC, Saltzherr TP, Reitsma JB (2012) Systematic review and meta-analysis of immediate total-body computed tomography compared with selective radiological imaging of injured patients. Br J Surg 99(Suppl 1):52-58.
8. Wurmb TE, Fruhwald P, Hopfner W et al (2009) Whole-body multislice computed tomography as the first line diagnostic tool in patients with multiple injuries: the focus on time. J Trauma 66:658-665.
9. Linsenmaier U, Reiser M (2009) Multislice computed tomography in emergency radiology. Radiologe 49:479-480.
10. Soto JA, Anderson SW (2012) Multidetector CT of blunt abdominal trauma. Radiology 265:678-693.
11. Boscak AR, Shanmuganathan K, Mirvis SE et al (2013) Optimizing trauma multidetector CT protocol for blunt splenic injury: need for arterial and portal venous phase scans. Radiology 268:79-88.
12. Loupatatzis C, Schindera S, Gralla J et al (2008) Whole-body computed tomography for multiple traumas using a triphasic injection protocol. Eur Radiol 18:1206-1214.
13. Marmery H, Shanmuganathan K, Mirvis SE et al (2008) Correlation of multidetector CT findings with splenic arteriography and surgery: prospective study in 392 patients. J Am Coll Surg 206:685-693.
14. Boscak A, Shanmuganathan K (2012) Splenic trauma: what is new? Radiol Clin North Am 50:105-122.
15. Karlo CA, Stolzmann P, Do RK, Alkadhi H (2013) Computed tomography of the spleen: how to interpret the hypodense lesion. Insights Imaging 4:65-76.
16. Yoon W, Jeong YY, Kim JK et al (2005) CT in blunt liver trauma. Radiographics 25:87-104.
17. Rekhi S, Anderson SW, Rhea JT, Soto JA (2010) Imaging of blunt pancreatic trauma. Emerg Radiol 17:13-19.
18. Wong YC, Wang LJ, Lin BC et al (1997) CT grading of blunt pancreatic injuries: prediction of ductal disruption and surgical correlation. J Comput Assist Tomogr 21:246-250.
19. To'o KJ, Duddalwar VA (2012) Imaging of traumatic adrenal injury. Emerg Radiol 19:499-503.
20. Kim HC, Shin HC, Park SJ et al (2004) Traumatic bowel perforation: analysis of CT findings according to the perforation site and the elapsed time since accident. Clin Imaging 28:334-339.
21. LeBedis CA, Anderson SW, Soto JA (2012) CT imaging of blunt traumatic bowel and mesenteric injuries. Radiol Clin North Am 50:123-136.
22. Marmery H, Shanmuganathan K, Alexander MT, Mirvis SE (2007) Optimization of selection for nonoperative management of blunt splenic injury: comparison of MDCT grading systems. AJR Am J Roentgenol 189:1421-1427.

# Congenital and Acquired Pathologies of the Pediatric Gastrointestinal Tract

Alan Daneman[1], Simon G.F. Robben[2]

[1] Radiology, University of Toronto and The Hospital for Sick Children, Toronto, Ontario, Canada
[2] Department of Radiology, Maastricht University Medical Centre. Maastricht, The Netherlands

## Introduction

The diagnosis of congenital and acquired pathologies of the gastrointestinal (GI) tract in children is quite challenging, and this is an understatement for many reasons. First, it involves a large number of diseases, many of which are not well known by general radiologists. Second, young children are not capable of verbal communication (although crying is a way of expressing discomfort, the authors do not consider this as an optimal means of communication). From this perspective, pediatric radiology has much in common with veterinary medicine. Third, children may not be as cooperative as one would desire, and the same goes for the parents who are often overanxious and demanding. Finally, pediatricians have the tendency to upgrade the meaning of "emergency".

There are many ways to cope with these challenges. Perhaps the best way is to correlate complaints and symptoms with the age of the child because pediatric diseases are often age-dependent:

- Neonates (0-1 month of age): atresias, malrotation and midgut volulus, Hirschsprung's disease, meconium ileus, meconium plug syndrome, meconium peritonitis, and necrotizing enterocolitis
- Infants and preschool children(1 month to 5 years): gastroenteritis, intussusception, malrotation and midgut volvulus, appendicitis, abdominal malignancies, hemolytic uremic syndrome (HUS), Meckel's diverticulum, and Henoch-Schönlein purpura (HSP)
- Children and adolescents (6-18 years): appendicitis, inflammatory bowel disease (IBD), ovarian torsion, pancreatitis (hereditary or secondary to congenital abnormalities), distal intestinal obstruction syndrome, Meckel's diverticulum, and HSP.

Another important way to cope with the above-mentioned challenges is imaging. Many diseases of the GI tract can be diagnosed with a combination of ultrasonography (US) and conventional radiography (including contrast studies). Magnetic resonance imaging (MRI) and computed tomography (CT) are considered problem solvers.

This chapter provides a brief overview of pediatric GI pathologies, from the esophagus to the anus, with emphasis on US. Also, special attention is paid to neonatal obstruction as a separate entity.

## Liver, Biliary System, and Pancreas

These subjects are discussed separately in the Kangaroo section of this syllabus (pp. 271-278).

## Esophagus and Gastroesophageal Junction

Pathology of the esophagus includes esophageal atresia, gastroesophageal reflux disease (GERD), duplication cysts, achalasia, foreign bodies, and narrowing by vascular rings. Initial examination is the upper GI series; however, the cervical esophagus can be visualized on conventional US in all children as an oval structure between trachea and vertebral column [1]. It can be seen to the best advantage using the thyroid gland as an acoustic window and rotating the head 45° to the opposite side [2]. The esophageal wall is recognized by its gut signature, with five clearly defined layers. Mean wall thickness is 2.8 (range 2.2-3.8) mm at all ages.

In patients with esophageal atresia without a tracheoesophageal fistula, there is no gas in the abdomen; therefore, the abdominal radiograph is useless for evaluating the digestive tract. The abdomen can be examined with US to reveal additional abnormalities.

The diagnosis of GERD is made by upper GI series and/or by PH-metry. However, the gastroesophageal junction can also be visualized with US in 87-95% of children with suspected GERD, and reflux of gastric content into the esophagus can be demonstrated [3, 4]. A threshold of three reflux periods within 10 min allows for a sensitivity of 82% and a specificity of 85% for GERD [3]. Sensitivity can be increased to 98% using color-Doppler US [5]. However, in premature infants, sensitivity is 38% and specificity 100% when compared with 24-h PH-metry [6].

*Diseases of the Abdomen and Pelvis 2014-2017*,
DOI: 10.1007/978-88-470-5659-6_28 

Moreover US can evaluate the postoperative situation after a fundoplication as well as gastric emptying, another important contributing factor to the pathogenesis of GERD.

## Stomach

### Gastric Duplication Cysts

The stomach is the second most common location of duplication cysts. A detailed discussion on duplication cysts is found in this chapter in the paragraph on small bowel.

### Gastric Volvulus

Gastric volvulus (mesenteroaxial and organoaxial) in children is rare. In the organoaxial type (more common), rotation is along the longitudinal axis of the stomach. In the mesenteroaxial type, the stomach twists along the axis of its mesentery and flips into an inverted position. Volvulus is facilitated by poor fixation by gastric ligaments and gastroperitoneal attachments. It is associated with diaphragmatic herniation, eventration, asplenia/polysplenia syndrome, and hypermobility of the spleen. Typical presentation is vomiting with epigastric distention. Upper GI series demonstrate the abnormal position of the stomach (e.g., antrum and pylorus above the fundus, or greater curvature above minor curvature, together with beaking at points of twist). US signs are gastric dilatation caused by gastric outlet obstruction and an abnormal position of the antrum in the mesenteroaxial type; ventral and superior to the fundus [7, 8].

### Gastric Wall Thickening

- Gastritis and peptic ulcer disease are uncommon in children. US shows a small lumen and a stratified wall thickening with hyperemia. In severe cases (i.e., accompanied by deep ulcer disease), stratification may become less distinct. When present, the ulcer is difficult to visualize. Eosinophilic gastritis is a rare disorder often involving the antropyloric region, and may even cause gastric outlet obstruction simulating hypertrophic pyloric stenosis. Stomach wall stratification is usually preserved. Detection of multifocal small-bowel involvement is highly suggestive of the diagnosis.
- Foveolar hyperplasia consists of a polypoid thickening of the mucosal layer. It may be seen after longstanding prostaglandin therapy, hypertrophic gastropathy, and cow's milk allergy, or it may be idiopathic. It may simulate pyloric hypertrophy, but on closer US examination, the obstruction will appear to be caused by thickened mucosa instead of thickened muscle.
- Other rare causes of gastric wall thickening and gastric outlet obstruction include pylorospasm, food allergy, chronic granulomatous disease, hyperlipidemia, chemotherapy, duplication cysts, ectopic pancreas, benign and malignant tumors, and bezoars. In infants, curding milk in the fundus of the stomach may mimic a solid tumor.

### Hypertrophic Pyloric Stenosis

Infantile hypertrophic pyloric stenosis (IHPS) [9] is a condition of unknown etiology. It affects young infants aged 2-8 weeks in whom the antropyloric portion of the stomach becomes abnormally thickened and causes obstruction to gastric emptying. The male-to-female ratio is approximately 4:1. Typically, infants with IHPS are clinically normal at birth; during the first few weeks of postnatal life, they develop nonbilious "projectile" vomiting that leads to weight loss, dehydration, hypochloremic alkalosis, and eventually to death. Surgical treatment is curative. In virtually all such patients, US is highly accurate in facilitating the diagnosis. It is important that the radiologist understand anatomic changes of the pyloric channel in affected infants as reflected by US, which shows pyloric muscle hypertrophy to a variable degree during the examination and also a certain amount of thickening of the mucosa (Fig. 1). A muscle thickness ⩾3 mm throughout the examination is considered to be diagnostic of IHPS, although some authors state that the overall morphologic and dynamic impression during the examination are as important, including length of the pyloric canal, relaxation, and peristalsis. The examination can be performed in a very short time, with an accuracy approaching 100%.

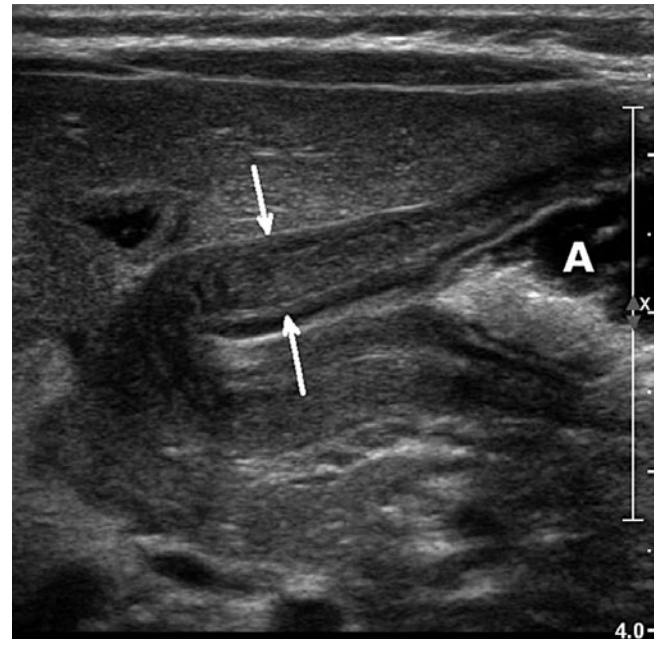


**Fig. 1.** Hypertrophic pyloric stenosis. Muscle thickening is indicated by *arrows*. *A* antrum of the stomach with retained fluid

## Small Bowel

Conventional radiographs, upper GI series, and US are the initial imaging modalities in children with abdominal pain or obstruction [3]. MR enterography may serve as a problem solver in older children. The most important additional value of US over conventional abdominal radiographs in these children is the capability to visualize peristalsis, vascularity, bowel wall characteristics, dilatation of fluid-filled loops, and extraintestinal abnormalities, e.g., ascites and other fluids. The jejunum and ileum can be distinguished from the colon based on its anatomical location, caliber, contents, folds, and peristalsis.

*Anatomical Location.* The colon has a peripheral location in which the ascending and descending colon lie dorsally in both flanks and the transverse colon is located ventrally in the upper abdomen. The sigmoid colon traverses the left psoas muscle and courses into the pelvis. In contrast, the small bowel has a more central position.

*Caliber.* The diameter of the small bowel is small, and that of the large bowel is relatively large (explains the nomenclature).

*Contents*. The small bowel is either empty or filled with liquid contents and little air, whereas the colon is generally filled with gas-filled bulky stools.

*Folds*. Folds in the jejunum are more numerous, thinner, and closer together than the ileal folds. In the terminal ileum, the mucosa may be thickened due to hyperplasia of lymphoid tissue. The colon is recognized by its haustrations. Infants have little to no haustrations.

*Peristalsis*. The small bowel is continuously moving due to peristaltic waves, whereas the colon shows sparse movements. In general, thickened small-bowel loops show decreased peristalsis and contain little air and are therefore easily visualized and measured. At least three patterns can be distinguished [10]:

- Stratified thickening of small bowel is found in infectious ileitis, advanced appendicitis, early Crohn's disease, and graft-versus-host disease
- Nonstratified thickening of the small bowel is found in HSP, advanced Crohn's disease, tuberculous ileitis, protein-loosing enteropathy, hereditary angioedema, ischemia, celiac disease, Burkitt lymphoma, Kawasaki's disease, and viral enteritis
- Nonstratified thickening with hyperplastic valvular folds is found in viral (and sometimes bacterial) lymphoid hyperplasia and Yersinia ileitis.

### Malrotation and Midgut Volvulus

This entity is discussed separately in the Kangaroo section of this syllabus (pp. 279-288).

### Crohn's Disease

Crohn's disease is a chronic IBD characterized by its granulomatous component, its transmural inflammation, its tendency to affect the surrounding tissues, and its formation of fistula and sinus tracts. The exact cause is still unknown. It can occur in children from the age of 5 years, but most often, adolescents and young adults are affected. The initial course is insidious, with recurrent diarrhea, abdominal pain, and weight loss. Also, atypical features such as growth failure, malnutrition, anorexia nervosa, amenorrhea, arthritis, and cutaneous and ocular manifestations may be present. Levels of calprotectin in stools are increased. Calprotectin is a neutrophil protein that is released from activated leukocytes [11].

Crohn's disease can affect the entire digestive tract but has a predilection for the terminal ileum. Initially, the inflammation starts as aphthoid ulcers in the mucosa and progresses to a transmural inflammation that eventually also involves the surrounding fat. Finally the inflammation may proceed to other surrounding structures, such as skin, other bowel loops, and urine bladder, forming sinus tracts and fistula and even abscesses. Diagnosis depends on US and MR enterography. US is of great value in diagnosis and follow-up in children with IBD [12, 13], with a sensitivity of 75-88% and a specificity of 82-93% [14-16]. Faure even reports a sensitivity of 100% for terminal ileitis in Crohn's disease [14]. On US, initially, bowel wall stratification is preserved. In advanced disease, stratification is lost, and the affected bowel loop is surrounded by thickened, inflamed, echogenic fat, more or less isolated from the other bowel loops (Fig. 2). Close attention should be paid to small hypoechoic spurs that extend into the echogenic fat. They probably represent an insidious sinus tract and predict future fistula or abscess formation.

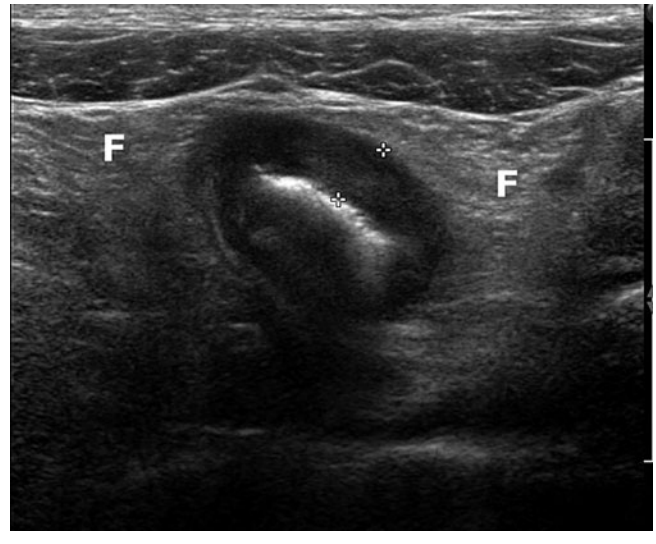


**Fig. 2.** Advanced Crohn's disease with loss of stratification and with wall thickening (5 mm, between calipers) and thickened surrounding echogenic fat (*F*)

### Intestinal Polyps

Intestinal polyps in the small bowel are usually hamartomatous polyps in patients with Peutz-Jeghers syndrome. They occur more often in the jejunum than in the ileum. US is able to detect moderate and large polyps and therefore may serve as a screening method for detecting uncomplicated polyps. However, one should take into account the high specificity but relatively low sensitivity. US is valuable in diagnosing complications associated with small-bowel polyps, e.g., intussusceptions [3]. One must be aware that specific particles within stools (e.g., undigested food, foreign bodies) may mimic polyps.

### Henoch-Schönlein Purpura

Henoch-Schönlein Purpura (HSP) is a systemic vasculitis of unknown cause involving the small vessels of the skin, gut, and kidneys. Mean age of presentation is approximately between 3 and 8 years, with a slight male predominance [17-19]. Patients develop a typical skin rash and intestinal complaints such as abdominal pain, nausea and vomiting, and melena or bloody stools. Proteinuria, hematuria, and arthralgia are additional findings. Abdominal complaints are present in two thirds of the patients and may be severe. Intestinal symptoms may precede the skin rash, and therefore, the radiologist may be the first to suggest the diagnosis. The small bowel is affected, including the duodenum [20]. Involvement is frequently multifocal, with skipped lesions. US findings include symmetrical thickening of the bowel wall up to 11 mm, loss of stratification, intramural hematoma, enlargement and smoothening of folds, hypoperistalsis, hyperemia, lymphadenopathy, and often, some clear peritoneal fluid. These US findings can subside within several days and exacerbations and remissions may occur. Sensitivity, specificity, and positive (PPV) and negative (NPV) predictive value of US for gastrointestinal involvement of HSP is 83%, 100%, 100%, and 54%, respectively [21]. Complications include pathological small-bowel intussusception (PSBI), bleeding, and rarely, necrosis and perforation, pancreatitis, cholecystitis, and appendicitis. It is a self-limiting disease, although persisting proteinuria due to nephritis is a well-known complication.

#### *Ascaris Lumbricoides*

*Ascaris lumbricoides* is the most common helminthic infestation world wide, mainly affecting children and young adults. Many children are asymptomatic or have minor nonspecific abdominal complaints. US images are quite characteristic depending on the image plane: in the longitudinal plane, the worms appear as parallel echogenic lines; in transverse images, they appear as round dots inside the lumen. Fluid administration prior to the examination improves visualization of the worms. Differentiation with intraluminal lines may be difficult, and worm movement can aid in differentiation; tubes and lines do not move by themselves. *Ascaris* residing in the small intestines may migrate into the biliary system, pancreatic duct, and appendix, causing symptoms of biliary stones, pancreatitis, or appendicitis [22].

### Meckel's Diverticulum, Ileocolic Intussusception, and Necrotizing Enterocolitis

These entities are also discussed separately in the Kangaroo section of this syllabus (pp. 279-288).

### Intestinal Duplication Cysts

Intestinal duplication cysts can occur anywhere along the alimentary tract, but the most common location is the ileum. Therefore, these cysts are discussed in this small-bowel section. Duplication cysts are spherical or tubular masses adherent to the GI tract, which sometimes communicate with it [23-25]. They are lined with intestinal epithelium, and there is smooth muscle within the wall. In 15-20% of cases, the cyst contains gastric mucosa that may cause hemorrhages. The most common site is the ileum, followed by the stomach. Most patients present within the first year of life, with symptoms including GI obstruction; less common presentations include a palpable mass, intussusception, hemorrhage, and abdominal distension. US and MRI readily appreciate the cystic nature of duplication cysts. The content is often anechoic but may contain debris after hemorrhage or due to mucoid material. Rarely, the cyst appears completely hyperechoic after hemorrhage. Two US signs are virtually diagnostic of a duplication cyst: first is the double-layer demonstration of its wall, consisting of echogenic mucosa and hypoechoic muscularis propria, the so-called "gut signature" (Fig. 3). Second is the demonstration of peristalsis in the cyst. Moreover, meticulous US examination may identify the primary bowel loop from which the cyst originates; the cyst shares the muscularis propria and serosa with the primary bowel loop. Ovarian, urachus and mesenteric cysts and lymphatic malformations can mimic duplication cysts.

### Benign Small-Bowel Intussusception

Benign small-bowel intussusception (BSBI) is a recently described entity and differs from the classic symptomatic ileocolic intussusception; BSBI occurs predominantly in the right lower quadrant or periumbilical region, has a smaller diameter than pathological (ileocolic) intussusceptions (mean 1.4 cm versus 2.5 cm), a small length (mean 2.5 cm), a thinner outer rim, and does not contain mesenteric lymph nodes (Fig. 4) [26, 27]; moreover, peristalsis in the intussuscepted loop persists, in contrast with ileocolic intussusceptions. Often, BSBI is an incidental finding, but it occurs with increased frequency and number in coeliac disease. In general, BSBI does not need immediate reduction because of its spontaneously resolving nature.


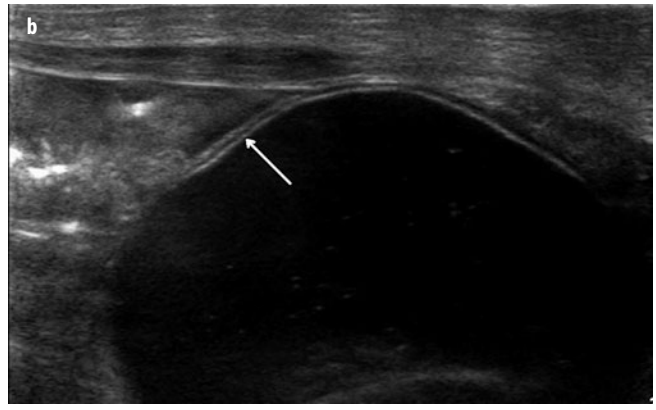


**Fig. 3 a, b.** Duplication cyst of ileum. **a** Prenatal magnetic resonance imaging (MRI) shows a cyst (*C*) in right abdomen. No other abnormalities are present. **b** Postnatal ultrasound (US) image shows gut signature of the cyst wall (*arrow*); during examination, intrinsic peristalsis of the cyst was seen

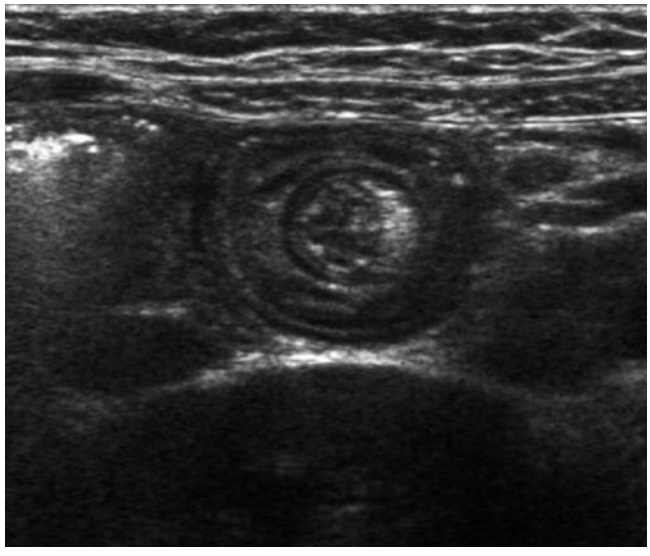

**Fig. 4.** Benign small-bowel intussusception in a patient without abdominal pain. Diameter 1.4 cm, persisting peristalsis, and no lymph nodes within the intussusception. The small central echogenic crescent is mesenteric fat

## Appendix

This entity is also discussed separately in the Kangaroo section of this syllabus (pp. 279-288).

## Large Bowel

The differences between normal small bowel and large bowel are described in the paragraph on the small bowel.

Three US patterns can be distinguished [28]:

- Stratified thickening is found in infectious colitis, advanced appendicitis, and IBD (both ulcerative colitis and Crohn's disease)
- Nonstratified thickening with loss of haustral folds is found in early HUS and advanced Crohn's disease
- Nonstratified imaging with preservation of normal haustral fold length is found in pseudomembranous colitis and neutropenic colitis (typhlitis).

### Crohn's Disease

Crohn's disease is also discussed in the paragraph describing the small bowel in this chapter. Right-sided colonic involvement is most common. In contrast to ulcerative colitis, Crohn's disease will eventually lead to loss of stratification and pericolic fat proliferation. Because of its anatomical location (descending and ascending colon), the pericolic inflammation can extend into the retroperitoneal space and cause hydronephrosis. However, in early Crohn's disease, these features are not yet present, and differentiation based on imaging findings is difficult, even impossible, when there is pancolitis without involvement of the terminal ileum.

### Ulcerative Colitis

Ulcerative colitis is a noninfectious inflammation with diffuse, uniform mucosal inflammation with involvement of the mucosa and superficial submucosa. It is limited to the colon. Onset may be insidious, with abdominal pain and recurrent diarrhea and weight loss. Nonintestinal symptoms may be present, such as growth failure, mal-

nutrition, amenorrhea, arthritis, and cutaneous and ocular manifestations. Rectal bleeding is more common in ulcerative colitis than in Crohn's disease. Ulcerative colitis begins in the rectum and advances proximally without skip lesions. Pancolitis is frequent in children. On US, mural stratification is clearly visible because the inflammation remains superficial. The inflammation causes an increased muscle tone, and the lumen is collapsed.

#### Infectious Colitis (*Salmonella, Campylobacter, Shigella, Escherichia coli, Yersinia*)

Infectious colitis has a similar US pattern as ulcerative colitis, with preserved stratification and normal pericolic fat. In contrast with ulcerative colitis, colonic involvement is often right sided, and in more than one third of patients, distal ileum/ileocecal valves are involved. Otherwise, the diagnosis of infectious colitis depends on stool and blood cultures and analysis.

#### Neutropenic Enterocolitis (Typhlitis)

Neutropenic enterocolitis is a severe infectious colitis in children with neutropenia. Mainly, the cecum and ascending colon are involved, but the small bowel can be involved also. The pathogenesis is complex and involves mucosal damage, compromised immunity, bacterial invasion, distensibility, and vascularization [29]. Also, clostridial toxins are proposed as causative agents. It is often found in children with leukemia during chemotherapy. Symptoms are fever, diarrhea, and right lower quadrant pain. US demonstrates severe colonic wall thickening with loss of stratification, a redundant inner layer of increased echogenicity, and intense mural hypervascularity [30-32].

#### Pseudomembranous Colitis

Pseudomembranous colitis is usually caused by overgrowth of *Clostridium difficile* (together with its toxin) in patients on antibiotic therapy. Symptoms include abdominal pain, watery diarrhea, fever, and leucocytosis after recent use of antibiotics. Pseudomembranes originate from deep crypt abscesses that erupt to the surface and are formed by coalescence of mucus, fibrin, epithelial cell debris, inflammatory cells, and exudate. Depending on its composition, the pseudomembrane can be of varying thickness and echogenicity. Haustrations are preserved and not shortened, as in many other types of colitis. The pattern of swollen preserved haustrae is known as the accordion sign.

#### Hemolytic Uremic Syndrome

Hemolytic Uremic Syndrome (HUS) is a triad of microangiopathic hemolytic anemia, thrombocytopenia, and acute renal failure. It is thought to be caused by systemic spread of bacterial toxins, e.g., Shiga-toxin-producing *E. coli* (STEC). Most cases occur in children younger than 5 years of age. US signs include considerable thickening of the colon wall and increased echogenicity of the renal parenchyma. The thickened wall shows loss of stratification and is strikingly avascular on color-Doppler US, especially in the prodromal phase [33]. Because the colitis often precedes the full-blown clinical presentation of HUS, the radiologist may be the first to suggest the diagnosis in a child with colitis and bloody diarrhea.

#### Juvenile Polyps

Juvenile polyps are the most common neoplasms in the large bowel in children. The sigmoid and rectum are preferential locations. The presenting symptom is rectal bleeding in >90% of patients; occasionally, a colocolic intussusception is the first manifestation. US will demonstrate a pedunculated spherical nodule with a diameter varying from 10 to 25 mm containing multiple 2- to 3-mm cysts. Administration of fluid within the bowel lumen will greatly improve visualization of these polyps; however, the assessment of rectal polyps is still unreliable. Specific particles within the stools may mimic polyps (e.g., undigested food, pellets of stool).

#### Epiploic Appendagitis

Epiploic appendagitis is a localized inflammation caused by torsion and ischemia of an epiploic appendage. These are small, peritoneal-covered fat tags at the serosal or antimesenteric border of the colon with a single artery and vein in the pedicle. Epiploic appendagitis is rare in children, but its recognition is important to prevent surgery in this self-limiting disease. It causes localized pain that will direct the sonographer toward the right site. The inflamed appendage is seen on US as a hyperechoic mass sometimes surrounded by thickened hyperechoic pericolic fat [34, 35]. In obese children, it is better appreciated with CT or MRI.

#### Meconium Calcifications

Meconium calcifications can be seen in patients with anal atresia and large rectourethral or rectovesical fistulae [36]. Apparently, the mixture of meconium and urine causes the meconium to calcify. This causes a specific pattern of discrete punctate flecks within the course of the colon that can be appreciated on abdominal radiographs and US. It should not be confused with meconium peritonitis, in which the calcifications are linear and plaque like along the peritoneum.

### Rectum

The rectum can be easily visualized by US when the bladder is filled with urine. Several studies measured the transverse diameter of the rectum with US. This measurement seems to be a reliable tool by which to identify rectal impaction and may replace digital rectal examination; all children with rectal impaction on digital examination had

a rectal diameter >30 mm [37]. Moreover, several studies show that in children with constipation, the mean diameter of the rectum is significantly larger than in normal children. In a series of 225 children, the mean rectal diameter in normal children was 32 mm [standard deviation (SD) 8.2] and in children with constipation 43 mm (SD 9.7) [38]. To overcome the problem of age dependency of rectal diameter in normal children, Bijos et al. proposed the rectopelvic ratio: i.e., the ratio of the rectal diameter (US) to the distance between the anterior superior iliac spines [38]. When the ratio is >0.189, the sensitivity for rectal impaction is 88% compared with proctoscopy. Rectal diameter can also be used to monitor therapy.

## Anus

### Anal Atresia

Anal atresia is a relatively frequent congenital abnormality in which the anus is absent and a rectoperineal, rectovestibular, rectovaginal, rectourethral, or rectovesical fistula may be identified in almost all cases. The "fistula" demonstrates an internal sphincter, and therefore, some prefer the terms ectopic anus or anorectal malformation instead of anal atresia. During preoperative evaluation, it is important to assess the type of anal atresia: high type (distal rectal pouch above the puborectal sling), intermediate type (at the sling), or low type (through the sling). Transperineal US is a good diagnostic modality for defining the type of anal atresia by measuring the distance between the rectal pouch and the perineum (P-P distance). A P-P threshold value of 15 mm discriminates low from intermediate and high types, with a sensitivity of 100% and a specificity of 86% [39]. Moreover, in 82% of patients with high type, the internal fistula can be correctly identified [40]. Transperineal sonography is also a useful method for differentiating between an anteriorly displaced anus, which is a normal anatomical variant, and a low-type imperforate anus with perineal fistula, which is a pathological developmental abnormality requiring surgical repair [41].

### Perianal Abscesses

In adults, transperineal US is a simple, painless, cost-effective, and real-time method by which to detect and classify perianal fluid collections, abscesses, fistulas, and sinus tracts [42-44]. These data probably may be extrapolated to the pediatric population, e.g., children with Crohn's disease, sometimes obviating the need for MRI.

## Neonatal Bowel Obstruction

Many neonatal bowel obstructions are caused by diseases already mentioned in previous paragraphs, e.g., duplication cysts, malrotation or volvulus, necrotizing enterocolitis, anal atresia, and pyloric hypertrophy. Additional causes include various types of atresia, annular pancreas, meconium ileus, meconium peritonitis, Hirschsprung's disease, and meconium plug syndrome. These diseases are diagnosed by conventional abdominal radiographs and/or conventional contrast studies, but US may be of additional value [45].

### Atresias

Atresias are congenital interruptions of the lumen of the alimentary canal caused by a failure of canalization during organogenesis or by a prenatal vascular event [46]. It results in dilatation proximal to the atresia and complete collapse distal to the atretic segment. The clinical and radiographic presentation is typical, but US may be used to demonstrate accompanying pathology:

- Exclusion of associated malrotation in cases of high obstruction
- Evaluation of colon and rectum in cases of high obstruction; single atresias are associated with a normal-sized colon, whereas multiple atresias are associated with microcolon
- Evaluation of associated malformations of heart, kidneys, and biliary tree
- Demonstration of extrinsic duodenal compression in cases of high obstruction, e.g., duplication cysts, preduodenal portal vein, annular pancreas
- Demonstration of signs of prenatal meconium peritonitis as a cause of small-bowel atresia (meconium cysts, small peritoneal or scrotal calcifications)
- Differentiation from meconium ileus by confirming the fluid content of the dilated bowel loops; in meconium ileus, contents consist of thick, echogenic meconium [45, 47] (see paragraph on meconium ileus).

### Inspissated Milk Syndrome (Milk Curd Syndrome)

This rare disease occurs in premature infants and usually results from high-caloric or concentrated powdered milk formula or expressed, fortified breast milk [48, 49]. Milk curds may also occur proximal to congenital or acquired stenosis. The inspissated milk curds in distal ileum and proximal colon obstruct the bowel. Compared with other neonatal obstruction syndromes, it has a somewhat delayed onset of symptoms. Because milk curds show little adherence to the bowel wall, air or fluid can be seen between the curds and the bowel wall on US or radiographs. The air between the curd and bowel wall may even simulate pneumatosis intestinalis. US depicts the milk curds as hyperechoic, spherical structures within the bowel loops, sometimes with a small rim of fluid surrounding it. Recognizing this entity is important, because therapeutic hypertonic iodine contrast enema may be used in these infants [50].

### Meconium Plug Syndrome

Meconium plug syndrome is best compared with neonatal obstipation. Most often, premature infants are affected

and present with a distended abdomen and failure to pass meconium without signs of peritonitis. The abdominal radiograph shows distal obstruction, with moderate dilatation of small-bowel loops, no wall thickening, and often no air-fluid levels. US can exclude meconium ileus and malrotation by visualizing hyperechoic meconium in the colon and confirming a normal position of the mesenteric vessels, cecum, and D3 duodenum segment. An enema with iodine contrast is diagnostic and therapeutic because of its laxative properties.

#### Meconium Ileus

Meconium ileus is a congenital intestinal obstruction caused by abnormally thick meconium and occurs in approximately 10-20% of newborns with cystic fibrosis (CF). A child with meconium ileus has CF until proven otherwise. Because of the CF, the meconium is very tenacious and adheres to the bowel wall. The relatively weak contractions of the small bowel are not capable of transporting the meconium distally, and obstruction is usually located in the distal ileum. Therefore, the colon is unused and remains a microcolon. Prenatal complications caused by antenatal obstruction are volvulus, atresia, and meconium peritonitis (antenatal perforation). Abdominal radiographs show nonspecific, lower-abdominal obstruction but less dilatation and air-fluid levels than in atresias. US reveals a microcolon (mean diameter 4 mm) and wide proximal small-bowel loops. The most proximal jejunal loops are wide but usually show peristalsis and are filled with fluid. However, more distally, the jejunal loops are wide but without peristalsis, and the content becomes more hyperechoic and heterogeneous. Finally, the distal ileum is filled with small, hyperechoic pellets of impacted meconium. The tenacious meconium creates a pseudothickening of the small-bowel wall, and small collections of air are trapped in the meconium. An important difference from small-bowel atresia is the echogenicity of the bowel content: hypoechoic in atresia, and hyperechoic in meconium ileus. In atresia, the bowel content is also less inspissated [45, 47].

#### Meconium Peritonitis

Meconium peritonitis is caused by antenatal gastrointestinal perforation, leading to a sterile peritonitis. This often results in peritoneal, and sometimes scrotal, calcifications. Approximately 50% of patients have CF, in contrast with meconium ileus, in which virtually 100% of patients have CF. Bowel perforation is secondary to intestinal obstruction (meconium ileus, atresia, or volvulus) or is idiopathic. Sometimes, the digestive tract remains normally patent, and only peritoneal calcifications are silent witnesses of antenatal perforation. There are several types of meconium peritonitis: generalized, cystic, and fibroadhesive. Meconium pseudocyst is a manifestation of the cystic type of meconium peritonitis that results from in utero bowel perforation. The spilled meconium is encapsulated and forms a large meconium-filled (hyperechoic) cyst lined by a thick inflammatory and fibrotic membrane, often containing calcifications. Postnatally, the perforation may still communicate with the cyst. If the perforation occurs when the processus vaginalis is still patent, meconium enters the tunica vaginalis and causes meconium periorchitis [23, 25, 51].

#### Hirschsprung's Disease

Hirschsprung's disease is caused by an absence of ganglion cells, resulting in abnormal motility and lack of relaxation. The length of the aganglionic segment is variable, but the distal end of the intestinal tract is always affected. In a small number of patients, the entire colon, even ileum and jejunum, is involved. Diagnosis depends on contrast enema, rectal manometry, and biopsy.

## Conclusion

Children are not small adults; they differ in anatomy, physiology, and psychology. Moreover, there is a great variety of diseases, many of which are uncommon in adults. Knowledge of these differences will result in choosing the most appropriate imaging studies and preventing any unnecessary delay in diagnosing pediatric GI diseases.

## References

1. Palabiyik FB, Bayramoglu S, Guner NT et al (2012) Use of sonography for evaluation of the cervical and thoracic esophagus in children. J Ultrasound Med 31:1375-1379.
2. Mateen MA, Kaffes AJ, Sriram PV et al (2006) Modified technique of high-resolution ultrasonography of the normal cervical esophagus. J Gastroenterol Hepatol 21:1660-1663.
3. Couture A, Baud C, Ferran J et al (2008) Gastrointestinal tract sonography in fetuses and children. Springer, Berlin, Heidelberg.
4. Westra SJ, Derkx HH, Taminiau JA (1994) Symptomatic gastroesophageal reflux: diagnosis with ultrasound. J Pediatr Gastroenterol Nutr 19:58-64.
5. Farina R, Pennisi F, La Rosa M et al (2008) Contrast-enhanced colour-Doppler sonography versus pH-metry in the diagnosis of gastro-oesophageal reflux in children. Radiol Med 113:591-598.
6. Pezzati M, Filippi L, Psaraki M et al (2007) Diagnosis of gastro-oesophageal reflux in preterm infants: sonography vs. pH-monitoring. Neonatology 91:162-166.
7. Anagnostara A, Koumanidou C, Vakaki M et al (2003) Chronic gastric volvulus and hypertrophic pyloric stenosis in an infant. J Clin Ultrasound 31:383-386.
8. Cribbs RK, Gow KW, Wulkan ML (2008) Gastric volvulus in infants and children. Pediatrics 122:e752-762.
9. Hernanz-Schulman M (2003) Infantile hypertrophic pyloric stenosis. Radiology 227:319-331.
10. Baud C (2008) Small bowel thickening. In: Couture A, Baud C, Ferran JL et al (Eds) Gastrointestinal tract sonography in fetuses and children, 1st edition. Springer, Berlin, Heidelberg, pp 253-296.
11. Aomatsu T, Yoden A, Matsumoto K et al (2011) Fecal calprotectin is a useful marker for disease activity in pediatric patients with inflammatory bowel disease. Dig Dis Sci 56:2372-2377.

12. Darge K, Anupindi S, Keener H, Rompel O (2010) Ultrasound of the bowel in children: how we do it. Pediatr Radiol 40:528-536.
13. Nylund K, Hausken T, Gilja OH (2010) Ultrasound and inflammatory bowel disease. Ultrasound Q 26:3-15.
14. Faure C, Belarbi N, Mougenot JF et al (1997) Ultrasonographic assessment of inflammatory bowel disease in children: comparison with ileocolonoscopy. J Pediatr 130:147-151.
15. Fraquelli M, Colli A, Casazza G et al (2005) Role of US in detection of Crohn disease: meta-analysis. Radiology 236:95-101.
16. Haber HP, Busch A, Ziebach R et al (2002) Ultrasonographic findings correspond to clinical, endoscopic, and histologic findings in inflammatory bowel disease and other enterocolitides. J Ultrasound Med 21:375-382.
17. Chen O, Zhu XB, Ren P et al (2013) Henoch Schonlein Purpura in children: clinical analysis of 120 cases. Afr Health Sci 13:94-99.
18. Trapani S, Micheli A, Grisolia F et al (2005) Henoch Schonlein purpura in childhood: epidemiological and clinical analysis of 150 cases over a 5-year period and review of literature. Semin Arthritis Rheum 35:143-153.
19. Yang YH, Hung CF, Hsu CR et al (2005) A nationwide survey on epidemiological characteristics of childhood Henoch-Schonlein purpura in Taiwan. Rheumatology Oxford) 44:618-622.
20. Karnsakul W, Fallon KB, Swart S (2008) Exudative hemorrhagic duodenitis as a primary event in a child with Henoch-Schonlein purpura. Clin Gastroenterol Hepatol 6:A24.
21. Nchimi A, Khamis J, Paquot I et al (2008) Significance of bowel wall abnormalities at ultrasound in Henoch-Schonlein purpura. J Pediatr Gastroenterol Nutr 46:48-53.
22. Wu S (2009) Sonographic findings of ascaris lumbricoides in the gastrointestinal and biliary tracts. Ultrasound Q 25:207-209.
23. Khong PL, Cheung SC, Leong LL, Ooi CG (2003) Ultrasonography of intra-abdominal cystic lesions in the newborn. Clin Radiol 58:449-454.
24. Segal SR, Sherman NH, Rosenberg HK et al (1994) Ultrasonographic features of gastrointestinal duplications. J Ultrasound Med 13:863-870.
25. Wootton-Gorges SL, Thomas KB, Harned RK et al (2005) Giant cystic abdominal masses in children. Pediatr Radiol 35:1277-1288.
26. Park NH, Park SI, Park CS et al (2007) Ultrasonographic findings of small bowel intussusception, focusing on differentiation from ileocolic intussusception. Br J Radiol 80:798-802.
27. Wiersma F, Allema JH, Holscher HC (2006) Ileoileal intussusception in children: ultrasonographic differentiation from ileocolic intussusception. Pediatr Radiol 36:1177-1181.
28. Baud C (2008) Infectious and inflammatory colitis. In: Couture A, Baud C, Ferran JL et al (Eds) Gastrointestinal tract sonography in fetuses and children, 1st edition. Springer, Berlin, Heidelberg, pp 297-339.
29. Dietrich CF (2009) Significance of abdominal ultrasound in inflammatory bowel disease. Dig Dis 27:482-493.
30. Alexander JE, Williamson SL, Seibert JJ (1988) The ultrasonographic diagnosis of typhlitis (neutropenic colitis). Pediatr Radiol 18:200-204.
31. Baud C, Saguintaah M, Veyrac C et al (2004) Sonographic diagnosis of colitis in children. Eur Radiol 14:2105-2119.
32. Suarez B, Kalifa G, Adamsbaum C et al (1995) Sonographic diagnosis and follow-up of diffuse neutropenic colitis: case report of a child treated for osteogenic sarcoma. Pediatr Radiol 25:373-374.
33. Friedland JA, Herman TE, Siegel MJ (1995) Escherichia coli O157:H7-associated hemolytic-uremic syndrome: value of colonic color Doppler sonography. Pediatr Radiol 25 Suppl 1:S65-67.
34. Fraser JD, Aguayo P, Leys CM et al (2009) Infarction of an epiploic appendage in a pediatric patient. J Pediatr Surg 44:1659-1661.
35. Hollerweger A, Macheiner P, Rettenbacher T, Gritzmann N (2002) Primary epiploic appendagitis: sonographic findings with CT correlation. J Clin Ultrasound 30:481-495.
36. Miller JP, Smith SD, Newman B, Sukarochana K (1988) Neonatal abdominal calcification: is it always meconium peritonitis? J Pediatr Surg 23:555-556.
37. Joensson IM, Siggaard C, Rittig S et al (2008) Transabdominal ultrasound of rectum as a diagnostic tool in childhood constipation. J Urol 179:1997-2002.
38. Bijos A, Czerwionka-Szaflarska M, Mazur A, Romanczuk W (2007) The usefulness of ultrasound examination of the bowel as a method of assessment of functional chronic constipation in children. Pediatr Radiol 37:1247-1252.
39. Haber HP, Seitz G, Warmann SW, Fuchs J (2007) Transperineal sonography for determination of the type of imperforate anus. AJR Am J Roentgenol 189:1525-1529.
40. Choi YH, Kim IO, Cheon JE et al (2009) Imperforate anus: determination of type using transperineal ultrasonography. Korean J Radiol 10:355-360.
41. Haber HP, Warmann SW, Fuchs J (2008) Transperineal sonography of the anal sphincter complex in neonates and infants: differentiation of anteriorly displaced anus from low-type imperforate anus with perineal fistula. Ultraschall Med 29:383-387.
42. Bonatti H, Lugger P, Hechenleitner P et al (2004) Transperineal sonography in anorectal disorders. Ultraschall Med 25:111-115.
43. Maconi G, Ardizzone S, Greco S et al (2007) Transperineal ultrasound in the detection of perianal and rectovaginal fistulae in Crohn's disease. Am J Gastroenterol 102:2214-2219.
44. Stewart LK, McGee J, Wilson SR (2001) Transperineal and transvaginal sonography of perianal inflammatory disease. AJR Am J Roentgenol 177:627-632.
45. Couture A (2008) Bowel obstruction in neonates and children. In: Couture A, Baud C, Ferran JL et al (Eds) Gastrointestinal tract sonography in fetuses and children, 1st edition. Springer, Berlin, Heidelberg, pp 131-251.
46. Sadler TW, Rasmussen SA (2010) Examining the evidence for vascular pathogenesis of selected birth defects. Am J Med Genet A 152A:2426-2436.
47. Neal MR, Seibert JJ, Vanderzalm T, Wagner CW (1997) Neonatal ultrasonography to distinguish between meconium ileus and ileal atresia. J Ultrasound Med 16:263-266.
48. Flikweert ER, La Hei ER, De Rijke YB, Van de Ven K (2003) Return of the milk curd syndrome. Pediatr Surg Int 19:628-631.
49. Wagener S, Cartwright D, Bourke C (2009) Milk curd obstruction in premature infants receiving fortified expressed breast milk. J Paediatr Child Health 45:228-230.
50. Swischuk LE (1997) Imaging of the newborn, infant, and young child. Williams & Wilkins, Baltimore.
51. Yang WT, Ho SS, Metreweli C (1997) Case report: antenatal sonographic diagnosis of meconium peritonitis and subsequent evolving meconium pseudocyst formation without peritoneal calcification. Clin Radiol 52:477-479.

# Imaging of the Urinary Tract in Children

Jeanne S. Chow[1], J. Damien Grattan-Smith[2]

[1] Departments of Urology and Radiology, Boston Children's Hospital, Boston, MA, USA
[2] Department of Radiology, Children's Healthcare of Atlanta at Scottish Rite, Atlanta, GA, USA

## Introduction and Techniques

The principle that guides imaging of the pediatric genitourinary tract is the same that guides imaging elsewhere in the body of the child: judicious use of imaging while minimizing ionizing radiation exposure [1] and unnecessary sedation. Ultrasound (US) is the main imaging modality of the genitourinary tract, providing excellent images of the kidneys and bladder. An abnormally dilated ureter is also easily imaged, especially at the levels of the kidney and bladder. Doppler provides additional information regarding vascular flow and is especially helpful in evaluating the main renal artery and veins as well as the arcuate vessels. US contrast agents are used to further evaluate vascular flow of the kidneys, intrarenal masses, and vesicoureteral reflux (VUR) [2]. The main downside of US is that it provides little functional imaging, instead mainly revealing the physical appearance of the urinary tract (UT).

If further imaging is necessary, magnetic resonance urography (MRU) provides exquisite, detailed images of the UT in addition to functional information. MRU has become very popular because it emits no ionizing radiation and yields both anatomical and functional information. When gadolinium is administered, the study provides uptake and excretion rates, relative function and indirect measurements of glomerular filtration rates, and overall provides more information than obtained from a technetium-99m-mercaptoacetyltriglycine ($^{99m}$Tc-MAG)-3/Lasix renogram alone [3]. However, because MRU is a long procedure that often requires sedation, technetium-99m dimercaptosuccinic acid ($^{99m}$Tc-DMSA) and MAG-3 are more commonly used to provide functional imaging of the genitourinary tract. In addition, functional information cannot be obtained by MRI without gadolinium, which places children with chronic renal failure and end-stage renal disease at risk for developing nephrogenic systemic fibrosis [4]. Although nephroureterolithiasis may be commonly studied by computed tomography (CT) in adults, US is the first-line imaging modality in children [5].

***Key Point***

- US is the main imaging modality of the genitourinary tract in children

## Managing in Utero-Renal-Pelvis Dilatation

Dilatation of the renal pelvis is a common finding on obstetrical US, with a frequency of around 1-4% of all pregnancies. Yet, not every dilatation has the same clinical relevance; furthermore, antenatal and postnatal evolution is variable. This has led to controversy in the literature about the best workup and follow-up after birth [6-8].

### Definition

A common criterion for measuring UT dilatation is the anteroposterior (AP) diameter of the renal pelvis, which is measured on a transverse scan of the fetal kidneys. The upper limit for normal (ULN) should be 4 mm in the second trimester and 7 mm in the third trimester. Other US evidence of UT abnormality are visibility of the fetal ureter, dilatation of the renal calyces, abnormal echogenicity of the renal parenchyma, and demonstration of an enlarged bladder.

### Findings on Obstetric US

Most mild hydronephrosis is transient and resolves. The greater the degree of hydronephrosis, the greater the likelihood of UT obstruction. The common sites of obstruction in the fetus and child are at the ureteropelvic junction and ureterovesical junctions. Vesicoureteral reflux (VUR) is also associated with UT dilatation; however, the risk does not change significantly with degree of hydronephrosis [9]. In male fetuses, urethral obstruction can cause hydronephrosis. In most cases, US evaluation will differentiate between etiologies. In some patients, especially those with bilateral and complex uropathies, fetal MR imaging (MRI) will provide additional information.

*Diseases of the Abdomen and Pelvis 2014-2017*,
DOI: 10.1007/978-88-470-5659-6_29 

Other organ malformations also can be associated with UT dilatation; therefore, the US survey should be as meticulous and complete as possible. Chromosomal analysis may be indicated in selected patients.

The prognosis of uropathy will depend upon type and extent of anomalies. Amniotic fluid volume is important to the prognosis, as well; oligohydramnios, thought to be related to decreased urine production, is a poor prognostic indicator.

It is of utmost importance that any relevant information is correctly transmitted to the postnatal team that will be in charge of the newborn.

### Management of Postnatal Fetal Pelvis Dilatation

Certain conditions require immediate postnatal confirmation and therapeutic maneuvers, such as obstructive posterior urethral valves and prolapsed ectopic ureterocele into the urethra. In those cases, US and voiding cystourethrography (VCUG) should be performed directly after birth. In all other cases, the workup can be planned without urgency, typically in the first month of life. The use of prophylactic antibiotics until the VCUG is performed, once routine, is now variable.

Additional VCUG is recommended if US shows a significant anomaly, such as greater than mild to moderate pelvicaliceal dilatation, ureteral dilatation, duplex kidney with dilatation, renal size discrepancy, or dysplasia. If VUR is not present, complementary imaging is necessary to determine the precise origin of the dilatation. Renal function is assessed through isotopic studies, whereas function and anatomy are best evaluated by MRI.

Treatment type (conservative or surgical) will depend upon diagnosis, renal function on follow-up, and complications. The trend is increasingly toward a conservative, nonsurgical approach, as many causes of UT dilatation resolve with time. The length of follow-up must be adapted to anomaly type and clinical and imaging follow-up.

#### *Key Points*

- Fetal renal dilatation is a common finding during obstetric US.
- Thresholds of 4 and 7 mm during the second and third trimester, respectively, are commonly used.
- Postnatally, these patients must be further evaluated by US; VCUG is performed only if an anomaly is present on postnatal US.
- The trend is toward a more conservative approach to treatment based on clinical and imaging follow-up.

## Imaging Cystic Kidneys in Children

Renal cystic diseases may be discovered or suspected at any stage during fetal life or at any age in childhood. Such diseases encompass a large number of conditions that can be separated into those with or without hereditary transmission. Imaging, mainly US, plays an important role in differentiating between the various types of cystic diseases, as it shows the features of renal involvement as well as associated anomalies.

### Cystic Kidneys in the Fetus

In the fetus (and during the perinatal period), cystic renal disease should be suspected whenever bilateral hyperechoic kidneys or cysts are discovered during an US examination. Many of these renal cystic diseases are ciliopathies, which are due to dysfunction of hair-like organelles called cilia [10]. The imaging approach to the diagnosis should be based on detailed sonographic analysis that includes measurement of renal length, presence or absence of normal corticomedullary differentiation (CMD), and presence, number, size, and location of cysts. This evaluation should be completed with an analysis of the entire fetus, looking for associated anomalies. Timing of detection and the amount of amniotic fluid are the most important prognostic factors. Furthermore, a detailed clinical and familial inquiry is essential in disease evaluation.

Autosomal recessive polycystic kidney disease (ARPKD) is the main diagnosis to consider in case of bilateral, markedly enlarged, hyperechoic kidneys without normal CMD. The prognosis is usually poor if amniotic fluid volume is markedly decreased.

In case of moderately enlarged hyperechoic kidneys, three diagnoses must be considered: (1) nephropathy due to a mutation in the *TCF2* gene, (2) a milder form of ARPKD, and (3) autosomal-dominant polycystic kidney disease (ADPKD).

- In *TCF2*-mediated nephropathy, CMD can be normal or abnormal, and whenever cysts are visible, they are typically subcortical.
- In the milder form of ARPKD, cysts may be observed in the medullary area.
- The main sonographic feature of ADPKD is a striking cortical hyperechogenicity associated with increased CMD.

Whenever cysts are the main US finding in the fetal kidney, number and location are the main criteria for differential diagnosis.

- The diagnosis of unilateral multiple cysts suggests a multicystic dysplastic kidney.
- Bilateral multiple cysts can be visualized in a large number of renal diseases, including bilateral multicystic dysplastic kidney, ADPKD, bilateral obstructive dysplasia, and glomerulocystic kidneys [10].

### Renal Cystic Diseases in Children

In children, renal cystic diseases are usually discovered during US examination performed in the follow-up of a known perinatally diagnosed disease, during the workup of syndromes diagnosed after birth, during screening in an at-risk family, or as an incidental finding. The US

approach is the same as that described for the fetus. The role of imaging in the diagnosis and follow-up of renal involvement is to search for complications such as hemorrhage or urolithiasis. Specifically, an important role for US is detecting hepatic-biliary complications.

***Key Points***

- Renal cystic diseases can be diagnosed prenatally or in childhood.
- Hyperechogenicity or cysts are cardinal findings.
- Familial history, detailed clinical inquiry, and associated findings help establish the diagnosis.

## Renal Ectopia and Duplications

One of the most interesting areas of pediatric uroradiology is studying and understanding the multitude congenital abnormalities of the UT. During normal renal development, the kidneys ascend from the renal pelvis while rotating medially. If the kidneys do not ascend or ascend past their normal location in the renal fossae, they are ectopic. In some cases, they are as low as the pelvis and in others as high as the thoracic cavity. If the kidneys fuse during ascent, pelvic cake kidneys, midline horseshoe kidneys, or left- or right-sided cross-fused ectopic kidneys form. As the embryological origin of the kidneys (metanephros) is separate from that of the ureters (ureteric buds), the site of ureteral insertion is normal, even if the kidney is ectopic. However, renal blood supply from the aorta will vary depending on the level of ectopia.

The ureteric bud must meet the metanephros in order for the kidney to form. Without this interaction, kidney formation is not induced. If two ureteric buds meet at the metanephric blastema, then the kidney becomes duplex. Ureteral duplication may be complete or, more commonly, incomplete.

### Incomplete Ureteral Duplication

In incomplete ureteral duplication, a single ureteric bud bifurcates and meets the metanephros during approximately the fifth to sixth week of gestation. The two branches of the ureter may join at the level of the renal pelvis (bifid pelvis) or at the proximal, mid, or distal ureter (bifid ureter) and terminate in a single distal ureter that inserts orthotopically into the bladder. As the two moieties of the kidney share a common distal ureter, they behave similarly and usually appear normal. Rarely, one of the ureteral buds may be blind-ending and never appear to reach the kidney (blind-ending ureteral duplication). The associated kidney has a single collecting system.

### Complete Ureteral Duplication

In complete ureteral duplication, two separate ureteric buds arise from the Wolffian duct. The lower-pole ureter is considered the analogue to the normal, single-system ureter. Thus, the lower pole of the kidney has all the same abnormalities that can affect a single-system kidney, including VUR, ureteropelvic junction obstruction (UPJO), and UVJO. The upper-pole ureter is abnormal and ectopic (Weigert-Meyer rule).

### Ectopic Ureter

The ectopic ureter inserts medially and inferiorly to the normal ureteral orifice, usually in the bladder. In girls, the ectopic ureter may insert below the bladder base, into the urethra or vagina. A vaginal ectopic ureter can cause constant urinary dribbling and is a cause of incontinence [11]. In boys, ectopic ureters never terminate below the urinary sphincter and thus never cause incontinence; however, the ureter can terminate in Wolffian duct derivatives, including seminal vesicals and vas deferens. Very rarely, three completely or incompletely separated ureters form, resulting in ureteral triplication [12].

Ectopic ureters are often obstructed but rarely reflux. If the ectopic ureter inserts into the urethra at the level of the urinary sphincter, urinary flow is obstructed or refluxes depending whether the sphincter is closed or open [13]. The more distal the ureteral insertion, the more dysplastic and dysfunctional the associated renal parenchyma. Ectopic ureters, and all the associated abnormalities, can also occur in single-system kidneys (single ectopic ureter) [14].

### Ureterocele

A ureterocele is the dilated submucosal terminal segment of the ureter. It causes varying degrees of ureteral obstruction and subsequent dilatation of the renal pelvis and calyces. In girls, ureteroceles are most commonly seen in association with ectopic upper-pole ureters. In boys, they are most commonly associated with single-system kidneys and are orthotopic. Although ureteroceles protrude into the bladder, when the intravesical pressure equals that of the ureterocele, the ureterocele can flatten and become imperceptible (efface). When the intravesical pressure exceeds that of the ureterocele, the latter everts or intussuscepts into its ureter. Ectopic bladder-neck ureteroceles or large, simple ureteroceles can prolapse into the urethra and cause bladder outlet obstruction.

***Key Points***

- Renal ectopia is due to abnormalities in the normal ascent of the kidney.
- Ureteral duplication may be incomplete (more common) or complete.
- The Weigert-Meyer rule states that the upper-pole ureter of a duplex kidney inserts ectopically, medially, and inferiorly to the orthotopic location.

- The lower-pole ureter is the analogue of the single-system kidney.

## Urinary Tract Obstruction

Urinary tract obstructions occur at three main areas: the ureteropelvic junction, the ureterovesical junction, and the bladder outlet (i.e., urethra). Rarely, the midureter can be obstructed by webs, fibrosis, or compression from the inferior vena cava; or there may be obstruction at the level of the infundibula in the kidney. On US, the normal hypoechoic medullary pyramids seen routinely in infancy and childhood should not be confused with dilated calyces or a sign of obstruction.

### Ureteropelvic Junction Obstruction

The most common congenital obstruction of the kidney is UPJO, which is due to stenosis at the junction of the renal pelvis and proximal ureter. As most children are now diagnosed prenatally and followed postnatally, they rarely present with symptoms and signs of obstruction, such as infection, pain, or renal stones. Some children have UPJO due to a crossing renal artery and present with intermittent pain from intermittent obstruction, with hydronephrosis only evident during obstruction. To be correctly diagnosed, these children must be imaged at the time of painful episodes [15].

### UPJO Imaging

The goal of UPJO imaging is to predict the degree of obstruction and whether its eventual effects on renal function will improve or worsen over time. US is routinely used to describe the degree of obstruction and appearance of the renal parenchyma. However, functional imaging studies, primarily, the MAG-3/Lasix renogram and MRU, are used to help quantify the degree of obstruction and the contributing function of each kidney.

### Ureterovesical Junction Obstruction

An obstruction of the distal ureter as it enters into the bladder results in a ureterovesical junction obstruction (UVJO). Most such cases are primary and due to a ureteral obstruction, although secondary UVJO can occur with an abnormally thickened bladder. Insertion of the obstructed ureter may be orthotopic (primary megaureter) or ectopic. An orthotopic or ectopic ureterocele may also be associated with obstruction. Primary megaureter accounts for the majority of cases of UVJO. In most patients with this condition, the degree of dilatation improves over time [16] such that surgical repair is required only for a minority of affected patients. Surgery is indicated if the degree of dilatation worsens, renal function is impaired, or the obstruction is thought to be contributing to stasis and UT infections.

#### *Key Points*

- Ureteropelvic junction obstruction is the most common cause of UT obstruction.
- Most cases of ureterovesical junction obstruction improve with time.

## Voiding Abnormalities and Secondary Vesicoureteral Reflux

Children with spinal abnormalities and tethered cord may have detrusor-sphincter dyssynergia, in which the bladder contracts but the urinary sphincter does not relax during voiding, resulting in chronic obstruction of the bladder outlet. The uncoordinated voiding causes urinary retention, increased bladder pressures, secondary VUR, and secondary UVJO. Similarly, children with voiding dysfunction without a neurogenic cause can also develop secondary reflux.

### Urethral Obstruction

Urethral obstruction can occur in the posterior or anterior urethra in boys whereas the urethra is rarely obstructed in girls. Posterior urethral valves are the most common congenital urethral obstructions and are caused by an obstructing membrane just below the level of the verumontanum. Anterior urethral obstruction is most commonly due to traumatic strictures and mostly located in the bulbar urethra. Anterior urethral valves or diverticula are rare. Depending on obstruction severity, the portion of the urethra proximal to the obstruction may be dilated, the bladder wall may be hypertrophied, and secondary reflux and UVJO may occur. In circumcised boys, meatal stenosis is another cause of urethral obstruction. Retrograde urethrogram under fluoroscopy or US is the best way of studying the anterior urethra, whereas the posterior urethra can only be studied during voiding.

#### *Key Points*

- Voiding dysfunction can lead to VUR.
- Most obstructions of the bladder outlet in boys are congenital (e.g., posterior and anterior urethral valves) or posttraumatic (bulbar urethral stricture).

## Renal Masses in Children

Once a mass is established to be intrarenal, its histology can be predicted based on its appearance and the patient's age. Most intrarenal masses occurring in the newborn period are benign. Although rare, the most common solid intrarenal mass seen in newborns is a mesoblastic nephroma [17]. These large, solid, enhancing masses are benign, although the cellular subtype is the most aggressive and

can cause paraneoplastic syndromes [18]. These must be removed, but the prognosis is excellent.

### Multicystic Dysplastic Kidney

In the newborn, the most frequently occurring cystic abnormality of the kidney is multicystic dysplastic kidney, which can be segmental or involve the entire kidney. The condition is due to a congenital abnormality of the kidney in which the collecting system forms as cysts, and the renal parenchyma is dysplastic and nonfunctional. Multicystic dysplastic kidney is now commonly diagnosed in utero. Over time, cyst fluid resorbs and a tiny nubbin of tissue remains. These are typically treated nonsurgically.

### Wilms' Tumor

The most common renal mass in toddlers is Wilms' tumor. Children with aniridia; Wilms' tumor, aniridia, genitourinary abnormalities, and mental retardation (WAGR); Deny-Drash syndrome; Beckwith-Weidemann syndrome; hemihypertrophy; or nephroblastomatosis are predisposed to developing this tumor. Wilms' tumor is a solid, cystic, and often hemorrhagic mass and is far more common but radiographically indistinguishable from either clear cell sarcoma or malignant rhabdoid tumor. However, if a tumor has a large subcapsular hematoma, and if there are brain metastases, malignant rhabdoid tumor should be considered [19]. Centrally located multilocular masses of the kidney may be a multilocular cystic nephroma, which is more common in boys in childhood and in women in adult life [20].

### Renal Cell Carcinoma

In children $>11$ years of age, renal cell carcinoma becomes more common than Wilms' tumor, although the likelihood of either tumor is extremely rare [21]. It is crucial to confirm that the child has no clinical indicators of UT infection, because focal pyelonephritis or lobar nephronia mimic a tumor in appearance and thus must always be considered in the differential diagnosis of a renal mass.

### Bilateral Renal Mass

If the renal mass is bilateral, appearance and clinical presentation are extremely helpful in predicting histology. If there are multiple large masses and the kidneys are also enlarged, bilateral nephrogenic rests due to nephroblastomatosis is most likely. Nephrogenic rests are remnant fetal renal tissue that never fully matured. As they have a high propensity to develop into Wilms' tumors, these masses need frequent surveillance. If the masses are partially echogenic, angiomyolipoma should be considered, especially if the patient has tuberous sclerosis. Wilms' tumors, lymphoma, and infections may also be bilateral.

### Solitary Simple Cysts

Solitary simple cysts are much less commonly seen in children than in adults. Calyceal diverticula may appear as simple cysts but actually communicate with the adjacent calyx and can become superinfected. Delayed intravenous pyelogram, CT, or MRI, which shows excretion of contrast within the cyst, is able to distinguish calyceal diverticula from simple cysts. If there are multiple simple cysts, especially in enlarged kidneys, ADPKD should be considered.

#### *Key Points*

- Most newborn renal masses are benign.
- The most common renal malignancy in toddlers is Wilms' tumor.
- Focal pyelonephritis mimics renal tumors.

## Imaging Renal Failure in Children

US plays a central role in differentiating between etiologies of renal failure. For some diseases, the US pattern will be specific; for others, there will be little or no parenchymal changes. US evaluation should therefore be highly meticulous and correlated to biological and clinical data [21-23].

### Acute Renal Failure

Acute renal failure (ARF) is defined as urine production $<1$ mg/kg per day. Its causes can be prerenal, renal, or postrenal in origin. In the case of ARF of renal origin, US is often diagnostic.

### Hemolytic Uremic Syndrome

Hemolytic microangiopathic anemia, thrombocytopenia, and ARF occurring together constitute hemolytic uremic syndrome (HUS), which is the commonest cause of ARF in the USA and in several European countries, especially in young infants. On US, during the acute phase of the disease, the renal cortex appears markedly hyperechoic with increased CMD. On Doppler analysis, there is no diastolic flow, which correlates well with the lack of urine production. Return of the diastolic wave indicates a return to normal diuresis. Other organs may be involved as well, including the gallbladder and digestive tract.

### Medullary or Cortical Necrosis: Shock Kidneys

Medullary and cortical necrosis in the neonate results from a lack of renal perfusion. On US, the cortex in cortical necrosis first appears hyperechoic, then shrinks, and finally calcifies. In medullary necrosis, calcifications develop within the medulla.

#### Renal Vein Thrombosis

While largely a neonatal disease, renal vein thrombosis may occur in utero. When both renal veins are involved, the condition is associated with ARF. In the acute phase on US, kidneys appear enlarged, CMD is absent, and hyperechoic streaks are demonstrated in the interlobar areas. Later, the kidneys may become atrophied, with residual calcified vessels.

#### Obstructive Uropathies

Anuria and ARF may follow ureterocele prolapse within the urethra, obstruction of a single renal system, tumoral entrapment of the ureters, or bilateral obstructive urolithiasis.

#### Chronic Renal Failure

Chronic renal failure (CRF) is defined as a glomerular filtration rate (GFR) $<$50 ml/min per 1.73 $m^2$/kidney. One of the most common causes of CRF is renal hypodysplasia. On US, kidneys are small, CMD absent, and small cysts can be visualized.

#### Renal Cystic Diseases (see above)

##### *Congenital Nephrotic Syndromes*

Congenital nephrotic syndromes (CNS) encompass diseases in which there is massive proteinuria occurring after birth. The most common form of CNS is the Finnish type. Proteinuria starts in utero and the placenta is thickened. On US, at birth, the kidneys are swollen and hyperechoic; CMD is present, but the pyramids are irregular and within weeks will "disappear."

Other causes of CNS include diffuse mesangial sclerosis (DMS), which can be part of Drash syndrome In some patients, CNS evolve toward end-stage renal disease and necessitate renal transplantation.

#### Syndromes Affecting Tubules and Metabolic Diseases

Renal diseases that include primary and secondary tubulopathy are numerous. Hypercalciuria is a constant finding and may lead to nephrocalcinosis, which is easily detected by US. For instance, type 1 primitive hyperoxaluria is seen as strikingly hyperechoic kidneys at birth and results in urolithiasis.

##### *Key Points*

- US is the key imaging examination in children with acute or chronic renal failure.
- Etiologies of renal failure are numerous.
- US patterns will orient the diagnosis.

## Urinary Tract Infection

UT infection is one of the commonest bacterial diseases in children: 5% of girls and 0.5% of boys will suffer at least one episode. Despite numerous studies and publications, the role of imaging is controversial. The main challenges of imaging are to identify patients with complicated UT infection, those with an underlying cause, and those at risk for recurrence [24-26]. Imaging may be done at the time of diagnosis of an acute episode, during treatment, or after treatment. No single imaging technique allows complete evaluation of the UT; instead, the use of each one must be optimized to obtain the maximum amount of information in association with the lowest risk of morbidity.

#### Imaging Acute Pyelonephritis

Pyelonephritis is a clinical diagnosis. The main role of conventional US is to diagnose any associated congenital anomalies and/or complications (abscess) of a UT infection. The gold standard examination for the diagnosis of renal lesions during an acute episode (as well as for detecting scars) is DMSA scintigraphy.

Because VUR is considered a risk factor for developing UT infections, patients with pyelonephritis are evaluated for reflux. There are two approaches: top down and bottom up. In the top-down approach, patients with focal abnormalities detected by DMSA scan proceed to VCUG. In the bottom-up approach, patients should undergo VCUG first. CT and MRI rarely play a role in the initial evaluation of pyelonephritis, other than occasionally, when these patients present with abdominal pain and fever, or when mass and other causes are being considered.

#### Complications of Acute Pyelonephritis

Renal abscess is the typical complication of delayed or nonresponsive antibiotic treatment. Lesions are demonstrated by US, although further, cross-sectional imaging (CT scan or MRI) is occasionally useful. Pyonephrosis corresponds to urine infection in a dilated UT. Suspicion of this diagnosis should prompt a diagnostic and therapeutic nephrostomy.

#### Late Complications of UT Infection

The development of renal scars is the long-term risk of untreated acute pyelonephrosis. Patients with renal scars are at risk for developing renal hypertension, complications during pregnancy, and renal failure. Both DMSA scintigraphy and MRU are excellent methods for evaluation, if performed at a time sufficiently removed from the acute episode.

Xanthogranulomatous pyelonephritis is an atypical chronic infectious renal lesion. It may appear as a focal mass and mimic tumor or present as a more diffuse abnormality of the kidney. Cross-sectional imaging by CT or MRI is helpful after initial evaluation by US.

***Key Points***

- Imaging of UT infections is controversial.
- US with Doppler, DMSA scintigraphy, and VCUG form the basis of imaging workup.

## Imaging Urolithiasis in Children

Urolithiasis is less common in children than in adults (1 child for every 20,000 adults). It is more frequent in certain geographic areas. Hematuria and pain are the presenting symptoms in about half of patients, whereas the disease is asymptomatic and an incidental finding in 20% of patients. A familial history is frequent and accounts for >50% of patients. Metabolic disorders and UT infections are common etiologies [27, 28].

The work-up of a patient with urolithiasis includes urinalysis, blood tests, and genetic analysis, looking for underlying diseases or infections. Imaging must be applied systematically, starting with US, and CT as a problem-solving tool.

## Imaging Modalities

US, with its entire spectrum of optimized techniques, is the ideal primary imaging modality in children. It allows reliable demonstration of kidneys and UT and is useful in diagnosis and posttherapeutic follow-up. Some kidney diseases have a specific, characteristic pattern, such as primary hyperoxaluria type 1.

CT serves as a complementary tool in cases of a nondiagnostic US examination or prior to treatment. When properly performed, radiation doses are minimized and optimally adapted to the child's size.

## Acknowledgements

Special thanks and acknowledgement to Dr. Fred Avni for his work on the previous version of this syllabus, and Rhonda Johnson for her excellent work in helping us prepare and submit this manuscript.

## References

1. Brenner D, Elliston C, Hall E et al (2001) Estimated risks of radiation-induced fatal cancer from pediatric CT. AJR Am J Roentgenol 176:289-296.
2. Ripolles T, Puig J (2009) Update on the use of contrast agents in ultrasonography: a review of the clinical guidelines of the European Federation of Societies for Ultrasound in Medicine and Biology (EFSUMB). Radiologia 51:362-375.
3. Grattan-Smith JD, Jones RA (2008) MR urography: technique and results for the evaluation of urinary obstruction in the pediatric population. Magn Reson Imaging Clin N Am 16:643-660, viii-ix.
4. Thomsen HS (2007) ESUR guideline: gadolinium-based contrast media and nephrogenic systemic fibrosis. Eur Radiol 17:2692-2696.
5. Passerotti C, Chow JS, Silva A et al (2009) Ultrasound versus computerized tomography for evaluating urolithiasis. J Urol 182:1829-1834.
6. Riccabona M, Avni FE, Blickman JG et al (2008) Imaging recommendations in paediatric uroradiology: minutes of the ESPR workgroup session on urinary tract infection, fetal hydronephrosis, urinary tract ultrasonography and voiding cystourethrography, Barcelona, Spain, June 2007. Pediatr Radiol 38:138-145.
7. Riccabona M, Avni FE, Blickman JG et al (2009) Imaging recommendations in paediatric uroradiology. Minutes of the ESPR uroradiology task force session on childhood obstructive uropathy, high-grade fetal hydronephrosis, childhood haematuria, and urolithiasis in childhood. ESPR Annual Congress, Edinburgh, UK, June 2008. Pediatr Radiol 39:891-898.
8. de Bruyn R, Marks SD (2008) Postnatal investigation of fetal renal disease. Semin Fetal Neonatal Med 13:133-141.
9. Lee RS, Cendron M, Kinnamon DD et al (2006) Antenatal hydronephrosis as a predictor of postnatal outcome: a meta-analysis. Pediatrics 118:586-593.
10. Hildebrandt F, Benzing T, Katsanis N (2011) Ciliopathies. N Engl J Med 364:1533-1543.
11. Carrico C, Lebowitz RL (1998) Incontinence due to an infrasphincteric ectopic ureter: why the delay in diagnosis and what the radiologist can do about it. Pediatr Radiol 28:942-949.
12. Gill RD (1952) Triplication of the ureter and renal pelvis. J Urol 68:140-147.
13. Wyly JB, Lebowitz RL (1984) Refluxing urethral ectopic ureters: recognition by the cyclic voiding cystourethrogram. AJR Am J Roentgenol 142:1263-1267.
14. Prewitt LH, Jr., Lebowitz RL (1976) The single ectopic ureter. AJR Am J Roentgenol 127:941-948.
15. Rooks VJ, Lebowitz RL (2001) Extrinsic ureteropelvic junction obstruction from a crossing renal vessel: demography and imaging. Pediatr Radiol 31:120-124.
16. Shukla AR, Cooper J, Patel RP et al (2005) Prenatally detected primary megaureter: a role for extended followup. J Urol 173:1353-1356.
17. Chaudry G, Perez-Atayde AR, Ngan BY et al (2009) Imaging of congenital mesoblastic nephroma with pathological correlation. Pediatr Radiol 39:1080-1086.
18. Ko SM, Kim MJ, Im YJ et al (2013) Cellular mesoblastic nephroma with liver metastasis in a neonate: prenatal and postnatal diffusion-weighted MR imaging. Korean J Radiol 14:361-365.
19. Eftekhari F, Erly WK, Jaffe N (1990) Malignant rhabdoid tumor of the kidney: imaging features in two cases. Pediatr Radiol 21:39-42.
20. Boggs LK, Kimmelstiel P (1956) Benign multilocular cystic nephroma: report of two cases of so-called multilocular cyst of the kidney. J Urol 76:530-541.
21. Estrada CR, Suthar AM, Eaton SH et al (2005) Renal cell carcinoma: Children's Hospital Boston experience. Urology 66:1296-1300.
22. Wedekin M, Ehrich JH, Offner G et al (2008) Aetiology and outcome of acute and chronic renal failure in infants. Nephrol Dial Transplant 23:1575-1580.
23. Ardissino G, Dacco V, Testa S et al (2003) Epidemiology of chronic renal failure in children: data from the ItalKid project. Pediatrics 111:e382-387.
24. Mercado-Deane MG, Beeson JE, John SD (2002) US of renal insufficiency in neonates. Radiographics 22:1429-1438.
25. Lim R (2009) Vesicoureteral reflux and urinary tract infection: evolving practices and current controversies in pediatric imaging. AJR Am J Roentgenol 192:1197-1208.
26. Lee MD, Lin CC, Huang FY et al (2009) Screening young children with a first febrile urinary tract infection for high-

grade vesicoureteral reflux with renal ultrasound scanning and technetium-99m-labeled dimercaptosuccinic acid scanning. J Pediatr 154:797-802.
27. Ajdinovic B, Jaukovic L, Krstic Z et al (2008) Impact of micturating cystourethrography and DMSA renal scintigraphy on the investigation scheme in children with urinary tract infection. Ann Nucl Med 22:661-665.
28. Hoppe B, Kemper MJ (2010) Diagnostic examination of the child with urolithiasis or nephrocalcinosis. Pediatr Nephrol 25:403-413.

# NUCLEAR MEDICINE SATELLITE COURSE
# “DIAMOND”

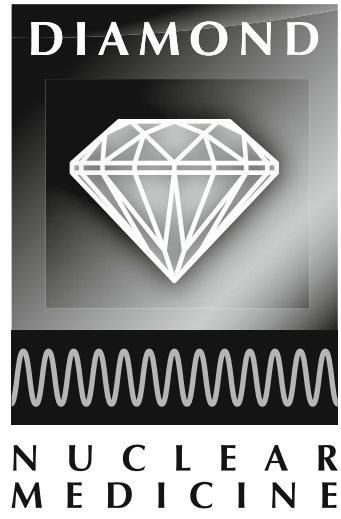

# Imaging and Therapy of Neuroendocrine Tumors of the Abdomen

Richard P. Baum, Harshad R. Kulkarni

THERANOSTICS Center for Molecular Radiotherapy and Molecular Imaging, Zentralklinik Bad Berka, Bad Berka, Germany

## Introduction

THERANOSTICS is an acronym that exemplifies the inseparability of diagnostics and therapeutics in the individualized management of disease. Neuroendocrine tumors (NETs) express somatostatin receptors (SSTRs), enabling the use of somatostatin (SMS) analogs for molecular imaging, when labeled with the positron emitter gallium-68 ($^{68}$Ga) for receptor positron emission tomography computed tomography (PET/CT) and targeted radionuclide therapy when labeled with beta-emitters $^{90}$Y and $^{177}$Lu (Fig. 1). Peptide receptor radionuclide therapy (PRRT) using $^{90}$Y- and $^{177}$Lu-labeled SMS analogs or a combination of the two (DUO-PRRT) is highly effective in the management of advanced or progressive NETs. Apart from benefit in overall survival from time of diagnosis of several years, significant improvement in clinical symptoms and excellent palliation can be achieved. In patients with progressive NETs, fractionated, personalized PRRT with lower doses of radioactivity given over a longer period of time results in good therapeutic responses. Using this concept, severe hematological and/or renal toxicity can be avoided and quality of life can be improved. PRRT should only be performed at specialized centers for individualized interdisciplinary treatment and long-term care.

## Targeted Imaging

NETs of the abdomen, i.e., gastroenteropancreatic (GEP) NETs, are relatively rare neoplasms typified by their endocrine metabolism and a distinct histological pattern [1]. Functional GEP-NETs cause symptoms due to secretion of neuroamines. On the other hand, many tumors are clinically silent, until they are identified later with mass effects. Therefore, better tumor localization and identification of small lesions is necessary. The morphologically oriented imaging modalities of ultrasound (US) (transabdominal, endoscopic, color Doppler), CT, and magnetic resonance imaging (MRI) provide valuable anatomical information and are therefore crucial for staging and restaging NETs. However, their shortcomings are in diagnosing an unknown neuroendocrine primary tumor and defining NET prognosis, where molecular imaging using radionuclides plays an important role.

Radionuclide imaging with gamma-emitting tracers, e.g., indium-labeled SMS analogs, and molecular imaging using diverse PET radiopharmaceuticals, e.g., gallium-labeled SMS analogs [2], is used for diagnostic workup of patients with NETs [3]. The foundation upon which molecular imaging of NETs is based, is the targeting of a metabolic pathway or a genuine molecular event (e.g., receptor binding of a peptide) that is specific for a certain kind of tumor or tissue/cells.

### Based on Somatostatin Receptor Expression of Neuroendocrine Tumors

Targeting NETs for THERANOSTICS is enabled by SSTR expression, mainly subtype 2, on their cell surfaces. Indium-111 diethylene triamine penta-acetic acid (DTPA)-D-Phe1-octreotide ($^{111}$In-pentetreotide; OctreoScan, Mallinckrodt, Inc, St. Louis, MO, USA) was the first radiolabeled SMS analog to be approved for NET scintigraphy and was shown in large clinical studies to be well suited for scintigraphic localization of primary and metastatic NETs [4]. Among $^{99m}$Tc-labeled SMS analogs, $^{99m}$Tc-EDDA-HYNIC-TOC (or -TATE) has been shown in a larger patient population to be superior to $^{111}$In-pentetreotide for detecting SSTR-positive tumors and metastases [5]. The next generation of SMS analogs, e.g., DOTA-D-Phe1-Tyr3-octreotide (DOTATOC) and DOTA-D-Phe$^{1}$-Tyr$^{3}$-Thr$^{8}$-octreotide (DOTATATE) were developed and labeled with different radionuclides for THERANOSTICS, i.e., diagnosis using PET/CT, as well as for therapy [6]. The advantage of PET/CT is its ability to quantify the disease at a molecular level. Therefore, SSTR PET/CT using $^{68}$Ga, a generator-produced radionuclide with convenient radiochemical characteristics for labeling with SMS analogs, clearly has an edge over single-photon-emission CT/CT (SPECT/CT) using gamma-emitting

*Diseases of the Abdomen and Pelvis 2014-2017*,
DOI: 10.1007/978-88-470-5659-6_30 

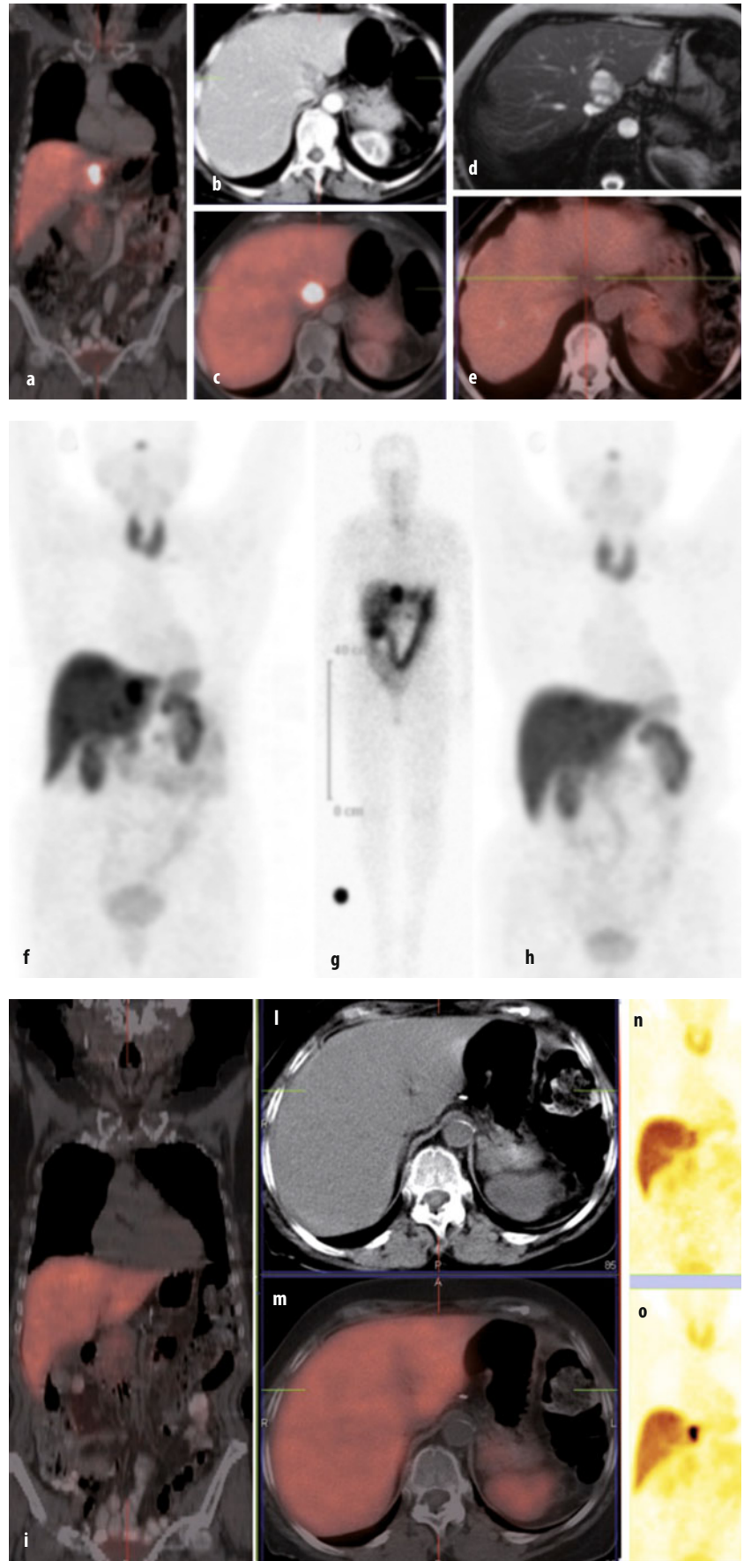


**Fig. 1 a-o.** Well-differentiated neuroendocrine neoplasm (NEN) of pancreatic tail, status post extended pancreatectomy and partial omentectomy, initial tumor stage (Union for International Cancer Control, UICC) pT2 (Ø 3.2 cm) pN1 (6/12) cM1 R0, Lx Vx, G2, proliferation rate (Ki-67) 10%, immunohistochemical expression of chromogranin A, synaptophysin, and somatostatin receptors (SSTRs), underwent peptide-receptor radionuclide therapy (PRRT). **a-e** Strongly SSTR-positive liver metastasis in S1 [standardized uptake value (SUV) 26.1] on gallium-68 DOTA-D-Phe1-Tyr3-octreotide ($^{68}$Ga-DOTATOC) positron emission tomography computed tomography (PET/CT) before therapy (**a**, coronal fused; **c**, transverse fused), hypodense on CT (**b**, transverse view), seen on T2-weighted magnetic resonance imaging (MRI) (**d**, transverse view), and importantly, ametabolic on $^{18}$F-2-fluoro-2-deoxyglucose ($^{18}$F-FDG) PET/CT with complete mismatch (**e**, transverse fused image). **f-h** The $^{68}$Ga-DOTATOC PET maximum intensity projection (MIP) image before PRRT (**f**) shows, in addition to the receptor-positive lesion in S1, discrete tracer uptake in S6. The $^{177}$Lu-DOTATOC whole-body planar scan 44 h after therapy also demonstrates an intense uptake in the liver metastasis described above. There was an excellent response after one PRRT cycle, as seen on the $^{68}$Ga-DOTATOC PET image after therapy (**h**). **i-o** Posttherapy $^{68}$Ga-DOTATOC PET/CT after one PRRT cycle (**i**, coronal fused; **m**, transverse fused and **n** coronal PET slice) compared with pretherapy SSTR PET (**o**, coronal PET before PRRT) shows complete remission

radionuclides. Hofmann et al. demonstrated this for the first time with $^{68}$Ga-DOTATOC as compared to $^{111}$In-octreotide SPECT (CT taken as reference) in detecting upper abdominal metastases [7]. In a more recent study, $^{68}$Ga-DOTATOC PET was proven to be superior to $^{111}$In-octreotide for detecting NET metastases in lung, bone, liver, and brain [8]. In our own experience with >8,000 SSTR PET/CT studies (currently >20 per week) performed at the Zentralklinik Bad Berka, $^{68}$Ga-SSTR PET is able to detect many lesions that are not routinely detected by CT, MRI, skeletal scintigraphy, or US. Our group [9] demonstrated for the first time a close correlation between maximum standard uptake value ($SUV_{max}$) and immunohistochemical scores for SSTR (particularly subtype 2A) quantification in NET tissue [8]. In a bicentric study, $^{68}$Ga-DOTA-1-Nal3-octreotide (DOTANOC) PET/CT localized the primary tumor in 59% of cases with cancer of unknown provenience (CUP-NET), significantly higher than the detection rate (39%) reported in the literature for $^{111}$In-Octreoscan [10].

#### Based on the Serotonin Production Pathway

Most clinical symptoms of NET are due to the excessive production of serotonin, i.e., 5-hydroxytryptamine (5-HT). The precursor for the production of 5-HT is tryptophan. One of the intermediates in the production pathway, 5-hydroxytryptophan labeled with carbon-11 ([$^{11}$C]), can be used for functionally active and serotonin-producing NETs, which accumulate the radiopharmaceutical, leading to visualization on PET images.

#### Based on Biogenic Amine Production and Storage Mechanism

NETs are characterized by the production and storage of several biogenic amines. One of the radiopharmaceuticals, metaiodobenzylguanidine (MIBG), labeled with iodine-131 ($^{131}$I) or with $^{123}$I, utilizes the structural resemblance of MIBG to norepinephrine (NE) [11]. As with NE, MIBG is taken up in an active amine uptake mechanism by the cell membrane of sympathomedullary tissue and by intracellular granules, which results in prolonged retention of the radiopharmaceutical in NETs. $^{123}$I is the preferred radionuclide for labeling MIBG because of its better physical imaging characteristics and ability to perform SPECT, whereas $^{131}$I-MIBG can also be used for therapy. $^{124}$I MIBG could be advantageous over $^{123}$I-MIBG in PET imaging. Carbon-11 ($^{11}$C)- or fluorine-18 ($^{18}$F)-labeled L-dihydroxyphenylalanine (DOPA) may be useful based on the increased activity of L-DOPA decarboxylase, one of the hallmarks of NETs [12].

#### Based on the Catecholamine Transport Pathway

Pheochromocytoma, neuroblastoma, and other chromaffin tumor tissues, due to their ability to produce epinephrine and NE, concentrate many synthetic amine precursors using catecholamine transporters. $^{11}$C-epinephrine and $^{11}$C-hydroxyepiphedrine ($^{11}$C-HED) are catecholamine analogs, and $^{18}$F-fluorodopamine is a catecholamine precursor, all of which concentrate, and thus help detect NETs [13].

#### Based on Increased Glucose Metabolism

The utilization of $^{18}$F-2-fluoro-2-deoxyglucose ($^{18}$F-FDG) for tumor imaging is based on the high glucose metabolism of many cancer cells for meeting their energy demand. $^{18}$F-FDG enters the glycolytic pathway like glucose in cytoplasm, where it is phosphorylated by the enzyme hexokinase to $^{18}$F-FDG-6-phosphate; however, it is not significantly metabolized, resulting in further accumulation (trapping) inside the cancer cell. $^{18}$F-FDG PET has a role in comprehensive tumor assessment in intermediate- and high-grade tumors: intense metabolic activity of tumors/metastases indicates a poor prognosis due to the presence of aggressive tumor clones [14].

Both conventional and functional imaging tools play a critical role in the diagnosis of NETs. CT or MRI alone cannot provide specific information regarding the functional status of the tumor. As knowing the functional status is essential in most cases prior to starting any of the available therapies, the current medical consensus should be to use PET/CT (or SPECT/CT or SPECT when PET is not available) at all tumor stages, and add MRI or other specific imaging modalities only when needed. Clinical indications for PET/CT in NETs are the following:

- Diagnosis and staging
- Follow-up of patients after surgery
- Follow-up of patients after octreotide, chemotherapy or targeted therapy (kinase inhibitors)
- Choosing the appropriate therapeutic regime of PRRT
- Predicting response to PRRT
- Defining patient prognosis.

## Targeted Radionuclide Therapy

Following scintigraphic localization of NETs with radiolabeled SST analogs, therapeutic approaches with radiolabeled peptides were developed. PRRT comprises systemic administration of a specific, well-defined radiopharmaceutical composed of a therapeutic radionuclide (e.g., a β-emitting radionuclide $^{177}$Lu or $^{90}$Y) chelated to a peptide for the purpose of delivering cytotoxic radiation to a tumor. The biological basis of PRRT is the SSTR 2A-mediated internalization and intracellular retention of the radiopeptide. PRRT can deliver adequate radiation doses to tumors to achieve volume reduction or even cure. Several clinical trials indicate that PRRT with radiolabeled SST analogs is among the most promising newly developed targeted tools for NETs [15-19]. PRRT is ideal for well-differentiated GEP and bronchial NETs (G1 or G2) according to the World Health Organization (WHO) 2010 classification [20]. Recently, as a joint effort of the International Atomic Energy Agency (IAEA), European Association

of Nuclear Medicine (EANM), and Society of Nuclear Medicine and Molecular Imaging (SNMMI), practical guidelines on PRRT in NETs were formulated based on recent literature and opinions of leading experts covering rationale, indications, and contraindications for PRRT, treatment response assessment, and patient follow-up [21].

Prerequisites for PRRT are as follows:

- Histologically proven NET
- High SSTR expression determined by functional imaging with OctreoScan (Krenning score) or $^{68}$Ga SSTR PET/CT
- Patient condition: Karnofsky-Lansky Performance Status >60% or Eastern Cooperative Oncology Group (ECOG) <2
- Tumor differentiation, preferably G1 or G2
- Proliferation rate (Ki-67/mitotic index) of the tumor, preferably ⩽20%.

Due to their small size, radiopeptides are filtered through glomerular capillaries in the kidneys and subsequently reabsorbed and retained in the proximal tubular cells, resulting in renal irradiation. Kidneys are the dose-limiting organs for PRRT due to their marked radiosensitivity [16, 22]. However, adequate renal protection can minimize the risk of renal damage. Positively charged molecules, such as L-lysine and/or L-arginine, competitively inhibit proximal tubular reabsorption of the radiopeptide and hence are coadministered with PRRT, reducing renal dose by 9-53% [23]. Besides renal toxicity, bone marrow involvement must be considered, although it appears not to be a principal dose-limiting factor. Acute mild hematological toxicity is not uncommon, especially after $^{90}$Y-labeled peptide therapy, and the possibility of a mild but progressive impoverishment in bone marrow reserves must be considered after repeated cycles. In addition, myelodysplastic syndrome (MDS) or overt leukemia may develop rarely in patients receiving high doses to bone marrow, especially in patients previously treated with alkylating chemotoxic agents [15]. PRRT should only be performed at specialized centers, as NET patients need highly individualized, interdisciplinary treatment and long-term care [24].

Many studies have already clearly substantiated the efficacy of PRRT in terms of response and survival benefit as a treatment option for progressive and metastasized NETs. Three months after the last therapy cycle in 310 patients, Kwekkeboom et al. [18] analyzed their response to PRRT with $^{177}$Lu-DOTATATE using a cumulative activity of 22.2-29.6 GBq (600-800 mCi). The objective tumor response [complete remission (CR), partial remission (PR), and minor response (MR)] was found in 46% of the patients. With very few adverse effects, there was a benefit in overall survival of several years (median survival from start of treatment was 46 months). In a study of a large cohort of 1,109 patients treated with $^{90}$Y-DOTATOC at the University Hospital Basel, morphological response was noted in 34.1% of patients, and stable disease (SD) in 5.2% patients was associated with longer survival (median survival in responders 3.8 years). Not only were morphological, biochemical, and clinical responses associated with longer median survival but also high tumor uptake on SSTR scintigraphy [19].

Due to the high energy and penetrating capacity of its beta particles, $^{90}$Y is suitable for larger tumors, with an optimal diameter of 34 mm. As receptor density and therefore tracer distribution could be heterogeneous, a better crossfire effect is helpful in these tumors. On the other hand, $^{177}$Lu has lower energy and smaller particle range, which allows better absorption in smaller tumors with an optimal diameter of 2 mm. The combination of $^{90}$Y- and $^{177}$Lu-labelled SMS analogs in an animal model demonstrated better tumor response than the use of each radiolabeled analog separately [25]. A conceivable solution to take this heterogeneity into account is the use of a combination of radionuclides $^{177}$Lu and $^{90}$Y, considerably different energies and tissue penetration ranges of the emitted beta particles. Sequential administration of $^{90}$Y- and $^{177}$Lu-labelled analogs also is helpful for treating larger tumors, followed by treatment of smaller metastases in further treatment cycles. This concept of DUO-PRRT refers to the use of $^{90}$Y- and $^{177}$Lu-labeled SMS analogs (DOTATATE or DOTATOC) in sequence, i.e., in two different settings 3-6 months apart. Tandem PRRT, on the other hand, specifically refers to concurrent use of these radioisotopes, i.e., in the same setting (Fig. 2). The results of a recent study by Kunikowska et al. indicate that tandem PRRT (with $^{90}$Y/$^{177}$Lu-DOTATATE) provided longer overall survival than with a single radioisotope ($^{90}$Y-DOTATATE), and the safety of both methods was comparable [26].

### Selective Targeting: Intra-Arterial PRRT

Intra-arterial PRRT involves radiopeptide administration in order to selectively target tumor receptors and minimize systemic toxicity. Intra-arterial administration of a mean cumulative activity of 58 GBq (1,570 mCi) $^{111}$In-octreotide in 16 patients with GEP-NETs and liver metastases showed objective tumor response (CR and PR) in 56% patients. Median survival for patients with CR, PR, or SD was 32 months [27].

### Radiosensitization

The 5-fluorouracil (5-FU) prodrug capecitabine has a radiosensitizing effect, as many tumors have a higher amount of thymidine phosphorylase (TP) needed to convert the inactive form (capecitabine) into its active form (5-FU). This leads to a higher concentration of the active form in tumors than in normal tissues. Synergistically, irradiation can induce an upregulation of TP and may enhance the effect of capecitabine [28].

### PRRT in Neoadjuvant and Adjuvant Settings

Neoadjuvant PRRT has also been administered in cases of inoperable NETs so that the tumor could be rendered operable by creating radiation-induced necrosis and

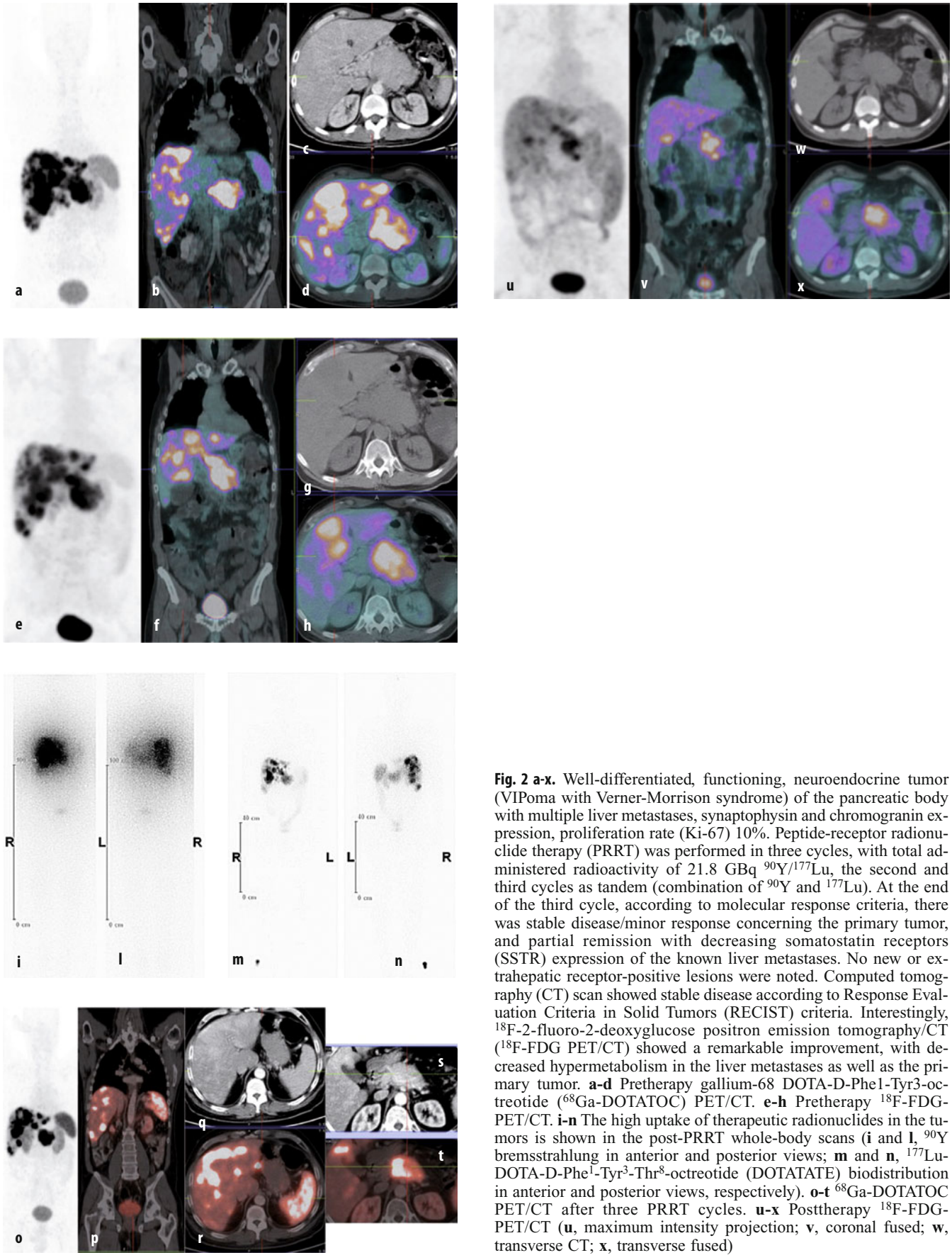


**Fig. 2 a-x.** Well-differentiated, functioning, neuroendocrine tumor (VIPoma with Verner-Morrison syndrome) of the pancreatic body with multiple liver metastases, synaptophysin and chromogranin expression, proliferation rate (Ki-67) 10%. Peptide-receptor radionuclide therapy (PRRT) was performed in three cycles, with total administered radioactivity of 21.8 GBq $^{90}$Y/$^{177}$Lu, the second and third cycles as tandem (combination of $^{90}$Y and $^{177}$Lu). At the end of the third cycle, according to molecular response criteria, there was stable disease/minor response concerning the primary tumor, and partial remission with decreasing somatostatin receptors (SSTR) expression of the known liver metastases. No new or extrahepatic receptor-positive lesions were noted. Computed tomography (CT) scan showed stable disease according to Response Evaluation Criteria in Solid Tumors (RECIST) criteria. Interestingly, $^{18}$F-2-fluoro-2-deoxyglucose positron emission tomography/CT ($^{18}$F-FDG PET/CT) showed a remarkable improvement, with decreased hypermetabolism in the liver metastases as well as the primary tumor. **a-d** Pretherapy gallium-68 DOTA-D-Phe1-Tyr3-octreotide ($^{68}$Ga-DOTATOC) PET/CT. **e-h** Pretherapy $^{18}$F-FDG-PET/CT. **i-n** The high uptake of therapeutic radionuclides in the tumors is shown in the post-PRRT whole-body scans (**i** and **l**, $^{90}$Y bremsstrahlung in anterior and posterior views; **m** and **n**, $^{177}$Lu-DOTA-D-Phe$^{1}$-Tyr$^{3}$-Thr$^{8}$-octreotide (DOTATATE) biodistribution in anterior and posterior views, respectively). **o-t** $^{68}$Ga-DOTATOC PET/CT after three PRRT cycles. **u-x** Posttherapy $^{18}$F-FDG-PET/CT (**u**, maximum intensity projection; **v**, coronal fused; **w**, transverse CT; **x**, transverse fused)

resultant complete remission after surgery [29]. A rationale for the adjuvant use of PRRT after surgery for NETs is to prevent metastases due to tumor spill as a result of surgical handling.

## References


1. Modlin IM, Oberg K, Chung DC et al (2008) Gastroenteropancreatic neuroendocrine tumours. Lancet Oncol 9:61-72.
2. Rufini V, Baum RP, Castaldi P et al (2012) Role of PET/CT in the functional imaging of endocrine pancreatic tumors. Abdom Imaging 37:1004-1020.
3. Baum RP, Prasad V (2008) PET and PET/CT imaging of neuroendocrine tumors. In: Wahl R, Beansland RSB (2008) Principles and practice of PET and PET/CT. Lippincott and Williams, Philadelphia, PA.
4. Krenning EP, Kwekkeboom DJ, Bakker WH et al (1993) Somatostatin receptor scintigraphy with [$^{111}$In-DTPA-D-Phe1]- and [$^{123}$I-Tyr3]-octreotide: the Rotterdam experience with more than 1000 patients. Eur J Nucl Med 20:716-731.
5. Decristoforo C, Melendez-Alafort L, Sosabowski JK et al (2000) $^{99m}$Tc-HYNIC-[Tyr3]-octreotide for imaging somatostatin-receptor-positive tumors: preclinical evaluation and comparison with $^{111}$In-octreotide. J Nucl Med 41:1114-1119.
6. Baum RP, Kulkarni HR, Carreras C (2012) Peptides and receptors in image-guided therapy: THERANOSTICS for neuroendocrine neoplasms. Semin Nucl Med 42:190-207.
7. Hofmann M, Maecke H, Borner R et al (2001) Biokinetics and imaging with the somatostatin receptor PET radioligand $^{68}$Ga-DOTATOC: preliminary data. Eur J Nucl Med Mol Imaging 28:1751-1757.
8. Buchmann I, Henze M, Engelbrecht S et al (2007) Comparison of $^{68}$Ga-DOTATOC PET and $^{111}$In-DTPAOC (Octreoscan) SPECT in patients with neuroendocrine tumours. Eur J Nucl Med Mol Imaging 34:1617-1626.
9. Kaemmerer D, Peter L, Lupp A et al (2011) Molecular imaging with $^{68}$Ga-SSTR PET/CT and correlation to immunohistochemistry of somatostatin receptors in neuroendocrine tumours. Eur J Nucl Med Mol Imaging 8:1659-1668.
10. Prasad V, Ambrosini V, Hommann M (2010) Detection of unknown primary neuroendocrine tumours (CUP-NET) using $^{68}$Ga-DOTA-NOC receptor PET/CT. Eur J Nucl Med Mol Imaging 37:67-77.
11. Shapiro B, Copp JE, Sisson JC et al (1985) Iodine-131 metaiodobenzylguanidine for the locating of suspected pheochromocytoma: experience in 400 cases. J Nucl Med 26:576-585.
12. Gazdar AF, Helman LJ, Israel MA et al (1988) Expression of neuroendocrine cell markers L-DOPA decarboxylase, chromogranin A, and dense core granules in human tumors of endocrine and nonendocrine origin. Cancer Res 48:4078-4082.
13. Kolby L, Bernhardt P, Levin-Jakobsen AM et al (2003) Uptake of meta-iodobenzylguanidine in neuroendocrine tumours is mediated by vesicular monoamine transporters. Br J Cancer 89:1383-1388.
14. Kayani I, Bomanji JB, Groves A et al (2008) Functional imaging of neuroendocrine tumours with combined PET/CT using $^{68}$Ga-DOTATATE (Dota-DPhe1, Tyr3-octreotate) and $^{18}$F-FDG. Cancer 112:2447-2455.
15. Kwekkeboom DJ, Mueller-Brand J, Paganelli G et al (2005) Overview of results of peptide receptor radionuclide therapy with 3 radiolabeled somatostatin analogs. J Nucl Med 46:62S-66S.
16. Bodei L, Cremonesi M, Grana C et al (2004) Receptor radionuclide therapy with $^{90}$Y-[DOTA]0-Tyr3-octreotide ($^{90}$Y-DOTATOC) in neuroendocrine tumors. Eur J Nucl Med Mol Imaging 31:1038-1046.
17. Khan S, Krenning EP, van Essen M et al (2011) Quality of life in 265 patients with gastroenteropancreatic or bronchial neuroendocrine tumors treated with [$^{177}$Lu-DOTA0,Tyr3]octreotate. J Nucl Med 52:1361-1368.
18. Kwekkeboom DJ, de Herder WW, Kam BL et al (2008) Treatment with the radiolabeled somatostatin analog [$^{177}$Lu-DOTA 0,Tyr3]octreotate: toxicity, efficacy, and survival. J Clin Oncol 26:2124-2130.
19. Imhof A, Brunner P, Marincek N et al (2011) Response, survival, and long-term toxicity after therapy with the radiolabeled somatostatin analogue [$^{90}$Y-DOTA]-TOC in metastasized neuroendocrine cancers. J Clin Oncol 29:2416-2423.
20. Anlauf M, Gerlach P, Raffel A et al (2011) Neuroendocrine neoplasia of the gastroenteropancreatic system. Pathology and classification. Onkologe 17:572-582.
21. Bodei L, Mueller-Brand J, Baum RP et al (2013) The joint IAEA, EANM, and SNMMI practical guidance on peptide receptor radionuclide therapy (PRRNT) in neuroendocrine tumours. Eur J Nucl Med Mol Imaging 40:800-816.
22. Valkema R, Pauwels SA, Kvols LK et al (2005) Long-term follow-up of renal function after peptide receptor radiation therapy with $^{90}$Y-DOTA(0),Tyr(3)-octreotide and $^{177}$Lu-DOTA(0), Tyr(3)-octreotate. J Nucl Med 46:83S-91S.
23. Rolleman EJ, Valkema R, de Jong M et al (2003) Safe and effective inhibition of renal uptake of radiolabelled octreotide by a combination of lysine and arginine. Eur J Nucl Med Mol Imaging 30:9-15.
24. Hörsch D, Bert T, Schrader J et al (2012) Pancreatic neuroendocrine neoplasms. Minerva Gastroenterol Dietol 58:401-426.
25. de Jong M, Breeman WA, Valkema R et al (2005) Combination radionuclide therapy using 177Lu- and 90Y-labeled somatostatin analogs. J Nucl Med 46:13S-7S.
26. Kunikowska J, Królicki L, Hubalewska-Dydejczyk A et al (2011) Clinical results of radionuclide therapy of neuroendocrine tumours with $^{90}$Y-DOTATATE and tandem $^{90}$Y/$^{177}$Lu-DOTATATE: which is a better therapy option? Eur J Nucl Med Mol Imaging 38:1788-1797.
27. Limouris GS, Chatziioannou A, Kontogeorgakos D et al (2008) Selective hepatic arterial infusion of In-111-DTPA- Phe1-octreotide in neuroendocrine liver metastases. Eur J Nucl Med Mol Imaging 35:1827-1837.
28. Claringbold PG, Brayshaw PA, Price RA et al (2011) Phase II study of radiopeptide 177Lu-octreotate and capecitabine therapy of progressive disseminated neuroendocrine tumours. Eur J Nucl Med Mol Imaging 38:302-311.
29. Kaemmerer D, Prasad V, Daffner W et al (2009) Neoadjuvant peptide receptor radionuclide therapy for an inoperable neuroendocrine pancreatic tumor. World J Gastroenterol 15:5867-5870.

# PET/CT in Hepatobiliary-Pancreatic Tumors

Stefano Fanti, Elena Tabacchi, Hanna Svirydenka, Cristina Nanni

Nuclear Medicine Unit, Policlinico St. Orsola-Malpighi; University of Bologna, Bologna, Italy

## Introduction

Primary hepatobiliary malignancies include liver tumors, cholangiocarcinoma (CCA), and gallbladder carcinoma (GBC). The prognosis for hepatobiliary and pancreatic malignancies is dismal, with a 5-year survival rate ranging from 5% to 20%. Accurate detection, diagnosis, and staging may lead to more appropriate treatments and improved clinical outcomes. As surgical resection is the primary curative option for most hepatobiliary/pancreatic cancers, earlier and more correct detection may increase the likelihood of timely intervention [1].

The assessment of hepatobiliary and pancreatic tumors is commonly obtained by ultrasound (US), computed tomography (CT), and magnetic resonance imaging (MRI). Functional imaging techniques are increasingly utilized for more precise patient assessment, such as metabolic imaging with positron emission tomography (PET), combined PET/CT (even with PET-contrast-enhanced CT scanning), PET/MRI and diffusion-weighted imaging (DWI) [2]. PET provides unique biological information that is different from current imaging modalities. Structural analysis forms the basis of conventional imaging, such as CT and MRI, exploiting the anatomic changes to detect disease. On the other hand, PET is based on identifying molecular biological changes. Undoubtedly, PET with $^{18}$F-fluorodeoxyglucose (FDG) has revolutionized imaging evaluation of patients with cancer. The utility of FDG-PET is based on the Warburg effect, which accounts for increased glucose metabolism of cancerous tissues. In normoxic conditions, tumors cells primarily use glycolysis for energy production instead of mitochondrial oxidative phosphorylation, as do normal cells. Most tumors cells have an increased glucose metabolism due to increased levels of glucose transporter proteins (GLUT-1) and increased levels of intracellular enzymes that promote glycolysis, such as hexokinase and phosphofructokinase. This, together with the relatively low levels of glucose-6-phosphatase in most cancer cells, leads to an accumulation and trapping of FDG in the cancer cell, with positron emission (PE) allowing visualization of increased FDG compared with normal cells [3]. The development and diffusion of hybrid PET/CT scanners incorporate the functional information of PET with the anatomical details of CT, thus combining the benefits of both modalities. Images produced of the entire body are obtained in a single examination. Fused PET/CT also provides certain anatomic delineation of FDG-avid lesions, improving the overall explanation, accuracy, and confidence of the image.

However, some cancers demonstrate low FDG avidity. Lesions that do not demonstrate FDG uptake may be described and characterized by the CT component. In addition PET permits accurate quantification of FDG uptake in tissue, and previous studies demonstrate that standardized uptake values (SUVs) provide highly reproducible parameters of tumor glucose use, useful data for clinical imaging, and research end points [4]. Finally, because PET tracers have very little pharmacologic side effects, PET can safely provide biological information about hepatobiliary and pancreatic tumors without the complications associated with other diagnostic interventions, such as fine-needle aspiration (FNA) biopsy, imaging with hyperosmolar contrast agents, or endoscopic retrograde cholangiopancreatography [4].

Thus, appropriate patient preparation, scanning protocol, combined assessment of PET and CT data, and the evaluation of conventional imaging findings are essential in defining the disease and avoiding diagnostic pitfalls [3].

## Liver Malignancy

Primary hepatic tumors (malignant or benign) are infrequent and include hepatocellular carcinomas (HCCs), hemangiomas, adenoma, and focal nodular hyperplasias. Imaging and differentiation of focal liver lesions is the domain of morphological imaging; despite high diagnostic accuracy of CT and MRI, difficulties remain in the diagnostic workup, and in recent years, the use of FDG-PET as an adjuvant to morphologic imaging has increased.

*Diseases of the Abdomen and Pelvis 2014-2017*,
DOI: 10.1007/978-88-470-5659-6_31 

## Hepatocellular Carcinoma

HCC is the most frequent primary liver cancer, with an increased incidence in patients with chronic liver diseases such as hepatitis, alcoholic cirrhosis, and systemic immune disease, particularly HIV, and has a poor prognosis in untreated patients [5]. Gold standard imaging modalities for differentiating HCC from other liver pathologies and delineating tumor extent are triple-phase contrast-enhanced CT (ce-CT) and MRI [4].

Many studies demonstrate inadequate sensitivity of FDG-PET in diagnosing primary HCC related to low FDG uptake due to the low expression of the enzyme glucose 6-phosphatase in both normal liver and in well-differentiated HCCs, in association with other limitations of the method represented by lesion size (spatial resolution 1 cm) and shape [3]. Therefore the addition of CT images is very important when the lesion is not FDG avid, because 70% of HCCs are visible on unenhanced CT, e.g., hypodense lesions, and an additional 20% is visible, e.g., hyperdense lesions [5]. As a result fusions of FDG-PET and CT images led to an improvement in detection, localization, and differentiation between physiologic and pathologic uptake on both CT and FDG-PET images alone. In particular, Torizuka et al. [6] showed that FDG uptake by HCC lesions correlates with the degree of HCC differentiation: high-grade HCCs have increased FDG uptake [mean ± standard deviation (SD) SUV 6.89 ± 3.39] compared with low-grade HCCs (mean SUV 3.21 ± 0.58) ($p<0.005$). For this reason, FDG-PET scans have an increased ability to detect higher-grade and a decreased ability to detect low-grade HCCs as a result of decreased FDG uptake. Sensitivity of FDG-PET/CT in detecting the amount of HCC lesions is about 50-65%.

Despite these considerations, FDG-PET is important in predicting clinical outcome and prognosis in patients with HCC: seeing that FDG uptake acts as a marker of differentiation, SUV can give an idea of the histopathologic nature of the tumor. Shiomi et al. [7] showed that SUV ratios (SUV ratio of tumor to nontumor in livers) of HCC tumors correlates with tumor volume-doubling time ($r=-0.582$; $p=0.006$) and that the cumulative survival rate can be predicted on the basis of SUV ratio [4, 5]. Additionally, Ho et al. [8] proposed that poorly differentiated HCCs, which are more likely to metastasize, tend to be FDG avid, and for this reason, metastases from HCCs in general are more likely to be detected with FDG-PET.

Furthermore, FDG-PET could be a good preoperative tool with which to ascertain the risks of posttransplantation tumor recurrence (higher probability if there is positivity in the images) and is useful in the follow-up after liver transplantation in terms of detecting extrahepatic metastases, thanks to the total body scan, especially if there is suspicion of recurrence not identified by conventional screening modalities. In particular, Kawaoka et al. [9] found FDG-PET/CT to have a higher sensitivity for detecting bone metastases from primary HCC compared with ce-CT and bone scintigraphy. In fact, it is able to detect metabolic changes preceding structural findings.

Furthermore, PET/CT is useful for restaging HCC after ablative procedures, e.g., radiofrequency ablation (RFA) or treatment with antiangiogenic drugs: the amount of FDG uptake correlates with the response to therapy, and a decreased uptake indicates a positive response.

Another use for PET/CT is related to the $^{90}$Y radioembolization consisting of using microspheres made of glass (TheraSpheres) or resin (SIR-Spheres) beads labeled with $^{90}$Y that emits β radiation and X-rays (bremsstrahlung) to treat unresectable liver tumors. This PE modality makes it possible to evaluate the $^{90}$Y microsphere distribution in the liver using PET/CT: a study by D'Arienzo et al. [10] show that $^{90}$Y-PET provided very good-quality images of liver tumors 2 h after the $^{90}$Y radioembolization, which correlated to FDG uptake in the target lesion on the pretreatment PET/CT. In that study, images obtained were used to calculate the target dose using voxel-based dosimetry, and it is proven that the calculated dose to target lesions on $^{90}$Y PET/CT predicts response to treatment on the 6-month follow-up PET/CT [4].

Seeing that FDG-PET has limited sensitivity for detecting some HCC tumors due to their variable FDG uptake, $^{11}$C-acetate-PET complements FDG-PET in a dual-tracer PET scan. $^{11}$C-acetate enters the Krebs cycle as a substrate for oxidation in fatty acid and cholesterol synthesis, and the former seems to be the major factor affecting its uptake by HCC [4, 11]. Ho et al. [8] found that well-differentiated HCCs preferably accumulate $^{11}$C- acetate, whereas poorly differentiated tumors tend to be FDG avid: HCC tumors with no evident FDG uptake were detected by $^{11}$C-acetate uptake and vice versa. Delbeke et al. [12] indicate that different uptake of tracers by lesions can restrict the differential diagnosis: when a tumor accumulates both tracers, or only $^{11}$C-acetate, HCC is high on the differential; lesions that accumulate only FDG suggest a non-HCC malignancy, and lesions that accumulate no tracer connote a benign pathologic abnormality.

Relying on tracer avidity to different types of HCC lesions, dual-tracer PET could increase the sensitivity in all HCC. The addition of $^{11}$C-acetate to FDG-PET/CT raises the global sensitivity for detecting primary HCC but not for extrahepatic metastases. Ho et al. [8] show that dual-tracer PET/CT has a sensitivity of 98%, a specificity of 86%, a positive predictive value (PPV) of 97%, a negative predicting value (NPV) of 90%, and an accuracy of 96%. Analogously, $^{11}$C-choline, which is incorporated into the cell membrane during phospholipid synthesis, seems to be useful when combined with FDG for detecting HCC lesions and is referred to have better detection for moderately differentiated HCC [3, 4, 11] (Fig. 1).

$^{18}$F-fluorothymidine is a marker of tumor proliferation and it was suggested, by a small sample size, that the level of its uptake has a prognostic value with reduced overall survival in lesions with a high uptake [4].

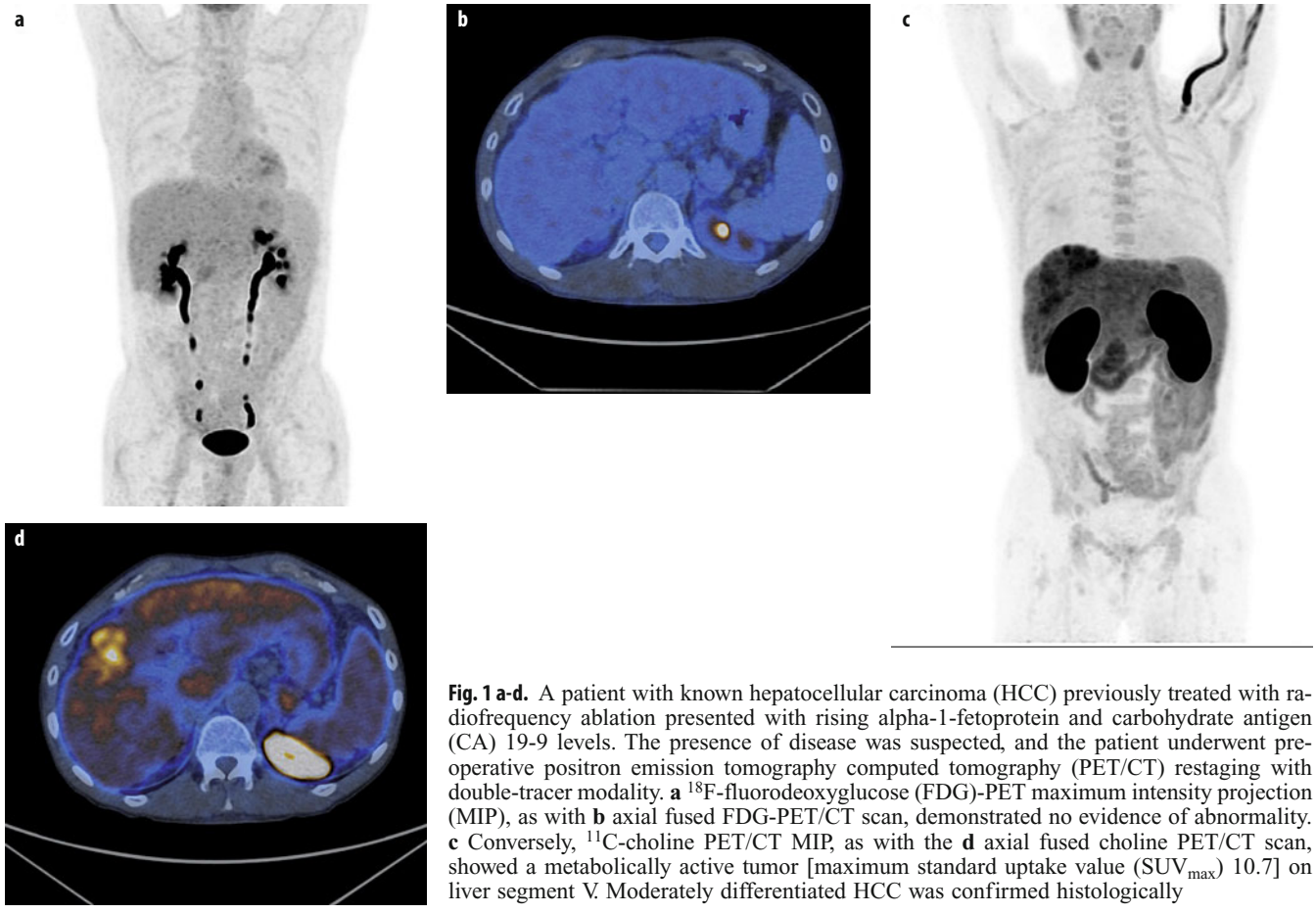


**Fig. 1 a-d.** A patient with known hepatocellular carcinoma (HCC) previously treated with radiofrequency ablation presented with rising alpha-1-fetoprotein and carbohydrate antigen (CA) 19-9 levels. The presence of disease was suspected, and the patient underwent preoperative positron emission tomography computed tomography (PET/CT) restaging with double-tracer modality. **a** $^{18}$F-fluorodeoxyglucose (FDG)-PET maximum intensity projection (MIP), as with **b** axial fused FDG-PET/CT scan, demonstrated no evidence of abnormality. **c** Conversely, $^{11}$C-choline PET/CT MIP, as with the **d** axial fused choline PET/CT scan, showed a metabolically active tumor [maximum standard uptake value ($SUV_{max}$) 10.7] on liver segment V. Moderately differentiated HCC was confirmed histologically

## Biliary System Malignancy

Primary neoplasms of the biliary system are a heterogeneous group mostly composed of GBC and CCA.

### Gallbladder Carcinoma

GBC is the fifth most common cancer of the gastrointestinal tract, with approximately 6,000 new cases each year. Only 10% of cancers are localized to the gallbladder upon detection. Hence, despite the poor ability of US and CT scanning to distinguish malignant from benign gallbladder disease, these studies are most commonly used to detect GBC. Despite preoperative assessment with traditional cross-sectional imaging modalities, up to a third of patients with primary biliary malignancy still undergo unnecessary surgery. The main contraindications to resectability found in surgery are occult peritoneal and liver metastases and, less commonly, vascular and lymph node invasion.

By contributing additional functional information, and when used in the correct context, FDG-PET/CT can allow earlier detection of tumors, identification of occult metastatic disease, characterization of equivocal lesions, assessment of therapeutic response, and globally more accurate staging for potential resection [3]. Some studies suggest that PET has a high sensitivity for detecting GBC (75-100%); however, several studies show poor sensitivity of FDG-PET/CT for detecting regional lymph node metastasis in GBC [14].

GBC is associated with a rate of peritoneal metastasis as high as 30-75 %, and the risk of metastasis strongly correlates with the presenting T stage. False-negative results can be related to mucinous adenocarcinoma; false-positive results can take place in patients with flogistic or granulomatous reactions and in cases of adenomyomatosis [1].

### Cholangiocarcinoma

CCA is a rare tumor arising from the epithelium of the intrahepatic or extrahepatic bile ducts, represents about 3% of all gastrointestinal malignancies, and is the second most common hepatic malignancy after HCC. Only a minority of patients who present with CCA have known risk factors, such as chronic biliary inflammation, cholestasis, and/or congenital abnormalities.

Despite advances in diagnostic techniques and new therapeutic strategies, a 5-year survival for CCA continues to be $<$5%. This is mainly attributed to the delayed

diagnosis, because the tumor remains silent until it is advanced and obstructs the bile duct. More than 90% of CCA are well- to moderately differentiated adenocarcinomas with a tendency to develop desmoplastic reaction and early perineural invasion. Diagnosis and accurate staging are improved with better imaging and advanced cytologic techniques [15].

CCAs are classified according to their anatomic location as: intrahepatic (ICCA), perihilar, or distal extrahepatic (ECCA). Perihilar CCAs, first described as a separate entity by Klatskin in 1965 [16], represent 60-70% of all CCAs, whereas ICCA represents 5-10% and ECCA 20-30%.

According to the morphologic classification system proposed by the Liver Cancer Study Group of Japan, CCA is classified into mass-forming, periductal infiltrating, and intraductal growth types [17].

Carbohydrate antigen (CA) 19-9 and carcinoembryonic antigen (CEA) are the most commonly used tumors marker, and MR-cholangiopancreatography is the best available imaging modality for CCA. Meticulous interpretation of all available clinical and radiological data is recommended to determine resectability and avoid unnecessary interventions. Memorial Sloan Kettering Cancer Center has shown that FDG-PET/CT had an overall sensitivity of 78% for identifying the primary tumor for CCA, which changed manageability in nearly a quarter of all patients [18].

Histopathology of the tumor is very important; in fact, PET has significant accuracy in diagnosing nodular tumor subtypes but may be less sensitive and produce false-negative scans due to poor FDG uptake in infiltrative and mucinous subtypes [19]. Additionally, PET/CT is vulnerable to diagnostic errors when biliary stents or postendoscopic cholangitis are present, as well as in the setting of chronic biliary inflammatory conditions such as primary sclerosing cholangitis, common in CCA patients. Regarding N staging, the predominance of lymph node involvement

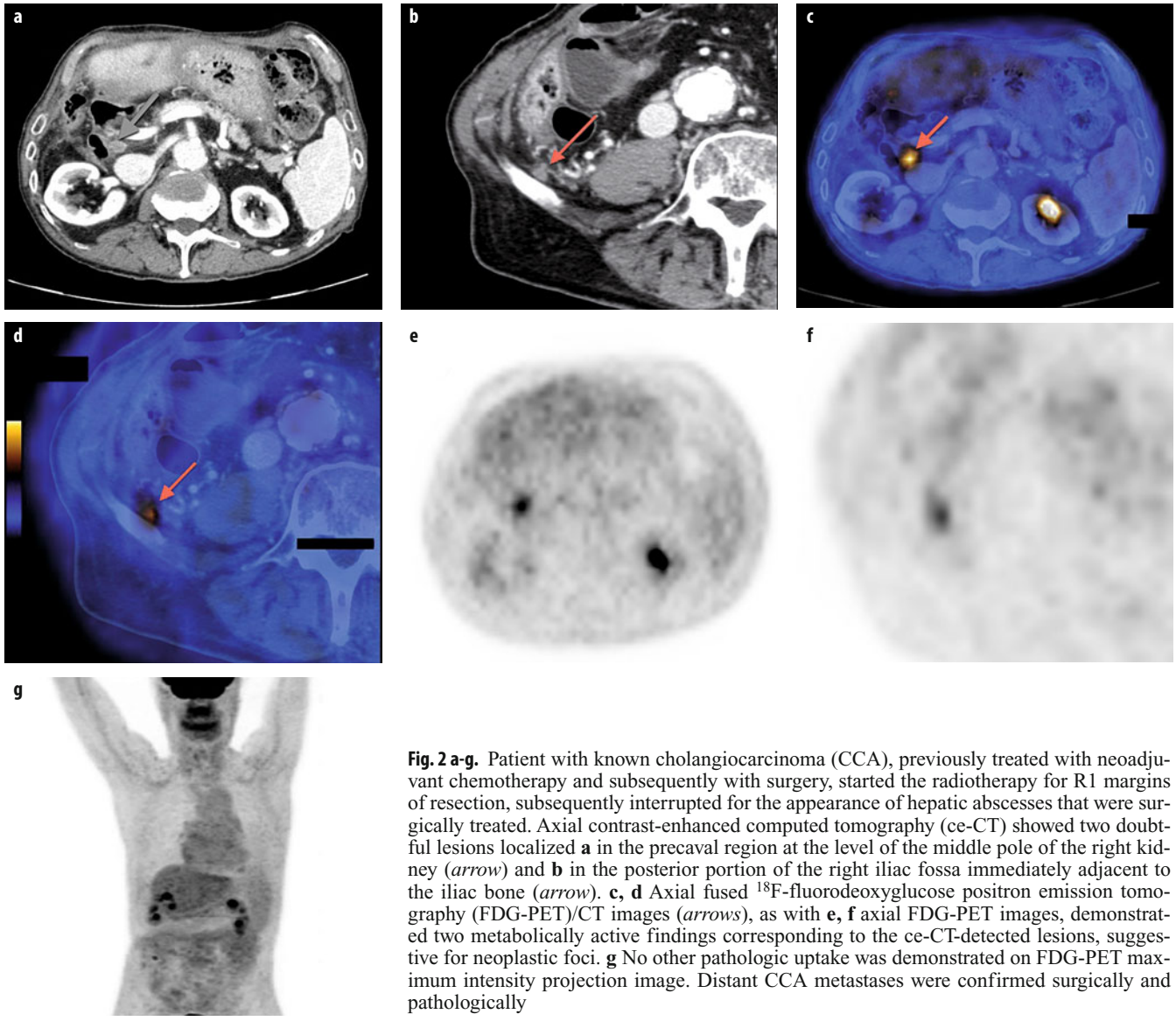


**Fig. 2 a-g.** Patient with known cholangiocarcinoma (CCA), previously treated with neoadjuvant chemotherapy and subsequently with surgery, started the radiotherapy for R1 margins of resection, subsequently interrupted for the appearance of hepatic abscesses that were surgically treated. Axial contrast-enhanced computed tomography (ce-CT) showed two doubtful lesions localized **a** in the precaval region at the level of the middle pole of the right kidney (*arrow*) and **b** in the posterior portion of the right iliac fossa immediately adjacent to the iliac bone (*arrow*). **c, d** Axial fused $^{18}$F-fluorodeoxyglucose positron emission tomography (FDG-PET)/CT images (*arrows*), as with **e, f** axial FDG-PET images, demonstrated two metabolically active findings corresponding to the ce-CT-detected lesions, suggestive for neoplastic foci. **g** No other pathologic uptake was demonstrated on FDG-PET maximum intensity projection image. Distant CCA metastases were confirmed surgically and pathologically

is around 45% for all CCA, with distal ECCA having the highest incidence of nodal metastases. It is difficult to detect microscopic lymph node metastases by PET/CT, and in extrahepatic CCA, difficulties can be encountered in distinguishing between extrahepatic parts of the tumor itself and FDG accumulation in perihilar lymph nodes. Presence of distant metastases (e.g., lung, bone, peritoneal, distant lymph nodes) is seen in 30% of patients at the time of diagnosis and connected with survival of only a few months. PET/CT has a sensitivity of 94-100% in detecting distal metastasis (Fig. 2). Additionally, $^{18}$F-FDG-PET/CT appears to be an encouraging method in postoperative monitoring of CCA recurrence. A small series by Chikamoto et al. [20] found that PET/CT had a sensitivity of 80%; in these cases, conventional imaging is limited because of difficulties in differentiating tumor tissue and postoperative changes [21-23].

## Pancreatic Malignancy

### Pancreatic Ductal Adenocarcinoma

Pancreatic ductal adenocarcinoma (PA) is the fourth leading cause of cancer-related death, with a 5-year survival rate <5% after initial diagnosis. PA is relatively aggressive, and even when <2 cm can present early infiltration of the retroperitoneum and surrounding anatomic structures, including nerves and vessels. Serum CA 19-9 and CEA are detectable in ~75% of patients with PA, and surgery remains the only curative treatment for locally resectable and nonmetastatic pancreatic cancer. In fact, <10-20% of PA is considered surgically resectable.

US, endoscopic retrograde cholangiopancreatography (ERCP), ce-CT, MRI, MR cholangiopancreatography (MRCP), and FDG-PET/CT are widely accepted imaging modalities accessible for PA diagnosis and staging. Unquestionably, PET/CT is valuable in PA management. In particular the potential indications for FDG-PET/CT include imaging-guided biopsy planning in cases with nondiagnostic FNA findings in patients with suspected pancreatic cancer, equivocal CT findings, tumor staging, depicting tumor recurrence, and monitoring response to therapy. Furthermore, it has proved useful in distinguishing postoperative fibrosis from recurrence. Actually, CT is limited in depicting small tumors (sensitivity 83% for lesions <2 cm) and isoattenuating lesions. About 10% of PA and pancreatic metastases are isoattenuating at ce-CT and, consequently, are not observed, even when >2 cm; differentiating mass-forming pancreatitis (MFP) from PA is commonly demanding. Both conditions are characterized by extensive fibrosis, with overlapping morphologic imaging findings. As PA may cause chronic obstructive inflammatory changes and MFP is associated with an increased risk for adenocarcinoma, the cross-sectional radiological detection remains challenging [24]. The reported sensitivity and specificity of FDG-PET/CT in assessing primary PA are 46-71% and 63-100%, respectively.

Staging pancreatic cancer is determined by local and distant spread of disease. Spread to lymph nodes is common and tends toward poor outcome. There are some limitations to current CT criteria for assessing lymph node involvement on the basis of size (>1 cm in the short axis) and in differentiating between benign and malignant lymph nodes. In N staging, some studies report PET/CT sensitivity and specificity ranging from 30% to 49% and 63% to 93%, respectively. The poor performance by FDG-PET may be determined by the small tumor burden in metastatic lymph nodes and intense photon scatter from the primary tumor (known as the penumbra effect). Fused PET/CT may enhance the specificity of nodal staging compared with CT alone and consequently facilitate identification of metastatic deposits in lymph nodes that manifest as nonspecific or borderline enlargement at CT.

PA tends to metastasize to the peritoneum, thus ruling out surgery or locoregional treatment, with the same treatment implications as other types of advanced systemic disease and a poor prognosis (mean survival 6 months) [24, 25].

Description of peritoneal implants remains challenging at CT, with reported sensitivity of 65-88% and specificity of 38-63%.

Analogously undefined lesions are frequently found in the liver at surveillance CT in patients with known malignancy. Description and characterization of hepatic lesions is challenging in patients with a fatty liver or contraindications for contrast agent. Nevertheless, liver or peritoneal spread is discovered during surgery in about 20% of patients with tumors that are deemed resectable at CT. Regarding metastatic liver lesions, increased FDG uptake is a powerful indication of malignancy, and a lack of FDG activity usually supports benignity; however, malignancy cannot be completely excluded in the absence of FDG uptake, especially in small lesions. FDG-PET for preoperative pancreatic cancer staging is cost beneficial because it depicts unexpected distant metastases in 43% of patients, thereby avoiding unnecessary surgery.

After surgery, 72-92% of PA recurs locally within 2 years. Locally recurrent tumors are not usually resectable; however, radiation therapy or ablation (radiofrequency or cryoablation) may be a palliative option. As the expected postoperative changes in the surgical bed and early tumor recurrence have similar morphologic characteristics, reliably in differentiating between them is demanding at CT. Moreover, it is often difficult to obtain an adequate tissue sample because desmoplastic reaction is known to be connected with pancreatic cancers. The reported sensitivity of FDG-PET for depicting tumor recurrence is 96%, compared with 39% for CT and MRI. Postoperative inflammatory changes in the pancreas, radiation therapy, or stent placement may also cause some FDG uptake. To minimize these false-positive results, it is recommended that follow-up PET or PET/CT be performed at least 6 weeks after surgery. Also, PET may play a role in monitoring response to chemo- and radiation therapy in patients with unresectable pancreatic cancer.

As in other neoplasms, a significant reduction in FDG uptake may precede morphologic changes and volumetric reduction at CT and may be proportional to the change in tumor size at subsequent follow-up examinations. FDG-PET/CT might also have prognostic value because tumors with a higher baseline $SUV_{max}$ are more likely to recur in the early postoperative period. $SUV_{max}$ is an independent predictor for overall survival in patients with locally advanced PA.

### Pancreatic Metastases

Pancreatic metastases are rare, accounting for 2% of all pancreatic neoplasms. Primary malignancies that most commonly metastasize to the pancreas are lung, breast, melanoma, gastric, colorectal, renal, and ovarian cancers. They usually occur in the setting of advanced metastatic disease and, rarely, as isolated pancreatic metastases. They may arise synchronously or metachronously and may occur singly (in 25% of patients) or in multiples (in 75% of patients).

### Cystic Neoplasms

Cystic neoplasms of the pancreas constitute <10% of all pancreatic neoplasms. Nevertheless, they have become more commonly reported because of the increased use and improved accuracy of imaging techniques. They encompass a wide range of pathologic conditions ranging from benign lesions (e.g., serous cystoadenomas) to malignant, potentially malignant, and borderline tumors, such as neuroendocrine tumors (NETs) with cystic features, mucinous cystic neoplasms, and intraductal papillary mucinous neoplasms (IPMNs). The accuracy of CT for determining malignancy ranges from 53% to 86%; studies show that FDG-positive cystic neoplasms are frankly malignant or invasive [24, 25].

### Pancreatic Neuroendocrine Tumors

Pancreatic NETs (PNETs) are rare, with an incidence of 1:100,000 individuals per year, and account for 1-2% of all pancreatic neoplasms. Pancreatic endocrine neoplasms are epithelial neoplasms, usually well differentiated, and classified as functional or nonfunctional on the basis of the presence of an associated clinical endocrine paraneoplastic syndrome. Pancreatic endocrine neoplasms are named according to the predominant hormone they produce (e.g., insulinoma, gastrinoma, VIPoma, glucagonoma, somatostatinoma).

Generally, well-differentiated, slow-growing PNETs demonstrate little or no FDG uptake, whereas poorly differentiated PNETs and metastases with a high proliferation index and dedifferentiated tumors, which rarely express somatostatin receptors (SSRs), are well recognized at FDG-PET. Novel radiolabeled somatostatin (SMS) analogs, such as gallium-68 DOTA-D-$Phe^1$-$Tyr^3$-$Thr^8$-octreotide ($^{68}$Ga-DOTATATE) (SSR-2 analogs), $^{68}$Ga-DOTA-D-$Phe^1$-$Tyr^3$-octreotide (DOTATOC) (SSR-2 and SSR-5 analogs), and $^{68}$Ga-DOTA-1-$Nal^3$-octreotide ($^{68}$Ga-DOTANOC) (SSR-2, SSR-3, and SSR-5 analogs) are available to study these tumors.

PNETs overexpress SSRs on their cell surface, and this represents the rationale for the use of SMS analogs for diagnosing and treating these tumors with direct therapeutic implications. $^{68}$Ga PET/CT appears to be a highly sensitive and specific modality for detecting NETs – better than conventional imaging techniques – and can have a significant impact on patient management (Fig. 3). New radiopharmaceutical agents, such as $^{11}$C-5-hydroxy-L-tryptophan ($^{11}$C-HTP) and L-3,4-dihydroxyphenylalanine (L-DOPA) are promising in their ability to help depict primary and metastatic NETs, but their availability remains an obstacle [26].

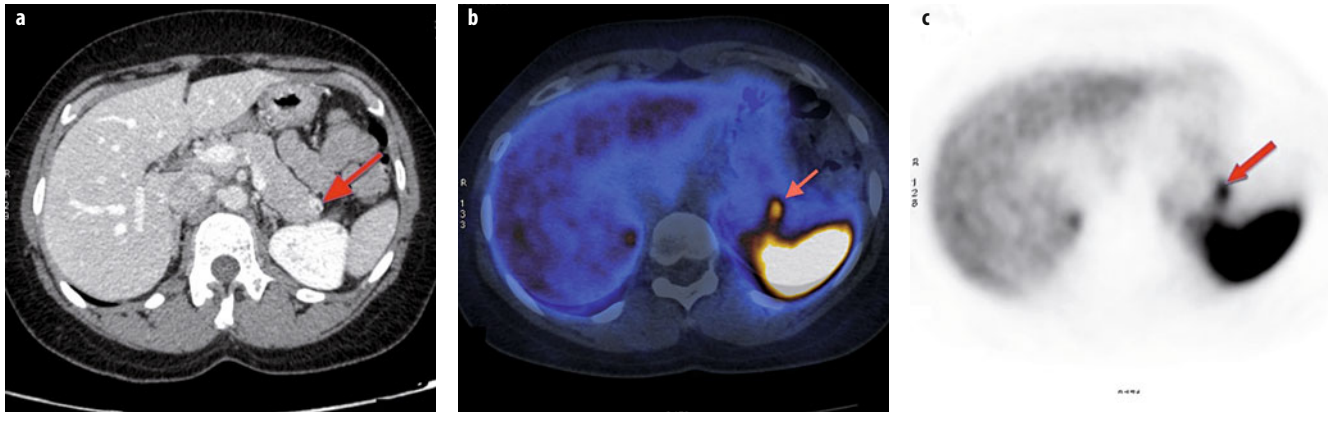


**Fig. 3 a-c.** A 38-year-old patient with a history of kidney lithiasis was studied with contrast-enhanced computed tomography (ce-CT) exam. **a** The presence of a homogeneously enhanced solid lesion at the level of pancreatic tail was incidentally revealed (*arrow*). This finding was suggestive for neoplasm. Chromogranin A marker was of uncertain significance; subsequently, gallium-68 ($^{68}$Ga) positron emission tomography (PET)/CT was performed. **b** Axial fused $^{68}$Ga PET/CT and **c** $^{68}$Ga PET images demonstrated the unique area of somatostatin receptor tracer uptake [maximum standard uptake value ($SUV_{max}$) 15.5] at the level of ce-CT-detected lesion (*arrows*). After 3 months, the patient underwent laparoscopic enucleation and resection of the pancreatic lesion. A well-differentiate neuroendocrine tumor was confirmed histologically

Whereas surgical therapy remains the most appropriate therapy for resectable PNETs, in incurable disease, multimodality treatment using a combination of surgery, liver-directed techniques, SMS analogs, and systemic chemotherapy is becoming more common. As a consequence, improving quality of life and long-term survival of PNET patients is now possible.

## References


1. Lan BY, Kwee SA, Wong LL (2012) Positron emission tomography in hepatobiliary and pancreatic malignancies: a review. Am J Surg 204:232-241.
2. Jadvar H (2012) Hepatocellular carcinoma and gastroenteropancreatic neuroendocrine tumors: potential role of other positron emission tomography radiotracers. Semin Nucl Med 42:247-254.
3. De Gaetano AM, Rufini V, Castaldi P et al (2012) Clinical applications of 18F-FDG-PET in the management of hepatobiliary and pancreatic tumors. Abdom Imaging 37:983-1003.
4. Sharma B, Martin A, Zerizer I (2013) Positron emission tomography-computed tomography in liver imaging. Semin Ultrasound CT MRI 34:66-80.
5. Sacks A, Peller PJ, Surasi DS et al (2011) Value of PET/CT in the management of primary hepatobiliary tumors, Part 2. AJR Am J Roentgenol 197:W260-W265.
6. Torizuka T, Tamaki N, Inokuma T et al (1995) In vivo assessment of glucose metabolism in hepatocellular carcinoma with FDG-PET. J Nucl Med 36:1811-1817.
7. Shiomi S, Nishiguchi S, Ishizu H et al (2001) Usefulness of positron emission tomography with fluorine-18-fluorodeoxyglucose for predicting outcome in patients with hepatocellular carcinoma. Am J Gastroenterol 96:1877-1880.
8. Ho CL, Chen S, Yeung DW, Cheng TK (2007) Dual-tracer PET/CT imaging in evaluation of metastatic hepatocellular carcinoma. J Nucl Med 48:902-909.
9. Kawaoka T, Aikata H, Takaki S et al (2009) FDG positron emission tomography/computed tomography for the detection of extraepatic metastases from hepatocellular carcinoma. Hepatol Res 39:134-142.
10. D'Arienzo M, Chiaramida P, Chiacchiararelli L et al (2012) 90Y PET-based dosimetry after selective internal radiotherapy treatments. Nucl Med Commun 33:633-640.
11. Grassi I, Nanni C, Allegri V et al (2012) The clinical use of PET with (11)C-acetate. Am J Nucl Med Mol Imaging 2:33-47.
12. Delbeke D, Pinson CW (2003) 11C-acetate: a new tracer for the evaluation of hepatocellular carcinoma. J Nucl Med 2003; 44:222-223.
13. Petrowsky H, Wildbrett P, Husarik DB et al (2006) Impact of integrated positron emission tomography and computed tomography on staging and management of gallbladder cancer and cholangiocarcinoma. J Hepatol 45:43-50.
14. Kluge R, Schmidt F, Caca K et al (2001) Positron emission tomography with [(18)F]fluoro-2-deoxy-D-glucose for diagnosis and staging of bile duct cancer. Hepatology 33:1029-1035.
15. Chung YE, Kim MJ, Park YN et al (2009) Varying appearance of cholangiocarcinoma: radiologic-pathologic correlation. RadioGraphics 29:673-700.
16. Klatskin G (1965) Adenocarcinoma of the hepatic duct at its bifurcation within the porta hepatis. An unusual tumor with distinctive clinical and pathological features. Am J Med 38:241-256.
17. Liver Cancer Study Group of Japan (1997) Classification of primary liver cancer. Kanehara, Tokyo.
18. Corvera CU, Blumgart LH, Akhurst T et al (2008) 18F-fluorodeoxyglucose positron emission tomography influences management decisions in patients with biliary cancer. J Am Coll Surg 206:57-65.
19. Fritscher-Ravens A, Bohuslavizki KH, Broering DC et al (2001) FDG PET in the diagnosis of hilar cholangiocarcinoma. Nucl Med Commun 22:1277-1285.
20. Chikamoto A, Tsuji T, Takamori H (2006) The diagnostic efficacy of FDG-PET in the local recurrence of hilar bile duct cancer. J Hepatobiliary Pancreat Surg 13:403-408.
21. Charbel H, Al-Kawas FH (2011) Cholangiocarcinoma: epidemiology, risk factors, pathogenesis, and diagnosis. Curr Gastroenterol Rep 13:182-187.
22. Aljiffry M, Walsh MJ, Molinari M (2009) Advances in diagnosis, treatment and palliation of cholangiocarcinoma: 1990-2009. World J Gastroenterol 15:4240-4262.
23. Valero V 3rd, Cosgrove D, Herman JM, Pawlik TM (2012) Management of perihilar cholangiocarcinoma in the era of multimodal therapy. Expert Rev Gastroenterol Hepatol 6:481-495.
24. Sahani DV, Bonaffini PA, Catalano OA et al (2012) State-of-the-Art PET/CT of the pancreas: current role and emerging indications. RadioGraphics 32:1133-1158.
25. Rufini V, Baum RP, Castaldi P et al (2012) Role of PET/CT in the functional imaging of endocrine pancreatic tumors. Abdom Imaging 37:1004-1020.
26. Milan SA, Yeo CJ (2012) Neuroendocrine tumors of the pancreas. Curr Opin Oncol 24:46-55.

# Tumors of the Adrenergic System: Imaging and Therapy

Cornelis A. Hoefnagel

Netherlands Cancer Institute, Amsterdam, The Netherlands

## Historical Background

The development and subsequent clinical uses of radioiodinated meta-iodobenzylguanidine (MIBG) represent a good example of truly molecular targeting *avant la lettre*. The credit for this goes to Prof. William Beierwaltes, whose group at the University of Michigan in Ann Arbor in the 1960s studied and developed tracers for the adrenal cortex, medulla, and heart. After working with $^{14}$C-epinephrine for neuroblastoma (1967) and $^{14}$C-dopamine for pheochromocytoma (1973) initially [1], they switched to radioiodinated bretylium analogs and quaternary ammonium derivatives for imaging. Don Wieland synthesized and compared $^{125}$I-labelled ortho-, para-, and metaisomers of iodobenzylguanidine and was the first to describe imaging of the dog's adrenal medulla using $^{131}$I-para-iodobenzylguanidine (1980); in 1981, Sisson et al. reported imaging of pheochromocytoma in humans using $^{131}$I-MIBG. The downside was that $^{131}$I-MIBG was a poor tracer for cardiac imaging and that initial attempts to image other neuroendocrine tumors (NETs) showed false-negative results.

Subsequent development occurred in Europe, where $^{131}$I-MIBG with specific low and high activity (for imaging and therapy, respectively) became commercially available and where from 1984 on several groups reported its successful use for scintigraphy and therapy in pheochromocytoma, paraganglioma, neuroblastoma, carcinoid tumors, and medullary thyroid carcinoma (MTC). In 1987, $^{123}$I-labeled MIBG became available, which had better imaging properties, allowing single-positron-emission computed tomography (SPECT) and proved to be a good cardiac agent after all when used as a specific tracer for sympathetic innervation of the myocardium. By 1999, combined therapeutic results in 534 patients demonstrated objective response rates of ~50% in malignant pheochromocytoma and paraganglioma, as well as in children with neuroblastoma, refractory to other forms of treatment. In contrast, in carcinoid tumors and MTC, objective responses were far fewer or even absent, although stabilization of disease, metabolic effects, and palliation (in 60% of patients) were associated with significantly prolonged survival [2].

## Targeting Mechanisms

NETs, such as with phaeochromocytoma, neuroblastoma, carcinoid, paraganglioma, chemodectoma, MTC, islet cell tumors, gastrinoma, small cell lung cancer, melanoma, and Merkel cell tumor, vary considerably in their clinical presentation, location, and histology; however, in common, they all arise from the same embryonic tissue, i.e., the neural crest. Therefore, they express several unique characteristics, which may be utilized to target radiopharmaceuticals both for diagnosis and therapy of these tumors [3]. Specific targeting of NETs may be achieved via the metabolic route (MIBG), receptor binding (peptides), or the immunological route (antibodies).

$^{123}$I- or $^{131}$I-MIBG and $^{111}$In-pentetreotide, being sensitive and highly specific tracers, are the most widely used. Comparative studies demonstrate the complementary role of these procedures [3]. An active uptake-1 mechanism at the cell membrane and neurosecretory storage granules in the cytoplasm of neural crest tumors are responsible for $^{123}$I- and $^{131}$I-MIBG uptake and retention, respectively. Although the radiopharmaceutical may be released from the granules, reuptake through this specific mechanism maintains prolonged intracellular concentration, in contrast to nonadrenergic tissues, which rely on passive diffusion only; this results in a high tumor/nontumor ratio. A number of drugs may interfere with uptake and/or retention of MIBG [4].

Targeting peptide receptors on the cell surface, somatostatin analogs can be used for diagnosis and therapy of a variety of NET and other tumor types in which peptide receptors have been demonstrated by autoradiography [5]. Unlike MIBG and antibodies, peptides are not specific for neural crest tumors. $^{111}$In-pentetreotide is mostly used for diagnostic scintigraphy, and $^{90}$Y-labeled octreotide or lanreotide and $^{177}$Lu-labeled octreotate are used for targeted therapy. Other peptides used for diagnostic

*Diseases of the Abdomen and Pelvis 2014-2017*,
DOI: 10.1007/978-88-470-5659-6_32 

scintigraphy include $^{111}$In-lanreotide, $^{99m}$Tc-depreotide, and $^{123}$I-vasoactive intestinal peptide (VIP).

Radiolabeled monoclonal antibodies target antigens on the cell surface of some NETs. Examples are the use of murine monoclonal antibodies $^{131}$I-UJ13A and $^{131}$I-3F8 in the 1980s and, more recently, of chimeric antibodies, such as $^{131}$I-chCE7, in neuroblastoma. Radioiodinated anti-carcinoembryonic antigen (CEA) antibodies/fragments may target CEA-producing MTC; bispecific anti-diethylenetriamine pentaacetic acid (anti-DTPA)/anti-CEA immunoconjugates demonstrate improved tumor/nontumor ratios and prolonged retention in MTC [6].

The role of radiolabeled peptides for imaging and therapy is discussed separately; this chapter focuses on diagnosis and therapy of NETs using $^{123}$I-MIBG or $^{131}$I-MIBG.

## Imaging Techniques

Several nuclear medicine procedures for the use of MIBG in NETs prevail.

- Conventional scintigraphy of the whole body, using either $^{123}$I-MIBG ($\gamma$-emitter, $T_{1/2fys}$=13 h, photon energy 159 KeV), or $^{131}$I-MIBG ($\alpha/\beta$-emitter, $T_{1/2fys}$=8 d, photon energy 364 KeV); $^{123}$I-MIBG scintigrams have better quality and results are more readily available, whereas $^{131}$I-MIBG enables delayed imaging over several days.
- SPECT/CT using $^{123}$I-MIBG enables improved detection, as well as accurate localization of NET sites by hybrid imaging.
- Positron emission tomography (PET)/CT and/or PET/magnetic resonance imaging (MRI) using novel, specific, PET tracers, e.g. $^{124}$I-MIBG, $^{11}$C-hydroxyephedrin, 6-$^{18}$F-dihydroxy-phenyl-alanine (DOPA), $^{11}$C-5-hydroxytryptophan (HTP), are the most accurate diagnostic modalities to date for NETs, linking great sensitivity and specificity with high-quality, hybrid imaging. [$^{18}$F]-fluorodeoxyglucose (FDG) does not have this high degree of specificity, but it may be used to detect dedifferentiating, rapidly growing tumors [7].
- Following reinjection with $^{123}$I-MIBG, the use of an intraoperative gamma probe may guide surgical resection of NET localizations.
- On posttherapy imaging, radionuclide therapy using high doses of $^{131}$I-MIBG is applied when tumors have a high concentration and prolonged retention of this radiopharmaceutical; they can be monitored by posttherapy total body scintigraphy with or without $^{131}$I-MIBG SPECT/CT fusion imaging.

## Diagnostic Imaging

### Pheochromocytoma

The place of $^{123}$I/$^{131}$IMIBG scintigraphy in the diagnosis of pheochromocytoma is not that of a screening test but is the best initial procedure in patients who, on the basis of clinical or familial history, are suspected of having pheochromocytoma and who are selected upon plasma levels or urinary excretion rates of catecholamines and catecholamine metabolites. The cumulative sensitivity of $^{123}$I/$^{131}$I-MIBG scintigraphy in patients suspected of pheochromocytoma is 88% [3]. Although CT and MRI of adrenal masses provide better anatomical detail to the surgeon, a positive $^{123}$I/$^{131}$I-MIBG scan is a highly specific finding. The scintigraphic technique is superior for localizing extra-adrenal, recurrent, multifocal, and malignant disease [8]. Hybrid imaging, either by $^{123}$I-MIBG SPECT/CT or fluorine-18-L-dihydroxyphenylalanine ([$^{18}$F]-DOPA) PET/CT, is currently the most reliable technique, where the one component can guide the other and help in characterizing findings [9]. Although cumulative results of $^{111}$In-pentetreotide scintigraphy also show a sensitivity of 88% in pheochromocytoma, a disadvantage in detecting an adrenal tumor is its renal, hepatic, and splenic accumulation. A recent prospective multicenter evaluation of $^{123}$I-MIBG in 150 patients with or suspected of having pheochromocytoma or paraganglioma demonstrated a sensitivity of 82-88% and specificity of 82-84%. In that series, the addition of SPECT (without CT) hardly affected these parameters [10].

### Neuroblastoma

The cumulative findings of $^{131}$I-MIBG scintigraphy reported in the literature [3] indicate that 92% of neuroblastomas concentrate MIBG. $^{123}$I/$^{131}$I-MIBG imaging allows detection of primary tumors, residual or recurrent disease, and metastases, regardless their localization, in a single procedure. Together with the urinalysis for catecholamine metabolites, MIBG imaging is the most sensitive and highly specific indicator of neuroblastoma [11]. MIBG uptake is so tissue specific that in a child presenting with a tumor of unknown origin, $^{123}$I/$^{131}$I-MIBG scintigraphy can noninvasively establish the diagnosis of neuroblastoma and rule out differential diagnoses, e.g. Wilms' tumor, Ewing sarcoma, rhabdomyosarcoma, osteosarcoma, and malignant lymphoma [12]. A prospective trial of $^{123}$I-MIBG scintigraphy in 100 neuroblastoma patients showed an overall sensitivity of 88%, which was slightly increased to 91% by the addition of SPECT. Patients with a recent diagnosis of neuroblastoma had a sensitivity of 93% and specificity of 92% [13]. At present, $^{123}$I/$^{131}$I-MIBG scintigraphy has an established role in disease staging and as a parameter in response criteria. Discrepant findings of MIBG and bone scintigrams have been described, either in favor of the first or the latter. As a positive finding on MIBG scintigram is more specific, the initial use of $^{123}$I/$^{131}$I-MIBG is preferred, but complementary bone scintigraphy may be indicated.

Radioimmunoscintigraphy with iodine 131-3F8 ($^{131}$I-3F8) [14] and, more recently, using radioiodinated chimeric antibodies directed against neuroblastoma, indicate results complementary to those of MIBG imaging [15].

### Carcinoid Tumors

Cumulative sensitivity of $^{111}$In-pentetreotide scintigraphy in patients with carcinoid (86%) is higher that that of $^{131}$I-MIBG scintigraphy (70%) [3]. Therefore, the first technique is preferred for initial diagnosis. $^{131}$I-MIBG scintigraphy should not be used as a screening test for the initial diagnosis of carcinoid, nor can it be relied upon to exclude disease. However, combined use of these techniques may serve as a key to therapy: a positive $^{111}$In-pentetreotide scintigram may predict a response to palliative octreotide therapy and indicate the feasibility of $^{90}$Y-octreotide or $^{177}$Lu-octreotate therapy, whereas $^{131}$I-MIBG scintigraphy has a role in the workup of patients with proven carcinoid to select those who may benefit from $^{131}$I-MIBG therapy.

### Other Neuroendocrine Tumors

For MTC, radioimmunoassays of serum calcitonin and CEA levels are the most sensitive parameters in diagnosis and follow-up; however, many nuclear medicine procedures have emerged for disease localization, i.e., in the abdomen, detection of liver metastases and adrenal pheochromocytomas, in particular. Total body scintigraphy with SPECT using $^{201}$Tl-chloride and/or $^{99m}$Tc-pentavalent dimercaptosuccinate (DMSA), $^{99m}$Tc-sestamibi, and PET using $^{18}$F-FDG can best be used initially; these are all relatively aspecific procedures, but sensitivities range from 80% to 90%. $^{111}$In-pentetreotide and radiolabeled anti-CEA antibodies, with sensitivities ranging 60% to 70%, may have a complementary role. Having the lowest sensitivity (35%), $^{131}$I-MIBG should only be used once MTC metastases have been confirmed and then it is used to evaluate its potential therapeutic role [3, 16].

Comparing results of $^{131}$I-MIBG and $^{111}$In-pentetreotide in a variety of other neural crest tumors [3], the highest sensitivities for $^{111}$In-pentetreotide are found in paraganglioma (97%), small cell lung cancer, and, to a lesser degree, in endocrine gastroenteropancreatic (GEP) tumors, Merkel cell tumor, melanoma, and functioning pituitary tumors. $^{123}$I/$^{131}$I-MIBG scintigraphy is useful for detecting ganglioneuroma, paraganglioma, and chemodectoma; it is of limited use in pancreatic islet cell tumors, retinoblastoma, Schwannoma, and Merkel cell tumors and has no place in the diagnosis of small cell lung cancer and melanoma [3].

Although high sensitivities for $^{111}$In-pentetreotide scintigraphy are found in non-neural-crest tumors, e.g. non-small-cell lung cancer, brain tumors and lymphomas, as well as in granulomatous and autoimmune diseases, $^{131}$I-MIBG scintigraphy, as a highly specific procedure for neural crest tumors, is virtually always negative in non-neural-crest tumors [3, 12].

### Rationale for Using MIBG and Somatostatin Receptor Imaging

Scintigraphy using $^{111}$In-pentetreotide is the best initial procedure in carcinoid and endocrine gastroenteropancreatic (GEP) tumors and (benign) paraganglioma. $^{131}$I-MIBG can be reserved to evaluate the feasibility of therapy and for radionuclide treatment of these tumors. $^{123}$I/$^{131}$I-MIBG scintigraphy remains the best initial procedure for pheochromocytoma, neuroblastoma, and malignant paraganglioma, both because of its high sensitivity/specificity and its effective therapeutic application in these conditions. For many indications, however, PET/CT using $^{18}$F-DOPA [17] and $^{11}$C-HTP [18] is taking over the diagnostic role, with high sensitivity and specificity and great anatomical detail.

## Radionuclide Therapy

### Indications/Contraindications for Therapy

Any malignant neural crest tumor showing sufficient uptake and prolonged retention of $^{131}$I-MIBG on a diagnostic tracer study (ideally $>$1% of the administered dose, depending on tumor volume) is a candidate for radionuclide therapy. Apart from tracer concentration, the availability and feasibility of other treatment modalities, as well as the patient's condition, determines the indication. The principle indications for $^{131}$I-MIBG therapy are malignant pheochromocytoma and paraganglioma, neuroblastoma stage III and IV, MTC, and symptomatic, metastatic carcinoid tumors [2]. Contraindications for radionuclide therapy in general are pregnancy, continued breast feeding, myelosuppression, and renal failure. In addition, unstable patient condition that does not allow isolation, as well as lack of understanding or cooperation with respect to radiation protection guidelines, are relative contraindications.

### Malignant Pheochromocytoma and Paraganglioma

The objective of $^{131}$I-MIBG therapy may be objective tumor volume reduction (complete or partial response), tumor arrest (stabilization of previously progressive disease), reducing the tumor's metabolic function (as the prognosis in pheochromocytoma may depend on long-term consequences of catecholamine hypersecretion, this may actually prolong survival), and symptom palliation (e.g., hypertension, bone pain, sweats, constipation) [2].

In 1991, the results of $^{131}$I-MIBG therapy in 117 patients with pheochromocytoma treated in 14 centers were pooled [19]. Objective response, defined as a $>$50% decrease in catecholamine excretion, a $>$50% reduction in tumor volume, or significant scintigraphic improvement if lesions could not be measured, was observed in 56% of patients. Soft tissue metastases responded better than skeletal metastases. In addition, subjective symptom improvement, decreased blood pressure, and better pain relief were achieved in $>$60% of patients. Also, in malignant paraganglioma, longstanding objective responses have been reported both in secreting and nonsecreting types [20]. These tumors may be treated either with $^{131}$I-MIBG or $^{90}$Y-/$^{177}$Lu-labeled octreotide/octreotate.

**Table 1.** Pooled results of radioiodinated meta-iodobenzylguanidine ($^{131}$I-MIBG) therapy

| Disease | Patients (534) | Objective response: tumor volume | Objective response: biochemical | Subjective response: palliation |
|---|---|---|---|---|
| Pheochromocytoma | 77 | 51% | 68% | 68% |
| Paraganglioma | 34 | 48% | 51% | 70% |
| Neuroblastoma | 229 | 51% | - | Most patients |
| Medullary thyroid ca. | 29 | 23% | 60% | 60% |
| Carcinoid | 159 | 8% | 24% | 60% |
| Other | 6 | 2/6 | – | – |

European Association of Nuclear Medicine (EANM) Radionuclide Therapy Committee, 1999 [2]

The European Association of Nuclear Medicine (EANM) Radionuclide Therapy Committee (1999) [2] gathered results of $^{131}$I-MIBG treatment in 534 patients with neural crest tumors, among whom 77 had malignant pheochromocytoma and 34 had paraganglioma (Table 1). The cumulative objective response rates with respect to tumor volume were 51% and 48%, respectively, with >50% decrease in catecholamine excretion observed in 68% and 51%; symptomatic palliation occurred in 68% of patients. These results compare favorably with the best reported results of combination chemotherapy and were attained with a treatment that is noninvasive and associated with minimal side effects.

Results in 20 patients with malignant pheochromocytoma or paraganglioma treated with moderate doses (7.4 GBq) at The Netherlands Cancer Institute (objective response 47%, metabolic response 67%, subjective response 89%) [21] compare well with those reported by the group at Duke University, USA, who treated 18 patients with moderate doses (7.4 GBq) and 15 with high doses (18.5 GBq) (objective response 38%, metabolic response 60%, subjective response 86%) [22]. Moreover, both a metabolic response and a subjective response may have an important influence on survival and quality of life (QOL), even in the absence of objective volume response.

## Neuroblastoma

Since 1984, therapeutic doses of $^{131}$I-MIBG have been administered to children with metastatic or recurrent neuroblastoma failing conventional treatment. In 1991, pooled results of the major centers (273 patients) indicated an objective response rate of 35% [15]; that rate increased to 51% (Table 1) [2]. Most of these patients had stage IV, progressive, and intensely pretreated disease and were only treated with $^{131}$I-MIBG after other treatment modalities failed. Both the $^{131}$I-MIBG therapy and isolation are generally well tolerated by children; hematological side effects may occur. Apart from objective response, the palliative effect was often impressive. For patients with recurrent and progressive disease after conventional treatment, $^{131}$I-MIBG therapy is probably the best palliative treatment, as the invasiveness and toxicity of this therapy compare favorably with those of chemotherapy and external-beam radiotherapy [23].

Some groups combined $^{131}$I-MIBG therapy with chemotherapy and/or total body irradiation, accepting more toxicity, and with myeloablative chemotherapy requiring autologous bone marrow or stem cell rescue [24]. Voûte et al. [25] combined $^{131}$I-MIBG therapy with oxygen treatment under hyperbaric conditions, aiming to improve survival in patients with recurrent stage IV neuroblastoma by adding the toxic effect of hydroxyl radicals to the radiation effect. Subsequently, high-dose vitamine C therapy was added to this regimen.

$^{131}$I-MIBG therapy has been integrated into the treatment protocol as the initial therapy instead of preoperative combination chemotherapy in children presenting with advanced disease/inoperable neuroblastoma. The objective is to reduce tumor volume, enabling adequate surgical resection, and avoiding toxicity and induction of multiple drug resistance. Chemotherapy is reserved to treat minimal residual disease postoperatively. Initial results demonstrate the feasibility and effectiveness of this approach: a higher objective response rate (>70%) and considerably less toxicity compared with $^{131}$I-MIBG therapy after conventional treatment [26]. By 2001, results in 56 patients showed that $^{131}$I-MIBG is equally as effective as chemotherapy in attaining operability of neuroblastoma: 43 of 56 evaluable patients (77%) had complete or >95% resection of the primary tumor or did not require surgery at all. At follow-up (13-144 months), the 5-year survival rate was 37% [2]. Based upon these results, upfront $^{131}$I-MIBG therapy was integrated into the treatment of neuroblastoma in two ways: patients with favorable parameters receive a less aggressive therapy, consisting of two cycles of $^{131}$I-MIBG followed by surgery, whereas patients with unfavorable parameters (high-risk group) receive intensified $^{131}$I-MIBG therapy combined with the topoisomerase I inhibitor topotecan to enhance radiation-induced cytotoxicity.

Compared to $^{131}$I-MIBG therapy after chemotherapy, upfront $^{131}$I-MIBG therapy has significantly less toxicity, the most frequent side effect now being nausea/vomiting (21%) and grade IV hematological toxicity in less than 5% of patients [27].

In 21 children with unresectable neuroblastoma, the contribution of $^{131}$I-MIBG therapy in the treatment regimen was acclaimed once more: the objective response rate was 95.2%, and the 10-year overall and event-free survival rate was 90.5% [28].

### Medullary Thyroid Carcinoma

In the abdomen, MTC may present with liver metastases. Results of combination chemotherapy are disappointing. Radionuclide therapy using $^{131}$I-MIBG or $^{131}$I-anti-CEA antibodies may provide both tumor regression and palliation. Pooled results in 29 patients with MTC treated with $^{131}$I-MIBG (Table 1) show an objective response rate of only 23% and a tumor-marker response of 60%; nevertheless, palliative effects, which may be quite meaningful, occurred in 60% of patients. However, only a minority of patients demonstrate sufficient $^{131}$I-MIBG uptake [2].

More patients may be amenable to radioimmunotherapy. In a phase I/II study of treatment using bispecific anti-DTPA/anti-CEA immunoconjugates followed by $^{131}$I-hapten in a two-step procedure in 26 MTC patients, some mixed responses, disease stabilization, and palliation were attained with limited hematological toxicity, but human anti-murine antibody (HAMA) response occurred in more than half of the patients [29]. As patients may require several of these treatments, the use of chimeric or humanized immunoconjugates would be more appropriate.

### Carcinoid Tumors

Palliative treatment for metastatic carcinoid tumors include long-acting somatostatin analogs (Sandostatin), alpha-interferon (IFN-$\alpha$), hepatic artery embolization, $^{131}$I-labeled and -unlabeled MIBG, and $^{90}$Y- or $^{177}$Lu-labeled octreotide therapy. Cumulative results of $^{131}$I-MIBG therapy in 159 patients with symptomatic metastatic disease show an objective response rate of only 8% and $>$50% decrease in 5-hydroxyindoleacetic acid (HIAA) excretion in 24% (Table 1). Despite the absence of objective response, palliation occurs in 60% of patients, without producing significant side effects [30]. In view of the often indolent character of this disease, the value of a prolonged symptomatic response should not be underestimated: in a study at Duke University Medical Center involving 98 patients with metastatic carcinoid treated with $^{131}$I-MIBG, subjective response was correlated with prolonged survival [31].

In carcinoid tumors not qualifying for $^{131}$I-MIBG therapy because of no or insufficient tumor uptake, palliative treatment with high doses of unlabeled MIBG also proved beneficial in 60% of cases, albeit with a shorter mean duration [32]. Improved biochemical and palliative effects of $^{131}$I-MIBG treatment due to enhanced tumor/nontumor ratios by predosing with non-labeled MIBG have also been reported [33]. Combination of higher doses of $^{131}$I-MIBG and unlabeled MIBG is used for therapy whenever comparative scintigraphy demonstrates a $>$20% increase in T/NT ratio by adding unlabeled MIBG.

## Outlook/Perspective

Despite the results described above, over recent years, a decline in the use of $^{131}$I-MIBG for NET therapy has occurred, possibly related to the development of radiolabeled peptides for diagnosis and therapy. In the individual patient, combined imaging of NETs using MIBG and octreotide is the key to selecting the therapy with the best dosimetric characteristics. Nevertheless, in clinical practice, in the literature, and at congresses, we see the use of radiolabeled peptides for therapy appearing more prominently. Although the indications for both therapies do not overlap completely, in radiolabeled peptide therapy, the objective response rates are relative low (up to 30%) and metabolic and palliative effects are more pronounced, with the latter also having bearing on patient survival, as was observed in $^{131}$I-MIBG therapy of carcinoid tumors.

Therefore, why is therapy using radiolabeled peptides more popular? Certainly, the availability of a good pair comprising PET tracer and therapeutic agent is an important factor, as high-quality PET/CT imaging using DOTA$^0$-phe$^1$-tyr$^3$-octreotide ($^{68}$Ga-DOTATOC) or octreotate, clearly showing tumor targeting and biodistribution, is indicative and promotional, convincing clinicians to refer their patients for treatment with $^{177}$Lu-octreotate, which has good properties for posttherapy imaging as well.

Therefore, a new increase in $^{131}$I-MIBG therapy may be foreseen. The similar use of a high-quality pair of a diagnostic tracer for PET/CT and/or PET/MR (e.g. $^{18}$F-DOPA and $^{124}$I-MIBG) and a therapeutic radiopharmaceutical may bring this mode of molecular tumor targeting to clinical attention and lead to a re-acclaim of $^{131}$I-MIBG therapy, not in competition with but parallel to peptide therapy.

## References


1. Raffel DM, Wieland DM (2010) Developmento of mIBG as a cardiac innervation imaging agent. J Am Coll Cardiol Img 3:111-116.
2. Hoefnagel CA, Lewington VJ (2004) MIBG therapy. In: Ell PJ, Gambhir SS (Eds) Nuclear medicine in clinical diagnosis and treatment, 3rd edition. Churchill Livingstone, Edinburgh, pp. 445-457.
3. Hoefnagel CA (1994) Metaiodobenzylguanidine and somatostatin in oncology: role in the management of neural crest tumours. Eur J Nucl Med 21:561-581.
4. Khafagi FA, Shapiro B, Fig LM et al (1989) Labetalol reduces Iodine-$^{131}$ MIBG uptake by pheochromocytoma and normal tissues. J Nucl Med 30:481-489.
5. Reubi JC (1995) Neuropeptide receptors in health and disease: the molecular basis for in vivo imaging. J Nucl Med 36:1825-1835.
6. Bardiès M, Bardet S, Faivre-Chauvet A et al (1996) Bispecific antibody and Iodine-$^{131}$-labeled bivalent hapten dosimetry in patients with medullary thyroid or small-cell lung cancer. J Nucl Med 37:1853-1859.
7. Goldsmith SJ (2009) Update on nuclear medicine imaging of neuroendocrine tumors. Future Oncol 5:75-84.
8. Troncone L, Rufini V, Montemaggi P et al (1990) The diagnostic and therapeutic utility of radioiodinated metaiodobenzylguanidine (MIBG). 5 years experience. Eur J Nucl Med 16:325-335.
9. Rozovsky K, Koplewitz BZ, Krausz Y et al (2008) Added value of SPECT/CT for correlation of MIBG scintigraphy and diagnostic CT in neuroblastoma and pheochromocytoma. Am J Roentgenol 190:1085-1090.

10. Wiseman GA, Pacak K, O'Dorisio MS et al (2009) Usefulness of 123I-MIBG scintigraphy in the evaluation of patients with known or suspected primary or metastatic pheochromocytoma or paraganglioma: results from a prospective multicenter trial. J Nucl Med 50:1448-1454.
11. Hoefnagel CA, De Kraker J (2004) Pediatric tumors. In: Ell PJ, Gambhir SS (Eds) Nuclear medicine in clinical diagnosis and treatment, 3rd edition. Churchill Livingstone, Edinburgh, pp. 195-206.
12. Leung A, Shapiro B, Hattner R et al (1997) The specificity of radioiodinated MIBG for neural crest tumors in childhood. J Nucl Med 38:1352-1357.
13. Vik TA, Pfluger T, Kadota R et al (2009) (123)I-mIBG scintigraphy in patients with known or suspected neuroblastoma: results from a prospective multicenter trial. Pediatr Blood Cancer 52:784-790.
14. Yeh SDJ, Larson SM, Burch L et al (1991) Radioimmunodetection of neuroblastoma with Iodine-$^{131}$-3F8: correlation with biopsy, Iodine-$^{131}$-Metaiodobenzylguanidine and standard diagnostic modalities. J Nucl Med 32:769-776.
15. Hoefnagel CA, Rutgers M, Buitenhuis CKM et al (2001) A comparison of targetting neuroblastoma with mIBG and anti L1-CAM antibody mAB chCE7: therapeutic efficacy in a neuroblastoma xenograft model and imaging of neuroblastoma patients. Eur J Nucl Med 28:359-368.
16. Hoefnagel CA, Delprat CC, Zanin D, van der Schoot JB (1988) New radionuclide tracers for the diagnosis and therapy of medullary thyroid carcinoma. Clin Nucl Med 13:159-165.
17. Kauhanen S, Seppänen M, Ovaska J et al (2009) The clinical value of [$^{18}$F]fluorodihydroxyphenylalanine positron emission tomography in primary diagnosis, staging and restaging of neuroendocrine tumors. Endocr Relat Cancer 16:255-265.
18. Koopmans KP, Neels OC, Kema IP et al (2008) Improved staging of patients with carcinoid and islet cell tumors with $^{18}$F-dihydroxy-phenyl-alanine and $^{11}$C-5-hydroxy-tryptophan positron emission tomography. J Clin Oncol 26:1489-1495.
19. Troncone L, Galli G (Eds) (1991) Proceedings International Workshop on the role of [$^{131}$I]metaiodobenzylguanidine in the treatment of neural crest tumors. J Nucl Biol Med 35:177-362.
20. Baulieu J-L, Guilloteau D, Baulieu F et al (1988) Therapeutic effectiveness of Iodine-$^{131}$ MIBG metastases of a nonsecreting paraganglioma. J Nucl Med 29:2008-2013
21. Gedik GK, Hoefnagel CA, Bais E, Olmos RA (2008) $^{131}$I-MIBG therapy in metastatic phaeochromocytoma and paraganglioma. Eur J Nucl Med Mol Imaging 35: 725-733.
22. Safford SD, Coleman RE, Gockerman JP et al (2003) Iodine-131 metaiodobenzylguanidine as an effective treatment for malignant pheochromocytoma and paraganglioma. Surgery 134:956-962.
23. Hoefnagel CA (1999) Nuclear medicine therapy of neuroblastoma. Q J Nucl Med 43:336-343.
24. Yanik GA, Levine JE, Matthay KK et al (2002) Pilot study of iodine-131 metaiodobenzylguanidine in combination with myeloablative chemotherapy and autologous stem-cell support for the treatment of neuroblastoma. J Clin Oncol 20:2142-2149.
25. Voûte PA, van der Kleij AJ, de Kraker J et al (1995) Clinical experience with radiation enhancement by hyperbaric oxygen in children with recurrent neuroblastoma stage IV. Eur J Cancer 31A:596-600.
26. Hoefnagel CA, de Kraker J, Valdés Olmos RA, Voûte PA (1994) $^{131}$I-MIBG as a first-line treatment in high-risk neuroblastoma patients. Nucl Med Commun 15:712-717.
27. Bleeker G, Schoot RA, Caron HN et al (2013) Toxicity of upfront $^{131}$I-metaiodobenzylguanidine ($^{131}$I-MIBG) therapy in newly diagnosed neuroblastoma patients: a retrospective analysis. Eur J Nucl Med Mol Imaging 40:1711-1717.
28. Schoot RA, Bleeker G, Caron HB et al (2013) The role of $^{131}$I-metaiodobenzylguanidine (MIBG) therapy in unresectable and compromising localized neuroblastoma. Eur J Nucl Med Mol Imaging 40:1516-1522.
29. Kraeber-Bodéré F, Bardet S, Hoefnagel CA et al (1999) Radioimmunotherapy in medullary thyroid cancer using bispecific antibody and iodine-131-labeled bivalent hapten: Preliminary results of a phase I/II clinical trial. Clin Cancer Res 5:3190s-3198s.
30. Zuetenhorst H, Taal BG, Boot H et al (1999) Long-term palliation in metastatic carcinoid tumours with various applications of Meta-idobenzylguanidine: pharmacological MIBG, $^{131}$I-labeled MIBG and the combination. Eur J Gastroenterol Hepatol 11:1157-1164.
31. Safford SD, Coleman RE, Gockerman JP et al (2004) Iodine-131 metaiodobenzylguanidine treatment for metastatic carcinoid. Results in 98 patients. Cancer 101:1987-1993.
32. Taal BG, Hoefnagel CA, Valdés Olmos RA et al (1996) Palliative effect of Metaiodobenzylguanidine in metastatic carcinoid tumors. J Clin Oncol 14:1829-1838.
33. Taal BG, Hoefnagel CA, Boot H et al (2000) Improved effect of $^{131}$I-MIBG treatment by predosing with non-radiolabeled MIBG in carcinoid patients, and studies in xenografted mice. Ann Oncol 11:1437-1443.

# PET/CT-Based Dose Planning in Radiation Therapy

Annika Loft[1], Anne Kiil Berthelsen[2]

[1] PET & Cyclotron Unit, Dept. of Clinical Physiology, Nuclear Medicine & PET, Rigshospitalet, Copenhagen University Hospital, Copenhagen, Denmark
[2] Dept. of Radiation Oncology, Rigshospitalet, Copenhagen University Hospital, Copenhagen, Denmark

## Introduction

Approximately 50% of cancer patients are estimated to receive radiation therapy as part of their total treatment regimen. External-beam treatment methods most commonly used at the Department of Radiation Oncology at Copenhagen University Hospital include 3D conformal radiation therapy (3D-CRT), intensity-modulated radiation therapy (IMRT), intensity-modulated arc therapy (IMAT), and stereotactic radiation therapy (SRT). Radiation therapy can either cure patients of malignant disease or palliate symptoms caused by malignant disease. Radiation therapy is an inexpensive treatment method compared with, for example, surgery, chemotherapy, and immunotherapy [1]. One of the most pronounced disadvantages of radiation therapy is the acute side effects in normal tissue, e.g., mucous membranes occurring during and after the treatment. Correctly identifying and including all tumor cells in the target volume and avoiding as much normal tissue as possible is the challenge of curative radiation therapy, especially when the new treatment methods, such as 3D-CRT, IMRT, IMAT, and SRT, are used.

Positron emission tomography (PET) with the tracer [$^{18}$F]-fluorodeoxyglucose (FDG) uses the fact that malignant cells have an increased metabolism and up-regulated membrane-bound glucose transporters [2]; therefore, they have a higher FDG uptake than normal tissue. PET is a functional imaging method without the precise anatomical resolution of computed tomography (CT) and magnetic resonance imaging (MRI). PET/CT scanners combine functional information from PET with anatomical information from CT, and the use of this imaging modality in cancer patients has increased very rapidly since it was introduce in 2001. PET/CT is increasingly used for radiation therapy dose planning.

## PET/CT-Based Dose-Planning Process

The planning process is carried out with utmost precision within the short time period between the scan and the treatment initiation. It is done by a team of qualified staff, including mould technicians, nuclear technologists, radiation technologists, nuclear physicians, radiologists, radiation oncologists, physicists, and dosimetrists.

It is of great importance that the PET/CT scan is carried out in the precise treatment position. For this reason, laser lights should be installed in the scanner, a flat tabletop should be placed on the scanner bed, and the patient must be positioned in the immobilization device precisely as for the treatment.

The scan is performed according to routine procedures; however, it is of great importance that the scan is performed with contrast enhancement and diagnostic quality, as the scan is used for radiotherapy-dose planning. We always perform the PET/CT scan as a whole-body examination, thereby allowing detection of possible unknown distant metastases, which typically would have an impact on further treatment planning.

After the scan patient setup marks are tattooed or marked on the immobilization device so the exact position can be reproduced during daily treatment.

## Radiation Therapy Dose-Planning Process

The dose planning process starts with the nuclear medicine physician the radiologist in consensus interpreting the PET/CT scan and depicting any malignant foci. The nuclear medicine physician then delineates the PET-positive tumor(s), gross tumor volume defined by PET, hereafter named gross tumor volume (GTV)-PET. CT scan and GTV-PET volumes are transferred to the dose planning system in the radiotherapy department.

On the CT scan, radiologist and radiation oncologist define the GTV-CT, which can include, for example, enlarged, necrotic lymph nodes that were non-FDG avid and therefore were not included in the GTV-PET. A final GTV including information from the GTV-PET and GTV-CT is then defined, a process also involving clinical information gained by physical examination, previous imaging studies (e.g., CT, MRI, US), and information from invasive diagnostic methods, including surgery.

*Diseases of the Abdomen and Pelvis 2014-2017*,
DOI: 10.1007/978-88-470-5659-6_33 

The radiation oncologist then defines the clinical target volume (CTV), including the GTV and any areas of suspected microscopic disease. There could be several CTVs receiving different doses, as is common in, for example, the head and neck area.

Hereafter, the dosimetrist continues the planning process by delineating the planning target volume (PTV), allowing a margin around the CTV for setup uncertainties, possible CTV movement due to respiration, or inter- and intratreatment variations. The organs at risk (OARs) are defined on the dose-planning computer system. These might be the spinal cord, kidneys, or any radiosensitive organ in the treatment area.

A treatment plan will be generated using a dose-planning system with the best technique available in the department for the individual patient. This could be 3D-conformal RT, 4D-conformal RT using gating (respiratory control during radiotherapy), IMRT, SRT, IMAT, or proton therapy. This process involves appropriate dose distribution to the CTV and OARs. The final plan will be checked at a conference with several radiotherapy experts, radiation oncologists, and physicists, before being digitally sent to the treatment machines.

## Results

It is our opinion that target definition is strongly facilitated by using PET/CT in the dose-planning process. We also believe that the working method we use for defining target, involving nuclear physicist, radiologist, and radiation oncologist, is a safer method that the one previously used by a single radiation oncologist. It is also our feeling that this working method allows more energy for the radiation oncologist to focus on the definition of proper CTV/CTVs.

The use of PET/CT frequently changes previously known tumor size and stage, including both presence of lymph node and distant metastases. These facts sometimes lead to changes in treatment modality with, for example, addition of concomitant chemotherapy or surgery and even to another treatment intention. In concordance with what others also have experienced, synchronous cancers are also detected when whole-body PET/CT is used for dose planning [3, 4].

Side effects most commonly seen are those of acute systemic allergic reactions due to iodine-containing contrast (not related to PET but to CT) and claustrophobic reactions during scanning, when the patient is immobilized and going through the gantry opening.

## Discussion

In our work to improve imaging techniques for radiation-therapy dose planning, we are using intravenous (IV) and orally applied contrast for CT scanning, our slice thickness is 3 mm, we have our own MRI scanner in our department. We also have a dedicated PET/CT scanner for whole-body PET/CT before dose planning, which has led to findings that change the intended treatment in approximately 30% of patients. This is confirmed by others using the same method [5]. One possible reason for this is that we not only use the older CT criteria for pathologic lymph node definition but also include increased metabolism in lymph nodes <10 mm in diameter [6]. Several studies [7-10] have shown increased conformity in target definition when using PET/CT instead of CT alone.

We find that the method we use for target definition in which a nuclear physicist and a radiologist work together and (often, but not always) the same radiologist works with a radiation therapist, is working very well. The radiation oncologist experiences a lot more energy and security when defining CTVs after GTV definitions together with the radiologist, compared with doing the entire procedure alone. We also experience that the teamwork makes the target definition more pleasant.

The effect of PET/CT has shown that the treated volume can either be smaller or larger, depending on additional information gained [5, 7]. We also believe that using PET/CT for radiotherapy dose planning is necessary if the patient is to have any gain from the new treatment techniques, such as IMRT, IMAT, IMPT, and SRT.

We strongly recommend the use of [$^{18}$F]-FDG-PET/CT in radiotherapy dose planning. In the future, we expect an increased use of PET/CT with tracers other than FDG for known prognostic factors such as hypoxia and tumor cell proliferation [11, 12]. It is of greatest importance to find tracers for genetically determined intrinsic tumor radiosensitivity, a significant prognostic factor for local control. These factors are all important for delivering radiotherapy with the so-called dose-painting technique [13, 14].

## Conclusion

In conclusion, we find whole-body PET/CT scanning for radiation-therapy dose planning a very useful tool in upfront radiation therapy and we believe it will be used even more in the future. We strongly believe in our working method involving different specialists in modern imaging techniques and specialists in radiation therapy, as described. The potential effects for patient outcome need to be observed in the future.

## References

1. Ringborg U, Bergqvist D, Brorsson B et al (2003) The Swedish Council on Technology Assessment in Health Care (SBU) systematic overview of radiotherapy for cancer including a prospective survey of radiotherapy practice in Sweden 2001—summary and conclusions. Acta Oncol 42:357-365.
2. Loft A, Berthelsen Kiil A, Roed H et al (2007) The diagnostic value of PET/CT scanning in patients with cervical cancer: a prospective study. Gynecol Oncol 106:29-34.

3. Adriaensen M, Schijf L, de Haas M et al (2008) Six synchronous primary neoplasms detected by FDG-PET/CT. Eur J Nucl Med Mol Imaging 35:1931.
4. Ishimori T, Patel P, Wahl R (2005) Detection of unexpected additional primary malignancies with PET/CT. J Nucl Med 46:752-757.
5. MacManus M, Nestle U, Rosenzweig KE et al (2009) Use of PET and PET/CT for radiation therapy planning: IAEA expert report 2006-2007. Radiat Oncol 91:85-94.
6. Berthelsen AK, Dobbs J, Kjellén E et al (2007) What's new in target volume definition for radiologists in ICRU Report 71? How can the ICRU volume definitions be integrated in clinical practice? Cancer Imaging 7:104-116.
7. Hutchings M, Loft A, Hansen M et al (2007) Clinical impact of FDG-PET/CT in the planning of radiotherapy for early-stage Hodgkin lymphoma. Eur J Haematol 78:206-212.
8. Caldwell CB, Mah K, Skinner M, Danjoux CE (2003) Can PET provide the 3D extent of tumor motion for individualized internal target volumes? A phantom study of the limitations of CT and the promise of PET. Int J Radiat Oncol Biol Phys 55:1381-1393.
9. Caldwell CB, Mah K, Ung YC et al (2001) Observer variation in contouring gross tumor volume in patients with poorly defined non-small-cell lung tumors on CT: the impact of 18FDG-hybrid PET fusion. Int J Radiat Oncol Biol Phys 51:923-931.
10. Leong T, Everitt C, Yuen K et al (2006) A prospective study to evaluate the impact of FDG-PET on CT-based radiotherapy treatment planning for oesophageal cancer. Radiother Oncol 78:254-261.
11. Souvatzoglou M, Grosu AL, Röper B et al (2007) Tumour hypoxia imaging with [18F]FAZA PET in head and neck cancer patients: a pilot study. Eur J Nucl Med Mol Imaging 34:1566-1575.
12. Rajendran JG, Schwartz DL, O'Sullivan J et al (2006) Tumor hypoxia imaging with [F-18] fluoromisonidazole positron emission tomography in head and neck cancer. Clin Cancer Res 12:5435-5441.
13. Grosu AL, Souvatzoglou M, Röper B et al (2007) Hypoxia imaging with FAZA-PET and theoretical considerations with regard to dose painting for individualization of radiotherapy in patients with head and neck cancer. Int J Radiat Oncol Biol Phys 69:541-551.
14. Grégoire V, Haustermans k, Geets X et al (2007) PET-based treatment planning in radiotherapy: a new standard? J Nucl Med 48(1suppl):68-77.

# Lymphoma: Management Using PET/CT

Niklaus G. Schaefer

Medical Oncology & Nuclear Medicine, Zurich, Switzerland

## Introduction

[$^{18}$F]-fluorodeoxyglucose (FDG)-positron emission tomography/computed tomography (PET/CT) is considered the standard imaging modality in Hodgkin's disease and aggressive non-Hodgkin's lymphoma. In the European Society of Medical Oncology guidelines, FDG-PET/CT is strongly recommended for staging and restaging Hodgkin's disease and diffuse large B-cell lymphoma [1]. FDG-PET/CT has further been tested in monitoring during therapy, surveillance after first-line therapy, transformation assessment, and response in salvage situations and in drug development studies. However, to understand CT, especially functional imaging, in lymphoma, a profound knowledge about lymphoma biology is mandatory.

## General Principles

Lymphomas are grouped into Hodgkin's (HL) and non-Hodgkin's (NHL) lymphoma. NHL derives from a diverse group of neoplasms: from B-cell progenitors, T-cell progenitors, mature B cells, mature T cells, or (rarely) natural killer (NK) cells. All of these different types of NHL have different clinical appearance, prognosis, therapy regimes, and FDG avidity. Aggressive NHL usually presents as a rapidly growing mass, often with symptoms of fever, weight loss, night sweats. Typical examples of aggressive NHL comprise diffuse large B-cell lymphoma, adult T-cell lymphoma, and precursor B- and T-cell lymphoblastic lymphomas or leukemias. Indolent lymphomas usually present as slow-growing masses in patients with hepatomegaly, splenomegaly, or cytopenias. Typical examples of indolent NHL are follicular lymphomas, chronic lymphocytic leukemias, and marginal-zone lymphomas. FDG-PET/CT has a different appearance in all of these subtypes.

HL, formerly called Hodgkin's disease, has a unique composition of inflammatory cells as background and a minority of neoplastic Reed-Sternberg cells. FDG-PET/CT is used in all subforms of HL.

## PET/CT in HL and NHL Staging

To plan appropriate therapies in patients with HL and NHL, accurate staging is mandatory. There are no large randomized trials to show the superiority of FDG-PET/CT over CT alone. Sensitivity and specificity of patients with HL and NHL using FDG-PET/CT is 92.2-100% and 98.8-100%, respectively [2-4]. The same studies report a sensitivity of 82-91% and 98-100%, respectively, for contrast-enhanced CT. However, there is no reported prospective study identifying any improved outcome or better overall survival in patients staged either with FDG-PET/CT or contrast-enhanced CT. These data are only valid for HL or aggressive NHL subtypes. There is no large amount of data for patients with rare lymphoma subtypes or indolent NHL.

## Bone Marrow Infiltration

Bone marrow infiltration is an important predictor of survival and often guides the choice of the lymphoma therapy. There are several publications about the value of bone marrow infiltration and of FDG-PET/CT. One prospective multicenter trial, by Rigacci et al., compared the value of bone marrow biopsy (BMB) with PET/CT in HL. In a patient collective of 186, 20 patients had discordant results on BMB compared with FDG-PET/CT [5]. However, a large number of HL and NHL patients with infiltration of the bone marrow have advanced disease, positive BMB or imaging does not alter the therapy choice; thus, BMB remains the clinical routine investigation in patients with HL and NHL. In indolent NHL, in particular, FDG-PET has a high false-negative rate in assessing bone marrow infiltration.

## PET/CT during Chemotherapy

Several prognostic scores are used to predict survival in lymphoma patients [6, 7]. However, these statistical

*Diseases of the Abdomen and Pelvis 2014-2017*,
DOI: 10.1007/978-88-470-5659-6_34 

considerations do not reflect response in a given patient. It is therefore important to monitor early response to determine successful from unsuccessful treatment. Several older studies prompted early midtreatment PET/CT scan to delineate responders. It has been consistently shown that midtreatment scanning has an important prognostic value [8-10]. However, more recent studies assess the role of midtreatment PET/CT more critically. In a study of diffuse large B-cell lymphoma (DLBCL), patients receiving rituximab plus cyclophosphamide, doxorubicin, vincristine, and prednisone every 21 days or 14 days (R-CHOP 21; R-CHOP 14), only the subgroup receiving R-CHOP 21 had a significant difference in progression-free survival [11]. In another study of 50 patients with DLBCL, interim PET/CT was considered a poor predictor [12]. It is unclear why earlier studies had different results than newer prospective trials: it may reflect the change in therapy, specifically the addition of rituximab, which entirely changed the therapeutic landscape in B-cell NHL. In HL, data on midtreatment PET/CT is more consistent: Gallamini et al. showed that PET/CT is the most important factor in prognosis, even more powerful than the International Prognostic Score [13]. Others have shown similar results [14]. There is no role for midtreatment PET/CT scanning in patients with low-grade histologies, such as follicular lymphoma, or in patients with T-cell NHL.

## PET/CT in Restaging HL and NHL

The largest amount of reported data using FDG-PET/CT is in HL and NHL restaging. Several studies show the superiority of FDG-PET compared with CT due to its ability to detect viable scar tissue after the end of induction therapy. Several studies report the clinical value of a negative FDG-PET/CT after the end of first-line therapy. Spaepen et al. show that patients achieving complete FDG-negative results after first-line treatment have a median complete remission of 653 days compared with 73 days in patients with FDG avidity in the end-of-treatment scan [15]. This finding has been repeatedly reported by many authors [16, 17]. Despite this interesting finding, in which interim FDG-PET/CT does predict prognosis, there is no paper describing an adaptation of therapy according to the interim scan. There is a phase II study by the Johns Hopkins group that went directly into salvage chemotherapy in patients not achieving complete remission in the interim scan. However, it has never been shown in a randomized trial whether this method results in better overall survival. In patients with incurable lymphomas, such as low-grade follicular lymphomas, no data support the value of the interim PET/CT.

## PET/CT in Surveillance after First-Line Therapy

Patients achieving complete remission after completion of first-line therapy often enter a disease-free phase and then enter a phase of regular clinical and radiological workup. PET surveillance is performed to detect early recurrence. Whereas there is no study supporting regular use of surveillance PET, Zinzani et al. [18] studied a series of patients after first-line therapy who were in complete remission after 6, 12, 18, and 24 months. A substantial number of patients with recurrence were detected. The paper provided no additional clinical data, and it is therefore unknown whether PET preceded clinical or laboratory signs of recurrence. It is furthermore not known whether recurrence detected early translates into a better overall survival for lymphoma patients. Petrausch et al. reported two retrospective series of patients with DLBCL [19] and HL [20]. These studies analyzed surveillance according to risk factors. Clinical signs of recurrence are the most important factor for predicting recurrence. According to current published data, regular PET scanning should be avoided.

## PET/CT in the Salvage Chemotherapy Setting

In recurrence after first-line therapy, patients enter salvage chemotherapy followed by autologous stem cell transplantation. There is still a curative intent; however, only patients with chemosensitive disease enter the stem cell program. It is therefore important to determine whether patients benefit from salvage chemotherapy, and FDG-PET does nicely fit into this treatment step. Several studies report a longer progression-free survival in patients achieving complete response after two or three cycles of salvage chemotherapy. In a meta-analysis of 12 studies with a total of 630 patients, functional imaging using PET did outperform conventional CT [21]. Still, the definitive procedure of how to treat PET-positive patients after salvage chemotherapy remains unclear. In all studies, there is a relevant subset of patients with positive PET before stem cell transplantation that achieve complete response after completion of therapy. It is therefore questionable whether patients with positive PET after salvage chemotherapy should not be transplanted. However, other risk factors must be considered as well, and alternative consolidation strategies, newer agents, and clinical trials must be considered. In patients undergoing allogeneic transplantation, there is no role for positive or negative pretransplantation scan, and the results do not predict relapse or overall survival [22].

## Interpretation of PET/CT in Lymphoma

FDG-PET/CT has become a standard tool in clinical trials. It is therefore important to identify clear and precise rules of FDG-PET/CT interpretation. One question regards the use of maximum standard uptake value ($SUV_{max}$) changes compared with visual assessment in patients with lymphoma. Reduction in of 66% of $SUV_{max}$ translates into better prognostic prediction compared with visual assessment

[23]. That trial, among others, showed the need for harmonization of response standards in FDG-PET/CT. The International Working Group (IWG) response criteria for assessment were developed to compare results among different clinical trials [24]. Cheson et al. added the PET information in patients with aggressive NHL in a retrospective analysis, showing that PET can increase the number of complete remissions. The earlier category of complete response unconfirmed (Cru) was eliminated, and the IWG-PET was initiated [25] and is now considered the standard, which is verified by several groups [26].

## Conclusion

For more than a decade FDG-PET has been used to stage, restage, and follow patients with NHL and HL. Its strengths are in HL and aggressive NHL staging, early response assessment, and restaging. Few studies report FDG-PET in surveillance. FDG-PET can guide treatment for patients undergoing salvage chemotherapy prior to stem cell transplantation. Response must be assessed using the IWG-PET criteria. Overlooking most of current studies, FDG-PET is still not considered as the mandatory standard in the named indication in patients with HL and NHL. There is still not enough prospective data to definitively predict the impact of FDG-PET/CT in HL and B-cell HL patients. Future study must focus on randomized intervention studies using PET as discriminator to select minimal required therapies to treat lymphoma patients sufficiently. Until these studies are complete, FDG-PET/CT will not be a mandatory standard for all HL and NHL patients. It is furthermore important to understand that most data is published in the field of HL and aggressive B-cell NHL. There is still insufficient data for indolent and T-cell NHL by which to definitely identify the role of FDG-PET in these separate lymphoma entities.

## References


1. ESMO Guidelines, www.esmo.org
2. Hutchings M, Loft A, Hansen M et al (2006) Positron emission tomography with or without computed tomography in the primary staging of Hodgkin's lymphoma. Haematologica 91:482-489.
3. Pelosi E, Pregno P, Penna D et al (2008) Role of whole body [18F] fluorodeoxyglucose positron emission tomography/computed tomography (FDG-PET/CT) and conventional techniques in the staging of patients with Hodgkin and aggressive non-Hodgkin lymphoma. Radiol Med 113:578-590.
4. Bangerter M, Moog F, Buchmann I et al (1998) Whole-body 2-[18F]-fluoro-2-deoxy-D-glucose positron emission tomography (FDG-PET) for accurate staging of Hodgkin's disease. Ann Oncol 9:1117-1122.
5. Rigacci L, Vitolo U, Nassi L et al (2007) Positron emission tomography in the staging of patients with Hodgkin's lymphoma: a prospective multicentric study by the Intergruppo Italiano Linfomi. Ann Hematol 86:897-903.
6. Shipp MA, Harrington DP, Anderson JR et al (1993) Development of a predictive model for aggressive lymphoma: The International Non-Hodgkin's Lymphoma Prognostic Factors Project. N Engl J Med 329:987-994.
7. Hasenclever D, Diehl V (1998) A prognostic score for advanced Hodgkin's disease: International Prognostic Factors Project on advanced Hodgkin's disease. N Engl J Med 339:1506-1514.
8. Spaepen K, Stroobants S, Dupont P et al (2002) Early restaging positron emission tomography with 18F-fluorodeoxyglucose predicts outcome in patients with aggressive non-Hodgkin's lymphoma. Ann Oncol 13:1356-1363.
9. Haioun C, Itti E, Rahmouni A et al (2005) [18F]fluoro-2-deoxy-D-glucose positron emission tomography (FDG-PET) in aggressive lymphoma: an early prognostic tool for predicting patient outcome. Blood 106:1376-1381.
10. Mikhaeel NG, Hutchings M, Fields PA et al (2005) FDG-PET after two to three cycles of chemotherapy predicts progression-free and overall survival in highgrade non-Hodgkin lymphoma. Ann Oncol 16:1514-1523.
11. Safar V, Dupuis J, Jardin F et al (2009) Early 18 fluourodeoxyglucose PET scan as a prognostic tool in diffuse large B-cell lymphoma patients treated with an anthracycline-based chemotherapy plus rituximab. Blood 114:45.
12. Cashen A, Dehdashti F, Luo J et al (2008) Poor predictive value of FDG-PET/CT performed after 2 cycles of R-CHOP in patients with diffuse large B-cell lymphoma (DLCL). Blood 112:144.
13. Gallamini A, Hutchings M, Rigacci L et al (2007) Early interim 2-[18F]fluoro-2-D-glucose positron emission tomography is prognostically superior to international prognostic score in advanced stage Hodgkin's lymphoma: a report from a joint Italian-Danish study. J Clin Oncol 25:3746-3752.
14. Cerci JJ, Pracchia LF, Linardi CCG et al (2010) 18F-FDG PET after 2 cycles of ABVD predicts eventfree survival in early and advanced Hodgkin lymphoma. J Nucl Med 51:1337-1343.
15. Spaepen K, Stroobants S, Dupont P et al (2001) Prognostic value of positron emission tomography (PET) with fluorine-18 fluorodeoxyglucose ([18F]FDG) after first-line chemotherapy in non-Hodgkin's lymphoma: is [18F]FDG-PET a valid alternative to conventional diagnostic methods? J Clin Oncol 19:414-419.
16. Engert A, Kobe C, Markova J et al (2010) Assessment of residual bulky tumor using FDG-PET in patients with advanced-stage Hodgkin lymphoma after completion of chemotherapy: final report of the GHSG HD15 trial. Blood 116:336.
17. Cerci JJ, Trindade E, Pracchia LF et al (2010) Cost effectiveness of positron emission tomography in patients with Hodgkin's lymphoma in unconfirmed complete remission or partial remission after firstline therapy. J Clin Oncol 28:1415-1421.
18. Zinzani PL, Stefoni V, Tani M et al (2009) The role of FDG-PET scan in the follow-up of lymphoma: experience on 421 patients. J Clin Oncol 27:1781- 1787.
19. Petrausch U, Samaras P, Haile SR et al (2010) Risk-adapted FDG-PET/CT-based follow-up in patients with diffuse large B-cell lymphoma after firstline therapy. Ann Oncol 21:1694-1698.
20. Petrausch U, Samaras P, Veit-Haibach P et al (2010) Hodgkin's lymphoma in remission afer first-line therapy: which patients need FDG-PET/CT for follow-up? Ann Oncol 21:1053-1057.
21. Spaepen K, Stroobants S, Dupont P et al (2003) Prognostic value of pretransplantation positron emission tomography using fluorine 18-fluorodeoxyglucose in patients with aggressive lymphoma treated with high-dose chemotherapy and stem cell transplantation. Blood 102:53-59.
22. Lambert JR, Bomanji JB, Peggs KS et al (2010) Prognostic role of PET scanning before and after reduced-intensity allogeneic stem cell transplantation for lymphoma. Blood 115:2763-2768.
23. Lin C, Itti E, Haioun C et al (2007) Early $^{18}$F-FDG PET for prediction of prognosis in patients with diffuse large B-cell lymphoma: SUV-based assessment versus visual analysis. J Nucl Med 48:1626-1632.

24. Cheson BD, Horning SJ, Coiffier B et al (1999) Report of an International Workshop to standardize response criteria for non-Hodgkin's lymphomas. J Clin Oncol 17:1244-1253.
25. Cheson BD, Pfistner B, Juweid ME et al (2007) Revised response criteria for malignant lymphoma. J Clin Oncol 25:579-586.
26. Dupuis J, Itti E, Rahmouni A et al (2009) Response assessment after an inductive CHOP or CHOP-like regimen with or without rituximab in 103 patients with diffuse large B-cell lymphoma: integrating $^{18}$fluorodeoxyglucose positron emission tomography to the International Workshop Criteria. Ann Oncol 20:503-507.

# PET Imaging in Prostate Cancer

H. Alberto Vargas

Radiology, Memorial Sloan-Kettering Cancer Center, New York, NY, USA

## Introduction

Positron emission tomography (PET) is a highly sensitive tool for detecting and quantifying molecular activity throughout the body, and its use in oncology is now widespread. PET imaging is based on the detection of probes that consist at minimum of a targeting agent (e.g., an antibody, peptide, or small molecule) and a positron-emitting radionuclide that provides the signal for imaging. A variety of radionuclides with different half-lives are available for labeling, including fluorine 18 ($^{18}$F), carbon 11 ($^{11}$C), nitrogen 13 ($^{13}$N), iodine 124 ($^{124}$I), zirconium 89 ($^{89}$Zr), and copper 64 ($^{64}$Cu), and different radionuclides may be used to label the same targeting agent. The glucose analog fluorodeoxyglucose (FDG), labeled with $^{18}$F, is at present the most common PET radiotracer used in routine clinical care. However, a number of other probes now in the pipeline promise to significantly expand the role of PET in prostate cancer management. Furthermore, prostate-specific probes that can be imaged with PET have been identified and are undergoing clinical translation. Designing such imaging probes can be challenging, as two key requirements need to be met: (1) identifying a suitable target specifically associated with prostate cancer and finding an appropriate ligand that will bind to it with high specificity; and (2) labeling this ligand with a label suitable for PET. For prostate cancer, several targets have been identified, which together with more established PET tracers are discussed in the following paragraphs.

## Fluorodeoxyglucose (FDG) PET

FDG is labelled with $^{18}$F and is a glucose analog that is transported into and then trapped within tumor cells that demonstrate increased expression of glucose transporters in the cellular membrane (e.g. GLUT1) and increased activity of the enzyme hexokinase [1]. GLUT1 overexpression is low in most prostate cancers, as it is present mainly in poorly differentiated or highly proliferative cancers [2]. These findings probably explain why, despite the positive correlation between FDG uptake and clinical outcomes identified in patients with castration-resistant metastatic prostate cancer [3, 4], [$^{18}$F]-FDG PET has a limited role in detecting and staging localized prostate cancer. Local staging is further hindered by overlap in [$^{18}$F]-FDG uptake between benign and malignant prostatic tissue (Fig. 1); the typical distribution of tumor foci

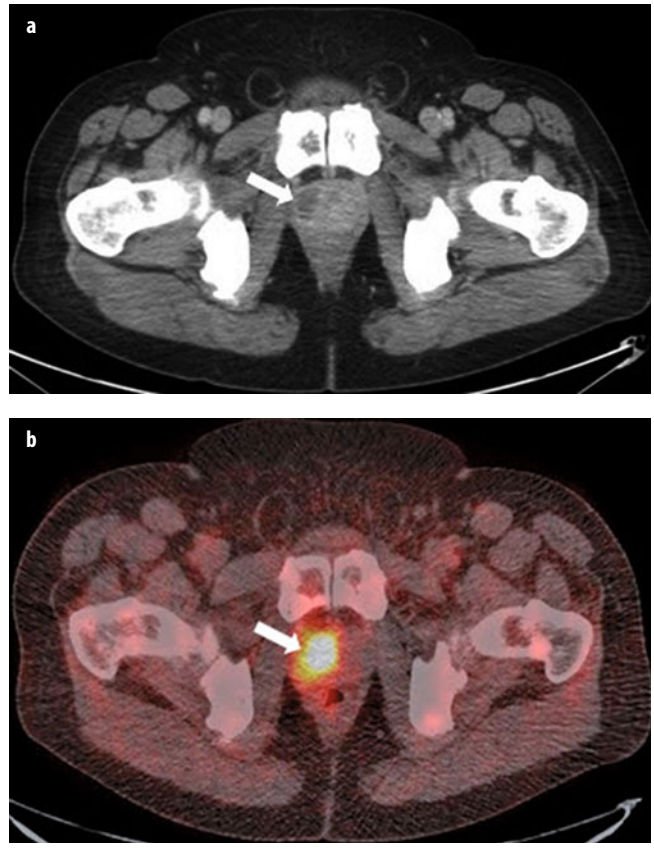


**Fig. 1 a, b.** **a** Axial computed tomography (CT) and **b** fused [$^{18}$F]-fluorodeoxyglucose (FDG) positron emission tomography computed tomography (PET/CT) images in a patient who had undergone transrectal ultrasound-guided prostate biopsy a few days earlier demonstrate abnormal FDG uptake in a prostatic abscess (*arrows*)

*Diseases of the Abdomen and Pelvis 2014-2017*,
DOI: 10.1007/978-88-470-5659-6_35 

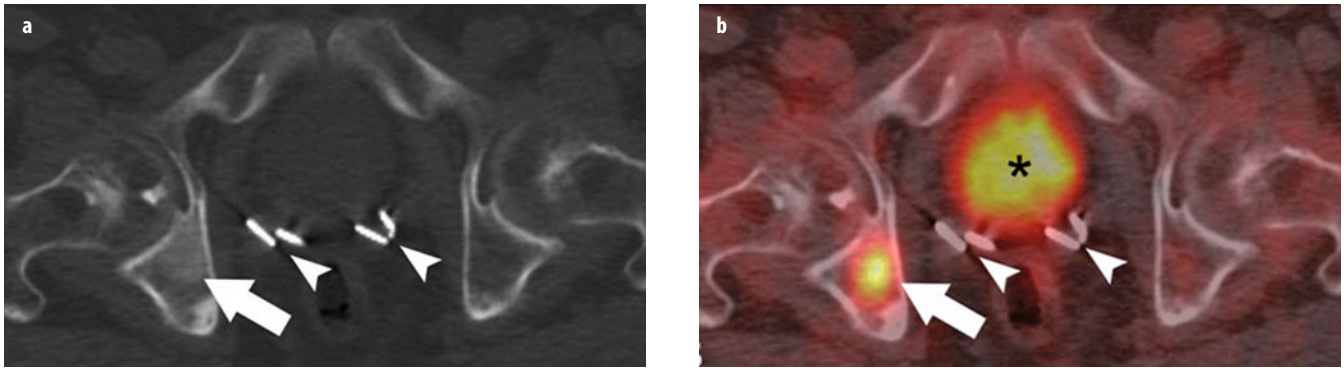


**Fig. 2 a, b.** **a** Axial computed tomography (CT) and **b** fused [$^{18}$F]-fluorodeoxyglucose (FDG) positron emission tomography computed tomography (PET/CT) images demonstrate a ground-glass-appearing density lesion in the right acetabulum on CT, with abnormal [$^{18}$F]-FDG accumulation (*arrow*) consistent with a bone metastasis in a patient with rising prostate-specific antigen (PSA) after prostatectomy. Prostatectomy clips (*arrowheads*) and physiological [$^{18}$F]-FDG excretion in the urinary bladder (*asterisk*) are also shown

intermixed with areas of benign hyperplastic prostate tissue and the prostate's close proximity to excreted tracer in the urethra and bladder. There may, however, be a correlation between prostate cancer aggressiveness and [$^{18}$F]-FDG uptake [5].

[$^{18}$F]-FDG PET has also been investigated for evaluating patients with biochemical recurrence after radical prostatectomy (Fig. 2) [6]. Also, in patients with castrate-resistant metastatic disease, a decline in [$^{18}$F]-FDG avidity of metastases treated with certain chemotherapeutic agents has been correlated with improved clinical response, whereas higher [$^{18}$F]-FDG uptake in tumors has been associated with shorter progression-free and overall survival [3, 4].

## Sodium Fluoride (NaF) PET

Sodium fluoride (NaF), typically labelled with $^{18}$F, is rapidly cleared from plasma in a biexponential manner. After a single pass, essentially, the entire amount of tracer administered is retained by bone. Bone uptake is related to chemisorption, with exchange of the $^{18}F^-$ ion for the $OH^-$ ion on the surface of the hydroxyapatite matrix of bone to form fluoroapatite and migration of $^{18}F^-$ ion into the crystalline matrix. The diagnostic performance of PET with [$^{18}$F]-NaF is superior to that of standard bone scintigraphy, yielding higher-quality images with rapid blood clearance and high bone-to-background ratio and requiring less time from tracer administration to imaging (Fig. 3). Even-Sapir and colleagues [7] compared technetium-99m ($^{99m}$Tc)-methylene diphosphonate planar bone scintigraphy, single-positron-emission computed tomography (SPECT), [$^{18}$F]-NaF PET, and [$^{18}$F]-NaF PET/CT in 25 men with newly diagnosed prostate cancer, with Gleason scores $\geqslant$8 or prostate-specific antigen (PSA) levels $\geqslant$20 ng/ml or nonspecific sclerotic lesions on CT, as well as 19 patients referred for evaluation of suspected disease recurrence or progression. In a patient-based analysis, sensitivity and specificity were 70% and 57%, respectively, for planar bone scintigraphy, 92% and 82%, respectively, for multiple field of view (FOV) SPECT, 100% and 62%, respectively, for [$^{18}$F]-NaF PET, and 100% and 100%, respectively, for [$^{18}$F]-NaF fluoride PET/CT. The high sensitivity and specificity of [$^{18}$F]-NaF PET/CT allows detection of occult bone metastases that are missed on standard bone scintigraphy (Fig. 3), with important implications for patient management.

[$^{18}$F]-NaF PET has also been used to monitor treatment response. A small pilot study of five patients with castrate-resistant metastatic prostate cancer showed that semiquantitative [$^{18}$F]-NaF PET was more accurate than qualitative comparison of scans in assessing response of bone metastases to $^{223}$Ra-chloride (Alpharadin, Algeta) therapy and correlated better with PSA and alkaline phosphatase changes [8]. Despite potential advantages of [$^{18}$F]-NaF PET/CT over standard bone scintigraphy in quantifying treatment response, it should be emphasized that the therapy-induced "flare" phenomenon described with bone scintigrams is also present on [$^{18}$F]-NaF [9].

## Choline PET

Choline can be labeled with $^{11}$C or $^{18}$F. It enters the cell through choline transporters and is the precursor for the biosynthesis of phospholipids, which are major components of the cellular membrane. Overexpression of choline kinase as a result of increased cellular membrane synthesis in tumors forms the biological basis for choline accumulation in prostate cancer [10].

In primary prostate cancer, reported detection rates using choline PET vary widely, probably in part because of heterogeneity in the different study populations with regard to tumor location, size, aggressiveness (e.g., Gleason score) and PSA kinetics [11, 12]. For detecting prostate cancer recurrence, sensitivities ranging between 38% and 98% have been reported using [$^{11}$C]- and [$^{18}$F]-choline PET [13, 14]. Similar diagnostic performance

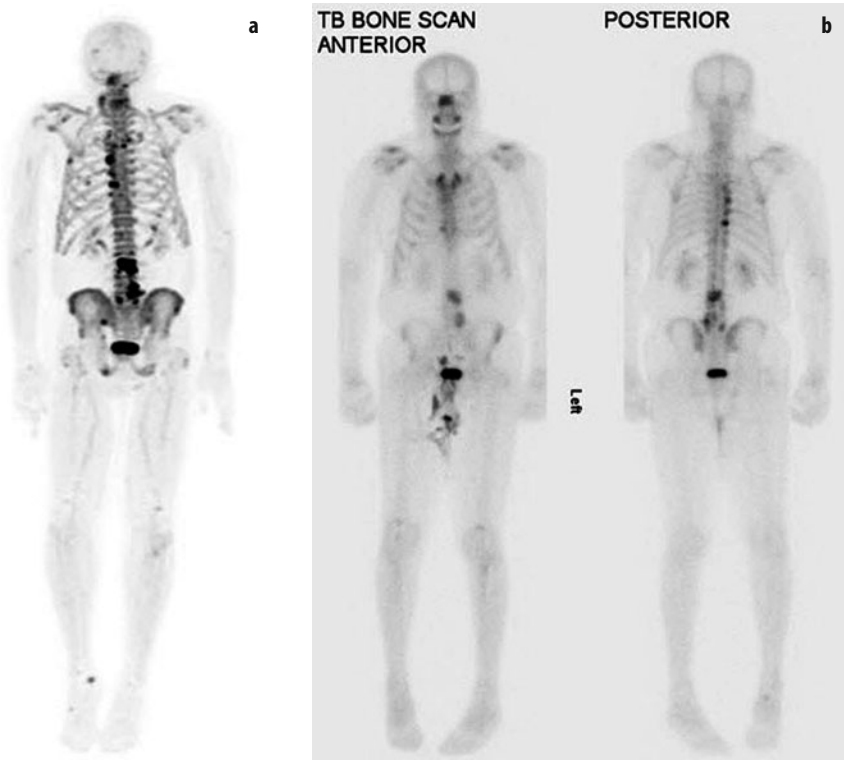


**Fig. 3 a, b.** **a** Three-dimensional maximum intensity projection (MIP) from [$^{18}$F]-sodium fluoride (NaF) positron emission tomography (PET) demonstrates an increased number and conspicuity of multiple bone lesions compared with anterior and posterior planar views from **b** technetium-99m ($^{99m}$Tc)-methylene diphosphonate bone scintigraphy in a patient with metastatic prostate cancer

for detecting prostate cancer have been reported in studies comparing [$^{11}$C]-choline or [$^{18}$F]-fluorocholine with [$^{11}$C]-acetate and [$^{18}$F]-NaF PET/CT [15, 16]. In prostate cancer bone metastases, the extent of choline uptake is inversely related to lesion attenuation on CT (lytic lesions on CT demonstrated higher choline uptake than blastic lesions) [17].

## Acetate PET

Acetate is preferentially transported across the cellular membrane through the monocarboxylate transporter. The major sources of acetate consumption are Krebs cycle and metabolic pathways related to production of phospholipids in cellular membranes. Acetate is typically labelled with [$^{11}$C]. An [$^{18}$F]-labeled formulation of acetate is also available (the 110-min half life of $^{18}$F is usually preferred over the 20-min half life of [$^{11}$C]), but experience with this tracer is limited [18]. Cancer-induced upregulation of fatty-acid synthase is the biologic basis for acetate uptake in prostate cancer. As with other tracers, there can be considerable overlap among uptake levels in primary prostate cancer, benign prostatic hyperplasia, and normal prostate gland, but generally, [$^{11}$C]-acetate uptake appears to be greater in cancerous than in noncancerous tissue [19]. Detection rates of up to 75% have been reported when using [$^{11}$C]-acetate for tumor recurrence assessment [20, 21]. As with all other imaging modalities, detection rates are dependent on serum PSA levels (in one study, positive findings occurred in 59% of patients with serum PSA levels $>$3 ng/ml and in 4% of patients with serum PSA levels $\leqslant$3 ng/ml) [22].

## Fluorothymidine (FLT) PET

FLT is phosphorylated by thymidine kinase (TK) 1, which is retained in proliferating cells without DNA incorporation [23]. FLT is typically labelled with $^{18}$F. Kukuk et al. [24] used PET to determine the pharmacokinetics of [$^{18}$F]-FLT, [$^{18}$F]-FDG, and [$^{11}$C]-choline in hormone-dependent and hormone-independent prostate cancer xenograft mouse models. The highest levels of [$^{18}$F]-FLT and [$^{18}$F]-FDG uptake were found in hormone-independent tumors. [$^{18}$F]-FDG uptake was also high in hormone-dependent tumors but decreased significantly after androgen deprivation therapy. A potential disadvantage to the use of [$^{18}$F]-FLT PET in assessing prostate cancer is the high level of physiologic accumulation in bone marrow, which may hinder detection of prostate cancer bone metastases.

## Fluoro-5-Methyl-1-β-D-Arabinofuranosyluracil (FMAU) PET

FMAU is a thymidine analog phosphorylated by TK and incorporated in DNA. Whereas FLT is phosphorylated by the cytosolic TK1, FMAU is phosphorylated by the mitochondrial TK2 [25]. FMAU is typically labelled with $^{18}$F and shows little physiologic accumulation in bone

marrow and urinary tract, which has theoretical advantages for imaging prostate cancer. Sun et al. [26], in a small study, showed that [$^{18}$F]-FMAU accumulated in locally recurrent prostate cancer tumors (tumor-to-background pelvis activity ratio 2.3-6.3) as well as in prostate cancer bone metastases (tumor-to-background normal bone activity ratio 2.4-3).

## Androgen Receptor (AR) PET

The androgen receptor (AR) plays a central role in the pathogenesis of castrate-resistant prostate cancer, and novel therapies directed against the androgen receptor have shown a clear survival benefit in this patient population. The effects of androgens are exerted via the nuclear AR, which is a ligand-dependent transcription activator involved in cellular proliferation and differentiation [27]. Almost all patients initially respond to androgen deprivation, but virtually all patients will eventually progress to a castration-resistant clinical state, which is thought to result from bypassing or sensitizing the AR pathway. Several ligands for the AR have been developed, including 16β-[$^{18}$F]-fluoro-5α-dihydrotestosterone ([$^{18}$F]-FDHT) [28]. Initial results from a study comparing [$^{18}$F]-FDHT and [$^{18}$F]-FDG PET in men with castration-resistant prostate cancer has shown that there are AR-predominant, glycolysis-predominant, and AR-glycolysis-concordant phenotypes (Fig. 4), which may have important prognostic and therapeutic implications [29]. Moreover, despite encouraging antitumor activity with enzalutamide in men with castration-resistant prostate cancer (e.g., decline in PSA, documented response in soft-tissue disease, stabilization of bone disease, and conversion from unfavorable to favorable circulating tumor cell counts), the enzalutamide-induced [$^{18}$F]-FDHT uptake changes in tumor did not necessarily parallel changes in tumor [$^{18}$F]-FDG uptake, suggesting that [$^{18}$F]-FDHT may be a pharmacodynamic marker as opposed to a treatment-response marker in this setting [30]. Further research is being conducted to elucidate the role of FDHT-PET in patients with advanced prostate cancer.

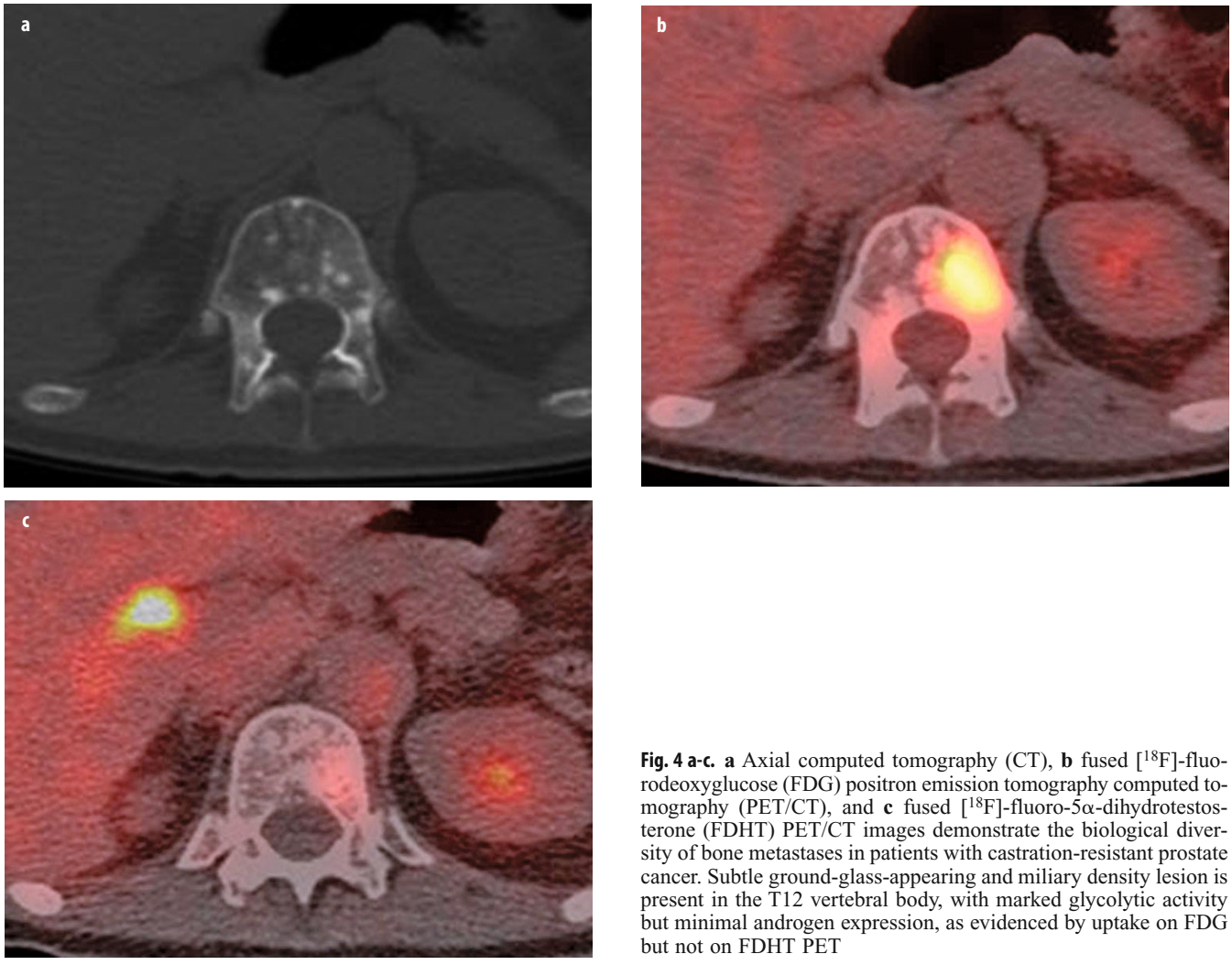


**Fig. 4 a-c.** **a** Axial computed tomography (CT), **b** fused [$^{18}$F]-fluorodeoxyglucose (FDG) positron emission tomography computed tomography (PET/CT), and **c** fused [$^{18}$F]-fluoro-5α-dihydrotestosterone (FDHT) PET/CT images demonstrate the biological diversity of bone metastases in patients with castration-resistant prostate cancer. Subtle ground-glass-appearing and miliary density lesion is present in the T12 vertebral body, with marked glycolytic activity but minimal androgen expression, as evidenced by uptake on FDG but not on FDHT PET

## Amino Acid PET

Enhanced amino acid transport and protein synthesis in tumor cells is the basis for labeling natural or synthetic amino acids for imaging with PET. Different amino acids have been used for this purpose. In one study [31], [$^{11}$C]-methionine was compared with [$^{18}$F]-FDG in ten patients with progressive prostate cancer. Index lesions demonstrated uptake of both tracers, but compared with [$^{18}$F]-FDG, [$^{11}$C]-methionine showed a higher tumor-to-blood ratio, more rapid tumor uptake after tracer administration, and a flatter uptake profile. There is increasing interest in the use of the synthetic amino acid anti-1-amino-3-[$^{18}$F]-fluorocyclobutyl-1-carboxylic acid (FACBC), an l-leucine analog [32]. The extent to which this tracer accumulates in prostate cancer tissue correlates with the expression level of alanine-, serine-, and cysteine-preferring system-mediated amino acid transport. Also, the tracer does not get incorporated into proteins. Schuster et al. [33] described their initial experience with anti-[$^{18}$F]-FACBC PET in prostate cancer. Visual analysis detected malignancy in all four men with local recurrence, corresponding to 40 of 48 prostate sextants, and in seven of nine pelvic nodal stations. More studies are being conducted to determine the potential incremental value of amino acid imaging over other established tracers, including evaluation of FACBC for detecting recurrent prostate cancer.

## Prostate-Specific Membrane Antigen (PSMA) PET

PSMA is a dimeric integral membrane glycoprotein highly expressed on prostate cancer cells and its expression is associated with prostate cancer progression and prognosis. PSMA protein expression can be imaged using labeled monoclonal antibodies (mAb) or small molecules. The most prominent of the mAb are 7E11 (indium-111 [$^{111}$In]-labeled capromab pendetide; ProstaScint®) and the more recently developed J591. 7E11 is a murine mAb specific for an epitope on the PSMA intracellular domain. As the binding site for this tracer is intracellular, it is only accessible if there is membrane disruption (e.g., dead or dying cells). As a result, the number of available targets for tracer binding is limited (i.e., tracer does not bind to cancer cells without membrane disruption); thus, SPECT with $^{111}$In-7E11 has shown low sensitivity for detecting viable tumor sites. Furthermore, $^{111}$In-capromab pendetide does not bind to viable prostate cancer sites in bone (the most common site of metastatic disease), and in contrast to PET, SPECT remains only semiquantitative in the clinical setting.

Recently, 7E11 was imaged using a new approach in which 7E11 is labelled with the PET nuclide zirconium-89 ($^{89}$Zr) [34]. $^{89}$Zr is ideally suited for targeted imaging probes, especially antibodies, as it has unique physical decay properties and energy (t1/2 = 78.43 h, $\beta+$ = 22.3%, E$\beta+$, max = 901 KeV, E$\gamma$ = 909 KeV). The greater half-life provides sufficient activity at the required circulation times for optimal targeting to disease sites, enabling imaging at later time points, including 120 h postinjection, an imaging window difficult to achieve with the shorter-lived PET nuclides such as $^{18}$F. The effects of chemotherapy, chemical castration, or radiotherapy may be monitored by observing 7E11 uptake, which increases with progressing cell membrane disruption resulting from treatment-induced cell death [34]. The uptake of $^{89}$Zr-7E11 correlates strongly with markers of cell death and apoptosis [34].

In contrast to 7E11, the humanized J591 mAb targets the extracellular domain of PSMA [35], which is accessible for binding regardless of cell membrane disruption and permeability. J591 has also been radiolabeled with $^{89}$Zr for immuno-PET imaging, demonstrating very high and specific tumor-to-background tissue ratios (Fig. 5) [36]. Overall, the novel radiotracers $^{89}$Zr-7E11 and -J591 represent promising candidates for translation to the clinic for noninvasively diagnosing prostate cancer and assessing its response to treatment.

In addition to antibodies, several small molecules have been described as ligands to PSMA. Low-molecular-weight imaging agents have several inherent advantages over bigger ligands such as antibodies, including faster tumor uptake and increased clearance from nontarget sites. Many low-molecular-weight inhibitors of PSMA are reported. A prominent example – now translated to the clinic – is N-[N-[(S)-1,3-dicarboxypropyl]carbamoyl]-4-[$^{18}$F]-fluorobenzyl-L-cysteine ([$^{18}$F]-DCFBC), a small-molecule inhibitor of PSMA's carboxypeptidase function [37]. As an inhibitor, this small molecule binds specifically and irreversibly to PSMA's active side. As tumor uptake and blood clearance are more rapid for small molecules than for antibodies, the pharmacodynamics of [$^{18}$F]-DCFBC are more favorable, with higher tumor-to-background ratios; however, a moderate degree of remaining blood pool activity has been noted, possibly due to binding to serum proteins.

Aptamers are another promising ligand for detecting PSMA. Aptamers are relatively short strands of oligonucleic molecules that bind to a specific target [38]. They are widely accepted as potential substitutes for antibodies, as they offer high stability, easy production, low immunogenicity, rapid clearance, and the possibility of binding to targets that are low in immunogenicity. An aptamer targeting PSMA (A10) was developed and, more recently, radiolabeled with $^{64}$Cu for possible PET imaging of PSMA-positive tumors [39].

## Prostate-Specific Antigen (PSA) PET

Standard prostate cancer screening is based on detecting raised levels of serum PSA. However, serum PSA is neither sensitive nor specific, and patients with prostate cancer may demonstrate normal serum PSA levels, and serum PSA may be raised in patients with noncancerous conditions, such as prostatitis. Although PSA expression

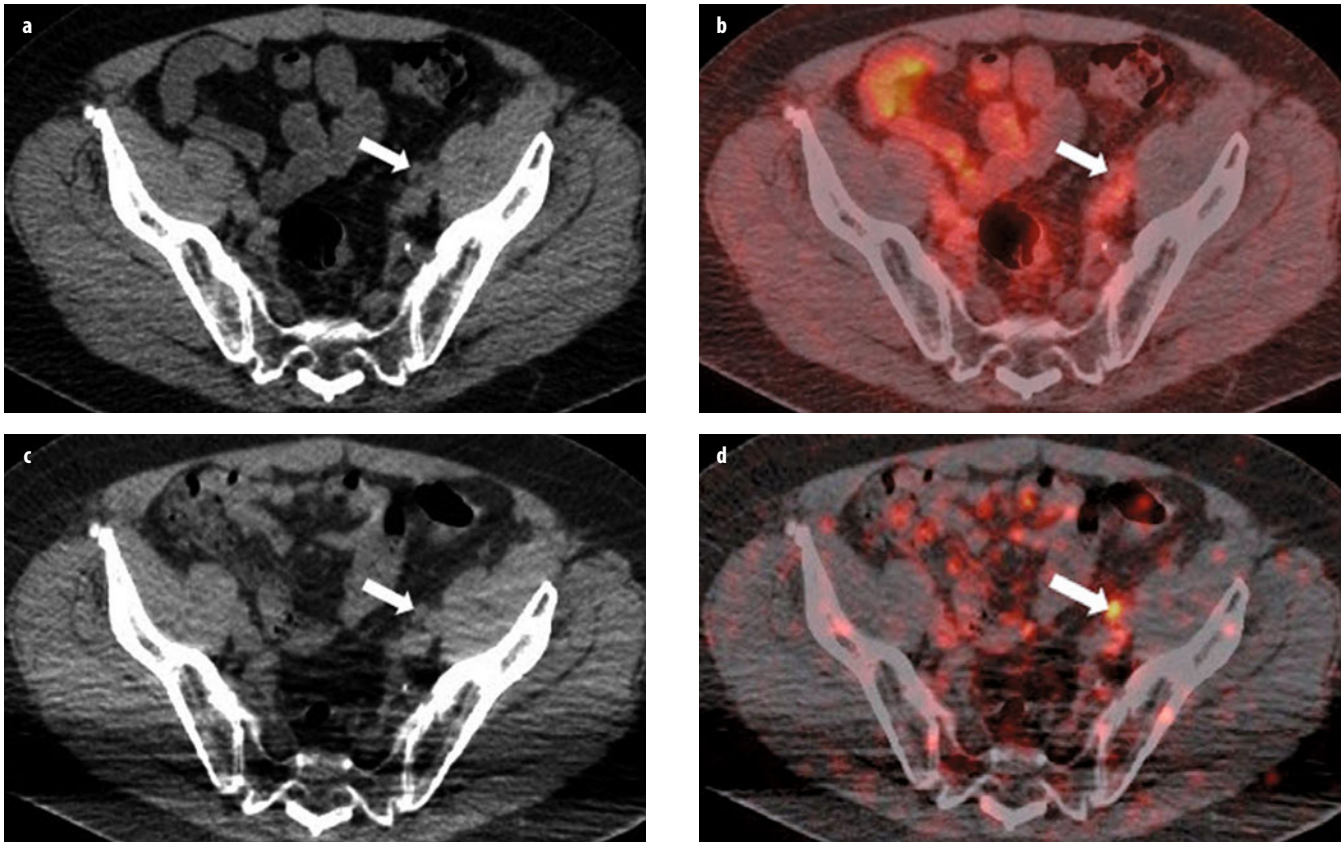


**Fig. 5 a-d.** **a** Axial computed tomography (CT) and **b** fused [$^{18}$F]-fluorodeoxyglucose (FDG) positron emission tomography computed tomography (PET/CT) images in a patient with prior prostatectomy for Gleason score 4+3 cancer undergoing evaluation for metastatic prostate cancer demonstrate a subcentimeter left external iliac lymph node without abnormal FDG uptake. **c** Axial CT and **d** fused zirconium 89 [$^{89}$Zr]-J591 PET/CT performed 8 days later demonstrate no change in size but abnormal J591 uptake in the same left external iliac lymph node. Fine-needle-aspiration biopsy confirmed the presence of metastatic prostate adenocarcinoma

is tightly coupled to AR signaling, and approximately 80-90% of prostate cancers are dependent on androgens, the ability to detect PSA in serum requires not only its expression within the cells but also its secretion and leakage into the circulation [40]. Only a very small amount of PSA is secreted into perivascular space and then ultimately into the serum. PSA is initially produced as an active protease ("free" PSA), and after its release into the perivascular space, it is quickly converted to its inactive forms ("complex" PSA). A mAb (5A10) recognizing an epitope near the catalytic cleft of PSA has been developed. This antibody only binds to free PSA, which remains associated with the tumor. $^{89}$Zr-labeled 5A10 exhibits excellent tumor uptake in multiple preclinical models of prostate cancer [40]. The androgen dependence of PSA could be visualized with PET. In one study, therapy with increasing amounts of the anti-androgen enzalutamide demonstrated a dose-dependent depression of tumor-associated $^{89}$Zr-5A10 uptake in primary tumors as well as bone lesions, whereas testosterone supplementation resulted in increased binding [40]. This study provided more evidence that therapy-dependent molecular changes of AR-targeted prostate-specific genes – the expression levels of PSA [40] – can be quantified noninvasively with radiolabeled antibodies and PET. As such tracers can be translated relatively quickly for clinical use, initial clinical trials are imminent.

## Other Targets

Several other targets on prostate cancer cells, as well as on neovasculature of prostate cancers, have been described. Prostate stem cell antigen is a cell-surface glycoprotein that is overexpressed in the majority of prostate cancers and most bone metastases. Antibodies against this antigen were raised [41] for PET imaging, although uptake in the tumor, at $<$5%, was relatively low. Another promising target is bombesin. The gastrin-releasing peptide receptor (GRPR) provides a promising target for staging and monitoring prostate cancer, as it is overexpressed only in prostate cancer and not in normal prostatic tissue. Bombesin is a 14-amino-acid peptide with a high binding affinity and specificity to the GRPR [42]. Radiopharmaceuticals containing bombesin or its analogues, labeled with several radionuclides including gallium 68, have been developed to target GRPR-expressing tumors for imaging with PET.

## References


1. Macheda ML, Rogers S, Best JD (2005) Molecular and cellular regulation of glucose transporter (GLUT) proteins in cancer. J Cell Physiol 202:654-662.
2. Reinicke K, Sotomayor P, Cisterna P et al (2012) Cellular distribution of Glut-1 and Glut-5 in benign and malignant human prostate tissue. J Cell Biochem 113:553-562.
3. Meirelles GS, Schoder H, Ravizzini GC et al (2010) Prognostic value of baseline [18F] fluorodeoxyglucose positron emission tomography and 99mTc-MDP bone scan in progressing metastatic prostate cancer. Clin Cancer Res 16:6093-6099.
4. Morris MJ, Akhurst T, Larson SM et al (2005) Fluorodeoxyglucose positron emission tomography as an outcome measure for castrate metastatic prostate cancer treated with antimicrotubule chemotherapy. Clin Cancer Res 11:3210-3216.
5. Shiiba M, Ishihara K, Kimura G et al (2012) Evaluation of primary prostate cancer using 11C-methionine-PET/CT and 18F-FDG-PET/CT. Ann Nucl Med 26:138-145.
6. Schoder H, Herrmann K, Gonen M et al (2005) 2-[18F]fluoro-2-deoxyglucose positron emission tomography for the detection of disease in patients with prostate-specific antigen relapse after radical prostatectomy. Clin Cancer Res 11:4761-4769.
7. Even-Sapir E, Metser U, Mishani E et al (2006) The detection of bone metastases in patients with high-risk prostate cancer: 99mTc-MDP Planar bone scintigraphy, single- and multi-field-of-view SPECT, 18F-fluoride PET, and 18F-fluoride PET/CT. J Nucl Med 47:287-297.
8. Cook G, Jr., Parker C, Chua S et al (2011) 18F-fluoride PET: changes in uptake as a method to assess response in bone metastases from castrate-resistant prostate cancer patients treated with 223Ra-chloride (Alpharadin). EJNMMI Res 1:4.
9. Wade AA, Scott JA, Kuter I, Fischman AJ (2006) Flare response in 18F-fluoride ion PET bone scanning. AJR Am J Roentgenol 186:1783-1786.
10. Contractor K, Challapalli A, Barwick T et al (2011) Use of [11C]choline PET-CT as a noninvasive method for detecting pelvic lymph node status from prostate cancer and relationship with choline kinase expression. Clin Cancer Res 17:7673-7683.
11. Scher B, Seitz M, Albinger W et al (2007) Value of 11C-choline PET and PET/CT in patients with suspected prostate cancer. Eur J Nucl Med Mol Imaging 34:45-53.
12. Martorana G, Schiavina R, Corti B et al (2006) 11C-choline positron emission tomography/computerized tomography for tumor localization of primary prostate cancer in comparison with 12-core biopsy. J Urol 176:954-960.
13. Picchio M, Briganti A, Fanti S et al (2011) The role of choline positron emission tomography/computed tomography in the management of patients with prostate-specific antigen progression after radical treatment of prostate cancer. Eur Urol 59:51-60.
14. Picchio M, Crivellaro C, Giovacchini G et al (2009) PET-CT for treatment planning in prostate cancer. Q J Nucl Med Mol Imaging 53:245-268.
15. Kotzerke J, Volkmer BG, Glatting G et al (2003) Intraindividual comparison of [11C]acetate and [11C]choline PET for detection of metastases of prostate cancer. Nuklearmedizin 42:25-30.
16. Wondergem M, van der Zant FM, van der Ploeg T, Knol RJ (2013) A literature review of 18F-fluoride PET/CT and 18F-choline or 11C-choline PET/CT for detection of bone metastases in patients with prostate cancer. Nucl Med Commun 34:935-945.
17. Beheshti M, Vali R, Waldenberger P et al (2010) The use of F-18 choline PET in the assessment of bone metastases in prostate cancer: correlation with morphological changes on CT. Mol Imaging Biol 12:98-107.
18. Matthies A, Ezziddin S, Ulrich EM et al (2004) Imaging of prostate cancer metastases with 18F-fluoroacetate using PET/CT. Eur J Nucl Med Mol Imaging 31:797.
19. Kato T, Tsukamoto E, Kuge Y et al (2002) Accumulation of [11C]acetate in normal prostate and benign prostatic hyperplasia: comparison with prostate cancer. Eur J Nucl Med Mol Imaging 29:1492-1495.
20. Kotzerke J, Volkmer BG, Neumaier B (2002) Carbon-11 acetate positron emission tomography can detect local recurrence of prostate cancer. Eur J Nucl Med Mol Imaging 29:1380-1384.
21. Sandblom G, Sorensen J, Lundin N et al (2006) Positron emission tomography with C11-acetate for tumor detection and localization in patients with prostate-specific antigen relapse after radical prostatectomy. Urol 67:996-1000.
22. Oyama N, Miller TR, Dehdashti F et al (2003) 11C-Acetate PET imaging of prostate cancer: detection of recurrent disease at PSA relapse. J Nucl Med 44:549-555.
23. Shields AF, Grierson JR, Dohmen BM et al (1998) Imaging proliferation in vivo with [F-18]FLT and positron emission tomography. Nat Med 4:1334-1336.
24. Kukuk D, Reischl G, Raguin O et al (2011) Assessment of PET tracer uptake in hormone-independent and hormone-dependent xenograft prostate cancer mouse models. J Nuclear Med 52:1654-1663.
25. Tehrani OS, Douglas KA, Lawhorn-Crews JM, Shields AF (2008) Tracking cellular stress with labeled FMAU reflects changes in mitochondrial TK2. Eur J Nucl Med Mol Imaging 35:1480-1488.
26. Sun H, Sloan A, Mangner TJ et al (2005) Imaging DNA synthesis with [18F]FMAU and positron emission tomography in patients with cancer. Eur J Nucl Med Mol Imaging 32:15-22.
27. Azzouni F, Mohler J (2012) Biology of castration-recurrent prostate cancer. Urol Clin North Am 39:435-452.
28. Larson SM, Morris M, Gunther I et al (2004) Tumor localization of 16beta-18F-fluoro-5alpha-dihydrotestosterone versus 18F-FDG in patients with progressive, metastatic prostate cancer. J Nucl Med 45:366-373.
29. Fox JJ, Autran-Blanc E, Morris MJ et al (2011) Practical approach for comparative analysis of multilesion molecular imaging using a semiautomated program for PET/CT. J Nucl Med 52:1727-1732.
30. Scher HI, Beer TM, Higano CS et al (2010) Antitumour activity of MDV3100 in castration-resistant prostate cancer: a phase 1-2 study. Lancet 375:1437-1446.
31. Macapinlac HA, Humm JL, Akhurst T et al (1999) Differential metabolism and pharmacokinetics of L-[1-(11)C]-methionine and 2-[(18)F] fluoro-2-deoxy-D-glucose (FDG) in androgen independent prostate cancer. Clin Positron Imaging 2:173-181.
32. Oka S, Hattori R, Kurosaki F et al (2007) A preliminary study of anti-1-amino-3-18F-fluorocyclobutyl-1-carboxylic acid for the detection of prostate cancer. J Nucl Med 48:46-55.
33. Schuster DM, Votaw JR, Nieh PT et al (2007) Initial experience with the radiotracer anti-1-amino-3-18F-fluorocyclobutane-1-carboxylic acid with PET/CT in prostate carcinoma. J Nucl Med 48:56-63.
34. Ruggiero A, Holland JP, Hudolin T et al (2011) Targeting the internal epitope of prostate-specific membrane antigen with 89Zr-7E11 immuno-PET. J Nucl Med 52:1608-1615.
35. Liu H, Moy P, Kim S et al (1997) Monoclonal antibodies to the extracellular domain of prostate-specific membrane antigen also react with tumor vascular endothelium. Cancer Res 57:3629-3634.
36. Holland JP, Divilov V, Bander NH et al (2010) 89Zr-DFO-J591 for immunoPET of prostate-specific membrane antigen expression in vivo. J Nucl Med 51:1293-1300.
37. Cho SY, Gage KL, Mease RC et al (2012) Biodistribution, tumor detection, and radiation dosimetry of 18F-DCFBC, a low-molecular-weight inhibitor of prostate-specific membrane anti-

gen, in patients with metastatic prostate cancer. J Nucl Med 53:1883-1891.
38. Song KM, Lee S, Ban C (2012) Aptamers and their biological applications. Sensors 12:612-631.
39. Rockey WM, Huang L, Kloepping KC (2011) Synthesis and radiolabeling of chelator-RNA aptamer bioconjugates with copper-64 for targeted molecular imaging. Bioorg Med Chem 19:4080-4090.
40. Ulmert D, Evans MJ, Holland JP et al (2012). Imaging androgen receptor signaling with a radiotracer targeting free prostate-specific antigen. Cancer discovery 2:320-327.
41. Lepin EJ, Leyton JV, Zhou Y et al (2010) An affinity matured minibody for PET imaging of prostate stem cell antigen (PSCA)-expressing tumors. Eur J Nucl Med Mol Imaging 37:1529-1538.
42. Smith CJ (2003) Radiochemical investigations of gastrin-releasing peptide receptor-specific [(99m)Tc(X)(CO)3-Dpr-Ser-Ser-Ser-Gln-Trp-Ala-Val-Gly-His-Leu-Met-(NH2)] in PC-3, tumor-bearing, rodent models: syntheses, radiolabeling, and in vitro/in vivo studies where Dpr = 2,3-diaminopropionic acid and X = H2O or P(CH2OH)3. Cancer Res (Baltimore) 63:4082-4088.

# PEDIATRIC RADIOLOGY SATELLITE COURSE
# "KANGAROO"

# Solid and Cystic Masses and Mass-Like Lesions of the Liver, Bile Ducts, and Pancreas

Jeanne S. Chow

Departments of Urology and Radiology, Boston Children's Hospital, Boston, MA, USA

## Introduction

This chapter focuses on the imaging of masses and mass-like entities of the upper abdomen arising from the liver, bile ducts, and pancreas. Radiologists play the crucial role in first discovering these masses, determining their site of origin, and providing the differential diagnosis. Masses in adults are different than those in children, and some masses arising from the biliary tree, liver, and pancreas even may be diagnosed prenatally.

The claw sign is a universal sign that helps show the organ of origin of a mass, and that organ should form a "claw" around or encircle the mass. Occasionally, a mass can be so large and abut multiple organs that the site of origin is difficult to determine. In children, ultrasound (US) is the initial imaging modality for abdominal masses and can be used to depict clearly masses from all three organs. If further evaluation is warranted, contrast-enhanced magnetic resonance imaging (MRI) is useful but in some children may require sedation. With faster sequences, proper patient preparation, and distraction techniques such as those provided by certified Child Life specialists, there is increasingly less need for sedation, even in young children [1]. Computed tomography (CT) is faster than MRI and rarely requires sedation, but it carries the risk of ionizing radiation. However, in the past decade, enormous improvements have been made in decreasing radiation dose by altering protocols and utilizing postprocessing software [2]. Nuclear medicine studies rarely play a role in the initial imaging of these masses.

## Liver Masses and Mass-Like Entities

In children, the histology of the liver mass can be predicted based on patient age at presentation, mass appearance, and elevated alpha-fetoprotein (AFP) [3] . Tumors that occur in the newborn period, some of which are discovered prenatally, include benign (infantile hemangioendothelioma/infantile hepatic hemangioma, mesenchymal hamartoma) and malignant (hepatoblastoma) tumors. The most common primary hepatic malignancy in toddlers is hepatoblastoma. In older children, hepatocellular carcinoma (HCC) is the most common primary malignancy and is typically associated with underlying liver disease. Hepatoblastoma and HCC can be distinguished from benign liver masses such as focal nodular hyperplasia (FNH) and hepatic adenoma by elevations in alpha-fetoprotein. A rare tumor, fibrolamellar HCC is a low-grade malignancy and does not cause AFP elevation. Many masses occurring in childhood have classic appearances, which are described below. In children, just as in adults, the most common liver tumors are not primary but secondary to metastases [4].

Imaging is extremely important in helping to diagnose a hepatic mass. Typically, US is the initial imaging modality and discovers the mass because US is the main screening modality of the abdomen in children. After it is determined that the mass arises from the liver, assessing size, location within the liver, vessel involvement and patency, and other anomalies in the abdomen are important. US contrast agents also help make liver masses more conspicuous, but this has mainly been studied in adults [5]. Elastography, often used in determining the character of the liver, specifically in distinguishing cirrhotic from normal livers, is not routinely used to better define liver masses in children [6].

In the past decade, advances in MRI techniques and new contrast agents have allowed for more specific diagnosis of liver masses. Contrast-enhanced MRI is fundamental for evaluating liver masses. The most widely available contrast agents are extracellular gadolinium chelates. The enhancement pattern using this contrast has been widely studied. Newer hepatocyte-specific contrast agents are taken up in variable quantities by functioning hepatocytes and are excreted by the bile. These agents give an increased contrast to noise ratio (CNR) for nonhepatocellular lesions compared with that of the background liver, which increases conspicuity on delayed T1-weighted images. Tumors that contain hepatocytes, such as adenomas, FNH, and nodular regenerative hyperplasia, demonstrate enhancement on delayed imaging. Some hepato-

*Diseases of the Abdomen and Pelvis 2014-2017*,
DOI: 10.1007/978-88-470-5659-6_36 

cyte-specific agents are first distributed into extracellular spaces and then taken up by hepatocytes, giving the benefit of dynamic imaging and delayed hepatobiliary-phase imaging [3, 7, 8]. Pediatric tumors have been recently described with such agents.

CT also beautifully depicts hepatic masses, with its main downside being ionizing radiation. However, CT rarely requires sedation and may be more readily available than MRI. Ionizing radiation can be kept to a minimum by adhering to low-dose principles [9] and eliminating unnecessary phases, such as scanning before administration of contrast.

Nuclear medicine rarely plays a role in the initial evaluation of liver masses, unless the mass originates from another organ, such as neuroblastoma or lymphoma, and if metastases are discovered in the liver using isotopes specific to the primary mass. Occasionally, FNH is distinguished from other tumors because Kupffer cells present within the mass take up radiotracer on sulfur colloid scintigraphy.

Benign and malignant hepatic masses can be distinguished by AFP elevation. This glycoprotein is normally synthesized by the fetal yolk sac, liver, and intestine. Thus, the value is normally elevated in the newborn period and gradually declines [10]. AFP is elevated in epithelial liver tumors (hepatoblastoma and HCC); however, its elevation is also associated with yolk-sac tumors (not arising from the liver), nonneoplastic conditions, including acute liver disease, and hereditary disorders [11]. The following discussion of hepatic masses is divided by patient age, with masses listed in order of frequency from common to uncommon.

This section on hepatic masses will primarily discuss tumors of the liver, with very little on infection.

### Hepatic Masses in Newborns

The most common masses in the newborn period are infantile hemangioma, infantile hemangioendothelioma, and mesenchymal hamartomas, which are benign lesions. Imaging characteristics, specifically enhancement patterns and presence of cysts help distinguish these from the less common tumor type, malignant hepatoblastoma. Elevations in AFP, which typically help distinguish hepatoblastoma from benign tumors, may be normally elevated during this period and therefore not helpful in distinguishing masses.

### Infantile Hemangiomas/Hemangioendotheliomas

Infantile hemangiomas and hemangioendotheliomas are both benign entities seen in infants. Occasionally, hemangioendotheliomas are seen prenatally. Although their names are similar, these represent two very different liver masses. Infantile hemangiomas are common, typically associated with other cutaneous "strawberry" hemangiomas. These small, uniform multifocal tumors follow a typical pattern of growth and involution. Hemangiomas are distinguished from hemangioendotheliomas by positive immunoreactivity to erythrocyte-type glucose transporter protein 1 (GLUT1). Infantile hemangioendotheliomas are now also referred to as RICH, or rapidly involuting congenital hemangiomas. These are large, solitary, focal lesions and represent vascular malformation rather than tumor, and they show no immunoreactivity to GLUT1. Because these large masses cause hemodynamic shunting, patients present with symptoms of congestive heart failure. However, as with infantile hemangiomas, the mass involutes, typically by 12-14 months of age [12].

Hepatic infantile hemangiomas are typically 1 cm in size and uniform in appearance. By US, they appear echogenic relative to adjacent liver parenchyma. After contrast administration, during either CT or MRI, these masses enhance rapidly and uniformly. Solitary infantile hemangioendothelioma are large and heterogeneous in appearance. The mass is composed of vascular channels and characterized by hemorrhage, necrosis, fibrosis, and calcification. US will show these characteristics. Contrast-enhanced MRI and CT typically show a large mass with rapid peripheral enhancement in a nodular pattern, which fills in centrally in a centripetal pattern. Adjacent hepatic vessels commonly dilate as they feed and drain the tumor [4].

### Mesenchymal Hamartoma

Mesenchymal hamartoma is the second most common benign lesion of the liver. This tumor is composed of disorganized hepatic tissue, fluid-filled mesenchyme, bile ducts, and cysts. As a result, these tumors appear highly heterogeneous and often cystic. The presence of cysts helps distinguish this tumor from other lesions. Most commonly discovered in children <2 years of age, 95% occur in children <5 years of age [4].

### Angiosarcoma

These large, heterogeneous, aggressive, rare tumors of infancy are often initially misdiagnosed as benign infantile hemangioendotheliomas; 60% of patients present with metastases to the lung and bones. Prognosis is dismal, with rapid decline within 6 months of diagnosis regardless of treatment [13]. Unlike adults who develop this tumor, after Thorotrast exposure children develop this tumor de novo.

### Hepatoblastoma

This type of tumor is the most common primary hepatic malignancy in infants and toddlers, with nearly 70% seen in the first year of life [14]. Most children have no history of liver disease. However, some predisposing conditions are familial adenomatous polyposis type 1A, glycogen storage disease, Gardner syndrome, fetal alcohol syndrome, Wilms' tumor, and Beckwith-Wiedemann syndrome [15]. There is also a strong association with low-birth-weight infants [16].

Hepatoblastoma most commonly presents as a large solitary mass and has a slight preference for the right lobe of the liver. More rarely, hepatoblastoma is multiple (20%) and infiltrative or diffuse. Tumors are of two main subtypes: epithelial and mixed epithelial mesenchymal. Epithelial tumors tend to be more homogeneous and the mixed subtype more heterogeneous, due to osteoid, cartilaginous, and fibrous components and propensity for hemorrhage and necrosis [13]. Evaluation of adjacent vessels is crucial to assess for thrombosis. Lungs are the first site of metastasis.

By US, the appearance of the mass depends on subtype, presence of disorganized mesenchymal tissue, and hemorrhage. These generally appear heterogeneous, as well as hypoechoic compared with normal adjacent liver parenchyma. These masses are commonly large at presentation, typically 30 cm in diameter. Similarly, CT and MRI will demonstrate a heterogeneously enhancing mass with variable quantities of calcification. Hepatocyte-specific agents are helpful in characterizing these masses [17].

### Hepatic Masses in Toddlers

Because vascular malformations (infantile hemangiomas and infantile hemangioendotheliomas) and mesenchymal hamartomas are less common in toddlers, a large hepatic mass is worrisome for a hepatoblastoma. Elevation of AFP will help distinguish hepatoblastoma and, less commonly, HCC from other typically benign entities.

Other hepatic masses seen in toddlers are listed here and described elsewhere in this chapter: hepatoblastoma, hepatocellular carcinoma, mesenchymal hamartoma, and FNH.

### Hepatic Masses in School-Aged Children and Teenagers

#### Focal Nodular Hyperplasia

FNH is a rare tumor in children and most commonly seen in adult women. Only 7% of cases occur in children, with a peak age range of 2-5 years. These benign epithelial tumors are composed of a polyclonal proliferation of hepatocytes, Kupffer cells, blood vessels, and malformed biliary ductules. The mass is encapsulated and thus well defined, and nodules within the mass are separated by fibrous septae that coalesce to form a characteristic central vascular scar. This central scar is characteristic but not specific to FNH. Masses tend to be otherwise homogeneous. These tumors may present as a solitary mass, or multiple masses in the setting of prior treated abdominal malignancy [18]. The etiology of this mass is uncertain, but one theory is the mass is a response to vascular injury [19].

Determining the presence of hepatocytes, central scar, and Kupffer cells is useful in imaging diagnosis. As the tumor is partially composed of hepatocytes, enhancement with a hepatocyte-specific MRI agent is useful for diagnosis, and the tumor remains isointense to hyperintense on delayed hepatocyte-phase imaging [3]. A central scar is a classic but inconsistent finding also seen with fibrolamellar HCC. The scar enhances on delayed images with traditional contrast agents but not on hepatocyte-specific agents, as the scar is devoid of hepatocytes. The presence of Kupffer cells in this tumor allows for increased uptake on technetium-99m ($^{99m}$Tc)-sulfur colloid scintigraphy. This is especially useful when distinguishing FNH from hepatic adenoma [13].

#### Hepatic Adenoma

These typically spherical masses are composed of hepatocytes with an increased amount of intracellular fat and glycogen, disorganized Kupffer cells, and a well-defined capsule. The presence of fat will allow these tumors to suppress on opposed-phase MRI. However, HCCs may contain intracellular fat and act similarly. With hepatic-specific contrast agents, these enhance rapidly initially, and enhancement persists on delayed images [20]; thus, the imaging pattern is similar to FNH. However, the presence of a focal scar favors the diagnosis of FNH. These are associated with the use of steroids, and adolescents who use contraceptives orally are the most frequent pediatric patients with liver adenomas [15].

#### Hepatocellular Carcinoma

This is the second most common primary liver malignancy in children after hepatoblastoma and occurs at two age groups: 4-5 years, and 12-14 years. Half of the patients have underlying liver disease, including cirrhosis, biliary atresia, hemochromatosis, glycogen storage disease, or viral hepatitis. Elevated AFP distinguishes this tumor from nonmalignant neoplasms but is elevated in only 70% of patients

Presentation may be solitary, multifocal, or diffuse and infiltrative. These lesions, especially large ones, appear heterogeneous. Vascular invasion is common. The appearance of HCC and hepatoblastoma are similar on US, CT, and MRI. Nuclear medicine gallium scans are useful in distinguishing these masses from benign regenerating nodules, as the tumors are gallium avid [15].

#### Fibrolamellar Carcinoma

This variant of HCC occurs in patients without underlying liver disease and usually in patients younger than those with typical HCC, peaking in the late teen years. Unlike HCC, these tumors do not have an elevated AFP. These large tumors do not have a characteristic appearance and mimic other liver tumors. They may be solitary, nodular, or diffuse. The presence of a nonenhancing central scar mimics FNH. Calcification may be present in 50%. However, age at presentation and lack of AFP elevation points to the diagnosis.

#### Undifferentiated Embryonal Sarcoma

This rare malignancy is the third most common tumor after hepatoblastoma and HCC. Peak patient age is between 6 and 10 years [21]. These large tumors tend to be hemorrhagic, cystic due to a large component of myxoid stroma.

#### Inflammatory Pseudotumor

These inflammatory masses consist of plasma cells and mononuclear leukocytes and are very rare. They may be singular or multiple and cannot be distinguished from metastases by imaging.

#### Multifocal Masses Occurring in All Age Groups

#### Metastasis

The most common liver malignancies are not primary but secondary to metastases. Common tumors that metastasize to the liver include neuroblastoma, leukemia, and Wilms' tumor [15]. The diagnosis is typically made after the primary tumor is found. Hepatocyte-specific contrast agents are useful for improving conspicuity of metastases from normal adjacent liver parenchyma and for distinguishing this mass from benign hepatic lesions, such as FNH, which can be seen after chemotherapy.

#### Infection

Infections tend to present as multifocal lesions within the liver. Abscesses may be necrotic centrally and thus exhibit peripheral enhancement. Presence of similar abnormalities in other organs, specifically lung, spleen, and kidneys, are helpful for further confirmation.

#### Nodular Regenerative Hyperplasia

These multifocal masses represent areas of benign hepatocellular proliferation typically present in a diseased liver due to cirrhosis, hepatotoxic medications, or collagen vascular disease. Vascular abnormalities can also lead to nodular regenerative hyperplasia. Because these masses contain hepatocytes, delayed postcontrast imaging demonstrates delayed, persistent enhancement when using hepatic-specific agents.

#### *Key Points*

Patient age, mass appearance, and tumor markers predict the histology of liver masses in children.

The main initial imaging modality for liver masses is US.

MRI with contrast agents that specifically target hepatocytes are excellent at characterizing and distinguishing benign and malignant masses.

## Biliary Masses and Mass-Like Lesions

In children, solid masses arising from the biliary system are extremely rare. The most common solid and cystic mass-like lesions of the biliary tract are due to congenital malformations of the small, medium, and large ducts of the biliary tree. Depending on the size of the affected duct, pathologic and radiographic appearances differ. When small ducts form abnormally, the finding is diffuse and results in congenital hepatic fibrosis and biliary hamartomas. When medium ducts are affected, polycystic liver disease manifests, often in association with polycystic kidneys. When large intra- and extrahepatic ducts are affected, the result is Caroli disease and choledochal cysts.

These congenital abnormalities of the biliary tree are secondary to abnormal development of the ductal plate, the primitive biliary duct. Ductal-plate malformations, also called fibrocystic liver disease, are due to abnormal formation of cilia organelles on the surface of the biliary epithelium. Defective ciliary proteins cause abnormalities in the smallest bile ducts, leading to congenital hepatic fibrosis, and in larger ducts, causing Caroli disease. This ciliopathy also causes abnormal tubule development in the kidneys and thus form the unifying cause of some diseases involving both the hepatic and renal organs, including autosomal recessive polycystic kidney disease, medullary sponge kidney, and nephronophthisis [7].

Multiple imaging modalities are useful in evaluating abnormalities of the biliary tree. US has a primary role in imaging and is excellent at depicting the multiple masses seen with biliary hamartomas or dilatation of the biliary tract. MRI with cholangiopancreatography (MRCP) using heavily T2-weighted sequences also evaluates the liver and biliary tree. The use of hepatocyte-specific contrast agents, which are excreted in the biliary tree, is useful in further characterizing the biliary tree [22]. Endoscopic retrograde cholangiopancreatography (ERCP) is an excellent method of evaluating the biliary tree but carries risk of pancreatitis and the inherent risks of sedation. By US and MRCP, cystic dilatation of the biliary tree is distinguished from multiple hepatic cysts by the central dot sign, in which the ectatic ducts surround the portal vein radicles and the radicles represent the central nonenhancing dot. Nuclear medicine hepatoiminodiacetic acid (HIDA) scans are helpful in showing the biliary tree, as the contrast agent is excreted in bile. CT is the least commonly used modality to evaluate the biliary tree.

The following discussion of mass-like lesions of the biliary tract progress from anomalies of the smallest to largest biliary ducts.

#### Congenital Hepatic Fibrosis

Malformation of the smallest biliary ducts, the interlobular ducts, leads to congenital hepatic fibrosis. Periportal fibrosis occurs from scarring between adjacent biliary tracts and ductal plate remnants. When associated with

abnormalities of the large ducts, the disease is called Caroli syndrome. The fibrotic liver appears heterogeneous, often with focal mass-like nodules, which represent focal regenerative hyperplasia. These not only appear as contour abnormalities but may enhance heterogeneously from the adjacent hepatic parenchyma on MRI or CT. However, in the background of hepatic fibrosis, the lesions are often assumed to be due to this cause rather than representing tumor, especially when AFP values are normal. When associated with dilatation of the larger intrahepatic biliary ducts of Caroli disease, the ducts will be dilated in a branching tree pattern with a central dot sign.

### Diffuse Hamartoma

Diffuse hamartomas are also known as microhamartomas and Von Meyenberg complex. These rare lesions are well defined, uniform in size, and multiple, with varying solid and cystic composition. They result from ductal plate malformations of the small bile ducts and are typically not associated with other anomalies. On US, lesions are typically hypoechoic with a comet-tail artifact; on T2-weighted MRI, they are hyperintense. These benign lesions are asymptomatic and require no treatment.

### Choledochal Cysts

Choledochal cysts are characterized by fusiform and saccular dilatation of the intrahepatic and extrahepatic biliary tree and categorized by five main subtypes of the Todani Classification [23].

#### Type 1

Todani choledochal cysts type 1 represent 80-90% of cases [24] and are characterized by common bile duct dilatation. Subtypes 1A, 1B, and 1C refer to common bile duct cystic dilatation, segmental dilatation below the cystic duct, and fusiform dilatation, respectively. Patients present in both infancy and childhood. Infants present with cholestatic jaundice, which is indistinguishable from biliary atresia and neonatal jaundice. The classic presentation triad described in older children of abdominal pain, obstructive jaundice, and fever occurs rarely.

#### Types 2-4

These types are much more rare: Todani choledochal cysts type 2 represent 2% of cases, with diverticula of the common bile duct. Type 3 involves dilatation of the intraduodenal portion of the distal common bile duct, which forms a cyst-like protrusion into the duodenum called a choledochocele, similar to a ureterocele in the urinary tract. Type 4 have extrahepatic biliary ductal dilatation, with type 4A being multiple intra- and extrahepatic biliary ductal dilatation, and type 4B showing no intrahepatic involvement.

#### Type 5

Todani choledochal cysts type 5 is Caroli disease, which is characterized by segmental, nonobstructive dilatation of the intrahepatic biliary ducts. The appearance is irregular fusiform dilatation or that of multiple intrahepatic cysts, which are in continuity with the biliary system. Caroli disease is associated with stone formation, cholangitis, and hepatic abscesses. In Caroli syndrome, there is associated congenital hepatic fibrosis and renal tubular ectasia and cysts, as described above.

#### *Key points*

Solid masses of the biliary tract are rare.

Many congenital anomalies of the biliary ducts are secondary to ciliopathies, which are associated with renal disease.

## Pancreatic Masses and Mass-Like Lesions

Pancreatitis, its sequelae, and primary and secondary masses of the pancreas are much less common in children than in adults.

The normal pancreas is a homogeneous-appearing organ, generally well visualized by US in children, especially if the child has been fasting. If overlying bowel gas obscures the organ, filling the stomach with fluid by asking the child to drink can provide a clearer acoustic window. The pancreas is slightly hypoechoic or isoechoic relative to the liver and more echogenic during the neonatal period [25]. Normal size measurements have been established [26]. Normally, the pancreatic duct can be faintly visualized.

MRI and MRCP can show the appearance of the pancreatic tissue, masses, and pancreatic duct. The appearance of the duct can be enhanced with administration of the hormone secretin, which stimulates a normal pancreas to secrete fluid while increasing the tone of the sphincter of Oddi [27]. Defining ductal anatomy is especially helpful in children who have congenital anomalies of the pancreatic duct or masses that may obstruct it. CT with contrast is another imaging option if the pancreas cannot be visualized by US and MRI is unavailable or the risk of sedation precludes it. Nuclear medicine is not typically indicated for evaluating the pancreas. ERCP is excellent for evaluating the pancreatic duct, but it is invasive.

Understanding the anatomical variants of the pancreas is important to avoid confusing masses with other anomalies. During normal embryologic development, the dorsal and ventral pancreatic tissues rotate and fuse to form a normal elongated pancreas. The dorsal and ventral pancreatic ducts fuse and normally form one major pancreatic duct, which joins with the common bile duct to drain through the ampulla of Vater into the second portion of the duodenum. Occasionally, the two ducts do not fuse and enter separately into the duodenum, with the dorsal

pancreatic duct becoming the accessory pancreatic duct of Santorini and the ventral duct becoming the main pancreatic duct of Wirsung. This configuration, called pancreatic divisum, is associated with increased risk of pancreatitis. When there is agenesis of the dorsal pancreatic anlage, the pancreas is short. This finding is common in patients with polysplenia. When the ventral pancreatic anlage rotates abnormally, an annular pancreas forms and wraps around the duodenum, which leads to duodenal obstruction in children.

### Acute Focal Pancreatitis

Pancreatitis is much less common in children than adults and is suspected on clinical grounds and elevation of pancreatic enzymes. The common causes of alcoholic and cholestatic pancreatitis in adults are replaced in children by multisystem disease, such as viruses, congenital anomalies, trauma, metabolic disease, and drug toxicity. The cause is idiopathic in one fourth of patients [28]. Imaging may be normal or abnormal. When abnormal, the pattern is typically of diffuse enlargement and inflammation but may be focal and appear mass like. Because congenital anomalies of the pancreatic duct are associated with pancreatitis, ERCP and MRCP (with secretin) are helpful in elucidating ductal anatomy if pancreatitis is recurrent. If pancreatic inflammation is secondary to trauma in a young child, and there is no obvious cause, nonaccidental trauma should be considered.

### Pancreatic Cysts

A cystic structure in the pancreas is secondary to inflammation, as in a pancreatic pseudocyst, rare developmental cysts, or systemic disease. Pancreatic pseudocyst is the most common cystic lesion of the pancreas and accounts for 75% of cystic lesions [29]. These occur typically after pancreatitis or pancreatic trauma.

When multiple cysts are present and there is no history of prior pancreatitis or trauma, cysts may be related to syndromes such as Beckwith-Wiedemann, autosomal-dominant polycystic kidney disease, or Meckel-Gruber syndrome. These diseases are ciliopathies and thus affect multiple organs [30]. Multiple pancreatic cysts may also be secondary to pancreatic cystosis in patients with cystic fibrosis.

### Pancreatic Tumors

The prognosis of a child with a pancreatic tumor is generally better than that of an adult. As with liver tumors, they can be predicted by patient age and elevated hormone levels. Unlike liver masses, which are relatively common, pancreatic tumors are rare and are broadly categorized into epithelial and nonepithelial tumors. Epithelial tumors arise from the pancreatic cells, with the most common examples being pancreatoblastoma and solid pseudopapillary tumor of the pancreas. Nonepithelial tumors are rare among this rare group of pancreatic tumors and include Burkitt's lymphoma, sarcoma, dermoid cyst, lymphangioma, and hemangioendothelioma. The epithelial tumors most common to adults – ductal adenocarcinoma, serous cystadenomas, and mucinous cystic neoplasms – are rare to unreported in children [31, 32].

#### Pancreatoblastoma

The most common tumor in infants and toddlers is pancreatoblastoma. However, this tumor is rare, and <100 have been reported in the literature. Half have been reported in Asians [33]. Children with Beckwith-Wiedemann syndrome have an increased incidence of these pancreatic tumors, though the histology is less aggressive [34]. These tumors are large at presentation and can be so large that their site of origin is often unclear. Most are heterogeneous. Cystic pancreatoblastomas are more characteristic in newborn patients with Beckwith-Wiedemann syndrome [35]. Although they cause mass effect on adjacent structures, they are rarely associated with dilatation of the pancreatic duct. The large masses may invade adjacent organs or metastasize to the liver or abdominal lymph nodes. Rarely, the lung and brain are involved [36]. Such tumors are removed surgically, with common recurrence and thus the need for continued surveillance.

#### Solid Pseudopapillary Tumor

These tumors tend to present in teenage girls and are more common than pancreatoblastoma; however, half the cases occur in adults, and there may be an increased incidence among Asians. This tumor is overall hypovascular and heterogeneous in appearance, with solid and cystic components, hemorrhage, and necrosis. There is a well-defined fibrous capsule that is characteristic and distinguishes it from other tumor types. They are slow growing and benign and best treated by surgical resection. Metastatic disease is rare in children [32].

#### Islet Cell Tumors

Islet cell tumors are distinguished from other pediatric masses of the pancreas by overproduction of peptide hormones, which causes symptoms and can be measured in blood serum. However, some islet cell tumors do not demonstrate such elevation. Unlike in adults, where a variety of islet cell tumors occur, in children, only gastrinomas and insulinomas have been reported. Patients with multiple endocrine neoplasia (MEN) type 1 are at greater risk for having islet cell tumors and present with the tumor at a younger age than patients without MEN type 1. Because these tumors are hormonally active, they are discovered when they are small. Insulinomas tend to be homogeneous, with intense enhancement after contrast administration. Gastrinomas tend to be slightly larger and heterogeneous [32]. Somatostatin receptor scintigraphy is also useful for finding these neuro-

endocrine tumors, with sensitivity depending on tumor type and somatostatin receptor expression. As with other pancreatic tumor types, they are rare and are surgically resected.

### Nesidioblastosis: Persistent Hyperinsulinemic Hypoglycemia of Infancy

Persistent hyperinsulinemic hypoglycemia of infancy is a rare but important cause of severe neonatal hypoglycemia. This abnormality may be diffuse or focal with a mass-like lesion and is caused by a proliferation of beta cells, which cause unregulated release of insulin. Recognition of this entity is important due to the fact that the hypoglycemia is so severe, it leads to severe neurological damage and may be life threatening.

### Nonepithelial Tumors

Of the nonepithelial tumors, non-Hodgkin's lymphoma is the most common [29] and is typically associated with multiple enlarged lymph nodes. As with lymphoma in other organs, the masses appear extremely hypoechoic on US, almost mimicking cysts, due to their homogeneity. Extremely rarely, lymphatic malformations, either macrocystic or microcystic, may occur in the pancreas, as may teratomas.

#### *Key Points*

Pancreatic tumors are rare in children. When a mass is discovered and found not to represent pancreatitis or cyst, pancreatoblastoma should be considered in infants and toddlers and pseudopapillary tumor in older females. Islet cell tumors are distinguished by elevated peptide hormones.

Multiple pancreatic cysts are frequently associated with multiorgan disease (cystic fibrosis and ciliopathies)

## References


1. Barnea-Goraly N, Weinzimer SA, Ruedy KJ et al (2013) High success rates of sedation-free brain MRI scanning in young children using simple subject preparation protocols with and without a commercial mock scanner–the Diabetes Research in Children Network (DirecNet) experience. Pediatr Radiol http://rd.springer.com/article/10.1007/s00247-013-2798-7
2. Zacharias C, Alessio AM, Otto RK et al (2013) Pediatric CT: strategies to lower radiation dose. AJR Am J Roentgenol 200:950-956.
3. Keup CP, Ratnaraj F, Chopra PR et al (2013) Magnetic resonance imaging of the pediatric liver: benign and malignant masses. Magn Reson Imaging Clin N Am 21:645-667.
4. Chung EM, Cube R, Lewis RB et al (2010) From the archives of the AFIP: Pediatric liver masses: radiologic-pathologic correlation part 1. Benign tumors. Radiographics 30:801-826.
5. Kim TK, Choi BI, Han JK et al (2000) Hepatic tumors: contrast agent-enhancement patterns with pulse-inversion harmonic US. Radiology 216:411-417.
6. Kim JE, Lee JY, Bae KS et al (2013) Acoustic radiation force impulse elastography for focal hepatic tumors: usefulness for differentiating hemangiomas from malignant tumors. Korean J Radiol 14:743-753.
7. Seale MK, Catalano OA, Saini S et al (2009) Hepatobiliary-specific MR contrast agents: role in imaging the liver and biliary tree. Radiographics 29:1725-1748.
8. Meyers AB, Towbin AJ, Serai S et al (2011) Characterization of pediatric liver lesions with gadoxetate disodium. Pediatr Radiol 41:1183-1197.
9. (2013) Image Gently Campaign. http://wwwpedradorg/associations/5364/ig/.
10. Blohm ME, Vesterling-Horner D, Calaminus G et al (1998) Alpha 1-fetoprotein (AFP) reference values in infants up to 2 years of age. Pediatr Hematol Oncol 15:135-142.
11. Ricafort R (2011) Tumor markers in infancy and childhood. Pediatr Rev. 32:306-308.
12. Kozakewich HPW (2001) The pathology of rapidly involuting congenital hemangioma (RICH) and non-involuting congenital hemangioma (NICH). Vascular Anomalies, New York, NY, USA.
13. Chung EM, Lattin GE, Jr., Cube R et al (2011) From the archives of the AFIP: Pediatric liver masses: radiologic-pathologic correlation. Part 2. Malignant tumors. Radiographics 31:483-507.
14. Stocker JT (2001) Hepatic tumors in children. Clinics in liver disease 5:259-281, viii-ix.
15. Dubois J, Lowe LH (2013) Neoplasia. In: Coley B (Ed) Caffey's Pediatric Diagnostic Imaging. Elsevier, Philadelphia, PA.
16. Spector LG, Puumala SE, Carozza SE et al (2009) Cancer risk among children with very low birth weights. Pediatrics 124:96-104.
17. Meyers AB, Towbin AJ, Geller JI et al (2012) Hepatoblastoma imaging with gadoxetate disodium-enhanced MRI—typical, atypical, pre- and post-treatment evaluation. Pediatr Radiol 42:859-866.
18. Towbin AJ, Luo GG, Yin H et al (2011) Focal nodular hyperplasia in children, adolescents, and young adults. Pediatr Radiol 41:341-349.
19. Ishak K, Goodman ZD, Stocker JT (2001) Benign hepatocellular tumors. In: Rosai J, Sobin L (Eds) Atlas of Tumor Pathology. Armed Forces Institute of Pathology, Wahington, DC.
20. Paulson EK, McClellan JS, Washington K et al (1994) Hepatic adenoma: MR characteristics and correlation with pathologic findings. AJR Am J Roentgenol 163:113-116.
21. Buetow PC, Buck JL, Pantongrag-Brown L et al (1997) Undifferentiated (embryonal) sarcoma of the liver: pathologic basis of imaging findings in 28 cases. Radiology 203:779-783.
22. Gupta RT, Brady CM, Lotz J et al (2010) Dynamic MR imaging of the biliary system using hepatocyte-specific contrast agents. AJR Am J Roentgenol 195:405-413.
23. Todani T, Watanabe Y, Narusue M et al (1977) Congenital bile duct cysts: classification, operative procedures, and review of thirty-seven cases including cancer arising from choledochal cyst. Am J Surg 134:263-269.
24. Gubernick JA, Rosenberg HK, Ilaslan H et al (2000) US approach to jaundice in infants and children. Radiographics 20:173-195.
25. Siegel MJ, Martin KW, Worthington JL (1987) Normal and abnormal pancreas in children: US studies. Radiology 165:15-18.
26. Khanna PC, Pruthi S (2013) The Pancreas. In: Caffey (Ed) Pediatric diagnostic imaging. Elsevier, Philadelphia, PA.
27. Tirkes T, Sandrasegaran K, Sanyal R et al (2013) Secretin-enhanced MR cholangiopancreatography: spectrum of findings. Radiographics 33:1889-1906.
28. Weizman Z, Durie PR (1988) Acute pancreatitis in childhood. J Pediatr 113:24-29.
29. Vaughn DD, Jabra AA, Fishman EK (1998) Pancreatic disease in children and young adults: evaluation with CT. Radiographics 18:1171-1187.
30. Hildebrandt F, Benzing T, Katsanis N (2011) Ciliopathies. New Engl J Med 364:1533-1543.

31. Vane DW, Grosfeld JL, West KW et al (1989) Pancreatic disorders in infancy and childhood: experience with 92 cases. J Pediatr Surg 24:771-776.
32. Chung EM, Travis MD, Conran RM (2006) Pancreatic tumors in children: radiologic-pathologic correlation. Radiographics 26:1211-1238.
33. Roebuck DJ, Yuen MK, Wong YC et al (2001) Imaging features of pancreatoblastoma. Pediatr Radiol 31:501-506.
34. Muguerza R, Rodriguez A, Formigo E et al (2005) Pancreatoblastoma associated with incomplete Beckwith-Wiedemann syndrome: case report and review of the literature. J Pediatr Surg 40:1341-1344.
35. Babyn P, Williams T (2000) The pancreas. In: Stringer D, Babyn P (Eds) Pediatric gastrointestinal imaging and intervention. Decker, Ontario, Canada.
36. Montemarano H, Lonergan GJ, Bulas DI et al (2000) Pancreatoblastoma: imaging findings in 10 patients and review of the literature. Radiology 214:476-482.

# An Approach to Imaging the Acute Abdomen in Pediatrics

Alan Daneman

University of Toronto, and Department of Diagnostic Imaging, The Hospital for Sick Children, Toronto, Ontario, Canada

## Introduction

The acute abdomen is a common and often extremely challenging emergency in pediatrics. This chapter outlines an approach to imaging evaluation and management of children with acute abdominal pain and focuses attention on the more common causes of abdominal pain that may require surgery.

## Causes of Acute Abdomen

A wide spectrum of pathology may give rise to acute abdominal pain in children. These include congenital and acquired lesions that may present in the immediate neonatal period or in older infants and children. The acute abdomen is not an uncommon event in neonatal intensive care units and may be the result of several causes, the three most significant being congenital bowel obstruction, complications of anomalies of midgut rotation and fixation, and necrotizing enterocolitis. In older infants and children, the common causes of acute abdominal pain that may require surgery include acute appendicitis, complications of anomalies of midgut rotation and fixation, intussusception, and Meckel diverticulum. Inflammatory bowel diseases may also present with acute abdominal symptomatology. Although these common causes of acute abdominal pain are due to lesions involving the gastrointestinal tract (GI), there are many causes of acute abdomen due to abnormalities of other viscera, e.g., gynecological abnormalities such as ovarian torsion (Fig. 1), omental lesions such as omental infarcts (Fig. 2), obstructions of the biliary and urinary tracts due to stones, and inflammatory processes such as pancreatitis or cholecystitis. Abdominal pain may also be due to referred pain from extra-abdominal pathology such as pneumonia or pleural effusion (Fig. 3). Medical diseases such as sickle cell disease, Henoch-Schönlein purpura, and hemolytic uremic syndrome (HUS) may also cause significant acute abdominal pain. Imaging of the child with acute abdominal pain should include a search for evidence of these other pathologies.

Abdominal trauma may also be the cause of an acute abdomen. Occasionally, mild abdominal trauma may cause abdominal pain out of proportion to the degree of trauma, and imaging in these children may reveal an underlying abnormality (such as a neoplasm) or an anomaly (such as ureteropelvic obstruction). Furthermore, one

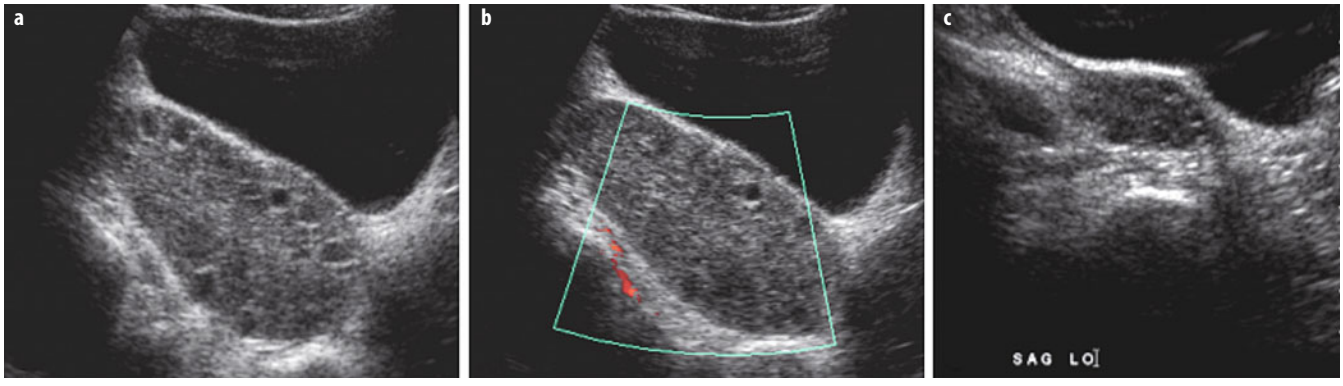


**Fig. 1 a-c.** Teenage girl who presented with right lower quadrant pain. **a, b** Sagittal ultrasound (US) views of right lower quadrant show markedly enlarged right ovary with peripheral follicles and no internal flow, consistent with right ovarian torsion. **c** Comparison sagittal US view of left lower quadrant shows normal sized left ovary

*Diseases of the Abdomen and Pelvis 2014-2017*,
DOI: 10.1007/978-88-470-5659-6_37 

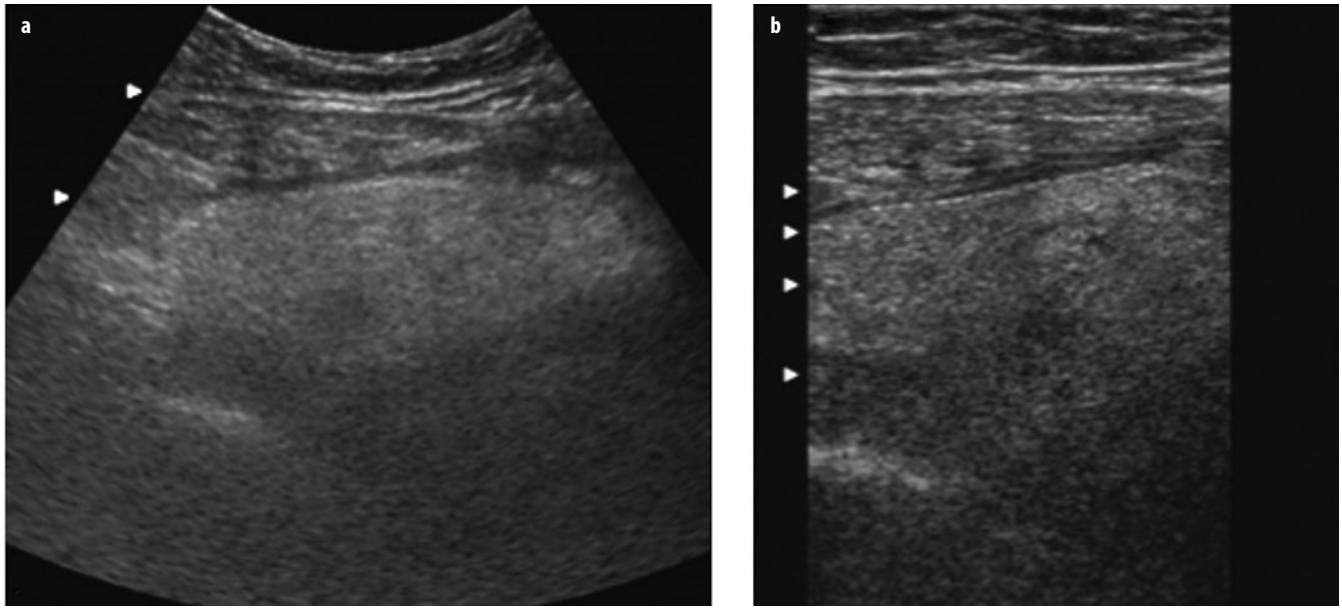


**Fig. 2 a, b.** Ultrasound (US) images of the right lower quadrant in an 11–year-old girl with right lower quadrant pain show an ill-defined, hyperechoic mass consistent with an omental infarct

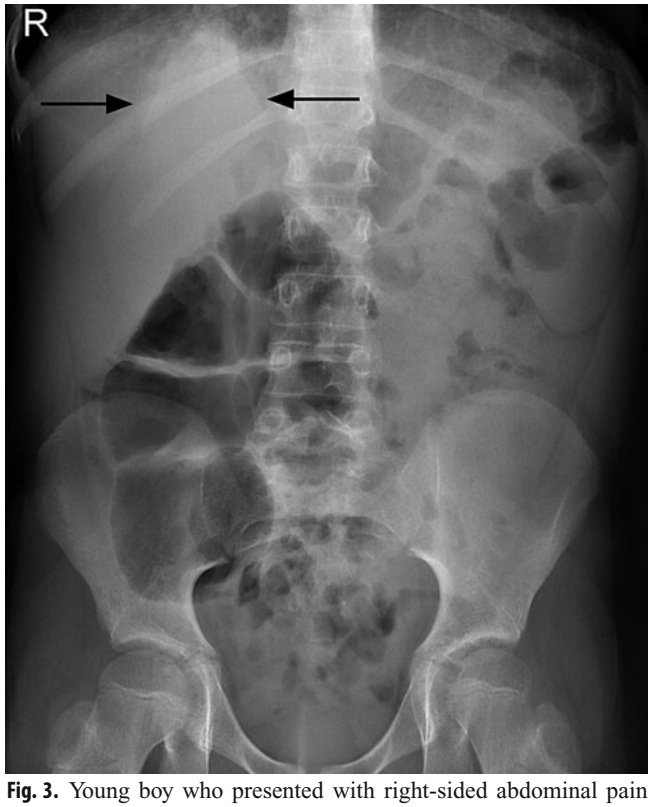


**Fig. 3.** Young boy who presented with right-sided abdominal pain and fever. The supine abdominal radiograph shows a triangular area of density at the right lung base (*arrows*), consistent with right lower-lobe pneumonia, the cause of referred pain into the abdomen

should consider nonaccidental injury or abuse when certain traumatic lesions are found, especially when in combination with presentations such as hematoma of the left lobe of the liver, duodenum, and pancreatitis.

## Imaging Modalities

### Sonography

Ultrasound (US) plays an ever-increasing role in managing children with acute abdominal pain and has replaced the plain abdominal radiograph as the modality of initial choice in many clinical situations. The major advantages of US are that it does not use ionizing radiation, is relatively inexpensive, and the abdominal viscera, including the bowel, can be well delineated in children. Therefore, many pathological entities can be easily confirmed or excluded on US.

### Plain Abdominal Radiograph

Abdominal radiography (AXR) remains a standard method for evaluating the acute abdomen in some clinical situations. It is essential when peritonitis is present and perforation is suspected.

All neonates with an acute abdomen are evaluated with AXR. This modality is essential for evaluating conditions such as necrotizing enterocolitis and congenital bowel obstruction. In the former, the AXR may be diagnostic; in the latter, findings may guide the choice of subsequent (if necessary) contrast examinations of the GI. Radiographic views with a horizontal beam are essential to exclude the presence of free air due to bowel perforation and can be performed with the neonate in the dorsal decubitus (lateral shoot-through view) or left lateral decubitus position.

In older children, the diagnosis of intestinal obstruction can often be made on the supine film alone. A search for air-fluid levels on the upright view does not always add extra information, and a search for free air in the abdomen is often more easily achieved with a lower radiation dose


**Fig. 4 a-c.** An 8-year-old boy with right lower quadrant pain. Ultrasound (US) images show **a** longitudinal and **b** transverse views of the enlarged appendix, which measured almost 1 cm in diameter. The surrounding tissue is ill defined and increased in echogenicity due to adjacent edema and inflammation. **c** The surrounding tissue is also hyperemic. Findings at operation were due to acute appendicitis

in a single, upright view of the chest, which will also serve to exclude lung pathology.

However, in both the neonate and older child, the AXR findings are often nonspecific, which limits the role of this modality.

### Contrast Examinations of the Gastrointestinal Tract

This imaging modality remains important in certain conditions. For example, in congenital low-bowel obstruction, the contrast enema is important in some neonates to establish a diagnosis; in others, it is also useful for therapy (e.g., meconium ileus or meconium plug syndrome). Contrast evaluating the upper GI may also be required to confirm or exclude anomalies of midgut rotation in symptomatic children in whom US is not conclusive (see below).

### Computed Tomography

Computed tomography (CT) may be reserved for the more complicated imaging situations when US may not provide all necessary information, e.g., appendicitis when gas obscures the right lower quadrant or in older, obese children; and children with abscesses. CT without contrast injection is also extremely helpful in delineating urinary stones when these are not well shown by US.

### Magnetic Resonance Imaging

Magnetic resonance imaging (MR**)** has a more limited role in children with acute abdominal pain. However, it can depict the anatomy exceptionally well in certain conditions in which it may be used to complement findings on US. These situations include biliary- and pancreatic-duct anomalies and gynecological disorders such as complex anomalies associated with hydrocolpos.

## Acute Appendicitis

Acute appendicitis is a common clinical entity in pediatrics. In many patients, it is easy to make the diagnosis clinically with certainty, and no imaging is required prior to appendicectomy. However, imaging of the abdomen is now commonly used in children with right lower quadrant pain, even when the clinical diagnosis may be clearcut; however, it is more important in children with nonspecific clinical features.

US is the modality of choice in evaluating children suspected of having acute appendicitis. CT should be reserved for patients in whom US examination is inconclusive or when abscesses are present, in order to better define the extent of the abscesses prior to drainage by the interventional radiology team.

The diagnosis of appendicitis is made on US when the diameter of the appendix is $>$6 mm and the appendix is noncompressible (Fig. 4). This should not be considered an absolute measurement, and other features should be considered, including edema of the mesentery, hyperemia of the wall of the appendix on color- or power-Doppler examination, presence of an appendicolith, and local fluid collections or abscess formation.

Other conditions may cause the appendix to become thick walled and dilated, and these include cystic fibrosis, Henoch-Schönlein purpura, and inflammatory bowel diseases (IBD).

## Anomalies of Midgut Rotation and Fixation (Malrotation)

The radiologist plays an exceptionally important role in diagnosing this condition, which can potentially lead to bowel necrosis that may require extensive bowel resection and even lead to death. During development, the midgut undergoes a process of growth and lengthening that involves:

- Herniation of the midgut into the umbilical cord along the axis of the superior mesenteric artery (SMA)
- Rotation of 270° in a counterclockwise direction
- Reduction of the midgut into the abdomen by 12 weeks' gestation
- Fixation of parts of the midgut by peritoneum.

The normal process of rotation and fixation is essential for the midgut to assume its normal mature position in the abdomen. However, abnormalities due to the arrest of rotation and/or fixation may occur at any phase of the process and may involve only part or all of the midgut. This may, therefore, lead to a number of variations of malrotation and/or malfixation. The vast majority of these variations are associated with clinical symptoms that usually present within the first few months of life and can be life threatening. Others may be associated with few or no symptoms, and the latter may only be found incidentally.

Malrotation usually leads to obstruction of the duodenum by: (1) peritoneal [Ladd] bands that anchor the cecum to the retroperitoneum across the duodenum in the right upper quadrant; (2) midgut volvulus due to the narrowed base of the mesentery; (3) internal hernia (much less commonly).

The clinical picture and imaging appearances depend upon the nature and degree of obstruction as well as the presence or absence of vascular compromise.

### Plain Abdominal Radiograph

In typical cases, there is gaseous distention of the duodenum, but often, appearances may be nonspecific or even normal. One should, therefore, never rely on the plain film findings to rule out malrotation. In some patients, the duodenum may be fluid filled and not visible, and only the stomach is distended with air, simulating a complete or partial gastric outlet obstruction. In children with severe vascular compromise due to volvulus, the entire small bowel may be dilated (with air-fluid levels), resembling a low-bowel obstruction or ileus, but vascular compromise may also produce a gasless abdomen. A volvulus with fluid-filled bowel may also appear as a soft tissue abdominal mass.

Because of the wide variation of appearances on plain radiographs with midgut malrotation, the clinician should never rely on plain radiographs to rule out this entity. Therefore, any child in whom there is a clinical suspicion of malrotation should be examined with modalities that will directly depict the position of the bowel and/or nature of the obstruction. Abdominal US and contrast examination of the upper GI tract are the most valuable modalities in this regard.

### Abdominal Sonography

Over the past decade, several sonographic findings have been described in malrotation and include:

- Fluid distention of the duodenum
- Inversion of the SMA and vein relationship; this can be seen in a small proportion of asymptomatic, normal individuals
- Whirlpool sign seen with midgut volvulus
- Ascites may rarely be present in neonates with chronic volvulus.

Yousefzadeh drew attention to US depiction of the third part of the duodenum (D3), in the angle between the aorta and SMA, and suggested that documentation of the presence of D3 in this normal position excludes the presence of malrotation. Further data regarding this is required.

### Contrast Examinations of the GI Tract

There was much debate about whether the upper GI series or the contrast enema is the most effective imaging modality to diagnose malrotation. Most institutions now rely more heavily upon the upper GI series, but if in doubt, it is prudent to do both. On the upper GI series, the duodenojejunal flexure is absent and the proximal small bowel typically lies in the midline (Fig. 5). Much less commonly, an internal hernia may be delineated (Fig. 6). On contrast enema, the cecum is usually in the right upper quadrant and the ascending colon and hepatic flexure are not correctly positioned. The major difficulty in making or excluding the diagnosis of malrotation is the variation in position that those structures may assume normally or with malrotation. It is beyond the scope of this chapter to describe them all. Meticulous technique is critical to either type of study in order to delineate these structures accurately. The use of too much or too little contrast material may render the study undiagnostic.

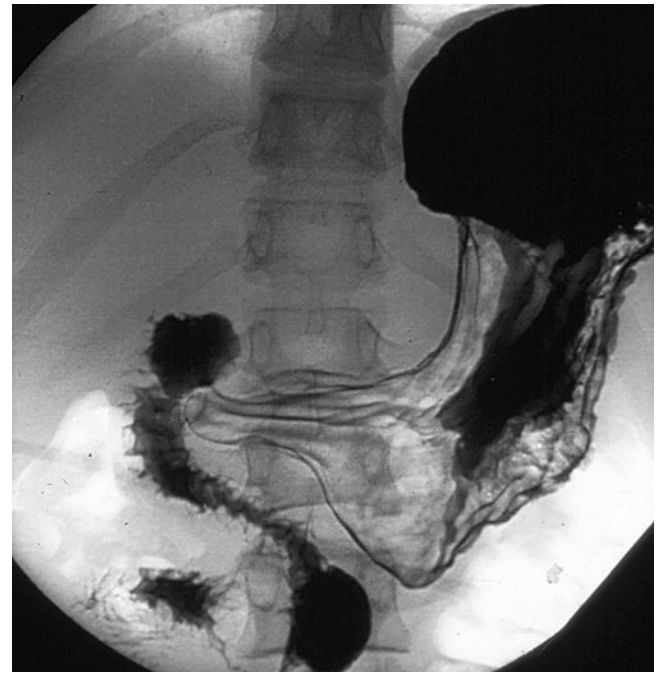

**Fig. 5.** A 16-year-old boy who presented with acute abdominal pain and bilious vomiting. Upper gastrointestinal series shows a normal stomach and proximal duodenum. However, the third part of the duodenum does not cross the midline normally to the left and, instead, courses inferiorly anterior to the spine and then to the right. Findings are typical of midgut malrotation, which was proven at surgery. There is no evidence of volvulus


**Fig. 6 a, b.** Upper gastrointestinal series in a teenage boy who presented with a history of chronic intermittent abdominal pain, occasionally accompanied by vomiting. **a** Duodenum and proximal small bowel are almost entirely to the right of the spine, consistent with midgut malrotation. **b** In a delayed image, the small bowel is filled with contrast and has a very rounded and well-defined shape, consistent with a paraduodenal internal hernia proven at surgery

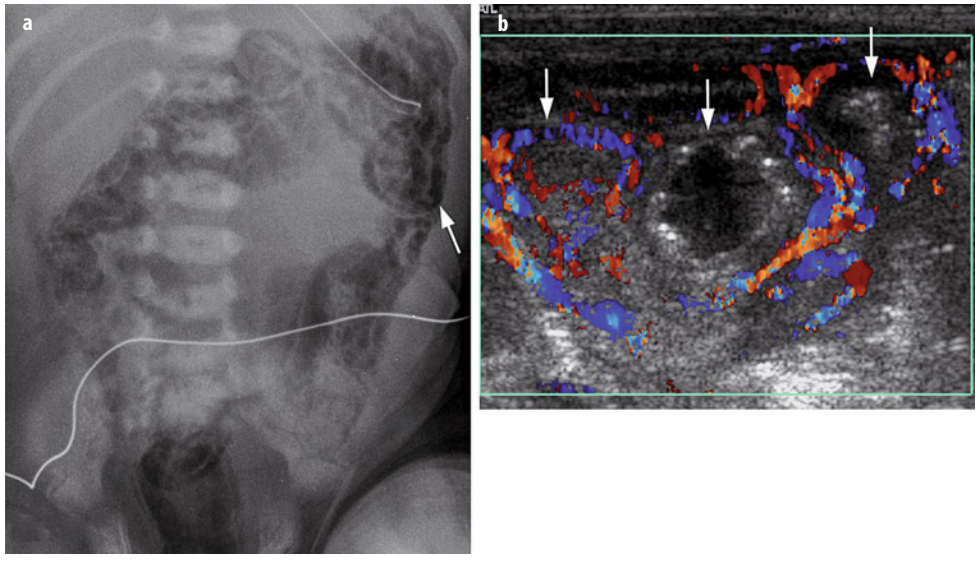


**Fig. 7 a, b.** **a** Plain radiograph in a 7-day-old neonate with necrotizing enterocolitis (NEC) shows a marked amount of intramural gas throughout the distribution of the large bowel and rectum. Intramural gas is very easily seen in the region of the descending colon (*arrow*). **b** Color-Doppler ultrasound (US) image in a 10-day-old neonate with NEC shows three loops of bowel (*arrows*). The two outer loops are well perfused and indeed are hyperemic, indicating viability. The central loop is distended with fluid and has some hyperechoic foci in the wall, consistent with intramural gas; this loop has no flow and was proven to be necrotic at surgery

## Necrotizing Enterocolitis

Necrotizing enterocolitis (NEC) usually presents in infants in the neonatal intensive care unit – more commonly in premature neonates. The classic presentation includes abdominal distention and blood in the stool. The radiologist plays an important role at the time of diagnosis of this condition, during follow-up, and in detecting later complications such as strictures.

### Abdominal Radiography

At the time of diagnosis, three abnormalities may be present on AXR: bowel dilatation, intramural gas, and portal venous gas (Fig. 7).

#### Bowel Dilatation

This abnormality is present in almost 100% of patients with NEC, and the degree of distention usually correlates well with clinical severity. Follow-up AXR may show asymmetric dilatation and fixed loops in infants whose condition deteriorates.

#### Intramural Gas

Intramural gas is not present in 100% of patients and the amount of intramural gas does not always correlate well with the degree of clinical severity.

### Portal Venous Gas

This finding is usually present in those with severe NEC. Disappearance of intramural and portal venous gas does not always correlate with clinical improvement, as the gas will eventually disappear even in children who deteriorate clinically

### Ultrasound

US is an extremely useful modality for investigating patients with NEC, as it can provide information regarding the presence of intraperitoneal fluid, bowel-wall thickness, and bowel perfusion (using color- or power-Doppler sonography) (Fig. 7).

US is much more accurate than AXR in documenting the presence of free and focal intraperitoneal fluid and can also define the character of this fluid. It is well known that following perforation, not all patients with NEC will demonstrate free intraperitoneal gas on AXR and may only present with the presence of free fluid.

In the early phases of NEC, the bowel wall will be quite thickened, but in patients who are more severely affected, bowel mucosa and submucosa slough into the bowel lumen, leaving a markedly thinned bowel wall. This is much more prone to perforation, and thinning of the bowel wall can be documented with sonography. The bowel (particularly the thickened bowel) becomes markedly hyperemic, indicating the presence of viable bowel. However, absence of bowel perfusion in single or multiple bowel loops (particularly when the bowel wall is thinned) indicates the presence of necrosis and may warrant surgical intervention, even if there is no free intraperitoneal gas present on the plain radiograph.

US, however, plays a more important role in the follow-up of patients with NEC who are not responding to medical management and those who deteriorate clinically. In these patients, US may provide information that cannot be depicted with AXR.

## Meckel Diverticulum

Meckel diverticulum most commonly presents as painless rectal bleeding due to ulceration because of the presence of ectopic gastric mucosa. These patients are usually adequately diagnosed and managed following a radionuclide scan.

In $<50\%$ of children presenting with Meckel diverticulum, clinical findings will be more complex, with a combination of abdominal pain, vomiting, and occasionally rectal bleeding. In children with acute pain, the diagnosis is often difficult and nonspecific. US can be used successfully to document the presence of an inflamed or hemorrhagic Meckel diverticulum. In this situation, the Meckel diverticulum has a variable appearance and may simulate the presence of an inflamed duplication cyst (Fig. 8), appendicitis, and sometimes a small intussusception. When one finds this somewhat atypical appearance on US, one should consider the diagnosis of a complicated Meckel diverticulum rather than the other pathologies it simulates. Meckel diverticulum is also the most common cause of a pathologic lead point of an intussusception in children.

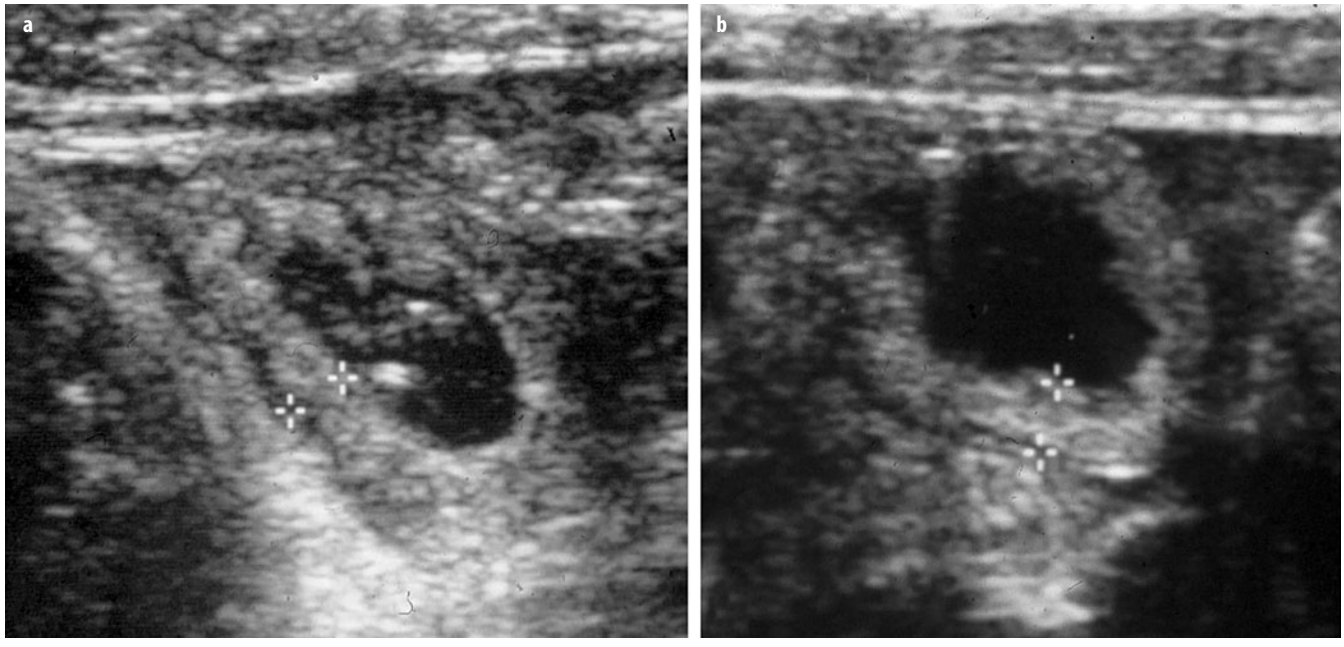


**Fig. 8 a, b.** Ultrasound (US) images of the lower abdomen in two young children with complicated Meckel's diverticulum. The *electronic cursors* delineate the thickened inflamed wall of the diverticulum in both images. **a** Diverticulum has a somewhat teardrop shape; **b** it appears more rounded, simulating a duplication cyst, although it is more irregular in outline

## Intussusception

Intussusception is one of the commoner causes of acute abdomen in children between 6 months and 5 years of age. The vast majority arise in the ileum and are either ileocolic or ileoileocolic. It is thought to occur due to hyperplasia of the lymphoid tissue in the ileum, possibly as a result of a viral infection. Other types of intussusceptions may relate to pathological lead points or gastrojejunostomy tubes, or those seen in the postoperative period. Another type is the benign small-bowel intussusception. This is often an incidental finding and does not present as an acute abdominal emergency.

Children presenting with ileocolic or ileoileocolic intussusceptions commonly do not present with the classic clinical triad of abdominal pain, red-currant-jelly stool, and palpable abdominal mass. Instead, presentation may be nonspecific. For this reason, the clinician must often rely on imaging procedures to diagnose or exclude intussusception.

### Ultrasound

According to many series, US is 100% accurate in depicting the presence or absence of the common types of ileocolic or ileoileocolic intussusceptions in children. These lesions have a characteristic sonographic appearance and are usually found just under the abdominal wall, most commonly on the right side of the abdomen (Figs. 9 and 10). As it is a noninvasive procedure, and because of its accuracy, sonography is the modality of choice for evaluating patients suspected of having an intussusception. The sonographic appearance of intussusception was excellently reviewed in the 1996 article by del-Pozo et al. (see "Suggested Reading").

### Plain Abdominal Radiographs

Plain AXR are required only in instances in which there is a clinical consideration of peritonitis. In this clinical setting, AXR is essential to exclude perforation, which is the major contraindication for attempted enema reduction.

According to the many series in the recent literature, the reduction rate of intussusception ranges from 80% to as high as 95%. These series used either fluoroscopic or sonographic guidance for reducing intussusceptions and either hydrostatic (barium, water-soluble, saline contrast) or pneumatic reduction. The fact that different techniques have been used with similar success rates suggests that technique is not important. Nonoperative reduction of an intussusception should only be attempted after the surgical team has evaluated the patient and the patient is clinically stable, well-hydrated, has no evidence of peritonitis, and has an intravenous line in place. The major contraindications to administering the enema are the clinical findings of peritonitis or shock or signs of perforation on an abdominal radiograph.

To improve the reduction rate, delayed, repeated reduction attempts can be used as long as the intussusceptions move in response to the initial attempted reduction and the child becomes asymptomatic and maintains stable vital signs. This approach is safe and effective, with a good success rate. We use this approach in approximately 15% of patients with intussusceptions, achieving successful reduction in 50% of intussusceptions not reduced on the first attempt. There does not appear to be a fixed optimal timing between attempts, and second or third attempts can be made several hours after the first.

Pathological lead points are found in about 5-7% of all intussusceptions. The most common are Meckel divertic-

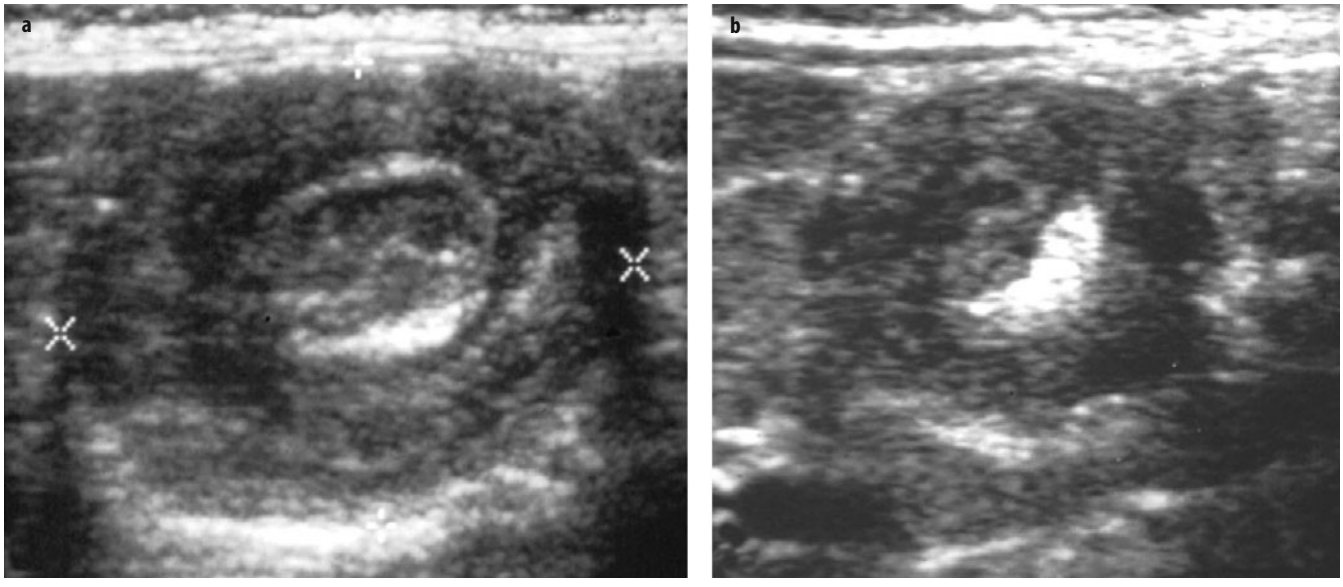


**Fig. 9 a, b.** Ultrasound (US) images of ileocolic intussusceptions in two children. In both, intussusceptions are seen in the transverse view and have a target appearance. The specific finding that characterizes this target appearance as an intussusception is the curvilinear hyperechoic mesenteric fat seen in both cases between the layers of the intussusceptum

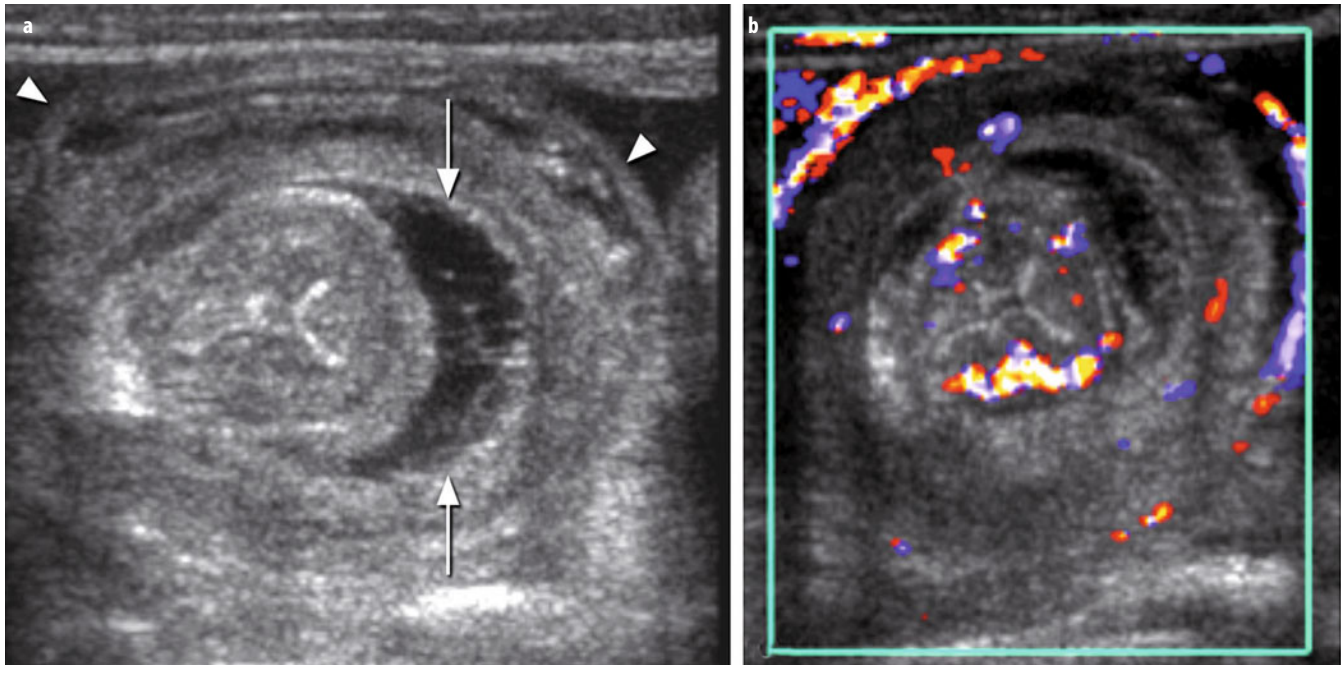


**Fig. 10 a, b.** **a** Grey-scale and **b** Doppler views of an ileocolic intussuscepiens seen in transverse view. **a** *Arrows* indicate a moderate amount of fluid between the layers of the intussusceptum; the amount of hyperechoic mesenteric fat is less than in Fig. 9. *Arrowheads* indicate the markedly thinned intussusceptions along the periphery, which is also separated from the intussusceptum by some fluid. **b** Doppler examination reveals very good flow to the intussusception, which was easily reduced by air enema

ulum, polyps, Henoch-Schönlein purpura, and cystic fibrosis. Less common causes are lymphoma, duplication cyst, and various inflammatory lesions of the bowel. Managing such patients remains a challenge.

Contrast or air enema techniques are not always diagnostic in documenting the presence of a pathological lead point. Sonography is extremely useful in this regard, as it may depict two thirds of pathological lead points, providing a specific diagnosis in one third of these cases.

However, it remains a diagnostic challenge as to how to search for pathological lead points in patients in whom there is a high index of suspicion for such a lesion and in whom the sonogram is negative. In such cases, the choice of which other imaging modalities to use will depend on the clinical situation in each particular patient. We recommend attempted enema reduction in all patients with a lead point if there is no contraindication to nonoperative reduction.

Intussusception may occur as a complication in $<1\%$ of laparotomies. These are usually more difficult to diagnose on sonography than the usual ileocolic intussusceptions, as they are small-bowel intussusceptions, which are often surrounded by large, dilated loops of obstructed bowel. They frequently require surgical reduction. Intussusceptions may complicate the presence of a gastrojejunostomy (GJ) tube. Most patients presenting with this complication are usually clinically stable and do not require urgent reduction of the intussusception. The majority can be managed by replacing the tube with a standard or a shortened GJ tube or with a gastrostomy tube. However, manipulation of the GJ tube and flushing with air or saline may also be helpful. Surgery is rarely required for reduction.

## Congenital Bowel Obstruction in the Neonate

Obstruction due to congenital lesions may occur at all levels of the GI tract and are, from a practical point of view, usefully divided into those termed “high” or “low” lesions. The high obstructions denote lesions of the esophagus, stomach, duodenum, and upper small bowel. The low obstructions include lesions of the lower small bowel, large bowel, and anorectal malformations (Fig. 11). The distribution of dilated bowel loops on plain radiographs usually enables differentiating high from low obstruction relatively easily (Fig. 11). This is done by evaluating the number of visible gas-filled loops. Fluid-filled loops may be difficult to visualize on plain radiographs and may masquerade as free fluid or masses; thus, they occasionally might confuse the picture. It should be emphasized that the differentiation of dilated gas-filled small- from large-bowel loops may be impossible in neonates. Free air is not usually evident in these patients unless the diagnosis is delayed. Intramural air (and even portal venous gas) may be seen proximal to a high-grade obstruction, but it is much more commonly seen in NEC. Calcification may be present in the peritoneum (meconium peritonitis) due to prenatal perforation, in the wall of the bowel proximal to an atresia, or in the bowel content

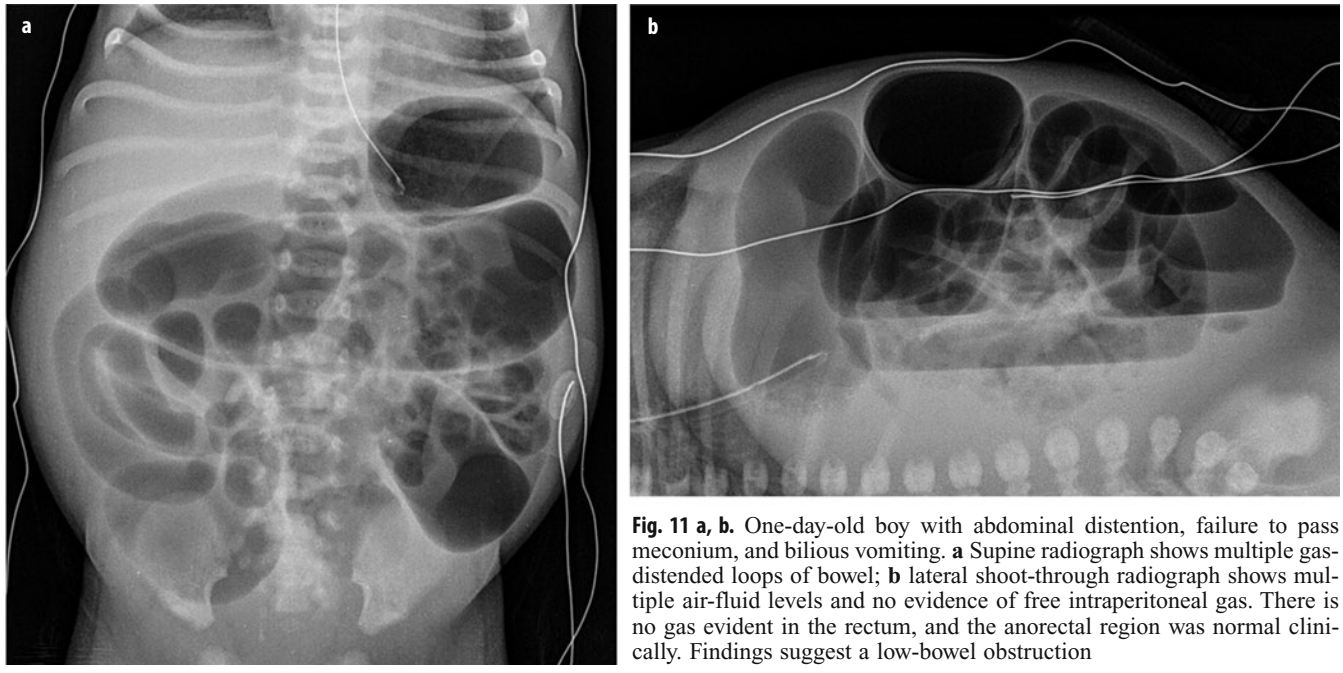


**Fig. 11 a, b.** One-day-old boy with abdominal distention, failure to pass meconium, and bilious vomiting. **a** Supine radiograph shows multiple gas-distended loops of bowel; **b** lateral shoot-through radiograph shows multiple air-fluid levels and no evidence of free intraperitoneal gas. There is no gas evident in the rectum, and the anorectal region was normal clinically. Findings suggest a low-bowel obstruction

within the lumen occasionally proximal to low obstruction.

### High Obstruction

Most complete high obstructions are easily diagnosed on plain radiographs. If the diagnosis is in doubt, air can be injected slowly via a feeding tube into the lumen of the GI tract to confirm or exclude an obstruction. In incomplete obstructions (e.g., malrotation and stenoses), positive water-soluble contrast agents are required to confirm the level and nature of obstruction.

### Low Obstruction

Low obstructions include ileal and colonic atresias meconium ileus, functional immaturity of the large bowel, Hirschsprung's disease, and anorectal malformations. Although there are some features on plain radiographs that might suggest each of the above conditions, the radiographic findings in all of the above may often be nonspecific. Differentiation of these conditions, therefore, will depend upon other factors, such as information from the clinical history and physical examination. Invariably, these conditions require the use of a water-soluble contrast enema to define the distal colon and ileum to increase one's confidence of diagnosis. The contrast enema may also prove therapeutic in patients with (1) meconium ileus, in which plugs of meconium are present in the distal ileum (most commonly in neonates with cystic fibrosis) or (2) meconium plug syndrome, in which the meconium plugs are in the large bowel in patients with functional immaturity of the large bowel, which often may give rise to a small left colon, mainly seen in premature infants or infants of diabetic mothers.

## Suggested Reading

Baldisserotto M, Marchiori E (2000) Accuracy of noncompressive sonography of children with appendicitis according to the potential positions of the appendix. AJR Am J Roentgenol 175:1387-1392.

Buonomo C (1999) The radiology of necrotizing enterocolitis. RCNA 37:1187-1198.

Daneman A (2009) Malrotation: the balance of evidence. Pediatr Radiol 39:S164-S166.

Daneman A, Lobo E, Alton DJ, Shuckett B (1998) The value of sonography, CT and air enema for detection of complicated Meckel diverticulum in children with nonspecific clinical presentation. Pediatr Radiol 28:928-932.

Daneman A, Myers M, Shuckett B, Alton DJ (1997) Sonographic appearances of inverted Meckel diverticulum with intussusception. Pediatr Radiol 27:295-298.

Daneman A, Alton DJ, Lobo E et al (1998) Patterns of recurrence of intussusception in children: a 17 year review. Pediatr Radiol 28:913-919.

Daneman A, Navarro O (2003) Intussusception Part 1: a review of diagnostic approaches. Pediatr Radiol 33:79-85.

Daneman A, Navarro O (2004) Intussusception Part 2: an update on the evolution of management. Pediatr Radiol 34:97-108.

del-Pozo G, Abillos JC, Tejedor D (1996) Intussusception: US findings with pathologic correlation – the crescent-in-doughnut sign. Radiology 199:688-692.

del-Pozo G, Albillos JC, Tejedor D et al (1999) Intussusception in children: current concepts in diagnosis and enema reduction. Radiographics 19:299-319.

Donnolly LF, Rencken IO, deLorimier AA, Gooding CA (1996) Left paraduodenal hernia leading to ileal obstruction. Pediatr Radiol 26:534-536.

Epelman M, Daneman A, Navarro OM et al (2007) Necrotizing enterocolitis: review of state-of-the-art imaging findings with pathologic correlation. Radiographics 27:285-305.

Faingold R, Daneman A, Tomlinson C et al (2005) Bowel viability assessment by colour doppler sonography in necrotizing enterocolitis. Radiology 235:587-594.

Kim G, Daneman A, Alton DJ et al (1997) The appearance of inverted Meckel diverticulum with intussusception on air enema. Pediatr Radiol 27:647-650.

Kornecki A, Daneman A, Navarro O et al (2000) Spontaneous reduction of intussusception: clinical spectrum, management and outcome. Pediatr Radiol 30:58-63.
Levy AD, Hobbs CM (2004) From the Archives of the AFIP. Meckel Diverticulum: radiologic features with pathologic correlation. Radiographics 24:565-587.
Long FR, Kramer SS, Markowitz RI et al (1996) Intestinal malrotation in children: tutorial on radiographic diagnosis in difficult cases. Radiology 198:775-780.
Long FR, Kramer SS, Markowitz RI, Taylor GE (1996) Radiographic patterns of intestinal malrotation in children. Radiographics 16:547-556
Navarro OM, Daneman A, Chae A (2004) Intussusception: the use of delayed, repeated reduction attempts and the management of intussusceptions due to pathologic lead points in pediatric patients. AJR Am J Roentgenol 182:1169-1176.
Navarro O, Daneman A (2004) Intussusception. Part 3: diagnosis and management of those with an identifiable or predisposing cause and those that reduce spontaneously. Pediatr Radiol 34:305-312.
Puylaert JB (1986) Acute appendicitis: US evaluation using graded compression. Radiology 158:355-360.
Rohrschneider WK, Troger J (1995) Hydrostatic reduction of intussusceptions under US guidance. Pediatr Radiol 25:530-534.
Sargent MA, Babyn P, Alton DJ (1994) Plain abdominal radiography in suspected intussusception: a reassessment. Pediatr Radiol 24:17-20.
Silva CT, Daneman A, Navarro OM et al (2007) Correlation of sonographic findings and outcome in necrotizing enterocolitis. Pediatr Radiol 37:274-282.
Sivit CJ (2004) Imaging the child with right lower quadrant pain and suspected appendicitis: current concepts. Pediatr Radiol 34:447-453.
Strouse PJ (2000) Disorders of intestinal rotation and fixation ("malrotation"). Pediatr Radiol 34:837-851.
Taylor GA (2004) Suspected appendicitis in children: in search of the Single Best Diagnostic Test. Radiology 231:293-295.
Todani T, Sato Y, Watanabe Y et al (1990) Air reduction for intussusceptions in infancy and childhood: Ultrasonographic diagnosis and management without X-ray exposure. Z Kinderchir 45:222-226.
Verschelden P, Filiatraut D, Garel L et al (1992) Intussusception in children: reliability of US in diagnosis – a prospective study. Radiology 184:741-744.
Yousefzadeh DK (2009) The position of the duodenojejunal junction; the wrong horse to back on in diagnosing or excluding malrotation. Pediatr Radiol 39:S172-S177.

# Tumor and Tumor-Like Lesions of the Pediatric Retroperitoneum

Simon G.F. Robben, Marjolein Dremmen

Department of Radiology, Maastricht University Medical Centre, Maastricht, The Netherlands

## Introduction

The retroperitoneal space literally means the (potential) space behind the parietal peritoneum of the abdominal cavity. It has no distinct borders; also, structures that lie between the parietal peritoneum and abdominal wall can be classified as retroperitoneal, at the ventral side sometimes referred to as properitoneal. It extends from the pelvic brim to the diaphragm. Embryologically, some organs have a retroperitoneal origin: adrenal glands, kidneys, ureters, bladder, aorta, inferior caval vein, and part of the rectum (primary retroperitoneal). Some organs were originally suspended in the abdominal cavity by a mesentery but migrated into a retroperitoneal position: head and body of the pancreas, duodenum, ascending and descending colon (secondary retroperitoneal) (Table 1).

The anatomy of the retroperitoneum can be further divided by means of the renal fascia into the perirenal space (between anterior and posterior leaf of the renal fascia), which contains adrenal glands, kidneys, and renal vessels; the anterior renal space (between peritoneum and anterior leaf of the renal fascia) containing pancreas, colon, and duodenum; the posterior renal space (between posterior leaf of renal fascia and fascia transversalis) containing fat. The extraperitoneal paravesical pelvic space is beyond the scope of this chapter.

Imaging is important because the retroperitoneal space is difficult to access with bedside modalities such as auscultation, palpation, or percussion. Symptoms and signs may be obscure, delayed, nonspecific, or misleading. Moreover, the peritoneal cavity reacts more acutely and severely than the retroperitoneal tissues.

**Table 1.** Retroperitoneal organs and structures

| Primary retroperitoneal | Secondary retroperitoneal |
|---|---|
| Kidneys | Head and body pancreas |
| Adrenal glands | Duodenum |
| Ureter | Ascending colon |
| Bladder | Descending colon |
| Aorta | |
| Inferior caval vein | |

## Imaging Techniques

Cross-sectional imaging techniques, such as ultrasonography (US), computed tomography (CT), and magnetic resonance imaging (MRI), dramatically improved the ability to evaluate the retroperitoneum. Selection of the optimal technique in each individual patient with a retroperitoneal mass is essential, and factors such as cost, radiation dose, and need for sedation should all be considered. Conventional radiography is of limited value, although it is the best technique to identify teeth in tumors with calcifications, which is virtually pathognomonic for mature teratomas. The initial modality to evaluate retroperitoneal masses is US because it is fast, inexpensive, has no radiation dose, and offers the possibility of fine-needle aspiration to confirm the infectious nature of a fluid collection or to perform histological biopsies in case of solid tumors. MRI and CT are not screening methods but are very useful in detailing osseous and soft tissue changes whenever conventional radiographs and US are not conclusive. CT provides good definition of possible bone destruction or sclerosis. The major drawback of CT is the radiation load. MRI is superior in defining soft tissue masses, bone marrow changes, cartilage destruction, and evaluating extension to the spinal canal (e.g., in neuroblastoma). The major drawback of MRI is the need for sedation in children $\leqslant$6 years. Scintigraphy, with specific radiopharmacy, has additional value in determining the nature of certain tumors and evaluating metastases. Positron emission tomography (PET)-CT and total-body MRI are promising and are valuable in lymphoma evaluation.

### Children versus Adults

Children are not small adults. There are significant anatomical, physiological, and psychological differences; and a large number of congenital and hereditary diseases may be added to the list of differences. Many of those differences have their adult radiological counterparts; therefore, it is not surprising that radiology in children is quite different from radiology in adults. This is true for the central nervous

*Diseases of the Abdomen and Pelvis 2014-2017*,
DOI: 10.1007/978-88-470-5659-6_38 

system (CNS), digestive tract, respiratory tract, urogenital tract, and retroperitoneal lesions, the latter being the topic of this chapter. Neonates are easy to handle, and all non-invasive imaging techniques can be used.

US is the initial modality in neonates for many clinical questions. The diagnostic value of US increases when the neonate is relaxed. Always use warm echogel, and in emergency cases, offering the infant a pacifier with syrup should do the trick.

Even MRI without anesthesia is feasible when performed immediately after feeding. Usually, newborn infants fall into a deep sleep after a meal, and this effect can be enhanced by some sleep and food deprivation prior to the meal. Intravenous access should be provided several hours prior to examination. However, this protocol fails after the age of 3-6 months. Older infants and preschool children usually need sedation for dedicated MRI examinations, although some clinical questions (control of hydrocephalus) can be answered with fast scanning techniques without the need for sedation.

CT techniques have been improved (dual-source CT), and scanning times $<1$ s are possible. Breathholding and motion lose their significance, and often radiation dose is much lower.

Once children go to school, their communication skills improve, and their voice should not be neglected by speaking only with the parents. However, do not even try to negotiate with a child (e.g., the amount of barium they have to drink): you will loose.

This chapter provides a brief overview of pediatric retroperitoneal pathologies in children.

## Pancreas

Pancreatic masses are discussed separately in pp. 271-278 of the Kangaroo section of this syllabus.

## Kidneys

### Nephroblastomatosis

Nephroblastomatosis is defined as the presence of foci of persistent embryological metanephric blastema (nephrogenic rests), which have the potential (1-5%) to develop into nephroblastomas (Wilms' tumor). Nephroblastomatosis presents as multinodular, peripheral, cortical lesions or as a subcapsular rind-like renal mass. On imaging, they are homogeneous and of low echogenicity on US, low density on CT, and low intensity on MRI. They are best appreciated on contrast-enhanced CT or T1-weighted MRI. Best diagnostic clue is its homogeneity.

### Wilms' Tumor

Wilms' tumor (nephroblastoma) is the most common pediatric abdominal tumor, with a peak incidence at 3-4 years of age. It contains blastemal, stromal, and epithelial elements. Patients typically present with a painless unilateral abdominal mass. The tumors are often very large, and the first task of the radiologist is to determine the organ of origin (Fig. 1). Also, the renal vein and inferior caval vein must be evaluated because of the tendency of Wilms' tumors to develop tumor extension into these veins and, rarely, into the ureter.

Imaging shows a large, heterogeneous, nephrogenic tumor that may contain cysts, calcifications, and fatty elements. The collecting system is stretched along the tumor, and other retroperitoneal structures, such as the aorta and inferior caval vein, are displaced. There is no encasement and no elevation of the aorta (features of neuroblastoma). Also, retroperitoneal lymph nodes need to be examined for lymphogenic spread. Hematogenous metastasis has a predilection for the lungs. Staging of Wilms' tumors is given in Table 2.

The contralateral kidney needs close inspection, because 4-13% of children have bilateral Wilms' tumor, particularly in some syndromes that are known to be associated with the risk of developing Wilms' tumor: Beckwith-Wiedemann syndrome and hemihypertrophy syndrome (both 5% risk), sporadic aniridia (30-40% risk), Drash syndrome,

**Table 2.** Children's Oncology Group (COG) staging of Wilms' tumor (summarized)

| Stage | Description |
|---|---|
| I | Limited to kidney; completely resectable with intact renal capsule |
| II | Infiltration beyond kidney; completely resectable |
| III | Residual; confined to abdomen without hematogenous metastasis |
| IV | Hematogenous spread |
| V | Bilateral disease |

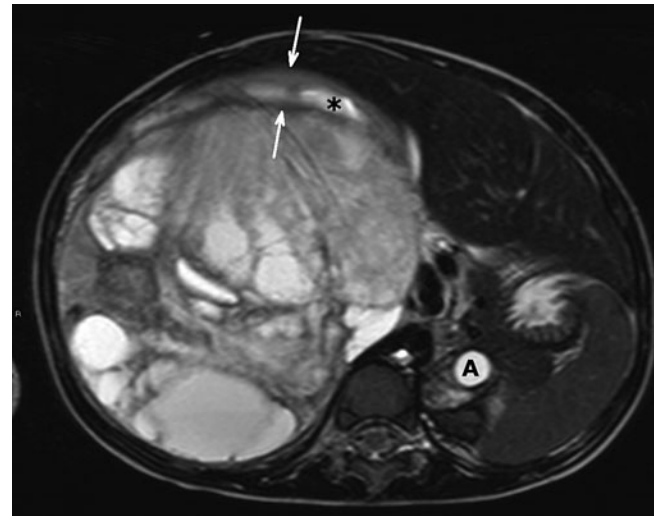


**Fig. 1.** Transverse T2-weighted magnetic resonance (MR) image. A 3-year-old girl with a right-sided palpable mass. Large Wilms' tumor with cystic components causes displacement of the aorta (*A*). A small rim of stretched, normal parenchyma of the upper pole can be recognized (*arrows*). The *asterisk* marks a dilated calyx

Perlman syndrome, Wilms' tumor, aniridia, genitourinary anomalies, and retardation (WARG) syndrome, and Fanconi anemia. In these patients, screening is performed from 6 months until 7 years every 3 months with US.

Other nephrogenic tumors are less frequent, like the following.

### Mesoblastic Nephroma

Mesoblastic nephroma commonly presents in the neonatal period (90% within first year of life) and is sometimes referred to as infantile Wilms' tumor, although histology (spindle cells) does not resemble Wilms' tumor. On imaging, it typically involves the renal sinus, is predominantly solid, and may contain cysts. These tumors seldom metastasize, and the prognosis is very good.

### Multilocular Cystic Renal Tumor

Multilocular cystic renal tumor (multilocular cystic nephroma) is a predominantly cystic tumor. If the cyst wall contains blastemic elements, it is called a cystic partially differentiated nephroblastoma; if the cyst wall is well differentiated, it is called cystic nephroma. There are two age peaks: in children aged 3 months to 4 years (predominantly boys with cystic partially differentiated nephroblastoma), and in adults (predominantly women with cystic nephroma). The prognosis is good.

### Rhabdoid Tumor

The rhabdoid tumor is considered a separate entity (it was formerly considered as a sarcomatous variant of Wilms' tumor) occurring in a slightly younger age group (80% in children $<$2 years, 25% between 6 and 12 months). Imaging findings resemble Wilms' tumor; however, it has other distinctive features. It has the worst prognosis of all childhood nephrogenic tumors and is often associated with primary or metastatic CNS lesions. Therefore, MRI of the brain is mandatory once histology is known.

### Clear Cell Sarcoma

Clear cell sarcoma is considered a separate entity (as rhabdoid tumor, it was formerly considered a sarcomatous variant of Wilms' tumor). Mean patient age is 1-4 years, and it has the same imaging characteristics as Wilms' tumor. The tumor is characterized by its aggressive behavior. The distinctive feature is the predilection for bone metastasis; it is also referred to as "bone-metastasizing tumor of infancy". Therefore, imaging the skeleton (nuclear medicine or total body MRI) is mandatory once histology is known.

### Renal Cell Carcinoma

Renal cell carcinoma (RCC) is rare in the first decade of life (as are most carcinomas). In the second decade of life, a nephrogenic tumor is equally likely to be a Wilms' tumor or renal cell carcinoma. Imaging features are not distinctive. RCC is associated with von-Hippel-Lindau disease (one of the phacomatoses), especially multiple and bilateral RCCs.

### Medullary Carcinoma

Medullary carcinoma of the kidney has been recently described as a separate entity that occurs almost exclusively in patients of African descent with sickle cell trait. It arises from the renal medulla, encases the renal pelvis (causing caliectasis), infiltrates the cortex, but often its reniform shape is maintained. The tumor metastasizes early to regional lymph nodes and lungs.

### Renal Lymphoma

Renal lymphoma is usually a regional metastatic deposit because the renal tissue does not contain lymphoid tissue and primary renal lymphoma is rare. Imaging shows round, homogeneous masses within the renal parenchyma. MRI and CT perform better than US in detecting small deposits. On US, nephromegaly may be the only finding.

### Renal Involvement in Leukemia

This situation usually results in nephromegaly, with some loss of corticomedullary demarcation without focal lesions (Fig. 2).

### Angiomyolipomas and Cysts

Angiomyolipomas and cysts are hamartomatous renal manifestations of tuberous sclerosis (TS), one of the

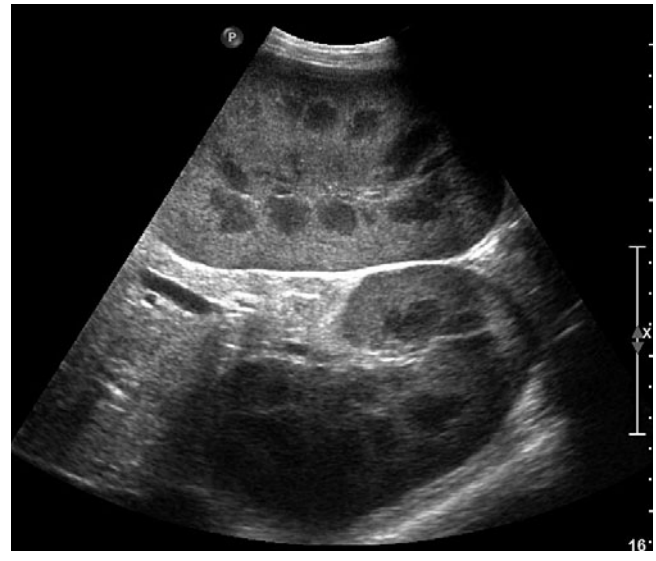

**Fig. 2.** Coronal ultrasound (US) image. Patient with acute lymphatic leukemia (T cell) and massive nephromegaly (kissing kidneys) caused by diffuse tumor infiltration. There are no focal lesions in the parenchyma, and renal vessels are patent

phakomatoses. Usually at birth, no abnormalities are seen, but at the age of 10 years, the majority of children with TS have angiomyolipomas. Angiomyolipomas contain a variable amount of fat and therefore may mimic Wilms' tumor on imaging. On US, angiomyolipomas have a strikingly hyperechoic appearance that resembles large calcifications. Other associated syndromes are neurofibromatosis and von-Hippel-Lindau disease. In patients with TS, syndromal screening is performed every 2-3 years until puberty and yearly thereafter with US. Lesions >4 cm have an increasing risk of fatal hemorrhage and may be selectively embolized or surgically removed.

## Adrenal Glands

Adrenal lesions include hemorrhage, cysts, neoplasms, abscesses, and hyperplasia. Neoplasms may arise from the adrenal medulla or cortex. Those arising from the medulla are of neural crest origin and may therefore also arise in sympathetic nerve chains (neuroblastoma, ganglioneuroma, and pheochromocytoma). Tumors arising from the cortex include adrenocortical carcinoma and adenoma, which may cause secondary symptoms such as Cushing syndrome, precocious puberty, and virilization. Adrenal hyperplasia occurs in adrenogenital syndrome (AGS), adrenal Cushing disease (primary hyperplasia), and in patients with increased adrenocorticotropic hormone (ACTH) levels (secondary hyperplasia as in Cushing's disease and ectopic ACTH production). Adrenal hemorrhage occurs in the neonatal period and is caused by birth trauma, perinatal asphyxia, renal vein thrombosis, septic shock, or dehydration and may resemble neuroblastoma, whereas adrenal cysts may be found in older children.

## Other Lesions of the Pediatric Retroperitoneum

Many retroperitoneal lesions do not originate in a specific organ. They include tumors with an extra-adrenal neuroectodermal origin, lipomatous tumors, rhabdomyosarcomas (RMS), undifferentiated sarcomas, germ cell tumors, mesenchymoma, lymphomas, and lymphatic malformations.

### Tumors Arising from Neuroectodermal Tissue

Such tumors include neuroblastoma, ganglioneuroblastoma, ganglioneuroma, extra-adrenal pheochromocytoma, paraganglioma, (plexiform) neurofibroma, neurofibrosarcoma, neurilemmoma, and schwannoma. Neuroblastoma tends to encase vascular structures and to extend into the spinal canal. Imaging shows heterogeneity, and calcification can be present. Neurofibromatous tumors are associated with neurofibromatosis type 1 (NF1). Abdominal involvement is found in 10-25% of patients with NF1, regardless of age. Neurofibromas present as heterogeneous masses or as multiple, rounded, hypoechoic, well-circumscribed variably sized nodules.

### Fat-Containing Retroperitoneal Tumors

In children, these tumors are lipoblastomas, teratomas, or angiomyolipomas. The latter two are described elsewhere in this chapter. Tumors of fatty origin in children are predominantly lipoblastomas; liposarcoma and retroperitoneal lipomas are rare in children. The majority of lipoblastomas are diagnosed before the age of 3 years, and children present with an increasing painless mass. Abdominal lipoblastoma predominantly involves the mesentery and omentum. It appears as finely lobulated, homogeneous tumor, or with fibrovascular septa. On imaging, the characteristic feature is the presence of variable amounts of fat within the tumor (depending on the cellular composition). This feature is best appreciated with CT or, preferably, with MRI. Calcification is not a feature of lipoblastoma, and this finding can be used in the differentiation with fat-containing teratomas.

### Rhabdomyosarcoma

Rhabdomyosarcoma (RMS) is a malignant tumor that originates from primitive mesenchyme with rhabdomyoma differentiation. There is a bimodal age distribution, with a peak at 7 years and at adolescence. RMS can occur anywhere in the body, and the retroperitoneum is involved in 7% of cases. RMS can histologically be characterized as embryonal (55%), a botryoid variant of embryonal (5%), alveolar (20%), or undifferentiated (20%). Alveolar RMS has the worst prognosis. Distant metastasis to bone, bone marrow, and lungs are frequently present. Imaging demonstrates a mass, with areas of calcification, necrosis, and heterogeneous enhancement. The botryoid type has cysts filled with mucosanguineous fluid.

### Germ Cell Tumors

These are benign or malignant tumors originating from primordial germinal epithelial layer cells. They may be gonadal or arising from primordial germ cells, sequestering during migration and mismigrating to extragonadal sites. Abdominal germ cell tumors are usually located in the retroperitoneum: these are germinoma, embryonal carcinoma, endodermal sinus tumor, choriocarcinoma, gonadoblastoma, and teratoma.

Teratomas are composed of a variety of tissues with poor organization in various stages of maturation and may be multicystic, solid, or even consist of a single large cyst. Abdominal teratomas arise from the retroperitoneum, presacral region, and ovary. Rare types are mesenteric and gastric teratomas. These tumors occur mainly in children, and 80% are benign. Mature, immature, and malignant types have been described. Most children present with a palpable abdominal mass. US will demonstrate a (multi)cystic or solid mass. Teratomas

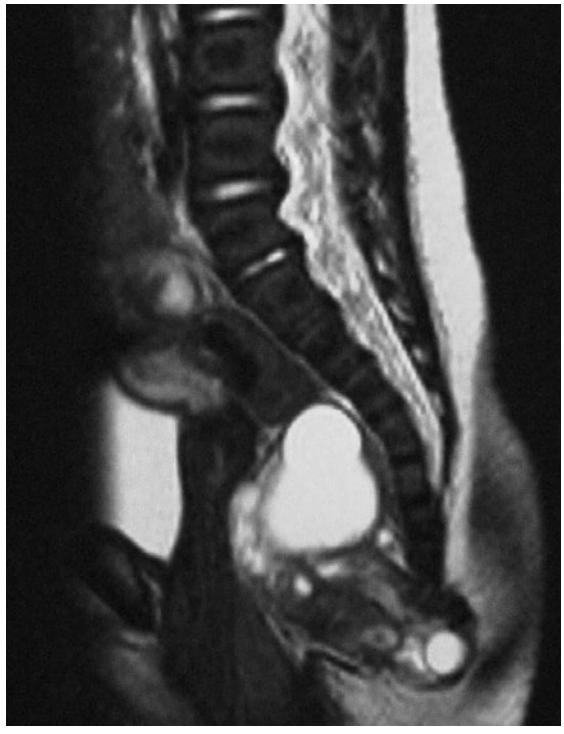

**Fig. 3.** Sagittal T2-weighted magnetic resonance (MR) image. A 2-month-old infant with presacral extension of a sacrococcygeal teratoma. The tumor is mixed solid/cystic

typically contain calcifications and fat. Calcifications may be seen in more than half of cases; fat is difficult to appreciate with US, but highly echogenic tissue can provide a clue for fatty tissue.

Sacrococcygeal teratomas arise from the coccygeal region and are usually detected on prenatal US or immediately after birth, with a large external cystic tumor at the coccyx. Approximately 80% of cases is diagnosed before the age of 6 months. However, some sacrococcygeal teratomas present with a large cystic intra-abdominal mass without any external mass (Fig. 3). These presacral tumors obstruct the rectum and bladder. A presacral extension of an intra-abdominal cyst provides a clue for the diagnosis of sacrococcygeal teratoma. Cystic tumors carry a better prognosis than do solid, hypervascular tumors. Hypertrophy of the median sacral artery may predict hemorrhagic complications during surgery. Patients diagnosed after the age of 6 months have an increased prevalence of malignancy.

### Lymphoma (Hodgkin's/non-Hodgkin's)

In children, non-Hodgkin's lymphoma is more commonly encountered than Hodgkin's lymphoma. Differentiation between them cannot solely be achieved by imaging, and tissue diagnosis is mandatory in all cases. Retroperitoneal involvement of lymph nodes is mostly seen as a mass, either single or multiple. Lymph nodes may show signs of central necrosis or calcification, and encasement of vessels is often encountered.

### Retroperitoneal Lymphadenopathy

Unlike mesenteric lymphadenopathy, enlargement of retroperitoneal lymph nodes should always be regarded as abnormal. Therefore, this finding warrants further follow-up. In children, the most common causes of retroperitoneal lymphadenopathy are malignancies, e.g., Wilms' tumor, neuroblastoma, rhabdomyosarcoma, and malignant lymphoma; however, infectious diseases can also cause lymph node enlargement. On US, lymphadenopathy can be obscured by gastrointestinal gas or obesity. In case of large abdominal tumors, the retroperitoneum can be difficult to visualize. In these children, disease staging using additional imaging, e.g., CT but preferably MRI, is mandatory.

### Fibromatosis, or Abdominal Desmoid

Fibromatosis, or abdominal desmoid, is part of the clinical-pathologic spectrum of deep fibromatoses. The deep fibromatoses encompass a group of benign fibroproliferative processes that are locally aggressive and have the capacity to infiltrate or recur but not metastasize. Mesenteric structures are the most common sites of origin of intra-abdominal fibromatosis, but the abdominal wall, pelvis, and retroperitoneum can also be involved. Thirteen percent of patients with mesenteric fibromatosis have familial adenomatous polyposis (FAP), specifically, the Gardner syndrome variant of FAP.

Prior abdominal surgery is an important risk factor for the development of fibromatosis in patients with FAP. US appearance of mesenteric fibromatosis is a solid, well-circumscribed mass of variable echotexture and homogeneity. Locally aggressive fibromatosis infiltrates the surrounding fat.

### Inflammatory Myofibroblastic Tumor

Inflammatory myofibroblastic tumors (IMT) most commonly occur in the lungs in children or young adults. IMTs that originate in the retroperitoneum are rare and may involve the kidney, ureter, and bladder. Such children complain of malaise, weight loss, or abdominal pain. Characteristics of IMT are nonspecific: solid, well-defined (sometimes lobulated) lesions with mixed echogenicity on US and frequent calcifications; infiltration of adjacent bowel may occur; prominent vascularity may be shown with Doppler US.

### Retroperitoneal Lymphatic Malformation

Cystic intra-abdominal masses originating from the alimentary canal are increasingly recognized because of the advent of routine prenatal US. Cystic intra-abdominal masses most often originate from solid organs (e.g., congenital splenic cyst) or from the alimentary canal (choledochal cyst, mesenteric cyst, etc.) and less frequently from the retroperitoneum. Predominantly cystic retro-

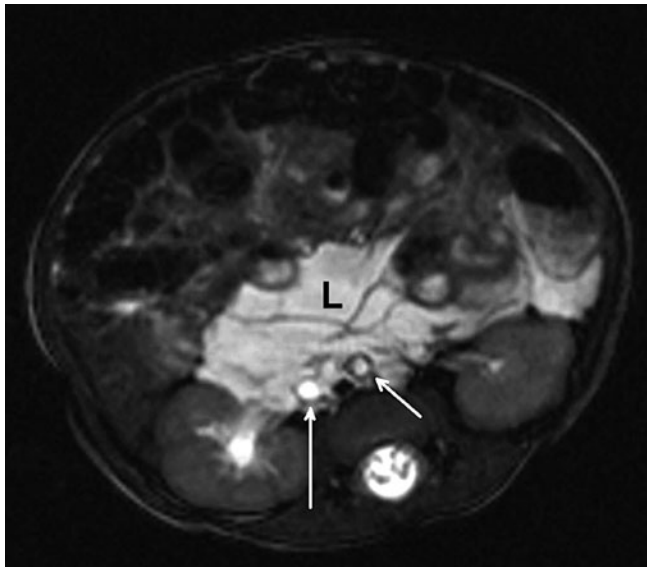


**Fig. 4.** Transverse T2-weighted magnetic resonance image. An infant with a retroperitoneal cystic lymphatic malformation (L). Aorta and inferior caval vein (ICV) are encased by the cysts (*arrows*)

peritoneal masses are most likely lymphatic malformations. These are not considered true neoplastic lesions but congenital, abnormally deformed lymphatics due to fetal blockage of lymph channels. They may change in size depending on fluid content, which varies over time and may extend into the mediastinum and groin. Lymphatic malformations may be composed of very small cystic components (microcystic) or of larger cystic spaces (macrocystic), the latter being referred to as cystic hygromas. Lymphatic malformations are commonly mixed with other vascular malformations. Septa are thin and better appreciated with US than CT. MRI is superior in defining lymphatic malformation extension (Fig. 4). Fluid may be clear or slightly turbid (best seen with US) because of small hemorrhages.

### Retroperitoneal Hematoma and Abscess

Retroperitoneal hematoma and abscesses often present as fluid collections within the psoas muscle. Imaging characteristics depend on the nature (blood, pus) and viscosity of the fluid. Hematoma is often seen in relation with hemophilia or other coagulation disorders, whereas a psoas abscess should raise the possibility of a tuberculous abscess (e.g., secondary to spinal infection).

## Conclusion

There is substantial overlap of imaging findings in various retroperitoneal masses. However, imaging is particularly useful in defining mass site of origin, extent, invasion of adjacent structures, and encasement of or extension into vessels. Moreover, clinical history and certain details seen at imaging can assist in making the correct diagnosis. Familiarity with the imaging features of retroperitoneal masses facilitates accurate diagnosis and treatment.

## Suggested Reading

Agrons GA, Lonergan GJ, Dickey GE, Perez-Monte JE (1999) Adrenocortical neoplasms in children: radiologic-pathologic correlation. Radiographics 19:989-1008.

Bittman ME, Lee EY, Restrepo R, Eisenberg RL (2013) Focal adrenal lesions in pediatric patients. AJR Am J Roentgenol 200:W542-W556.

Craig WD, Fanburg-Smith JC, Henry LR et al (2009) Fat-containing lesions of the retroperitoneum: radiologic-pathologic correlation. Radiographics 29:261-290

Donnely LF (2012) Diagnostic imaging pediatrics. Lippincott William & Wilkins/Amirsys.

Kocaoglu M, Frush DP (2006) Pediatric presacral masses. Radiographics 26:833-857.

Laffan EE, Ngan BY, Navarro OM (2009) Pediatric soft-tissue tumors and pseudotumors: MR imaging features with pathologic correlation part 2. Radiographics 29 e36:1-35.

Lowe LH, Isuani BH, Heller RM et al (2000) Pediatric renal masses: Wilms tumor and beyond. Radiographics 20:1585-1603.

Meyers MA, Oliphant M, Charnsangavej C (2010) Meyer's dynamic radiology of the abdomen. Springer.

Moholkar S, Sebire NJ, Roebuck DJ (2006) Radiological-pathological correlation in lipoblastoma and lipoblastomatosis. Pediatr Radiol 36:851-856.

Navarro OM, Laffan EE, Ngan BY (2009) Pediatric soft-tissue tumors and pseudotumors: MR imaging features with pathologic correlation part 1. Radiographics 29:887-906.

Rajiah P, Sinha R, Cuevas C (2011) Imaging of uncommon retroperitoneal masses. Radiographics 31:949-976.

Rohrschneider WK, Weirich A, Rieden K (1998) US, CT and MR imaging characteristics of nephroblastomatosis. Pediatr Radiol 28:435-443.

Ueno T, Tanaka YO, Nagata M (2004) Spectrum of germ cell tumors: from head to toe. Radiographics 24:387-404.

Yang DM, Jung DH, Kim H et al (2004) Retroperitoneal cystic masses: CT, clinical, and pathologic findings and literature review. Radiographics 24:1353-1365.

KANGAROO PEDIATRIC RADIOLOGY

IDKD 2014-2017

# MR Urography in Children

Richard A. Jones[1,2], J. Damien Grattan-Smith[1,2], Stephen Little[1]

[1] Department of Radiology, Children's Healthcare of Atlanta, Atlanta, GA, USA
[2] Department of Radiology, Emory University School of Medicine, Atlanta, GA, USA

## Introduction

Magnetic resonance urography (MRU) is a powerful clinical tool that fuses anatomic information with functional data in a single test without the use of ionizing radiation. This chapter provides an overview of the technical aspects, as well as common clinical applications, of MRU, with an emphasis on evaluating hydronephrosis. A fluid challenge is an essential part of our MRU protocol and enables the definition of compensated or decompensated kidneys within the spectrum of hydronephrosis. This classification may have prognostic implications when surgery is being considered. In addition, underlying uropathy can be identified on the anatomical scans, and renal scarring can be seen on both anatomical and dynamic scans. MRU can identify and categorize dysmorphic kidneys in vivo and may provide insight into congenital abnormalities seen in conjunction with vesicoureteric reflux (VUR). MRU is still in its infancy, and as the technique develops and becomes widely available, it seems likely that it will supplant renal scintigraphy for evaluating renal tract disorders in children.

MRU represents the next step in the evolution of uroradiology in children because it fuses superb anatomic and functional imaging in a single test that does not use ionizing radiation. MRU has advantages over other modalities in that it generates tissue contrast from a variety of sources. In addition to spin-echo T1 and T2 images, dynamic imaging is performed in conjunction with the injection of a gadolinium-based contrast agent (GBCA) in order to assess the concentrating and excretory functions of the kidney. Evaluating contrast dynamics is similar to renal scintigraphy but with the important distinction that signals originating from the renal parenchyma can be separated from those originating from the collecting system. Whereas MR is not used routinely to assess the degree of VUR, it can detect the anatomical consequences of VUR in terms of dilated ureters, distorted anatomy of the collecting system, and renal scarring and its functional consequences.

We have performed MRU on ~2,000 children over the last 8 years, finding that meticulous attention to patient preparation and scanning technique is essential if high-quality images are to be reliably obtained, with appropriate hydration and sedation being key factors in the success of the examination. There are several publications assessing the ability of MRU to reliably quantify glomerular filtration rate (GFR) using an arterial input function (AIF) derived from the aorta and signal curves measured in the renal parenchyma [1-3]. However, there are still a number of problems to be addressed before this examination becomes a clinical reality [4]. Thus, we base our approach on deriving measures that can be thought of as indices of renal function in that they are correlated with, but not necessarily equal to, GFR. We use these measures to derive several measures of differential renal function (DRF) in the same manner as is used for nuclear medicine, assessing them in terms of response to the fluid challenge provided by hydration and diuretic challenge provoked by furosemide administration. Because of the clinical importance of viewing individual volumes from the dynamic series in order to assess features such as renal scarring, areas of delayed uptake of contrast, and accurately delimiting the boundaries of duplex kidneys, we use a higher spatial resolution, and hence lower temporal resolution, than that used in many other recent studies. An advantage of studying the infant kidney is that it exhibits little respiratory motion, such that motion artifacts are minimal.

## Protocol

### Hydration

As a fluid challenge is an integral part of our protocol, hydration needs to be as reproducible as possible. For this reason, we use standardized intravenous (IV)-applied hydration. If children are to be sedated, we correct their nil per os (NPO) deficit using Ringer's solution according to the following formula:

- 4 cc/kg/h for first 10 kg of patient's weight
- 2 cc/kg/h for next 10 kg of patient's weight
- 4 cc/kg/h for each kilogram >20 kg patient's weight.

*Diseases of the Abdomen and Pelvis 2014-2017*,
DOI: 10.1007/978-88-470-5659-6_39 

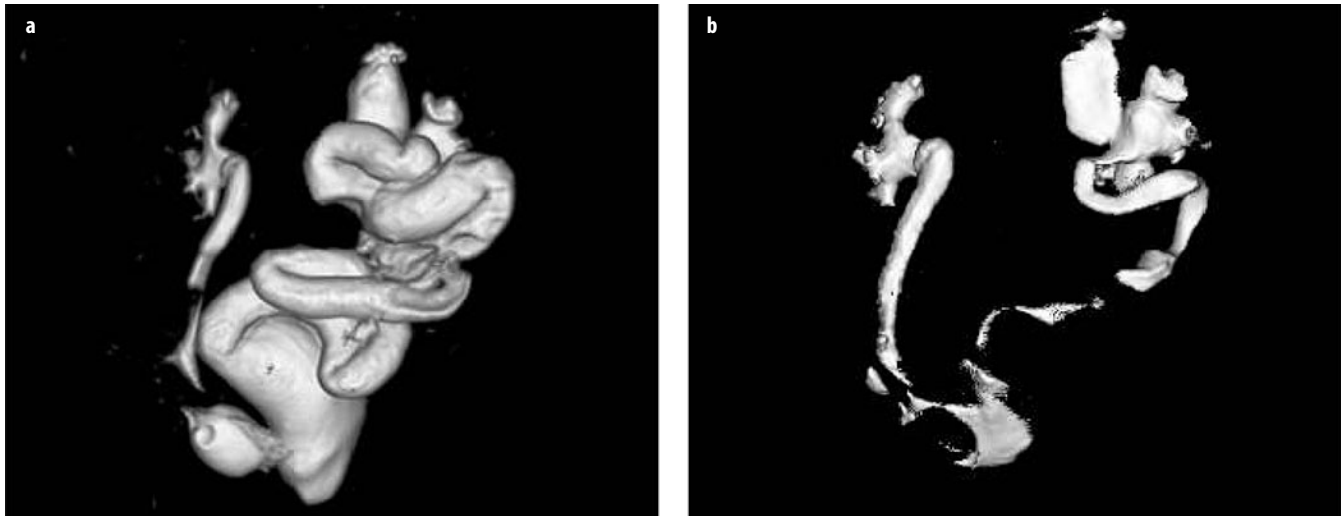


**Fig. 1 a, b.** T2-weighted (**a**) and postcontrast T1-weighted (**b**) 3D magnetic resonance urograms (MRU) show the anatomy and morphology of hydronephrotic and poorly functioning systems

If the child is a nonsedate candidate, we hydrate with Ringer's solution at a dose of 10 cc/kg given IV over 30-40 min.

### Furosemide

We use a standard dose of 1 mg/kg up to a maximum dose of 20 mg injected 15 min prior to the injection of the GBCA. In addition to being an integral part of the fluid challenge, the early administration of furosemide distends the urinary tract and minimizes the duration of the study [5]. Although the maximum onset of diuresis occurs at between 15 and 18 min after injection, there is substantial diuresis from 5 to 30 min, which provides some latitude in the timing of the contrast injection [6].

### Sedation

Almost all children <7 years of age will need to be sedated. We are fortunate to have dedicated sedation physicians who use propofol in most cases and are able to titrate the dose for the individual patient. Many of our patients are referred for antenatal hydronephrosis evaluation. In this population, our sedation physicians usually like to wait until the patient is at least 3 months of age before scheduling the MRU. Older children who are not sedated are asked to either breathe quietly, or if they are able to co-operate, we perform breath-hold imaging. One group reported some success with performing MRU on nonsedated infants [7].

### Bladder Catheterization

A bladder catheter is placed whenever possible. The main reason for placing a catheter is that children become uncomfortable and tend to wake from sedation if the bladder is full. There are additional imaging benefits from using a bladder catheter in that interpretation of the images is easier, as confounding issues, such as VUR and transmitted bladder pressure, are eliminated. If there is a question of bladder abnormality, the catheter can be clamped and images of the distended urinary bladder obtained. In older children, the bladder catheter is often not placed, and the patient is requested to void their bladder prior to the examination and, if necessary, prior to contrast administration.

### Precontrast Imaging

One of the strengths of MRU is the ability to combine both contrast-enhanced imaging with T2-weighted images so that both static and dynamic evaluation of the urinary tract is obtained [8, 9]. This is particularly helpful in cases of marked hydronephrosis or poorly functioning systems. We obtain a 3D T2 urogram, which is used to generate maximum intensity projection (MIP) and volume-rendered (VR) images of the pelvicalyceal system and ureters. VR images are very helpful in analyzing duplex systems or complicated anatomical variants (Fig. 1). We also perform an axial T2-weighted turbo spin-echo (TSE) image through the bladder to identify abnormalities of the bladder base, including ureteroceles and ectopic ureteric insertion. Additionally, we have come to rely on axial high-resolution T2-weighted images for assessing renal parenchyma (Fig. 2). These are typically performed immediately after the half-Fourier-acquisition single-shot turbo spin-echo (HASTE) scouts and are obtained prior to the furosemide injection, so we have a baseline evaluation of the degree of hydronephrosis to which we can compare the delayed images.

### Contrast Administration

One of the fundamental relationships that must be understood is the nonlinear relationship between signal inten-

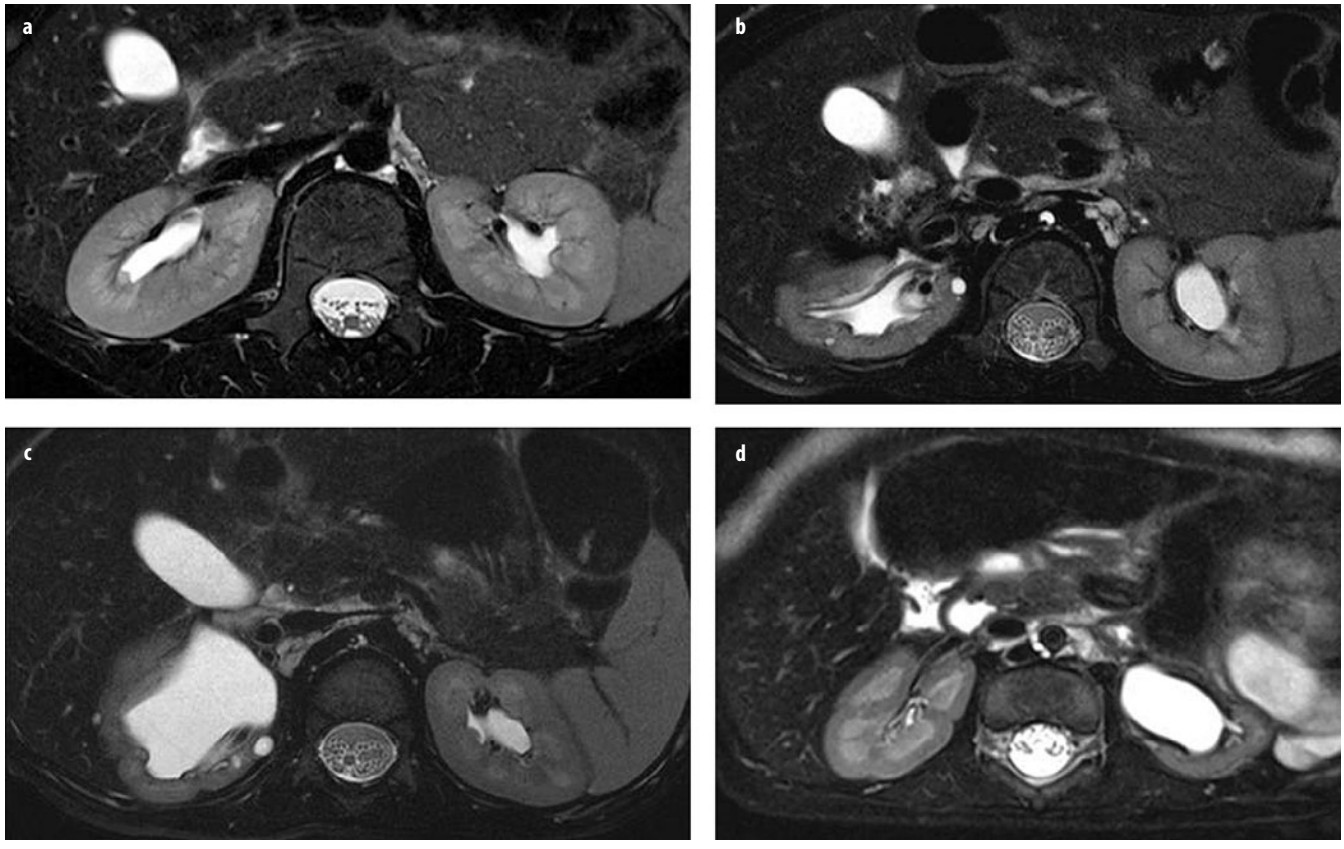


**Fig. 2 a-d.** High-resolution T2-weighted magnetic resonance urograms (MRU) of the kidney. The image **a** shows a patient with normal renal anatomy; the other three images are examples of patients with renal dysplasia. The high-resolution T2-weighted images can be used to assess renal parenchyma quality. Excellent corticomedullary differentiation allows assessment of both the renal cortex and medulla, as well as detection of cysts, scarring, edema, and architectural disorganization

sity and GBCA concentration when using gradient-echo (GRE) imaging. At low concentrations, T1 effects predominate, and the relationship is relatively linear. However, as the concentration increases, T2* effects become increasingly important, leading to signal dephasing and an increasingly nonlinear relationship between signal and GBCA concentration. If the signal is to be used to estimate GBCA concentration, then it is important to keep the concentration low enough to ensure it is within linear range. If we want to operate in the nonlinear range, then a precontrast measurement of relaxation time is used to convert the measured signals to a concentration. In our implementation, hydration and furosemide injection, along with suitable pulse-sequence parameters, are used to keep the gadolinium signal within the linear range and hence allow the signal to be used as a measure of GBCA concentration.

We use the standard dose of a GBCA (Magnevist), as it provides excellent enhancement of the kidneys and allows evaluation of the MR nephrogram by differentiating the enhancing parenchyma from the background. Others use smaller doses of contrast, but we found the contrast to be inferior when using a lower dose, particularly when trying to segment poorly functioning kidneys. Because of the risks associated with using GBCA on patients in renal failure, a serum creatinine test is used on all patients to estimate glomerular filtration rate (GFR). If creatinine GFR is $<$60ml/min, we change the contrast agent to ProHance. To date, we have had no cases in which creatinine GFR was $<$30 ml/min, as patients with renal failure are not typically referred for an MRU. Caution should be used when using a GBCA, such as Eovist or MultiHance, which exhibit some degree of protein binding in order to enhance their relaxivity [10]. Whereas this enhances the aortic signal, similar binding will not occur in the tubular compartment unless proteinuria is present (and in this case, the degree of enhancement will depend on proteinuria concentration), thus negating the use of the arterial signal as the renal input function.

Initially we gave the contrast as a rapid bolus injection but found that the aortic signal intensity exceeded the linear portion of the curve and that the arterial signal was poorly characterized with the temporal resolution of 8-9 s typically used for our studies. Therefore, in order to obtain a well-characterized AIF that falls within the linear range, we now slowly inject the contrast agent using a power injector to control the infusion rate. We typically use a rate between 0.1 and 0.2 ml/s, and the injection usually takes between 20 and 60 s; we do not exceed a rate of 0.25 ml/s for small children.

### Dynamic Contrast-Enhanced Imaging

As the GBCA is being injected, we acquire sequential dynamic 3D T1-weighted GRE sequences in the oblique coronal plane (Fig. 3). We typically use an acquisition time of 8-9 s per volume, using parallel imaging with a factor of 2. The flip angle is set at 30° in order to improve linearity of the signal intensity, and we use a high bandwidth to minimize TE. Our slice thickness is typically 2 mm, and we typically acquire 50 volume acquisitions in the first 10 min after contrast injection. We acquire continuous volumes for the first 5 min of scanning and then insert delays of increasing duration between the dynamics, as high temporal resolution is not required for the washout phase. An MIP image of each dynamic series is automatically generated, which facilitates a rapid review of data sets. We term this MIP image of each volumetric data set a concatenated MIP. Occasionally, if we want to outline the ureter and there is a fluid level within the renal pelvis, we turn the patients prone to promote drainage from the collecting system.

The dynamic data sets are reviewed to assess kidney perfusion, filtration, concentration, and excretion (Fig. 3). The aorta and renal arteries are usually well visualized on

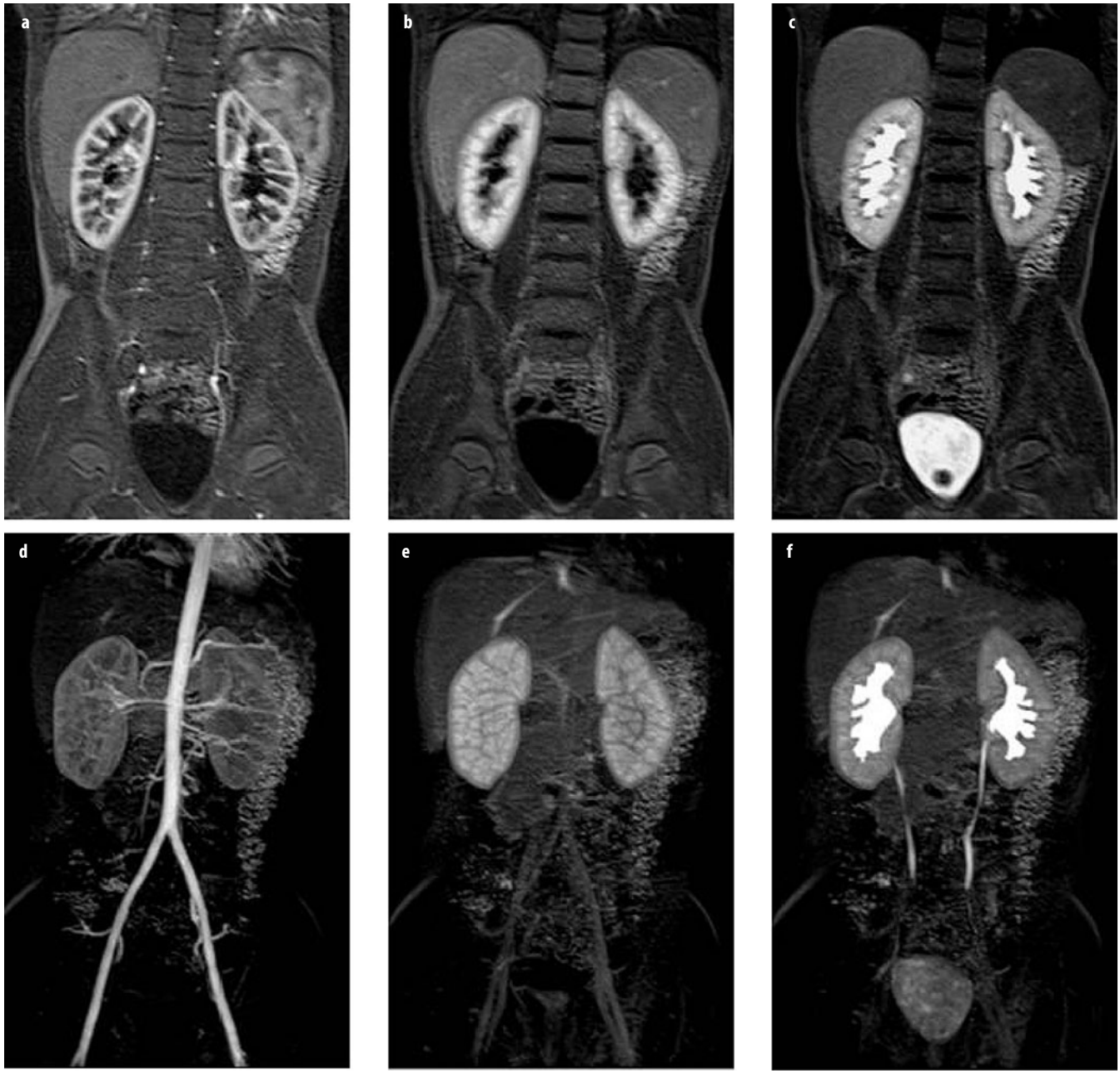


**Fig. 3 a-f.** Normal magnetic resonance urogram (MRU) in an 8-year-old girl. **a-c** The same slice from three volume acquisitions acquired at time points corresponding to cortical (arterial), parenchymal, and excretory phases of renal function, respectively. **d-f** Maximum intensity projections derived from the total volume for the same three time points

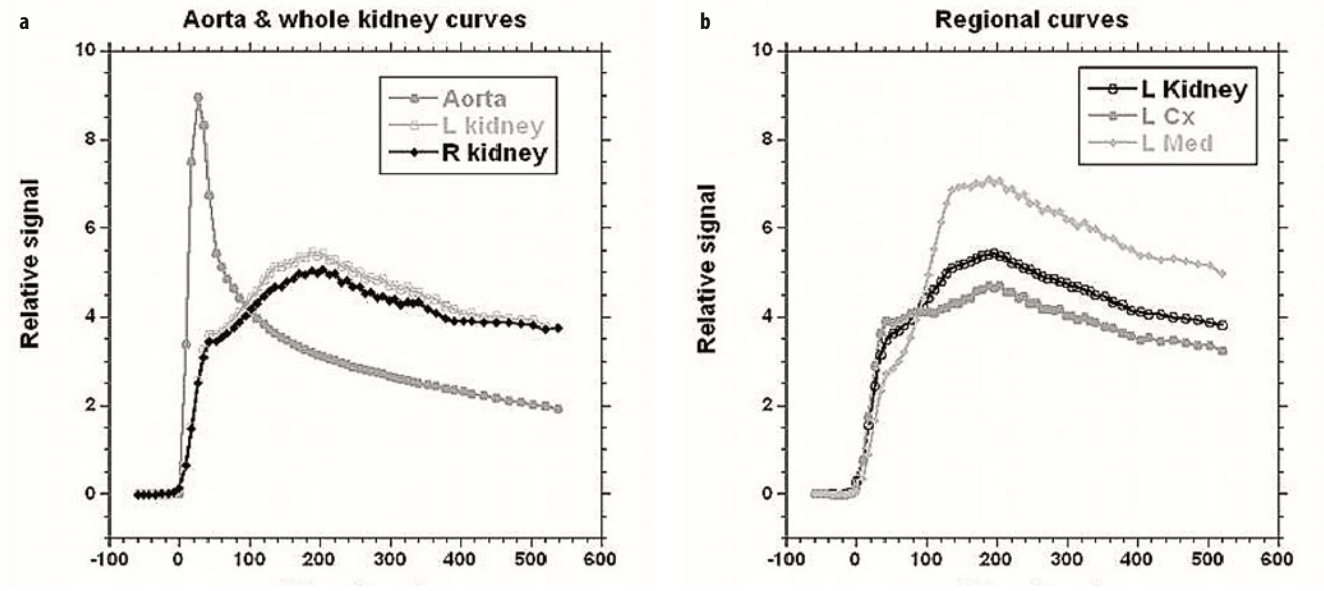


**Fig. 4 a, b.** Time intensity curves for patient shown in Fig. 3. These allow assessment and comparison of renal perfusion, concentration, and excretion similar to the time activity curves generated with diuretic renal scintigraphy. For this patient, volumetric differential renal function (vDRF) and Patlak (p)DRF were both 53:47 (*L:R*); unit Patlak per milliliter of tissue (up)DRF and tubular output (to)DRF were both 50:50

early dynamic images. This is helpful in identifying accessory arteries and crossing vessels associated with ureteropelvic junction (UPJ) obstruction [11]. The parenchymal phases are typically divided into cortical, medullary, and excretory phases. The cortical phase reflects both renal perfusion and glomerular filtration. The medullary phase typically occurs 45-90 s later and reflects perfusion of the renal medulla and concentration of the contrast agent in the loop of Henle. In the normal kidney, signal intensity in the renal medulla is always greater than in the cortex in this phase. After a further 30-60 s, contrast medium is excreted into the pelvicalyceal system and ureter in normal kidneys. Typically, signal intensity versus time curves are generated for the whole kidney but can be generated for specific tissues or regions of the kidney, if necessary (Fig. 4).

## High-Spatial-Resolution Imaging

Once contrast is excreted into the ureters, we obtain high spatial resolution images in order to delineate optimally urinary tract anatomy. We are able to define the renal cortex, medulla, and pelvicalyceal system, as well as the course of the ureters to the bladder. These images are excellent for 3D VR either on the scanner or on an independent workstation (Fig. 1). For infants and small children, data is acquired using isotropic voxels 0.9 mm in size. In older children, we are limited to breath-hold imaging, which requires shorter imaging time and therefore decreased spatial resolution. In older children, we typically acquire voxels with a nominal spatial resolution of approx. 1.5 × 1.5 × 2.5 mm.

## Postprocessing

The basic steps in postprocessing dynamic series are kidney segmentation, derivation of arterial and parenchymal curves, and fitting these to an appropriate model in order to derive indices of renal function. Segmentation provides both an estimate of renal volume, which is required when calculating GFR for the whole kidney, and a mask that determines the pixels contributing to the average time course for the kidney. We use a statistical approach in which the user selects a time point and outlines kidney location; then, statistical distribution of the signal in the selected dynamic (time point) and time-course information from each pixel are used to segment the kidneys [12]. The user then reviews the segmentation and if further refinement is required, then additional constraints can be added and the segmentation repeated until an acceptable segmentation is obtained. For most kidneys, little or no segmentation refinement is required, but for poorly functioning kidneys, achieving an acceptable segmentation can be quite time consuming. Rusinek et al. reported achieving good results with an algorithm based on the graph-cuts method [13]. Prior to fitting the signals for the kidney(s) and the AIF (see below) to a model, the signals must be converted into concentrations of contrast agent. This is usually done in one of two ways: (1) assuming a linear relationship between contrast agent concentration and signal change with respect to precontrast signal; (2) signal changes are converted, with the help of additional scans, to changes in T1, which can then be converted to changes in contrast agent concentration. The main disadvantage to method 1 is that it is only true for a restricted range of

concentrations [14]; thus, a reduced dose of contrast and/or a slow injection protocol are required to limit the peak concentration of both AIF and kidneys, whereas hydration and the effect of furosemide provide additional reductions in renal concentration of contrast. The main advantage of this method is that it is simple to implement and does not require any additional images other than one or more precontrast images (which will generally be acquired anyway). Method 2 potentially offers greater precision and latitude in choosing contrast dose and injection protocol. However, this approach generally requires additional scans prior, and in some case after, the dynamic series, such that T1 values can be derived and then used to derive the equilibrium magnetization so T1 can be calculated for each dynamic volume [15]. Additionally, for clinical applications, time constraints will generally limit the amount of additional data that can be acquired, which in turn limits the precision of the T1 calculation. It should also be noted that the method also uses values for relaxivity of the contrast agent, which are typically derived from ex vivo experiments and may well not apply to the very different environment encountered in the kidney, where relaxivity value will vary between different tissues [16]. It should be noted that some models of renal function require a compact bolus of contrast, resulting in high first-pass concentrations of contrast, which hence require the use of the T1 conversion.

For our studies, we use method 1 in conjunction with a slow injection of contrast (minimum duration 20 s) and the use of hydration and furosemide to help restrict the maximum renal concentration. Baseline (precontrast) signal ($S_0$) is averaged over the precontrast dynamics and the relative signal (change in signal) is calculated as $[(S(t)-S_0)/S_0]$. At a field strength of 1.5 T with our standard dynamic sequence, we found a linear relationship between relative signal and contrast agent up to concentrations of ~1.5 mM in phantom studies [14].

## Arterial Input Function (AIF)

In order to model renal function, an estimate of GBCA vascular concentration time course is required, and this is generally referred to as the AIF. The AIF is required, as vascular concentration affects GBCA filtration rate by the kidneys; even with a standardized dose and injection protocol, there will be idiosyncratic variations in AIF caused by physiological differences. For renal studies, the arterial signal is usually measured in a region of interest (ROI) in the descending aorta, the renal arteries being typically too small for reliable measurements in children. The aorta is viewed in both coronal and sagittal planes in order to minimize partial volume effects by excluding, if possible, regions where the aorta cuts through the imaging plane. The ROI consists of an arbitrary number of points – the points typically being positioned at or below the level of the renal arteries in order to minimize inflow effects. Even with careful selection of ROI location, pulsatility effects can still be present, and it is not always possible to eliminate partial volume and inflow effects. Imprecision in the AIF is one of the main factors that prohibit a reliable quantification of GFR with MRU. Several methods have been suggested to address this problem [17, 18], but none of these are yet close to routine clinical use. For methods based on the differential function then, AIF imperfections are common to both kidneys and hence are cancelled out [19].

In order to smooth out signal fluctuations and allow an estimate of the aortic signal at any given time point, the signal measured in the ROI is fitted to the model outlined below in order to generate a smooth AIF.

$$C_a(t) = C_{am} t_{am}^{-\alpha} \exp(\alpha) t^{\alpha} \exp(-\alpha t / t_{am}) \quad t < \tau \quad (1)$$

$$C_a(t) = \sum_{n=1}^{N} A_n \exp(-K_n(t-\tau)) \quad t \geqslant \tau \quad (2)$$

where $N = 2$, $C_{am}$ is the maximum arterial concentration, and $t_{am}$ is the time of maximum arterial concentration. The upper expression is a modified form of a gamma variate in which there is no coupling between parameters, and hence, the parameter $\alpha$ can be varied without affecting $C_{am}$ or $t_{am}$ [20]. This is not the case for the more usual form of the gamma variate function. This, along with the fact that initial estimates for $C_{am}$ and $t_{am}$ can be accurately estimated from the ROI data, leads to more robust curve fitting. After the time, $\tau$, GBCA concentration is described by a biexponential expression that accounts for the GBCA distribution through the vasculature, interactions with fast and slow exchange components within the body, and clearance through the kidneys [21, 22]. This model works well for the slow-injection protocol used for our studies (Fig. 5). However, for a compact bolus, peaks corresponding to GBCA recirculation can often be seen, and more complicated models may be required to describe fully the AIF [23].

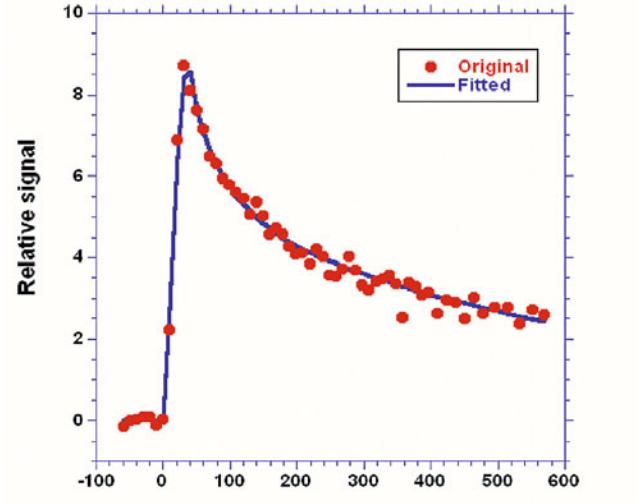


**Fig. 5.** Arterial input function. Measured data is shown by the *dots*, whereas the *line* is the best fit to Eqs. 1 and 2 using a nonlinear fitting procedure

The measured AIF is the whole blood AIF, but when the AIF is applied to models of renal function, plasma concentration is required, as GBCA is confined to plasma. Plasma concentration ($C_p$) is derived by correcting for hematocrit (Hct) using the formula given below:

$$C_p = \frac{C_a}{1 - Hct} \tag{3}$$

Standard values for hematocrit are frequently assumed, but in young children, in whom hematocrit shows considerable variation with age, or in disease states in which hematocrit may be altered, using a standard value may lead to significant errors when trying to calculate an absolute GFR value.

### Concentration versus Time Curves

Deriving the mean signal from the segmented volumes and converting the signal values to concentrations allows concentration versus time curves to be derived. Although the contrast dynamics can be assessed visually, the curves can provide extra information that is not always apparent from a visual inspection. Figure 4 shows both whole-kidney curves and segmental curves for the renal cortex and medulla (with the latter requiring additional segmentation). For all curves, the initial sharp increase in signal predominantly reflects the perfusion phase, with the renal cortex enhancing more than the medulla due to its higher blood volume. Because we use a slow injection of contrast, the vascular peak is less prominent than that seen when a compact bolus is used [24]. Following the vascular phase, a slight peak is seen in the cortical phase around 90 s after the initial arrival of contrast, and this represents GBCA arrival into proximal tubules. The main cortical peak, which occurs ~100 s later, represents contrast in the distal tubules. As the GBCA passes through the loop of Henle, the peak signal for the medullary curve occurs prior to the main cortical peak. After the peaks in both curves, there is a general decline in signal intensity due to contrast excretion into the urine and the ongoing decline in GBCA plasma concentration.

Although it is possible to segment the cortex and medulla separately (Fig. 4), it is time consuming, and for this reason, we evaluate only whole kidney curves for the majority of cases. These curves are rapidly generated and enable assessment of perfusion, concentration, and excretion for each kidney and are analogous to the time activity curves of renal scintigraphy. These curves reflect the changes that occur in the renal parenchyma only, rather than in the parenchyma and collecting systems as seen with renal scintigraphy. As postprocessing becomes easier, segmental analysis will become more practical and provide greater insights into the anatomic and pathophysiologic changes occurring in the different compartments with various renal diseases. Similarly, fitting the models on a pixel-by-pixel basis to produce statistical parametric maps of the model parameters is yet too time consuming for routine clinical use, but as increased computational power becomes available, these will also become clinically feasible.

## Modeling Renal Function

Several models of renal function have been developed and compared in the literature [3] and described in a review [25]. Therefore, we only briefly describe the specific techniques we use for clinical applications. The Rutland-Patlak model [26-28], which is widely used in single-photon-emission computed tomography (SPECT) and CT has been applied to dynamic contrast-enhanced magnetic resonance imaging (DCE-MRI) data [1, 29]. With this model, GFR is measured as the transfer of GBCA from arterial blood to renal tubules, and the fact that the kidney includes both vascular and tubular components is taken into account. The amount of GBCA in any one kidney at a time point, $C_k(t)$, prior to GBCA excretion, can be expressed as the sum of the GBCA in the vascular space and nephrons. Assuming GBCA plasma concentration in the vascular space is proportional to plasma concentration in the aorta, $C_p(t)$, then defining the constants $k_1$ and $k_2$ to represent the vascular volume within the kidney and GBCA clearance from the vascular space, respectively, one can write

$$C_k(t) = k_1 c_p(t) + k_2 . \int_0^t c_p(u)\, du \tag{4}$$

where $t = 0$ is GBCA arrival time. The values for $C_p(t)$ and $C_k(t)$ are derived from the AIF and renal curves, respectively. Equation 4 can be rewritten in the form of a linear equation, and values for $k_1$and $k_2$ derived from the plot of this equation. However, this requires choosing a start point (time when contrast agent is uniformly distributed in the vasculature) and an end point (excretion of contrast) for the plot, and it is simpler to apply a nonlinear fit of Eq. 4 to all data points between GBCA arrival and excretion in order to derive values for $k_1$ and $k_2$ [30].

Typically, one measures the average GBCA concentration within the kidney; thus, $k_2$ represents clearance per unit volume of tissue, which we refer to as the unit GFR. We believe this quantity is related to the single-nephron GFR and note that this quantity is reduced in decompensated, as well as dysplastic and uropathic, kidneys. An estimate of single-kidney GFR (SK-GFR) can be obtained by multiplying $k_2$ by renal volume ($V_r$). The Patlak model breaks down after a certain time because it fails to take account of the onward transport of GBCA (i.e., drop in signal seen at later time points in the parenchymal curves). Annet et al. developed a model that includes an additional term that accounts for the onward transport of GBCA and hence allows the whole time course to be modeled [2]. Their equation is of the form:

$$C_k(t) = k_1 c_p(t) + k_2 \cdot \int_0^t c_p(u) \cdot \exp(k_{ep}(t-u))du \qquad (5)$$

In their original article, Annet et al. confined their analysis to the renal cortex, and the term $k_{ep}$ represented the rate constant of GBCA transport out of the renal cortex and into the medulla. We apply the model to the whole kidney, and in this context, $k_{ep}$ is the rate constant of GBCA excretion from the kidney, which we refer to as the tubular output. A nonlinear fit of Eq. 5 can be applied to all points acquired after GBCA arrival, and hence, no preselection of the range of data points is required. In addition, Annet et al. modified $C_p$ by including a delay time (δ) to account for transit time from the arterial ROI to the renal parenchyma and a term to account for GBCA dispersion during this time. If only the delay term is incorporated, then $C_p(t)$ is replaced by a time-shifted plasma concentration $C_p(t\text{-}\delta)$. Because the transit times are exponentially distributed [31], the dispersion term can be expressed as a convolution of the time-shifted plasma concentration with the mean transit time of the plasma compartment ($MTT_p$) [2, 32]. The plasma concentration corrected for delay and dispersion ($C_p'$) is given by:

$$C_p'(t) = C_p(t-\delta) \otimes \frac{1}{MTT_p} \exp\left(\frac{-t}{MTT_p}\right) \qquad (6)$$

The vascular contribution is determined primarily by the aortic concentration scaled by the plasma fractional volume, and if dispersion is not accounted for, then an artificially low plasma volume is often derived in order to achieve the required scaling of the arterial concentration. This results in a vascular component with a low peak and a low "tail", causing most of the rest of the renal curve to be attributed to glomerular filtration. When dispersion is accounted for, the vascular component is broader, with a more pronounced tail leading to less of the curve being attributed to glomerular filtration. Thus, accounting for dispersion is expected to result in more accurate GFR values. However, due to the less stable fitting caused by introducing the convolution and the extra terms (δ and $MTT_p$) to the fitting process, combined with the limited temporal resolution used in our studies, we do not model dispersion, using a fixed delay instead.

## GFR Index

The majority of studies assessing the accuracy of the GFR estimates derived using MRU used measurements based on multiple blood samplings as the gold standard [1, 3]. However, such measurements are not routinely performed in a clinical setting (and only tend to be acquired for small numbers of volunteers in research studies). Absolute measurement of GFR is difficult, and the only clinical measure of GFR obtained on our patients is serum creatinine. There are several well-known shortcomings of this method, but when combined with suitable corrections, a reasonable estimate of GFR can be obtained [33]. Figure 6 shows the results of comparing total GFR as estimated from serum creatinine using the Brandt-Qualls formula, with the combined (i.e., sum of both kidneys) Patlak slope of the two kidneys for 195 patients. As hematocrit was not measured for these patients, no hematocrit correction (Eq. 3) was performed. For the correlation plot, the relationship can be seen to be linear to a good approximation, but with the Patlak values being lower than the Brandt-Qualls values. The Bland-Altman plot shows both offset (−6.6 ml/min) due to GFR underestimation by the Patlak techniques, and the 95% confidence intervals (CI) (±10.1 ml/min). Because of these fairly wide confidence limits and the presence of a number of outliers, it seems reasonable to use the functional measurements as an index, rather than an absolute measure, of GFR. We and others [30] found that the linear and nonlinear Patlak techniques produce similar GFR index values. We prefer to use the

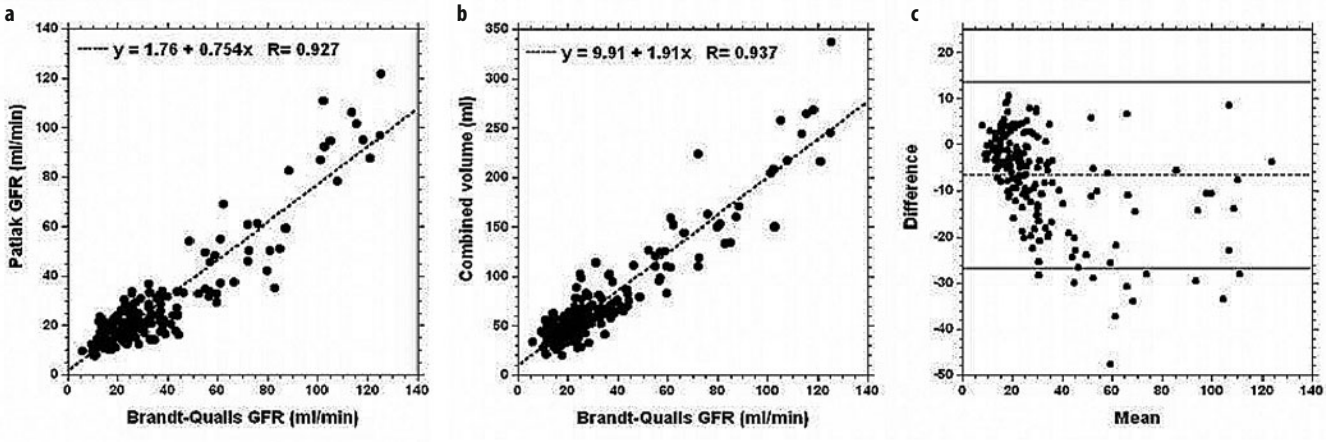


**Fig. 6 a-c.** **a** Correlation plot of glomerular filtration rate (GFR) values derived from serum creatinine values using the Brant-Qualls method, and GFR index calculated using the Patlak method. **b** Correlation of GFR values derived from serum creatinine values using the Brant-Qualls method and total (sum of both kidneys) segmented renal volume. **c** Bland-Altman plot of data shown in **a**. *Lines* represent mean (−6.56) and 95% confidence limits

nonlinear technique, as it requires choosing only an end time point, rather than start and end time points, and it uses more points. The Annet model produces systematically higher values for the GFR index in our implementation. Figure 6 also shows that there is a reasonable correlation between total renal volume (i.e., sum of the volume of both kidneys) and GFR.

## Differential Renal Function

The differential renal function (DRF) is widely used in nuclear medicine and simply expresses the results of functional measurements for each kidney as a percentage of total function (i.e., sum of both kidneys). Despite the obvious shortcomings, which include the assumption of a normal contralateral kidney as a reference and hence neglects the effect of compensatory changes in the contralateral kidney, the DRF is very useful clinically, as it removes the effect of the main source of error in the functional calculation, the AIF [19]. As the AIF is common to both kidneys, any distortion of the AIF will equally affect both kidneys. We routinely calculate the DRF in terms of:

- Volumetric DRF (vDRF)
- Patlak DRF of the whole kidney (pDRF)
- Unit Patlak per milliliter of tissue (upDRF)
- Rate constant of tubular output derived from the Annet model (toDRF).

The vDRF is simply the relative volume of enhancing renal parenchyma above a user-defined threshold and is considered to represent the functioning renal mass. The volume is calculated at the last time point prior to contrast being first excreted into the calyces, and the time point is independently selected for each kidney. pDRF is calculated using the SK-GFR estimate derived by combining the Patlak slope and kidney volume. However, as the volume is also correlated with GFR (Fig. 6), it is useful to calculate also a Patlak DRF based on the upDRF estimate, as this removes the volume effect and provides insight into the kidney workload. The vDRF appears to be relatively stable, whereas the pDRF changes in response to acute alterations in GFR.

## Transit Times

Two other parameters, renal transit time (RTT) and calyceal transit times (CTT), are derived manually from the images by the radiologist. RTT is defined as the time it takes for the contrast agent to pass from the renal cortex to the proximal ureters [34]. We previously used RTT to broadly classify renal drainage into obstructed, nonobstructed, and equivocal categories [34]. Our experience with RTT emphasizes that obstruction represents a spectrum of impairment to urinary flow and that drainage into the ureter is largely determined by UPJ anatomy. Interpreting drainage times is influenced by the ureteric insertion into the renal pelvis; in many cases, a delayed RTT may simply reflect stasis with resultant fluid levels within the renal pelvis, and if the child is turned prone, rapid drainage occurs. When there is significant loss of renal parenchyma and little urine is being produced, calculating RTT is of limited value in evaluating the presence of underlying obstruction. RTT in the normal range ($\leqslant$240 s) demonstrates that no significant obstruction is present. CTT is defined as the time it takes for the contrast agent to pass from the renal cortex to its first appearance in the collecting system. CTT seems to be determined by both GFR and tubular function. CTT is most useful when the contralateral kidney is normal and we can classify it as symmetric, delayed, or rapid on the hydronephrotic side. If CTT is symmetric, it usually indicates that the system remains compensated during the diuretic challenge. If CTT is delayed, it suggests an acute decrease in GFR and increased urine reabsorption by renal tubules in response to increased intrapelvic pressure. Rapid CTT is most often seen in patients with concentration defects, although we have seen several cases that are thought to be related to glomerular hyperfiltration.

### Evaluation of Hydronephrosis and Obstructive Uropathy

Hydronephrosis is the most common indication for MRU in infants and children [35]. Some degree of dilation of the renal pelvis is found in ~2% of all maternal US scans, and 0.2% have a significant urological problem, with approximately half of these being UPJ obstructions [36]. Approximately two thirds of these cases are confirmed on postpartum US scans. UPJ obstruction is defined as impaired urine flow from the renal pelvis into the proximal ureter and is the most common cause of neonatal hydronephrosis [35]. In patients in whom persistent hydronephrosis is demonstrated on postpartum US, the most commonly ordered radiological examinations are a voiding cystourethrogram (VCUG) and a nuclear renogram. As a spectrum of obstruction degree is found, a diagnosis of obstructed/unobstructed is not possible. Rather, it is necessary to attempt to determine whether the degree of obstruction will lead to either a loss of renal function in the future or, in the case of children, limit future kidney development.

Obstructive uropathy occurs in a subset of children with hydronephrosis and refers to obstruction of urine flow from the kidney to the bladder resulting in injury to the kidney [37]. Urinary tract obstruction is difficult to define clinically in children. Kidney damage is not simply a result of mechanical impairment of urine flow but occurs secondarily to a complex syndrome caused by the interaction of a variety of vasoactive factors and cytokines leading to alterations of both glomerular hemodynamics and tubular function [38]. In evaluating hydronephrotic systems with MRU, we analyze both anatomic and physiologic information to try to determine whether obstruction is present, evaluate its severity, and identify its location and – if possible – its cause.

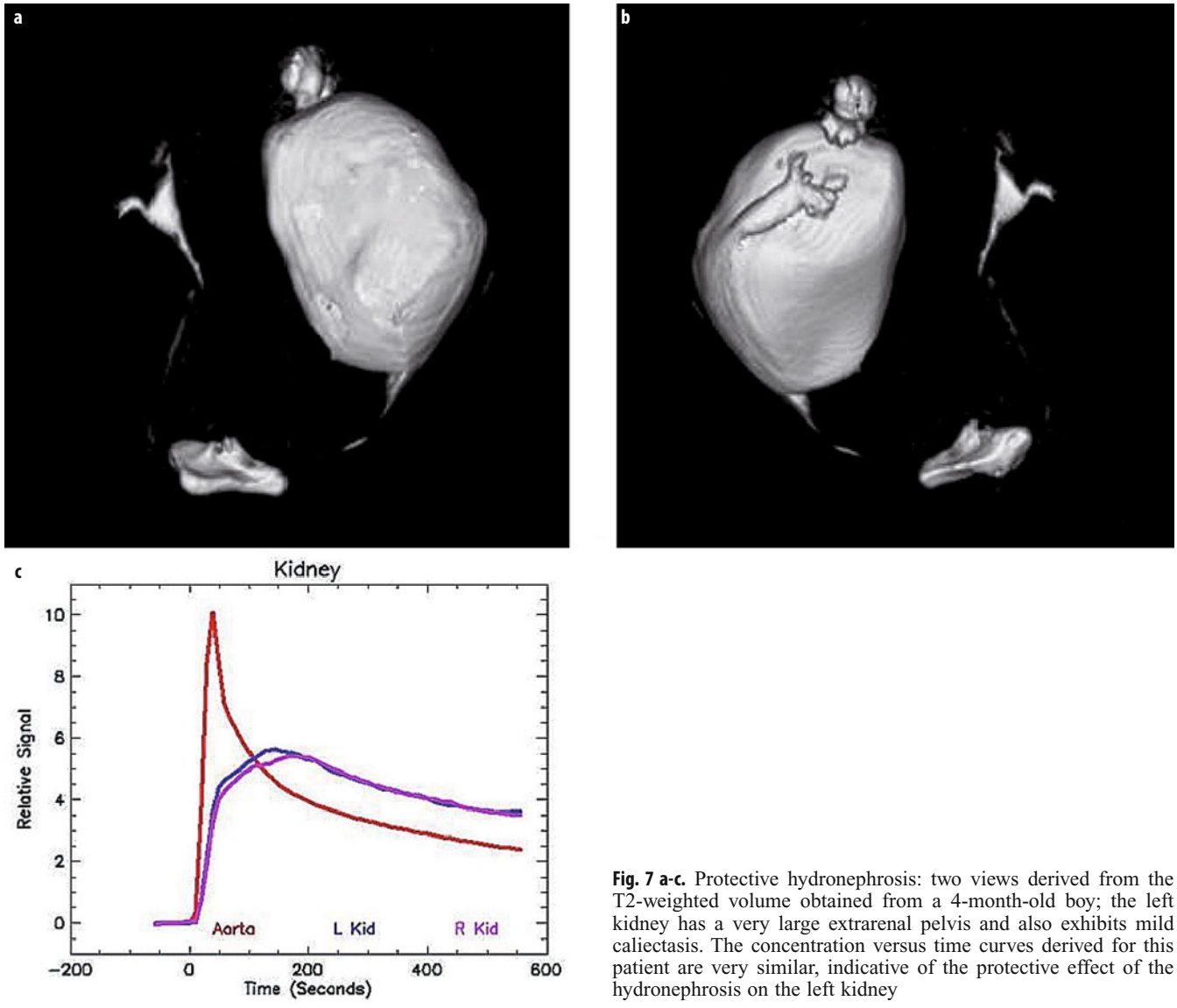


**Fig. 7 a-c.** Protective hydronephrosis: two views derived from the T2-weighted volume obtained from a 4-month-old boy; the left kidney has a very large extrarenal pelvis and also exhibits mild caliectasis. The concentration versus time curves derived for this patient are very similar, indicative of the protective effect of the hydronephrosis on the left kidney

We typically see hydronephrosis in two distinct populations: infants and young children diagnosed with antenatal hydronephrosis, and older children who present because they are symptomatic with abdominal pain, urinary tract infection (UTI), or hematuria. The effects of obstruction on the developing kidney depend on time of onset, location, and degree of obstruction [38]. Ureteral obstruction early in gestation results in dysplasia and a reduction in the number of nephrons. Most experts advocate primary conservative management for infants with hydronephrosis with close follow-up, and recommend surgery only if there is evidence of decreased renal function or progressive hydronephrosis [39, 40]. Typically, between 25% and 50% of children with antenatal hydronephrosis ultimately require surgery [41, 42]. It is important to understand that in children, obstruction is usually both chronic and partial. Partial obstruction results in equilibrium between urine production, impaired outflow, and pelvic reservoir capacity [43]. A steady state is reached between the amount of urine produced and the volume of the renal pelvis, so that pressure in the renal pelvis is in the normal range. Koff elegantly shows that hydronephrosis is a protective measure against increases in pressure [43] and that chronic partially obstructed kidneys typically have normal or low pressure within the renal pelvis and collecting system (Fig. 7). Glomerular filtration depends on the difference in hydrostatic pressure between the glomerulus and Bowman's space. This dynamic balance may be upset during diuresis or when the obstruction is exacerbated, as is seen with a ureteric kink. The loss of balance may result in transient increase in pelvic pressure. It is unclear whether frequency, duration, or severity of these transitory elevations in renal pelvic pressure is responsible for renal damage and progressive loss of renal function.

### Pathophysiology of Acute or Chronic Urinary Tract Obstruction: Compensated versus Decompensated Hydronephrosis

One of the key strengths of MRU in evaluating hydronephrosis and obstructive uropathy is its ability to dynamically assess signal intensity changes occurring within the renal parenchyma after contrast administration: i.e., we can rapidly evaluate changes in the MR nephrogram produced by perfusion, filtration, and concentration of the contrast agent. We are able to focus on pathophysiologic changes in the kidney itself as opposed to a simple evaluation of renal drainage. With MRU, the hydronephrotic kidney is subjected to both a fluid and diuretic challenge prior to contrast administration. How the kidney responds to this challenge determines MR nephrogram appearance. One concept that has been most helpful for us when analyzing MRU is to define subcategories within the general category of hydronephrosis. In particular, we developed criteria for defining compensated and decompensated systems (Fig. 8; Table 1). If there are symmetric changes in signal intensity of the nephrogram, we classify it as a compensated hydronephrotic system – the fluid challenge has been accommodated without increasing the pressure in the pelvicalyceal system. However, when signal intensity changes are asymmetric, they most often indicate acute or chronic obstruction – the fluid challenge has exceeded the capacity for renal drainage, and the pressure in the collecting system rises. These we classify as decompensated hydronephrotic systems. Near-normal renal blood flow, glomerular filtration, and tubular function are required to develop an obstructive nephrogram, and so findings of decompensation usually indicate significant recoverability of renal function. Signs associated with decompensation

**Table 1.** Compensated versus decompensated hydronephrosis

| SMRU findings | Compensated | Decompensated |
|---|---|---|
| Parenchyma on T2 | Normal | Edema |
| CTT | Symmetric, rapid | Delayed |
| MR Nephrogram | Normal | Delayed and dense |
| vDRF – pDRF | <4% | >4% |
| RTT | Delayed | Delayed |

*MRU* magnetic resonance urography, *CTT* calyceal transit times, *vDRF* volumetric differential renal function, *pDRF* Patlak differential renal function, *RTT* renal transit time

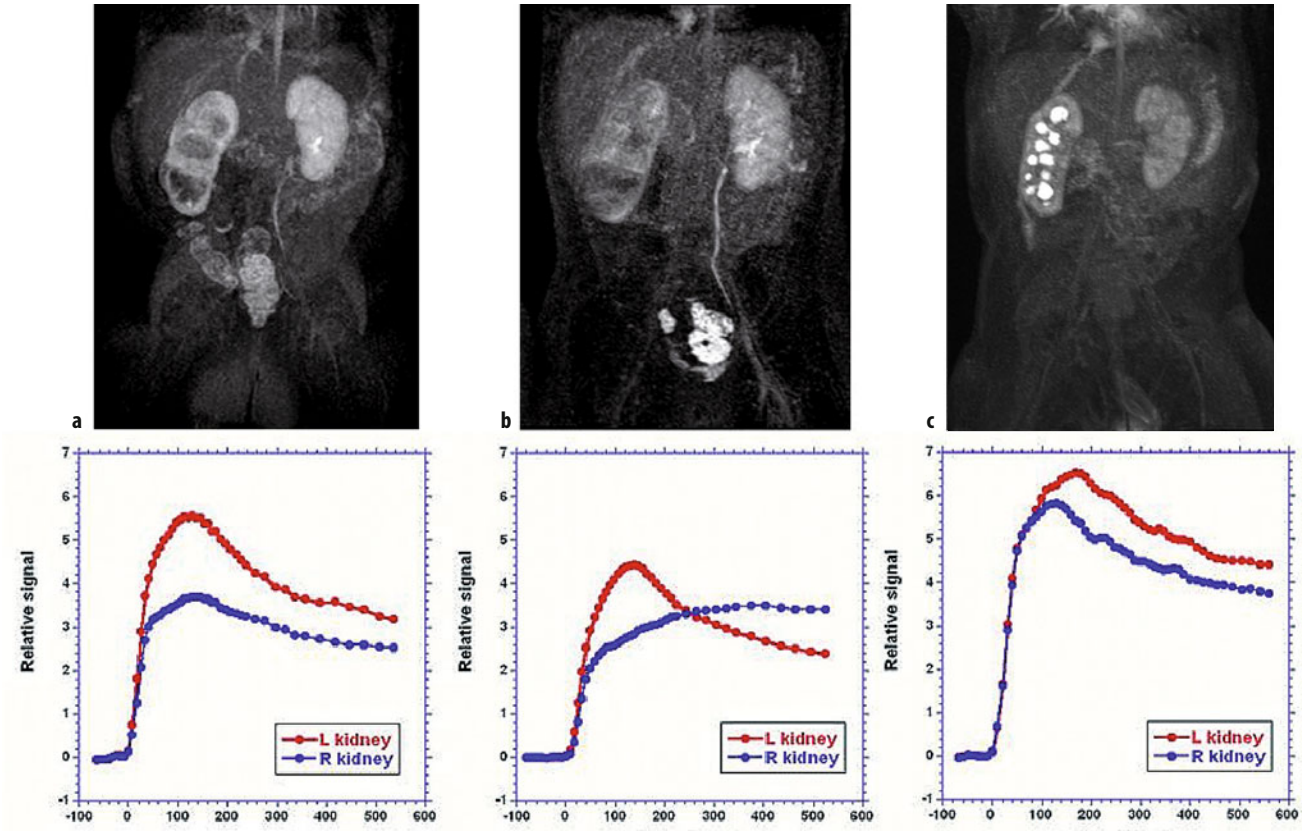


**Fig. 8 a-c.** Three scans performed on a female patient at the ages of 12, 22 and 40 months, respectively, with a pyeloplasty having been performed before the last scan. For each scan a MIP of the delayed, contrast enhanced, T1 weighted volume and the concentration versus time curves are shown. The first preoperative scan shows a compensated hyronephrotic system with rapid excretion of contrast into the right pelvicalyceal system with the signal intensity curve showing a concentration defect. The second preoperative scan then showed a decompensated system with a delayed nephrogram on the right. The signal intensity curve shows an obstructive pattern. Following the pyeloplasty, once again there is rapid excretion of contrast into the collecting system and the curves for the two kidneys are similar, but with a mild concentration defect on the right. These findings indicate that the physiologically significant obstruction resolved following pyeloplasty

include parenchymal edema on T2-weighted images, delayed calyceal transit time, delayed and increasingly dense nephrogram, and asymmetry in upDRF and toDRF values. These changes can also be used to grade obstruction severity and may coexist with anatomical abnormalities.

## Anatomic Evaluation

Anatomic information includes hydronephrosis grading, identifying transition in ureter caliber, evaluating underlying causes such as kinks, strictures, or crossing vessels, and morphologic assessment of renal parenchyma quality. We use both T2-weighted and delayed postcontrast images to define the pelvicalyceal and ureteric anatomy. T2-weighted images are particularly helpful in children with severe hydronephrosis and/or poorly functioning systems. Volumetric T2 and postcontrast images can be used to generate exquisite VR images of the pelvicalyceal systems and ureters. We grade the degree of hydronephrosis as mild, moderate, or severe, as opposed to the Society for Fetal Urology classification, which emphasizes calyceal dilatation as a discriminating factor [44]. Changes in ureteric caliber are useful indicators of the level of obstruction that most commonly occur at the UPJ, followed by vesicoureteric junction, and, rarely, midureter. UPJ obstruction may be idiopathic, a neuromuscular defect at the ureteropelvic junction, or associated with abnormalities such as aberrant lower-pole vessels, kinks, adhesions, or abnormal angulations. The vascular phase of the DCE series is used to identify crossing vessels that may be associated with UPJ obstruction [11].

Renal parenchyma quality is assessed both on high-resolution T2-weighted images and during the parenchymal phase of the nephrogram. We typically categorize the renal parenchyma as normal, uropathic, or edematous. With MRU, signs to suggest underlying uropathy and permanent damage on T2-weighted images include architectural disorganization with loss of the corticomedullary differentiation, small subcortical cysts, and low cortical T2 signal intensity (Fig. 2). The nephrogram in these cases usually shows dim and patchy contrast enhancement, reflecting damage to the microvasculature as well as glomeruli and tubules. These imaging findings probably reflect the histologic changes of renal damage based on reduced glomerular number, glomerular hyalinization, cortical cysts, and interstitial inflammation and fibrosis [45]. In contrast to uropathic kidneys, the edematous kidney typically shows increased signal intensity on T2-weighted images, as well as a delayed dense nephrogram. In our experience, the edematous pattern is almost always seen in decompensated hydronephrosis. These two patterns have different prognostic implications: little improvement in renal function can be expected following pyeloplasty in uropathic kidneys, but significant improvement is seen in decompensated systems [46].

## Functional Evaluation

### Differential Renal Function

Calculating DRF by renal scintigraphy is one of the key determinants in the decision of when to operate in children with hydronephrosis. With MRU, DRF is calculated on the basis of a number of parameters, as described earlier. The vDRF represents the functioning renal mass. As a threshold is used for segmenting the kidneys, vDRF tends to underestimate function of very poorly enhancing kidneys. The same renal segmentation is used to calculate Patlak index, and hence, pDRF also tends to underestimate the function of very poorly functioning kidneys. In this context, upDRF is generally a more useful parameter, as it is independent of renal volume. In decompensated systems, there tends to be a significant amount of asymmetry in upDRF, with the asymmetry being more pronounced in severely decompensated systems. Similarly, as the onward transport of the contrast is slow, as evidenced by the delayed peak in the time-intensity curve, to DRF also exhibits a marked asymmetry in decompensated systems.

With MRU, we can now diagnose compensated and decompensated hydronephrotic systems and identify uropathic changes. This classification has prognostic implications: following a technically successful pyeloplasty, there is little change in function for compensated UPJs, improvement in both volumetric and Patlak DRF in decompensated UPJs, and generalized loss of function in uropathic kidneys. Further study is required to fully understand the prognostic implications of this classification.

## Reflux Nephropathy and Renal Dysplasia

For the last 40 years, nephrologists, urologists, pediatricians, and radiologists have focused a great deal of attention on the relationship between VUR, pyelonephritis, and renal damage, with the aim of developing techniques to detect and therapies to prevent recurrent UTI and renal damage. The underlying rationale was that this approach would decrease the number of children who develop complications, such as hypertension and end-stage renal disease. However, the perceived relationship among these entities remains the source of much confusion and contentious debate, and recent literature is replete with conflicting data. One of the fundamental flaws underpinning our understanding of these diseases is the imperfect characterization of lesions in vivo because of limitations in imaging techniques. This has been compounded by the fact that no controlled study of VUR that includes a no-treatment arm has been performed.

The term reflux nephropathy was coined in 1973 by Bailey to describe the relationship between VUR, pyelonephritis, and renal damage [47]. The initial descriptions were based on intravenous urography (IVU), and the classic lesion demonstrated cortical contour deformity associated with a clubbed calyx, indicating transmantle parenchymal

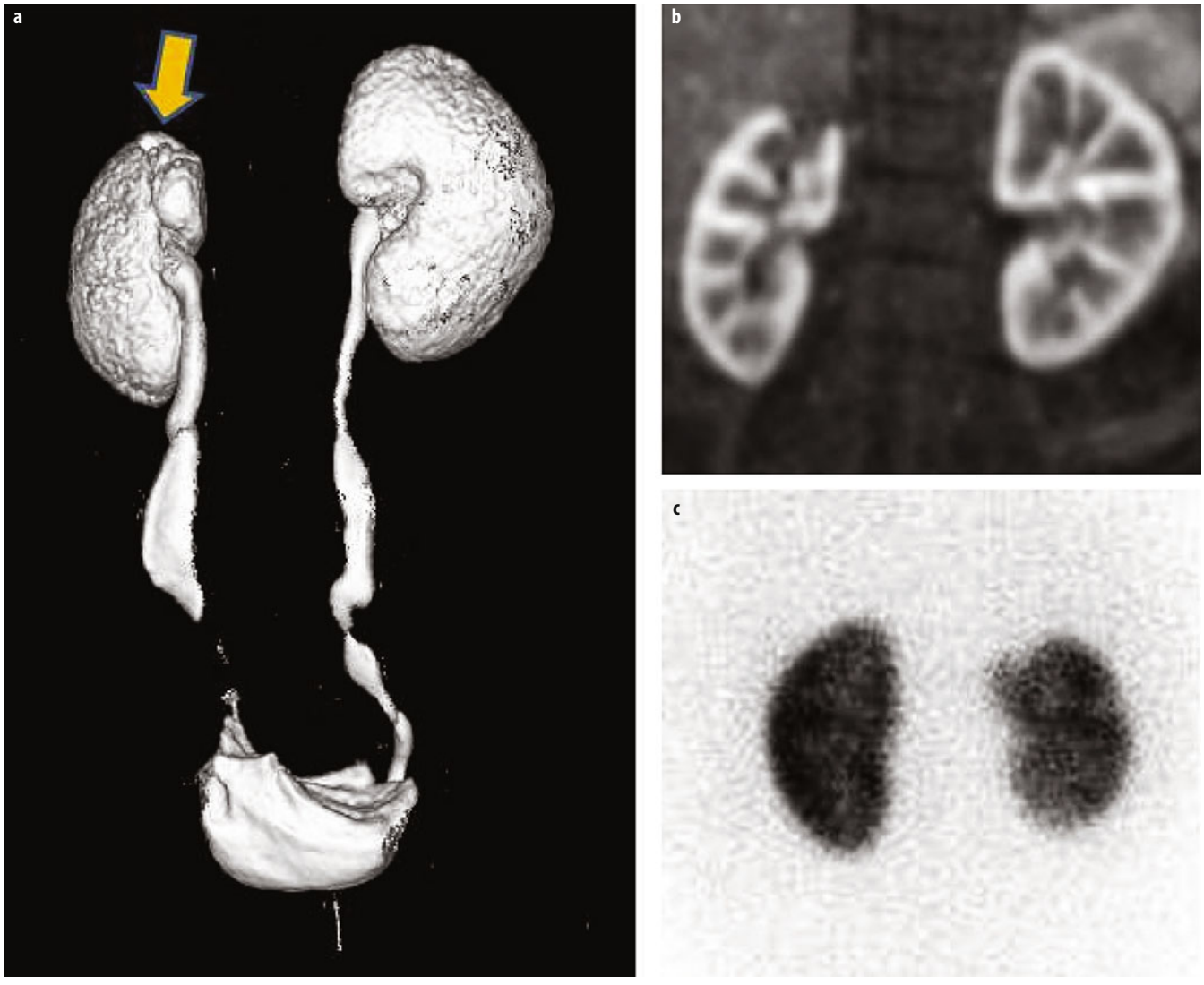


**Fig. 9 a-c.** Cortical renal scarring. The right kidney has a scar in the upper part of the kidney which is clearly seen on the maximum intensity projection (MIP) derived from the delayed, T1-weighted volume (*arrow*) (**a**) and on the arterial phase MR images (**b**). For comparison a nuclear medicine dimercaptosuccinate (DMSA) study is shown (**c**); this image follows the nuclear medicine convention which corresponds to a posterior view and hence the scarred kidney is now on the reader's right

loss. In most cases, scarring was established at initial diagnosis, new scars were rare, and – in some cases – the children progressed to renal failure despite aggressive treatment. Over time, it became apparent that children with VUR could be divided into two groups [48]: the first group has dilating VUR, typically presents with antenatal hydronephrosis, and up to 30% have defects on dimercaptosuccinate (DMSA) scan, even in the absence of a UTI. This group is almost entirely comprised of boys and makes up the majority of cases that proceed to end-stage renal disease [49]. The second group has VUR diagnosed after presenting with UTI. This group is predominantly girls, and renal damage is determined by a combination of factors: virulence of the organism, patient age, host inflammatory reactions, treatment delay, and genetic susceptibility.

MRU is able to identify the acquired segmental scars most often associated with VUR and infection in older girls (Fig. 9). The cortical scars seen in this group are identical to those seen in children who have developed pyelonephritis in the absence of VUR. These scars are characterized by volume loss and a contour defect of the kidney on T2-weighted images, perfusion defects on dynamic contrast-enhanced images, and exhibit dilatation of the adjacent calyx, indicating transmural parenchymal loss – i.e., the typical pyelonephritic scar of reflux nephropathy. Affected regions demonstrate no appreciable contrast enhancement. When scarring is diffuse, there is significant loss of renal function and renal reserve.

Renal damage is also seen in infants evaluated for antenatal hydronephrosis on renal scintigraphy, even in the absence of infection [50]. Renal damage detected by scintigraphy in infants with no demonstrable UTI is termed congenital reflux nephropathy [51]. Its appearance is peculiar because it is usually characterized by

generalized parenchymal loss, although there are cases of focal scarring [51]. MRU performed in children with antenatal hydronephrosis and VUR usually demonstrates a small kidney on the side with VUR. The affected kidney may have either a smooth appearance or may show focal cortical loss. Occasionally, the affected kidney is markedly hypoplastic and contains extensive focal scarring. It remains controversial whether these congenital renal abnormalities are due to poor nephrogenic differentiation of a congenital origin or from the backpressure effect on the developing fetal kidney from refluxed urine. Because MRU provides superior definition of anatomic and morphologic abnormalities, it enables more precise and accurate characterization of these congenital lesions. Thus, MRU has an important potential role because it can subdivide what was previously regarded as homogeneous patient groups into several subcategories, allowing a more precise identification of children at risk for progressive renal damage, as well as guiding and monitoring treatment aimed at preserving renal function in these children.

The diagnosis of renal dysplasia is based on histological identification of primitive tubules surrounded by stroma, smooth muscle collars, metaplastic cartilage, dysmorphic nerves, and vessels and erythropoietic cells [52]. It is a descriptive term of a heterogeneous group of disorders with diverse etiologies and represents one of the most common causes of end-stage renal disease in children. However, because the diagnosis is made only after biopsy, nephrectomy, or autopsy, there is no practical or clinically useful classification [52].

There are two main theories regarding dysplasia: it is thought to occur either as a result of failure of primary ureteric bud interaction with the metanephric mesenchyme, or as being secondary to obstruction [38]. The appearance of dysplasia secondary to obstruction is thought to be related to both timing and severity of the obstruction. The various forms of renal dysplasia include multicystic dysplastic kidney (MCDK), cystic obstructive dysplasia, hypodysplasia, and solid renal dysplasias. Experience gained in the course of our clinical studies with MRI leads us to believe that renal dysplasia can be categorized using MRU and that a combination of morphologic and dynamic data can be used to develop parameters that identify renal dysplasia based on anatomical and functional criteria. One problem is that typically biopsies are not obtained for these patients, so a histological confirmation of dysplasia is not available. This parallels the situation in characterizing cerebral cortical dysplasia with MRI, in which a system was developed to allow clinicians to classify their patients despite little histological data being available [53]. This imaging-based classification of cerebral dysplasia exists in parallel with classifications based on pathology or genetic material and is now widely used to classify MRI findings.

## Congenital Malformations and Renal Dysplasia

Anomalies of renal position and rotation are well demonstrated with MRU. Horseshoe and ectopic kidneys can be easily separated from the background and overlying tissues (Fig. 10). Pelvic kidneys, in particular, are well

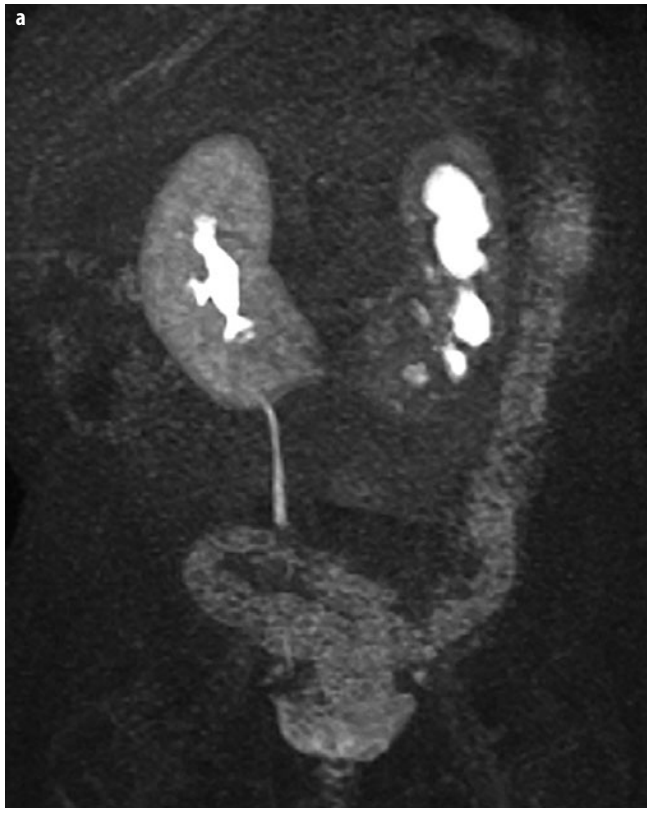


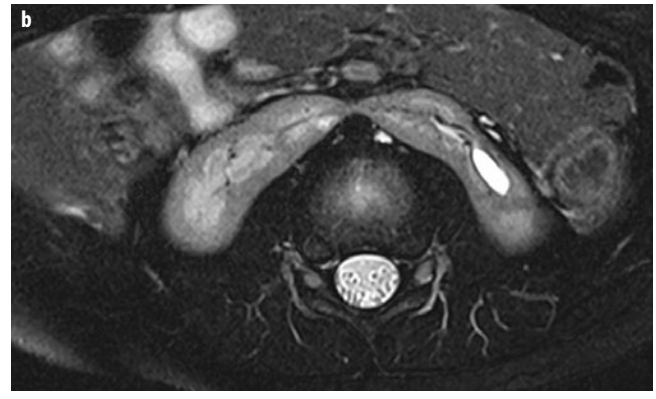


**Fig. 10 a, b.** A 5 year old boy with horseshoe kidney (**a**), demonstrating the abnormal orientation of the kidneys with an isthmus connecting the lower poles (**b**)

demonstrated with MRU. These ectopic kidneys are often significantly smaller than the normally positioned kidney. Hypoplastic kidneys associated with ureteric ectopia and supernumerary kidneys, which have been difficult to demonstrate with other imaging modalities, can usually be demonstrated even if there is minimal renal function. As described earlier, renal dysplasia is traditionally based on histological identification of undifferentiated mesenchyme, such as cartilage and immature tubules. However, we believe that MRU can be used to develop a classification that will allow these malformations to be studied, and categorized, in vivo. Typical imaging features associated with dysplastic kidneys include small size, disorganized architecture with loss of normal corticomedullary differentiation, small subcortical cysts, decrease in signal intensity on T2-weighted images, poor perfusion, dim and patchy nephrogram with minimal excretion on dynamic contrast-enhanced images, and dysmorphic calyces. These are similar to the features we previously described as representing uropathy in children with antenatally diagnosed UPJ obstruction. In many cases, additional clues for underlying malformations are seen with MRU, including small renal size and anomalous calyceal development. Anomalous calyceal development is better defined on MRU than on other imaging studies and includes decreased number of calyces as well as dysmorphic, malrotated, and blunted calyces. Calyceal anatomy is best demonstrated on 3D VR images. Calyces develop from the ureteric bud in a complex process of growth, branching, and remodeling termed branching morphogenesis [54]. Each successive division of the ureteric bud is binary to form the entire collecting system. Abnormal calyceal development is almost universally associated with small kidneys and reflects abnormal interaction between ureteric bud and metanephric mesenchyme.

## Conclusion

The ability of MRU to provide a more complete characterization of renal anatomy and physiology has provided insights into the pathophysiology of hydronephrosis as well as the complex interaction of renal development, VUR, and pyelonephritis. MRU is used to assess the response of the hydronephrotic kidney to a fluid and diuretic challenge. Although it is relatively straightforward to determine whether a system is not obstructed on the basis of RTT, no single parameter is adequate to fully characterize obstruction. MRU provides prognostic information by assessing the quality of the renal parenchyma and identifying uropathy preoperatively. MRU is capable of providing a wealth of information in evaluating obstructive uropathy that may ultimately help select patients most likely to benefit from surgical intervention and predict outcome in individual patients. We believe that renal dysplasia can be diagnosed and categorized using MRU and that a classification system will be developed that will permit patients previously assigned to the general category of reflux nephropathy to be assigned to one of several subcategories of renal dysplasia. It is important to remember that this clinical application is in its infancy and will improve significantly with further technical development.

## References


1. Hackstein N, Heckrodt J, Rau WS (2003) Measurement of single-kidney glomerular filtration rate using a contrast-enhanced dynamic gradient-echo sequence and the Rutland-Patlak plot technique. J Magn Reson Imag 18:714-725.
2. Annet L, Hermoye L, Peeters F et al (2004) Glomerular filtration rate: assessment with dynamic contrast enhanced MRI and a cortical compartment model in the rabbit kidney. J Magn Reson Imag 20:843-849.
3. Bokacheva L, Rusinek H, Zhang JL et al (2009) Estimates of glomerular filtration rate from MR renography and tracer kinetic models. J Magn Reson Imag 29:371-382.
4. Mendichovszky I, Pedersen M, Frøkiær J et al (2008) How accurate is dynamic contrast enhanced MRI in the assessment of renal glomerular filtration rate? A critical appraisal. J Magn Reson Imag 27:925-931.
5. English PJ, Testa HJ, Lawson RS et al (1987) Modified method of diuresis renography for the assessment of equivocal pelviureteric junction obstruction. Br J Urol 59:10-14.
6. Brown SC, Upsdell SM, O'Reilly PH (1992) The importance of renal function in the interpretation of diuresis renography. Br J Urol 69:121-125.
7. Vivier PH, Dolores M, Taylor M et al. MR urography in children. Part 1: how we do the F0 technique. Ped Radiol (in-press).
8. Rohrschneider WK, Hoffend J, Becker K et al (2000) Combined static-dynamic MR urography for the simultaneous evaluation of morphology and function in urinary tract obstruction. I. Evaluation of the normal status in an animal model. Pediatr Radiol 30:511-522.
9. Rohrschneider WK, Becker K, Hoffend J et al (2000) Combined static-dynamic MR urography for the simultaneous evaluation of morphology and function in urinary tract obstruction. II. Findings in experimentally induced ureteric stenosis. Pediatr Radiol 30:523-532.
10. Giesel FL, Von Tengg-Koblig H, Wilkinson ID et al (2006) Influence of human serum albumin on longitudinal and transverse relaxation rates (R1 and R2) of magnetic resonance contrast agents. Invest Radiol 41:222-228.
11. Mitterberger M, Pinggera GM, Neururer R et al (2008) Comparison of contrast enhanced colour Doppler imaging (CDI), computed tomography (CT) and magnetic resonance imaging (MRI) for the detection of crossing vessels in patients with ureteropelvic junction obstruction (UPJO). Eur Urol 53:1254-1262.
12. Jones RA, Schmotzer B, Little S, Grattan-Smith JD (2008) MRU post-processing. Ped Radiol 38(Suppl. 1):S18-27.
13. Rusinek H, Boykov Y, Kaur M et al (2007) Performance of an automated segmentation algorithm for 3D MR renography. Magn Reson Med 57:1159-1167.
14. Jones RA, Easley K, Little SB et al (2005) Dynamic contrast-enhanced MR urography in the evaluation of pediatric hydronephrosis: Part 1, Functional assessment. AJR Am J Roentgenol 185:1598-1607.
15. Parker GJM, Padhani AR (2004) T1-W DCE MRI: T1 weighted dynamic contrast enhanced MRI. In: Toft P (Ed) Quantitative MRI of the brain, 1st edition. Wiley, Chichester, UK, pp 341-344.
16. Mørkenberg J, Taagehø JF, Væver PN et al (1998) In-vivo measurement of T1 and T2 relaxivity in the kidney cortex of the pig-based on a two compartment steady state model. Magn Reson Imag 16:933-942.

17. Yang C, Karczmar GS, Medved M et al (2009) Reproducibility assessment of a multiple reference tissue method of quantitative dynamic contrast enhanced MRI analysis. Magn Reson Med 61:851-859.
18. Zhang JL, Rusinek H, Bokacheva L et al (2009) Use of cardiac output to improve measurement of input function in quantitative dynamic contrast enhanced MRI. J Magn Reson Imag 30:656-665.
19. Pedersen M, Shi Y, Anderson P et al (2004) Quantitation of differential renal blood flow and renal function using dynamic contrast-enhanced MRI in rats. Magn Reson Med 51:510-517.
20. Madsen MT (1992) A simplified formulation of the gamma variate function. Phys Med Biol 37:1597-1600.
21. Weinmann HJ, Laniado M, Mutzel W (1984) Pharmacokinetics of Gd-DTPA/dimeglumine after intraveneous injection into healthy volunteers. Physiol Chem Phys Med 16:167-172.
22. Wedeking P, Eaton S, Covell D et al (1990) Pharmokinetic analysis of blood distribution of intraveneously administered 153-Gd labeled Gd(DTPA)2 and 99M-Tc(DTPA) in rats. Magn Reson Imag 8:567-575.
23. Hosfield MA, Thornton JS, Gill A et al (2009) A functional form for injected MRI Gd-chelate contrast agent concentration incorporating recirculation, extravasation and excretion. Phys Med Biol 54:2933-2949.
24. Krier JD, Ritman EL, Bajzer Z et al (2001) Noninvasive measurement of concurrent single-kidney perfusion, glomerular filtration, and tubular function. Am J Physiol Renal Physiol 281:F630-638.
25. Jones RA, Votaw JR, Salman K et al. MRI evaluation of renal structure and function related to disease: Technical review of image acquisition, post-processing and mathematical modeling steps. JMRI (in-press).
26. Patlak CS, Blasberg RG, Fenstermacher JD (1983) Graphical evaluation of blood-to-brain transfer constants from multiple time uptake data. J Cereb Blood Flow Metab 3:1-7.
27. Rutland MD (1979) A single injection technique for subtraction of blood background in 131I-hippuran renograms. Br J Radiol 52:34-137.
28. Peters AM (1994) Graphical analysis of dynamic data: the Patlak-Rutland plot. Nucl Med Commun15:669-672.
29. Hackstein N, Kooijman H, Tomaselli S, Rau WS (2005) Glomerular filtration rate measured using the Patlak plot technique and contrast-enhanced dynamic MRI with different amounts of gadolinium-DTPA. J Magn Reson Imag 22:406-414.
30. Buckley DL, Shurrab A, Cheung CM (2006) Measurement of single kidney function using dynamic contrast enhanced MRI: Comparison of two models in human subjects. J Magn Reson Imag 24:1117-1123.
31. Lassen NA, Perl WP (1979) Tracer kinetic methods in medical physiology. Raven Press, New York, NY.
32. Sourbron, SP, Michaely HJ, Reiser MF, Schoenberg SO (2008) MRI-measurement of perfusion and glomerular filtration in the human kidney with a separable compartment model. Invest Radiol 43:40-48.
33. Brandt JR, Wong CS, Hanrahan JD et al (2006) Estimating absolute glomerular filtration rate in children. Ped Nephrol 21:1865-1872.
34. Jones RA, Perez-Brayfield MR, Kirsch AJ, Grattan-Smith JD (2004) Renal transit time with MR urography in children. Radiology 233:41-50.
37. O'Reilly PH. Obstructive uropathy. Q J Nucl Med 2002; 46, 295-303.
38. Peters CA (2010) Congenital urine flow impairments of the upper urinary tract : pathophysiology and experimental studies. In: Pediatric Urology. Elsevier. Philadelphia
39. Csaicsich D, Greenbaum LA, Aufricht C (2004) Upper urinary tract: when is obstruction obstruction? Curr Opin Urol 14:213-217.
40. Eskild-Jensen A, Gordon I, Piepsz A, Frokiaer J (2005) Congenital unilateral hydronephrosis: a review of the impact of diuretic renography on clinical treatment. J Urol 173:1471-1476.
41. Chertin B, Pollack A, Koulikov D, et al (2006) Conservative treatment of ureteropelvic junction obstruction in children with antenatal diagnosis of hydronephrosis: lessons learned after 16 years of follow-up. Eur Urol 49:734-738; discussion 739.
42. Ulman I, Jayanthi VR, Koff SA (2000) The long-term followup of newborns with severe unilateral hydronephrosis initially treated nonoperatively. J Urol 164:1101-1105.
43. Koff SA (1990) Pathophysiology of ureteropelvic junction obstruction. Clinical and experimental observations. Urol Clin North Am 17:263-272.
44. Fernbach SK, Maizels M, Conway JJ (1993) Ultrasound grading of hydronephrosis: introduction to the system used by the Society for Fetal Urology. Pediatr Radiol 23:478-480.
45. Elder JS, Stansbrey R, Dahms BB, Selzman AA (1995) Renal histological changes secondary to ureteropelvic junction obstruction. J Urol 154:719-722.
46. Little SB, Jones RA, Grattan-Smith JD (2008) Evaluation of UPJ obstruction before and after pyeloplasty using MR urography. Pediatr Radiol 38 Suppl 1:S106-124.
47. Bailey RR (1973) The relationship of vesico-ureteric reflux to urinary tract infection and chronic pyelonephritis-reflux nephropathy. Clin Nephrol 1:132-141.
48. Fanos V, Cataldi L (2004) Antibiotics or surgery for vesicoureteric reflux in children. Lancet 364:1720-1722.
49. Marra G, Oppezzo C, Ardissino G et al (2004) Severe vesicoureteral reflux and chronic renal failure: a condition peculiar to male gender? Data from the ItalKid Project. J Pediatr 144:677-681.
50. Greenfield SP, Wan J (2010) The diagnosis and medical management of primary vesicoureteral reflux. In: Pediatric Urology. Elsevier, Philadelphia.
51. Yeung CK, Godley ML, Dhillon HK et al (1997) The characteristics of primary vesico-ureteric reflux in male and female infants with pre-natal hydronephrosis. Br J Urol 80:319-327.
52. Woolf AS, Price KL, Scambler PJ, Winyard PJ (2004) Evolving concepts in human renal dysplasia. J Am Soc Nephrol 15:998-1007.
53. Barkovich AJ, Kuzniecky RI (1996) Neuroimaging of focal malformations of cortical development. J Clin Neurophysiol 13:481-494.
54. Costantini F (2006) Renal branching morphogenesis: concepts, questions, and recent advances. Differentiation 74:402-421.

# BREAST IMAGING SATELLITE COURSE
# “PEARL”

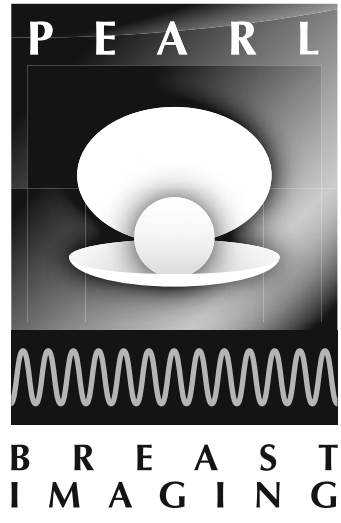

# Mammography: How to Interpret Microcalcifications

Ulrich Bick

Institut für Radiologie, CCM, Charité, Universitätsmedizin Berlin, Berlin, Germany

## Introduction

Almost half of all breast cancers are associated with calcifications on mammography; in many cases, calcifications are the only sign of breast cancer. However, calcifications may also occur in a variety of benign breast changes [1], and careful classification and interpretation of breast calcifications is the key to a correct diagnosis. It is also important to realize that a large overlap between benign and malignant calcifications exists (Fig. 1), and often, confirmation or exclusion of malignancy can only be achieved by obtaining tissue for histological analysis. There are several criteria by which benign and malignant breast calcifications can be distinguished, such as size, number, morphology, distribution, change over time, and associated findings or symptoms [2]. The Breast Imaging Reporting and Data System (BI-RADS®) Atlas of the American College of Radiology (ACR) provides an organized framework for description and classification of mammographic calcifications [3] and has found wide-spread acceptance around the world. Wherever applicable, standardized terms from the BI-RADS® lexicon are used in this manuscript. The mammography part of the BI-RADS® Atlas is available in its fourth edition, which was published in 2003 [4]. A new edition is in preparation but was not available at the time of writing.

## Artefacts and Changes Mimicking Breast Calcifications

It is important to realize that a number of artefacts, foreign material outside of breast and skin changes, may mimic suspicious breast calcifications. Typical examples

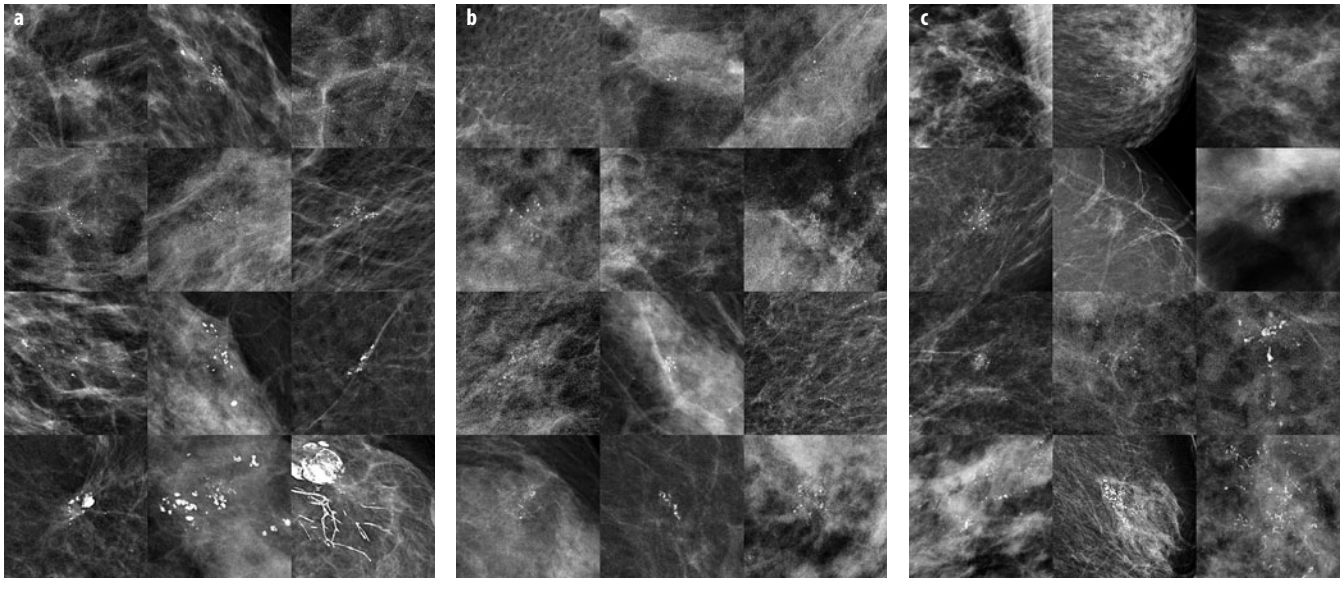


**Fig. 1 a-c.** Spectrum of histologically confirmed **a** benign and **b, c** malignant calcifications. There is a large overlap, especially between benign changes (**a**) and low-grade ductal carcinoma in situ (DISC) (**b**). **c** High-grade DCIS is more likely associated with calcifications with higher probability of malignancy

*Diseases of the Abdomen and Pelvis 2014-2017*,
DOI: 10.1007/978-88-470-5659-6_40 

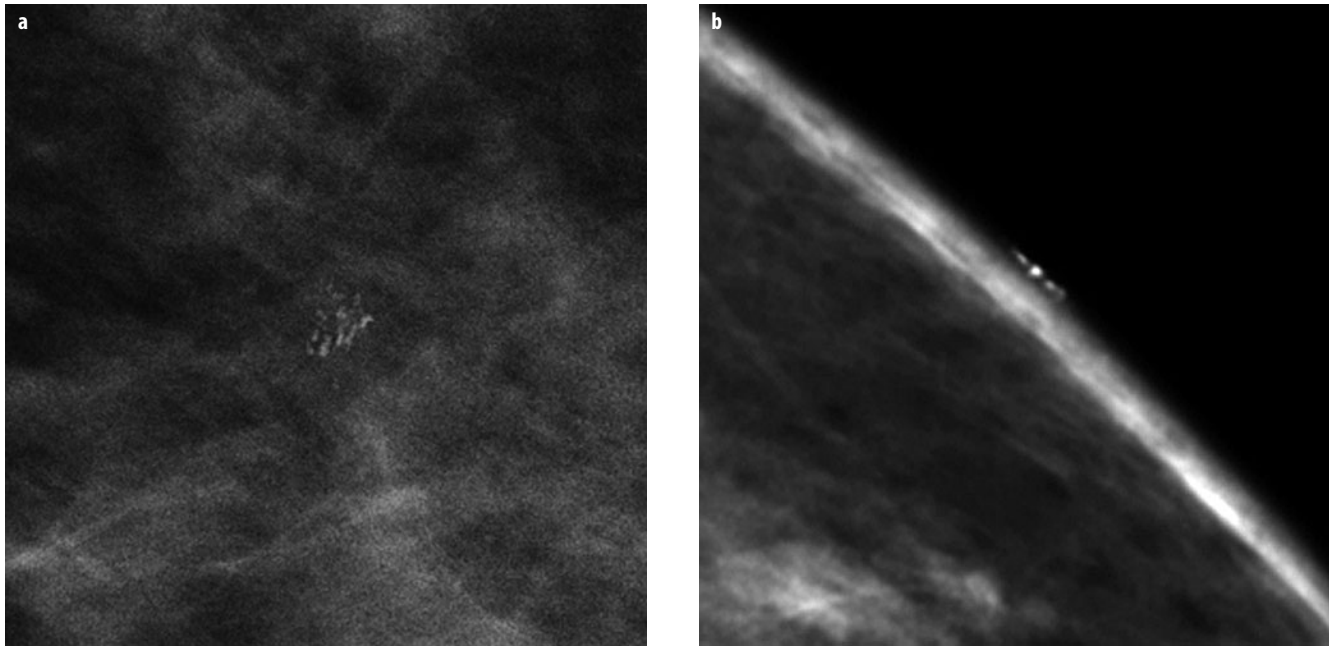


**Fig. 2 a, b.** **a** Small group of suspicious calcifications in the left breast seen on a magnification view. **b** Additional tangential view clearly demonstrates the superficial location of the calcifications on the skin surface, definitively proving their benign nature

are aluminium-based deodorants, zinc-containing skin ointments, calcifications within skin lesions (e.g., seborrheic warts) or benign calcifications within or on the surface of the skin. If it is unclear whether a calcification is actually located within the breast or on the surface, additional tangential views may be employed to demonstrate or exclude skin calcifications [5] (Fig. 2).

## Size

Oftentimes, breast calcifications are separated into larger (usually benign) macrocalcifications and smaller (possibly malignant) microcalcifications [6]. Usually, a size threshold of somewhere between 0.5 and 2 mm is used to distinguish between micro- and macrocalcifications; however, no clear guidelines for this exist [2, 7, 8]. The smallest calcifications visible on mammography have a size of ~0.1 mm [9, 10], although this will vary somewhat with the type of imaging system and parameters used as well as breast density and compressed thickness.

As histopathology is able to identify calcifications much smaller than this 0.1-mm threshold for calcification visibility on mammography, it is important for accurate radiologic-pathologic correlation to specify the size of calcifications seen on histopathology. The co-occurrence of very small microcalcifications at the mammographic detection threshold and larger calcifications within the same cluster increases the likelihood of malignancy (Fig. 3). Benign microcalcifications, e.g., in sclerosing adenosis, are more likely uniform in size.

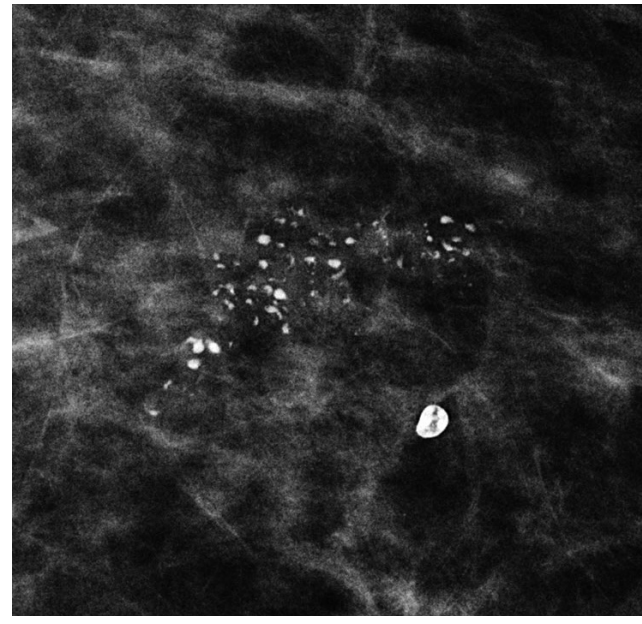

**Fig. 3.** Group of suspicious calcifications with coarse, heterogeneous morphology and varying individual sizes in a case of high-grade ductal carcinoma in situ (DCIS). In the vicinity, a typical benign macrocalcification is seen

## Number

The likelihood of calcification malignancy is strongly dependent on the number of calcifications within a certain area. Typically, a minimum of five calcifications within a cubic centimeter is considered sufficient to define a

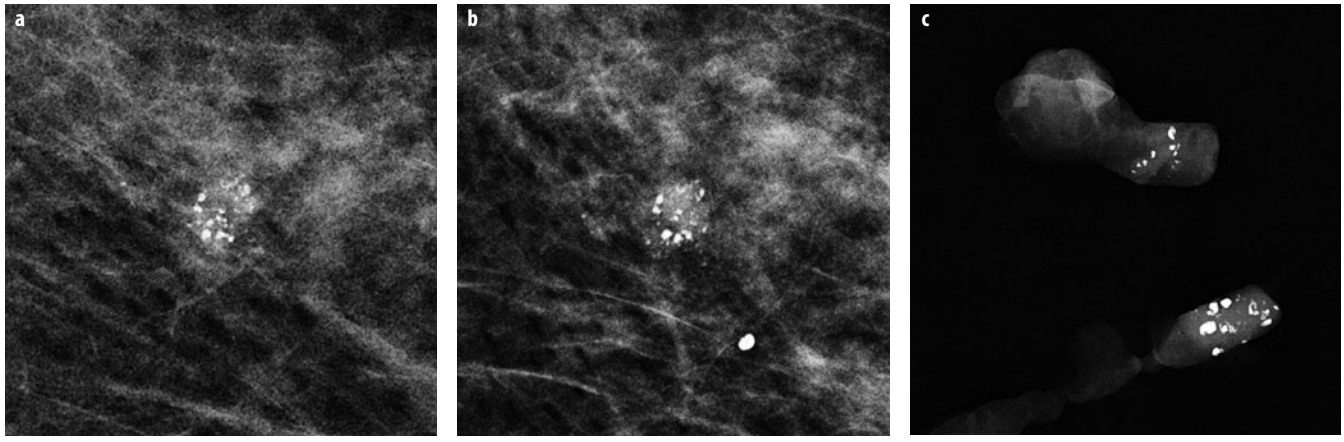


**Fig. 4 a-c.** **a** Small group of suspicious calcifications of varying size and shape detected on screening mammography. **b** On the additional magnification view, the shape of the calcifications is much better defined, and additional smaller calcifications are seen. **c** Vacuum-assisted stereotactic biopsy with specimen radiography was performed, confirming a high-grade ductal carcinoma in situ (DCIS)

group (cluster) of calcifications in which malignancy should at least be considered [8]. Individual, loosely distributed calcifications are almost always benign. Only in very rare instances may biopsy be required in diagnosing groups with fewer than five calcifications, e.g., if the individual calcifications are highly suspicious of malignancy based on morphology. The more individual calcifications are found within a group of calcifications, the higher the probability of malignancy [8]. In malignant calcifications, the magnification views will often show additional small calcifications (Fig. 4), whereas in benign cases, the number of individual calcifications in a cluster will typically be similar in the overview image as well as in the magnification view. The only exception are amorphous (powder-like) benign calcifications typically found in sclerosing adenosis, in which numerous, very small (usually at or below the detection threshold of mammography) calcifications are tightly packed within a small area. Sometimes, these are only detected on mammography because multiple overlying calcifications within the group add up to a sufficient density to be visible on mammography.

## Morphology

Calcification morphology is probably one of the strongest predictors of malignancy. Typically benign calcifications are popcorn-like coarse calcifications commonly encountered in involuting fibroadenomas; coarse foreign body (suture), or coarse dystrophic (posttraumatic) calcifications; tram-like vascular calcifications; benign, rodlike, periductal calcifications [11]; skin calcifications with lucent center; small cysts with milk-of-calcium deposits; and fat necrosis with eggshell or rim calcifications [1, 2, 8]. Round or punctate (lobular) calcifications, especially those with diffuse, bilateral distribution, are also very likely to be benign, although small, isolated clusters of round calcifications may sometimes represent malignancy and should at least be placed on short-term follow-up if not biopsied. Calcifications with high probability of malignancy that more often encountered in high-grade ductal carcinoma in situ (DCIS) (Fig. 1c) are fine pleomorphic or linear-branching calcifications [12, 13]. All other calcifications, which cannot be classified as either typically benign or highly suspicious of malignancy, are of intermediate concern. Typical examples of this category are coarse heterogeneous (Fig. 3) and amorphous (indistinct) calcifications [14]. Unless size stability over a longer period of time (usually at least 5 years) can be demonstrated, these calcifications usually require histological confirmation to exclude malignancy. Often, additional views (e.g., spot magnification, mediolateral view) are necessary to reliably categorize calcification morphology. If calcifications with different morphology are present within the same area, the decision whether to perform biopsy should be based on the most suspicious calcifications present.

## Distribution

Calcification distribution is an important factor in distinguishing between benign and malignant calcifications. Linear, segmental, clustered, and – to a lesser degree – regional distribution may indicate malignancy, whereas diffuse scattered, especially bilateral, distribution is usually, but not always, associated with benign disease [15]. Careful follow-up of cases with extensive calcifications should be performed to exclude malignancy developing within an area of preexisting benign calcifications (Fig. 5). In particular, sclerosing adenosis, columnar-cell change, and low-grade DCIS may sometimes coexist within the same area of calcifications.

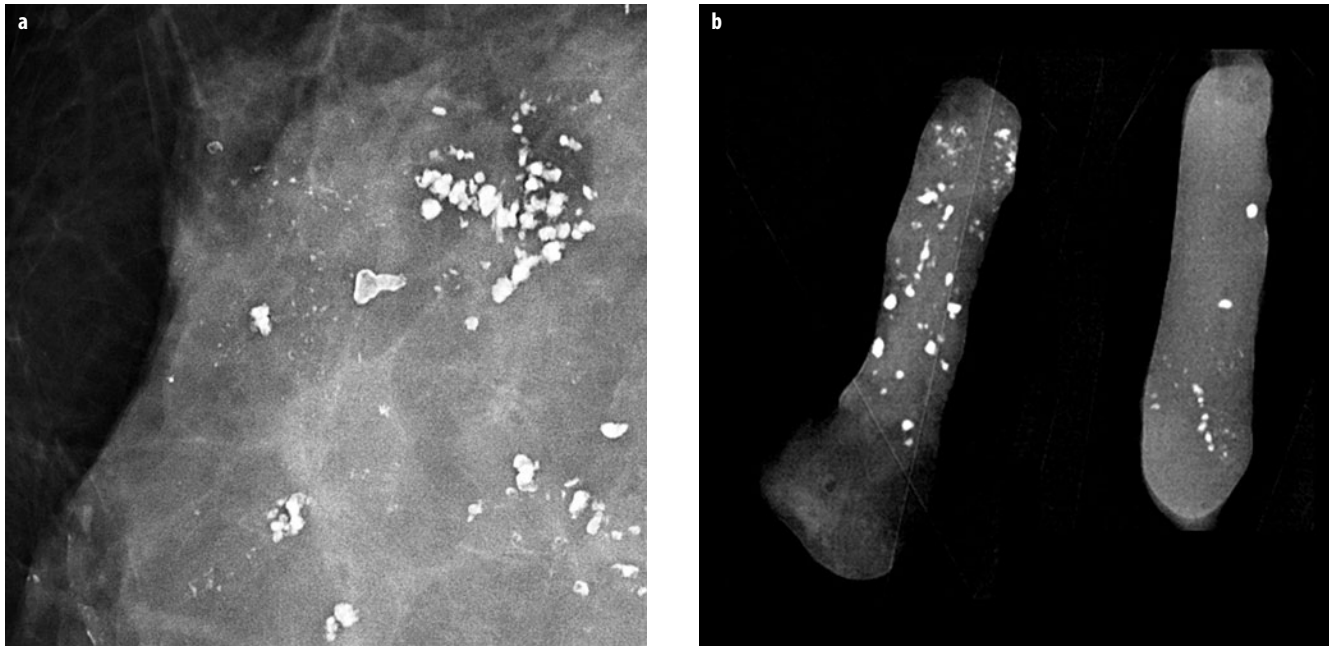


**Fig. 5 a, b.** Patient with known extensive, bilateral, coarse, dystrophic, benign calcifications. **a** In one area, additional suspicious fine pleomorphic and linear microcalcifications developed. **b** Stereotactic vacuum-assisted biopsy confirmed high-grade ductal carcinoma in situ (DCIS) with focal invasion

## Change Over Time

Interval progression of calcifications within a defined area may indicate malignancy, especially if the number of individual calcifications and the size of the involved area increase over time. If just the size of the individual existing calcifications increases but the number does not, the underlying abnormality will usually be benign (e.g., an increasingly calcified fibroadenoma or fat necrosis). Diagnostic difficulties may occur when a benign lesion such as a fibroadenoma is just beginning to calcify. In these cases, a short-term follow-up may be helpful to define more clearly the benign nature of the calcifications. Due to the sometimes very slow growth of DCIS, even documented calcification stability over a period of 2-3 years may not entirely rule out malignancy. Another potential pitfall is suspicious but stable calcifications within dense breast parenchyma, as progression of a noncalcified (invasive) tumour component may go undetected on mammography due to the surrounding dense breast parenchyma. In these cases, additional imaging such as ultrasound (US) or magnetic resonance imaging (MRI) may be beneficial.

## Associated Findings or Symptoms

The presence of suspicious calcifications, even if not reaching the threshold for biopsy itself, will significantly increase the likelihood of malignancy of other abnormalities seen on mammography (densities, asymmetries, architectural distortions) present in the same area as the calcifications. Digital breast tomosynthesis may be helpful in confirming that the calcifications and the other mammographic abnormality are truly located in the same area. In these cases, existing calcifications within the lesion may facilitate stereotactic biopsy, with the possibility of confirming the correct biopsy location through specimen radiography. If clinical symptoms such as bloody nipple discharge or palpable lump are present, and otherwise benign-appearing calcifications are the only detectable abnormality on imaging, biopsy of the calcification be considered despite the otherwise benign appearance.

## Image Quality and Technical Factors

A prerequisite for successfully detecting and characterizing calcifications on mammography is optimal image quality. Despite its nominally lower spatial resolution, digital mammography is superior for detecting small microcalcifications [16-18], especially in women with dense parenchyma. The is due to the possibility of postprocessing in digital mammography, which allows equal contrast optimization in all areas of the breast and improves the visibility of microcalcifications through tailored enhancement of small, high-frequency details in the image. However, both film-screen and digital mammography are vulnerable to motion artefacts, which may render subtle microcalcifications indistinct or invisible. In digital mammography, insufficient dose will significantly impair visibility of microcalcifications due to the higher noise

component in the image [19]. Due to the inherent limitations of contact-projection mammography, additional true geometric (air-gap) magnification views may be necessary to optimally depict microcalcifications. In digital mammography, these cannot be fully substituted for by electronic magnification (zooming) during softcopy reading [20]. Although visualization of individual, small microcalcifications may – depending on the dose applied – be slightly inferior in digital breast tomosynthesis compared with 2D projection mammography [21], the 3D nature of tomosynthesis images may provide important additional information on the spatial composition of a group of calcifications.

## Managing Suspicious Calcifications

If calcifications are found on mammography, the most important question to answer is whether histological confirmation is necessary or whether calcifications can be safely followed up. All calcifications that can clearly be placed in the typically benign category are considered a normal finding and do not even require any short-term follow-up. A short-term (e.g., 6-month) follow-up approach for calcifications may be feasible in cases with a small round cluster with only punctate or round individual calcifications [15], as they likely represent benign lobular calcifications and also in cases in which it is believed likely that the calcifications in question may develop into typically benign calcifications in a short time frame (e.g., early calcifications within an area of postsurgical or posttraumatic fat necrosis) [22]. In all other calcifications of intermediate concern, the likelihood of malignancy is above the threshold of 2%, usually considered safe for short-term follow-up, and histological confirmation should at least be considered. For determining whether to biopsy or follow-up, the individual patient's underlying breast cancer risk, age, and possible comorbidities should be taken into consideration to avoid overdiagnosis. Although the majority of highly suspicious calcifications, especially if new or increasing over time, will represent breast cancer (either in situ or invasive), these calcification should – if technically possible – always be subjected to percutaneous biopsy first to avoid unnecessary benign surgeries and to allow definitive surgical treatment if necessary, including sentinel node biopsy.

Large-gauge vacuum-assisted stereotactic biopsy has become the default biopsy approach for suspicious calcifications. Compared with standard core biopsy, both the false-negative rate as well as the underestimation rates regarding invasion are lower with large-gauge vacuum-assisted biopsy [23]. Especially for larger areas of suspicious calcifications, additional US or MRI may help to detect possible invasion and thus determine the best area for biopsy. In up to 15% of calcifications, biopsy may identify histological changes with unknown malignant potential – the so-called high-risk lesions such as atypical ductal hyperplasia (ADH), lobular neoplasia, flat epithelial atypia (FEA; also called columnar cell change with atypia), radial scar, and papilloma [24]. In these cases, repeat open-surgical biopsy may be necessary to fully exclude malignancy. The decision of whether to perform repeat open surgical biopsy or to opt for short-term follow-up should be made in a dedicated multidisciplinary conference, taking into account the size of the original mammographic abnormality and whether it was completely excised by the percutaneous biopsy [25]; whether the high-risk lesion was associated with the radiographic abnormality; or whether it represented an accidental finding on histopathology. In addition, the patient's underlying risk situation, age, comorbidities, and preferences should be taken into consideration. Although the false-negative rate of a successful large-gauge (≥11-gauge) vacuum-assisted stereotactic biopsy with representative calcification sampling is very low (<1%) [26], the possibility of undersampling has to at least be considered in large areas of calcifications, which may contain different – both benign and malignant – abnormalities within the same lesion. In these cases, careful follow-up and, if necessary, repeat biopsy should be performed.

## References


1. Tse GM, Tan PH, Pang AL et al (2008) Calcification in breast lesions: pathologists' perspective. J Clin Pathol 61:145-151.
2. Demetri-Lewis A, Slanetz PJ, Eisenberg RL (2012) Breast calcifications: the focal group. AJR Am J Roentgenol 198:W325-W343.
3. Burnside ES, Ochsner JE, Fowler KJ et al (2007) Use of microcalcification descriptors in BI-RADS 4th edition to stratify risk of malignancy. Radiology 242:388-395.
4. American College of Radiology (2003) ACR BI-RADS®. Breast Imaging and Reporting Data System, Breast Imaging Atlas. Mammography, Breast Ultrasound, Magnetic Resonance Imaging. American College of Radiology, Reston, VA.
5. Diekmann F, Diekmann S, Bick U, Hamm B (2002) Reduced-dose digital mammography of skin calcifications. AJR Am J Roentgenol 178:473-474.
6. Monsees BS (1995) Evaluation of breast microcalcifications. Radiol Clin North Am 33:1109-1121.
7. Bassett LW (1992) Mammographic analysis of calcifications. Radiol Clin North Am 30:93-105.
8. Sickles EA (1986) Breast calcifications: mammographic evaluation. Radiology 160:289-293.
9. Cowen AR, Launders JH, Jadav M, Brettle DS (1997) Visibility of microcalcifications in computed and screen-film mammography. Phys Med Biol 42:1533-1548.
10. Karssemeijer N, Frieling JTM, Hendriks JHCL (1993) Spatial resolution in digital mammography. Invest Radiol 28:413-419.
11. Graf O, Berg WA, Sickles EA (2013) Large rodlike calcifications at mammography: analysis of morphologic features. AJR Am J Roentgenol 200:299-303.
12. Hofvind S, Iversen BF, Eriksen L et al (2011) Mammographic morphology and distribution of calcifications in ductal carcinoma in situ diagnosed in organized screening. Acta Radiol 52:481-487.
13. Bent CK, Bassett LW, D'Orsi CJ, Sayre JW (2010) The positive predictive value of BI-RADS microcalcification descriptors and final assessment categories. AJR Am J Roentgenol 194:1378-1383.
14. Berg WA, Arnoldus CL, Teferra E, Bhargavan M (2001) Biopsy of amorphous breast calcifications: pathologic outcome and yield at stereotactic biopsy. Radiology 221:495-503.

15. Sickles EA (1991) Periodic mammographic follow-up of probably benign lesions: results in 3,184 consecutive cases. Radiology 179:463-468.
16. Del Turco MR, Mantellini P, Ciatto S et al (2007) Full-field digital versus screen-film mammography: comparative accuracy in concurrent screening cohorts. AJR Am J Roentgenol 189:860-866.
17. Vigeland E, Klaasen H, Klingen TA et al (2008) Full-field digital mammography compared to screen film mammography in the prevalent round of a population-based screening programme: the Vestfold County Study. Eur Radiol 18:183-191.
18. Bluekens AM, Holland R, Karssemeijer N et al (2012) Comparison of digital screening mammography and screen-film mammography in the early detection of clinically relevant cancers: a multicenter study. Radiology 265:707-714.
19. Bick U, Diekmann F (2007) Digital mammography: what do we and what don't we know? Eur Radiol 17:1931-1942.
20. Fallenberg EM, Dimitrijevic L, Diekmann F et al (2013) Impact of magnification views on the characterization of microcalcifications in digital mammography. Fortschr Röntgenstr Doi:10.1055/s-0033-1350572.
21. Spangler ML, Zuley ML, Sumkin JH et al (2011) Detection and classification of calcifications on digital breast tomosynthesis and 2D digital mammography: a comparison. AJR Am J Roentgenol 196:320-324.
22. Gunhan-Bilgen I, Oktay A (2007) Management of microcalcifications developing at the lumpectomy bed after conservative surgery and radiation therapy. AJR Am J Roentgenol 188:393-398.
23. Schueller G, Schueller-Weidekamm C, Helbich TH (2008) Accuracy of ultrasound-guided, large-core needle breast biopsy. Eur Radiol 18:1761-1773.
24. Weigel S, Decker T, Korsching E (2011) Minimal invasive biopsy results of "uncertain malignant potential" in digital mammography screening: high prevalence but also high predictive value for malignancy. Fortschr Röntgenstr 183:743-748.
25. Penco S, Rizzo S, Bozzini AC et al (2010) Stereotactic vacuum-assisted breast biopsy is not a therapeutic procedure even when all mammographically found calcifications are removed: analysis of 4,086 procedures. AJR Am J Roentgenol 195:1255-1260.
26. Jackman RJ, Marzoni FA, Jr., Rosenberg J (2009) False-negative diagnoses at stereotactic vacuum-assisted needle breast biopsy: long-term follow-up of 1,280 lesions and review of the literature. AJR Am J Roentgenol 192:341-351.

# MRI of the Breast: Current Indications and Outlook to the Future

Karen Kinkel

Clinique des Grangettes, Chêne-Bougeries, Geneva, Switzerland

## Introduction

Magnetic resonance imaging (MRI) of the breast has gained widespread clinical acceptance due to a large effort in standardization of image acquisition and interpretation partly due to the extensive use of the Breast Imaging Reporting and Data System (BI-RADS) lexicon. The role of MRI of the breast has evolved from the traditional question about local recurrence of breast cancer to a variety of indications such as high-risk screening, evaluating response to neoadjuvant chemotherapy, staging and screening for contralateral cancer, occult primary breast cancer, and implant evaluation [1, 2]. This jump from a third-line breast-imaging technique to a primary imaging technique is also due to the increased availability of MRI-guided biopsy systems and an increasing awareness for standardized follow-up protocols and quality assurance for MRI-only lesions [3]. This trend has encouraged newer indications, such as discordant radiopathologic findings, nipple discharge, or high-risk lesions after breast biopsy, for MRI of the breast to help solve complex clinical situations.

## Screening the High-Risk Patient

Since the early 2000s, multiple prospective studies in patients at high risk for breast cancer have shown higher sensitivity of MRI compared with mammography and US in early detection of breast cancer (Table 1). Patients are considered at high risk if the cumulative lifetime risk of breast cancer exceeds 20% or if they were treated for Hodgkin's disease between the age of 8 and 30 years with mantle radiation therapy. Patients are sent to an oncologic genetic counselling consultation if the family history strongly indicates a suspicion of genetic mutation for breast cancer. This is the case for three instances of first- or second-degree relatives of patients with breast/ovarian cancer from the same parental side or two cases of first-degree relatives with breast cancer that occurred before the age of 40, or if the cancer was bilateral. A family history of two first-degree relatives of ovarian cancer, of one male breast cancer or one breast and ovarian cancer also suggests a possible genetic mutation. *BRCA* mutations affect a tumor suppressor gene, with dominant autosomic transmission by either the father or the mother, with a 50% chance of transmission. Breast cancer risk starts at the age of 25 (mean 45-48) years and 55 years for ovarian cancer. Male breast cancer is only seen in patients with the *BRCA2* mutation.

The lifetime risk for breast cancer in patients with *BRCA1* or *BRCA2* mutation is 60-85% but for ovarian cancer is 40-60% in *BRCA1* patients versus 10-30% in *BRCA2* patients. The risk of contralateral breast cancer is 30% within 5 years of the first breast cancer. Risk-reduction options include either bilateral mastectomy with (95% reduction) or without (90% reduction) oophorectomy, oophorectomy alone before the age of 50 years, or tamoxifen chemo-

**Table 1.** Sensitivity of screening magnetic resonance imaging (MRI)

| Study | Year | No. patients | Cancer | N+ | Mammography | MRI |
|---|---|---|---|---|---|---|
| Warner | 2004 | 236 *BRCA* | 22 | 9% | 36% | 77% |
| Kriege | 2004 | 1,909 | 51 | 14% | 40% | 71% |
| Kuhl | 2005 | 613 | 12 | 8% | 42% | 83% |
| Maribs | 2005 | 349 | 35 | 14% | 40% | 77% |
| Lehman | 2005 | 367 contralateral | 4 | | 25% | 100% |
| Hagen | 2007 | 491 *BRCA* | 25 | 26% | 50% | 86% |
| Riedl | 2007 | 327 | 28 | | 50% | 86% |
| Kuhl | 2009 | 687 | 27 | 11% | 33% | 93% |
| Sardanelli | 2011 | 501 | 52 | 22% | 50% | 91% |

*Diseases of the Abdomen and Pelvis 2014-2017*,
DOI: 10.1007/978-88-470-5659-6_41 

prevention (38% risk reduction). Other options include more intense and earlier screening starting at the age of 30 years with annual MRI of the breast. The role of mammography in *BRCA1* mutation carriers is controversial due to an increased risk of radiation-induced breast cancer in vitro. Compared with MRI as a screening method alone, the majority of comparative imaging screening trials shows a small number of additional cancers with mammography but no or very little value of US after annual MRI and mammography [4, 5]. Imaging features of breast cancer in high-risk women are often more benign appearing, particularly in *BRCA1* mutation carriers, in whom 23% of invasive ductal cancer demonstrates a fibroadenoma-like appearance with an oval or round shape and smooth margins but no dark septations [6]. Moreover, no mammographic calcifications are seen in invasive cancer. A posterior prepectoral location of breast cancer is seen in 67% of *BRCA1* mutation carriers [6]. Second-look US is crucial to identify suspicious lesions on MRI to allow subsequent US-guided biopsy. If US remains negative, spot-compression mammography or tomosynthesis may help identify MRI lesions. If no traditional imaging method identifies the suspicious MRI-only lesion, then MRI-guided biopsy with clip positioning and postbiopsy mammography allows adequate patient management. A 6-months' follow-up, MRI remains important to demonstrate no increase in size after a negative MRI-guided biopsy. The benefit of high-risk screening was shown in a study comparing breast cancer in *BRCA1* and *BRCA2* patients diagnosed with and without MRI. The group with MRI had significantly smaller tumors and less chemotherapy; however, the slightly higher 3-year and disease-free and overall survival was not significant [7].

## Implant Evaluation

MRI of the breast for implant evaluation has a sensitivity of 89% and a specificity of 97% in the diagnosis of implant rupture [8]. The incidence of rupture increases with implant age, with most ruptures occurring between 10 and 15 years after implantation. The imaging protocol includes four T2-weighted sequences: native, fat-suppressed, water-suppressed, and dedicated to silicone only (fat and water suppression). The silicone-only sequence should be performed in two different slice orientations to differentiate a rupture from implant folds.

Intracapsular implant rupture is defined as rupture of the implant shell, with silicone leakage that does not extend beyond the fibrous capsule. The most reliable MRI criterion for intracapsular rupture is the presence of multiple curvilinear low-signal-intensity lines within the high-signal-intensity silicone gel, the so-called linguine sign. These curvilinear lines represent the collapsed implant shell floating within the silicone gel [9]. The linguine sign is missing in an uncollapsed rupture, and instead, MRI shows free silicone outside the implant shell but still contained by the fibrous capsule. Focal silicone invagination between the inner shell and fibrous capsule are common, resulting in the teardrop sign and the key-hole sign. Extracapsular silicone implant rupture is defined as rupture of both the implant shell and the fibrous capsule, with macroscopic silicone leakage that extends beyond the fibrous capsule into surrounding tissues. Focal areas of high signal intensity in the silicone-only sequence represent free silicone. Capsular contracture can be confirmed at MRI in the event of a round breast implant with increased capsular thickness. Implant infection is more common in oncoplastic procedures and demonstrates rim enhancement around the implant. Contrast-enhanced MRI is indicated in addition to the four T2 sequences whenever there is an oncoplastic question about the glandular breast tissue, a mass in the breast, or an associated high-risk situation.

## Breast Cancer Staging

MRI of the breast has several roles in this situation:

- To measure the extent (size and location) of the known breast cancer
- To identify additional foci of cancer elsewhere in the breast (multifocality)
- To define adequate resection margins of the cancer
- To screen the contralateral breast for breast cancer.

A large number of papers confirm the superiority of MRI compared with US and mammography to fulfil these tasks, particularly in patients with invasive lobular cancer [10], cancer in high-risk patients, patients with a size discrepancy $>1$ cm between mammography and US, and patients eligible for partial breast irradiation. However, there are no randomized trials that demonstrate evidence for reduced recurrence rate or mortality from breast cancer. Moreover, the Comparative Effectiveness of MRI in Breast Cancer (COMICE) trial, a multicenter trial from the UK, demonstrated no difference in re-operation rate between breast cancer patients with and without breast MRI [11]. The study was limited by poor design and absent MRI quality assurance, as most centers started the use of breast MRI and had no MRI-guided biopsy. Therefore, the study represents poor use of MRI technology and should not be considered. Identifying occult foci of breast cancer in the ipsilateral or contralateral breast does not necessarily increase the percent of patients undergoing mastectomy.

Indeed, multiple lumpectomies for several small breast cancers within a large breast volume may represent a valid surgical alternative to mastectomy. Moreover according to the initial tumor size before vacuum-assisted biopsy, watchful waiting for very small lesions treated by radiation therapy and adjuvant therapy may be another alternative.

## Neoadjuvant Chemotherapy

Patients with locally advanced tumors undergo neoadjuvant chemotherapy to increase the rate of breast-conserving

surgery. Surgical success depends on breast volume and residual disease after the end of neoadjuvant chemotherapy. Assessing the type of shrinkage pattern is important because it impacts the type of surgery: if the shrinkage pattern is concentric, lumpectomy can be performed; if the shrinkage pattern consists of tumor fragmentation, there is no change in the widest tumor margins and mastectomy is required. Comparison between pre- and postchemotherapy MRI is crucial for adequate residual tumor assessment. Moreover, the decreased enhancement rate of residual tumor after chemotherapy should lower the threshold for residual tumor diagnosis to avoid underestimation of tumor volume. This situation is increased in patients with estrogen-receptor-positive and human epidermal growth factor receptor (HER2)-negative tumors. The inclusion of diffusion-weighted imaging has shown promising results for assessing residual disease after chemotherapy [12]. Another potential indication of MRI is the early prediction of response to avoid delay in surgical treatment if the chemotherapy regimen is not efficient. However, this indication requires larger studies to establish the value of MRI in distinguishing responders from nonresponders [13].

## Occult Primary Cancer

Histopathology of metastases helps determine the mammary origin of the primary cancer. However, clinical examination, mammography, and US are not able to identify the cancer. MRI sensitivity for detecting unknown breast cancer ranges from 25% to 86% [14]. When MRI is positive, adequate surgical treatment consists of lumpectomy or mastecomy according to lesion size and location. When MRI is negative, breast surgery is not performed and axillary dissection and breast radiation therapy are performed instead.

## Outlook to the Future

New emergent indication of breast MRI include nipple discharge and high-risk lesions at breast biopsy (stage B3). Cancer is present in 10% of patients with spontaneous, unilateral, discharge from one nipple orifice that is of various colors but not white.

Cytology, mammography, and US demonstrate false-negative results in 30-50% of cases. Performing a ductography helps demonstrate the extent of an abnormal milk channel but does not exclude cancer. MRI of the breast has therefore been suggested in demonstrating both suspicious lesions and the abnormal duct in performing an indirect ductography through heavily T2-weighted sequences [15]. This technique has high sensitivity and negative predictive value for cancer in patients with otherwise negative conventional imaging findings.

There is a large group of heterogeneous benign breast lesions (stage B3) diagnosed with percutaneous biopsy and at variable risk of being upgraded to malignancy at surgical excision. They include lobular neoplasia, atypical ductal hyperplasia, radial sclerosing lesions, and papillary lesions. Several studies show the high negative predictive value of MRI in excluding cancer, particularly in patients with radial scars and papillomas. These patients can safely undergo follow-up examination rather than surgical excision [16].

Higher field strengths (3T) offer greater signal-to-noise ratio (SNR), enabling fast acquisition strategies and the opportunity of introducing new imaging techniques, which can help differentiate and characterize breast lesions, e.g., diffusion-weighted imaging (DWI) and magnetic resonance spectroscopy (MRS). The combination of DWI, proton MRS, and contrast-enhanced MRI show increased sensitivity and specificity in detecting and differentiating breast cancer from benign disease [17, 18]. These promising technical advances require further technical standardization and teaching to become part of routine clinical practice in MRI.

## References


1. Mann RM, Kuhl CK, Kinkel K, Boetes C (2008) Breast MRI: guidelines from the European Society of Breast Imaging. Eur Radiol 18:1307-1318.
2. Sardanelli F, Boetes C, Borisch B et al (2010) Magnetic resonance imaging of the breast: recommendations from the EUSOMA working group. Eur J Cancer 46:1296-1316.
3. Heywang-Köbrunner SH, Sinnatamby R, Lebeau A et al; Consensus Group (2009) Interdisciplinary consensus on the uses and technique of MR-guided vacuum-assisted breast biopsy (VAB): results of a European consensus meeting. Eur J Radiol 72:289-294.
4. Kuhl C, Weigel S, Schrading S et al (2010) Prospective multicenter cohort study to refine management recommendations for women at elevated familial risk of breast cancer: the EVA trial. J Clin Oncol 28:1450-1457.
5. Sardanelli F, Podo F, Santoro F et al; High Breast Cancer Risk Italian 1 (HIBCRIT-1) Study (2011) Multicenter surveillance of women at high genetic breast cancer risk using mammography, ultrasonography, and contrast-enhanced magnetic resonance imaging (the high breast cancer risk Italian 1 study): final results. Invest Radiol 46:94-105.
6. Schrading S, Kuhl CK (2008) Mammographic, US, and MR imaging phenotypes of familial breast cancer. Radiology 246:58-70.
7. Chéreau E, Uzan C, Balleyguier C et al (2010) Characteristics, treatment, and outcome of breast cancers diagnosed in BRCA1 and BRCA2 gene mutation carriers in intensive screening programs including magnetic resonance imaging. Clin Breast Cancer 10:113-118.
8. Hölmich LR, Vejborg I, Conrad C et al (2005) The diagnosis of breast implant rupture: MRI findings compared with findings at explantation. Eur J Radiol 53:213-225.
9. Juanpere S, Perez E, Huc O et al (2011) Imaging of breast implants: a pictorial review. Insights Imaging 2:653-670.
10. Bedrosian I, Mick R, Orel SG et al (2003) Changes in the surgical management of patients with breast carcinoma based on preoperative magnetic resonance imaging. Cancer 98:468-473.
11. Turnbull L, Brown S, Harvey I et al (2010) Comparative effectiveness of MRI in breast cancer (COMICE) trial: a randomised controlled trial. Lancet 375:563-571.

12. Woodhams R, Kakita S, Hata H et al (2010) Identification of residual breast carcinoma following neoadjuvant chemotherapy: diffusion-weighted imaging—comparison with contrast-enhanced MR imaging and pathologic findings. Radiology 254:357-366.
13. Prevos R, Smidt ML, Tjan-Heijnen VC et al (2012) Pre-treatment differences and early response monitoring of neoadjuvant chemotherapy in breast cancer patients using magnetic resonance imaging: a systematic review. Eur Radiol 22:2607-2616.
14. de Bresser J, de Vos B, van der Ent F, Hulsewé K (2010) Breast MRI in clinically and mammographically occult breast cancer presenting with an axillary metastasis: a systematic review. Eur J Surg Oncol 36:114-119.
15. Hirose M, Otsuki N, Hayano D et al (2006) Multi-volume fusion imaging of MR ductography and MR mammography for patients with nipple discharge. Magn Reson Med Sci 5:105-112.
16. Linda A, Zuiani C, Furlan A et al (2012) Nonsurgical management of high-risk lesions diagnosed at core needle biopsy: can malignancy be ruled out safely with breast MRI? AJR Am J Roentgenol 198:272-280.
17. Bogner W, Gruber S, Pinker K et al (2009) Diffusion-weighted MR for differentiation of breast lesions at 3.0 T: how does selection of diffusion protocols affect diagnosis? Radiology 253:341-351.
18. Gruber S, Debski BK, Pinker K et al (2011) Three-dimensional proton MR spectroscopic imaging at 3 T for the differentiation of benign and malignant breast lesions. Radiology 261:752-761.

# BI-RADS: Ultrasound Update Including Elastography. Where Do We Stand Now?

Alexander Mundinger

Radiological Department and Breast Centre, Niels-Stensen-Clinics, Osnabrueck, Germany

## Introduction

New developments in ultrasound (US) encompass 3D automated US as an adjunct to screening, handheld high-frequency transducers in whole breast US, and hybrid systems. High-frequency US is relevant for assessing small mammographic masses and for preoperative staging to detect accompanying focal or ductal changes due to ductal carcinoma in situ (DCIS) and metastatic axillary lymph nodes (ALN). Advanced modes such as compounding, tissue harmonic imaging (THI), and speckle reduction increase the signal to contrast ratio. Doppler techniques and elastography are additional tools to recategorize Breast Imaging Reporting and Data System (BI-RADS) 3 vs. 4a lesions, suggesting upgrading the former if the lesion is stiff or hypervascularized and downgrading the latter if the lesion is soft and not vascularized. Modern US assessment of architecture, flow, elasticity, and redefinition of special cases are among the highlights of the updated BI-RADS lexicon. The most relevant descriptors for characterizing a US lesion continue to comprehend shape, margin, and orientation together. Handheld and 3D automated US increase the cancer detection rate following negative mammography by three to four per 1,000 in a multimodality approach to examine women with dense breast tissue within breast cancer screening studies. US is indicated and routinely used in breast centers for preoperative staging, to monitor therapy, and to observe patients after breast conservation surgery or mastectomy. US-guided core needle biopsy (CNB) is the standard interventional technique for all breast lesions that correlate with findings of other imaging modalities. Sensitivity of US-guided large-core needle biopsy (LCNB) is 93-98%; specificity ranges from 95% to 100%. The diagnostic accuracy of US-guided vacuum-assisted biopsy is close to 100%. US-guided needle aspiration and CNB of the axilla should be used preoperatively to define metastatic lymph node involvement.

## Basics of Breast Ultrasound Anatomy

Breast anatomy is the basis for understanding breast US. The breast is a modified skin gland enveloped in fibrous fascia. The undersurface of the breast lies on the deep pectoralis fascia. The superficial pectoralis fascia is located beneath the skin and nipple. The breast is composed of three major structures: skin, subcutaneous tissue, and breast tissue, the latter containing parenchyma and stroma. The parenchyma is divided into 15-20 lobes or segments that converge at the nipple in a radial arrangement. Each lobe contains 20-40 lobules. Each lobule contains 10-100 ductules or acini. The terminal duct lobular unit (TDLU) is the functional unit and is composed of a lobule and its terminal duct. Major ducts join below the nipple in a netlike pattern and widen in a portion named the lactiferous sinus before opening into the orifices of the nipple. The converging larger ducts drain the segmental ducts arising from subsegmental ducts and terminal ducts. To date, definition of ducts and associated TDLUs within a segment using a ductal or radial scanning examination technique complements the transverse and sagittal examination [1, 2]. Several proliferative breast diseases, including DCIS arise from the TDLUs. Only DCIS cells expand throughout all ducts. However, distended TDLUs due to DCIS develop rarely, and high-resolution US (HRUS) detects distended TDLUs frequently in various benign lesions. Therefore, additional information is necessary, such as suspicious segmental distribution or correlation, when imaging findings with mammography or magnetic resonance imaging (MRI) may indicate malignancy. Tiny changes, as small as 2-5 mm in diameter, can be dismissed in analogy with MRI-detected foci. On the contrary, such small pseudocystic changes must be assessed when there is concern about multifocality or ductal extension of DCIS.

The echogenicity of fat is the reference by which to compare other anatomical structures on breast US [1, 2]:

*Diseases of the Abdomen and Pelvis 2014-2017*,
DOI: 10.1007/978-88-470-5659-6_42 

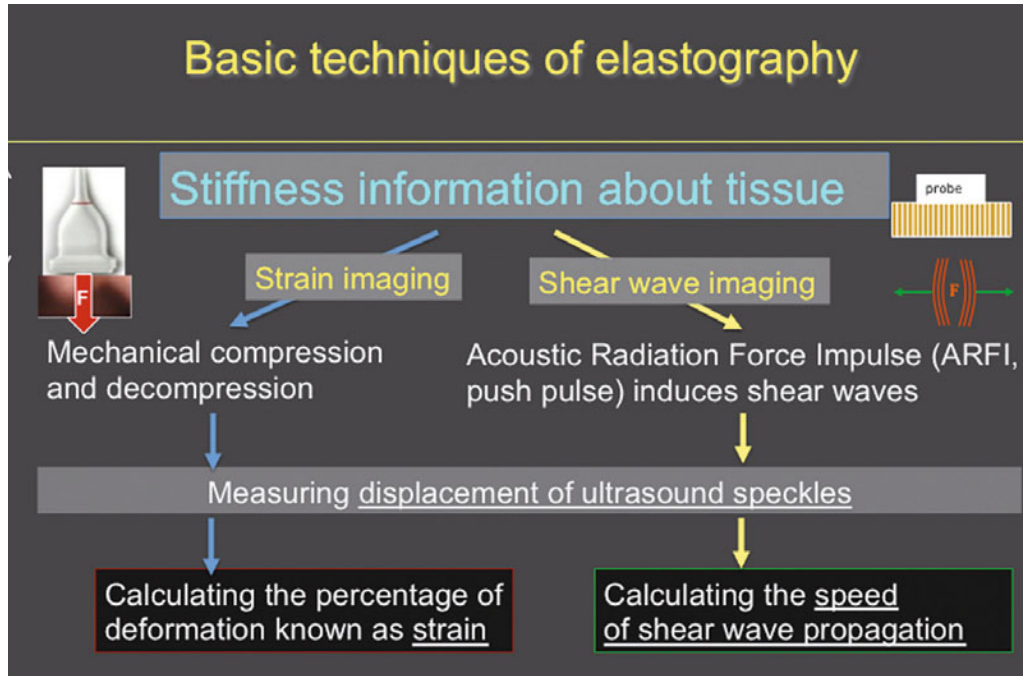


**Fig. 1.** Basic techniques of elastography. Differences between strain and shear-wave elastography

- Isoechoic echogenicity is found in fat, epithelium, loose periductal, and intralobular fibrous tissue and some TDLUs.
- Hyperechoic echogenicity is found in skin, Cooper's ligaments, stromal fibrous tissue (interlobular), and some TDLUs.
- Hypoechoic echogenicity is found in nipple and blood in vessels.
- Anechoic echogenicity is found in dilated TDLUs (cysts), ducts, and lymphatics.

## Physics and Equipment

US of the breast provides physical information about the impedance of tissue interfaces that influence US transmission and reflection across the breast. Scanning with 15 MHz in comparison with 7.5 MHz results in a lateral (0.4 mm) and axial (0.2 mm) spatial resolution that is twice as high as the spatial resolution at 7.5 MHz at the cost of identifying penetration depth, which is reduced to half. Compounding and THI in combination with speckle reduction enhances contrast resolution and can detect fat isoechogenic lesions masked with fundamental US. The high spatial and contrast resolution of modern breast US equipment has increased the detection and conspicuity of subtle lesions the size of expanded terminal duct lobular units, such as DCIS and microinvasive lesions. Color Doppler techniques detect and characterize blood flow within lesions, providing valuable discrimination information between solid nodules and complicated cysts. Three-dimensional diagnostic imaging includes multidimensional reformations, reconstructions, and tomographic US. The additional diagnostic information of 3D US encompasses the demonstration of suspicious retractions around a tumour in the coronal plane, which is unique to this technique. New horizons in high-end US technology encompass miniaturized and portable US systems and imaging fusion of US information with digital mammography, tomosynthesis, contrast-enhanced (CE) dual-energy mammography, MRI, and positron emission tomography (PET) [1, 3].

## Elastography

Elasticity is defined as the ability of a material to deform under a given shear force and return to the original shape due to elastic-restoring forces of the tissue. The decompression phase represents elasticity in mathematical terms. The integrity of the tissue matrix and the tension placed upon it are also important for shear-wave propagation that is set up within the body by any motion, internal or external, and correlate with elasticity. An update of current elastography methods has been adopted according to the European Federation of Societies for Ultrasound in Medicine and Biology (EFSUMB) guidelines (Figs. 1, 2). The applied force in strain elastography relies on active external hand movement of the transducer parallel to the breast skin to produce slight vibrations, resulting in periodic distortions of the underlying tissue. Semistatic elastography relies on passive, tiny displacements of tissue due to periodic physiologic tissue movements due to heart or vessel pulsations or inspiration. Acoustic radiation-force impulses (ARFI) apply minute mechanical pushes to tissue. Responses are displacement (i.e., strain) and shear waves traveling away from

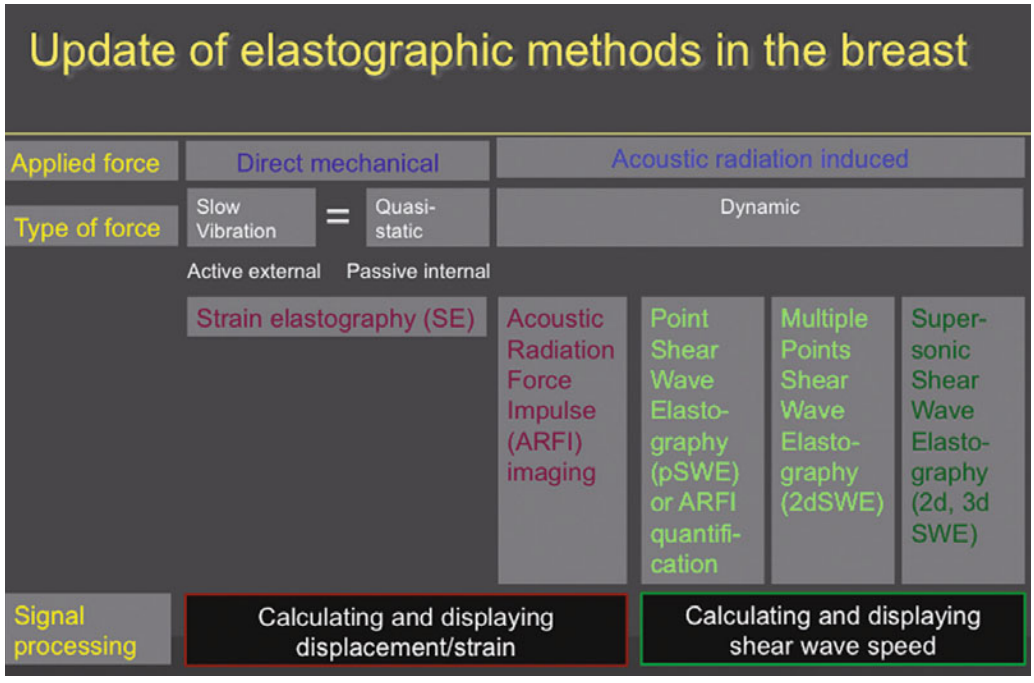


**Fig. 2.** Update of elastographic methods focussing on application of force, type of force, and signal processing, Adoption according to the European Federation of Societies for Ultrasound in Medicine and Biology (EFSUMB) guidelines and recommendations on the clinical use of ultrasound elastography [3, 4]

the line of these push pulses. Strain can be assessed estimating displacement by radiofrequency echo correlation tracking and Doppler processing. The speed of shear is subject to measurements using ultrafast B-mode techniques that track the way the speckle pattern changes in a small region of interest (ROI) [2D echo (2DE)] or in a large area (2DE or 3DE). The latter is realized in the supersonic method that tracks the speed of the shear-wave front (Mach cone) in centimeters per second or converted to kilo-Pascal (kPa), which is the standard unit for tissue stiffness. For clinical purposes, a five-point subjective score between benignity and malignancy for color-coded strain elastograms has been proposed by the Tsukuba group [3, 4] and became standard in the early days of elastography. Current users of elastography apply other qualitative, semiquantitative, or quantitative criteria extracted by the stiffness images. Numerous studies attest to the value of both strain and shear-wave elastography. The role of elastography comprises an add on to conventional US, particularly in helping reclassify BI-RADS 3 and 4a lesions, upgrading the former to biopsy if the lesion is stiff, and downgrading the latter to follow-up if the lesion is very soft. Using lesion stiffness in context of conventional features is important because in vitro bench measurements of the stiffness of breast lesions demonstrate that there is overlap, with some fibroadenomas and fibrotic lesions being quite stiff and some cancers, especially high-grade and DCIS, being soft [4].

## Indications for Breast Ultrasound

A list of updated recommendations pertaining to indications is given in Table 1. US is the first-line imaging technique for women <40 years presenting with symptoms or clinical signs. In the presence of a suspicious lesion, US is the method of choice to guide core biopsy to harvest tissue. US-guided vacuum-assisted biopsy (VAB) is used increasingly to diagnose intraductal lesions, small architectural distortions, and borderline lesions; to complete preoperative staging in patients with extensive ductal component; and for therapeutic excision. Stereotactic-

**Table 1.** Updated indications for high-resolution ultrasound (HRUS)

| |
|---|
| – Differentiation of cysts and solid tumors |
| – Differentiation between solid, benign, and malignant lesions |
| – Characterization of palpable abnormalities |
| – Assessment of mammographic screening abnormalities |
| – Dense breasts showing reduced mammographic sensitivity |
| – Diagnosis and follow-up of women with benign breast disease or risk lesions |
| – During pregnancy or lactation |
| – Significant nipple discharge |
| – Under hormonal replacement therapy |
| – Inflamed breast and abscess formation |
| – Extended screening for high-risk patients |
| – Second look after magnetic resonance mammography |
| – Guidance of interventional procedures, such as fine-needle aspiration, core biopsy, diagnostic and therapeutic vacuum biopsy, preoperative tumor localization, axillary lymph node biopsy |
| – Preoperative lesion staging; skin and nipple distance for planning breast-conserving surgery, mastectomy, or oncoplastic reconstruction with implants; assessment of multifocality, multicentricity, intraductal extension, lymph node changes, and contralateral lesions |
| – Preoperative staging and follow-up under neoadjuvant chemotherapy |
| – Surveillance after breast-conserving therapy |
| – Silicone implants |

guided VAB is the method of choice by which to sample screen-detected microcalcifications and architectural distortions not seen on US. In the dense breast, the combination of US and screening mammography improves cancer detection considerably compared with mammography alone but with an increase in biopsy rate. The additional diagnostic yield of US after negative mammography is 3.2:1,000 women with dense breasts. Intraoperative surgeon-performed US focuses on accurately defining the resection segment or sector and margin analysis of the resection specimen. MRI is useful preoperatively to assess the extent of ipsilateral disease and exclude contralateral breast cancer, particularly for women at increased risk of mammographically occult disease. Second-look US can detect up to 50% of MR-enhancing cancers with negative mammography [5-8].

## Examination Technique

The International Breast Ultrasound School (IBUS) and American College of Radiology (ACR) guidelines for breast US examination advise a systematic, comprehensive, and reproducible examination technique, followed by documentation, description, reporting, classification, and recommendation. The examination starts with proper positioning of the patient in a supine or anterior oblique position depending on breast volume, with elevation of the ipsilateral arm. Positioning should result in a maximum flattening of the breast portion being examined. Automated tissue optimization and focal-zone and field of view (FOV) settings should be optimized before scanning, with the transducer perpendicular to skin. A minimum of two scan planes is recommended in whole-breast US. Image analysis of a detected lesion or pseudolesion requires rotation of the transducer over the entire lesion using changing compression intensities and angulations. Radial imaging of adjacent ducts is mandatory to assess ductal extensions. BI-RADS descriptors and further criteria of additional elastography, 3D tissue criteria, vascularization, and associated lymph node morphology characterize a state-of-the-art lesion assessment by US. The o'clock position and distances to skin and nipple describe the exact localization of a lesion within the volume of the breast. Indication of palpability and imaging correlation to other modalities complete the documentation [9-12].

## Concepts of Interpretation Based on Ultrasound BI-RADS Descriptors

The categorization of a mass found in all modalities relates to a 3D macropathological tissue lesion. The pathology defines lesion shape, margin, and texture. These features have already been described individually for the varying modalities. Uniform wording of the major diagnostic criteria for all modalities would be logical. The BI-RADS concept stepped first in this direction and was designed primarily as a mammographic language with a clear, defined terminology. In 2003, the ACR published the *Breast Imaging Atlas*, which is a BI-RADS lexicon for mammography, US, and MRI. The US chapters were originally arranged under the chair of Ellen B. Mendelson [11], and descriptors and diagnostic criteria are presented with increasing probability of malignancy. Descriptors of a mass include shape, orientation, margin, boundary, echo pattern, posterior acoustic features, and characteristics of surrounding tissue, as well as associated distinguishing findings. The combination of several descriptors predicts malignancy better than one single descriptor. However, the most relevant descriptors for characterizing a US lesion continue to comprehend shape, margin, and orientation taken together. The reader should use further explanatory elements indicated in the guidance chapters of the atlas, such as clinical context conditions, tumour biology, and epidemiological prevalence, to cover the complex field of breast lesions. Assumptions regarding the expected prevalence and individual risk for cancer in a patient drive the intuitive recommendation for or against a biopsy and influence the choice of a final BI-RADS assessment category. In other words, the threshold for performing a biopsy is lower for a probably benign lesion compared with a screening setting if advanced patient age, large lesion, palpability, or individual high-risk situation are concerns to the reader. BI-RADS categories 3-5 imply a defined probability of malignancy for each category. For BI-RADS 3, these probabilities are $<2\%$, for BI-RADS 4 between 3% and 94%, and for BI-RADS 5 $\geqslant 95\%$.

Most European US societies have adopted or modified the ACR BI-RADS US guidelines. In addition to the 2003 US descriptors, various features have been suggested, such as elastic compressibility, movability, 3D criteria, detailed lymph node morphology, and others. Further prospective multicenter studies still have to validate the complementary diagnostic importance of such associated features as an adjunct to the basic characteristics of a lesion [12, 13]. Several authors disclosed that interobserver agreement with the new BI-RADS terminology is good and validated the lexicon in retrospect following landmark studies in the 1990s. Only fair agreement exists in most studies for margin evaluation. Further, a trend toward lower concordance was noted for evaluating small masses. Classification into subdivisions 4a, 4b, and 4c was more or less reproducible. Despite limitations of the BI-RADS lexicon, most authors agree that stratification predicting the likelihood of malignancy could be useful for decision making and communication with patients and between researchers, physicians, and physicians of different specialties [14-16]. The updated second edition of BI-RADS US guidelines [17] will reemphasize the importance of basic features, such as mass shape, margins, and orientation on one hand, and associated findings such as an adjunct on the other. The amended chapters cover expanded

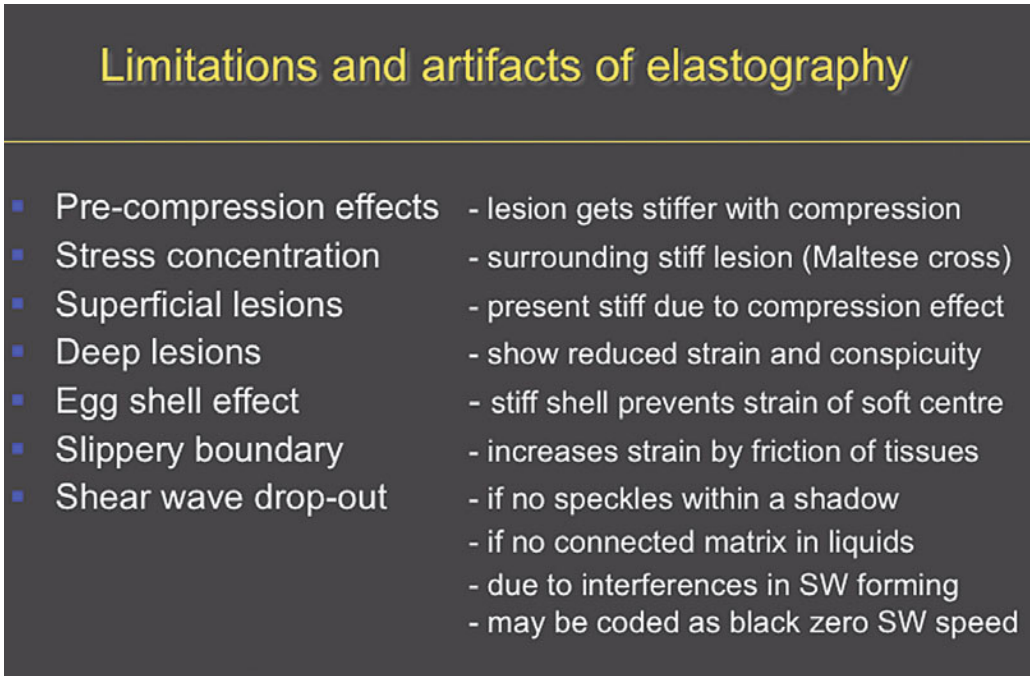


**Fig. 3.** Limitations and artefacts of elastography

general issues, detailed lexicon images and US descriptors, reporting system, and guidance. Figure 3 presents a training schema for beginners in the field of breast diagnostics that can be used to learn standardized BI-RADS US reading of larger masses. This schema has no scientific proof for use in daily workup. Table 2 highlights some underlying intrinsic and extrinsic concepts of BI-RADS US assessment categories that must be considered in daily work.

**Table 2.** Underlying concepts of Breast Imaging and Reporting Data System ultrasound (BI-RADS US) assessment categories

| |
|---|
| – Categorization and management depend on the most suspicious diagnostic criterion |
| – Benign lesions must look typically benign; no suspicious image descriptor |
| – Malignant lesions frequently show one or more suspicious criterion |
| – Predefined thresholds for positive predictive value or cancer risk influence classification in categories 2-5 |
| – Overall BI-RADS category must consider further clinical context conditions, expected prevalence, and other risk factors besides morphological criteria of each imaging modality assessment category |
| – Typical indicators of benignity, such as cysts, fat in a lesion (hamartoma, lipoma), or benign macrocalcification (popcorn calcification with fibroadenoma) diagnosed by multimodality evaluation can downgrade overall assessment category compared with US category |
| – Indicators of potential malignancy in other modalities or high-risk patients can upgrade overall assessment category compared with US category |
| – Overall assessment category should also be based on the most urgently needed procedure. This point of view ensures critical re-evaluation of final assessment category |

## Concepts of Interpretation and Clinical Decision Making

The US characterization of a lesion in daily routine follows a reproducible diagnostic algorithm and should involve fundamental US and all advanced applications of the used US system, preferably on a one-click basis.

First, the reader must define whether or not the lesion resembles a typical benign finding, such as cyst, lipoma, lymph node, or previously know scar or fibroadenoma (Fig. 3). Complicated cysts with internal debris are challenging: when the debris is mobile or a fluid-debris level is seen, complicated cysts can be dismissed as benign findings, i.e., BI-RADS US category 2 [11, 18].

Second, a typical oval-shaped, hypoechoic lesion with circumscribed margins and horizontal orientation in young women is most likely a fibroadenoma (Fig. 4). Short-term follow-up can be used. Several studies concluded that short-term follow-up of such BI-RADS US category 3 lesions is associated with a cancer rate $<2\%$ [19-21]. Being $>45$ years, having palpability, or any preselection that enriched cancer cases in the collective, are associated with cancer rates $>2\%$. In a recent study, 0.8% of 4,000 women with lesions that were initially classified as probably benign proved to be malignant at follow-up. The most frequent reason for a false-negative assessment on US was failure to recognize suspicious margin characteristics (28 of 32 malignancies; 87.5%). Malignancy was more frequent in palpable (2.4%; 21 of 859) than nonpalpable (0.4%; 11 of 3141) lesions [22]. As an isolated finding, homogeneous complicated cysts and clustered microcysts can be classified as probably benign, particularly if the lesion is new or rather small or deep, i.e., diagnostic uncertainty exists [18].

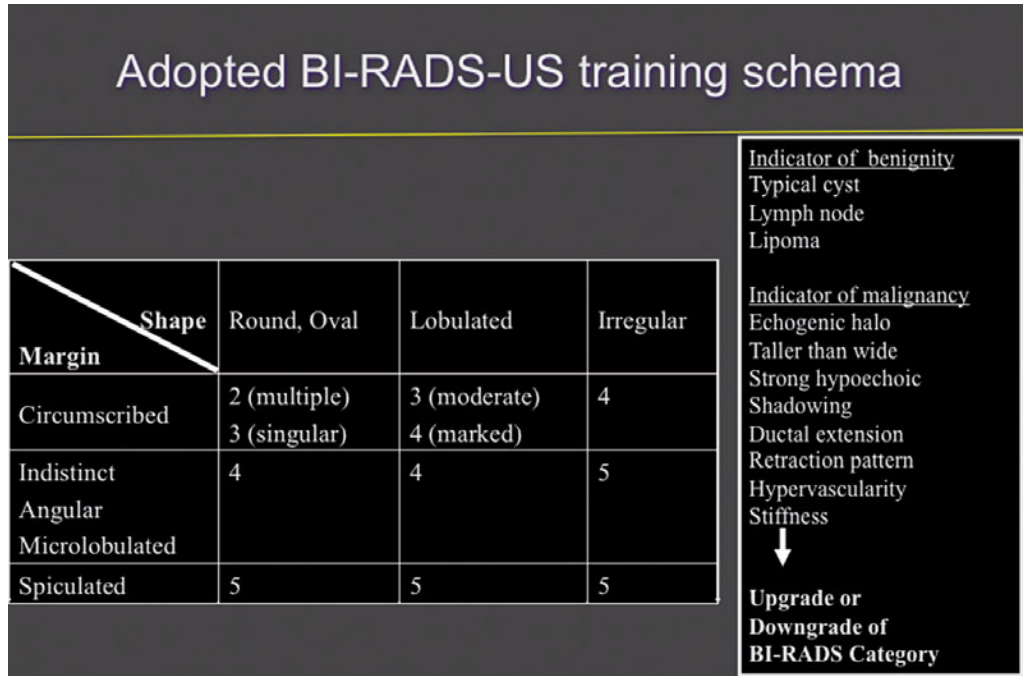


**Fig. 4.** Adopted Breast Imaging Reporting and Data System Ultrasound (BI-RADS US) training schema. BI-RADS characterization of a mass can be taught using basic descriptors and associated findings that upgrade or downgrade overall assessment category. The teaching schema aims to support beginners in the field of breast diagnosis. This schema provides no scientific proof to be used in daily workup, as it can miss cancers

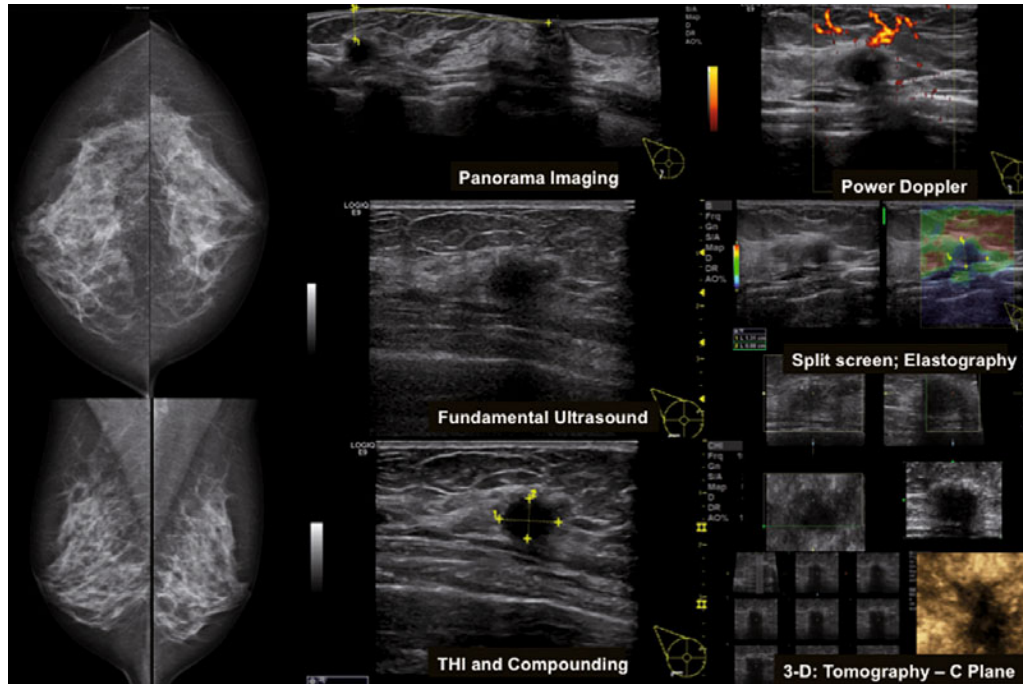


**Fig. 5.** A 53-year-old patient presenting with mammographic-negative and ultrasound (US)-positive invasive cancer. Histology is not otherwise specified (NOS), formerly named ductal invasive cancer and ductal carcinoma in situ (DCIS). No palpable finding. Diagnostic US criteria including elastography point to malignancy. American College of Radiology (ACR) density 2 (scattered fibroglandular tissue composition); Breast Imaging Reporting and Data System mammography (BI-RADS MG) 1; BI-RADS US 5. This lesion had been misinterpreted at another facility as a cyst in the presence of other fibrocystic findings. *THI* tissue harmonic imaging

Third, detailed analysis of US morphology, vascularity, and elasticity of a lesion should disclose any suspicious basic descriptor or suspicious associated finding. The presence of suspicious descriptors results in a BI-RADS US category 4 or 5, depending on the total number and character of these descriptors. A biopsy is recommended in these cases and also in benign-looking lesions that are significantly increasing in size during follow-up (Fig. 5) [11].

## Updated Role of Ultrasound

US studies in up to 12,000 asymptomatic patients yielded tumour detection rates of only 0.3-0.4%; however, a similar size and stage was reported compared with mammography-detected clinically occult cancers. The advantage of US as an adjunct to mammography is greatest in women with palpable lesions and those at high risk, including women with dense breasts, which is a risk factor.

US signs of malignancy develop with increasing tumour size. No single diagnostic sign can pick up all cancers due to their heterogeneous appearance. Patients with a high mammographic density (>75%) present in meta-analyses with fourfold increased risk compared with women with low-radiodense breasts and a twofold increased risk compared with women with scattered fibroglandular breasts [7]. The sensitivity of standard US for breast cancer is 55-95%. US transfers an additional diagnostic yield of 30-40% in comparison with mammography to patients with radiodense breasts in the incidence setting (Fig. 5). The updated American College of Radiology Imaging Network (ACRIN) follow-up study focuses on cancer detection in patients at increased risk due to radiodense breasts and those under surveillance after breast cancer or other conditions. Of 111 imaging-detected cancers, 33 cancers were found by mammography only, 32 by US only, 26 by both methods, and nine by MRI only [23]. In national screening programs, mammography is still the method of choice of early breast cancer detection. The upcoming Austrian national screening program will add US examination for all women presenting with an ACR density level 3 and 4 (dense and extremely dense).

To date, mammography still provides the best compromise between advantages, disadvantages, and costs [24]. Breast US is indicated for further assessment of mammographic abnormalities and guiding minimally invasive biopsy. Masses in mammography and on MRI can be correlated with US confidently with increasing size, starting at a diameter of 0.5 cm [25-27]. Although advanced US is suitable for detecting subtle changes in DCIS, the detection rate of DCIS by US is low without prior knowledge of focal DCIS at mammography. Targeted US of suspected DCIS depicts frequently hypoechoic lesions that represent dilated TDLUs and look similar to them, such as fibroadenoma, papilloma, ductectasia, and microcystic changes. US is the method of choice when assessing and puncturing such solid-looking small masses, dilated ducts, pseudomicrocystic lesions, and dense accumulations of microcalcifications that correspond with mammographic changes.

A radiogram of large-core cylinders is mandatory to correlate the US finding with index calcifications [3]. Underestimation of US-guided 14-guage LCNB in comparison with VAB is an unsolved problem in the preoperative diagnosis of DCIS compared with the gold standard of surgical excision. Therefore, such patients should be directed toward VAB rather than LCNB. Underestimation rates in DCIS are reported as being between 9% and 16% for VAB and 22% and 48% for LCNB [3, 27, 28].

For localization of nonpalpable breast cancer, intraoperative US is a reliable alternative to guidewire localization, as it achieves similar results in terms of complete tumour removal (93%), reexcision rate (11%), and excised volume [29]. Intraoperative breast US can guide segmental surgery with wide distances to the malignant lesions. HRUS shows a comparable diagnostic performance in preoperative staging with MRI in invasive ductal cancer. MRI performs better in preoperative staging of lobular invasive cancer, DCIS, multifocality, multicentricity, and posterior breast-wall involvement, as well as diagnosing recurrence, failing silicon prosthesis, and monitoring during neoadjuvant therapy. The median additional detection yield for MRI is estimated as 16% in meta-analyses.

To date, there is no evidence that preoperative MRI improves surgical care or prognosis [30-32]. The analog statement is probably true for the role of US in preoperative staging. The presence of Doppler blood flow increases the malignancy pickup rate, but at the expense of a significant decrease in specificity and diagnostic accuracy and an increase in biopsy rate prognosis [33].

CEUS does not appear to be superior to conventional US as a diagnostic tool overall; however, it is a very rarely used adjunct without a role in daily routine work. The overall true-positive rate for conventional US and CEUS is 88% and 86%, respectively. DCIS, medullary carcinoma, and intraductal papillary carcinoma achieved an improved true-positive rate, with 94%, 100%, and 100%, respectively [34].

Elastography can increase specificity of US examination. Two meta-analyses on strain elastography respectively reported summary sensitivities of 88% and 83% and specificities of 83% and 84% [35, 36]. Also, several studies based on shear-wave elastography shed light on the old experience that soft should be benign and stiff resembles malignancy. In BI-RADS 4a and 3 US lesions, the certainty of benignity is being increased in an elastographic, very soft lesion [37]. On the contrary, the presence of an elastographic, very stiff malignant lesion is associated with poor prognosis measured by histologic parameters [38]. All elastographic techniques aim to characterize breast lesions that have been detected and categorized previously according to BI-RADS by real-time US. Therefore, the role of elastography in its various applications resembles an additional characterizing tool such as Doppler, which has no role in population-based breast cancer screening or primary detection of US lesions.

In summary, elastography is going to enter clinical routine and, in combination with Doppler, will increase the potential of advanced US to better characterize breast lesions. Currently, elastography is just one additional feature among various BI-RADS descriptors. It will be a wise addition to everyday practices performing LCNB in lesions with any suspicious feature or in a patient with a pretest probability resembling high risk due to the inevitable overlap between benign and malignant lesions. The future role of elastography in low-prevalence collectives needs to be determined by population-based randomized studies. Automated breast US acquires data of the 3D breast volume that will be analyzed on a workstation subsequent to the examination. This technology has the potential to develop US to a primary screening tool and seems to show similar potential in characterizing lesions according to Bi-RADS US at similar or only slightly reduced diagnostic accuracy [39, 40].

Sentinel lymph node biopsy (SLNB) is associated with a low local recurrence and similar survival rates to those of ALN dissection and is now the standard of care. All patients with invasive breast cancer should have US of the axilla to exclude obvious local nodal spread. The presence of asymmetric focal hypoechoic cortical lobulations >3 mm, or a completely hypoechoic node with US, should direct further examination to fine-needle aspiration (FNA) of the index lymph node. Cortical thickness >3 mm reveals an approximately four-times increased risk of the presence of an ALN metastasis compared with cortical thickness <3 mm. Further, the absence of a hilum shows the highest specificity for ALN metastasis (94.6%) but low sensitivity [41]. The combination of tissue harmonics and compounding postprocessing increases sensitivity for lymphadenopathy. US-guided biopsy of ALN has a sensitivity that varies between 30.6% (22.5-39.6%) and 62.9% (49.7-74.8%) and a specificity of 100% (94.8-100%) [42]. When the cytological or histological finding is positive, SLNB can be omitted and primary ALN dissection performed in patients with intermediate- and high-risk disease. In negative US findings, SLNB should be performed due to the substantial number of false-negative results in patients with invasive breast cancer, although preoperative axillary US alone may exclude most cases of N2 and N3 disease [43, 44]. Surgical SLNB is the expected standard for axillary staging. Selecting patients who may not need ALN biopsy with proven low-risk axillary metastases or following neoadjuvant chemotherapy is the subject of ongoing debate.

HRUS presents an additional diagnostic yield compared with mammography in postoperative surveillance after breast-conserving and oncoplastic surgery. MRI would be the method of choice for surveillance with respect to its better diagnostic performance in comparison with mammography and US [45]. However, costs and availability restrict the use of MRI to high-risk patients and for differentiation between scar and recurrence with a problematic diagnostic background presented by the other modalities. Most surveillance guidelines rely on mammography alone or mammography in combination with US.

To detect one locoregional recurrence or second primary breast cancer preclinically, 1,349 physical examinations versus 262 mammography and/or MRI tests were performed. Follow-up provided by only one discipline may decrease the number of unnecessary follow-up visits. Breast imaging plays a major role and physical examination a minor role in early detection of second primary breast cancers and locoregional recurrences. The yield of the physical examination to detect relapses early is low and should therefore be minimized.

## Conclusion

Modern breast care requires definitive nonoperative diagnosis of all potential breast abnormalities in a timely and cost-effective way. The combination of mammography and/or US remains the mainstay in breast cancer diagnosis. New US technologies, including Doppler and elastography, improve the diagnosis and management of breast diseases due to the tight loop between examination and definitive histological diagnosis. Breast density shows a profound effect on imaging performance, with mammographic sensitivity falling from 90% to 46% and US sensitivity reducing from 95% to 72% with increasing breast density in symptomatic patients [46].

US-guided CNB has developed as the minimally invasive biopsy method of choice for all breast lesions (sensitivity 93-98%; specificity 95-100%). US-guided VAB is increasingly used for diagnosing borderline lesions, for complete preoperative staging in patients with extensive ductal component, and for therapeutic excision of biopsy-proven benign lesions such as fibroadenomas and some papillary lesions and radial scars. The diagnostic accuracy of US-guided VAB for invasive cancers is close to 100% [3, 25, 27].

## References


1. Mundinger A (2013) Advanced breast ultrasound and interventions: an update. In Hodler J, von Schulthess GK, Zollikofer CH L (Eds) Muskuloskeletal diseases. 2013-2016. Springer-Verlag Italia, Milan, pp 282-289.
2. Weismann C, Mayr C, Egger H, Auer A (2011) Breast sonography -2D,3D,4D ultrasound or elastography? Breast Care 6:98-103.
3. Bamber J, Cosgrove D, Dietrich CF et al (2013) EFSUMB guidelines and recommendations on the clinical use of ultrasound elastography. Part 1: Basic principles and technology. Ultraschall Med 34:169-184.
4. Cosgrove D, Piscaglia F, Bamber J et al (2013) EFSUMB guidelines and recommendations on the clinical use of ultrasound elastography. Part 2: Clinical applications. Ultraschall Med 34:238-253.
5. Mundinger A, Wilson ARM, Weismann C et al (2012) Where do we stand in advanced breast ultrasound? EJC 48(Suppl 1):15-17.
6. Abe H, Schmidt RA, Shah RN et al (2010) MR-directed ("Second-Look") ultrasound examination for breast lesions detected initially on MRI: MR and sonographic findings. AJR Am J Roentgenol 194:370-377.
7. Price ER, Hargreaves J, Lipson JA et al (2013) The California breast density information group: a collaborative response to the issues of breast density, breast cancer risk, and breast density notification legislation. Radiology 269:887-892.
8. Heywang-Köbrunner SH, Schreer I, Heindel W, Katalinic A (2008) Imaging studies for the early detection of breast cancer. Dtsch Arztebl Int 105:541-547.
9. Madjar H, Rickard M, Jellins J et al (1999) IBUS guidelines for the ultrasonic examination of the breast. Eur J Ultrasound 9:99-102.
10. Sencha AN, Evseeva EV, Mogutov M, Patrunov YN (2013) Breast ultrasound. Springer, Heidelberg, New York, Dordrecht, London, pp 23-42.
11. D'Orsi CJ, Sickles EA, Mendelson EB, Morris EA (2013) Breast imaging reporting and data system: ACR BI-RADS–breast imaging atlas, 5th ed. American College of Radiology, Reston, VA (in press).
12. Madjar H, Ohlinger R, Mundinger A et al (2006) BI-RADS-analogue DEGUM criteria for findings in breast ultrasound -

consensus of the DEGUM Committee on Breast Ultrasound. Ultraschall Med 27:374-379.
13. Wojcinski S, Farrokh A, Weber S et al (2010) Multicenter study of ultrasound real-time tissue elastography in 779 cases for the assessment of breast lesions: improved diagnostic performance by combining the BI-RADS®-US classification system with sonoelastography. Ultraschall Med 31:484-491.
14. Lazarus E, Mainiero MB, Schepps et al (2006) BI-RADS lexicon for US and mammography: interobserver variability and positive predictive value. Radiology 239:385-391.
15. Lee HJ, Kim EK, Kim MJ et al (2008) Observer variability of Breast Imaging Reporting and Data System (BI-RADS) for breast ultrasound. Eur J Radiol 65:293-298.
16. Santana Montesdeoca JM, Gómez Arnáiz A, Fuentes Pavón R et al (2009) Diagnostic accuracy and interobserver variability in the BI-RADS ultrasound system. Radiologia 51:477-486.
17. Mendelson EB, Baum JK, Berg WA et al (2003) Breast imaging reporting and data system, BI-RADS. American College of Radiology, Reston.
18. Berg WA, Sechtin AG, Marques H et al (2010) Cystic breast masses and the ACRIN 6666 experience. Radiol Clin North Am 48:931-987.
19. Gruber R, Jaromi S, Rudas M et al (2012) Histologic work-up of non-palpable breast lesions classified as probably benign at initial mammography and/or ultrasound (BI-RADS category 3). Eur J Radiol [Epub ahead of print].
20. Fu CY, Hsu HH, Yu JC et al (2010) Influence of age on PPV of sonographic BI-RADS Categories 3, 4, and 5. Ultraschall Med 32:8-13.
21. Moon HJ, Kim MJ, Kwak JY et al ( 2010) Probably benign breast lesions on ultrasonography: a retrospective review of ultrasonographic features and clinical factors affecting the BI-RADS categorization. Acta Radiol 51:375-382.
22. Moon HJ, Kim MJ, Kwak JY et al (2010) Malignant lesions initially categorized as probably benign breast lesions: retrospective review of ultrasonographic, clinical and pathologic characteristics. Ultrasound Med Biol 36:551-559.
23. Berg WA, Zhang Z, Lehrer D et al; ACRIN 6666 Investigators (2012) Detection of breast cancer with addition of annual screening ultrasound or a single screening MRI to mammography in women with elevated breast cancer risk. JAMA 07:1394-1404.
24. El Saghir NS, Anderson BO (2012) Breast cancer early detection and resources: where in the world do we start? The Breast 21:423-425.
25. Mundinger A (2006) Staging the breast and axilla. EJC Supplements 4:35-37.
26. Lehman CD, DeMartini W, Anderson BO et al (2009) Indications for breast MRI in the patient with newly diagnosed breast cancer. J Natl Compr Canc Netw 7:193-201.
27. Cho N, Moon WK, Cha JH et al (2009) Ultrasound-guided vacuum-assisted biopsy of microcalcifications detected at screening mammography. Acta Radiol 50:602-609.
28. Suh YJ, Kim MJ, Kim EK et al (2012) Comparison of the underestimation rate in cases with ductal carcinoma in situ at ultrasound-guided core biopsy: 14-gauge automated core-needle biopsy vs. 8- or 11-gauge vacuum-assisted biopsy. Br J Radiol 85:e349-356.
29. Barentsz MW, van Dalen T, Gobardhan PD et al (2012) Intraoperative ultrasound guidance for excision of non-palpable invasive breast cancer: a hospital-based series and an overview of the literature. Breast Cancer Res Treat 135:209-219.
30. Houssami N, Hayes DF (2009) Review of preoperative magnetic resonance imaging (MRI) in breast cancer: should MRI be performed on all women with newly diagnosed, early stage breast cancer? CA Cancer J Clin 59:290-302.
31. Turnbull L, Brown S, Harvey I et al (2010) Comparative effectiveness of MRI in breast cancer (COMICE) trial: a randomised controlled trial. Lancet 375:563-571.
32. Peters NH, van Esser S, van den Bosch MA et al (2011) Preoperative MRI and surgical management in patients with nonpalpable breast cancer: the MONET - randomised controlled trial. Eur J Cancer 47:879-886.
33. Tozaki M, Fukuma E (2011) Does power Doppler ultrasonography improve the BI-RADS category assessment and diagnostic accuracy of solid breast lesions? Acta Radiol 52:706-710.
34. Wang X, Xu P, Wang Y, Grant EG (2011) Contrast-enhanced ultrasonographic findings of different histopathologic types of breast cancer. Acta Radiol 52:248-255.
35. Sadigh G, Carlos RC, Neal CH, Dwamena BA (2012) Ultrasonographic differentiation of malignant from benign breast lesions: a meta-analytic comparison of elasticity and BIRADS scoring. Breast Cancer Res Treat 133:23-35.
36. Gong X, Xu Q, Xu Z et al (2011) Real-time elastography for the differentiation of benign and malignant breast lesions: a meta-analysis. Breast Cancer Res Treat 130:11-18.
37. Berg WA, Cosgrove DO, Doré CJ et al for the BE1 Investigators (2012) Shear-wave elastography improves the specificity of breast US: the multinational study of 939 masses. Radiology 262:435-449.
38. Evans A, Whelehan P, Thomson K (2012) Invasive breast cancer: relationship between shear-wave elastographic findings and histologic prognostic factors. Radiology 263:673-677.
39. Prosch H, Halbwachs C, Strobl C et al (2011) Automated breast ultrasound vs. handheld ultrasound: BI-RADS classification, duration of the examination and patient comfort. Ultraschall Med 32:504-510.
40. Giuliano V, Giuliano C (2012) Improved breast cancer detection in asymptomatic women using 3D-automated breast ultrasound in mammographically dense breasts. Clin Imaging [Epub ahead of print].
41. Choi YJ, Ko EY, Han BK et al (2009) High-resolution ultrasonographic features of axillary lymph node metastasis in patients with breast cancer. Breast 18:119-122.
42. Alvarez S, Añorbe E, Alcorta P et al (2006) Role of sonography in the diagnosis of axillary lymph node metastases in breast cancer: a systematic review. AJR Am J Roentgenol 186:1342-1348
43. Choi JS, Kim MJ, Moon HJ et al (2012) False negative results of preoperative axillary ultrasound in patients with invasive breast cancer: correlations with clinicopathologic findings. Ultrasound Med Biol 38:1881-1886.
44. Cody HS 3rd, Houssami N (2012) Axillary management in breast cancer: what's new for 2012? Breast 21:411-415.
45. Pan L, Han Y, Sun X et al (2010) FDG-PET and other imaging modalities for the evaluation of breast cancer recurrence and metastases: a meta-analysis. J Cancer Res Clin Oncol 136:1007-1022.
46. Britton P, Warwick J, Wallis MG et al (2012). Measuring the accuracy of diagnostic imaging in symptomatic breast patients: team and individual performance. Br J Radiol 85:415-22.

# Tomosynthesis: Should it Be Integrated into Screening and Clinical Routine Imaging?

Per Skaane

Oslo University Hospital Ullevaal, University of Oslo, Oslo, Norway

## Introduction

Digital breast tomosynthesis (DBT) is a new and promising technique for breast imaging based on a full-field digital mammography (FFDM) platform. It was more than 15 years ago that this modality was first presented as a promising technique for breast imaging, having the potential to improve specificity and early detection of breast cancer [1]. DBT has been investigated in several clinical settings during the last few years [2-4]. Some studies focused on the great potential that tomosynthesis might have in breast cancer screening.

Digital breast tomosynthesis has the potential to overcome some major limitations of conventional mammography, including false-positive interpretations caused by superimposed breast tissue and false-negative interpretations due to the poor sensitivity of conventional mammography in women with dense breasts [5]. The great advantage of DBT is the elimination of superimposed tissue and improved detection of lesions otherwise hidden by dense parenchyma, as well as improvement in lesion interpretation due to elimination of overlapping breast tissue. DBT images are obtained in the same standard projections [craniocaudal (CC) and mediolateral oblique (MLO)] as conventional screening mammography. For DBT acquisition, the X-ray tube moves through a proscribed arc, and several low-dose projection images are acquired [2]. The arc of movement and the number of exposures vary among equipment manufacturers. Tomosynthesis is often called 3D mammography, but it is important to keep in mind that DBT is only a quasi-3D examination due to the limited angle of scanning. Images are reconstructed into a stack of 1-mm slices. The reconstructed 1-mm slices may also be displayed as volume, consisting of several slices (slabs).

Different reconstruction methods are applied for tomosynthesis image reconstruction. The most commonly used algorithms include filtered backprojection and iterative reconstruction algorithms. Thus, tomosynthesis image quality is a complex issue and is determined by several interrelated factors. As expected, the amount of tomosynthesis data is much larger than for 2D images. A four-view DBT examination requires about 1 GB in storage space, and consequently, implementing DBT in a high-volume breast cancer screening program requires more Picture Archiving and Communication System (PACS) space. Data compression would partially solve this challenge.

There has been much debate as to whether tomosynthesis should or would replace 2D FFDM images, or whether DBT should provide a supplemental view to conventional imaging [6, 7]. From a theoretical point of view, one might think that 1-mm-thin slices through the breast would detect far most abnormalities. Experience so far, however, has been that several malignancies are quite obvious in one of the standard projections but hardly or not on the other one. Consequently, two projections seem to be superior to one-view imaging. Experience so far indicates that improved diagnostic performance is more substantial when 2D images are combined with tomosynthesis in both views [8].

The mean glandular dose for mammography and DBT depends on several factors, including thickness of the compressed breast, glandular fraction of breast tissue, and exposure parameters. In general, the glandular dose for a DBT projection is approximately the same as for a conventional FFDM image. One study reported a mean glandular dose of 1.70 mGy for FFDM compared with 1.74 mGy for tomosynthesis [9]. Consequently, the combined application of FFDM and DBT means a doubling of the radiation dose. Radiation dose has been of much concern, and radiation exposure is a critical issue if DBT is going to be implemented in breast cancer screening.

The potential of DBT to improve sensitivity and specificity is of great interest for breast cancer screening. Reduction in recall rate would be of most interest in the USA, which has higher recall rates than most European screening programs. In European mammography screening with low recall rates, implementation of DBT would only be justified if a significant improvement in the cancer detection rate can be achieved. The first publications from tomosynthesis in breast cancer screening are very promising, showing improved recall and cancer detection

*Diseases of the Abdomen and Pelvis 2014-2017*,
DOI: 10.1007/978-88-470-5659-6_43 

rates [3]. The very different study designs and techniques used may explain the great variation in results for DBT screening reported so far.

## Tomosynthesis in a Clinical Setting

### Tomosynthesis and Soft-Tissue Lesions

Mammographic identification and characterization of breast masses is often difficult in women with dense breast parenchyma. DBT reduces the obscuring effect of overlying and underlying breast tissue. Because overlapping tissue is eliminated, masses and their margins are frequently more clearly delineated. Margins of benign masses, including cysts and fibroadenomas, which might not appear sharp and distinct on conventional FFDM due to superimposition of surrounding breast tissue, often present as well-circumscribed masses with an obvious benign etiology on DBT.

Clinical studies indicate that DBT may replace additional view and cone-down views when assessing suspicious lesions demonstrated on conventional 2D mammograms [10]. Tomosynthesis can eliminate the need for spot compression, as the borders of masses are much better shown at DBT [11]. Of interest is that DBT also might have the potential to eliminate the need for supplemental ultrasonography (US) in a fraction of cases [5].

Preoperative imaging for assessing cancer size and extent include supplemental mammographic views as well as US and occasionally magnetic resonance imaging (MRI). Cancer conspicuity and visibility is superior on DBT compared with conventional FFDM [12]. Another study confirmed that tomosynthesis correlated better with the pathologic size of breast cancers, and consequently, staging was significantly more accurate with DBT than with FFDM [13]. Tomosynthesis is significantly superior to digital mammography for assessing breast cancer extent, especially for small tumors and lesions in dense breast parenchyma [14].

### Tomosynthesis and Microcalcifications

Initially, there was some concern regarding identification and characterization of small clusters of fine, punctate, microcalcifications due to the so-called thin-slice effect. Each slice 1-mm thick may include very few calcifications, so that the reader will not get the impression of a 3D cluster. The thin 1-mm slices in tomosynthesis could make the perception of small clusters with punctate microcalcifications more problematic, especially in women with dense breast parenchyma. The reconstructed 1-mm slices may be displayed as volume consisting of several slices (slabs), and this quasi-3D of grouping adjacent 1-mm slices into slabs of varying thickness, a kind of maximum intensity projection (MIP) technique, might overcome the perception challenge. However, studies are needed to evaluate whether such slabs offer any advantages regarding perception and characterization of microcalcifications.

Studies comparing the sharpness and contrast of calcifications seen on FFDM and tomosynthesis conclude that calcifications can be demonstrated with equal or even greater clarity on DBT than on conventional mammography [15]. One study reported that FFDM was slightly more sensitive than DBT for detecting calcifications, but the diagnostic performance as measured by the area under the curve (AUC) using the Breast Imaging Reporting and Data System (BI-RADS) categories was not significantly different [16]. Similar results were found in a study on lesions recalled for assessment following routine screening, in which the addition of DBT to FFDM did not show significant improvement for microcalcifications, which is in contrast to the improvement in diagnostic accuracy for soft-tissue lesions [17].

### Tomosynthesis and Workup of Screening-Detected Lesions

There is much interest in implementing DBT to assess suspicious abnormalities detected at screening mammography, as studies show that tomosynthesis may replace spot compression and magnification views for nonpalpable abnormalities. These studies conclude that DBT can be used as a valuable additional technique for assessing screening-detected abnormalities [9]. The significantly improved diagnostic accuracy for noncalcified lesions suggests that tomosynthesis may replace conventional supplemental imaging in such lesions [18].

Distortion detected at tomosynthesis can occasionally represent a great diagnostic challenge if an abnormality is not confirmed at conventional mammographic workup or US. MRI might be used as a problem solver, but even normal findings at dynamic contrast-enhanced MRI do not rule out malignancy. Tomosynthesis-guided biopsy represents a time-saving procedure for assessing lesions visible only on tomosynthesis.

## Tomosynthesis in Breast Cancer Screening

Mammography has a reduced sensitivity in women with dense breast parenchyma, and alternatives or supplemental techniques were a hot topic in recent years. Two modalities have been the focus of individualized or personalized screening: MRI and US. MRI has the highest sensitivity and has been implemented in screening programs for women at increased risk for breast cancer. High costs and limited availability of MRI are limiting factors for implementing this modality in high-volume screening programs for women at normal risk. US is well tolerated by patients and is highly available, but the two main limiting factors for implementation in screening are the time-consuming examination and interpretation time and the many false-positive findings and low positive predictive value (PPV) for US-detected lesions.

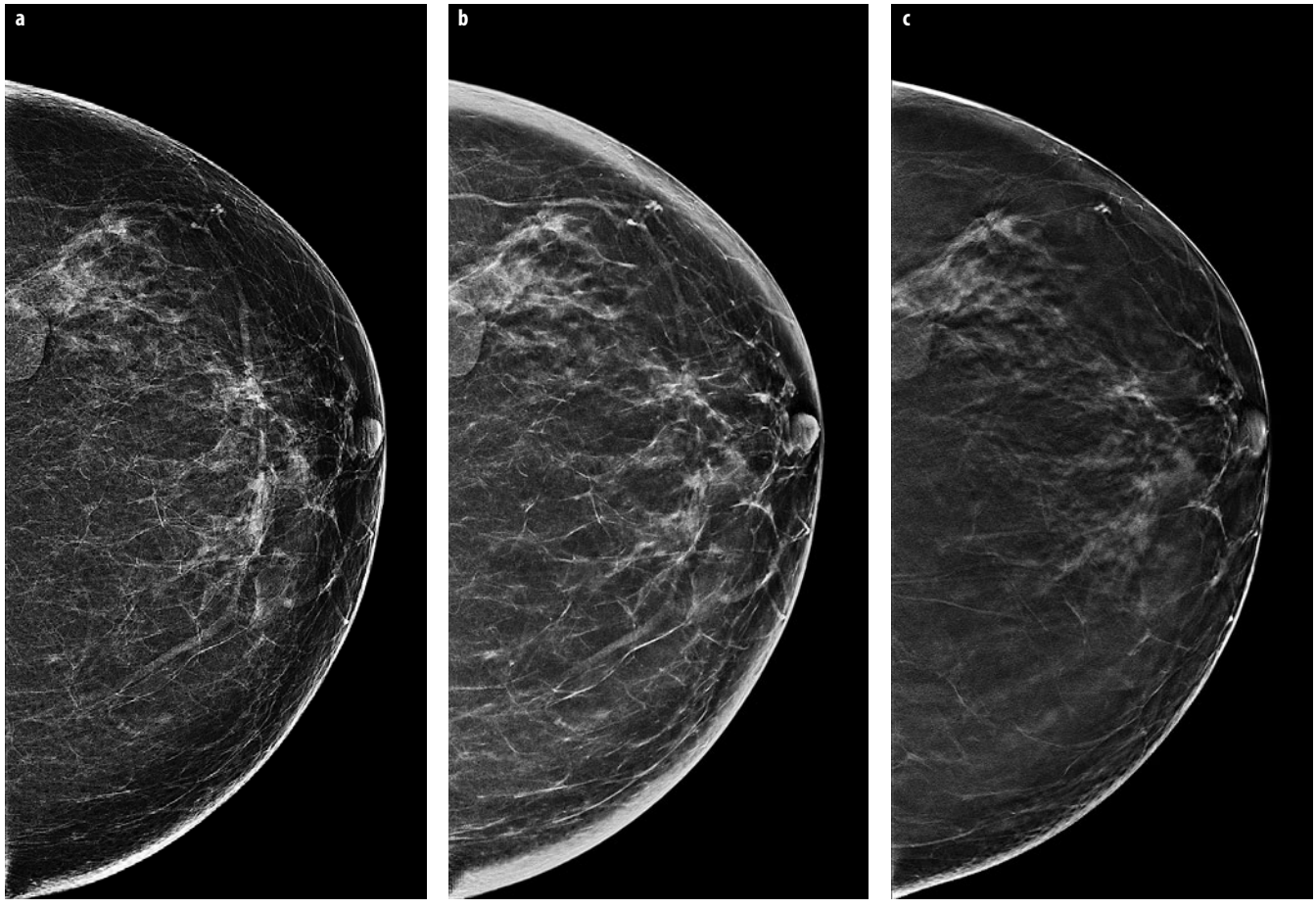


**Fig. 1 a-c.** Breast cancer screening: asymptomatic 60-year-old woman. A spiculated mass with microcalcifications is shown in the lateral part of the left breast on these craniocaudal (CC) images. **a** Conventional full-field digital mammography (FFDM). **b** Synthetic 2D (C-view). **c** Tomosynthesis (DBT). Microcalcifications are highlighted on the C-view, making the perception much easier, and spiculations are best seen on tomosynthesis. The combined synthetic 2D plus DBT show the cancer much better than conventional FFDM, with comparable radiation dose. Histology revealed invasive lobular carcinoma grade 3 with a diameter of 8 mm and pleomorphic lobular carcinoma in situ of 10 mm

The improved visibility of suspicious lesions with the potential for increased sensitivity and specificity and, consequently, for decreasing recall rates makes DBT very interesting for breast cancer screening [8, 12]. The potential for increased sensitivity with tomosynthesis seems to be especially applicable for cancers manifesting as spiculated masses and distortions [4]. It has been postulated that tomosynthesis might become the next gold standard for screening.

The consequence of combining two-view FFDM plus two-view DBT in a screening setting would mean doubling the radiation dose, which is not acceptable. A solution to this problem is synthetic 2D images reconstructed from the 3D dataset of DBT [19]. The synthesized images are created by summing and filtering the stack of reconstructed DBT slices. Thus, an image comparable with a maximum intensity projection (MIP) image is created. Using synthetic 2D instead of conventional 2D images allows combined 2D plus 3D images to be implemented with approximately the same radiation dose as for conventional FFDM. The perception of fine, small, punctate microcalcifications is significantly improved by the highlighting seen on such synthetic 2D images (Fig. 1).

So far, few studies have reported results from implementing tomosynthesis in breast cancer screening. These results are very promising and confirm that DBT may become the next gold standard for breast cancer screening. A brief overview of these DBT screening studies are summarized in Table 1.

The Italian Screening with Tomosynthesis OR Standard Mammography (STORM) trial recruited women ≥48 years attending the population-based screening program in Trento and Verona. Screen-reading was carried out in two sequential phases: first 2D only, and soon afterward, integrated 2D and DBT [20]. A remarkable increase in the cancer detection rate was reported: 5.3 per 1,000 women for 2D only compared with 8.1 per 1,000 screens for integrated 2D and 3D [20]. Stratified analysis revealed that integrated 2D plus 3D mammography was associated with an increased cancer detection rate in both younger and elderly age groups and both breast-density groups. Inte-

**Table 1.** Studies comparing conventional full-field digital mammography (FFDM) (2D) and digital breast tomosynthesis (DBT) (3D) in breast cancer screening

| Study | Population: (n) | Study design | Examination mode | Reading mode | Cancer: (n) 2D | Cancer: (n) 2D+3D | Cancer: (n/1,000) 2D | Cancer: (n/1,000) 2D+3D | Cancer: rel. increase (%) |
|---|---|---|---|---|---|---|---|---|---|
| Trento/Verona [20] | 7,292 | Prospective; paired | 2D: 2-view<br>3D: 2-view | Double; sequential | 39 | 59 | 5.3 | 8.1 | 51.0 |
| Oslo [21] | 12,631 | Prospective; paired | 2D: 2-view<br>3D: 2-view | Double; independent | 90 | 119 | 7.1 | 9.4 | 32.0 |
| TOPS, Houston [23] | 2D: 13,856<br>3D: 9,499 | Retrospective; non-paired | 2D: 2-view<br>3D: 2-view | Single; independent | 56 | 51 | 4.0 | 5.4 | 32.0 |
| Yale, New Haven [24] | 2D: 7,058<br>3D: 6,100 | Retrospective; non-paired | 2D: 2-view<br>3D: 2-view | Single; independent | 37 | 35 | 5.2 | 5.7 | 9.5 |
| Malmø [25] | 5,700 | Prospective; paired | 2D: 2-view<br>3D: 1-view | Double; sequential | – | – | 4.7 | 6.8 | 45.0 |

grated 2D and 3D may have reduced false-positive callbacks by approximately 17% [20].

The Oslo Tomosynthesis Screening Trial (OTST) is a large, prospective, single-institution study that is part of the population-based Norwegian Breast Cancer Screening Program (NBCSP). This program invites women aged 50-69 years to biennial two-view mammography. The OTST included independent double reading of 2D FFDM as well as independent double reading of combined 2D and DBT [21]. Preliminary results showed a significantly improved sensitivity, with a relative increase in cancer detection of about 30% [22]: the detection rate for FFDM alone was 6.1 cancers per 1,000 examinations compared with 8.0 cancers per 1,000 examinations for combined FFDM plus tomosynthesis [21]. The additional cancers detected using combined 2D plus 3D reading mode were invasive cancers mainly presenting as distortion and spiculated masses, whereas ductal carcinoma in situ (DCIS) detection was the same using the two reading modalities [21].

A USA observational study from a multisite community-based breast center compared performance measures at screening mammography without and with the use of digital breast tomosynthesis [23]. The cancer detection rate increased from 4.0 to 5.4 per 1,000 screening examinations using combined 2D plus 3D mode (Table 1). Interestingly, the detection of invasive cancers increased from 2.8 to 4.3 per 1,000 examinations [23]. Furthermore, a significant reduction in recall rates from 8.7% to 5.5% was found [23].

A retrospective USA study including four sites compared FFDM at sites without DBT and combined FFDM plus tomosynthesis at sites having DBT [24]. This study also applied a single reading, as is usually done in the USA. The overall recall rate revealed a significantly lower rate of 8.4% for combined 2D plus 3D mode compared with conventional FFDM alone [24]. The cancer detection rate increased from 5.2 per 1,000 patients for FFDM alone to 5.7 per 1,000 examinations for the tomosynthesis group, but this 9.5% increase in cancer detection was nonsignificant (Table 1).

The Malmø Breast Tomosynthesis Screening Trial (MBTST) [25] is a large, ongoing, single-institution trial. The estimated enrollment is 15,000 women aged 40-74 years invited to its population-based mammography screening program (Table 1). So far, only preliminary results have been presented as oral presentations at international radiological congresses.

Tomosynthesis has the potential to overcome the limitations of MRI and US in high-volume breast cancer screening. MRI has the highest sensitivity, but availability and high costs restricts its use to screening of high-risk women. US is available and easily tolerated by patients, but examinations are time consuming and consequently would represent a high-cost modality in population-based screening programs. Acquisition time for DBT is only some few seconds longer than for conventional FFDM [16, 21]. On the other hand, interpretation time is regarded as a challenge for implementing tomosynthesis in high-volume screening programs [2]. Average reading time for 2D plus 3D combo mode is reported to be 77 s, compared with 33 s for 2D only [26]. Preliminary results from the population-based OTST reported average interpretation times of 89 s and 48 s per examination for combo mode and 2D only, respectively [21]. Thus, reading time for combined two-view 2D plus DBT is approximately double that for FFDM only. This increased reading time must be considered with respect to the significantly higher cancer detection rate for the combined use of FFDM plus tomosynthesis.

## Conclusion

Tomosynthesis has the potential in the clinical setting to replace conventional supplemental mammograms in the workup of screening-detected abnormalities and to improve the assessment of cancer size and multifocality preoperatively. In the screening setting, the combined use of conventional or synthetic 2D imaging with tomosynthesis

has the potential to improve the cancer detection rate as well as reduce the recall rate in breast cancer screening. Future implementation of tomosynthesis-guided biopsy will make the diagnostic workup of lesions seen only on DBT faster and easier [27].

## References


1. Niklason LT, Christian BT, Niklason LE et al (1997) Digital tomosynthesis in breast imaging. Radiology 205:399-406.
2. Baker JA, Lo JY (2011) Breast tomosynthesis: state-of-the-art and review of the literature. Acad Radiol 18:1298-1310.
3. Houssami N, Skaane P (2013) Overview of the evidence on digital breast tomosynthesis in breast cancer screening. The Breast 22:101-108.
4. Skaane P, Gullien R, Bjørndal H et al (2012) Digital breast tomosynthesis (DBT): initial experience in a clinical setting. Acta Radiol 53:524-529.
5. Hakim CM, Chough DM, Ganott MA et al (2010) Digital breast tomosynthesis in the diagnostic environment: A subjective side-by-side review. AJR Am J Roentgenol 195:172-176.
6. Gennaro G, Hendrick RE, Ruppel P et al (2013) Performance comparison of single-view digital breast tomosynthesis plus single-view digital mammography with two-view digital mammography. Eur Radiol 23:664-672.
7. Svahn T, Andersson I, Chakraborty D et al (2010) The diagnostic accuracy of dual-view digital mammography, single-view breast tomosynthesis, and a dual-view combination of breast tomosynthesis and digital mammography in a free-response observer performance study. Radiat Prot Dosim 139:113-117.
8. Rafferty EA, Park JM, Philpotts LE et al (2013) Assessing radiologist performance using combined digital mammography and breast tomosynthesis compared with digital mammography alone: results of a multicenter, multireader trial. Radiology 266:104-113.
9. Teertstra HJ, Loo CE, van den Bosch MAAJ et al (2010) Breast tomosynthesis in clinical practice: initial results. Eur Radiol 20:16-24.
10. Noroozian M, Hadjiiski L, Rahnama-Moghadam S et al (2012) Digital breast tomosynthesis is comparable to mammographic spot views for mass characterization. Radiology 262:61-68.
11. Brandt KR, Craig DA, Hoskins TL et al (2013) Can digital breast tomosynthesis replace conventional diagnostic mammography views for screening recalls without calcifications? A comparison study in a simulated clinical setting. AJR Am J Roentgenol 200:291-298.
12. Andersson I, Ikeda DM, Zackrisson S et al (2008) Breast tomosynthesis and digital mammography: a comparison of breast cancer visibility and BI-RADS classification in a population of cancers with subtle mammographic findings. Eur Radiol 18:2817-2825.
13. Fornvik D, Zackrisson S, Ljungberg O et al (2010) Breast tomosynthesis: accuracy of tumor measurement compared with digital mammography and ultrasonography. Acta Radiol 51:240-247.
14. Mun HS, Kim HH, Shin HJ et al (2013) Assessment of extent of breast cancer: comparison between digital breast tomosynthesis and full-field digital mammography. Clin Radiol 68:1254-1259.
15. Kopans D, Gavenonis S, Halpern E et al (2011) Calcifications in the breast and digital breast tomosynthesis. Breast J 17:638-644.
16. Spangler ML, Zuley ML, Sumkin JH et al (2011) Detection and classification of calcifications on digital breast tomosynthesis and 2D digital mammography: a comparison. AJR Am J Roentgenol 196:320-324.
17. Michell MJ, Iqbal A, Wasan RK et al (2012) A comparison of the accuracy of film-screen mammography, full-field digital mammography, and digital breast tomosynthesis. Clin Radiol 67:976-981.
18. Zuley ML, Bandos AI, Ganott MA et al (2013) Digital breast tomosynthesis versus supplemental diagnostic mammographic views for evaluation of noncalcified breast lesions. Radiology 266:89-95.
19. Gur D, Zuley ML, Anello MI et al (2012) Dose reduction in digital breast tomosynthesis (DBT) screening using synthetically reconstructed projection images: an observer performance study. Acad Radiol 19:166-171.
20. Ciatto S, Houssami N, Bernardi D et al (2013) Integration of 3D digital mammography with tomosynthesis for population breast-cancer screening (STORM): a prospective comparison study. Lancet Oncol 14:583-589.
21. Skaane P, Bandos AI, Gullien R et al (2013) Prospective trial comparing full-field digital mammography (FFDM) versus combined FFDM and tomosynthesis in a population-based screening programme using independent double reading with arbitration. Eur Radiol 23:2061-2071.
22. Skaane P, Bandos AI, Gullien R et al (2013) Comparison of digital mammography alone and digital mammography plus tomosynthesis in a population-based screening program. Radiology 267:47-56.
23. Rose SL, Tidwell AL, Bujnoch LJ et al (2013) Implementation of breast tomosynthesis in a routine screening practice: an observational study. AJR Am J Roentgenol 200:1401-1408.
24. Haas BM, Kalra V, Geisel J et al (2013) Comparison of tomosynthesis plus digital mammography and digital mammography alone for breast cancer screening. Radiology 269:694-700.
25. Zackrisson S; ECR Vienna (2013) Interim analysis; Malmø Breast Tomosynthesis Screening Trial.
26. Bernardi D, Ciatto S, Pellegrini M et al (2012) Application of breast tomosynthesis in screening: incremental effect on mammography acquisition and reading time. Br J Radiol 85:e1174-1178.
27. Dershaw DD (2013) Large core needle biopsy with tomosynthesis guidance: Another development in breast imaging technology. Breast J 19:1-3.